
Applied Superconductivity:

Josephson Effect and Superconducting Electronics

**Manuscript to the Lectures during WS 2003/2004, WS 2005/2006, WS 2006/2007,
WS 2007/2008, WS 2008/2009, and WS 2009/2010**

Prof. Dr. Rudolf Gross

and

Dr. Achim Marx

Walther-Meißner-Institut

Bayerische Akademie der Wissenschaften

and

Lehrstuhl für Technische Physik (E23)

Technische Universität München

Walther-Meißner-Strasse 8

D-85748 Garching

Rudolf.Gross@wmi.badw.de

Contents

Preface	xxi
I Foundations of the Josephson Effect	1
1 Macroscopic Quantum Phenomena	3
1.1 The Macroscopic Quantum Model	3
1.1.1 Coherent Phenomena in Superconductivity	3
1.1.2 Macroscopic Quantum Currents in Superconductors	12
1.1.3 The London Equations	18
1.2 Flux Quantization	24
1.2.1 Flux and Fluxoid Quantization	26
1.2.2 Experimental Proof of Flux Quantization	28
1.2.3 Additional Topic: Rotating Superconductor	30
1.3 Josephson Effect	32
1.3.1 The Josephson Equations	33
1.3.2 Josephson Tunneling	37
2 JJs: The Zero Voltage State	43
2.1 Basic Properties of Lumped Josephson Junctions	44
2.1.1 The Lumped Josephson Junction	44
2.1.2 The Josephson Coupling Energy	45
2.1.3 The Superconducting State	47
2.1.4 The Josephson Inductance	49
2.1.5 Mechanical Analogs	49
2.2 Short Josephson Junctions	50
2.2.1 Quantum Interference Effects – Short Josephson Junction in an Applied Magnetic Field	50

2.2.2	The Fraunhofer Diffraction Pattern	54
2.2.3	Determination of the Maximum Josephson Current Density	58
2.2.4	Additional Topic: Direct Imaging of the Supercurrent Distribution	62
2.2.5	Additional Topic: Short Josephson Junctions: Energy Considerations	63
2.2.6	The Motion of Josephson Vortices	65
2.3	Long Josephson Junctions	68
2.3.1	The Stationary Sine-Gordon Equation	68
2.3.2	The Josephson Vortex	70
2.3.3	Junction Types and Boundary Conditions	73
2.3.4	Additional Topic: Josephson Current Density Distribution and Maximum Josephson Current	79
2.3.5	The Pendulum Analog	84
3	JJs: The Voltage State	89
3.1	The Basic Equation of the Lumped Josephson Junction	90
3.1.1	The Normal Current: Junction Resistance	90
3.1.2	The Displacement Current: Junction Capacitance	92
3.1.3	Characteristic Times and Frequencies	93
3.1.4	The Fluctuation Current	94
3.1.5	The Basic Junction Equation	96
3.2	The Resistively and Capacitively Shunted Junction Model	97
3.2.1	Underdamped and Overdamped Josephson Junctions	100
3.3	Response to Driving Sources	102
3.3.1	Response to a dc Current Source	102
3.3.2	Response to a dc Voltage Source	107
3.3.3	Response to ac Driving Sources	107
3.3.4	Photon-Assisted Tunneling	112
3.4	Additional Topic: Effect of Thermal Fluctuations	115
3.4.1	Underdamped Junctions: Reduction of I_c by Premature Switching	117
3.4.2	Overdamped Junctions: The Ambegaokar-Halperin Theory	118
3.5	Secondary Quantum Macroscopic Effects	122
3.5.1	Quantum Consequences of the Small Junction Capacitance	122

3.5.2	Limiting Cases: The Phase and Charge Regime	125
3.5.3	Coulomb and Flux Blockade	128
3.5.4	Coherent Charge and Phase States	130
3.5.5	Quantum Fluctuations	132
3.5.6	Macroscopic Quantum Tunneling	133
3.6	Voltage State of Extended Josephson Junctions	139
3.6.1	Negligible Screening Effects	139
3.6.2	The Time Dependent Sine-Gordon Equation	140
3.6.3	Solutions of the Time Dependent Sine-Gordon Equation	141
3.6.4	Additional Topic: Resonance Phenomena	144
II	Applications of the Josephson Effect	153
4	SQUIDs	157
4.1	The dc-SQUID	159
4.1.1	The Zero Voltage State	159
4.1.2	The Voltage State	164
4.1.3	Operation and Performance of dc-SQUIDs	168
4.1.4	Practical dc-SQUIDs	172
4.1.5	Read-Out Schemes	176
4.2	Additional Topic: The rf-SQUID	180
4.2.1	The Zero Voltage State	180
4.2.2	Operation and Performance of rf-SQUIDs	182
4.2.3	Practical rf-SQUIDs	186
4.3	Additional Topic: Other SQUID Configurations	188
4.3.1	The DROS	188
4.3.2	The SQIF	189
4.3.3	Cartwheel SQUID	189
4.4	Instruments Based on SQUIDs	191
4.4.1	Magnetometers	192
4.4.2	Gradiometers	194
4.4.3	Susceptometers	196

4.4.4	Voltmeters	197
4.4.5	Radiofrequency Amplifiers	198
4.5	Applications of SQUIDs	200
4.5.1	Biomagnetism	200
4.5.2	Nondestructive Evaluation	204
4.5.3	SQUID Microscopy	206
4.5.4	Gravity Wave Antennas and Gravity Gradiometers	208
4.5.5	Geophysics	210
5	Digital Electronics	215
5.1	Superconductivity and Digital Electronics	216
5.1.1	Historical development	217
5.1.2	Advantages and Disadvantages of Josephson Switching Devices	219
5.2	Voltage State Josephson Logic	222
5.2.1	Operation Principle and Switching Times	222
5.2.2	Power Dissipation	225
5.2.3	Switching Dynamics, Global Clock and Punchthrough	226
5.2.4	Josephson Logic Gates	228
5.2.5	Memory Cells	234
5.2.6	Microprocessors	236
5.2.7	Problems of Josephson Logic Gates	237
5.3	RSFQ Logic	239
5.3.1	Basic Components of RSFQ Circuits	241
5.3.2	Information in RSFQ Circuits	246
5.3.3	Basic Logic Gates	247
5.3.4	Timing and Power Supply	249
5.3.5	Maximum Speed	249
5.3.6	Power Dissipation	250
5.3.7	Prospects of RSFQ	250
5.3.8	Fabrication Technology	253
5.3.9	RSFQ Roadmap	254
5.4	Analog-to-Digital Converters	255
5.4.1	Additional Topic: Foundations of ADCs	256
5.4.2	The Comparator	261
5.4.3	The Aperture Time	263
5.4.4	Different Types of ADCs	264

6 The Josephson Voltage Standard	269
6.1 Voltage Standards	270
6.1.1 Standard Cells and Electrical Standards	270
6.1.2 Quantum Standards for Electrical Units	271
6.2 The Josephson Voltage Standard	274
6.2.1 Underlying Physics	274
6.2.2 Development of the Josephson Voltage Standard	274
6.2.3 Junction and Circuit Parameters for Series Arrays	279
6.3 Programmable Josephson Voltage Standard	281
6.3.1 Pulse Driven Josephson Arrays	283
7 Superconducting Photon and Particle Detectors	285
7.1 Superconducting Microwave Detectors: Heterodyne Receivers	286
7.1.1 Noise Equivalent Power and Noise Temperature	286
7.1.2 Operation Principle of Mixers	287
7.1.3 Noise Temperature of Heterodyne Receivers	290
7.1.4 SIS Quasiparticle Mixers	292
7.1.5 Josephson Mixers	296
7.2 Superconducting Microwave Detectors: Direct Detectors	297
7.2.1 NEP of Direct Detectors	298
7.3 Thermal Detectors	300
7.3.1 Principle of Thermal Detection	300
7.3.2 Bolometers	302
7.3.3 Antenna-Coupled Microbolometers	307
7.4 Superconducting Particle and Single Photon Detectors	314
7.4.1 Thermal Photon and Particle Detectors: Microcalorimeters	314
7.4.2 Superconducting Tunnel Junction Photon and Particle Detectors	318
7.5 Other Detectors	328
8 Microwave Applications	329
8.1 High Frequency Properties of Superconductors	330
8.1.1 The Two-Fluid Model	330
8.1.2 The Surface Impedance	333
8.2 Superconducting Resonators and Filters	336
8.3 Superconducting Microwave Sources	337

9 Superconducting Quantum Bits	339
9.1 Quantum Bits and Quantum Computers	341
9.1.1 Quantum Bits	341
9.1.2 Quantum Computing	343
9.1.3 Quantum Error Correction	346
9.1.4 What are the Problems?	348
9.2 Implementation of Quantum Bits	349
9.3 Why Superconducting Qubits	352
9.3.1 Superconducting Island with Leads	352
 III Anhang	 355
 A The Josephson Equations	 357
 B Imaging of the Maximum Josephson Current Density	 361
 C Numerical Iteration Method for the Calculation of the Josephson Current Distribution	 363
 D Photon Noise	 365
I Power of Blackbody Radiation	365
II Noise Equivalent Power	367
 E Qubits	 369
I What is a quantum bit ?	369
I.1 Single-Qubit Systems	369
I.2 The spin-1/2 system	371
I.3 Two-Qubit Systems	372
II Entanglement	373
III Qubit Operations	375
III.1 Unitarity	375
III.2 Single Qubit Operations	375
III.3 Two Qubit Operations	376
IV Quantum Logic Gates	377
IV.1 Single-Bit Gates	377
IV.2 Two Bit Gates	379
V The No-Cloning Theorem	384
VI Quantum Complexity	385
VII The Density Matrix Representation	385

F Two-Level Systems	389
I Introduction to the Problem	389
I.1 Relation to Spin-1/2 Systems	390
II Static Properties of Two-Level Systems	390
II.1 Eigenstates and Eigenvalues	390
II.2 Interpretation	391
II.3 Quantum Resonance	394
III Dynamic Properties of Two-Level Systems	395
III.1 Time Evolution of the State Vector	395
III.2 The Rabi Formula	395
G The Spin 1/2 System	399
I Experimental Demonstration of Angular Momentum Quantization	399
II Theoretical Description	401
II.1 The Spin Space	401
III Evolution of a Spin 1/2 Particle in a Homogeneous Magnetic Field	402
IV Spin 1/2 Particle in a Rotating Magnetic Field	404
IV.1 Classical Treatment	404
IV.2 Quantum Mechanical Treatment	406
IV.3 Rabi's Formula	407
H Literature	409
I Foundations of Superconductivity	409
I.1 Introduction to Superconductivity	409
I.2 Early Work on Superconductivity and Superfluidity	410
I.3 History of Superconductivity	410
I.4 Weak Superconductivity, Josephson Effect, Flux Structures	410
II Applications of Superconductivity	411
II.1 Electronics, Sensors, Microwave Devices	411
II.2 Power Applications, Magnets, Transportation	412
II.3 Superconducting Materials	412
I SI-Einheiten	413
I Geschichte des SI Systems	413
II Die SI Basiseinheiten	415
III Einige von den SI Einheiten abgeleitete Einheiten	416
IV Vorsätze	418
V Abgeleitete Einheiten und Umrechnungsfaktoren	419

J Physikalische Konstanten**425**

List of Figures

1.1	Meissner-Effect	19
1.2	Current transport and decay of a supercurrent in the Fermi sphere picture	20
1.3	Stationary Quantum States	24
1.4	Flux Quantization in Superconductors	25
1.5	Flux Quantization in a Superconducting Cylinder	27
1.6	Experiment by Doll and Naebauer	29
1.7	Experimental Proof of Flux Quantization	29
1.8	Rotating superconducting cylinder	31
1.9	The Josephson Effect in weakly coupled superconductors	32
1.10	Variation of n_s^* and γ across a Josephson junction	35
1.11	Schematic View of a Josephson Junction	36
1.12	Josephson Tunneling	39
2.1	Lumped Josephson Junction	45
2.2	Coupling Energy and Josephson Current	46
2.3	The Tilted Washboard Potential	48
2.4	Extended Josephson Junction	51
2.5	Magnetic Field Dependence of the Maximum Josephson Current	55
2.6	Josephson Current Distribution in a Small Josephson Junction for Various Applied Magnetic Fields	56
2.7	Spatial Interference of Macroscopic Wave Funktions	57
2.8	The Josephson Vortex	57
2.9	Gaussian Shaped Josephson Junction	59
2.10	Comparison between Measurement of Maximum Josephson Current and Optical Diffraction Experiment	60
2.11	Supercurrent Auto-correlation Function	61
2.12	Magnetic Field Dependence of the Maximum Josephson Current of a YBCO-GBJ	63

2.13 Motion of Josephson Vortices	66
2.14 Magnetic Flux and Current Density Distribution for a Josephson Vortex	70
2.15 Classification of Junction Types: Overlap, Inline and Grain Boundary Junction	74
2.16 Geometry of the Asymmetric Inline Junction	77
2.17 Geometry of Mixed Overlap and Inline Junctions	78
2.18 The Josephson Current Distribution of a Long Inline Junction	80
2.19 The Maximum Josephson Current as a Function of the Junction Length	81
2.20 Magnetic Field Dependence of the Maximum Josephson Current and the Josephson Current Density Distribution in an Overlap Junction	83
2.21 The Maximum Josephson Current as a Function of the Applied Field for Overlap and Inline Junctions	84
 3.1 Current-Voltage Characteristic of a Josephson tunnel junction	91
3.2 Equivalent circuit for a Josephson junction including the normal, displacement and fluctuation current	92
3.3 Equivalent circuit of the Resistively Shunted Junction Model	97
3.4 The Motion of a Particle in the Tilt Washboard Potential	98
3.5 Pendulum analogue of a Josephson junction	99
3.6 The IVCs for Underdamped and Overdamped Josephson Junctions	101
3.7 The time variation of the junction voltage and the Josephson current	103
3.8 The RSJ model current-voltage characteristics	105
3.9 The RCSJ Model IVC at Intermediate Damping	107
3.10 The RCJ Model Circuit for an Applied dc and ac Voltage Source	108
3.11 Overdamped Josephson Junction driven by a dc and ac Voltage Source	110
3.12 Overdamped Josephson junction driven by a dc and ac Current Source	111
3.13 Shapiro steps for under- and overdamped Josephson junction	112
3.14 Photon assisted tunneling	113
3.15 Photon assisted tunneling in SIS Josephson junction	113
3.16 Thermally Activated Phase Slippage	116
3.17 Temperature Dependence of the Thermally Activated Junction Resistance	119
3.18 RSJ Model Current-Voltage Characteristics Including Thermally Activated Phase Slippage	120
3.19 Variation of the Josephson Coupling Energy and the Charging Energy with the Junction Area	124
3.20 Energy diagrams of an isolated Josephson junction	127
3.21 The Coulomb Blockade	128

3.22 The Phase Blockade	129
3.23 The Cooper pair box	131
3.24 Double well potential for the generation of phase superposition states	132
3.25 Macroscopic Quantum Tunneling	134
3.26 Macroscopic Quantum Tunneling at Large Damping	138
3.27 Mechanical analogue for phase dynamics of a long Josephson junction	141
3.28 The Current Voltage Characteristic of an Underdamped Long Josephson Junction	145
3.29 Zero field steps in IVCs of an annular Josephson junction	147
4.1 The dc-SQUID	160
4.2 Maximum Supercurrent versus Applied Magnetic Flux for a dc-SQUID at Weak Screening	162
4.3 Total Flux versus Applied Magnetic Flux for a dc SQUID at $\beta_L > 1$	163
4.4 Current-voltage Characteristics of a dc-SQUID at Negligible Screening	165
4.5 The pendulum analogue of a dc SQUID	167
4.6 Principle of Operation of a dc-SQUID	169
4.7 Energy Resolution of dc-SQUIDs	172
4.8 The Practical dc-SQUID	173
4.9 Geometries for thin film SQUID washers	174
4.10 Flux focusing effect in a $\text{YBa}_2\text{Cu}_3\text{O}_{7-\delta}$ washer	175
4.11 The Washer dc-SQUID	176
4.12 The Flux Modulation Scheme for a dc-SQUID	177
4.13 The Modulation and Feedback Circuit of a dc-SQUID	178
4.14 The rf-SQUID	180
4.15 Total flux versus applied flux for a rf-SQUID	182
4.16 Operation of rf-SQUIDS	183
4.17 Tank voltage versus rf-current for a rf-SQUID	184
4.18 High T_c rf-SQUID	187
4.19 The double relaxation oscillation SQUID (DROS)	188
4.20 The Superconducting Quantum Interference Filter (SQIF)	190
4.21 Input Antenna for SQUIDS	191
4.22 Various types of thin film SQUID magnetometers	193
4.23 Magnetic noise signals	194
4.24 Magnetically shielded room	195
4.25 Various gradiometers configurations	196

4.26 Miniature SQUID Susceptometer	197
4.27 SQUID Radio-frequency Amplifier	198
4.28 Multichannel SQUID Systems	201
4.29 Magnetocardiography	203
4.30 Magnetic field distribution during R peak	204
4.31 SQUID based nondestructive evaluation	205
4.32 Scanning SQUID microscopy	207
4.33 Scanning SQUID microscopy images	208
4.34 Gravity wave antenna	209
4.35 Gravity gradiometer	210
 5.1 Cryotron	217
5.2 Josephson Cryotron	218
5.3 Device performance of Josephson devices	220
5.4 Principle of operation of a Josephson switching device	222
5.5 Output current of a Josephson switching device	224
5.6 Threshold characteristics for a magnetically and directly coupled gate	229
5.7 Three-junction interferometer gate	230
5.8 Current injection device	230
5.9 Josephson Atto Weber Switch (JAWS)	231
5.10 Direct coupled logic (DCL) gate	231
5.11 Resistor coupled logic (RCL) gate	232
5.12 4 junction logic (4JL) gate	232
5.13 Non-destructive readout memory cell	234
5.14 Destructive read-out memory cell	235
5.15 4 bit Josephson microprocessor	237
5.16 Josephson microprocessor	238
5.17 Comparison of latching and non-latching Josephson logic	240
5.18 Generation of SFQ Pulses	242
5.19 dc to SFQ Converter	243
5.20 Basic Elements of RSFQ Circuits	244
5.21 RSFQ memory cell	245
5.22 RSFQ logic	246
5.23 RSFQ OR and AND Gate	247

5.24 RSFQ NOT Gate	248
5.25 RSFQ Shift Register	249
5.26 RSFQ Microprocessor	253
5.27 RSFQ roadmap	254
5.28 Principle of operation of an analog-to-digital converter	256
5.29 Analog-to-Digital Conversion	257
5.30 Semiconductor and Superconductor Comparators	262
5.31 Incremental Quantizer	263
5.32 Flash-type ADC	265
5.33 Counting-type ADC	266
6.1 Weston cell	271
6.2 The metrological triangle for the electrical units	273
6.3 IVC of an underdamped Josephson junction under microwave irradiation	275
6.4 International voltage comparison between 1920 and 2000	276
6.5 One-Volt Josephson junction array	277
6.6 Josephson series array embedded into microwave stripline	278
6.7 Microwave design of Josephson voltage standards	279
6.8 Adjustment of Shapiro steps for a series array Josephson voltage standard	281
6.9 IVC of overdamped Josephson junction with microwave irradiation	282
6.10 Programmable Josephson voltage standard	283
7.1 Block diagram of a heterodyne receiver	288
7.2 Ideal mixer as a switch	288
7.3 Current response of a heterodyne mixer	289
7.4 IVCs and IF output power of SIS mixer	290
7.5 Optimum noise temperature of a SIS quasiparticle mixer	293
7.6 Measured DSB noise temperature of a SIS quasiparticle mixers	294
7.7 High frequency coupling schemes for SIS mixers	295
7.8 Principle of thermal detectors	301
7.9 Operation principle of superconducting transition edge bolometer	302
7.10 Sketch of a HTS bolometer	305
7.11 Specific detectivity of various bolometers	305
7.12 Relaxation processes in a superconductor after energy absorption	307
7.13 Antenna-coupled microbolometer	308

7.14 Schematic illustration of the hot electron bolometer mixer	309
7.15 Hot electron bolometer mixers with different antenna structures	311
7.16 Transition-edge sensors	315
7.17 Transition-edge sensors	317
7.18 Functional principle of a superconducting tunnel junction detector	319
7.19 Circuit diagram of a superconducting tunnel junction detector	319
7.20 Energy resolving power of STJDS	321
7.21 Quasiparticle tunneling in SIS junctions	323
7.22 Quasiparticle trapping in STJDS	326
7.23 STJDS employing lateral quasiparticle trapping	326
7.24 Superconducting tunnel junction x-ray detector	327
 8.1 Equivalent circuit for the two-fluid model	332
8.2 Characteristic frequency regimes for a superconductor	332
8.3 Surface resistance of Nb and Cu	335
 9.1 Konrad Zuse 1945	341
9.2 Representation of a Qubit State as a Vector on the Bloch Sphere	342
9.3 Operational Scheme of a Quantum Computer	344
9.4 Quantum Computing: What's it good for?	345
9.5 Shor, Feynman, Bennett and Deutsch	346
9.6 Qubit Realization by Quantum Mechanical Two level System	349
9.7 Use of Superconductors for Qubits	352
9.8 Superconducting Island with Leads	354
 E.1 The Bloch Sphere S^2	370
E.2 The Spin-1/2 System	371
E.3 Entanglement – an artist's view.	373
E.4 Classical Single-Bit Gate	377
E.5 Quantum NOT Gate	378
E.6 Classical Two Bit Gate	380
E.7 Reversible and Irreversible Logic	380
E.8 Reversible Classical Logic	381
E.9 Reversible XOR (CNOT) and SWAP Gate	382
E.10 The Controlled U Gate	382

E.11 Density Matrix for Pure Single Qubit States	386
E.12 Density Matrix for a Coherent Superposition of Single Qubit States	387
F.1 Energy Levels of a Two-Level System	392
F.2 The Benzene Molecule	394
F.3 Graphical Representation of the Rabi Formula	396
G.1 The Larmor Precession	400
G.2 The Rotating Reference Frame	404
G.3 The Effective Magnetic Field in the Rotating Reference Frame	405
G.4 Rabi's Formula for a Spin 1/2 System	408

List of Tables

5.1	Switching delay and power dissipation for various types of logic gates.	233
5.2	Josephson 4 kbit RAM characteristics (organization: 4096 word \times 1 bit, NEC).	236
5.3	Performance of various logic gates	237
5.4	Possible applications of superconductor digital circuits (source: SCENET 2001).	251
5.5	Performance of various RSFQ based circuits.	252
7.1	Characteristic materials properties of some superconductors	325
8.1	Important high-frequency characteristic of superconducting and normal conducting . . .	334
E.1	Successive measurements on a two-qubit state showing the results <i>A</i> and <i>B</i> with the corresponding probabilities $P(A)$ and $P(B)$ and the remaining state after the measurement. . . .	373

Part I

Foundations of the Josephson Effect

Chapter 1

Macroscopic Quantum Phenomena

1.1 The Macroscopic Quantum Model

One of the main principles of quantum mechanics is the fact that physical quantities such as energy or momentum are, under certain conditions, quantized. That is, they can have only discrete values. However, for a long time it was believed that quantization is relevant only for microscopic objects such as nuclei, atoms or molecules. Indeed, if we are considering the behavior of macroscopic objects consisting of a large number of atoms, quantization effects cannot be observed, although every single atom obeys the laws of quantum mechanics. This is due to the fact that thermal motion masks quantum regularities. However, for a number of phenomena, in particular superconductivity, it has been found that it is possible to observe macroscopic quantization. That is, we can observe quantization of parameters that characterize macroscopic objects (for example the flux through a superconducting ring of macroscopic dimension) many orders of magnitude larger than microscopic objects like atoms. As will be discussed in the following, this is caused by the fact that the electron system in a superconductor is highly correlated due to coherence effects. Then we have to consider all superconducting electrons as a single quantum mechanical entity.

1.1.1 Coherent Phenomena in Superconductivity

Although superconductivity has been discovered already in 1911,¹ it took many decades until a modern concept for the superconducting state has been developed. The main milestones along the way towards a deeper understanding of superconductivity have been the discovery of the ***Meißner-Ochsenfeld effect***² by **Walther Meißner** and **Robert Ochsenfeld** in 1933, the development of the phenomenological theories by **Fritz** and **Heinz London**³ and **V.L. Ginzburg** and **L.D. Landau**⁴ and finally the creation of the microscopic BCS theory by **J. Bardeen**, **L.N. Cooper** and **J.R. Schrieffer**^{5,6} with later important

¹H. Kammerlingh Onnes, *The resistance of pure mercury at helium temperatures*, Communication from the Physical Laboratory at the University of Leiden, Nos. **120b**, **122b**, and **124c** (1911).

²Walther Meißner, Robert Ochsenfeld, *Ein neuer Effekt bei Eintritt der Supraleitfähigkeit*, Naturwissenschaften **21** (44), 787–788 (1933).

³F. London, H. London, *The Electromagnetic Equations of the Superconductor*, Proc. Roy. Soc. Lond. A **149**, 71 (1935); see also F. London, *Superfluids*, Wiley, New York (1950).

⁴V.L. Ginzburg, L.D. Landau, *On the theory of superconductivity*, Zh. Eksp. Teor. Fiz. **20**, 1064 (1950).

⁵J. Bardeen, L.N. Cooper, and J.R. Schrieffer, *Microscopic Theory of Superconductivity*, Phys. Rev. **106**, 162–164 (1957).

⁶J. Bardeen, L. N. Cooper, and J. R. Schrieffer, *Theory of Superconductivity*, Phys. Rev. **108**, 1175–1205 (1957).

contributions by **N.N. Bogolyubov**⁷ and **L.P. Gor'kov**⁸ as well as by **A.A. Abrikosov**⁹.

A great deal of our knowledge on superconductivity can be obtained from phenomenological models (e.g. electrodynamics of superconductors) such as the ***London-Laue-theory*** developed by Fritz and Heinz London, but also by Max von Laue. However, these models have just been formulated to agree with the fundamental observations, namely perfect conductance, the Meißner-Ochsenfeld effect and the thermodynamic nature of the superconducting transition. That is, the models do not show us how these phenomena are related to each other. Historically, the theoretical predictions and experimental observation of coherent phenomena in superconductors such as flux quantization^{10,11} have been proven to be the key for the final formulation of the macroscopic quantum concept of superconductivity. It was already realized in 1935 by **Fritz London** that the phenomenon of superconductivity cannot be understood in terms of classical concepts. By 1948 he was able to derive the ***London equations*** from more fundamental ideas, if the superelectron fluid was treated as a quantum mechanical entity. London made this development, since he realized that

superconductivity is an inherently quantum phenomenon manifesting itself on a macroscopic scale.

We know that although quantum mechanics has replaced Newtonian mechanics as the appropriate physical theory, the classical laws are very good approximations on length scales much larger than atomic dimensions. Therefore, it is not evident on first sight why quantum mechanics is required to describe the properties of a macroscopic superconductor. However, superconductivity is like the coherent light emitted by a laser. There is no way to describe the phenomenon by the laws of classical physics alone. The reason for that is that superconductivity is a ***macroscopic quantum phenomenon*** and this is precisely the reason why we can observe the unusual quantum phenomena on a macroscopic scale.

The macroscopic quantum model of superconductivity is based on the hypothesis that there is a macroscopic wave function $\psi(\mathbf{r}, t)$, which describes the behavior of the whole ensemble of superconducting electrons. Of course, this hypothesis can be justified by the microscopic theory of superconductivity (BCS-theory). This theory is based on the idea that in superconducting metals there is an attractive force between electrons near the Fermi level. At temperatures below the critical temperature T_c this attractive force creates a new quantum state differing from the Fermi sea of a normal metal. Roughly we can say that a small portion of the electrons close to the Fermi level are bound to Cooper pairs. In the simplest case, the internal motion of the pairs has no orbital angular momentum (symmetric s -state) and consequently Pauli's principle requires that the two spins must be in a singlet (antisymmetric) spin state. In contrast to binding of two atoms to a molecule, the orbital state of the pair has a much larger radius typically between 10 nm and 1 μm so that the individual pairs overlap strongly in space and consequently the binding turns cooperative. In particular, the binding energy of any pair depends on how many other pairs have condensed and, furthermore, the center of mass motion of the pairs is so strongly correlated that each pair resides in the same state with the same center of mass motion.¹² It is this state which we are describing by a macroscopic wave function and which gives the system its superfluid properties. For example, the center of mass motion can be described by the wave function

⁷N.N. Bogoliubov *A new method in the theory of superconductivity*, Zh. Eksp. Teor. Fiz. **34**, 58 (1958).

⁸see e.g. A.A. Abrikosov, L.P. Gor'kov, I.E. Dzyaloshinskii in *Quantum Field Theoretical Models in Statistical Physics*, Pergamon Press, London (1965).

⁹A.A. Abrikosov, Zh. Eksp. Teor. Fiz. **32**, 1141 (1957)

¹⁰R. Doll, M. Nähbauer, *Experimental Proof of Magnetic Flux Quantization in a Superconducting Ring*, Phys. Rev. Lett. **7**, 51 (1961)

¹¹B.S. Deaver, W.M. Fairbank, *Experimental Evidence for Quantized Flux in Superconducting Cylinders*, Phys. Rev. Lett. **7**, 43 (1961).

¹²This is possible since the pairs represent bosons. We then can say that these bosons undergo a Bose-Einstein condensation, i.e. many pairs condense in the same quantum state like in the condensation which occurs for purely statistical reasons in an ideal Bose gas.

Walther Meißner (1882 -1974):

Walther Meißner was born on December 16, 1882 in Berlin.

He studied mechanical engineering at the Technische Hochschule Berlin Charlottenburg from 1901 - 1904 as well as mathematics and physics at the University of Berlin from 1904 - 1906. In 1907 he finished his Ph.D. in the group of Max Planck. Then he joined the National Bureau of Standards at Berlin. From 1922 - 1925 he set up a helium liquifier which was the third one worldwide. In 1933 he discovered the perfect diamagnetism in superconductors together with Robert Ochsenfeld. Today, this effect therefore is denoted as Meißner-Ochsenfeld effect.

In 1934 he was offered a full professor position at the Technische Hochschule München. After the second world war Walther Meißner was the first president of the Bavarian Academy of Sciences and founded in 1946 the Commission for Low Temperature Research. The laboratories of this commission first were at Herrsching close to Munich. In 1965, the new Central Institute for Low Temperature Research was build on the research campus at Garching. On the occasion of Walther-Meißner's 100. birthday this institute was renamed Walther-Meißner-Institute in 1982.

Walther Meißner died on November 15, 1974 in Munich.



$\psi(\mathbf{r}, t) = \psi_0 \exp(i\theta(\mathbf{r}, t)) = \psi_0 \exp(i\mathbf{k}_s \cdot \mathbf{r} - i\omega t)$ with every pair having the same momentum $\hbar\mathbf{k}_s$ or pair velocity $\mathbf{v}_s = \hbar\mathbf{k}/m^*$.

We note that the macroscopic quantum model can not only be applied to charged superfluids but also to uncharged superfluids such as superfluid ^4He and ^3He , or Bose-Einstein condensates.^{13,14} The development and understanding of the macroscopic quantum model of superconductivity requires the sound knowledge of quantum mechanics. Therefore, in the following we briefly review the most fundamental concepts of quantum mechanics that have direct relevance to superconductivity.

Schrödinger's Equation

In 1900 **Max Planck** introduced the concept of quantization to explain the radiation emitted by a black body at a given temperature. In order to explain the experimental observations he had to abandon the classical concept that radiation can be emitted in arbitrarily small quanta. Instead he had to postulate that the electromagnetic field can exchange energy only in certain discrete amounts. Planck did not feel comfortable with this postulation and considered it as a mathematical trick. However, **Albert Einstein** considered Planck's departure from classical physics as something far more fundamental. In 1905 he postulated that electromagnetic radiation has to be considered as a collection of particles known as **photons**. A single photon of a known angular frequency ω represents the smallest amount of energy namely

$$E = \hbar\omega \quad \text{with} \quad \hbar = 1.054\,571\,596(82) \times 10^{-34} \text{ J s} . \quad (1.1.1)$$

that can be radiated from a black body. That is, Planck has not merely postulated a mathematical trick but discovered a very fundamental characteristic of nature.

¹³D. Einzel, *Supraleitung und Suprafluidität*, in Lexikon der Physik, Spektrum Akademischer Verlag, Heidelberg, Berlin (2000).

¹⁴D. Einzel, *Superfluids*, Encyclopedia of Mathematical Physics (2005).

Later on, **Louis de Broglie**¹⁵ realized in 1924 that, just by reasons of symmetry, it should be possible to describe classical particles as waves, in the same way as classical waves can be described as particles. In his doctoral thesis he introduced the concept of **matter waves**, which was completely outside normal experience that time. Today, there is overwhelming experimental evidence for the **wave-particle duality** and we are used to this concept. The **de Broglie relations** linking the particle quantities energy E and momentum \mathbf{p} to the wave quantities frequency ω and wave vector \mathbf{k} , resp. wavelength λ , are given by

$$E = \hbar\omega , \quad (1.1.2)$$

$$\mathbf{p} = \hbar\mathbf{k} = \frac{h}{\lambda} \hat{\mathbf{k}} . \quad (1.1.3)$$

with $h = 2\pi \cdot \hbar = 6.6262 \times 10^{-34} \text{ Js}$ and $\hat{\mathbf{k}} = \mathbf{k}/|\mathbf{k}|$. In both equations the constant of proportionality is related to the Planck's constant. It is due to the small value of Planck's constant that we usually do not notice quantum effects in our macroscopic world.

Based on these ideas we have to find an equation of motion for a quantum system playing the role of Newton's equation of motion for a classical system. Based on the existence of matter waves, **Erwin Schrödinger** initiated in 1926 the development of the wave mechanics by using the analogy to wave optics. According to Schrödinger a quantum particle can be described by the complex wave function $\Psi(\mathbf{r}, t)$, where in analogy to wave optics the relations

$$\Psi(\mathbf{r}, t) = A \exp[i(\mathbf{k} \cdot \mathbf{r} - \omega t)] = A \exp\left[\frac{i}{\hbar}(\mathbf{p} \cdot \mathbf{r} - Et)\right] \quad (1.1.4)$$

are valid.

We first consider the case of a free particle without any spin effects for which the potential energy $E_{\text{pot}} = 0$ and hence $E = E_{\text{kin}}$. According to the analogy to wave optics it is natural to start with the wave equation

$$\nabla^2\Psi - \frac{1}{v_{\text{ph}}^2} \frac{\partial^2\Psi}{\partial t^2} = 0 \quad (1.1.5)$$

for waves with the phase velocity v_{ph} . For stationary problems, for which \mathbf{p} and E do not vary with time, the wave function can be separated into two parts depending on space and time. Thus we can write

$$\Psi(\mathbf{r}, t) = \Psi(\mathbf{r}, 0) \exp(-i\omega t) . \quad (1.1.6)$$

Using this Ansatz in the above wave equation and by using

$$k^2 = \frac{\omega^2}{v_{\text{ph}}^2} = \frac{p^2}{\hbar^2} = \frac{2mE_{\text{kin}}}{\hbar^2} = \frac{2m\omega}{\hbar} \quad (1.1.7)$$

we obtain the expression

$$\nabla^2\Psi = -k^2\Psi = -\frac{2mE_{\text{kin}}}{\hbar^2}\Psi . \quad (1.1.8)$$

¹⁵**Louis Victor Prince de Broglie**, born on August 15, 1892 in Dieppe, died on March 19, 1987, Nobel Prize in Physics 1929.

In the more general case the particle can move in the potential V . If the potential is conservative, we can attribute each position a potential energy E_{pot} with the total energy $E = E_{\text{kin}} + E_{\text{pot}}$ being constant. With $E_{\text{kin}} = E - E_{\text{pot}}$ we obtain from (1.1.8) the ***stationary Schrödinger equation***

$$\left(-\frac{\hbar^2}{2m} \nabla^2 + E_{\text{pot}} \right) \Psi(\mathbf{r}) = E \Psi(\mathbf{r}) . \quad (1.1.9)$$

By using the time derivative of (1.1.6) we obtain

$$i\hbar \frac{\partial}{\partial t} \Psi(\mathbf{r}, t) = E_{\text{kin}} \Psi(\mathbf{r}, t) . \quad (1.1.10)$$

Then, with (1.1.8) we obtain the time dependent equation

$$i\hbar \frac{\partial}{\partial t} \Psi(\mathbf{r}, t) = -\frac{\hbar^2}{2m} \nabla^2 \Psi(\mathbf{r}, t) . \quad (1.1.11)$$

For non-stationary problems (i.e. $E_{\text{kin}} = E_{\text{kin}}(t)$ and $p = p(t)$) we can no longer express $\partial^2 \Psi / \partial t^2$ by $-\omega^2 \Psi$ and hence derive the wave equation for matter waves. Schrödinger postulated that even in the case of a time dependent potential energy the equation

$$i\hbar \frac{\partial}{\partial t} \Psi(\mathbf{r}, t) = \left(-\frac{\hbar^2}{2m} \nabla^2 + E_{\text{pot}}(\mathbf{r}, t) \right) \Psi(\mathbf{r}, t) \quad (1.1.12)$$

is valid. This general ***time dependent Schrödinger equation*** was noted by Schrödinger for the first time in 1926. Up to now this equation has been confirmed in a huge number of experiments and represents the basic equation of quantum mechanics. Often the Schrödinger equation is written as $i\hbar \frac{\partial \Psi}{\partial t} = \hat{H} \Psi$ with $\hat{H} \equiv -\frac{\hbar^2}{2m} \nabla^2 + E_{\text{pot}}(\mathbf{r}, t)$ being the ***Hamilton operator***.

Probability Currents

In the last section we have seen that the Schrödinger equation governs the evolution of the wave function Ψ in space and time. The wave function Ψ is somehow descriptive of the quantum system but its interpretation is not obvious. On the first sight we might consider it as a quantum field similar to the fields encountered in electromagnetism. However, this is not the case. It is evident that Ψ cannot be a real scalar function as a result of the factor i in the Schrödinger equation. Therefore, if Ψ is a scalar function, it must have both real ***and*** imaginary parts. For a plane wave this implies

$$\Psi(\mathbf{r}, t) = \Psi_0 e^{i(\mathbf{k} \cdot \mathbf{r} - \omega t)} . \quad (1.1.13)$$

In contrast, electromagnetic fields always can be represented as the real ***or*** imaginary part of a complex expression:

$$\mathbf{E}(\mathbf{r}, t) = \Re \left\{ \mathbf{E}_0 e^{i(\mathbf{k} \cdot \mathbf{r} - \omega t)} \right\} . \quad (1.1.14)$$

Erwin Schrödinger (1887 -1961), Nobel Price in Physics 1933:

Erwin Schrödinger was born on August 12, 1887, in Vienna. He was a highly gifted man with a broad education. After having finished his chemistry studies, he devoted himself for years to Italian painting. After this he took up botany, which resulted in a series of papers on plant phylogeny. Schrödinger's wide interests dated from his school years at the Gymnasium, where he not only had a liking for the scientific disciplines, but also appreciated the severe logic of ancient grammar and the beauty of German poetry. (What he abhorred was memorizing of data and learning from books.)

From 1906 to 1910 he was a student at the University of Vienna, during which time he came under the strong influence of Fritz Hasenöhrl, who was Boltzmann's successor. It was in these years that Schrödinger acquired a mastery of eigenvalue problems in the physics of continuous media, thus laying the foundation for his future great work. Hereafter, as assistant to Franz Exner, he, together with his friend K. W. F. Kohlrausch, conducted practical work for students (without himself, as he said, learning what experimenting was). During the First World War he served as an artillery officer.

In 1920 he took up an academic position as assistant to Max Wien, followed by positions at Stuttgart (extraordinary professor), Breslau (ordinary professor), and at the University of Zurich (replacing von Laue) where he settled for six years. In later years Schrödinger looked back to his Zurich period with great pleasure - it was here that he enjoyed so much the contact and friendship of many of his colleagues, among whom were Hermann Weyl and Peter Debye. It was also his most fruitful period, being actively engaged in a variety of subjects of theoretical physics. His papers at that time dealt with specific heats of solids, with problems of thermodynamics (he was greatly interested in Boltzmann's probability theory) and of atomic spectra; in addition, he indulged in physiological studies of colour (as a result of his contacts with Kohlrausch and Exner, and of Helmholtz's lectures). His great discovery, Schrödinger's wave equation, was made at the end of this epoch-during the first half of 1926.

It came as a result of his dissatisfaction with the quantum condition in Bohr's orbit theory and his belief that atomic spectra should really be determined by some kind of eigenvalue problem. For this work he shared with Dirac the Nobel Prize for 1933.

In 1927 Schrödinger moved to Berlin as Planck's successor. Germany's capital was then a center of great scientific activity and he enthusiastically took part in the weekly colloquies among colleagues, many of whom "exceeding him in age and reputation". With Hitler's coming to power (1933), however, Schrödinger decided he could not continue in Germany. He came to England and for a while held a fellowship at Oxford. In 1934 he was invited to lecture at Princeton University and was offered a permanent position there, but did not accept. In 1936 he was offered a position at University of Graz, which he accepted only after much deliberation and because his longing for his native country outweighed his caution. With the annexation of Austria in 1938, he was immediately in difficulty because his leaving Germany in 1933 was taken to be an unfriendly act. Soon afterwards he managed to escape to Italy, from where he proceeded to Oxford and then to University of Ghent. After a short stay he moved to the newly created Institute for Advanced Studies in Dublin, where he became Director of the School for Theoretical Physics. He remained in Dublin until his retirement in 1955.

All this time Schrödinger continued his research and published many papers on a variety of topics, including the problem of unifying gravitation and electromagnetism, which also absorbed Einstein and which is still unsolved; (he was also the author of the well-known little book "What is Life?", 1944). He remained greatly interested in the foundations of atomic physics. Schrödinger disliked the generally accepted dual description in terms of waves and particles, with a statistical interpretation for the waves, and tried to set up a theory in terms of waves only. This led him into controversy with other leading physicists.

After his retirement he returned to an honored position in Vienna. He died on the 4th of January, 1961, after a long illness.



The fact that the quantum wave function is necessarily a complex quantity does not generate any problems with mathematics. However, recalling that Ψ_0 is just the amplitude of a plane wave we see from Schrödinger's equation that the absolute phase of this quantity cannot be arbitrarily. This is quite astonishing. Usually we do not discuss the absolute phase, since it does not change the physics of the problem. Schrödinger's equation in contrast seems to suggest that the absolute phase is not arbitrary but rather a measurable quantity with physical significance. To remove this problem, **Max Born** was proposing that the absolute square of the wavefunction corresponds to the probability $\rho(\mathbf{r},t)$ of a quantum object to be

at the location \mathbf{r} at time t . That is, we can write

$$\rho(\mathbf{r},t) = |\Psi(\mathbf{r},t)|^2 = \Psi^*(\mathbf{r},t)\Psi(\mathbf{r},t) \quad (1.1.15)$$

$$\int \Psi^*(\mathbf{r},t)\Psi(\mathbf{r},t) dV = 1 . \quad (1.1.16)$$

Here, (1.1.16) represents a normalization condition, since the probability to find the particle somewhere in space must be unity at all times.

We now will discuss how $\rho(\mathbf{r},t)$ evolves in space and time. In order to do so we perform the following steps:

- We first multiply the Schrödinger equation from the left side by $\Psi^*(\mathbf{r},t)$.
- We next multiply the complex conjugate of the Schrödinger equation from the left side by $\Psi(\mathbf{r},t)$.
- We then subtract both equations from each other.

In this way we obtain

$$\frac{\partial}{\partial t}(\Psi^*\Psi) + \frac{\hbar}{2mi}(\Psi^*\Delta\Psi - \Psi\Delta\Psi^*) = 0 . \quad (1.1.17)$$

Because any scalar function f and vector field \mathbf{F} obeys the vector identity

$$\nabla \cdot (f\mathbf{F}) = f \nabla \cdot \mathbf{F} + \mathbf{F} \cdot \nabla f$$

and $\Delta \equiv \nabla \cdot \nabla$ we can rewrite (1.1.17) to

$$\frac{\partial}{\partial t}(\Psi^*\Psi) + \nabla \cdot \left[\frac{\hbar}{2mi}(\Psi^*\nabla\Psi - \Psi\nabla\Psi^*) \right] = 0 . \quad (1.1.18)$$

This equation has the form of a continuity equation for the probability

$$\frac{\partial\rho}{\partial t} + \nabla \cdot \mathbf{J}_\rho = 0 ,$$

(1.1.19)

where the **probability current** \mathbf{J}_ρ is defined as

$$\mathbf{J}_\rho \equiv \frac{\hbar}{2mi}(\Psi^*\nabla\Psi - \Psi\nabla\Psi^*) = \Re \left\{ \Psi^* \frac{\hbar}{im} \nabla \Psi \right\} = \Re \left\{ \Psi^* \frac{\hat{\mathbf{p}}}{m} \Psi \right\} .$$

(1.1.20)

Equation 1.1.19 is the desired expression describing the evolution of the probability in space and time. It gives the local constraint on ρ , whereas (1.1.16) gives the global constraint on ρ . Eq.(1.1.20) says that the probability of a quantum objects at a certain point cannot change instantaneously but rather has to change in a continuous fashion by the flow of a probability current. Then, expression (1.1.19) can be viewed as a statement of the **conservation of probability**.

It is obvious that (1.1.19) resembles the familiar expression for the conservation of charge. However, this similarity is only mathematical. Whereas the electrical current is a real, physical measurable quantity the probability current is only a theoretical construct. It is not possible to measure \mathbf{J}_ρ for a single particle.

The probability current (1.1.20) describes the probabilistic flow of a quantum object which is subjected to forces varying in space and time. However, it still does not describe the situation we are interested in namely the motion of a charged particle in an electromagnetic field. This is caused by the fact that a charged particle moving in an electromagnetic field is subjected to forces depending on the motion of the particle itself. To find \mathbf{J}_ρ for this situation we first have to find the appropriate form of the Schrödinger equation. In order to do so we start with the general classical equation of motion

$$\frac{d}{dt} \mathbf{p} = -\nabla V . \quad (1.1.21)$$

Here, \mathbf{p} is the canonical momentum and V the externally applied potential, which are used in writing the total energy of the system. We will see that this formalism is useful for the considered case, since the electromagnetic field represents a non-conservative potential making the formulation of energy relationships difficult.

We begin with the classical equation of motion for a particle of charge q and mass m in an electromagnetic field given by the **Lorentz's law**

$$m \frac{d\mathbf{v}}{dt} = q [\mathbf{E} + (\mathbf{v} \times \mathbf{B})] . \quad (1.1.22)$$

In order to obtain the Schrödinger equation for this problem we first rewrite (1.1.22) into the form suggested by (1.1.21). The first step is to express the field quantities \mathbf{E} and \mathbf{B} in terms of potentials. According to **Gauss's law** the flux density \mathbf{B} always can be written as

$$\mathbf{B} = \nabla \times \mathbf{A} , \quad (1.1.23)$$

where \mathbf{A} is a *vector potential*. \mathbf{A} can be used to write **Faraday's law** $\nabla \times \mathbf{E} = -\partial \mathbf{B} / \partial t$ as

$$\nabla \times \left(\mathbf{E} + \frac{\partial \mathbf{A}}{\partial t} \right) = 0 . \quad (1.1.24)$$

Using the fact that the curl of the gradient of any single-valued scalar field ϕ is zero, (1.1.24) is equivalent to the statement

$$\mathbf{E} = -\frac{\partial \mathbf{A}}{\partial t} - \nabla \phi . \quad (1.1.25)$$

Then, Lorentz's law in terms of these potentials can be written as

$$m \frac{d\mathbf{v}}{dt} = -q \left(\nabla \phi + \frac{\partial \mathbf{A}}{\partial t} - \mathbf{v} \times (\nabla \times \mathbf{A}) \right) . \quad (1.1.26)$$

In order to bring this equation into the form of (1.1.21) we have to group all time derivatives together. Using the chain rule of differentiation

$$\frac{d\mathbf{A}}{dt} = \frac{\partial \mathbf{A}}{\partial t} + (\mathbf{v} \cdot \nabla) \mathbf{A} \quad (1.1.27)$$

we obtain

$$\frac{d}{dt} (m\mathbf{v} + q\mathbf{A}) = -q[\nabla\phi - (\mathbf{v} \cdot \nabla)\mathbf{A} - \mathbf{v} \times (\nabla \times \mathbf{A})] . \quad (1.1.28)$$

Now eq. (1.1.28) is close to the desired form and we can suspect that the ***canonical momentum*** is given by

$$\mathbf{p} = m\mathbf{v} + q\mathbf{A} . \quad (1.1.29)$$

To verify this we must be able to express the right hand side of (1.1.28) as the gradient of a scalar function. We therefore rewrite it in terms of the canonical momentum and obtain

$$\frac{d\mathbf{p}}{dt} = -q\nabla\phi + \frac{q}{m}(\mathbf{p} \cdot \nabla)\mathbf{A} - \frac{q^2}{m}(\mathbf{A} \cdot \nabla)\mathbf{A} + \frac{q}{m}\mathbf{p} \times (\nabla \times \mathbf{A}) - \frac{q^2}{m}\mathbf{A} \times (\nabla \times \mathbf{A}) . \quad (1.1.30)$$

Using the vector identities

$$\mathbf{a} \times (\nabla \times \mathbf{b}) = \nabla(\mathbf{a} \cdot \mathbf{b}) - (\mathbf{a} \cdot \nabla)\mathbf{b} - (\mathbf{b} \cdot \nabla)\mathbf{a} - \mathbf{b} \times (\nabla \times \mathbf{a}) \quad (1.1.31)$$

$$\mathbf{a} \times (\nabla \times \mathbf{a}) = \frac{1}{2}\nabla(\mathbf{a} \cdot \mathbf{a}) - (\mathbf{a} \cdot \nabla)\mathbf{a} \quad (1.1.32)$$

we can rewrite (1.1.30) as

$$\frac{d\mathbf{p}}{dt} = -q\nabla\phi + \frac{q}{m}\nabla(\mathbf{p} \cdot \mathbf{A}) - \frac{q^2}{2m}\nabla(\mathbf{A} \cdot \mathbf{A}) - \frac{q}{m}(\mathbf{A} \cdot \nabla)\mathbf{p} - \frac{q}{m}\mathbf{A} \times (\nabla \times \mathbf{p}) . \quad (1.1.33)$$

At this point we have to recall that we are using a set of independently specified variables (\mathbf{r}, \mathbf{p}) to describe the problem. Therefore, the spatial derivative of the canonical momentum is zero and we obtain

$$\frac{d\mathbf{p}}{dt} = -\nabla \left\{ q\phi - \frac{q}{m}(\mathbf{p} \cdot \mathbf{A}) + \frac{q^2}{2m}(\mathbf{A} \cdot \mathbf{A}) \right\} . \quad (1.1.34)$$

That is, we have achieved our initial goal of writing Lorentz's law in the generic form of eq. (1.1.21).

We briefly will discuss the physical meaning of (1.1.34). First, the canonical momentum \mathbf{p} given by (1.1.29) is composed of two parts. The first part, $m\mathbf{v}$, is the usual ***kinetic momentum*** and is associated with the momentum in elementary mechanics. The second part, $q\mathbf{A}$, is denoted as the ***field momentum***, which is a direct result of the charge of the particle. Any change of the velocity of the particle produces an electromagnetic field that must be considered self-consistently. Therefore, the generalized potential of the problem

$$V = q\phi - \frac{q}{m}(\mathbf{p} \cdot \mathbf{A}) + \frac{q^2}{2m}(\mathbf{A} \cdot \mathbf{A}) \quad (1.1.35)$$

is not only a function of space and time but also of the canonical momentum. In this way the interaction of the externally applied field and the induced current created by the motion of the charged particle is accounted for self-consistently.

The next step in obtaining the Schrödinger equation is to use the expressions for \mathbf{p} and V to write down the total energy:

$$E = E_{\text{kin}} + E_{\text{pot}} = \frac{\mathbf{p} \cdot \mathbf{p}}{2m} + \left\{ q\phi - \frac{q}{m}(\mathbf{p} \cdot \mathbf{A}) + \frac{q^2}{2m}(\mathbf{A} \cdot \mathbf{A}) \right\} . \quad (1.1.36)$$

This purely classical expression can be rewritten as

$$E = \frac{1}{2m}(\mathbf{p} - q\mathbf{A}) \cdot (\mathbf{p} - q\mathbf{A}) + q\phi . \quad (1.1.37)$$

The last step is to replace energy and momentum by the corresponding quantum mechanical operators

$$E \Rightarrow i\hbar \frac{\partial}{\partial t} \quad \mathbf{p} \Rightarrow -i\hbar \nabla . \quad (1.1.38)$$

Using these expression we expect the quantum form of the Lorentz's law to be

$$i\hbar \frac{\partial \Psi}{\partial t} = \frac{1}{2m} \left(\frac{\hbar}{i} \nabla - q\mathbf{A} \right)^2 \Psi + q\phi \Psi . \quad (1.1.39)$$

This equation corresponds to the Schrödinger equation of a charge particle in an electromagnetic field. We finally can use now eq. (1.1.39) to derive the probability current of a charged particle in an electromagnetic field to

$$\mathbf{J}_p = \Re \left\{ \Psi^* \left(\frac{\hbar}{im} \nabla - \frac{q}{m} \mathbf{A} \right) \Psi \right\} = \Re \left\{ \Psi^* \frac{\hat{\mathbf{p}}}{m} \Psi \right\} . \quad (1.1.40)$$

In deriving this equation we have to take into account that ϕ represents a portion of the applied potential field and therefore is a real quantity. We will see in the following section that Eq. (1.1.40) is the central expression in the quantum mechanical description of superconductivity.

1.1.2 Macroscopic Quantum Currents in Superconductors

After having recalled some basic concepts of quantum mechanics we can apply these concept to superconductors. Before doing so let us first consider the situation in a normal conductor. Of course, the electrons in a normal metal move according to the laws of quantum mechanics. In the usual approximation of weakly or non-interacting particles this motion can be described in terms of the ordinary Schrödinger equation

$$i\hbar \frac{\partial \Psi}{\partial t} = \hat{H} \Psi , \quad (1.1.41)$$

where

$$\Psi(\mathbf{r}, t) = \Psi_0(\mathbf{r}, t) e^{i\theta(\mathbf{r}, t)} \quad (1.1.42)$$

is the complex wave function of a particle. According to quantum mechanics $|\Psi|^2$ can be interpreted as the probability density of the particles. In the stationary situation $|\Psi|^2$ can be assumed constant and \hat{H} can be replaced by the energy E of the particle. As a result we can write

$$\hbar \frac{\partial \theta}{\partial t} = -E . \quad (1.1.43)$$

That is, the quantum specific character is reduced to that of the wave function phase θ .

The important point is that in normal metals (1.1.43) does not result in quantum correlations for the macroscopic variables because the electrons obey Fermi-Dirac statistics and their energies can never be exactly equal. Therefore, according to (1.1.43) the temporal evolution of the phases of the particle wave functions differs for all particles. That is, the phases are uniformly distributed and since all macroscopic quantities are sums over all the particles the phases drop out in these quantities.

We now discuss that this is not the case for superconductors. In superconductors bound pairs of electrons (Cooper pairs) are formed with opposite momenta and spins in the simplest case. These pairs with zero net spin obey the Bose-Einstein statistics and therefore can occupy the lowest energy state at low temperatures. As a result, their rates $\partial \theta / \partial t$ are identical. Furthermore, the Cooper pairs have a relatively large size of the order of 10 to 1000 nm, which is much larger than the typical distance between the pairs. Therefore, the wave functions of the individual pairs are strongly overlapping. As a result of these two factors, all the pairs are forming a ***phase-locked*** state that can be described by a single wave function Ψ , which is frequently denoted as the order parameter. In this situation the phases do not drop out during summation over all particles and therefore macroscopic variables, in particular current, can depend on the phase θ , which changes in a quantum manner under the action of an electromagnetic field. This quantum dependence leads not only to the zero resistance of superconductors and the Meißner-Ochsenfeld effect but also to specific coherent effects such as the ***flux quantization*** and the ***Josephson effect***.

The qualitative discussion of the previous paragraph shows that the situation for superconductors is somehow similar to the situation in atoms. For the latter, the fact that electrons can orbit the nucleus without decaying and letting the atom collapse could not be explained classically. Only quantum mechanics provided the necessary framework. In the same way, the infinite conductivity of superconductors cannot be explained classically. If one would try to do so, one has to postulate that the superelectrons do not scatter. Although the results of this assumption are consistent with the experimental fact, it seems to us arbitrary to postulate an infinite scattering time. In the same way as Schrödinger's equation provides the explanation for stable microscopic currents created by orbiting electrons, it was hypothesized by **Fritz London** that the macroscopic currents in superconductors might be explained in a similar way. This was the starting point of the ***macroscopic quantum model*** of superconductivity.

The central hypothesis behind the macroscopic quantum model of superconductivity can be stated as follows:

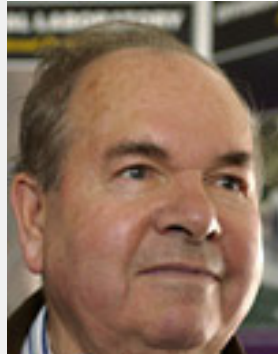
There exists a macroscopic quantum wave function

$$\psi(\mathbf{r}, t) = \psi_0(\mathbf{r}, t) e^{i\theta(\mathbf{r}, t)} \quad (1.1.44)$$

that describes the behavior of the entire ensemble of superelectrons in a superconductor.

The motivation for this assumption is that superconductivity is a ***coherent phenomenon*** of all superelectrons. This situation is analogous to the quantum description of electromagnetism. According to wave-particle dualism we can envision a photon as a quantum particle. Then, when a large number of photons interact coherently such as in a laser, the entire collection of these quantum particles can be adequately described in terms of an electromagnetic field with amplitude and phase. As we will see, the macroscopic wave function ψ is a field-like quantity that similarly describes the whole ensemble of superelectrons.

The Nobel Prize in Physics 2003 has been given to Alexei A. Abrikosov, Vitaly L. Ginzburg, and Anthony J. Leggett *for their pioneering contributions to the theory of superconductors and superfluids.*



Alexei A. Abrikosov



Vitaly L. Ginzburg



Anthony J. Leggett

Alexei A. Abrikosov, born 1928 in Moscow, the former Soviet Union, American (and Russian) citizen. Doctor's degree in physics in 1951 at the Institute for Physical Problems, Moscow. Distinguished Argonne Scientist, Argonne National Laboratory, Argonne, Illinois, USA.

Vitaly L. Ginzburg, born 1916 in Moscow, Russia (Russian citizen). Doctor's degree in physics at the University of Moscow. Former Head of the Theory Group at the P.N. Lebedev Physical Institute, Moscow, Russia.

Anthony J. Leggett, born 1938 in London, England (British and American citizen). Doctor's degree in physics in 1964 at the University of Oxford. MacArthur Professor at the University of Illinois at Urbana-Champaign, USA.

We have now to examine the consequences of postulating a macroscopic wave function describing the whole ensemble of superelectrons. We first discuss the meaning of $|\psi|^2$. For a single quantum particle described by the wave function Ψ the absolute square $|\Psi(\mathbf{r},t)|^2$ has been interpreted as the probability to find the particle at the location \mathbf{r} at a given time t . As a result we have the global constraint or normalization condition $\int \Psi^* \Psi dV = 1$ (compare (1.1.16)) stating that the particle exists somewhere in space at any time. Along this line it is natural to assume that the wave function ψ representing the whole ensemble of superelectrons satisfies the normalization condition

$$\int \psi^*(\mathbf{r},t) \psi(\mathbf{r},t) dV = N_s^* \quad (1.1.45)$$

$$|\psi(\mathbf{r},t)|^2 = \psi^*(\mathbf{r},t) \psi(\mathbf{r},t) = n_s^*(\mathbf{r},t) \quad (1.1.46)$$

Here, $n_s^*(\mathbf{r},t)$ is the local density and N_s^* the total number of superconducting electrons. Condition (1.1.45) says that if we are searching the whole space we have to find all superelectrons. Since the superelectrons are discrete objects, there must be of course a sufficiently large density in order to make the definition of a local density sense. This concern is similar to the situation in fluid mechanics. Although we know that all fluids consist of discrete atoms or molecules, it is convenient to describe the system by a local fluid density. Due to the analogy to fluid mechanics the collection of superelectrons is often referred to as a **charged superfluid**. Therefore, the theoretical description of superconductors (charged superfluid) and uncharged superfluids such as superfluid helium has many similarities. Indeed, the Nobel Prize in Physics 2003 was given to **Vitaly L. Ginzburg, Alexei A. Abrikosov and Anthony J. Leggett** for their pioneering contributions to the theory of superconductors and superfluids.

Note that the macroscopic quantum model of superconductivity does not explain the microscopic origin of superconductivity, which is not discussed here. That is, it does not explain the microscopic origin of

the attractive interaction of electrons in a solid resulting in the formation of Cooper pairs. This mechanism, which may be different for the classical metallic superconductors, the novel high temperature superconductors or the heavy fermion superconductors is not relevant for the macroscopic quantum phenomena discussed in the following. The only relevant issue is the possibility to describe the superelectron fluid as a quantum mechanical entity irrespective of the detailed pairing mechanism.

The analogy to superfluids is powerful to establish an intuitive picture about the macroscopic quantum model. Instead of a single particle wave function describing the probabilities for single particles we are now considering so many quantum objects that we have a wave function describing the actual location of a complete subset of the whole ensemble. Then, the continuity equation (1.1.19) for the probability becomes a continuity equation for the condensate density n_s^* . Furthermore, we do not have a probability flow \mathbf{J}_ρ but rather a flow of particles, which is nothing more than a physical current. Following (1.1.40) we can immediately write down the macroscopic quantum current density \mathbf{J}_s in an electromagnetic field, which is equivalent to the supercurrent density. We only have to multiply the ensemble probability current describing the particle flux by the charge q^* of the superelectron:

$$\begin{aligned}\mathbf{J}_s &= q^* \Re \left\{ \Psi^* \left(\frac{\hbar}{m^* i} \nabla - \frac{q^*}{m^*} \mathbf{A} \right) \Psi \right\} \\ &= \frac{q^* \hbar}{2m^* i} (\Psi^* \nabla \Psi - \Psi \nabla \Psi^*) - \frac{q^{*2}}{2m^*} \Psi \Psi^* \mathbf{A} .\end{aligned}\quad (1.1.47)$$

Here, m^* is the mass of the superelectrons. This expression can be brought in a more useful form by making some assumption on Ψ . According our discussion the macroscopic wavefunction $\Psi(\mathbf{r}, t)$ obeys the Schrödinger-like equation for the ensemble in an electromagnetic field:

$$i\hbar \frac{\partial \Psi(\mathbf{r}, t)}{\partial t} = \frac{1}{2m^*} \left(\frac{\hbar}{i} \nabla - q^* \mathbf{A}(\mathbf{r}, t) \right)^2 \Psi(\mathbf{r}, t) + q^* \phi(\mathbf{r}, t) \Psi(\mathbf{r}, t) .\quad (1.1.48)$$

Because of the phase factor i in this expression the macroscopic wave function Ψ in the same way as the microscopic one is a complex quantity. Therefore, $\Psi(\mathbf{r}, t)$ is of the form

$$\Psi(\mathbf{r}, t) = \sqrt{n_s^*(\mathbf{r}, t)} e^{i\theta(\mathbf{r}, t)} .\quad (1.1.49)$$

Here, we have used an amplitude satisfying the condition that the absolute square of the wave function is equivalent to the density of superelectrons. We also note that θ is a real function representing the phase of the complex number.

Substitution of (1.1.49) into the expression (1.1.47) for the supercurrent we obtain the supercurrent equation

$$\mathbf{J}_s = q^* n_s^*(\mathbf{r}, t) \left\{ \frac{\hbar}{m^*} \nabla \theta(\mathbf{r}, t) - \frac{q^*}{m^*} \mathbf{A}(\mathbf{r}, t) \right\} .\quad (1.1.50)$$

Since a current density always can be written as $\mathbf{J}_s = q^* n_s^* \mathbf{v}_s$, the expression in parentheses corresponds to the velocity of the superelectrons:

$$\mathbf{v}_s \equiv \frac{\hbar}{m^*} \nabla \theta(\mathbf{r}, t) - \frac{q^*}{m^*} \mathbf{A}(\mathbf{r}, t) .\quad (1.1.51)$$

Additional Topic: Gauge Invariance

We briefly address a rather technical point, which is however of particular importance for superconductors. We have to recall that quantities such as \mathbf{A} , ϕ or θ describe physical variables but are not themselves observable. We also can find formal transformations for these quantities that have no effect on the observable quantities such as \mathbf{B} , \mathbf{E} , or \mathbf{J}_s . Such transformations are called *gauge transformations*. Unobservable quantities such as \mathbf{A} , ϕ or θ , which change in a well defined way under a gauge transformation, are denoted as *gauge covariant*.

Let us consider eq.(1.1.50). It states that the supercurrent \mathbf{J}_s only depends on the phase of the macroscopic wave function and the vector potential. That is, the observable quantity \mathbf{J}_s is related to two quantities, which cannot be determined directly from the experiment. Moreover, because any single-valued scalar field f satisfies the condition $\nabla \times (\nabla f) = 0$, we know that for an arbitrary scalar function χ

$$\mathbf{B} = \nabla \times \mathbf{A} = \nabla \times (\mathbf{A} + \nabla \chi) . \quad (1.1.52)$$

That is, there exists an infinite number of possible vector potentials that can describe the correct magnetic flux density. This suggests that we can obtain a well defined value for the measurable quantity \mathbf{J}_s only if we can measure both θ and \mathbf{A} , which have been introduced only for mathematical convenience and are not physical observables.

The way out of this dilemma is to recognize the fact that the relation between phase and vector potential is not arbitrary but fixed. In this way we can measure the supercurrent but still are not able to determine θ and \mathbf{A} . That is, we demand that expression (1.1.50) is independent of the special choice of \mathbf{A} . The specific choice of \mathbf{A} is usually referred to as the gauge and, hence, we have to make the expression for the supercurrent *gauge invariant*. Mathematically this is straightforward. Suppose we define a new vector potential \mathbf{A}' as

$$\mathbf{A}' \equiv \mathbf{A} + \nabla \chi . \quad (1.1.53)$$

Then, according to (1.1.52) this new vector potential correctly gives the magnetic flux density. In addition, the new vector potential also must correctly describe the electric field. Therefore, we define a new scalar potential ϕ' so that the electric field is given by

$$\mathbf{E} = -\frac{\partial \mathbf{A}'}{\partial t} - \nabla \phi' . \quad (1.1.54)$$

Comparing this expression to the original expression $\mathbf{E} = -\frac{\partial \mathbf{A}}{\partial t} - \nabla \phi$ (1.1.25) we see that the two scalar potentials are related by

$$\phi' \equiv \phi - \frac{\partial \chi}{\partial t} . \quad (1.1.55)$$

According to (1.1.53) and (1.1.55) we can separately specify the temporal and spatial dependence of a scalar function χ to generate new sets of the scalar and the vector potentials which still describe the original electric and magnetic fields.

By rewriting (1.1.48) in terms of the new potentials with the new wave function $\psi'(\mathbf{r},t) = \sqrt{n_s^*(\mathbf{r},t)} e^{i\theta'(\mathbf{r},t)}$ we can easily derive a new expression for the supercurrent density given by

$$\mathbf{J}_s = q^* n_s^*(\mathbf{r},t) \left\{ \frac{\hbar}{m^*} \nabla \theta'(\mathbf{r},t) - \frac{q^*}{m^*} \mathbf{A}'(\mathbf{r},t) \right\} . \quad (1.1.56)$$

Since the supercurrent, the experimentally measurable quantity, must be the same in (1.1.56) and (1.1.50), we have to satisfy the condition

$$\theta' = \theta + \frac{q^*}{m^*} \chi . \quad (1.1.57)$$

This in turn results in

$$\psi'(\mathbf{r}, t) = \psi(\mathbf{r}, t) e^{i(q^*/\hbar)\chi} . \quad (1.1.58)$$

That is, the same scalar function χ is changing both the phase and the vector potential. In this way the supercurrent always has the same value and can be measured regardless the specific gauge chosen. The important conclusion that can be drawn is that the expression for the supercurrent is gauge invariant and therefore we do no longer be concerned about this issue.

From the expression (1.1.56) and (1.1.50) for the supercurrent density we obtain the condition

$$\nabla \theta' - \frac{q^*}{\hbar} \mathbf{A}' = \nabla \theta - \frac{q^*}{\hbar} \mathbf{A} . \quad (1.1.59)$$

We therefore can introduce a *gauge invariant phase gradient*

$$\gamma = \nabla \theta - \frac{q^*}{\hbar} \mathbf{A} = \nabla \theta - 2\pi \frac{(-2e)}{h} \mathbf{A} = \nabla \theta - \frac{2\pi}{\Phi_0} \mathbf{A} , \quad (1.1.60)$$

where we have used $q^* = -2e$ and

$$\Phi_0 = \frac{h}{|q^*|} = \frac{h}{2e} \quad (1.1.61)$$

is the flux quantum. We see that the supercurrent is then given by

$$\mathbf{J}_s = \frac{q^* n_s^* \hbar}{m^*} \gamma = \frac{\hbar}{q^* \Lambda} \gamma , \quad (1.1.62)$$

where

$$\Lambda \equiv \frac{m^*}{n_s^* q^{*2}} \quad (1.1.63)$$

is the *London coefficient* and

$$\lambda_L \equiv \sqrt{\frac{m^*}{\mu_0 n_s^* q^{*2}}} \quad (1.1.64)$$

the *London penetration depth*. We see that the supercurrent density is proportional to the gauge invariant phase gradient.¹⁶

¹⁶Note that $\nabla \theta - \frac{q^*}{\hbar} \mathbf{A}$ cannot be written as $\nabla \gamma$, that is, as the gradient of a gauge invariant phase. In this case we would have $\mathbf{A} \propto \nabla \theta - \nabla \gamma$ and hence $\nabla \times \mathbf{A} = \mathbf{B} = 0$.

1.1.3 The London Equations

The two **London equations** formulated by **Fritz London** to describe the behavior of superconductors based on classical physics can be easily derived from the expression (1.1.50) for the supercurrent density by assuming $n_s^* = \text{const}$. Note that (1.1.50) includes the cases where the superelectron density varies in space and time.

By using the London coefficient $\Lambda = \frac{m^*}{n_s^* q^{*2}}$ we can rewrite (1.1.50) as

$$\Lambda \mathbf{J}_s = - \left\{ \mathbf{A}(\mathbf{r}, t) - \frac{\hbar}{q^*} \nabla \theta(\mathbf{r}, t) \right\} . \quad (1.1.65)$$

Second London Equation and Meißner-Ochsenfeld-Effect

By taking the curl of this expression we obtain the **second London equation**

$$\nabla \times (\Lambda \mathbf{J}_s) = - \nabla \times \mathbf{A} = -\mathbf{B} , \quad (1.1.66)$$

Taking the curl of the Maxwell equation $\nabla \times \mathbf{B} = \mu_0 \mathbf{J}_s$ we obtain $\nabla \times \nabla \times \mathbf{B} = \nabla \times \mu_0 \mathbf{J}_s$. With the vector identity $\nabla \times \nabla \times \mathbf{B} = \nabla(\nabla \cdot \mathbf{B}) - \nabla^2 \mathbf{B}$ and using $\nabla \cdot \mathbf{B} = 0$ and the second London equation we arrive at

$$\nabla^2 \mathbf{B} = \frac{\mu_0}{\Lambda} \mathbf{B} = \frac{1}{\lambda_L^2} \mathbf{B} . \quad (1.1.67)$$

This equation describes the Meißner-Ochsenfeld effect.^{17,18} An applied field decays exponentially inside a superconductor with the characteristic decay length given by the London penetration depth λ_L . For example, near a plane surface extending in the yz -plane the magnetic field B_z parallel to the z -direction decays exponentially with x as $B_z(x) = B_{z,0} e^{-x/\lambda_L}$ (see Fig. 1.1). With $\nabla \times \mathbf{B} = \mu_0 \mathbf{J}_s$ we obtain also an exponential decay of the supercurrent density flowing in y -direction as $J_{s,y}(x) = \frac{B_{z,0}}{\mu_0 \lambda_L} e^{-x/\lambda_L} = \frac{H_{z,0}}{\lambda_L} e^{-x/\lambda_L} = J_{y,0} e^{-x/\lambda_L}$.

First London Equation and Perfect Conductivity

In order to get the first London equation from (1.1.50) we have to take the partial derivative with respect to time:

$$\frac{\partial}{\partial t} (\Lambda \mathbf{J}_s) = - \left\{ \frac{\partial \mathbf{A}(\mathbf{r}, t)}{\partial t} - \frac{\hbar}{q^*} \nabla \left(\frac{\partial \theta(\mathbf{r}, t)}{\partial t} \right) \right\} . \quad (1.1.68)$$

From the Schrödinger-like equation (1.1.48) we obtain for $n_s^* = \text{const}$

$$-\hbar \frac{\partial \theta}{\partial t} = \frac{1}{2n_s^*} \Lambda \mathbf{J}_s^2 + q^* \phi . \quad (1.1.69)$$

¹⁷Walther Meißner, born on December 16, 1882 in Berlin, died on November 15, 1974 in Munich.

¹⁸Robert Ochsenfeld, born on May 18, 1901 in Helberhausen, died on December 5, 1993 in Helberhausen.

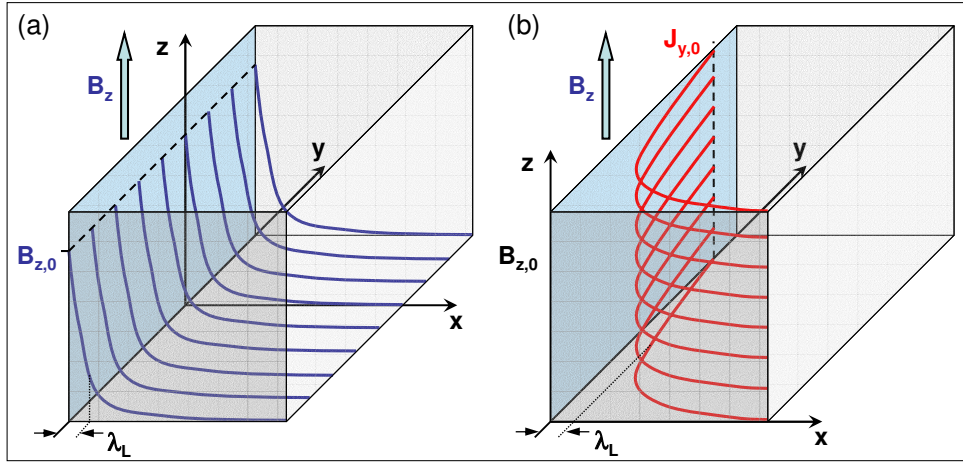


Figure 1.1: Exponential decay of the magnetic field \mathbf{B} (a) and the supercurrent density \mathbf{J}_s (b) with distance x into a bulk superconductor.

This expression is known as the *energy-phase relationship*, since the first term on the right hand side represents the kinetic energy ($\frac{1}{2}m^*v_s^2$) and the second the potential energy. By substituting (1.1.69) into (1.1.68) and using $\mathbf{E} = -\partial \mathbf{A}/\partial t - \nabla \phi$ we obtain the *first London equation*

$$\frac{\partial}{\partial t}(\Lambda \mathbf{J}_s) = \mathbf{E} - \frac{1}{n_s^* q^*} \nabla \left(\frac{1}{2} \Lambda \mathbf{J}_s^2 \right) . \quad (1.1.70)$$

As discussed below the second term on the right hand side usually can be neglected. Then, the 1. London equation reads $\frac{\partial}{\partial t}(\Lambda \mathbf{J}_s) = \mathbf{E}$. We hence see that for a time-independent supercurrent the electric field inside the superconductor vanishes and we therefore have a dissipationless current.¹⁹

The fact that a supercurrent flowing in a superconductor does not decay in time is interesting and not obvious at first sight. Therefore, we briefly consider processes that could cause a decay. In order to do so we consider the Fermi sphere which is shown in Fig. 1.2 in two-dimensions in the $k_x k_y$ -plane. The allowed \mathbf{k} -states are represented by points. At $T = 0$, all states within the Fermi sphere (Fermi circle in two dimensions) are occupied. Without any current the Fermi sphere is centered around the origin (dashed line). However, for a finite current e.g. in x -direction it is slightly shifted along the k_x -direction by δk_x . In the normal state of a metal the charge carriers can relax into states of lower energy, where the Pauli principle has to be taken into account (see Fig. 1.2a). Since there is a large variety of possible scattering processes, the system rapidly will relax into the situation with the Fermi sphere centered around the origin, i.e. the current will relax rapidly. In contrast, in the superconducting state all the Cooper pairs have the same center of mass momentum. Therefore, they can be scattered only around the sphere as shown in Fig. 1.2b. However, these scattering processes do not result in a shift of the center of the Fermi sphere and hence in a decay of the current. That is we have a non-decaying supercurrent. Note that other scattering processes are only possible if we destroy the Cooper pairs what however requires the supply of its binding energy.

We emphasize that the two London equations, although closely related to each other, are independent and neither can be deduced from the other. For example, if we take the time derivative of the 2. London

¹⁹Based on this result we can derive the 1. London equation by a simple classical consideration. For a dissipationless motion of charge carriers we can neglect the friction and can write the equation of motion as $m^* \ddot{\mathbf{v}}_s = q^* \mathbf{E}$. With $\mathbf{J}_s = n_s^* q^* \mathbf{v}_s$ we find $\mathbf{E} = \frac{m^*}{q^* n_s^*} \dot{\mathbf{J}}_s = \frac{\partial}{\partial t}(\Lambda \mathbf{J}_s)$, i.e., the 1. London equation. However, one has to take into account that in this derivation we already have made use of the existence of a dissipationless current, which is an essential result of the 1. London equation.

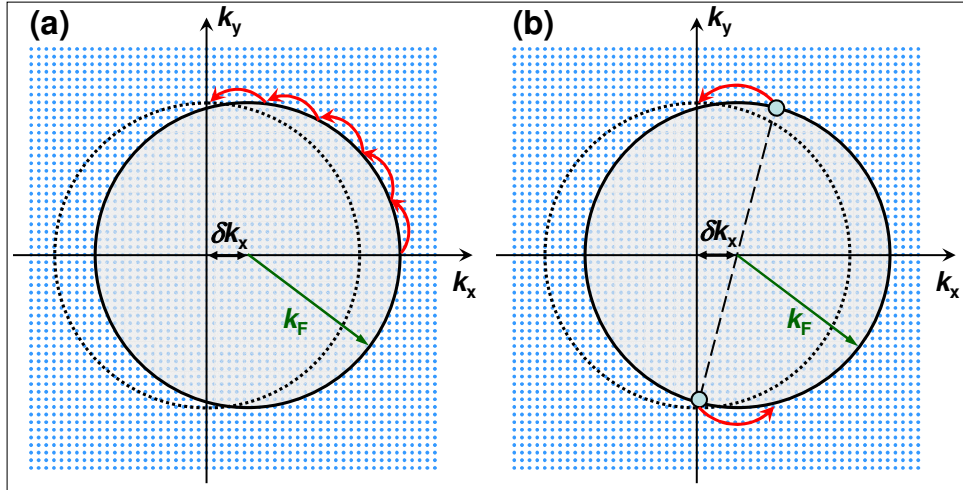


Figure 1.2: Intuitive picture for the decay of a current in the normal state (a) and the superconducting state (b) of a metal. In (b) the electrons are correlated to Cooper pairs relative to the center of the shifted Fermi sphere since they all have the same center of mass velocity.

equation (1.1.66) to derived the 1. London equation (1.1.70), we cannot fix the term $\nabla\phi$ on the right hand side of (1.1.70) with certainty. That is, although it is obvious that the screening currents on the surface of the superconductor must flow resistanceless because they do not decay, we cannot prove that $\mathbf{E} = 0$ inside the superconductor from (1.1.66) alone. On the other hand, by taking the curl of (1.1.70) we can get the time derivative of (1.1.66) but not (1.1.66) itself. Using the time derivative of Ampère's rule, we further can get the time derivative of (1.1.67). By integration over time we then can deduce that changes in \mathbf{B} are screened from the bulk of the superconductor. However, eq.(1.1.66) is stronger since it implies that not only changes in \mathbf{B} but the field \mathbf{B} itself is screened. This is the difference between a perfect conductor, which is screening changes in \mathbf{B} , and a superconductor (perfect diamagnet), which also screens \mathbf{B} .

Additional Topic: Linearized 1. London Equation

Usually, the first London equation is given as

$$\frac{\partial}{\partial t}(\Lambda \mathbf{J}_s) = \mathbf{E}, \quad (1.1.71)$$

that is, without the second term on the right hand side of (1.1.70) which contains the kinetic energy of the superelectrons. Since this term does not contain \hbar , it is not of quantum mechanical origin.

In order to discuss the origin of the extra term in (1.1.70) we use the vector identity

$$\mathbf{a} \times (\nabla \times \mathbf{a}) = \frac{1}{2} \nabla(\mathbf{a} \cdot \mathbf{a}) - (\mathbf{a} \cdot \nabla)\mathbf{a} \quad (1.1.72)$$

to write $\frac{1}{2} \nabla \mathbf{J}_s^2 = \mathbf{J}_s \times (\nabla \times \mathbf{J}_s) + (\mathbf{J}_s \cdot \nabla) \mathbf{J}_s$. Then, by using the second London equation we can rewrite (1.1.70) as

$$\frac{\partial}{\partial t}(\Lambda \mathbf{J}_s) = \mathbf{E} - \frac{1}{n_s^* q^*} (\mathbf{J}_s \cdot \nabla) (\Lambda \mathbf{J}_s + \frac{1}{n_s^* q^*} (\mathbf{J}_s \times \mathbf{B})). \quad (1.1.73)$$

Fritz London (1900 -1954):

Fritz London was born on March 7, 1900 in Breslau, Germany (now Wroclaw, Poland). He was a German-American physicist who, with Walter Heitler, devised (1927) the first quantum mechanical treatment of the hydrogen molecule. London was educated at the universities of Bonn, Frankfurt, Göttingen, Munich (Ph.D., 1921), and Paris. He was a Rockefeller research fellow at Zürich and Rome and a lecturer at the University of Berlin. From 1933 to 1936 he was a research fellow at the University of Oxford and then went to the University of Paris as master and director of research.

In 1939 he immigrated to the United States to become professor of theoretical chemistry at Duke University, Durham, N.C., and from 1953 he was James B. Duke professor of chemical physics there. He became a U.S. citizen in 1945. His publications include two volumes on Superfluids (1950, 1954).

London's theory of the chemical binding of homopolar molecules marked the beginning of modern quantum mechanical treatment of the hydrogen molecule and is considered one of the most important advances in modern chemistry. With his brother, Heinz London, he developed (1935) the phenomenological theory of superconductivity, providing a new foundation for the understanding of molecular forces and clarifying the connection between pure quantum phenomena and many of the most striking facts of chemistry.

London died on March 30, 1954, at Durham, N.C., USA.



With $\frac{d}{dt}(\Lambda \mathbf{J}_s) = \frac{\partial}{\partial t}(\Lambda \mathbf{J}_s) + (\mathbf{v}_s \cdot \nabla)(\Lambda \mathbf{J}_s)$ and $\mathbf{J}_s = n_s^* q^* \mathbf{v}_s$ we obtain

$$m^* \frac{d\mathbf{v}_s}{dt} = q^* \mathbf{E} + q^* \mathbf{v}_s \times \mathbf{B} , \quad (1.1.74)$$

This expression corresponds to the Lorentz's law. From this we can conclude that

- the nonlinear first London equation results from the Lorentz's law and the second London equation. Therefore, (1.1.70) must be the exact form of the expression describing the phenomenon of zero dc resistance in superconductors.
- The first London equation is derived using the second London equation. This shows that the Meißner-Ochsenfeld effect is the more fundamental property of superconductors than the vanishing dc resistance.²⁰

Since the nonlinear first London equation represents the correct expression the question arises, whether conclusions derived from the more frequently used linear London equation (1.1.71) are wrong. Fortunately, the answer is no, since in most cases the nonlinear term can be neglected. However, one has to be aware that we cannot always neglect the nonlinear term. In some cases it even plays an important role.

In order to elucidate the relevance of the nonlinear term in the first London equation we can state the following:

1. Situations dealing with superconductors in an applied magnetic field (e.g. slab in a parallel field) we usually can treat without using the first London equation. Electric fields are not important in this case. They are derived using Faraday's law after having calculated the magnetic fields and the corresponding currents. The first London equation only would yield small corrections to the supercurrent density distribution.

²⁰Since the vanishing dc resistance has been discovered already in 1911, whereas the Meißner-Ochsenfeld effect was found only in 1933, the phenomenon was not denoted as "superdiamagnetism" but as superconductivity.

2. It is evident from eq.(1.1.70) that the nonlinear term can always be neglected if

$$|\mathbf{E}| \gg \left| \frac{1}{n_s^* q^*} \nabla (\Lambda \mathbf{J}_s^2) \right|. \quad (1.1.75)$$

Assuming that the spatial variation of the supercurrent occurs on a length scale ℓ , we have $\nabla \cdot \mathbf{J}_s \sim J_s / \ell$. Then, the condition can be written as

$$|\mathbf{E}| \gg |\mathbf{v}_s| \left| \frac{\Lambda \mathbf{J}_s}{\ell} \right|. \quad (1.1.76)$$

With the same assumption we obtain

$$\left| \frac{\Lambda \mathbf{J}_s}{\ell} \right| \sim |\mathbf{B}| \quad (1.1.77)$$

from the second London equation. As a result, we obtain the condition

$$|\mathbf{E}| \gg |\mathbf{v}_s| |\mathbf{B}| \quad (1.1.78)$$

for neglecting the nonlinear term. This is not surprising, since this condition is equivalent to the usually made assumption that the magnetic contribution to the Lorentz's law can be neglected compared the electric one in deriving the first London equation.

Additional Topic: The London Gauge

Although we usually keep all expressions gauge invariant, i.e. they hold in all gauges, in some cases it is convenient to use a special gauge. If the macroscopic wavefunction is single valued (this is the case for a simply connected superconductor containing no flux) we can choose $\chi(\mathbf{r}, t)$ so that $\theta = \theta' - \frac{q^*}{m^*} \chi = 0$ everywhere. This is sometimes called the rigid gauge, since the phase of ψ never changes and therefore $\hbar \nabla \theta = 0$ when we switch on a magnetic field or introduce a finite supercurrent. Hence (1.1.65) reads

$$\Lambda \mathbf{J}_s = -\mathbf{A}(\mathbf{r}, t). \quad (1.1.79)$$

Frequently we also have $\nabla \cdot \mathbf{J}_s = 0$ (this is the case when no supercurrent is converted into a normal current or vice versa). Then we obtain from (1.1.79)

$$\nabla \cdot \mathbf{A} = 0 \quad \text{and} \quad A_n = \Lambda J_{sn}. \quad (1.1.80)$$

Here, the second relation is just a boundary condition. A_n is the component of \mathbf{A} normal to the boundary and J_{sn} is the supercurrent density normal to the boundary. A vector potential which satisfies the conditions (1.1.80) is said to be in the **London gauge**. Together with $\nabla \times \mathbf{A} = \mathbf{B}$ the conditions of the London gauge fix \mathbf{A} unambiguously. One can easily show that in the London gauge the vector potential obeys the equations $\nabla^2 \mathbf{A} = 0$ and $\nabla^2 \mathbf{A} = \mathbf{A}/\lambda_L^2$ outside and inside the superconductor, respectively.

We briefly use the London gauge to compare the perfect diamagnetism of a superconductor to the diamagnetism of a single atom. When we are placing an atom in a uniform magnetic field \mathbf{B} , the electrons perform a Larmor precession with angular frequency $eB/2m_e$ giving the atom a diamagnetic moment. We can describe the uniform field by the vector potential $\mathbf{A} = \frac{1}{2}\mathbf{B} \times \mathbf{r}$, which is in the London gauge. For weak fields we can neglect the effect of the magnetic field on the wavefunctions (for the superconductor

we say the wavefunction is rigid). Then, the formal angular momentum quantum numbers stay the same and locally the canonical momentum is not changed. However, since $\mathbf{p} = m_e \mathbf{v} - e\mathbf{A}$, the electrons of the atom have now an extra local velocity $e\mathbf{A}/m_e$ in the same way as in the superconductor. For the atom the velocity is $(e\mathbf{B}/2m_e) \times \mathbf{r}$, i.e. the expected precession velocity. The only difference between the atom and the superconductor is the fact that for the atom the diamagnetic screening current is much too small to screen the applied field on the atomical length scale, whereas in the superconductor it is strong enough to restrict the field to a region within a penetration depth λ_L from the surface.

1.2 Flux Quantization

In the previous section we have shown that the macroscopic quantum model of superconductivity is consistent with the phenomenological laws deduced using classical reasoning. We now examine the quantum mechanical consequences of the model. The first example is ***fluxoid quantization*** in multiply connected superconductors (see Fig. 1.3).

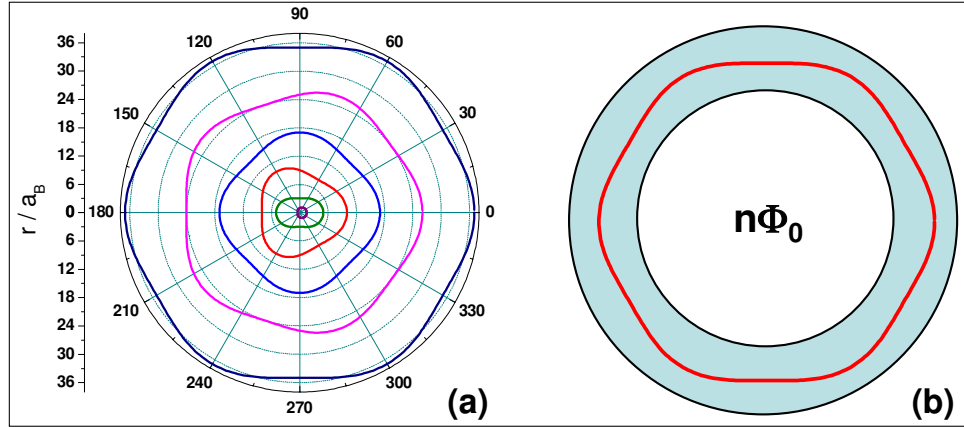


Figure 1.3: Stationary quantum states: (a) The standing electron wave around the nucleus of an atom at $r = 0$ resulting in the Bohr-Sommerfeld quantization of the angular momentum. (b) The standing wave of the macroscopic wave function representing the superconducting state in a superconducting cylinder resulting in flux quantization.

We start our discussion with a simple ***Gedanken*** experiment. We take a superconducting ring and generate (just by magnetic induction) a supercurrent in the ring. Since the superconductor has zero dc resistance this supercurrent should be stable, that is, the considered system is in a stationary state. Of course we can change this state by changing the induction process generating the supercurrent. Classically we would expect that in this way we can generate arbitrary supercurrents in the ring. However, after having learnt that we have to consider the superconductor as a macroscopic quantum system, we have to revise the expectation. The quantum mechanical treatment of microscopic systems teaches us that stationary states are determined by certain quantum conditions. Within Bohr's model for atoms the stationary states for the electrons are determined by the quantization condition for the angular momentum. As shown in Fig. 1.3a this is equivalent to the requirement that the electron wave is not interfering destructively. In the same way we expect a stationary state for the supercurrent along the ring only if the macroscopic wave function describing the whole ensemble of superelectrons is not interfering destructively (see Fig. 1.3b). Therefore, we immediately expect a quantization condition. This has been first supposed by **Fritz London**.²¹ He came to the conclusion that the magnetic flux enclosed by a superconducting ring can only have discrete values given by multiples of a flux quantum Φ_0^L . London suggested the value

$$\Phi_0^L = \frac{h}{e} \simeq 4 \times 10^{-15} \text{ Vs} . \quad (1.2.1)$$

London derived this value for the flux quantum, since he presumed that single electrons are carrying the supercurrent. The fact that Cooper pairs are carrying the supercurrent became clear only after the development of the BCS theory in 1957.²²

Before discussing the experimental observation of flux quantization, we use the macroscopic quantum model of superconductivity to mathematically derive the quantization condition. For simplicity we will

²¹F. London, *Superfluids*, Wiley, New York (1950).

²²J. Bardeen, L.N. Cooper, J.R. Schrieffer, Phys. Rev. **108**, 1175 (1957).

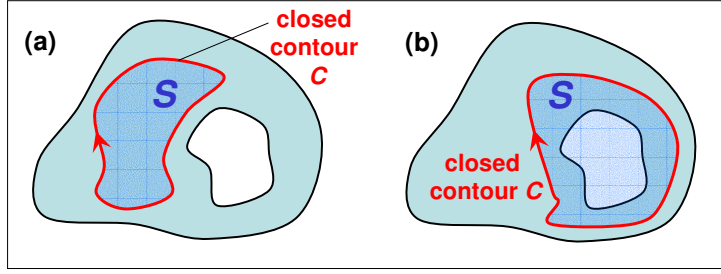


Figure 1.4: Different possibilities for closed contours within a superconducting medium: (a) The path is in a simply connected superconducting region. (b) The path is in a multiply connected region.

assume a homogeneous and isotropic superconductor. We start with the expression (1.1.65) for the supercurrent density

$$\Lambda \mathbf{J}_s = - \left\{ \mathbf{A}(\mathbf{r}, t) - \frac{\hbar}{q^*} \nabla \theta(\mathbf{r}, t) \right\} \quad (1.2.2)$$

and integrate this expression around a closed contour C . From **Stoke's theorem** we know that

$$\oint_C \mathbf{A} \cdot d\mathbf{l} = \int_S (\nabla \times \mathbf{A}) \cdot d\mathbf{s} = \int_S \mathbf{B} \cdot d\mathbf{s} , \quad (1.2.3)$$

where S is the surface defined by the closed contour C (see Fig. 1.4) and \mathbf{B} is the flux density associated with the vector potential \mathbf{A} . Using Stoke's theorem we can rewrite (1.2.2) as

$$\oint_C (\Lambda \mathbf{J}_s) \cdot d\mathbf{l} + \int_S \mathbf{B} \cdot d\mathbf{s} = \frac{\hbar}{q^*} \oint_C \nabla \theta \cdot d\mathbf{l} . \quad (1.2.4)$$

We first evaluate the integral on the right hand side of (1.2.4). We know from the vector calculus that the integral of the gradient of a scalar function along the path defined by points \mathbf{r}_1 and \mathbf{r}_2 is given by

$$\int_{\mathbf{r}_1}^{\mathbf{r}_2} \nabla \theta \cdot d\mathbf{l} = \theta(\mathbf{r}_2, t) - \theta(\mathbf{r}_1, t) . \quad (1.2.5)$$

We see that if $\mathbf{r}_1 \rightarrow \mathbf{r}_2$ such that a closed path is formed the integral is zero. However, in general this is not true, since the specific value of the phase of ψ is not well defined. Indeed there exists an infinite amount of possible phase values, because for integer values of n all values $\theta_n = \theta_0 + 2\pi n$ give the same value of

$$\psi(\mathbf{r}, t) = \sqrt{n_s^*} e^{i(\theta_0 + 2\pi n)} . \quad (1.2.6)$$

That is, although the macroscopic wavefunction ψ is well defined, this is not the case for the phase:

$$\theta(\mathbf{r}, t) = \theta_0(\mathbf{r}, t) + 2\pi n . \quad (1.2.7)$$

The phase is specified only within modulo 2π of its principal value θ_0 ranging in the interval $[-\pi, \pi]$. Since θ_0 is single valued, we obtain for the integral of the phase gradient along a closed contour

$$\oint_C \nabla \theta \cdot d\mathbf{l} = \lim_{\mathbf{r}_2 \rightarrow \mathbf{r}_1} [\theta(\mathbf{r}_2, t) - \theta(\mathbf{r}_1, t)] = 2\pi n . \quad (1.2.8)$$

With this result (1.2.4) becomes

$$\oint_C (\Lambda \mathbf{J}_s) \cdot d\mathbf{l} + \int_S \mathbf{B} \cdot d\mathbf{s} = n \frac{h}{q^*} = n \Phi_0 \quad (1.2.9)$$

with the *flux quantum*

$$\Phi_0 \equiv \frac{h}{|q^*|} = \frac{h}{2e} = 2.067\,833\,636(81) \times 10^{-15} \text{ Vs} . \quad (1.2.10)$$

Here, we have set $|q^*| = 2e$ in giving a value for the flux quantum and have replace n by $-n$ in (1.2.9) with no loss of generality. The quantity Φ_0 represents the flux quantum and is the smallest amount of flux included by the closed contour line.

The consequences of (1.2.9) can be easily seen by considering Fig. 1.4:

1. We first consider the case (a), where the surface S defined by the contour C is in a simply connected superconducting region (see Fig. 1.4a). We have to recall that we are performing the integration along the closed contour by imagining a line integration between two points \mathbf{r}_1 and \mathbf{r}_2 including the limit $\mathbf{r}_2 \rightarrow \mathbf{r}_1$. Since (1.2.9) holds for all contour lines, we also have to include the case where the size of the contour just has shrunk to zero. In this case both integrals in (1.2.9) vanish and we find $n = 0$ for the simply connected superconductor.²³ This result is expected since the condition $n = 0$ just yields the integral form of the second London equation.
2. We next consider the case of a multiply connected superconductor as illustrated in Fig. 1.4b. Here, the important point is that the surface S defined by the contour C now contains both superconducting and nonsuperconducting regions (in the most simple case the nonsuperconducting region is just a hole). Thus, if we are closing the line integral by applying the limit $\mathbf{r}_2 \rightarrow \mathbf{r}_1$, we somehow have built in a “memory” in our path: We know that we have enclosed a nonsuperconducting region into the contour. In other words, the phases at the points \mathbf{r}_2 and \mathbf{r}_1 are now distinct. Therefore, although the principal value of the two phases is the same, the difference between them is $2\pi n$.

1.2.1 Flux and Fluxoid Quantization

Fluxoid Quantization

The left-hand side of (1.2.9) is denoted as the *fluxoid* and hence this equation is a statement of *fluxoid quantization*. Note that the externally applied magnetic flux is not necessarily quantized. However, we have to take into account *both* the external applied flux *and* the flux generated by the induced supercurrent in our calculation. Then, the total flux threading the multiply connected superconductor cannot be arbitrary but must have discrete values corresponding to integer multiples of the flux quantum.

Flux Quantization

We now discuss a superconducting cylinder as sketched in Fig. 1.5. We assume that the wall of the cylinder is much thicker than the London penetration depth λ_L . If we apply a small magnetic field (much

²³Of course this is only true, if there are no singularities in the supercurrent density \mathbf{J}_s or the flux density \mathbf{B} .

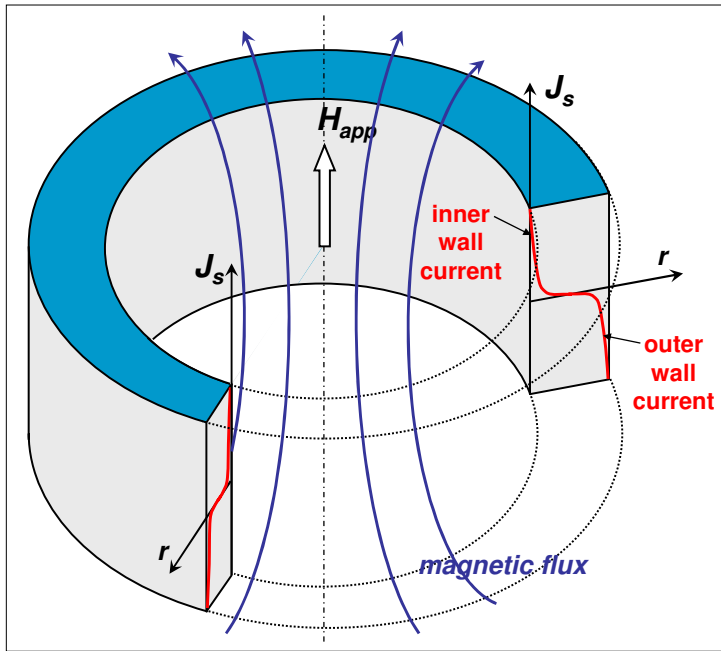


Figure 1.5: Sketch of a superconducting cylinder in the presence of an applied magnetic field along the cylinder axis. Also shown is the expected supercurrent distribution in the wall of the cylinder. For a wall thickness much larger than the superconducting screening length λ_L , the supercurrent density in the center of the wall is negligible.

smaller than the critical field of the superconducting material) after cooling down the cylinder below the transition temperature of the superconducting material, no flux will thread the superconducting cylinder. There are screening currents flowing on the outer surface of the cylinder wall screening the magnetic field.

The more interesting case is obtained by applying the magnetic field during cooling down. In this case below the transition temperature a screening current flows on the outer surface of the cylinder to expel the applied magnetic field from the superconducting material. In the same way, a screening current with opposite direction is flowing on the inner surface of the cylinder to keep the applied magnetic field outside the superconducting material.

We now use (1.2.9) to analyze the amount of flux trapped in the superconducting cylinder. In the classical case the currents flowing on the inner surface would be constraint only by Ampère's law. Then, classically we could trap arbitrary amounts of magnetic flux in the cylinder by simply varying the magnetic field applied during cooling down. However, in an exact quantum mechanical treatment we have to satisfy also the fluxoid quantization condition (1.2.9). Since the thickness of the superconducting material is much larger than the London penetration depth λ_L , we can choose a closed contour deep inside the superconducting material, where in very good approximation we have $\mathbf{J}_s = 0$. The fluxoid quantization condition then simplifies to

$$\int_S \mathbf{B} \cdot d\mathbf{s} = n \Phi_0 . \quad (1.2.11)$$

That means, if we are removing the applied magnetic field after cooling down, the magnetic flux trapped in the cylinder exactly is an integer multiple of the flux quantum. Therefore, (1.2.11) can be considered as a statement of ***flux quantization***.

Flux Trapping

We briefly discuss the question why the superconducting ring does not expel the magnetic flux but keeps it trapped inside the ring after switching off the magnetic field. The answer can be derived from the 1. London equation saying that the electric field deep inside the body of the superconducting cylinder must be zero, since $\partial \mathbf{J}_s / \partial t = 0$ there. This applies also for situations where the supercurrent in the ring is changing, since this supercurrent is only flowing on the surface within λ_L (see Fig. 1.5). With $\mathbf{E} = -\partial \mathbf{A} / \partial t - \nabla \phi = 0$ we can obtain

$$\oint \mathbf{E} \cdot d\mathbf{l} = -\frac{\partial}{\partial t} \oint \mathbf{A} \cdot d\mathbf{l} = -\frac{\partial}{\partial t} \int_S \mathbf{B} \cdot d\mathbf{s} = -\frac{\partial \Phi}{\partial t}, \quad (1.2.12)$$

where Φ is the magnetic flux enclosed within the contour. Taking the contour deep inside the superconductor we have $\mathbf{E} = 0$ and hence $\frac{\partial \Phi}{\partial t} = 0$. That is, the flux enclosed in the cylinder has to stay constant. The supercurrents flowing on the surface of the cylinder are adjusting themselves so that the flux in the ring is not changing, i.e. the flux stays trapped.

1.2.2 Experimental Proof of Flux Quantization

In 1961 the flux quantization in superconducting cylinders has been experimentally proved by two groups, **R. Doll** and **M. Nähbauer** at the Walther-Meißner-Institute in Munich and **B. S. Deaver** and **W. M. Fairbank** at Stanford.^{24,25} These very difficult experiments not only have demonstrated the quantization of magnetic flux in a superconducting cylinder but also for the first time proved the existence of Cooper pairs with charge $q^* = 2e$ thereby confirming the prediction of the microscopic theory developed by **John Bardeen**, **Leon Cooper** and **Robert Schrieffer** (BCS-theory) in 1957.

The aim of the experiments was to show that the flux enclosed by a superconducting cylinder of wall thickness $d \gg \lambda_L$ can have only discrete values $\Phi_n = n \cdot \Phi_0$. In order to do so different amounts of magnetic flux have to be frozen in during cooling down the cylinder in an applied magnetic field B_{cool} and then the amount of trapped flux has to be measured with a precision much better than a single flux quantum. In order to obtain a large relative change of the magnetic flux from measurement to measurement only small values of B_{cool} have to be used resulting in a small number of trapped flux quanta. Since $\Phi = B \cdot S$, both small applied fields and a small cross-sectional area S , resp. diameter d of the cylinder have to be used. Note that for a cylinder area of $S = 1 \text{ mm}^2$ a flux density B of only about 10^{-9} T is required to generate one flux quantum. This flux density is much smaller than that due to the earth magnetic field $B_e \simeq 2 \times 10^{-5} \text{ T}$.

Both experimental groups were using small hollow cylinders with an outer diameter of the order of $10 \mu\text{m}$. For such diameter, a flux density of $B \simeq 2 \times 10^{-5} \text{ T}$ is required to generate one flux quantum $\Phi_0 = 2 \times 10^{-15} \text{ T m}^2$. Since this flux density is of the same order of magnitude as the one due to the earth magnetic field, a careful shielding of the earth magnetic field and other perturbing fields was necessary.

In the experiment of Doll and Nähbauer a hollow Pb cylinder was used (see Fig. 1.6). The cylinder was obtained by evaporating Pb on a quartz fiber. In this cylinder they were trapping magnetic flux by cooling down the sample below the transition temperature in a small magnetic field applied parallel to the axis of the cylinder. The magnitude of the trapped magnetic flux has been determined by measuring the torque

²⁴R. Doll, M. Nähbauer, *Experimental Proof of Magnetic Flux Quantization in a Superconducting Ring*, Phys. Rev. Lett. **7**, 51 (1961)

²⁵B.S. Deaver, W.M. Fairbank, *Experimental Evidence for Quantized Flux in Superconducting Cylinders*, Phys. Rev. Lett. **7**, 43 (1961).

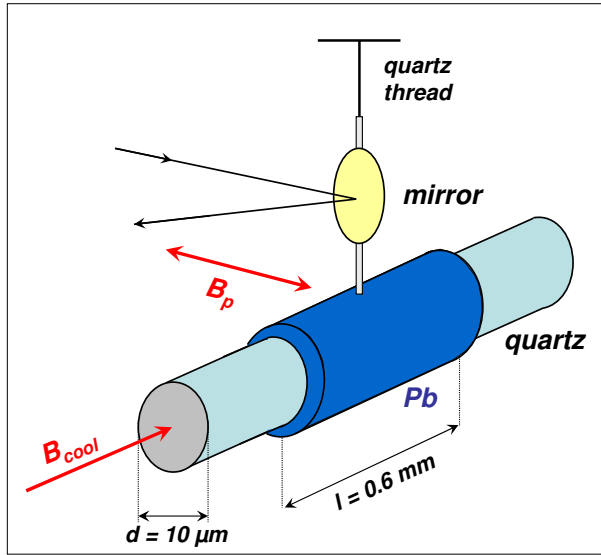


Figure 1.6: Sketch of the experimental configuration used by Doll and N  bauer in 1961 for the determination of the flux quantization in a superconducting cylinder (according to R. Doll, M. N  bauer, Phys. Rev. Lett. 7, 51 (1961)).

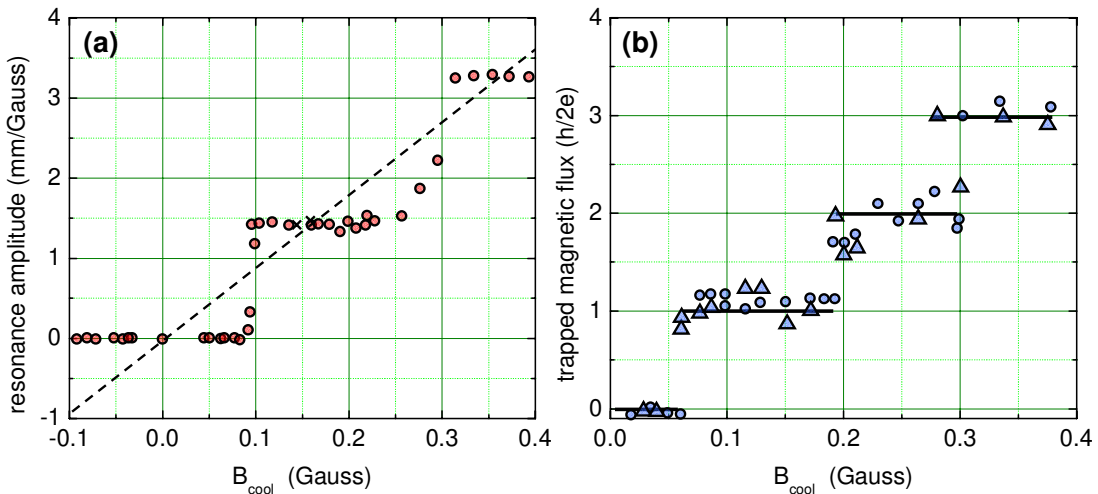


Figure 1.7: Magnetic flux trapped in a superconducting cylinder as a function of the applied magnetic flux density during cooling down the cylinder below the superconducting transition temperature. (a) Experiment by Doll and N  bauer (according to R. Doll, M. N  bauer, Phys. Rev. Lett. 7, 51 (1961) and Zeitschrift f  r Physik **169**, 526 (1962)). (b) Experiment by Deaver and Fairbank (according to B. S. Deaver, W. M. Fairbank, Phys. Rev. Lett. 7, 43 (1961)).

$\mathbf{D} = \mu \times \mathbf{B}_p$ due to a probe field B_p applied perpendicular to the cylinder axis. Here, μ is the magnetic moment of the trapped magnetic flux. The measurement has been done by hanging up the cylinder using a thin quartz thread. The rotation of the cylinder has been measured by shining light on a mirror attached to the quartz thread. Since the torque is very small, static measurements of the torque could not be performed. Therefore, Doll and N  bauer used a so-called self-resonance method. In this method they were using the small torque created by the probe field B_p for the excitation of a torque vibration of the system. In case of resonance the resulting resonance amplitude is becoming large enough to be measured. The resonance amplitude is proportional to the exciting torque, which in turn is proportional to the flux trapped in the cylinder. Of course, in order to excite the vibration the direction of the probe field \mathbf{B}_p has to be switched at the resonance frequency.

In the experiment by Deaver and Fairbank a tiny Sn tube with a length of about 0.9 mm, an inner diameter of $13\ \mu\text{m}$ and a wall thickness of $1.5\ \mu\text{m}$ was used. The cylinder was vibrated in the axial direction at a frequency of about 100 Hz and the resulting rf signal was detected via a pair of pick-up coils. The experimental results of both experiments are shown in Fig. 1.7. The results of both experiments were essentially identical and convincing. Although the cylinders were cooled down in different magnetic fields, the net magnetic flux trapped in the cylinder always occurred in quantized amounts. In this way the two groups experimentally demonstrated the limitations of a purely classical treatment of superconductivity.

1.2.3 Additional Topic: Rotating Superconductor

We consider the interesting case when a superconducting cylinder is rotating at an angular frequency Ω (see Fig. 1.8). In this case we have to modify our analysis given in Section 1.1.3. We have to rewrite Faraday's law as

$$\nabla \times \mathbf{B} = \mu_0 \mathbf{J} = \mu_0 n_s^* q^* (\mathbf{v}_s - \mathbf{v}_\Omega) = \mu_0 (\mathbf{J}_s - n_s^* q^* \mathbf{v}_\Omega) . \quad (1.2.13)$$

Here, \mathbf{J} is the net current density and $\mathbf{v}_s - \mathbf{v}_\Omega$ is the velocity of the superfluid relative to the velocity \mathbf{v}_Ω of the positively charged lattice. We can take the curl of (1.2.13) and take into account that $\nabla \times \mathbf{v}_\Omega = 2\Omega$ to arrive at

$$\nabla \times \nabla \times \mathbf{B} = \mu_0 \nabla \times \mathbf{J}_s - \mu_0 n_s^* q^* \nabla \times \mathbf{v}_\Omega = \frac{\mu_0}{\Lambda} \left(\nabla \times (\Lambda \mathbf{J}_s) - \frac{2m^*}{q^*} \Omega \right) . \quad (1.2.14)$$

With $\nabla \times \nabla \times \mathbf{B} = -\nabla^2 \mathbf{B}$, $\mu_0/\Lambda = 1/\lambda_L^2$, and the 2. London equation $\nabla \times (\Lambda \mathbf{J}_s) = -\mathbf{B}$ we obtain

$$\nabla^2 \mathbf{B} = \frac{\mathbf{B} - \frac{2m^*}{q^*} \Omega}{\lambda_L^2} = \frac{\mathbf{B} - \mathbf{B}_L}{\lambda_L^2} . \quad (1.2.15)$$

Here, $\mathbf{B}_L = \frac{2m^*}{q^*} \Omega$ is the **London field**.

The modified screening equation shows that the field inside the superconductor does no longer decay to zero but to the London field \mathbf{B}_L . That means that there is a finite field in a rotating superconductor. We can understand this from our discussion on page 22. The additional field is just required to give the electron systems a precession equal to the rotating lattice. For an observer in the reference frame rotating with the superconductor, the effect of this field is to compensate for the effect of the Coriolis force acting on the electrons. That means that for such an observer the dynamics of the electrons appear to be unaffected by the rotation.

Since the London field is spatially uniform, it follows from Ampère's rule that there is no net current flowing deep inside the superconductor. However, if there is no external magnetic field ($\mathbf{B} = 0$), there must be a screening current flowing on the outside surface of the superconductor (see Fig. 1.8).

We now discuss how the flux quantization is affected by the rotation. We have to replace eq.(1.2.9) by

$$\oint_C \Lambda(\mathbf{J}_s - n_s^* q^* \mathbf{v}_\Omega) \cdot d\mathbf{l} + \int_S \mathbf{B} \cdot d\mathbf{s} = n \Phi_0 \quad (1.2.16)$$

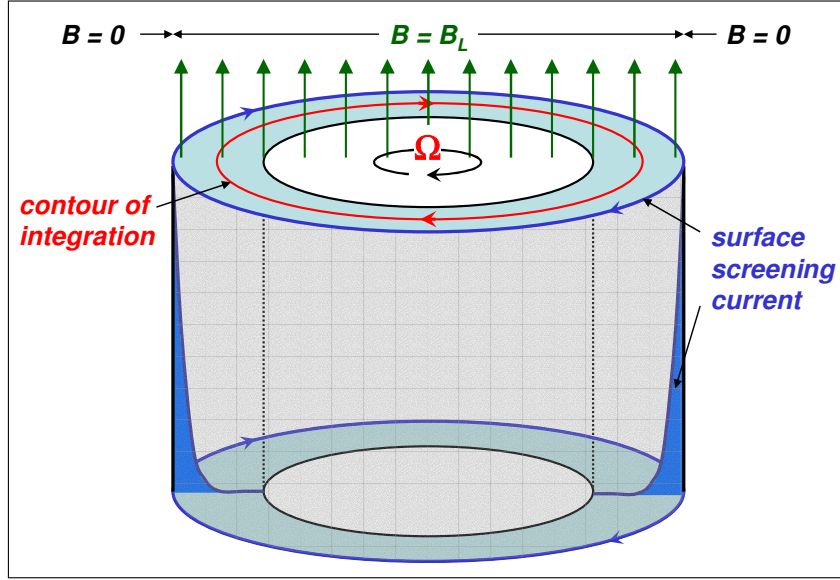


Figure 1.8: Magnetic fields and currents in a superconducting cylinder rotating at angular frequency Ω . The London field \mathbf{B}_L fills the superconductor and the hole. A corresponding screening current flows only on the outer surface of the cylinder and decays exponentially inside the cylinder within the decay length λ_L .

For a contour deep inside the superconductor, where $\mathbf{J}_s = 0$, we obtain²⁶

$$\Phi = n\Phi_0 + 2\frac{m^*}{q^*} \Omega \cdot \mathbf{S}, \quad (1.2.17)$$

where \mathbf{S} is the area enclosed by the contour of integration. We see that the hole contains the usual quantized flux plus a non-quantized term due to the London field filling the hole as well as the bulk superconductor. For $n = 0$ the field in the hole is the same as in the bulk superconductor so that no screening current flows on the inner surface of the superconducting cylinder.²⁷

²⁶We use $\oint \mathbf{v}_\Omega \cdot d\mathbf{l} = \int_S (\nabla \times \mathbf{v}_\Omega) \cdot d\mathbf{s} = 2\Omega \cdot \mathbf{S}$.

²⁷In principle the field inside the hole should be detectable using e.g. a SQUID detector. However, a detailed analysis shows that the SQUID can only detect the relative angular velocities of the cylinder and the SQUID detector making the experimental setup difficult (see e.g. R.M. Brady, IEEE Trans. Magn. **MAG 17**, 861 (1981)).

1.3 Josephson Effect

In section 1.2 we have discussed the fluxoid quantization in multiply connected superconductors as the first consequence of the macroscopic quantum nature of superconductivity. It became evident that this phenomenon is a direct manifestation of the macroscopic quantum coherence of the superconducting state. In this section we discuss the ***Josephson effect*** as a second coherent phenomenon. The Josephson effect has been predicted by **Brian D. Josephson** in 1962 and is equally important as flux quantization.²⁸ Today, the Josephson effect is used for many applications of superconductivity in electronics, sensors and high frequency devices. The Josephson effect is observed, if two superconductors are weakly connected by an electrical contact. Such contact can be established in many different ways. Prominent examples are tunneling barriers, point contacts or normal conducting layers connecting the two superconducting electrodes. In the following we will denote such contact as ***Josephson junction***. The initial theoretical work by Josephson has considered only superconductor-insulator-superconductor (SIS) junctions.

Suppose we consider a SIS contact between two identical superconductors as sketched in Fig. 1.9. For a normal metal-insulator- normal metal (NIN) tunnel junction it is well known that for a thin enough tunneling barrier the normal electrons can tunnel through the barrier with the tunneling current density decaying exponentially with increasing barrier thickness. Now, for a SIS tunnel junction at zero temperature we do no longer have normal electrons at the Fermi level. Therefore, we expect that there is no tunneling current as long as the applied voltage V is smaller than twice the energy gap voltage $2\Delta/e$. For $eV \geq 2\Delta$ Cooper pairs can be broken up into to normal electrons, which in turn can tunnel through the barrier. As will be discussed later, this effect is indeed observed.

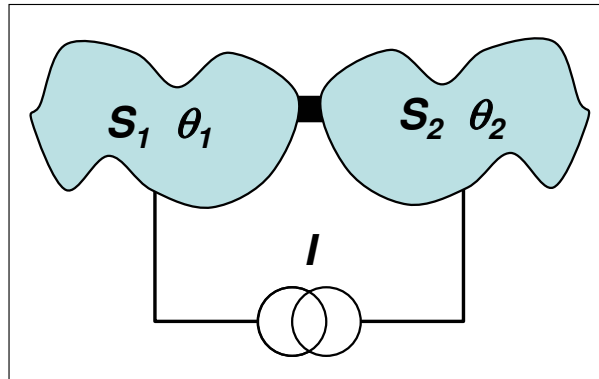


Figure 1.9: The Josephson effect: coherent phenomenon for two weakly coupled superconductors S_1 and S_2 with wave functions $\psi_1 = \sqrt{n_s^{*1}} e^{i\theta_1}$ and $\psi_2 = \sqrt{n_s^{*2}} e^{i\theta_2}$.

We also have to ask ourselves, whether or not it is possible for Cooper pairs to tunnel through a thin insulating barrier. The consensus in 1962 was that such events would not happen often enough to be measurable. The reason for that seems to be evident. Even the probability of a single electron to tunnel through a thin barrier is very small. Typically, the tunneling probability is $p_t \lesssim 10^{-4}$. Then, for a Cooper pair one would expect a probability p_t^2 , which again is orders of magnitude smaller. However, in 1962 Brian Josephson changed this common reasoning. He discovered that the probability of a Cooper pair tunneling through the barrier is the same as that for a single electron. The reason is that the tunneling of Cooper pairs is a coherent process. That is, we should not consider the Cooper pair as two incoherent electron waves leaking through the barrier. Instead, it is the macroscopic wave function describing

²⁸Brian D. Josephson, *Possible new effects in superconductive tunnelling*, Phys. Lett. **1**, 251–253 (1962).

For his theoretical predictions of the properties of a supercurrent through a tunnel barrier, in particular those phenomena which are generally known as the Josephson effects, Brian Josephson received the Nobel Price in physics in 1973 together with **Leo Esaki** and **Ivar Giaever**.

Brian David Josephson (born 1940):

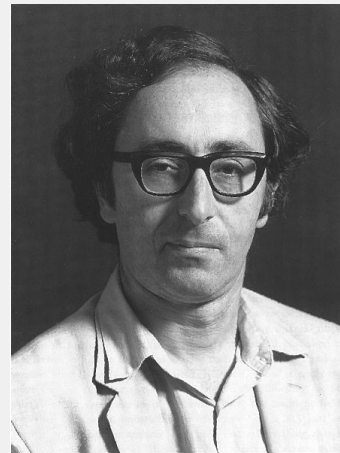
Brian David Josephson was born on January 4, 1940 in Cardiff, Glamorgan, Wales. He is a British physicist whose discovery of the Josephson effect while a 22-year-old graduate student won him a share (with Leo Esaki and Ivar Giaever) of the 1973 Nobel Prize for Physics.

He entered Trinity College, Cambridge, in pursuit of an education in physics and received his bachelor's (1960) and master's and Ph.D. degrees (1964) there, publishing his first work while still an undergraduate. It dealt with certain aspects of the special theory of relativity and the Mößbauer effect. He was elected a fellow of Trinity College in 1962. He was a brilliant and assured student; one former lecturer recalled a special need for precision in any presentation to a class that included Josephson – otherwise, the student would confront the instructor politely after class and explain the mistake.

While still an undergraduate, Josephson became interested in superconductivity, and he began to explore the properties of a junction between two superconductors that later came to be known as a Josephson junction. Josephson extended earlier work in tunneling, the phenomenon by which electrons functioning as radiated waves can penetrate solids, done by Esaki and Giaever. He showed theoretically that tunneling between two superconductors could have very special characteristics, e.g., flow across an insulating layer without the application of a voltage. If a voltage is applied, the current stops flowing and oscillates at high frequency. This was the Josephson effect. Experimentation confirmed it, and its confirmation in turn reinforced the earlier BCS theory of superconductor behavior. Applying Josephson's discoveries with superconductors, researchers at International Business Machines Corporation had assembled by 1980 an experimental computer switch structure, which would permit switching speeds faster than those possible with conventional silicon-based chips, increasing data processing capabilities by a vast amount.

He went to the United States to be a research professor at the University of Illinois in 1965-66 and in 1967 returned to Cambridge as assistant director of research. He was appointed reader in physics in 1972 and professor of physics in 1974. He was elected a fellow of the Royal Society in 1970.

A few years before the Nobel award, Josephson grew interested in the possible relevance of Eastern mysticism to scientific understanding. In 1980 he and V.S. Ramachandran published an edited transcript of a 1978 international symposium on consciousness at Oxford under the title *Consciousness and the Physical World*.



the entire ensemble of superconducting electrons that is tunneling through the barrier. Only one year later, **Philip W. Anderson** and **John M. Rowell**²⁹ had experimentally confirmed the prediction of Brian Josephson, which again is a direct consequence of the macroscopic quantum nature of the superconducting state.

We can consider two weakly coupled superconductors as sketched in Fig. 1.9 also as a molecule. In the same way as we obtain molecular binding due to the overlap of the wavefunctions of the electrons of two hydrogen atoms, the overlap of the macroscopic wavefunctions of the two superconductors results in a finite binding energy. This binding energy is called the **Josephson coupling energy** and will be derived later in chapter 2.

1.3.1 The Josephson Equations

In deriving the Josephson equations we follow general arguments introduced by **L.D. Landau** and **E.M. Lifschitz**.³⁰

²⁹P. W. Anderson and J. M. Rowell, *Probable Observation of the Josephson Superconducting Tunneling Effect*, Phys. Rev. Lett. **10**, 230–232 (1963).

³⁰L.D. Landau, E.M. Lifschitz, *Lehrbuch der Theoretischen Physik*, Bd. IX, Akademie-Verlag, Berlin (1980).

First Josephson Equation: current-phase relation

We first speculate what determines the supercurrent between two weakly connected superconductors. It certainly can depend on the Cooper pair densities $|\psi_1|^2 = n_{s,1}^*$ and $|\psi_2|^2 = n_{s,2}^*$ in the junction electrodes. However, since the coupling between the two superconductors is weak and, hence, the supercurrent density between them is small, we can assume that the supercurrent density between the two junction electrodes is not changing $|\psi|^2$. However, although the amplitude of the wave functions in the electrodes does not play a role, the supercurrent density certainly is expected to depend on the phase of the wave functions.

We already have learnt that the supercurrent density in a bulk superconductor depends on the gauge invariant phase gradient (compare (1.1.50) and (1.1.62)) as

$$J_s(\mathbf{r}, t) = \frac{q^* n_s^* \hbar}{m^*} \left[\nabla \theta(\mathbf{r}, t) - \frac{2\pi}{\Phi_0} \mathbf{A}(\mathbf{r}, t) \right] = \frac{q^* n_s^* \hbar}{m^*} \gamma(\mathbf{r}, t) . \quad (1.3.1)$$

We simplify our discussion by assuming that (i) the current density can be considered homogeneous. We will see later that this assumption can be always made if the junction area is small enough. We are now applying expression (1.3.1) to the case of two weakly connected superconductors. Doing so, we further assume that (ii) the phase gradient γ is varying negligibly in the superconducting electrodes (see Fig. 1.10). This is always a good assumption as long as the Cooper pairs density n_s^* in the electrodes is much larger than in the coupling region as shown in Fig. 1.10. Since \mathbf{J}_s is the same in the electrodes and the junction area (current conservation), according to (1.3.1) the gauge-invariant phase gradient is negligibly small in the electrodes compared to the junction region. Then, we can replace the gauge invariant phase gradient $\gamma = \nabla \theta - \frac{2\pi}{\Phi_0} \mathbf{A}$ just by the **gauge-invariant phase difference** φ given by

$$\begin{aligned} \varphi(\mathbf{r}, t) &= \int_1^2 \gamma(\mathbf{r}, t) = \int_1^2 \left(\nabla \theta - \frac{2\pi}{\Phi_0} \mathbf{A} \right) \cdot d\mathbf{l} \\ &= \theta_2(\mathbf{r}, t) - \theta_1(\mathbf{r}, t) - \frac{2\pi}{\Phi_0} \int_1^2 \mathbf{A}(\mathbf{r}, t) \cdot d\mathbf{l} . \end{aligned} \quad (1.3.2)$$

We note that the integration path is along the direction of current (see Fig. 1.11). That is, for a SIS-type Josephson junction the path is across the insulating barrier from the superconductor one with phase θ_1 to the superconductor 2 with phase θ_2 . For the geometry of Fig. 1.11 the integration path is from $-d/2$ to $+d/2$ and the differential line element is $d\mathbf{l}$.

According to (1.3.1) we expect the supercurrent density J_s to be a function only of φ , that is, $J_s = J_s(\varphi)$. Actually, according to (1.3.1) we expect $J_s \propto \varphi$. However, we have to take into account that any phase change of 2π in the wave functions of the junction electrodes results in the same wave function $\psi_{1,2}$. From this we can conclude that $J_s(\varphi)$ should not be a linear but a 2π -periodic function:

$$J_s(\varphi) = J_s(\varphi + n \cdot 2\pi) . \quad (1.3.3)$$

Finally, in the absence of any current the phase gradient must be zero and both electrodes form a single superconductor with a common phase. That is, in this case we have $\theta_1 = \theta_2$ and hence

$$J_s(0) = J_s(n \cdot 2\pi) = 0 . \quad (1.3.4)$$

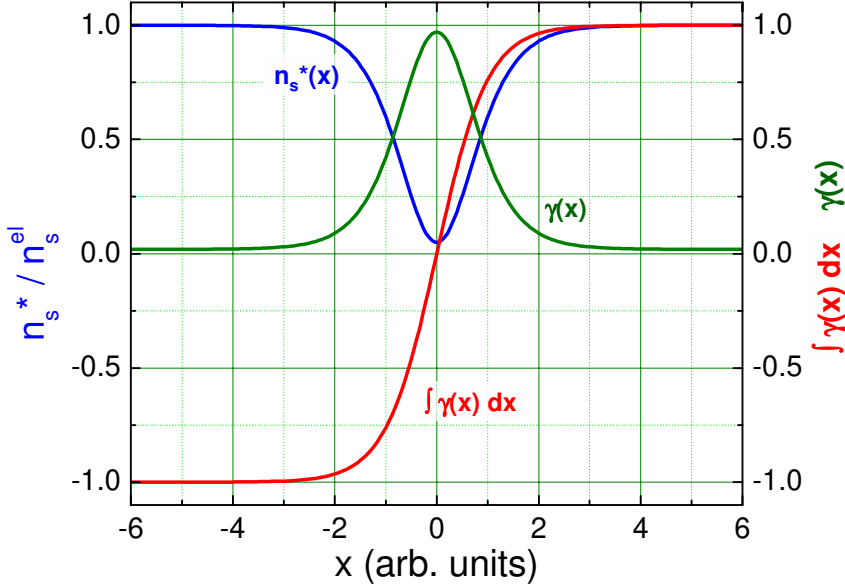


Figure 1.10: Sketch of the variation of the Cooper pair density n_s^* and the gauge-invariant phase gradient γ across a one-dimensional Josephson junction extending in x -direction. Also shown is the integral $\int \gamma dx$ of the gauge invariant phase gradient.

Summarizing our discussion we can conclude that the supercurrent density between the two junction electrodes in the most general case should have the form³¹

$$J_s(\varphi) = J_c \sin \varphi + \sum_{m=2}^{\infty} J_m \sin(m\varphi) . \quad (1.3.5)$$

Here, J_c is the ***critical or maximum Josephson current density***, which is determined by the coupling strength between the two junction electrodes. Expression (1.3.5) is the general formulation of the ***1. Josephson equation***. It also is denoted as the ***current-phase relation***, since it relates the supercurrent density to the phase difference. Rigorous theoretical treatment shows that in most cases (in particular in the case of weak coupling) the second term on the right hand side can be neglected. Then, (1.3.5) obtains the form

$$J_s(\varphi) = J_c \sin \varphi , \quad (1.3.6)$$

which was derived by Josephson in his original paper for the particular case of an insulating barrier. Here, due to the rapid decay of the wave function in the insulator, weak coupling was explicitly assumed. We will discuss this case in more detail in section 1.3.2.

The basic essence of (1.3.6) can be summarized as follows:

The supercurrent density through a Josephson junction varies sinusoidally with the phase difference $\varphi = \theta_2 - \theta_1$ across the junction in the absence of any scalar and vector potentials.

³¹In general we could write J_s as a Fourier series of sine and cosine terms. However, eq.(1.3.4) requires that all the coefficients of the cosine terms vanish. The same conclusion can be drawn from the requirement of time reversal symmetry. Upon inversion of time, the Josephson current flows in opposite direction. Furthermore, since the time evolution of the macroscopic wavefunction is given by $\exp(-i\omega t)$, inversion of time requires that we are inverting the sign of the phase of the wavefunction. Then, time-invariance of the Josephson current requires that $J_s(\gamma) = -J_s(-\gamma)$ what excludes all cosine terms in a Fourier series.

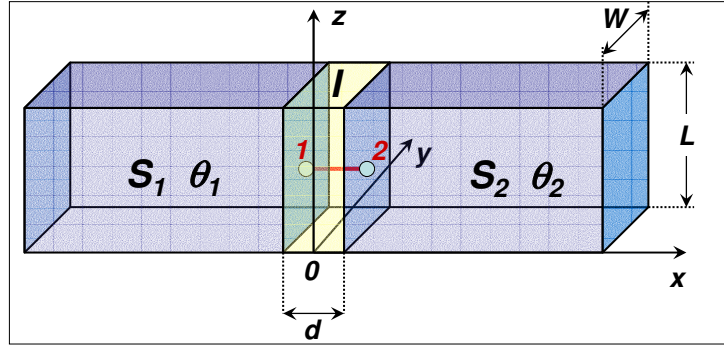


Figure 1.11: Sketch of a superconductor-insulator-superconductor (SIS) Josephson junction with a current source driving a current through the junction.

Above we have made the assumption of a homogenous supercurrent density allowing a one-dimensional treatment. This assumption can be relaxed by noting that the argument given above still holds if applied *locally* to each point (y, z) of the junction area. In particular, we can generalize the critical current density J_c to $J_c(y, z)$ (the junction area extends in the yz -plane, see Fig. 1.11). The current flow is always in x -direction so that there is no divergence of current density. That is, for any given y and z the supercurrent is flowing straight across the junction area. However, the current density given by (1.3.6) may now depend on y and z and we have to generalize the current-phase relation to

$$J_s(y, z, t) = J_c(y, z) \sin \varphi(y, z, t) . \quad (1.3.7)$$

Second Josephson Equation: voltage-phase relation

In order to derive the 2. Josephson equation we use the time derivative of the gauge invariant phase difference

$$\frac{\partial \varphi}{\partial t} = \frac{\partial \theta_2}{\partial t} - \frac{\partial \theta_1}{\partial t} - \frac{2\pi}{\Phi_0} \frac{\partial}{\partial t} \int_1^2 \mathbf{A}(\mathbf{r}, t) \cdot d\mathbf{l} . \quad (1.3.8)$$

Substitution of the energy-phase relation (1.1.69)

$$-\hbar \frac{\partial \theta}{\partial t} = \frac{1}{2n_s^*} \Lambda \mathbf{J}_s^2 + q^* \phi \quad (1.3.9)$$

into (1.3.8) yields

$$\frac{\partial \varphi}{\partial t} = -\frac{1}{\hbar} \left(\frac{\Lambda}{2n_s^*} [\mathbf{J}_s^2(2) - \mathbf{J}_s^2(1)] + q^* [\phi(2) - \phi(1)] \right) - \frac{2\pi}{\Phi_0} \frac{\partial}{\partial t} \int_1^2 \mathbf{A} \cdot d\mathbf{l} . \quad (1.3.10)$$

Since the supercurrent density across the junction is continuous, we can use $\mathbf{J}_s(2) = \mathbf{J}_s(1)$ and obtain with $q^* = 2e$ and $\Phi_0 = h/2e$

$$\frac{\partial \varphi}{\partial t} = \frac{2\pi}{\Phi_0} \int_1^2 \left(-\nabla \phi - \frac{\partial \mathbf{A}}{\partial t} \right) \cdot d\mathbf{l} . \quad (1.3.11)$$

Here, we have expressed the difference in the scalar potential ϕ as a line integral of its gradient. Since the term in parentheses is just the electric field (compare (1.1.54)), we can write

$$\frac{\partial \phi}{\partial t} = \frac{2\pi}{\Phi_0} \int_1^2 \mathbf{E}(\mathbf{r}, t) \cdot d\mathbf{l} \quad (2. \text{ Josephson equation}) . \quad (1.3.12)$$

This equation is known as the ***second Josephson equation***. We note that $\int_1^2 \mathbf{E}(\mathbf{r}, t) \cdot d\mathbf{l}$ corresponds to a voltage drop across the junction resulting in the difference $\Delta\mu = \mu_2 - \mu_1 = eV$ between the electrochemical potentials of the two superconductors. That is, the time derivative of ϕ is determined by $\Delta\mu$ as expected from the general energy-phase relation. Since $\Delta\mu$ is determined by the voltage drop across the junction, the second Josephson equation also is called the ***voltage-phase relation***. The ***voltage-phase relation*** and the ***current-phase relation*** (1.3.6) together with the expression for the ***gauge-invariant phase difference*** (1.3.2) represent the set of basic equations governing the behavior of Josephson junctions. The fact that $\dot{\phi} \propto \Delta\mu$ can be viewed as a quantum interference effect of the macroscopic wave function in the two superconducting electrodes.

If a constant voltage V is applied to the Josephson junction, we obtain

$$\frac{\partial \phi}{\partial t} = \frac{2\pi}{\Phi_0} V . \quad (1.3.13)$$

and the phase difference is growing linearly in time:

$$\phi(t) = \phi_0 + \frac{2\pi}{\Phi_0} V \cdot t . \quad (1.3.14)$$

Then, the Josephson current $I_s(t) = I_c \sin \phi(t)$ is oscillating at the ***Josephson frequency***

$$\frac{\nu}{V} = \frac{\omega}{2\pi V} = \frac{1}{\Phi_0} \simeq 483.597\,898(19) \frac{\text{MHz}}{\mu\text{V}} . \quad (1.3.15)$$

We see that the Josephson junctions can be considered as a voltage controlled oscillator that can be used to generate very high frequencies (500 GHz at 1 mV). The linewidth and the power that can be achieved with Josephson junctions will be discussed later, when we are discussing applications of the Josephson effect. By taking two Josephson junctions made of different materials the proportionality constant between frequency and voltage has been compared and found to agree within 2×10^{-16} .³² More recent experiments even found an agreement in the range of 10^{-19} .

1.3.2 Josephson Tunneling

So far we have not discussed the magnitude of the ***maximum Josephson current density*** J_c . In this subsection we derive an expression of this quantity for the case of Josephson junction with an insulating tunneling barrier of thickness d . That is, we consider the supercurrent density across a superconductor-insulator-superconductor Josephson junction as sketched in Fig. 1.11. To solve the problem we are using

³²J.S. Tsai, A.K. Jain, J.E. Lukens, Phys. Rev. Lett. **51**, 316 (1983).

the so-called **wave matching method**. Here, we solve the Schrödinger equation in the three regions, namely the two superconducting electrodes and the insulating barrier. The solutions will contain coefficients that can be determined by matching the solutions at the boundaries between the three regions.

We first start with the wave function in the superconducting electrodes. The supercurrent density at the edges of the junction electrodes at the positions $x = \pm d/2$ is given by the supercurrent density equation (1.1.50)

$$\mathbf{J}_s = q^* n_s^*(\mathbf{r}, t) \left\{ \frac{\hbar}{m^*} \nabla \theta(\mathbf{r}, t) - \frac{q^*}{m^*} \mathbf{A}(\mathbf{r}, t) \right\} . \quad (1.3.16)$$

We already have found the relationship between the current density at the boundary to the insulator and the phase of the wave functions at each boundary. It is given by the current-phase relation. In order to derive the magnitude of the maximum Josephson current density J_c we make the same assumptions as in section 1.3.1. That is, we assume a uniform tunneling barrier. We further assume that the junction area $L \cdot W$ is small enough, so that the Josephson current density can be assumed uniform within the junction area. It will be discussed later, up to which length scale this approximation is valid.

We start our discussion with the energy-phase relation (1.1.69) for the superconducting electrodes, which directly follows from the Schrödinger equation. In the absence of any electric and magnetic field this equation can be written as

$$-\hbar \frac{\partial \theta}{\partial t} = \frac{1}{2n_s^*} \Lambda \mathbf{J}_s^2 . \quad (1.3.17)$$

The term on the right hand side corresponds to the kinetic energy $E_0 = m^* v_s^2 / 2$ of the moving superelectrons and therefore we can write

$$\frac{\partial \theta}{\partial t} = -\frac{E_0}{\hbar} . \quad (1.3.18)$$

Consequently, the time dependent macroscopic wave function can be written as

$$\psi(\mathbf{r}, t) = \psi(\mathbf{r}) e^{-i(E_0/\hbar)t} , \quad (1.3.19)$$

where $\psi(\mathbf{r})$ is the time independent amplitude of the wave function.

We must now determine the wavefunction within the insulating barrier of thickness d . The barrier height V_0 is assumed larger than E_0 . Then, the variation of the potential along the x -direction is given by a step-like function $V(x)$, which is zero outside and V_0 inside the barrier region (see Fig. 1.12). We know that classically for $V_0 > E_0$ the superelectrons cannot penetrate the barrier region. However, quantum mechanically the situation is different. Here, the superelectrons can tunnel through the barrier. In our discussion we consider only elastic processes, that is, the superelectrons maintain their energy. Therefore, the time evolution of the wavefunction is the same outside and inside the barrier and we have to consider only the time independent part. Moreover, since within the barrier we are in a region of constant potential energy V_0 , the time dependent Schrödinger-like equation (1.1.48) can be written as the time independent Schrödinger equation

$$-\frac{\hbar^2}{2m^*} \nabla^2 \psi(\mathbf{r}) = (E_0 - V_0) \psi(\mathbf{r}) . \quad (1.3.20)$$

Using now our simplifying assumptions of a homogeneous barrier and homogeneous supercurrent flow we have to consider only the x -dependence, i.e. we have to solve only a one-dimensional problem.

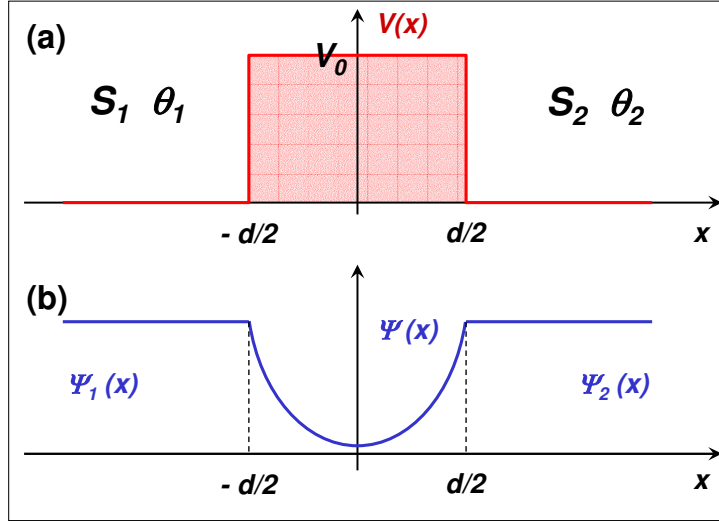


Figure 1.12: (a) Sketch of the model potential $V(x)$ of a superconductor-insulator-superconductor junction. (b) Time independent part of the wave function.

The solution of (1.3.20) can be written as a sum of decaying and growing exponentials or equivalently as

$$\psi(x) = A \cosh(\kappa x) + B \sinh(\kappa x), \quad (1.3.21)$$

where the **characteristic decay constant** κ is determined by the barrier properties and is given by

$$\kappa = \sqrt{\frac{2m^*(V_0 - E_0)}{\hbar^2}}. \quad (1.3.22)$$

The coefficients A and B are determined by the boundary conditions at $x = \pm d/2$:

$$\psi(-d/2) = \sqrt{n_1^*} e^{i\theta_1} \quad (1.3.23)$$

$$\psi(+d/2) = \sqrt{n_2^*} e^{i\theta_2}. \quad (1.3.24)$$

Here, $\sqrt{n_{1,2}^*}$ and $\theta_{1,2}$ are the magnitude and the phase of the wave function at the boundaries $x = \pm d/2$.

With these boundary conditions we obtain from (1.3.21)

$$\sqrt{n_1^*} e^{i\theta_1} = A \cosh(\kappa d/2) - B \sinh(\kappa d/2) \quad (1.3.25)$$

$$\sqrt{n_2^*} e^{i\theta_2} = A \cosh(\kappa d/2) + B \sinh(\kappa d/2) \quad (1.3.26)$$

and hence by solving for A and B

$$A = \frac{\sqrt{n_1^*} e^{i\theta_1} + \sqrt{n_2^*} e^{i\theta_2}}{2 \cosh(\kappa d/2)} \quad (1.3.27)$$

$$B = -\frac{\sqrt{n_1^*} e^{i\theta_1} - \sqrt{n_2^*} e^{i\theta_2}}{2 \sinh(\kappa d/2)}. \quad (1.3.28)$$

We now have to recall that for the supercurrent density is given by (compare (1.1.47))

$$\mathbf{J}_s = \frac{q^*}{m^*} \Re \left\{ \psi^* \left(\frac{\hbar}{i} \nabla \right) \psi \right\}. \quad (1.3.29)$$

With the wavefunction from (1.3.21) the current density is obtained to

$$\mathbf{J}_s = \frac{q^*}{m^*} \kappa \hbar \Im \{A^* B\} . \quad (1.3.30)$$

Substituting (1.3.27) and (1.3.28) in (1.3.30) yields the supercurrent density

$$\boxed{\mathbf{J}_s = \mathbf{J}_c \sin(\theta_2 - \theta_1)} \quad (1.3.31)$$

with the ***maximum Josephson current density***

$$\boxed{\mathbf{J}_c = -\frac{q^*}{m^*} \kappa \hbar \frac{\sqrt{n_1^* n_2^*}}{2 \sinh(\kappa d/2) \cosh(\kappa d/2)} = -\frac{q^* \hbar \kappa}{m^*} \frac{\sqrt{n_1^* n_2^*}}{\sinh(2\kappa d)} .} \quad (1.3.32)$$

Here we have used $2 \sinh(x) \cosh(x) = \sinh(2x)$. We see that from our analysis we not only obtain the value for the maximum Josephson current density but also the current-phase relation, which has been derived from our qualitative discussion above.

In real junctions the barrier height V_0 typically is of the order of a few eV and therefore the decay length $1/\kappa$ less than a nanometer. Since the thickness of the tunnel barrier is usually a few nanometer, we have $\kappa d \gg 1$. In this case we can use the approximation $\sinh(2\kappa d) \simeq \frac{1}{2} \exp(2\kappa d)$. Hence, the maximum Josephson current density decays exponentially with increasing thickness of the tunneling barrier. With $q^* = -2e$ and $m^* = 2m$ we obtain

$$\mathbf{J}_c = \frac{e \hbar \kappa}{m} 2 \sqrt{n_1^* n_2^*} \exp(-2\kappa d) . \quad (1.3.33)$$

We note that the Josephson equations also can be derived by considering two separate quantum mechanical systems that are weakly coupled by a coupling Hamilton operator (transfer Hamiltonian approach). This derivation is discussed in Appendix A

Summary

- Macroscopic quantum model of superconductors:

Superconductors can be described by a macroscopic wave function

$$\psi(\mathbf{r}, t) = \psi_0(\mathbf{r}, t) e^{i\theta(\mathbf{r}, t)} .$$

The wave function describes an ensemble of a macroscopic number of superconducting particles of mass q^* and mass m^* moving in the electromagnetic potentials ϕ and \mathbf{A} .

In contrast to the usual quantum mechanics interpretation of $|\psi|^2$ as the probability to find a particle at position \mathbf{r} at time t , $|\psi|^2$ is associated with the density $n_s^*(\mathbf{r}, t)$ of the superconducting particles.

- By considering the current density in a superconductor as a quantum mechanical probability current, the current density

$$\mathbf{J}_s = \frac{\hbar n_s^* q^*}{m^*} \left\{ \nabla \theta(\mathbf{r}, t) - \frac{q^*}{\hbar} \mathbf{A}(\mathbf{r}, t) \right\} = \frac{\hbar n_s^* q^*}{m^*} \left\{ \nabla \theta(\mathbf{r}, t) - \frac{2\pi}{\Phi_0} \mathbf{A}(\mathbf{r}, t) \right\}$$

is obtained. That is, the current density in a superconductor is proportional to the gauge invariant phase gradient

$$\gamma(\mathbf{r}, t) = \nabla \theta(\mathbf{r}, t) - \frac{q^*}{\hbar} \mathbf{A}(\mathbf{r}, t) = \nabla \theta(\mathbf{r}, t) - \frac{2\pi}{\Phi_0} \mathbf{A}(\mathbf{r}, t) .$$

- The phenomenological London equations are obtained by taking the time derivative and the curl of the expression for the supercurrent density. In its linearized form they are given by

$$\begin{aligned} \frac{\partial}{\partial t} (\Lambda \mathbf{J}_s) &= \mathbf{E} && \text{(1. London equation)} \\ \nabla \times (\Lambda \mathbf{J}_s) &= -\mathbf{B} && \text{(2. London equation)} \end{aligned} \quad (1.3.34)$$

Here, $\Lambda = m^*/n_s^* q^{*2} = \mu_0 \lambda_L^2$ is the London parameter and λ_L the London penetration depth. The 1. and 2. London equation phenomenologically describe the perfect conductivity and perfect diamagnetism of superconductors.

- Fluxoid and flux quantization:

The fluxoid $\oint_C (\Lambda \mathbf{J}_s) \cdot d\mathbf{l} + \int_S \mathbf{B} \cdot d\mathbf{s}$ threading a multiply connected superconductor is quantized in units of the flux quantum $\Phi_0 = 2.068 \times 10^{-15} \text{ Vs}$:

$$\oint_C (\Lambda \mathbf{J}_s) \cdot d\mathbf{l} + \int_S \mathbf{B} \cdot d\mathbf{s} = n \Phi_0$$

If the integration path can be taken in a region where $\mathbf{J}_s = 0$, we arrive at the flux quantization:

$$\Phi = \int_S \mathbf{B} \cdot d\mathbf{s} = n \Phi_0$$

- The Josephson effect:

The current between two weakly coupled superconductors is proportional to the sine of the gauge invariant phase difference φ (1. Josephson equation):

$$\begin{aligned}\mathbf{J}_s(\mathbf{r},t) &= \mathbf{J}_c(\mathbf{r},t) \sin \varphi(\mathbf{r},t) \\ \varphi(\mathbf{r},t) &= \theta_2(\mathbf{r},t) - \theta_1(\mathbf{r},t) - \frac{2\pi}{\Phi_0} \int_1^2 \mathbf{A}(\mathbf{r},t) \cdot d\mathbf{l}\end{aligned}$$

In the presence of a finite potential difference $\Delta\mu = eV$ between the two superconductors, the gauge invariant phase difference φ changes in time as (2. Josephson equation)

$$\frac{\partial \varphi}{\partial t} = \frac{2eV}{\hbar} = \frac{2\pi}{\Phi_0} V .$$

The Josephson current then oscillates in time as $\mathbf{J}_s = \mathbf{J}_c \sin(\omega t + \varphi_0)$ at a frequency $\omega/2\pi = 483.6 \text{ GHz/mV}$.

Chapter 2

Physics of Josephson Junctions: The Zero Voltage State

In this chapter we discuss the physics of Josephson junctions in the zero voltage state. In this situation the Josephson current density J_s always is smaller than the maximum Josephson current density J_c so that the current is flowing as supercurrent that can be described by the macroscopic quantum approach. The voltage state of Josephson junctions will be discussed in chapter 3. In the case of a finite junction voltage the situation is more complex, since besides the Josephson current other types of current such as a normal current or a displacement current have to be taken into account. These currents vanish in the zero voltage state and hence make the treatment of this situation simple.

In section 2.1 we first restrict ourselves to cases where the junction area is small enough so that the junction can be considered as a zero-dimensional or lumped element. Then the integral current rather than the current density is sufficient to describe the Josephson junction properties. We will introduce the ***Josephson coupling energy*** and the ***Josephson inductance*** as well as mechanical analogs for lumped Josephson junctions.

In sections 2.2 and 2.3 we then relax the restriction on the junction area and discuss the junctions as distributed systems, where the currents have a spatial dependence inside the junction itself. Here, the discussion of the magnetic field dependence of the Josephson current density is the main topic.

2.1 Basic Properties of Lumped Josephson Junctions

In many superconducting devices and circuits Josephson junctions with very small spatial dimensions are used. Such small Josephson junctions can be understood by considering the gauge invariant phase difference and the current density to be uniform over the junction area. We will show later (see sections 2.2 and 2.3) that small means that the spatial extension of the junction area must be much smaller than a characteristic screening length, the so-called **Josephson penetration depth** λ_J . This screening length of a weak superconducting system is the analog of the **London penetration depth** λ_L of a bulk superconductor and sets the length scale over which variations of the supercurrent density occur. Therefore, the supercurrent density across a Josephson junction can be assumed to be constant, if the junction area is much smaller than this screening length. In the same way the supercurrent density in a bulk superconductor always can be assumed constant, if the spatial dimensions of the bulk superconductor are much smaller the London penetration depth.

We recall that the London penetration depth $\lambda_L = \sqrt{m^*/\mu_0 n_s^* q^{*2}}$ defines the length scale over which an applied field can penetrate a bulk superconductor. Equivalently, it defines the surface layer, in which the screening currents are flowing. This length scale typically ranges between several 10 nm and about 1 μm for most superconductors. For a weak superconducting system as a Josephson junction the equivalent screening length is much larger. This can be understood simply by the fact that in the weak region connecting two bulk superconductors the density of Cooper pairs is strongly reduced. Since the screening length is proportional to $1/\sqrt{n_s^*}$, the corresponding screening length λ_J is strongly increased. It easily can be larger than 100 μm . That is, even Josephson junctions with spatial dimensions of the order of several 10 μm can be considered small.

2.1.1 The Lumped Josephson Junction

We call Josephson junctions with spatially homogeneous supercurrent density and phase difference **lumped junctions**. Such junctions can be described by a supercurrent

$$I_s = \int_S \mathbf{J}_s \cdot d\mathbf{s} . \quad (2.1.1)$$

The region of integration is the junction area S . The current-phase relation (1.3.7) can be rewritten in terms of the currents as

$$I_s(t) = I_c \sin \varphi(t) . \quad (2.1.2)$$

The gauge-invariant phase difference is still given by

$$\varphi(t) = \theta_2(t) - \theta_1(t) - \frac{2\pi}{\Phi_0} \int_1^2 \mathbf{A}(\mathbf{r}, t) \cdot d\mathbf{l} . \quad (2.1.3)$$

The voltage-phase relation $\frac{\partial \varphi}{\partial t} = \frac{2\pi}{\Phi_0} \int_1^2 \mathbf{E}(\mathbf{r}, t) \cdot d\mathbf{l}$ can be simplified by noting that $\int_1^2 \mathbf{E}(\mathbf{r}, t) \cdot d\mathbf{l}$ is just the voltage $V(t)$ across the junction. Note that the voltage is constant across the junction area extending for example in the yz -plane, since for a lumped junction the electric field is independent of y and z . The voltage-phase relation then becomes

$$\frac{d\varphi}{dt} = \frac{2\pi}{\Phi_0} V . \quad (2.1.4)$$

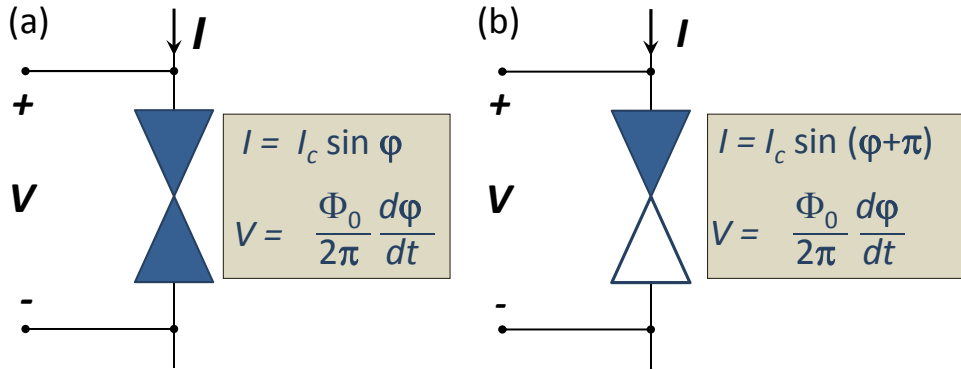


Figure 2.1: The Josephson junction as a lumped circuit element, which is characterized by the crossed symbol in circuit diagrams and is governed by the two Josephson equations. Left: “0”-junction, right: “ π ”-junction.

Note that we are now using the total derivative because for a lumped junction the phase difference φ does not depend on any spatial coordinate.

Fig. 2.1 shows the symbol for a lumped Josephson junction along with the two equations describing the junction. As we discuss later, we have to distinguish between “0”-junctions, for which $I_s = I_c \sin(0 + \varphi) = I_c \sin \varphi$, and so-called “ π ”-junctions, for which $I_s = I_c \sin(\pi + \varphi) = -I_c \sin \varphi$. That is, for the same phase difference φ the Josephson current I_s is flowing in opposite directions for “0”- and “ π ”-junctions. In the following subsections we discuss how energy can be stored in a lumped junction and how it behaves when it is driven by external current or voltage sources.

2.1.2 The Josephson Coupling Energy

Due to the zero junction voltage, no energy will be dissipated in the junction residing in the superconducting (S) state. However, there is a finite energy stored in the junction. This energy can be considered as a molecular binding energy caused by the finite overlap of the macroscopic wavefunctions of the two weakly coupled superconductors. The magnitude of the binding energy becomes immediately evident by considering the process of increasing the junction current from zero to a finite value I . Let the initial value of the phase difference φ be zero at zero junction current. As we are increasing the current, according to the current-phase relation also the phase difference φ has to change. Furthermore, according to the voltage-phase relation a changing phase difference corresponds to a finite junction voltage. That is, on increasing the current the external source has to supply energy that is determined by the integral of the power $I \cdot V$ during the current increase. Although the superelectrons can flow across the junction without causing any resistance, on increasing the current we have to accelerate the superelectrons in the sample and this requires a certain amount of energy. This energy is then stored by the moving superelectrons. The described process can be viewed as a conversion of potential into kinetic energy. Upon reaching the critical current I_c , the whole potential (“binding”) energy is converted into kinetic energy.

In order to calculate the energy stored in the Josephson junction we have to integrate the power from time $t = 0$ when we start the current increase to time $t = t_0$ when we are stopping the increase:

$$E_J = \int_0^{t_0} I_s V dt . \quad (2.1.5)$$

Here, V is the voltage applied during increasing the current from zero at $t = 0$ to the final value I at time

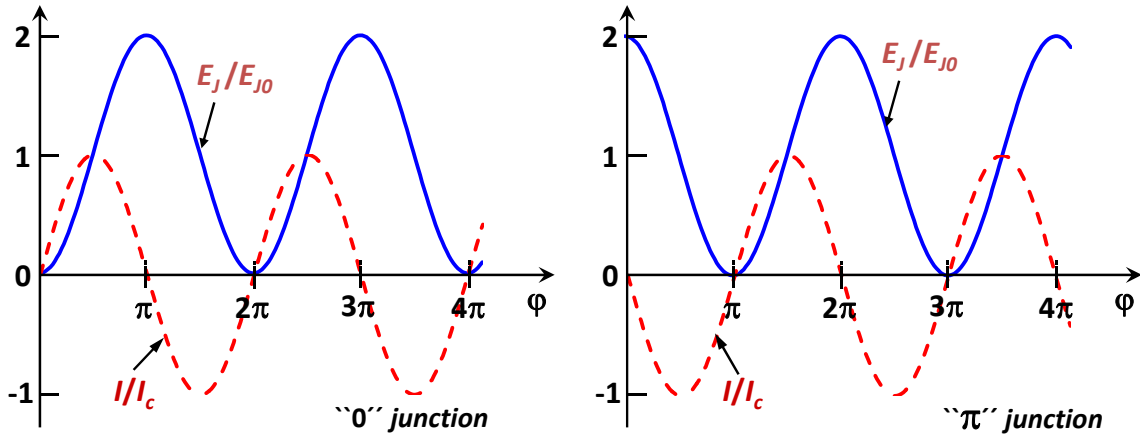


Figure 2.2: The normalized Josephson current I_s/I_c and the normalized coupling energy E_J/E_{J0} plotted versus the phase difference φ . Left: “0”-junction, right: “ π ”-junction

t_0 . Using the current-phase and the voltage-phase relation we obtain

$$E_J = \int_0^{t_0} (I_c \sin \tilde{\varphi}) \left(\frac{\Phi_0}{2\pi} \frac{d\tilde{\varphi}}{dt} \right) dt . \quad (2.1.6)$$

With the phase difference $\varphi(0) = 0$ and $\varphi(t_0) = \varphi$ we can write the integral as

$$E_J = \frac{\Phi_0 I_c}{2\pi} \int_0^{\varphi} \sin \tilde{\varphi} d\tilde{\varphi} . \quad (2.1.7)$$

Integration gives the energy stored in the junction as

$$E_J = \frac{\Phi_0 I_c}{2\pi} (1 - \cos \varphi) = E_{J0} (1 - \cos \varphi) . \quad (2.1.8)$$

This energy is usually denoted as the **Josephson coupling energy**. Similar to the binding energy of a molecule this energy results from the overlap (or coupling) of the wave functions of the two superconducting electrodes.

In Fig. 2.2 we have plotted the coupling energy and the Josephson current as a function of the phase difference. The energy is lowest, if no current flows and φ is zero or a multiple of 2π . Therefore, such junctions are denoted as “0” junctions. There are also other junctions (e.g. junctions with ferromagnetic barrier layers) for which the state of lowest coupling energy is obtained for a phase difference of π or $(2n+1)\pi$. These junctions are named “ π ” junctions.

We briefly discuss the order of magnitude of the Josephson coupling energy. For a junction with a typical critical current of 1 mA we have $E_{J0} \simeq 3 \times 10^{-19} \text{ J}$ what corresponds to the thermal energy $k_B T$ of around 20 000 K. Therefore, thermal smearing effects are negligible. However, for junctions with very small critical current this is different. For example, for $I_c = 1 \mu\text{A}$ the coupling energy corresponds to the thermal energy at around 20 K and, hence, thermal smearing effects become prominent as discussed in chapter 3.

2.1.3 The Superconducting State

According to the current-phase relation (2.1.2) a constant dc current imposed on a Josephson junction by an external current source results in a constant phase difference

$$\varphi = \varphi_n = \arcsin\left(\frac{I}{I_c}\right) + 2\pi n \quad (2.1.9)$$

$$\varphi = \tilde{\varphi}_n = \pi - \arcsin\left(\frac{I}{I_c}\right) + 2\pi n \quad (2.1.10)$$

for

$$-I_c \leq I \leq +I_c . \quad (2.1.11)$$

The constant phase difference results in $d\varphi/dt = 0$. Hence, each of the solutions corresponds to zero junction voltage and describes the superconducting state. We will call this situation the *zero voltage state* or stationary (*S*) state.

In order to analyze the stability of the zero voltage state we use the potential energy E_{pot} of the system Josephson junction + current source. To find E_{pot} we use the rule, which is general for any subsystem (the Josephson junction in our case) under the action of a constant external force F (the applied current in our case), saying that the total energy G is equal to the difference of the two terms:¹

$$G = E - F \cdot x . \quad (2.1.12)$$

Here, E is the intrinsic (free) energy of the subsystem and x is its generalized coordinate corresponding to the generalized force $F = I$. The coordinate should be chosen in a way that the product $F\dot{x}$ gives the power P flowing into the subsystem. Since for the Josephson junction the latter product equals to $I \cdot V$, the desirable coordinate is

$$x = \int V dt = \frac{\hbar}{2e} \varphi + c = \frac{\Phi_0}{2\pi} \varphi + c , \quad (2.1.13)$$

where c is an integration constant. The potential energy of the system is thus given by

$$E_{\text{pot}}(\varphi) = E_J(\varphi) - I \left(\frac{\Phi_0}{2\pi} \varphi + c \right) = E_{J0} \left[1 - \cos \varphi - \frac{I}{I_c} \varphi \right] + \tilde{c} . \quad (2.1.14)$$

As shown by Fig. 2.3, the function $E_{\text{pot}}(\varphi)$ has the shape of a tilted washboard and is therefore often called the *tilted washboard potential*. The washboard has minima and maxima for the values of the phase difference given by (2.1.9) and (2.1.10), respectively. It is evident that the former solutions are stable and the latter are unstable. We further note that the states corresponding to different n are physically equivalent and therefore we usually only refer to the $n = 0$ solution.

¹Note that in thermodynamics G is called the Gibbs energy (potential) of the subsystem, which has to be distinguished from the free energy (Helmholtz energy) E .

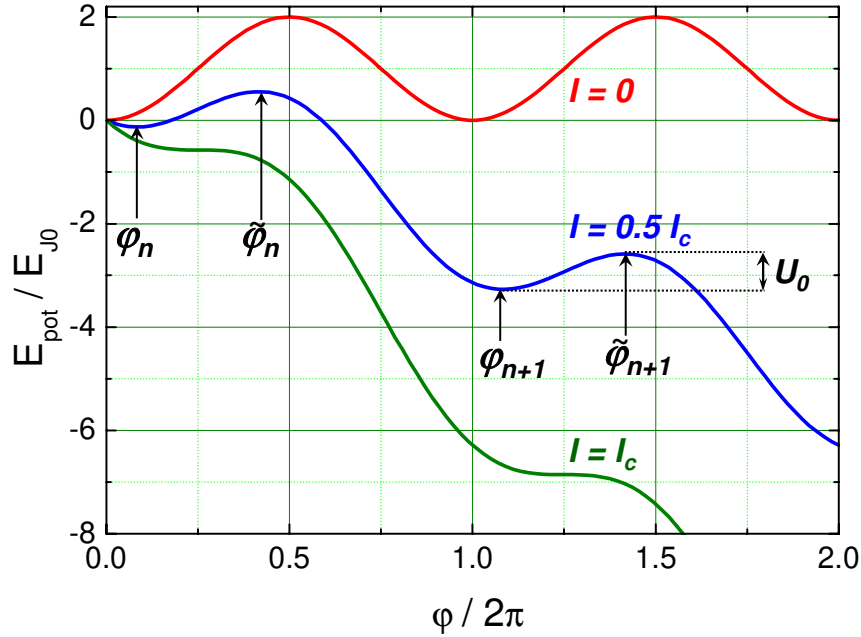


Figure 2.3: The potential energy $E_{\text{pot}}(\phi)$ of a current biased lumped Josephson junction at various values of the applied current. The potential is named tilted washboard potential.

By analyzing the tilted washboard potential, from (2.1.14) we can easily derive the difference $U_0 = E_{\text{pot}}(\varphi_n) - E_{\text{pot}}(\tilde{\varphi}_n)$ and the curvature $k \equiv \partial^2 E_{\text{pot}} / \partial \varphi^2$ of the potential at the potential minimum. We obtain²

$$U_0 \equiv E_{\text{pot}}(\varphi_n) - E_{\text{pot}}(\tilde{\varphi}_n) = 2E_{J0} \left[\sqrt{1 - \left(\frac{I}{I_c} \right)^2} - \frac{I}{I_c} \arccos \left(\frac{I}{I_c} \right) \right] \quad (2.1.15)$$

$$k \equiv \frac{\partial^2 E_{\text{pot}}}{\partial \varphi^2} = E_{J0} \sqrt{1 - \left(\frac{I}{I_c} \right)^2}. \quad (2.1.16)$$

We see that these quantities approach zero for $I \rightarrow I_c$. Close to the critical current we have $\alpha \equiv 1 - I/I_c \ll 1$ and can use the following approximations

$$\varphi_0 = \frac{\pi}{2} - \sqrt{2\alpha}, \quad \tilde{\varphi}_0 = \frac{\pi}{2} + \sqrt{2\alpha} \quad (2.1.17)$$

$$U_0 = \frac{2}{3} E_{J0} (2\alpha)^{2/3} \quad (2.1.18)$$

$$k = E_{J0} (2\alpha)^{1/2}. \quad (2.1.19)$$

We will see in chapter 3 that the tilted washboard potential is very useful for describing the dynamics of Josephson junctions at $I > I_c$. It is evident from (2.1.14) and Fig. 2.3 that in this case there are no longer any minima in the potential and consequently the phase will continuously increase resulting in a finite junction voltage. The dynamics can be described by considering the phase as a particle moving down the tilted washboard potential. However, in order to describe this process we have to determine the mass of the particle and the damping of the motion. This can be done only after introducing the other current components as the normal current and the displacement current in chapter 3.

²Here we use the equality $\arcsin(x) = (\pi/2) - \arccos(x) = \arccos(\sqrt{1-x^2})$.

2.1.4 The Josephson Inductance

Energy storage and conservation in the Josephson junction suggests that it can be considered as a *non-linear reactance*. In order to clarify this we consider the time derivative of the current-phase relation

$$\frac{dI_s}{dt} = I_c \cos \varphi \frac{d\varphi}{dt}. \quad (2.1.20)$$

Using the voltage-phase relation we obtain

$$\frac{dI_s}{dt} = I_c \cos \varphi \frac{2\pi}{\Phi_0} V. \quad (2.1.21)$$

This immediately shows that for small variations of the current around the value $I_s = I_c \sin \varphi$ the Josephson junction behaves as an inductance

$$L_s = \frac{\Phi_0}{2\pi I_c \cos \varphi} = L_c \frac{1}{\cos \varphi} \quad \text{with} \quad L_c = \frac{\hbar}{2eI_c}. \quad (2.1.22)$$

A very unusual property of this *Josephson inductance* is the fact that it can have negative values in the intervals $\pi/2 + 2\pi n < \varphi < 3\pi/2 + 2\pi n$. Note that from the electrotechnical point of view the energy E_J can be considered as stored in the inductance L_s . The fact that the Josephson inductance can have negative values results in a behavior that is completely different from an ordinary nonlinear inductance. This is immediately seen, if we apply a constant voltage V to the Josephson junction. In this case we obtain an oscillating Josephson current as discussed already in section 1.3.1. Note that for an ordinary inductance the current would not oscillate but just gradually increase. The oscillations of the supercurrent are called *Josephson oscillations* and have been predicted in the original paper by Brian Josephson. These oscillations accompany most processes in Josephson junctions and are of particular importance for their dynamics as we will see in chapter 3.

2.1.5 Mechanical Analogs

The unusual properties of the supercurrent has stimulated the search for mechanical analogs that can be used to better understand the dynamics of the Josephson junction. The first example is a plane mechanical pendulum in a uniform gravity field. Here, the phase difference φ plays the role of the angle of the pendulum with respect to its equilibrium position. The supercurrent corresponds to the torque and the voltage to the angular velocity of the pendulum.

A second useful analog is a particle moving along the coordinate φ with velocity $v \propto d\varphi/dt \propto V$ in a potential given by (2.1.14).

2.2 Short Josephson Junctions

So far we only have considered zero-dimensional Josephson junctions with a spatially homogeneous supercurrent density. We could describe these lumped elements by the integral Josephson current I_s with its maximum value I_c and the gauge-invariant phase difference φ . In this section we relax the condition of spatially homogeneous values of the Josephson current density and the gauge-invariant phase difference and allow now for spatial variations $J_s(\mathbf{r})$ and $\varphi(\mathbf{r})$ of these quantities. We refer to such junctions as *extended Josephson junctions*.

Discussing the physics of extended Josephson junctions we have to distinguish between two cases:

- ***Short Josephson junctions:***

For short junctions the magnetic field generated by the Josephson current itself (self-field) is negligible compared to the externally applied magnetic field. We will show below that junctions can be considered as short junctions, if the spatial dimensions of the junction area are smaller than a characteristic length scale named *Josephson penetration depth* λ_J .

- ***Long Josephson junctions:***

For long Josephson junctions the magnetic field generated by the Josephson current itself is no longer negligible. Long Josephson junctions have spatial dimensions larger than the *Josephson penetration depth* λ_J .

2.2.1 Quantum Interference Effects – Short Josephson Junction in an Applied Magnetic Field

The description of superconductors by a macroscopic wave function manifests itself in a number of interference effects. We already have seen in section 1.3 that the oscillation of the Josephson current in the presence of a finite potential difference between the junction electrodes can be viewed as a *temporal interference* between the macroscopic wave functions of the two superconducting electrodes. In the following we show that we also can observe *spatial interference* in Josephson junctions, if we generate spatial changes of the gauge invariant phase difference by applying an external magnetic field. We will see that the observed interference effect is completely analogous to the diffraction at a slit in optics.

We consider the cross section of an extended Josephson junction as sketched in Fig. 2.4. The two junction electrodes are separated by a thin insulating barrier of thickness d . The junction area $L \cdot W$ extends in the yz -plane and the current is flowing in the x -direction. We assume $W, L \gg d$ so that effects of the edges of the junction can be neglected. Each superconducting electrode is assumed to have thickness t_1 and t_2 larger than the London penetration depth λ_{L1} and λ_{L2} of the electrode material, respectively. An external magnetic field is applied parallel to the y -direction, that is, $\mathbf{B}_e = (0, B_y, 0)$. Since the applied field penetrates the superconducting electrode up to a thickness given by the London penetration depth, we can define a magnetic thickness of the junction given by $t_B = d + \lambda_{L1} + \lambda_{L2}$.

In order to discuss the effect of the applied magnetic field on the Josephson current density J_s we have to determine the phase shift introduced between two positions P and Q along the z -axis separated by an infinitesimal distance dz . The shift $\varphi(Q) - \varphi(P)$ of the gauge-invariant phase difference between the two points can be determined by considering the line integral along the contour shown in Fig. 2.4. We have to demand that the total phase change along the closed contour is $2\pi n$, that is

$$\oint_C \nabla \theta \cdot d\mathbf{l} = 2\pi n$$

$$= (\theta_{Q_b} - \theta_{Q_a}) + (\theta_{P_c} - \theta_{Q_b}) + (\theta_{P_d} - \theta_{P_c}) + (\theta_{Q_a} - \theta_{P_d}) + 2\pi n \quad (2.2.1)$$

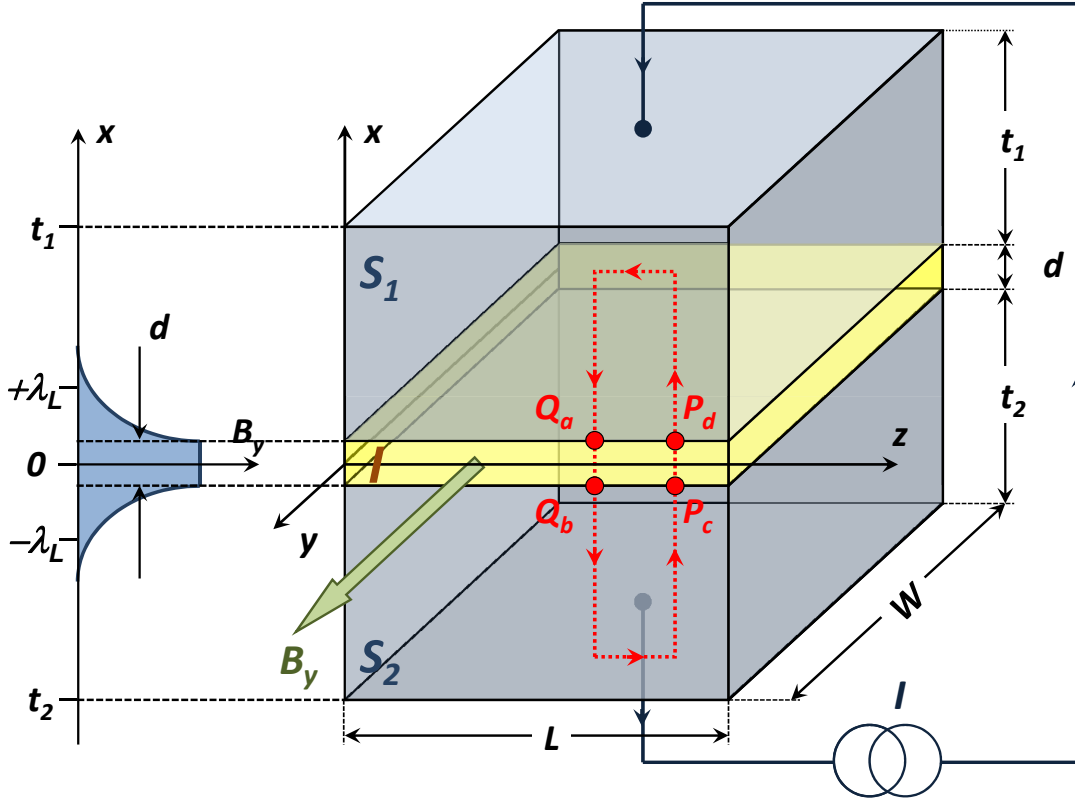


Figure 2.4: Cross section of an extended Josephson junction. The current flows in x - direction, the magnetic field is applied in y -direction. The broken line indicates the closed contour of integration. On the left hand side the decay of the magnetic field in the junction electrodes over the length scale λ_L is indicated.

For the determination of the various terms we use the expressions for the gauge invariant phase gradient in the bulk superconductors (compare (1.1.65))

$$\nabla\theta = \frac{2\pi}{\Phi_0} (\Lambda \mathbf{J}_s + \mathbf{A}) \quad (2.2.2)$$

and the gauge-invariant phase difference across the barrier (compare (1.3.2))

$$\varphi = \theta_2 - \theta_1 - \frac{2\pi}{\Phi_0} \int_1^2 \mathbf{A} \cdot d\mathbf{l} . \quad (2.2.3)$$

The first and third term in (2.2.1) are the differences across the Josephson junction barrier and directly follow from (2.2.3):

$$\theta_{Q_b} - \theta_{Q_a} = +\varphi(Q) + \frac{2\pi}{\Phi_0} \int_{Q_a}^{Q_b} \mathbf{A} \cdot d\mathbf{l} \quad (2.2.4)$$

$$\theta_{P_d} - \theta_{P_c} = -\varphi(P) + \frac{2\pi}{\Phi_0} \int_{P_c}^{P_d} \mathbf{A} \cdot d\mathbf{l} . \quad (2.2.5)$$

The second and fourth term are differences in the superconducting material and are found from the supercurrent equation (2.2.2) for $\nabla\theta$:

$$\theta_{P_c} - \theta_{Q_b} = \int_{Q_b}^{P_c} \nabla\theta \cdot d\mathbf{l} = +\frac{2\pi}{\Phi_0} \int_{Q_b}^{P_c} \Lambda \mathbf{J}_s \cdot d\mathbf{l} + \frac{2\pi}{\Phi_0} \int_{Q_b}^{P_c} \mathbf{A} \cdot d\mathbf{l} \quad (2.2.6)$$

$$\theta_{Q_a} - \theta_{P_d} = \int_{P_d}^{Q_a} \nabla\theta \cdot d\mathbf{l} = +\frac{2\pi}{\Phi_0} \int_{P_d}^{Q_a} \Lambda \mathbf{J}_s \cdot d\mathbf{l} + \frac{2\pi}{\Phi_0} \int_{P_d}^{Q_a} \mathbf{A} \cdot d\mathbf{l} . \quad (2.2.7)$$

Substituting (2.2.4) – (2.2.7) into (2.2.3) yields

$$\varphi(Q) - \varphi(P) = -\frac{2\pi}{\Phi_0} \oint_C \mathbf{A} \cdot d\mathbf{l} - \frac{2\pi}{\Phi_0} \int_{Q_b}^{P_c} \Lambda \mathbf{J}_s \cdot d\mathbf{l} - \frac{2\pi}{\Phi_0} \int_{P_d}^{Q_a} \Lambda \mathbf{J}_s \cdot d\mathbf{l} . \quad (2.2.8)$$

The integration of \mathbf{A} is around a close contour and therefore is equal to the total flux Φ inside the area enclosed by the contour. The integration of \mathbf{J}_s follows the same contour C but excludes the integration over the insulating barrier. We rewrite this integral as an integral along the incomplete contour C' :

$$\oint_{C'} \Lambda \mathbf{J}_s \cdot d\mathbf{l} = \int_{Q_b}^{P_c} \Lambda \mathbf{J}_s \cdot d\mathbf{l} + \int_{P_d}^{Q_a} \Lambda \mathbf{J}_s \cdot d\mathbf{l} . \quad (2.2.9)$$

Then, the difference of the gauge-invariant phase difference between point Q and P is obtained to

$$\varphi(Q) - \varphi(P) = -\frac{2\pi\Phi}{\Phi_0} - \frac{2\pi}{\Phi_0} \oint_{C'} \Lambda \mathbf{J}_s \cdot d\mathbf{l} . \quad (2.2.10)$$

Discussing the magnitude of the line integral of the current density we can note the following: First, the integration of the current density along one segment of the path in x -direction cancels with the contribution of the adjacent path, which is only an infinitesimal distance dz away. Second, each part of the integration in the z -direction is taken deep inside ($\gg \lambda_L$) the superconducting electrode, where the current density induced by the applied field is exponentially small. Furthermore, the applied current is in the negative x -direction. That is, it is perpendicular to the integration path along z and therefore contributes nothing to the integral of the current density. Therefore, the line integral of the current density vanishes and we obtain

$$\varphi(P) - \varphi(Q) = \frac{2\pi\Phi}{\Phi_0} . \quad (2.2.11)$$

We see that the normalized shift $[\varphi(P) - \varphi(Q)]/2\pi$ of the gauge invariant phase difference is just given by the normalized magnetic flux Φ/Φ_0 threading the junction between the positions z and $z + dz$.

Since the magnetic field decays exponentially into each superconducting electrodes the total flux enclosed by the contour line is

$$\Phi = B_y(d + \lambda_{L1} + \lambda_{L2}) dz = B_y t_B dz . \quad (2.2.12)$$

Then, with $\varphi(P) - \varphi(Q) = \frac{2\pi}{\Phi_0} B_y t_B dz = \frac{\partial \varphi}{\partial z} dz$ we obtain

$$\frac{\partial \varphi}{\partial z} = \frac{2\pi}{\Phi_0} B_y t_B \quad (2.2.13)$$

We can use a similar argument by choosing point Q and P at an infinitesimal distance dy in the y -direction and obtain

$$\frac{\partial \varphi}{\partial y} = -\frac{2\pi}{\Phi_0} B_z t_B . \quad (2.2.14)$$

In general, we can write

$$\nabla \varphi(\mathbf{r}, t) = \frac{2\pi}{\Phi_0} t_B [\mathbf{B}(\mathbf{r}, t) \times \hat{\mathbf{x}}] , \quad (2.2.15)$$

where $\hat{\mathbf{x}}$ is the unit vector in x -direction, that is the unit vector perpendicular to the junction area (anti-parallel to the current flow in our case).

Integration of (2.2.13) gives

$$\varphi(z) = \frac{2\pi}{\Phi_0} B_y t_B z + \varphi_0 , \quad (2.2.16)$$

where the integration constant φ_0 is the phase difference at $z = 0$. Using the current-phase relation we obtain the supercurrent density to

$$J_s(y, z, t) = J_c(y, z) \sin\left(\frac{2\pi}{\Phi_0} t_B B_y z + \varphi_0\right) = J_c(y, z) \sin(kz + \varphi_0) \quad (2.2.17)$$

with $k = \frac{2\pi}{\Phi_0} t_B B_y$. We see that J_s varies sinusoidally along the z -direction with the oscillation period $\Delta z = 2\pi/k$ given by $\Phi_0/t_B B_y$. That is, Δz is inversely proportional to the product of the applied field and the effective magnetic thickness. We also immediately see that $\Delta z t_B B_y = \Phi = \Phi_0$, i.e. the magnetic flux through the junction within a single oscillation period corresponds to a single flux quantum.

So far we have assumed that the thickness of the junction electrodes is much larger than the London penetration depth. If $t_1 < \lambda_{L1}$ and $t_2 < \lambda_{L2}$ the magnetic field penetrates the complete electrode and the Meissner shielding currents are less than those in thick electrodes. As a result the effective value of the magnetic thickness of the junction increases and the magnetic thickness t_B has to be replaced by

$$\tilde{t}_B = d + \lambda_{L1} \coth \frac{t_1}{\lambda_{L1}} + \lambda_{L2} \coth \frac{t_2}{\lambda_{L2}} . \quad (2.2.18)$$

2.2.2 The Fraunhofer Diffraction Pattern

In this subsection we discuss, how the integral current $I_s = \iint J_s(y, z) dy dz$ across the junction depends on the applied magnetic field. We first integrate the maximum Josephson current density $J_c(y, z)$ in the direction of the applied magnetic field. If the external field is in y -direction ($\mathbf{B}_e = (0, B_y, 0)$) we obtain

$$i_c(z) = \int_{-W/2}^{W/2} J_c(y, z) dy . \quad (2.2.19)$$

With this expression, according to (2.2.17) we obtain

$$I_s(B_y) = \int_{-L/2}^{L/2} i_c(z) \sin(kz + \varphi_0) dz . \quad (2.2.20)$$

This expression is equivalent to

$$I_s(B_y) = \Im \left\{ e^{i\varphi_0} \int_{-\infty}^{\infty} i_c(z) e^{ikz} dz \right\} , \quad (2.2.21)$$

where $k = \frac{2\pi}{\Phi_0} t_B B_y$. Since $i_c(z)$ is zero outside the junction, i.e. for $|z| > L/2$, we have replaced the integration limits by $\pm\infty$.

In general, the integral in (2.2.21) is a complex number with magnitude and phase. When the integral is multiplied by $e^{i\varphi_0}$, only the phase but not the magnitude changes. Therefore, the maximum Josephson current I_s^m is just given by the magnitude of the integral, that is by

$$I_s^m(B_y) = \left| \int_{-\infty}^{\infty} i_c(z) e^{ikz} dz \right| . \quad (2.2.22)$$

This integral represents a Fourier integral, that is, the magnetic field dependence of the maximum Josephson current I_s^m is given by the Fourier transform of the function $i_c(z)$. This is completely analogous to optics, where the intensity of the light behind a slit of width L and transmission function $i_c(z)$ is given by the Fourier transform of the transmission function.

If the maximum Josephson current density $J_c(y, z)$ of the junction is spatially homogeneous, the magnitude of $i_c(z)$ is constant for $-L/2 \leq z \leq +L/2$ and zero for $|z| > L/2$. In this case the $I_s^m(B_y)$ dependence is equivalent to the diffraction pattern of a slit of width L with constant transmission i_c . The diffraction pattern is the well known **Fraunhofer diffraction pattern** shown by Fig. 2.5:

$$I_s^m(\Phi) = I_c \left| \frac{\sin \frac{kL}{2}}{\frac{kL}{2}} \right| = I_c \left| \frac{\sin \frac{\pi\Phi}{\Phi_0}}{\frac{\pi\Phi}{\Phi_0}} \right| . \quad (2.2.23)$$

Here, $\Phi = B_y t_b L$ is the flux through the junction and $I_c = i_c L$. We note that the experimental observation of the Fraunhofer diffraction pattern $I_s^m(\Phi)$ given by (2.2.23) was very important to prove the Josephson

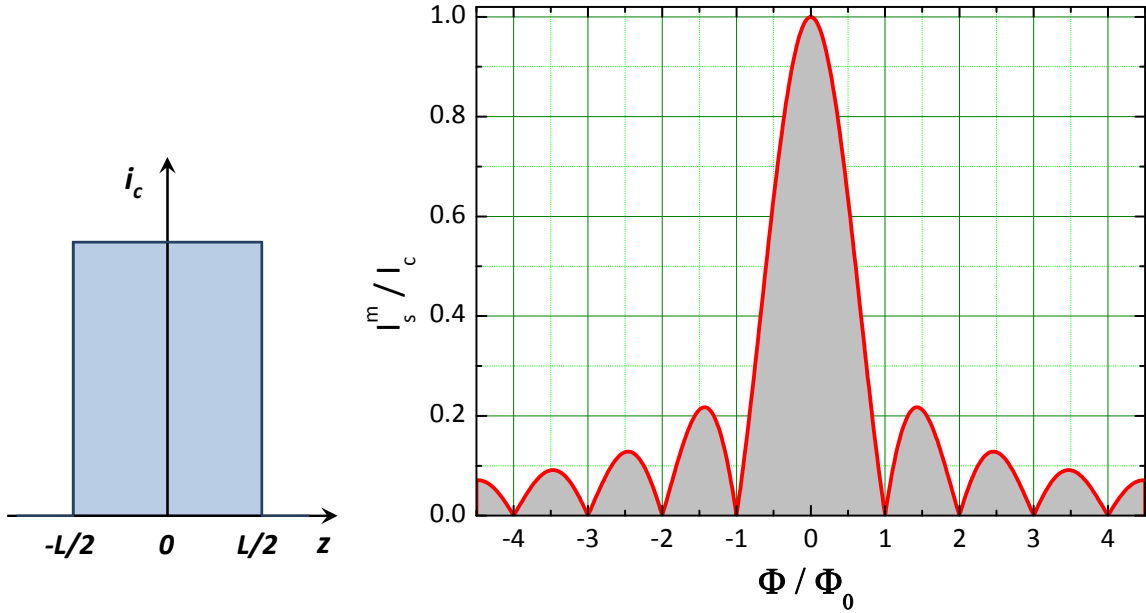


Figure 2.5: Magnetic field dependence of the maximum Josephson current I_s^m of a short Josephson junction. On the left the maximum current density integrated along the magnetic field direction, $i_c(z) = \int J_c(y, z) dy$, is shown for the case of a spatially homogeneous maximum current density $J_c(y, z)$.

tunneling of Cooper pairs. From the experimental point of view it was unclear whether the measured supercurrent in a superconductor/insulator/superconductor tunnel junction is flowing as a homogeneous Josephson tunneling current or just through small pinholes in the tunneling barrier. However, if the latter would have been true, no Fraunhofer diffraction pattern would have been observed for the $I_s^m(\Phi)$ dependence.

To understand the shape of the $I_s^m(\Phi)$ dependence we consider the spatial distribution of $i_s(z) = \int J_s(y, z) dy$ along the z -direction for a magnetic field applied in y -direction. For zero field, that is $\Phi = 0$ the gauge-invariant phase difference is constant, $\varphi(z) = \varphi_0$, and hence $i_s(z) = \text{const}$. The maximum Josephson current is obtained for $\varphi_0 = -\pi/2$, that is, $J_s(y, z) = -J_c(y, z)$ (note that the current is flowing in negative x -direction, see Fig. 2.6a). If we feed a current less than the maximum Josephson current through the junction, we have $\varphi_0 \neq \pi/2$ and the local current density is just $J_s(y, z) = J_c(y, z) \sin \varphi_0 < J_c(y, z)$.

We next consider the case of an externally applied magnetic flux of $\Phi = \Phi_0/2$. In this case according to (2.2.16) the gauge-invariant phase difference $\varphi(z)$ varies as

$$\varphi(z) = \frac{2\pi\Phi}{\Phi_0} \frac{z}{L} + \varphi_0 = \frac{\pi z}{L} + \varphi_0 . \quad (2.2.24)$$

Therefore, the supercurrent density varies sinusoidally with z . The difference of the phases between the two edges of the junction is

$$\varphi(L/2) - \varphi(-L/2) = \pi . \quad (2.2.25)$$

That means that half of a full oscillation period fits into the junction. This situation is shown in Fig. 2.6b. Which half period to put into the junction depends on the choice of φ_0 . In Fig. 2.6b we have made the choice $\varphi_0 = -\pi/2$. In this case the phase difference increases from $-\pi$ at $z = -L/2$ to 0 at $z = +L/2$. This choice gives the maximum possible Josephson current I_c^m in negative x -direction. Note that for $\varphi = 0$ we obtain a vanishing total Josephson current.

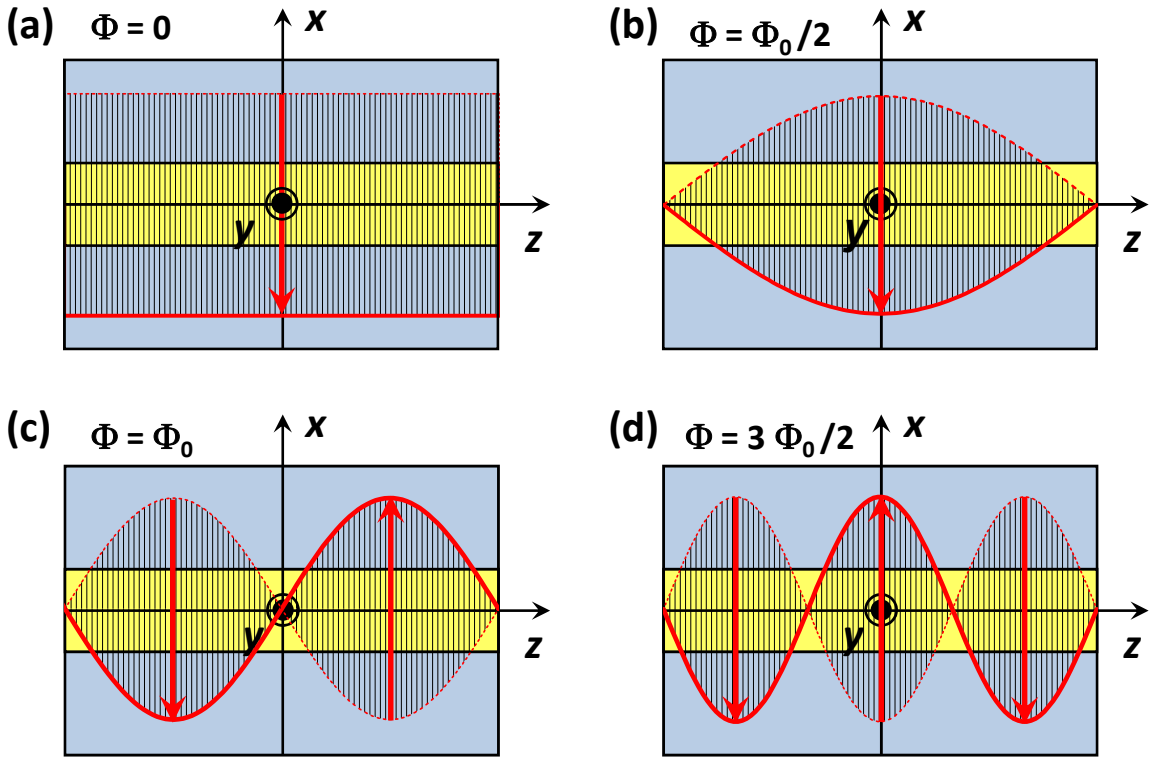


Figure 2.6: The Josephson current density distribution along a small Josephson junction extending from $-L/2$ to $+L/2$ in z -direction. (a) $\Phi = 0$, $\phi_0 = -\pi/2$ (b) $\Phi = \frac{1}{2}\Phi_0$, $\phi_0 = -\pi/2$, (c) $\Phi = \Phi_0$, $\phi_0 = 0$ and (d) $\Phi = \frac{3}{2}\Phi_0$, $\phi_0 = +\pi/2$. The magnetic field is applied in y -direction. The external current is applied in negative x -direction.

In Fig. 2.6c and d we show the situation for $\Phi = \Phi_0$ and $\Phi = \frac{3}{2}\Phi_0$, respectively. For $\Phi = \Phi_0$ the total phase difference from one edge of the junction to the other is 2π and a complete oscillation period of the Josephson current density fits into the junction. In this case the total Josephson current is zero irrespective of the choice of ϕ_0 . For $\Phi = \frac{3}{2}\Phi_0$ the total phase difference from one edge to the other is 3π and one and a half oscillation periods of the Josephson current density fit into the junction. The current from the full period is zero and the total current is determined by a half period. Of course, the total current is smaller than for $\Phi = \Phi_0/2$ when a half period fits the whole junction. This shows that the Josephson current generally tends to decrease with increasing applied magnetic field as shown in Fig. 2.5.

In order to illustrate the magnetic field dependence of the maximum Josephson current as the result of a spatial interference effect of the macroscopic wave functions in the two superconducting electrodes we consider Fig. 2.7. Superconductor 1 is described by a plane wave with the plane of constant phase parallel to the barrier. In the same way, superconductors 2 is described by a plane wave, however, with the plane of constant phase tilted due to the phase shift caused by the magnetic field B_y . The phase shift at position z is given by $\delta\phi(z) = \frac{2\pi}{\Phi_0}B_y t_B z + \phi_0$. For the situation shown in Fig. 2.7 we immediately see that each partial wave has a counterpart with a phase shift of π causing destructive interference. This is just the situation where the total Josephson current through the junction is zero.

We discuss in more detail the situation for $\Phi = \Phi_0$ shown in Fig. 2.6c. Evidently in this situation the Josephson current density flows in negative and positive x -direction on the left and right side of the junction, respectively. The question is, how the supercurrent density can have such pattern across the insulating barrier without any net driving current. The solution is shown in Fig. 2.8. The supercurrent on the left side turns around in the bottom electrode so as to match the supercurrent density in the insulator on the right side. Actually the supercurrent has to bend to avoid the penetration of the applied magnetic field into the electrode material over a length scale larger than the London penetration depth.

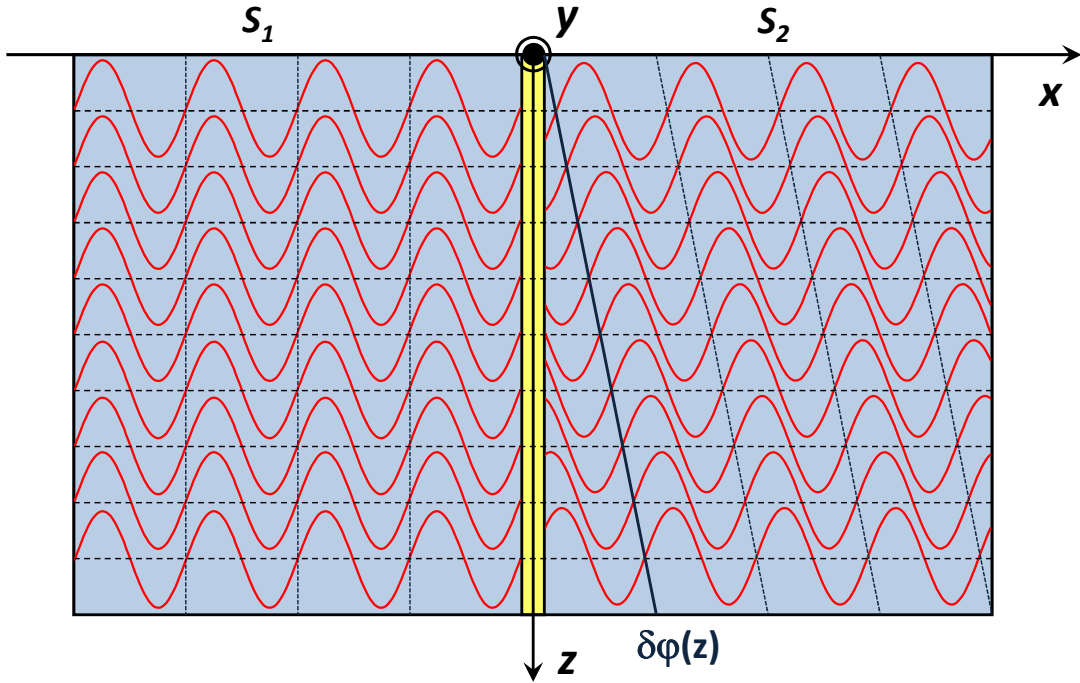


Figure 2.7: Illustration of the magnetic field dependence of the maximum Josephson current as a spatial quantum interference phenomenon. The applied magnetic field B_y causes a position dependent phase shift $\delta\phi(z) = \frac{2\pi}{\Phi_0} B_y t_B z + \phi_0$ (we have chosen $\phi_0 = 0$ for simplicity).

The resulting supercurrent density pattern resembles the pattern of an Abrikosov vortex in a type-II superconductor and is known as **Josephson vortex**. Note that in contrast to an Abrikosov vortex the Josephson vortex does not need to have a normal core. The vortex core is located in the barrier region where the pair density is exponentially small.

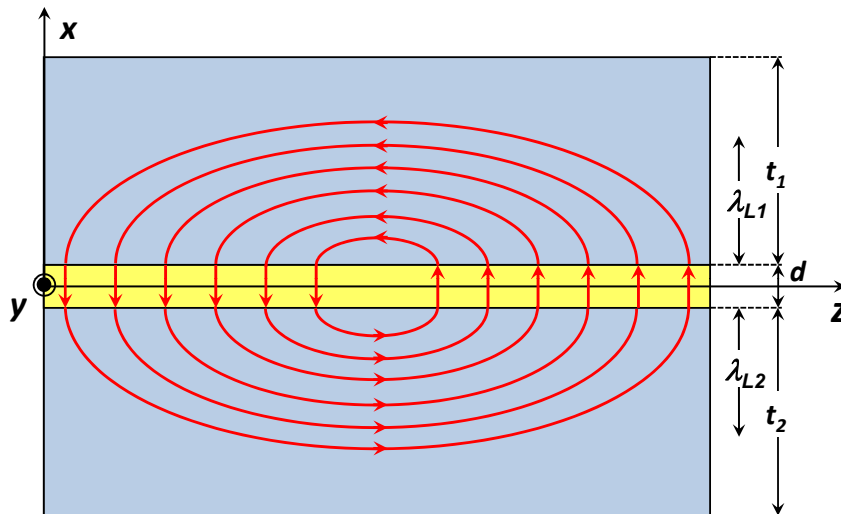


Figure 2.8: The supercurrent distribution in the superconducting electrodes and across the insulator for the case $\Phi = \Phi_0$. The pattern is known as the Josephson vortex.

Arbitrary Magnetic Field Direction

We consider a short Josephson junction as shown in Fig. 2.4 and let the applied magnetic field lie in an arbitrary direction within the plane of the junction barrier so that

$$\mathbf{B}_e = B_y \hat{\mathbf{y}} + B_z \hat{\mathbf{z}} . \quad (2.2.26)$$

Here, $\hat{\mathbf{y}}$ and $\hat{\mathbf{z}}$ are the unit vectors in y - and z -direction. By generalizing the arguments given above, for this situation the magnetic field dependence of the maximum Josephson current can be expressed as

$$I_s^m(\Phi) = I_c \left| \frac{\sin \frac{\pi \Phi_y}{\Phi_0}}{\frac{\pi \Phi_y}{\Phi_0}} \right| \left| \frac{\sin \frac{\pi \Phi_z}{\Phi_0}}{\frac{\pi \Phi_z}{\Phi_0}} \right| , \quad (2.2.27)$$

where $\Phi_y = B_y t_b L$ and $\Phi_z = B_z t_b W$. Equivalently, we can write

$$I_s^m(\mathbf{B}_e) = \left| \int_S J_c(y, z) e^{i\mathbf{k} \cdot \mathbf{r}} dS \right| . \quad (2.2.28)$$

Here, $S = L \cdot W$ is the junction area, \mathbf{r} the position vector in the two-dimensional yz -plane, and dS the differential area element in that plane.

2.2.3 Determination of the Maximum Josephson Current Density

In real Josephson junctions usually the critical current density $J_c(y, z)$ is spatially inhomogeneous due imperfections of the fabrication process or a spatially varying thickness of the tunneling barrier. That is, this quantity usually is not known. Therefore, for researchers fabricating Josephson junctions it would be very desirable to be able to determine the spatial distribution $J_c(y, z)$ experimentally. A suitable method would be the measurement of the $I_s^m(\Phi)$ dependence. However, it is evident from (2.2.22) or (2.2.23) that the distribution $J_c(y, z)$ cannot be derived from the measured $I_s^m(\Phi)$ dependence by performing an inverse Fourier transformation. The reason for that is that in a measurement only the amplitude of the complex function $I_s(\Phi)$ is measured but not the phase. Therefore, the back transformation of $I_s^m(\Phi)$ to obtain $i_c(y, z)$ is not possible.³

By making some assumptions about the properties of the function $i_c(z)$ one can restore $i_c(z)$ approximately from the measured $I_s^m(\Phi)$ dependence. For example, if $i_c(z)$ is symmetrical with respect to the junction midpoint, we obtain

$$i_c(z - L/2) = \frac{1}{\pi} \int_0^\infty |I_s^m(k)| \cos(kz) (-1)^{n(k)} dk , \quad (2.2.29)$$

where $k = \frac{2\pi}{\Phi_0} t_B B_y$ and n is the number of zeros of $|I_s^m(k)|$ between 0 and k . Analyzing this equation we see that the secondary maxima of the diffraction pattern are increased or reduced, if $i_c(z)$ increases or

³We note that in principle also the phase can be measured directly using specific junction configurations. However, this has not yet been used in experiments. See e.g. L. D. Jackel, R. A. Buhrman, W. W. Webb, Phys. Rev. **B 10**, 2782 (1974); J. R. Waldram, J. M. Lumley, Rev. Phys. Appl. **10**, 7 (1975); J. E. Meservey, P. W. Tedrow, D. Paraskevopoulos, IEEE Trans. Magn. **11**, 720 (1975); R. Rifkin, B.S. Deaver, Phys. Rev. **B 13**, 3894 (1976).

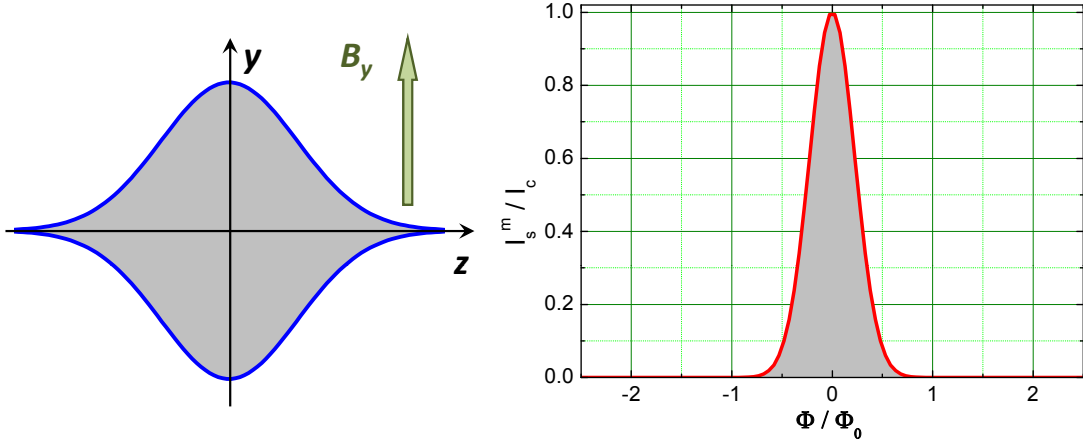


Figure 2.9: Left: Gaussian shaped junction area extending in the yz -plane. For spatially homogeneous $J_c(y, z)$ the current density integrated in y -direction, $i_c(z) = \int J_c(y, z) dy$ corresponds to a Gaussian profile. Right: Magnetic field dependence of the maximum Josephson current as a function of the flux through junction. The magnetic field is applied in y -direction.

decreases towards the junction edges, respectively.⁴ Note that $i_c(z)$ is determined by applying the field in y -direction and measuring $I_s^m(\Phi)$. In the same way, we can determine $i_c(y)$ by applying the magnetic field in z -direction and measuring the corresponding $I_s^m(\Phi)$. The two-dimensional distribution $J_c(y, z)$ can be determined by measuring $I_s^m(\Phi)$ for various field directions.

In order to get information on $J_c(y, z)$ on a very small length scale, we have to measure the $I_s^m(\Phi)$ dependence up to high magnetic fields. If we could do a Fourier back transformation, the spatial resolution would be given by $2\pi/k$. With $k = \frac{2\pi}{\Phi_0} t_B B_y$ and $\Phi = B_y t_B L$ we obtain

$$\frac{2\pi}{k} = \frac{\Phi_0}{t_B} \frac{1}{B_y} = L \frac{\Phi_0}{\Phi} . \quad (2.2.30)$$

We see that the spatial resolution is proportional to $1/B_y$. If we are measuring the $I_s^m(\Phi)$ dependence only up to $\Phi/\Phi_0 = 1$, we obtain a spatial resolution only of the order of the junction length L .

In some applications of Josephson junction (e.g. x-ray detectors) the Josephson current has to be suppressed by an applied magnetic field. Therefore, a $I_s^m(\Phi)$ dependence having only a central maximum and vanishing side lobes is desirable. This can be achieved by generating a $i_c(z)$ dependence that is close to a Gaussian profile

$$i_c(z) = i_c(0) \exp\left(-\frac{z^2}{2\sigma^2}\right) . \quad (2.2.31)$$

Since the Fourier transform of a Gaussian profile again is a Gaussian profile, we obtain a $I_s^m(\Phi)$ dependence that has no side lobes

$$I_s^m(\Phi) = \sqrt{\frac{1}{2\pi}} i_c(0) L \exp(-\sigma k^2) = \sqrt{\frac{1}{2\pi}} i_c(0) L \exp\left(-\sigma \frac{4\pi^2 \Phi^2}{L^2 \Phi_0^2}\right) . \quad (2.2.32)$$

As shown in Fig. 2.9, a Gaussian profile of $i_c(z)$ can be achieved by not choosing a rectangular shaped junction geometry but a shape that well approaches a Gauss curve. For homogeneous $J_c(y, z)$ then $i_c(z)$ is close to a Gauss profile resulting in a good suppression of the side lobes of the $I_s^m(\Phi)$ curve.

⁴A. Barone, G. Paterno, M. Russo, R. Vaglio, physica status solidi A **41**, 393 (1977).

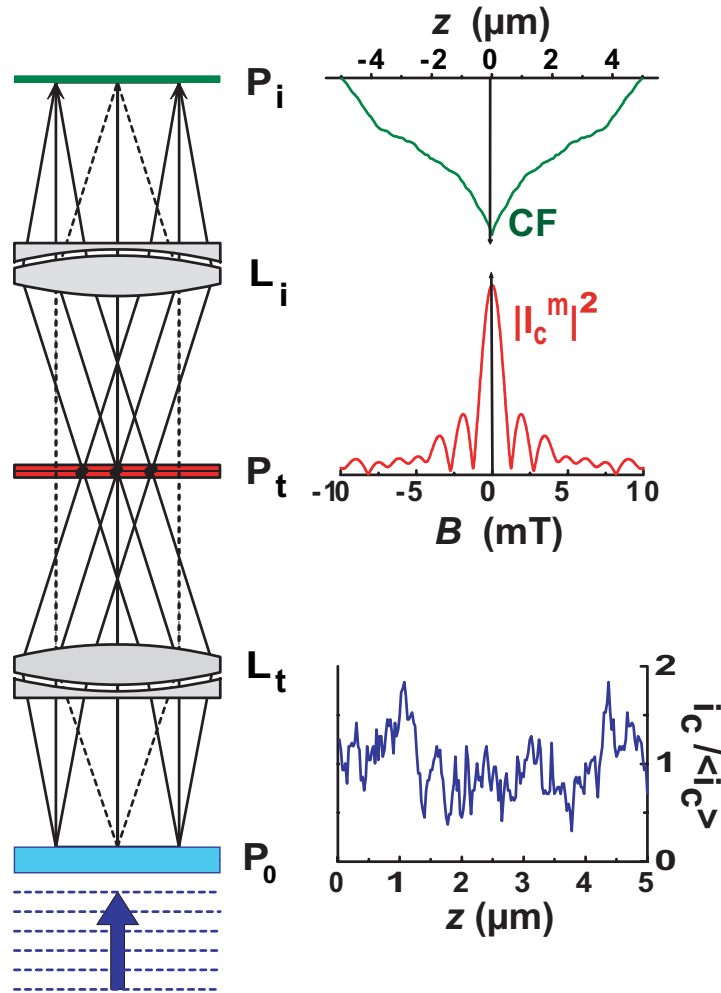


Figure 2.10: Comparison of the measurement of the maximum Josephson current (right) and an optical diffraction experiment (left). Note that in optics the second Fourier transformation recovers an image P_i of the transmission function P_0 .

Additional Topic: The Supercurrent Auto-correlation Function

We briefly compare the measurement of the maximum Josephson current as a function of an applied magnetic field to an optical diffraction experiment (see Fig. 2.10). In the optical diffraction experiment a plane wave is illuminating an object (e.g. a slide) with a transmission function $P_0(z)$. This transmission function corresponds to the spatial distribution $i_c(z)$ of the maximum Josephson current density integrated along the field direction (y -direction for the situation shown in Fig. 2.10). In the simplest case the transmission function is that of an ideal slit, which is constant inside and zero outside the slit. This would correspond to an ideal rectangular shaped junction with spatially homogeneous $J_c(y, z)$. In the more general case the transmission probability or equivalently $i_c(z)$ may vary along z as shown in Fig. 2.10.

For the optics experiment, the measurement of the $I_s^m(B_y)$ dependence corresponds to the observation of the square root of the light intensity P_t in the focal plane after the first lens system L_t . However, in optics in the focal plane both the amplitude and the phase are recovered and, hence, a back-transformation of P_t can be made by a second lens system L_i resulting in an image P_i of the original transmission function P_0 . This is just the well known optical imaging process. The spatial resolution of this imaging process

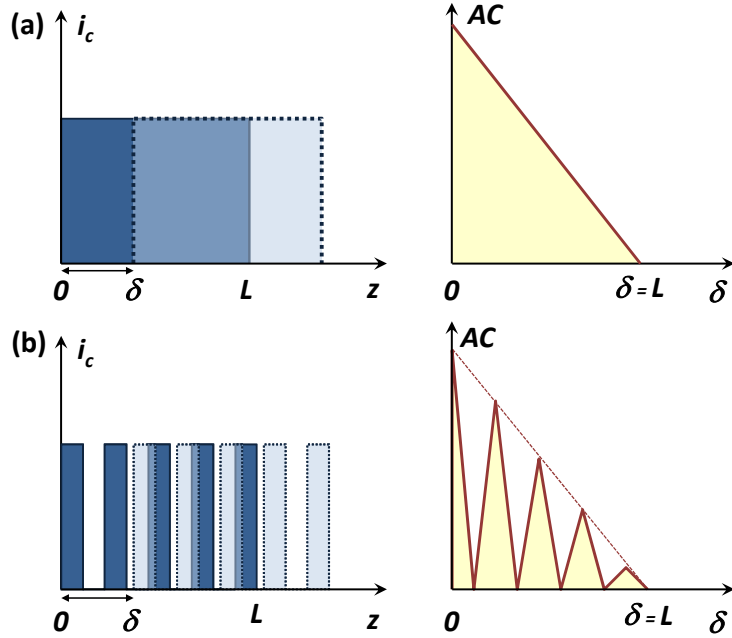


Figure 2.11: (a) The supercurrent auto-correlation function for an ideal slit function $i_c(z)$ obtained for a rectangular shaped Josephson junction with homogeneous critical current density $J_c(y, z)$. (b) The supercurrent auto-correlation function for a periodic function $i_c(z)$. The auto-correlation function shows a modulation with the periodicity of the periodic function.

depends on how many diffraction orders are used for reconstructing the image. In Fig. 2.10 we only have shown the 0^{th} as well as the $\pm 1^{st}$ order for simplicity. For the $I_c^m(B_y)$ measurement, in principle the same process could be performed, if both the amplitude and the phase of $I_c^m(B_y)$ could be measured. Then, in the imaging process the spatial resolution of the $i_c(z)$ image would be given by the number of side lobes of the diffraction pattern used for the reconstruction process. However, as already discussed above, in an experiment we are only measuring the amplitude of $I_c^m(B_y)$ and not the phase. Therefore, in a second Fourier transformation we can back-transform only the intensity $(I_c^m)^2(B_y)$. As we discuss now, the Fourier transform of the intensity distribution is just the auto-correlation function of the supercurrent distribution along the junction.

In general, the auto-correlation function is defined as

$$AC(\delta) = \int_{-\infty}^{\infty} i_c(z) i_c(z + \delta) dz . \quad (2.2.33)$$

This expression shows, that the auto-correlation function is just obtained by calculating the overlap between the function $i_c(z)$ and the same function shifted by δ . This is illustrated in Fig. 2.11a, where we have plotted the auto-correlation function for a simple slit function. It is evident that the auto-correlation function is a linearly decreasing function. If the function $i_c(z)$ is not constant across the width L of the slit but varies strongly as schematically shown in Fig. 2.11b, the auto-correlation function no longer shows a linear decrease but a rich fine structure. Only the envelop shows a linear decay.

Using the **Wiener-Khintchine theorem**^{5,6} we can express the auto-correlation function of the supercur-

⁵N. Wiener, *Generalized harmonic analysis*, Acta Mathematica **55**, 117 (1930).

⁶A. Khintchine, *Korrelationstheorie der stationären stochastischen Prozesse*, Math. Ann. **109**, 604 (1934).

rent distribution $i_c(z)$ in terms of the intensity of the $I_s^m(B_y)$ dependence:

$$\text{AC}(\delta) = \int_{-\infty}^{\infty} |I_s^m(k)|^2 e^{ik\delta} dk , \quad (2.2.34)$$

where $k = \frac{2\pi}{\Phi_0} t_B B_y = \frac{1}{L} 2\pi \frac{\Phi}{\Phi_0}$. We immediately see that the spatial information contained in the autocorrelation function depends on the k , or equivalently the magnetic field interval, used in the measurement of the $I_s^m(B_y)$ dependence. According to (2.2.30) we have the spatial resolution $2\pi/k = L \frac{\Phi_0}{\Phi}$. That is, recording the $I_s^m(B_y)$ dependence up to the 100^{th} side lobe (equivalent to $\frac{\Phi_0}{\Phi} = 0.01$) we have a spatial resolution of 0.01 times the junction width.

Note that already the envelop of the $|I_s^m(B_y)|^2$ curve contains valuable statistical information on the supercurrent distribution.⁷ If we have for example inhomogeneities of $i_c(z)$, which have a probability distribution $p(a) \propto 1/a$, that is, if the probability times the characteristic length scale a of the inhomogeneity is constant, then the envelop of the $|I_s^m(B_y)|^2$ curve follows a $1/B_y$ dependence. Therefore, we speak about “spatial $1/f$ noise”.⁸ The presence of such inhomogeneities can be checked easily in the experiment by plotting $\log |I_s^m(B_y)|^2$ versus $\log B_y$. In such a plot one should obtain a straight line with a slope of -1 . If, in contrast, the supercurrent distribution would be formed by a random distribution of filaments of width a , then the envelop of the autocorrelation function should be a constant function up to $k = 2\pi/a$ and then should fall off proportional to $1/B_y^2$. In this case we speak of “spatial shot noise”.⁹ These two examples show that the analysis of the autocorrelation function can yield valuable statistical information on inhomogeneities of the critical current density.

An experimental example is shown in Fig. 2.12. Here, the $I_s^m(B_y)$ dependence of a $\text{YBa}_2\text{Cu}_3\text{O}_{7-\delta}$ grain boundary Josephson junction has been measured up to an applied magnetic field of 5 Tesla. In a $\log |I_s^m(B_y)|$ versus $\log B_y$ plot one obtains a slope of about -0.65 corresponding to $\log |I_s^m(B_y)|^2 \propto 1/B_y^{1.3}$. From this observation one can conclude that there are spatial inhomogeneities in the supercurrent distribution that have a probability distribution $p(a) \propto 1/a^{1.5}$. That is, inhomogeneities with smaller characteristic length scale a have higher probability.

2.2.4 Additional Topic: Direct Imaging of the Supercurrent Distribution

Since it is difficult to derive the spatial distribution of the maximum Josephson current density from measurements of $I_s^m(\Phi)$, direct imaging methods have been developed.¹⁰ In these imaging methods the Josephson junction is scanned by a focused electron or laser beam and the change $\delta I_s^m(y, z)$ of the maximum Josephson current is measured as a function of the beam position (y, z) . As discussed in more detail in Appendix B, the measured change $\delta I_s^m(y, z)$ of the integral junction current in first approximation

⁷see e.g. O. M. Fröhlich, H. Schulze, A. Beck, R. Gerdemann, R. Gross, R. P. Huebener, IEEE Trans. Appl. Supercond. **5**, 2188 (1995); O. M. Fröhlich, H. Schulze, A. Beck, B. Mayer, L. Alff, R. Gross, R. P. Huebener, Appl. Phys. Lett. **66**, 2289 (1995).

⁸In the analysis of fluctuating time signals one is plotting the intensity of the Fourier transform of the time signal (the power spectral density S) versus frequency and often obtains a $1/f$ dependence. This is the signature of so-called $1/f$ noise that is ubiquitous in nature. The power spectral density $S(f)$ corresponds to $|I_c^m(B_y)|^2$.

⁹In the analysis of time signals the random appearance of spikes of constant width δt is known to appear due to the discrete nature of physical quantities (e.g. the electronic charge in charge transport). The resulting noise is called shot noise. This noise is white, that is, frequency independent up to high frequencies $f \propto 1/\delta t$ and then falls off as $1/f^2$.

¹⁰for a review see R. Gross, D. Kölle, *Low Temperature Scanning Electron Microscopy of Superconducting Thin Films and Josephson Junctions*, Reports on Progress in Physics **57**, 651-741 (1994).

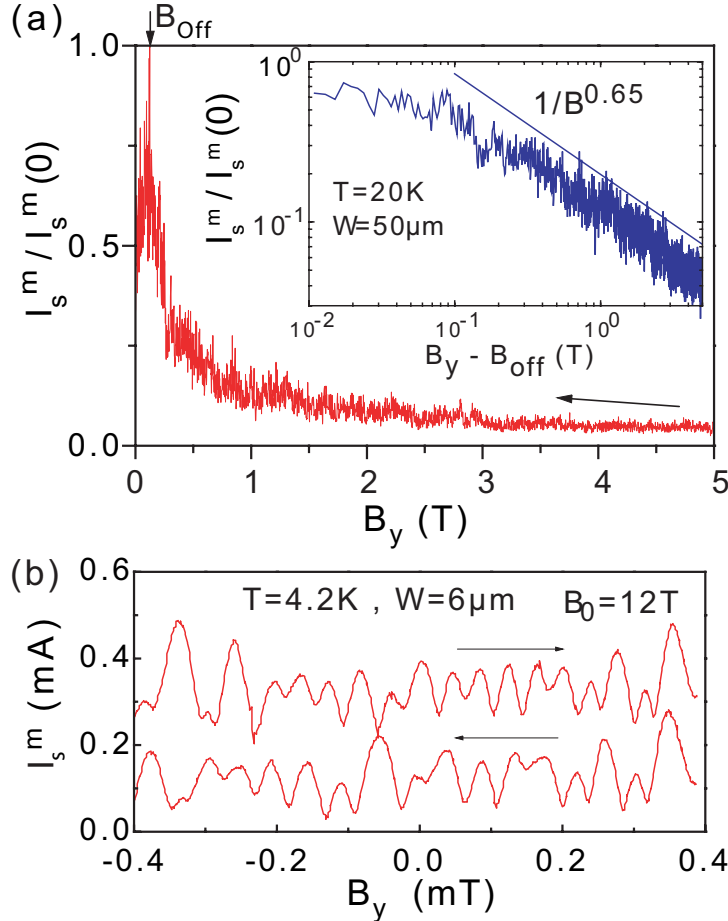


Figure 2.12: (a) I_s^m vs B_y dependence of a $\text{YBa}_2\text{Cu}_3\text{O}_{7-\delta}$ grain boundary Josephson junction recorded for decreasing magnetic field at $T = 20 \text{ K}$. The inset shows I_s^m vs $B_y - B_{\text{off}}$ on a log-log scale. (b) Modulation of I_s^m with varying B_y for opposite sweep directions as indicated by the arrows at a base field $B_0 = 12 \text{ T}$. The curve for increasing field is shifted vertically by $0.2 \mu\text{A}$ for clarity (from O. Fröhlich *et al.*, Appl. Phys. Lett. **66**, 2289 (1995)).

is directly proportional to the local critical current density $J_c(y, z)$. Hence, by scanning the junction and measuring $\delta I_s^m(y, z)$ simultaneously, a two-dimensional image of $J_c(y, z)$ is obtained.

The local perturbation of the focused electron or laser beam can be modeled in most cases by a local thermal heating effect. Therefore, the spatial resolution of the imaging technique is not determined by the diameter of the focused electron or laser beam, but by the so-called thermal healing length, which determines the diameter of the heated sample region. Typically, for superconducting thin film structures this length scale is of the order of $1 \mu\text{m}$.

2.2.5 Additional Topic: Short Josephson Junctions: Energy Considerations

After having found the spatial distribution of the maximum Josephson current density we now discuss the energy E associated with a short Josephson junction. Doing so, we derive a criterion for the notation ‘‘short’’. We will see that short means smaller than a characteristic length scale λ_J , the **Josephson penetration depth**.

The junction energy is given by the sum

$$E = E_S + E_I , \quad (2.2.35)$$

where E_S is the energy stored in the superconducting electrodes and E_I the energy stored in the insulating barrier. The energy stored in the superconducting electrodes is the sum of the magnetic field energy and the kinetic energy of the superelectrons. It is given by

$$E_S = \frac{1}{2\mu_0} \int_{V_s} (\mathbf{B}^2 + \mu_0 \Lambda \mathbf{J}_s^2) dV , \quad (2.2.36)$$

where the integration is over the superconducting volume V_s . This expression, which can be derived from the first London equation, is not valid for the insulating barrier. Here, instead of the kinetic energy of the superelectrons we have to use the Josephson coupling energy E_J . We obtain

$$E_I = \frac{1}{2\mu_0} \int_{V_i} \mathbf{B}^2 dV + \int_{V_i} \frac{1}{d} \frac{E_J}{A_i} dV . \quad (2.2.37)$$

Here, $V_i = A_i \cdot d$ is the volume of the insulator with A_i the junction area and d the barrier thickness. With $E_J/A_i = \frac{\Phi_0 J_c}{2\pi} (1 - \cos \varphi)$ (compare (2.1.8)) we obtain

$$E_I = \frac{1}{2\mu_0} \int_{V_i} \mathbf{B}^2 dV + \int_{A_i} \frac{\Phi_0 J_c(y, z)}{2\pi} [1 - \cos \varphi(z)] dy dz . \quad (2.2.38)$$

Here, the second term has been integrated over the barrier thickness d thus leaving only an integral over the junction area A_i extending in the yz -plane.

With (2.2.36) and (2.2.38) we obtain the total energy

$$E = \frac{1}{2\mu_0} \int_{V_s+V_i} \mathbf{B}^2 dV + \frac{1}{2} \int_{V_s} \Lambda \mathbf{J}_s^2 dV + \int_{A_i} \frac{\Phi_0 J_c(y, z)}{2\pi} [1 - \cos \varphi(z)] dy dz . \quad (2.2.39)$$

We are now able to give a definition of a short junction by comparing the different energy contributions. We will call a junction short, if the energy E_B stored in the junction due to the external field (first and second term on the right hand side) is much larger than the Josephson coupling energy E_J (third term on the right hand side), that is $E_B \gg E_J$.

We first consider E_B given by the first two integrals in (2.2.39). If the thickness of the superconducting electrodes is larger than the London penetration depth, the first integral dominates so that

$$E_B = \frac{1}{2\mu_0} \int_{V_s+V_i} \mathbf{B}^2 dV . \quad (2.2.40)$$

Note that the magnetic flux density penetrates the superconducting electrodes only up to a length given by the London penetration depth. Therefore, the integration volume is given by $W \cdot L \cdot (d + 2\lambda_L) = A_i \cdot t_B$ (compare Fig. 2.4). Hence, we obtain

$$E_B = \frac{1}{2\mu_0} B_y^2 W L t_B = \frac{1}{2\mu_0} \frac{\Phi^2 W}{t_B L} , \quad (2.2.41)$$

where we have used $\Phi = B_y L t_B$.

We next consider the Josephson coupling energy (energy due to the currents in the junction) given by the last integral in (2.2.39). If we assume for simplicity a spatially homogeneous $J_c(y, z)$, we obtain

$$\begin{aligned} E_J &= \frac{\Phi_0 I_c}{2\pi} - \int_{-W/2}^{W/2} \int_{-L/2}^{L/2} \frac{\Phi_0 J_c(y, z)}{2\pi} \cos \varphi(z) dy dz \\ &= \frac{\Phi_0 I_c}{2\pi} - \int_{-L/2}^{L/2} \frac{\Phi_0 i_c(z)}{2\pi} \cos \varphi(z) dz = \frac{\Phi_0 I_c}{2\pi} - \frac{\Phi_0 I_c}{2\pi} \frac{\sin \frac{\pi \Phi}{\Phi_0}}{\frac{\pi \Phi}{\Phi_0}} \cos \varphi(0) , \end{aligned} \quad (2.2.42)$$

where we have used $\varphi(z) = \frac{2\pi\Phi}{\Phi_0} \frac{z}{L} + \varphi_0$ (compare (2.2.24)).

Comparing E_J and E_B for the typical flux of one flux quantum in the junction area, the condition $E_B \gg E_J$ can be written as

$$\frac{1}{2\mu_0} \frac{\Phi_0^2 W}{t_B L} \gg \frac{\Phi_0 I_c}{2\pi} . \quad (2.2.43)$$

With the critical current density $J_c = I_c/WL$ this inequality can be expressed as

$$L \ll \tilde{\lambda}_J \equiv \sqrt{\frac{\pi \Phi_0}{\mu_0 J_c t_B}} . \quad (2.2.44)$$

Hence, a junction is considered short, if its length L is small compared to the characteristic length scale $\tilde{\lambda}_J$. This length is equal to the so-called **Josephson penetration depth** λ_J introduced in section 2.3 within a factor of the order of unity. In the discussion of long Josephson junctions in section 2.3 we will see, how λ_J is entering the equations describing these junction as a natural length scale.

2.2.6 The Motion of Josephson Vortices

Above we have seen that vortices can be used to visualize the Josephson current density in a current driven junction. We now discuss the situation, where Josephson vortices are moving along the junction in z -direction at a constant velocity v_z .

For a short Josephson junction the magnetic field due to the Josephson current density itself can be neglected compared to the external field and we can therefore assume that the flux density in the junction is given by the external field $\mathbf{B}_e = (0, B_y, 0)$. Hence, the gauge-invariant phase difference must satisfy equation (2.2.14):

$$\frac{\partial \varphi}{\partial z} = \frac{2\pi}{\Phi_0} B_y t_B . \quad (2.2.45)$$

Due to the motion of the vortices a temporal change of the phase difference at a specific position is obtained. Since the passage of a complete vortex with flux content Φ_0 changes the phase difference by 2π we can write

$$\frac{\partial \varphi}{\partial t} = \frac{2\pi}{\Phi_0} \frac{\partial \Phi}{\partial t} . \quad (2.2.46)$$

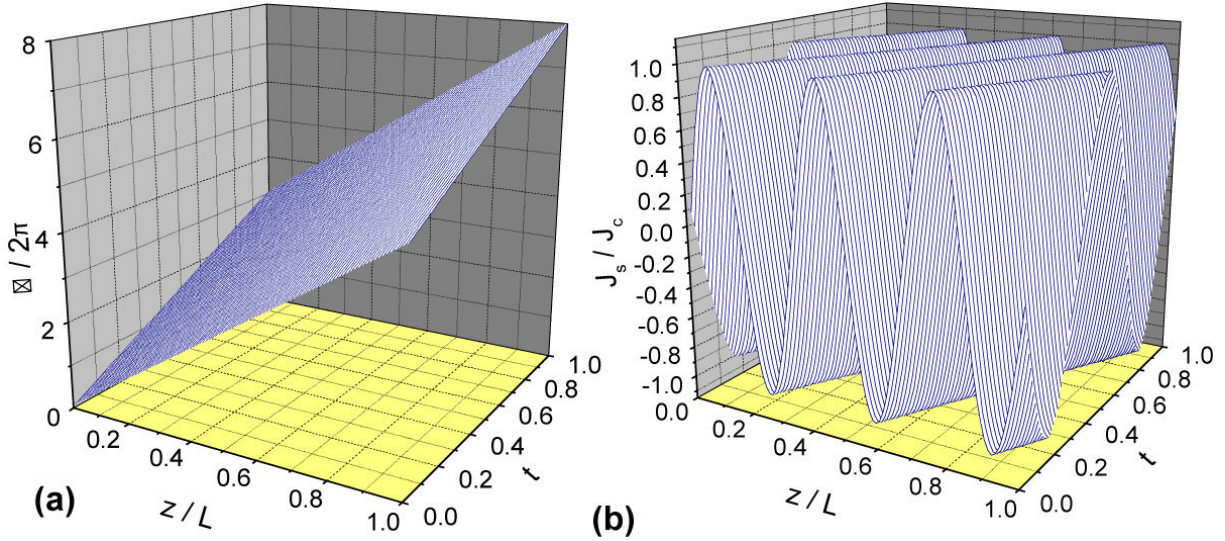


Figure 2.13: (a) The linear increase of the gauge-invariant phase difference along the junction and with increasing time. (b) The corresponding Josephson current density J_s along the junction as a function of time.

With the magnetic flux given by $\Phi = B_y t_B z$ we obtain

$$\frac{\partial \varphi}{\partial t} = \frac{2\pi}{\Phi_0} B_y t_B \frac{\partial z}{\partial t} = \frac{2\pi}{\Phi_0} B_y t_B v_z . \quad (2.2.47)$$

The solution to (2.2.45) and (2.2.47) is

$$\varphi(z, t) = \frac{2\pi}{\Phi_0} B_y t_B (z - v_z t) + \varphi(0) = k(z - v_z t) + \varphi(0) . \quad (2.2.48)$$

That is, the gauge-invariant phase difference is increasing linearly in space and time. This situation is shown in Fig. 2.13a, where we have plotted $\varphi(z, t)$. In order to obtain the temporal and spatial evolution of the Josephson current density, we have to use the current-phase relation and obtain

$$J_s(y, z, t) = J_c(y, z) \sin[k(z - v_z t)] . \quad (2.2.49)$$

Comparing (2.2.49) to (2.2.17) shows that the current density through the junction has the same spatial pattern as for the stationary vortices but the pattern itself moves at a constant velocity v_z according to our assumption (see Fig. 2.13b).

The current density pattern can be considered as a vortex with a period $p = L \frac{\Phi_0}{\Phi}$. That is, if the flux in the junction corresponds to one flux quantum, $\Phi = \Phi_0$, the period is L . For $\Phi > \Phi_0$ and $\Phi < \Phi_0$ the period is smaller and larger than the junction length L , respectively. With the period p we can define the number of vortices in the junction as

$$N_V = \frac{L}{p} = \frac{\Phi}{\Phi_0} . \quad (2.2.50)$$

The amount $\Delta\varphi$ the gauge-invariant phase difference changes along the junction is then given by

$$\Delta\varphi = 2\pi \frac{\Phi}{\Phi_0} = 2\pi N_V . \quad (2.2.51)$$

That is, the change of φ is just given by 2π times the number of vortices in the junction. We can now consider the rate, at which vortices are passing the junction. This rate is given by

$$\frac{dN_V}{dt} = \frac{1}{2\pi} \frac{d\Delta\varphi}{dt}. \quad (2.2.52)$$

Since according to the voltage-phase relation a temporal change of the gauge-invariant phase difference is equal to $\frac{2\pi}{\Phi_0}V$, where V is the junction voltage, we obtain

$$\frac{dN_V}{dt} = \frac{V}{\Phi_0}. \quad (2.2.53)$$

That is, the constant motion of the vortices across the junction is causing a constant junction voltage proportional to the rate, at which vortices are moving across the junction. We note that this relationship is completely analogous to the motion of Abrikosov vortices across a type-II superconductor perpendicular to the current direction resulting in the so-called flux-flow voltage. A more detailed discussion is given in chapter 3.

2.3 Long Josephson Junctions

In section 2.2 we have neglected the self-field effect by the Josephson current density. This is possible only if the spatial dimensions W, L of the junction are small compared to the Josephson penetration depth. In this section we relax this assumption and discuss long Josephson junctions with spatial dimensions larger than the Josephson penetration depth.

2.3.1 The Stationary Sine-Gordon Equation

We again consider the junction geometry shown in Fig. 2.4. We also note that the derivation of expression (2.2.15) describing the spatial variation of the gauge-invariant phase difference due to a magnetic flux density is general. That is, for the geometry shown in Fig. 2.4 with the external magnetic field applied parallel to the y -direction we can write

$$\frac{\partial \varphi}{\partial z} = \frac{2\pi}{\Phi_0} B_y t_B . \quad (2.3.1)$$

However, in contrast to short junctions now the magnetic flux density results both from the externally applied field **and** the Josephson current density and must satisfy Ampère's law. With $\mathbf{B} = \mu_0 \mathbf{H}$ and $\mathbf{D} = \epsilon_0 \mathbf{E}$ we obtain

$$\nabla \times \mathbf{B} = \mu_0 \mathbf{J} + \epsilon \epsilon_0 \mu_0 \frac{\partial \mathbf{E}}{\partial t} . \quad (2.3.2)$$

Here, μ_0 and ϵ_0 are the permeability and permittivity in vacuum, respectively, and ϵ is the dielectric constant of the barrier material.

As in section 2.2 we only consider the zero voltage state, that is, we have $\partial \mathbf{E} / \partial t = 0$. Then, for the geometry of Fig. 2.4 Ampère's law gives

$$\frac{\partial B_y(z)}{\partial z} = -\mu_0 J_x(z) . \quad (2.3.3)$$

With this expression we can write the spatial derivative of (2.3.1) as

$$\frac{\partial^2 \varphi(z)}{\partial z^2} = \frac{2\pi t_B}{\Phi_0} \frac{\partial B_y(z)}{\partial z} = -\frac{2\pi \mu_0 t_B}{\Phi_0} J_x(z) . \quad (2.3.4)$$

Assuming that $J_c(y, z) = \text{const}$ and remembering that the current is flowing in negative x -direction, that is, $J_x(y, z) = -J_s(y, z)$ so that $J_x(z) = -J_c \sin \varphi(z)$ expression (2.3.4) can be rewritten as

$$\frac{\partial^2 \varphi(z)}{\partial z^2} = \frac{2\pi \mu_0 t_B J_c}{\Phi_0} \sin \varphi(z) = \frac{1}{\lambda_J^2} \sin \varphi(z) \quad (2.3.5)$$

with the **Josephson penetration depth**

$$\lambda_J \equiv \sqrt{\frac{\Phi_0}{2\pi \mu_0 t_B J_c}} . \quad (2.3.6)$$

Note that λ_J is about equal to the characteristic length scale $\tilde{\lambda}_J$ derived in section 2.2 (compare (2.2.44)) within a factor of the order unity. Equation (2.3.5) shows that the gauge-invariant phase difference follows a nonlinear differential equation called ***stationary Sine-Gordon equation*** (SSGE).¹¹ Formally, solutions of this equation can be expressed in terms of elliptic Jacobi functions.^{12,13} A typical boundary problem for this equation admits, however, several such solutions and only some of them can be realized. In many situations, the stationary Sine-Gordon equation has to be solved numerically.

We close this subsection by emphasizing that for a two-dimensional junction we have the two-dimensional ***stationary Sine-Gordon equation***

$$\frac{\partial^2 \varphi(y,z)}{\partial y^2} + \frac{\partial^2 \varphi(y,z)}{\partial z^2} = \frac{1}{\lambda_J^2} \sin \varphi(y,z) . \quad (2.3.7)$$

Additional Topic:

Analytical Solutions of the SSGE

We consider a few simple cases where we can solve the SSGE (2.3.5) analytically. First we note that we can linearize (2.3.5) for small arguments. Then, with $\sin \varphi \simeq \varphi$ we have

$$\frac{\partial^2 \varphi(z)}{\partial z^2} = \frac{1}{\lambda_J^2} \varphi(z) \quad (2.3.8)$$

with the solution

$$\varphi(z) = \varphi(0) e^{-z/\lambda_J} . \quad (2.3.9)$$

Then, from (2.3.1) we obtain for the magnetic field $B_y(z)$ along the junction to

$$B_y(z) = -\frac{\varphi(0)}{2\pi} \frac{\Phi_0}{\lambda_J t_B} e^{-z/\lambda_J} . \quad (2.3.10)$$

This expression shows that λ_J is a decay length for the magnetic field justifying the expression penetration depth.

With $\frac{\partial B_y(z)}{\partial z} = -\mu_0 J_x(z)$, for the current flowing at the edges of the junction we obtain

$$J_x(z=0) = \frac{1}{\lambda_J} \frac{B_y(z=0)}{\mu_0} . \quad (2.3.11)$$

Since the junction can stay in the Meißner state as long as $J_x \leq J_c$, Meißner solutions are possible for

$$B_y(z=0) \leq \mu_0 J_c \lambda_J . \quad (2.3.12)$$

We next consider the case of a small junction with $L \ll \lambda_J$. Equation (2.3.5) can then be approximated by $\frac{\partial^2 \varphi(z)}{\partial z^2} \simeq 0$ resulting in $\frac{\partial \varphi(z)}{\partial z} \simeq \text{const}$. That is, we obtain the well known result of the short junction. Note that according to (2.3.4) the approximation $\frac{\partial^2 \varphi(z)}{\partial z^2} \simeq 0$ is equivalent to neglecting the self-field effect of the current. This again demonstrates that the condition for a short junction is equivalent to the assumption of neglecting self-fields.

¹¹J. Rubinstein, J. Math. Phys. **11**, 258 (1970).

¹²I.O. Kulik, Sov. Phys. JETP **51**, 1952 (1966).

¹³C.S. Owen, D.J. Scalapino, Phys. Rev. **164**, 538 (1967).

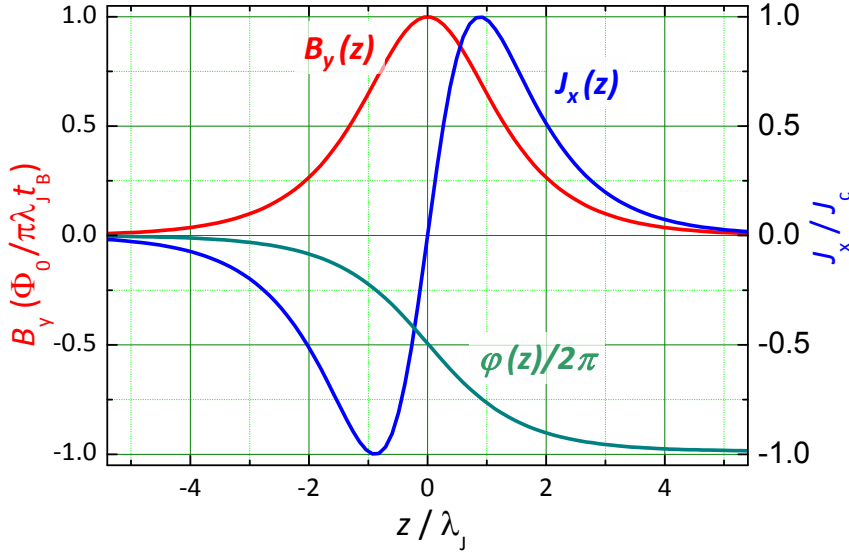


Figure 2.14: Magnetic flux and current density distribution as well as the variation of the gauge-invariant phase difference for a the Josephson vortex solution of the stationary Sine-Gordon equation.

2.3.2 The Josephson Vortex

A possible solution of the SSGE is the particular solution

$$\varphi(z) = \pm 4 \arctan \left\{ \exp \left(\frac{z-z_0}{\lambda_J} \right) \right\} + 2\pi n \quad (2.3.13)$$

which can be verified by substitution into (2.3.5). The corresponding magnetic field can be found from (2.3.1) to

$$B_y(z) = \pm \frac{\Phi_0}{\pi \lambda_J t_B} \frac{1}{\cosh \left(\frac{z-z_0}{\lambda_J} \right)} . \quad (2.3.14)$$

The Josephson current density is obtained form (2.3.3) to

$$J_x(z) = -J_s(z) = \pm \frac{\Phi_0}{\pi \mu_0 \lambda_J^2 t_B} \frac{\sinh \left(\frac{z-z_0}{\lambda_J} \right)}{\cosh \left(\frac{z-z_0}{\lambda_J} \right)} \quad (2.3.15)$$

$$= \pm 2J_c \frac{\sinh \left(\frac{z-z_0}{\lambda_J} \right)}{\cosh \left(\frac{z-z_0}{\lambda_J} \right)} . \quad (2.3.16)$$

Note that for a general solution of a differential equation we not only have to know the particular solution but also the homogeneous solutions in order to match the boundary conditions. However, we will restrict ourselves here to those cases where only the particular solution is needed.

A particular important example is the case where the origin is chosen at z_0 and $\varphi(z)$ is chosen to vanish at $z = \pm\infty$ in a junction of infinite length. In this case the particular solution is the full solution satisfying the boundary conditions. The corresponding magnetic field and current distribution is shown in Fig. 2.14.

The magnetic field and the Josephson current density decay with the characteristic length scale λ_J . Interestingly, the Josephson current density does not have a maximum at the position where the magnetic field has its maximum. Integrating the magnetic flux density and the current density along the junction we see that the total Josephson current is zero and the total flux is equal to Φ_0 . That is, we have a situation similar to that shown in Fig. 2.6c and Fig. 2.8. Therefore, we can interpret this special solution of the SSGE as a ***Josephson vortex*** in a long Josephson junction. The different signs in (2.3.13) – (2.3.16) correspond to different orientations or polarizations of the vortex. It is evident that the Josephson vortex is confined to a length of the order of the Josephson penetration depth λ_J .

Additional Topic: Energy of the Josephson Vortex Solution

As we have done for a short junction, we can calculate the energy E for a long Josephson junction. In fact the expression (compare (2.2.39))

$$E = \frac{1}{2\mu_0} \int_{V_s+V_i} \mathbf{B}^2 dV + \frac{1}{2} \int_{V_s} \Lambda \mathbf{J}_s^2 dV + \int_{A_i} \frac{\Phi_0 J_c(y, z)}{2\pi} [1 - \cos \varphi(z)] dy dz \quad (2.3.17)$$

also holds for long Josephson junctions with the energy (compare (2.2.36))

$$E_s = \frac{1}{2\mu_0} \int_{V_s} (\mathbf{B}^2 + \mu_0 \Lambda \mathbf{J}_s^2) dV \quad (2.3.18)$$

stored in the superconductor and the energy (compare (2.2.38))

$$E_I = \frac{1}{2\mu_0} \int_{V_i} \mathbf{B}^2 dV + \int_{A_i} \frac{\Phi_0 J_c(y, z)}{2\pi} [1 - \cos \varphi(z)] dy dz . \quad (2.3.19)$$

stored in the insulator.

In the following we calculate the stored energy for the vortex solution of the long junction. Here, we again assume that the junction electrodes are much thicker than the London penetration depth so that the first term dominates in the expression for E_s . Then we have

$$E = \frac{1}{2\mu_0} \int_{V_s+V_i} \mathbf{B}^2 dV + \int_{A_i} \frac{\Phi_0 J_c(y, z)}{2\pi} [1 - \cos \varphi(z)] dy dz . \quad (2.3.20)$$

Using $\partial \varphi / \partial z = 2\pi B_y t_B / \Phi_0$ to express the magnetic flux density B_y in terms of the gauge-invariant phase difference φ , we obtain after integrating over y and x ¹⁴

$$E = \frac{\Phi_0 J_c W}{2\pi} \int_{-\infty}^{\infty} \left\{ \frac{1}{2} \lambda_J^2 \left(\frac{\partial \varphi(z)}{\partial z} \right)^2 + [1 - \cos \varphi(z)] \right\} dz . \quad (2.3.21)$$

¹⁴We obtain $B_y^2 / 2\mu_0 = (\partial \varphi / \partial z)^2 \Phi_0^2 / 8\pi^2 t_B^2 \mu_0 = (\partial \varphi / \partial z)^2 (\Phi_0 J_c / 2\pi t_B) \frac{1}{2} \lambda_J^2$. Integration over y gives just the junction width W and integration over x gives the magnetic thickness t_B . That is $\iint (\Phi_0 J_c / 2\pi t_B) \frac{1}{2} \lambda_J^2 dx dy = (\Phi_0 J_c W / 2\pi) \frac{1}{2} \lambda_J^2$.

With the expression (2.3.13) for $\varphi(z)$ we can now calculate the energy stored in the vortex solution. In order to do so we use the trigonometric identity $1 - \cos \varphi = 2 \sin^2(\varphi/2)$. With $\varphi(z) = 4 \arctan \left\{ \exp \left(\frac{z-z_0}{\lambda_J} \right) \right\} = -2 \sin^{-1}(1/\cosh(z/\lambda_J))$ we obtain

$$1 - \cos \varphi(z) = 2 \frac{1}{\cosh^2 \left(\frac{z}{\lambda_J} \right)} . \quad (2.3.22)$$

Furthermore, the first term in the integral can be simplified by using (2.3.14):

$$\frac{1}{2} \lambda_J^2 \left(\frac{\partial \varphi}{\partial z} \right)^2 = 2 \frac{1}{\cosh^2 \left(\frac{z}{\lambda_J} \right)} . \quad (2.3.23)$$

Hence, we obtain

$$E = \frac{2\Phi_0 J_c W}{\pi} \int_{-\infty}^{\infty} \frac{1}{\cosh^2 \left(\frac{z}{\lambda_J} \right)} dz = \frac{4\Phi_0 J_c W \lambda_J}{\pi} . \quad (2.3.24)$$

With this expression we can write down the energy per unit length of the Josephson vortex to

$$E_{\text{Vortex}} = \frac{E_I}{W} = \frac{4\Phi_0 J_c \lambda_J}{\pi} . \quad (2.3.25)$$

Note that the energy of the vortex is positive. That is, its formation is impossible without external fields and/or currents supplying the required energy.

With expression (2.3.25) for the vortex energy per unit length we can find the magnetic flux density B_{c1} , at which the vortex will first enter the junction in complete analogy to the lower critical field of a type-II superconductor.¹⁵ For a type-II superconductor the lower critical field is given by

$$B_{c1} = \frac{\mu_0}{\Phi_0} E_{\text{Vortex}} . \quad (2.3.26)$$

Hence, in analogy the lower critical field of a long Josephson junction is

$$B_{c1} = \frac{4\mu_0 J_c \lambda_J}{\pi} = \frac{2\Phi_0}{\pi^2 \lambda_J t_B} . \quad (2.3.27)$$

This result can be understood intuitively. B_{c1} is just about the magnetic flux density of a single flux quantum distributed over an area $t_B \cdot \lambda_J$.

¹⁵see e.g. T. P. Orlando, K. A. Delin, *Foundations of Applied Superconductivity*, Addison-Wesley, New York (1991); section 6.5.

2.3.3 Junction Types and Boundary Conditions

If we consider the stationary Sine-Gordon equation (SSGE) we see that only the properties of the tunneling barrier (barrier thickness d or equivalently J_c) and the junction electrodes (London penetration depth λ_L) are entering. In contrast, the geometry of the junction electrodes are not entering the differential equation. However, the geometry of the junction electrodes determine how the current is flowing into the junction area and therefore is entering the boundary conditions.

In order to solve the SSGE we have to know the magnetic flux density at the edges of the junction. That is, we have to know the boundary conditions (compare (2.2.15))

$$\left. \frac{\partial \varphi}{\partial z} \right|_{z=0} = \left. \frac{2\pi t_B}{\Phi_0} B_y \right|_{z=0} \quad (2.3.28)$$

$$\left. \frac{\partial \varphi}{\partial z} \right|_{z=L} = \left. \frac{2\pi t_B}{\Phi_0} B_y \right|_{z=L} \quad (2.3.29)$$

$$\left. \frac{\partial \varphi}{\partial y} \right|_{y=0} = - \left. \frac{2\pi t_B}{\Phi_0} B_z \right|_{y=0} \quad (2.3.30)$$

$$\left. \frac{\partial \varphi}{\partial y} \right|_{y=W} = - \left. \frac{2\pi t_B}{\Phi_0} B_z \right|_{y=W} . \quad (2.3.31)$$

The main problem is that the magnetic flux density is determined by both the external applied flux density \mathbf{B}^{ex} **and** the flux density \mathbf{B}^{el} of the current density in the junction electrodes:

$$\mathbf{B} = \mathbf{B}^{ex} + \mathbf{B}^{el} . \quad (2.3.32)$$

In contrast to short junctions we no longer can neglect \mathbf{B}^{el} . Unfortunately, in many cases the geometry of the junction electrodes is complicated and, hence, it is difficult to calculate the magnetic flux density at the junction edges. Moreover, the current density distribution in the junction electrodes is determined by the spatial distribution of the Josephson current density itself. That is, the boundary conditions depend on the solution of the SSGE. Therefore, in many cases numerical iteration methods have to be used to solve the SSGE self-consistently.^{16,17,18}

In the following we discuss the boundary conditions for a few simple one-dimensional junction geometries. Here, one-dimensional means that the junction dimension in one direction (the y -direction in the following) is much smaller than the Josephson penetration depth. Then, for this junction direction self-field effects of the current can be usually neglected. In the following subsections we classify the junctions into three main types, namely

- *overlap junctions*,
- *inline junctions*, and
- *grain boundary junctions*.

¹⁶J. Mannhart, J. Bosch, R. Gross, R. P. Huebener, *Calculation of the Josephson Current Distribution in Two-dimensional Tunnel Junctions*, Phys. Lett. A **121**, 241 (1987).

¹⁷J. Mannhart, J. Bosch, R. Gross, R. P. Huebener, *Spatial Distribution of the Maximum Josephson Current in Superconducting Tunnel Junctions*, J. Low Temp. Phys. **70**, 459 (1988).

¹⁸B. Mayer, H. Schulze, G. M. Fischer, R. Gross, *Nonlocal Response of Grain Boundary Type Josephson Junctions to Local Perturbation*, Phys. Rev. B **52**, 7727 (1995).

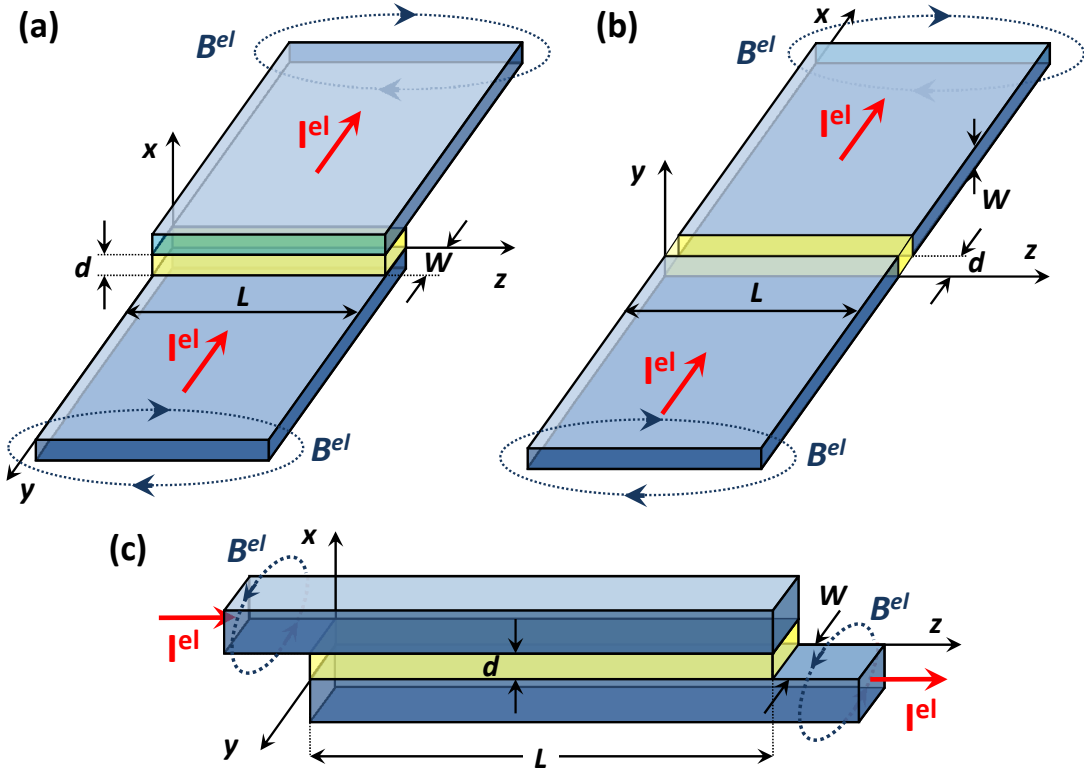


Figure 2.15: The geometry of the overlap (a), the grain boundary (b) and the inline Josephson junction (c). The junction plane always extends in the yz -plane. The width W of the junction is small, whereas the length L of the junction is large compared to the Josephson penetration depth λ_J . Also indicated is the direction of the electrode current I^{el} and the resulting magnetic field B^{el} .

We discuss the boundary conditions for these junction types and the resulting stationary Sine-Gordon equation.

The geometries of the three main junction types are shown in Fig. 2.15. For the **overlap junction** the junction area is formed by a short overlap of width W of the bottom and the top junction electrodes extending in y -direction. The one-dimensional junction of length L extends in z -direction, that is, perpendicular to the direction of the current flow in the electrodes (x -direction). Therefore, the magnetic field B^{el} generated by the electrode current I^{el} at the junction edges is parallel to the z -direction and, hence, perpendicular to the short side of the junction. Therefore, the magnetic flux $\Phi^{el} = B^{el}Wt_B$ is negligibly small due to the very small width W of the junction. Note that the field component B_x^{el} is perpendicular to the junction area and has no influence on the gauge-invariant phase difference (compare (2.2.15)).

For the **inline junction** the situation is different. Here, the junction area is formed by a long overlap of length L of the bottom and the top junction electrodes extending in the z -direction. The width W again is very small so that we have a one-dimensional junction extending in the z -direction. The important point is that in contrast to the overlap junction the long side of the junction now is parallel to the direction of the current flow in the electrodes (z -direction). Therefore, the magnetic field B^{el} generated by the electrode current I^{el} at the junction edges is parallel to the y -direction and, hence, perpendicular to the long side of the junction. Therefore, the magnetic flux $\Phi^{el} = B^{el}Lt_B$ is significant due to the large length $L \gg \lambda_J$ of the junction and has to be taken into account. As for the overlap junction the field component B_x^{el} is perpendicular to the junction area and therefore has no influence on the gauge-invariant phase difference.

For the **grain boundary junction** geometry we have somehow a mixture of the overlap and inline geometry. Here, the junction area is not formed by an overlap of the bottom and the top electrode, but both

electrodes are attached to each other face to face. This junction configuration has been widely used for the high temperature superconductors. For these materials a Josephson junction could be obtained by putting an epitaxial film on a bicrystalline substrate. Since the high temperature superconducting film takes the in-plane orientation of the bicrystalline substrate, an individual grain boundary could be introduced into the epitaxial film with the grain boundary angle determined by the substrate. This artificial grain boundary was found to act as junction barrier resulting in a Josephson junction.¹⁹ Therefore, this junction type is called grain boundary Josephson junction. In the grain boundary geometry the junction area extending in the yz -plane is not parallel to the surface of the electrodes (xz -plane) as for the overlap and inline geometry but perpendicular to it. Therefore, the electrode current I^{el} is now flowing perpendicular to the junction area and not parallel to it as for the overlap and inline geometry. The width W of the junction is small and the length L of the junction large compared to the Josephson penetration depth resulting in a one-dimensional junction extending in the z -direction. In contrast to the overlap and inline geometry now both the y - and z -component of the magnetic field B^{el} generated by the electrode current I^{el} lie in the junction plane. Whereas the component B_z^{el} can be neglected due to the small width W of the junction, the component B_y^{el} has to be taken into account, since it is perpendicular to the long side of the junction.

Overlap Junctions

For the overlap junction the magnetic field B_z^{el} due to the electrode current flowing in the bottom and top electrode can be expressed as²⁰

$$B_z^{el} \simeq \pm \frac{\mu_0}{2} \frac{I^{el}}{L} . \quad (2.3.33)$$

We see that the electrode current is generating only a field component in z -direction. With the external magnetic field applied in y -direction, the total field in z -direction is only determined by B_z^{el} and we can write the boundary conditions (2.3.30) and (2.3.31) as²¹

$$\left. \frac{\partial \varphi}{\partial y} \right|_{y=0} = + \frac{2\pi t_B}{\Phi_0} B_z^{el} \Big|_{y=0} = + \frac{1}{\lambda_J^2} \frac{I^{el}}{2J_c L} \quad (2.3.34)$$

$$\left. \frac{\partial \varphi}{\partial y} \right|_{y=W} = - \frac{2\pi t_B}{\Phi_0} B_z^{el} \Big|_{y=W} = - \frac{1}{\lambda_J^2} \frac{I^{el}}{2J_c L} . \quad (2.3.35)$$

With $W \ll \lambda_J$, the gauge-invariant phase difference φ can have only a very small variation in y -direction. Therefore, we can use the Ansatz

$$\varphi(y, z) = \varphi(z) + f(y) .$$

With the boundary conditions (2.3.34) and (2.3.35) we obtain for an arbitrary y position between the two edges

$$\frac{\partial f}{\partial y} = \frac{2\pi t_B}{\Phi_0} \frac{\mu_0 I^{el}}{2L} \left(1 - \frac{2y}{W} \right)$$

¹⁹For a review see R. Gross, Grain Boundary Josephson Junctions in the High Temperature Superconductors in *Interfaces in High-T_c Superconducting Systems*, S. L. Shinde and D. A. Rudman eds., Springer Verlag, New York (1994), pp. 176-210.

²⁰We use $\oint B ds = \mu_0 I^{el}$ and $\oint B ds \simeq B_z^{el} \cdot 2L$. We also assume that the current distribution in the electrodes is homogeneous. The case of an inhomogeneous current distribution will be discussed below in the subsection on mixed overlap and inline junction geometries.

²¹Note that B_z^{el} is in negative z -direction for $y = 0$ and in positive z -direction for $y = W$.

and hence

$$\frac{\partial^2 \varphi}{\partial y^2} = -\frac{2\pi t_B}{\Phi_0} \frac{\mu_0 I^{el}}{LW} = -\frac{2\pi t_B \mu_0 J_c}{\Phi_0} \frac{I^{el}}{I_c} = -\frac{1}{\lambda_J^2} \frac{I^{el}}{I_c} = -\frac{1}{\lambda_J^2} \gamma , \quad (2.3.36)$$

where $\gamma \equiv I^{el}/I_c$. With the solution for $\frac{\partial^2 \varphi}{\partial y^2}$ we obtain from (2.3.7)

$$\frac{\partial^2 \varphi(z)}{\partial z^2} - \frac{1}{\lambda_J^2} \sin \varphi(y, z) = \frac{1}{\lambda_J^2} \gamma . \quad (2.3.37)$$

For the field component in y -direction we have $B_y = B_y^{ex}$ and we obtain the boundary conditions

$$\left. \frac{\partial \varphi}{\partial z} \right|_{z=0} = +\frac{2\pi t_B}{\Phi_0} B_y^{ex} \Big|_{z=0} \quad (2.3.38)$$

$$\left. \frac{\partial \varphi}{\partial z} \right|_{z=L} = +\frac{2\pi t_B}{\Phi_0} B_y^{ex} \Big|_{z=L} . \quad (2.3.39)$$

Inline Junctions

For the inline junction the magnetic field B_y^{el} due to the electrode current flowing in the bottom and top electrode can be expressed as

$$B_y^{el} \simeq \pm \frac{\mu_0}{2} \frac{I^{el}}{W} . \quad (2.3.40)$$

We see that the electrode current is generating only a field component in y -direction. With the external magnetic field applied in y -direction, the total field in y -direction is then determined by the sum $B_y^{ex} + B_y^{el}$.

Since $W \ll \lambda_J$ and since we have no magnetic field component in z -direction, we can assume $\frac{\partial^2 \varphi}{\partial y^2} \simeq 0$ and we arrive at the differential equation for the inline junction

$$\frac{\partial^2 \varphi(z)}{\partial z^2} - \frac{1}{\lambda_J^2} \sin \varphi(y, z) = 0 . \quad (2.3.41)$$

For the field parallel to the y -direction we have $B_y = B_y^{ex} + B_y^{el}$ and we can write the boundary conditions (2.3.28) and (2.3.29) as²²

$$\left. \frac{\partial \varphi}{\partial z} \right|_{z=0} = +\frac{2\pi t_B}{\Phi_0} \left(B_y^{ex} - \frac{\mu_0 I^{el}}{2W} \right)_{z=0} \quad (2.3.42)$$

$$\left. \frac{\partial \varphi}{\partial z} \right|_{z=L} = +\frac{2\pi t_B}{\Phi_0} \left(B_y^{ex} + \frac{\mu_0 I^{el}}{2W} \right)_{z=L} . \quad (2.3.43)$$

These are the boundary conditions for a so-called symmetric inline junction, where the current in the top and bottom electrode are flowing in the same direction. In an **asymmetric inline junction** the current in

²²Note that the field due to the electrode current is in negative y -direction at $z = 0$ and in positive y -direction for $z = L$.

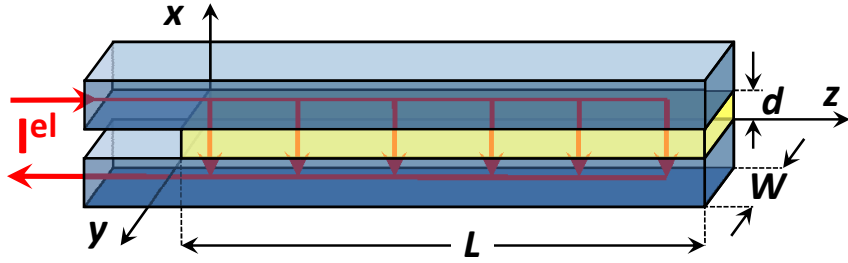


Figure 2.16: The geometry of an asymmetric inline junction. In contrast to the symmetric inline junction the electrode currents in the top and bottom electrode are flowing in opposite direction. At $z = L$ the electrode current density becomes zero, since along the junction length the current injected at $z = 0$ in the top electrode is tunneling to the bottom electrode and flowing back in opposite direction.

the top and bottom electrode are flowing in opposite direction as shown in Fig. 2.16. In this case we have the boundary conditions

$$\frac{\partial \varphi}{\partial z} \Big|_{z=0} = +\frac{2\pi t_B}{\Phi_0} \left(B_y^{ex} - \frac{\mu_0 I_{el}}{W} \right)_{z=0} \quad (2.3.44)$$

$$\frac{\partial \varphi}{\partial z} \Big|_{z=L} = +\frac{2\pi t_B}{\Phi_0} (B_y^{ex})_{z=L}. \quad (2.3.45)$$

These boundary conditions are evident, since now the field at $z = 0$ is twice of that of the symmetric inline junction, whereas the field at $z = L$ vanishes.

Mixed Overlap and Inline Junctions

We can have two situations, where we obtain an inline admixture to an overlap junction geometry:

1. Overlap junctions for which the width of the junction electrodes is larger or smaller than the actual junction length L (see Fig. 2.17a and b).
2. The electrode current is not distributed homogeneously over the cross-section of the electrode. This is the case, if the thickness of the electrodes is larger than the London penetration depth λ_L . Then, the current density distribution in the junction electrodes is peaked at the edges of the junctions (see Fig. 2.17c).

Note that for the overlap geometry the electrode current always flows only in y -direction resulting in a magnetic field component B_z^{el} which is perpendicular to the short side of the junction. However, as shown in Fig. 2.17 for the two cases mentioned above there is always a finite electrode current I_z^{el} at the edges of the junction area, which is parallel to the z -direction and results in a magnetic field component B_y^{el} in y -direction. This field component is perpendicular to the long side of the junction and corresponds to the field component of the inline geometry. Therefore, for the situations shown in Fig. 2.17 we speak about a ***mixed overlap and inline geometry***.

The inline admixture to an overlap type junction can be formally characterized by a dimensionless parameter s which ranges between 0 and 1. Here, $s = 0$ corresponds to a pure overlap junction and $s = 1$ to a pure inline junction. With this parameter we obtain the stationary Sine-Gordon equation to

$$\frac{\partial^2 \varphi(z)}{\partial z^2} - \frac{1}{\lambda_J^2} \sin \varphi(z) = (1-s) \frac{1}{\lambda_J^2} \gamma \quad (2.3.46)$$

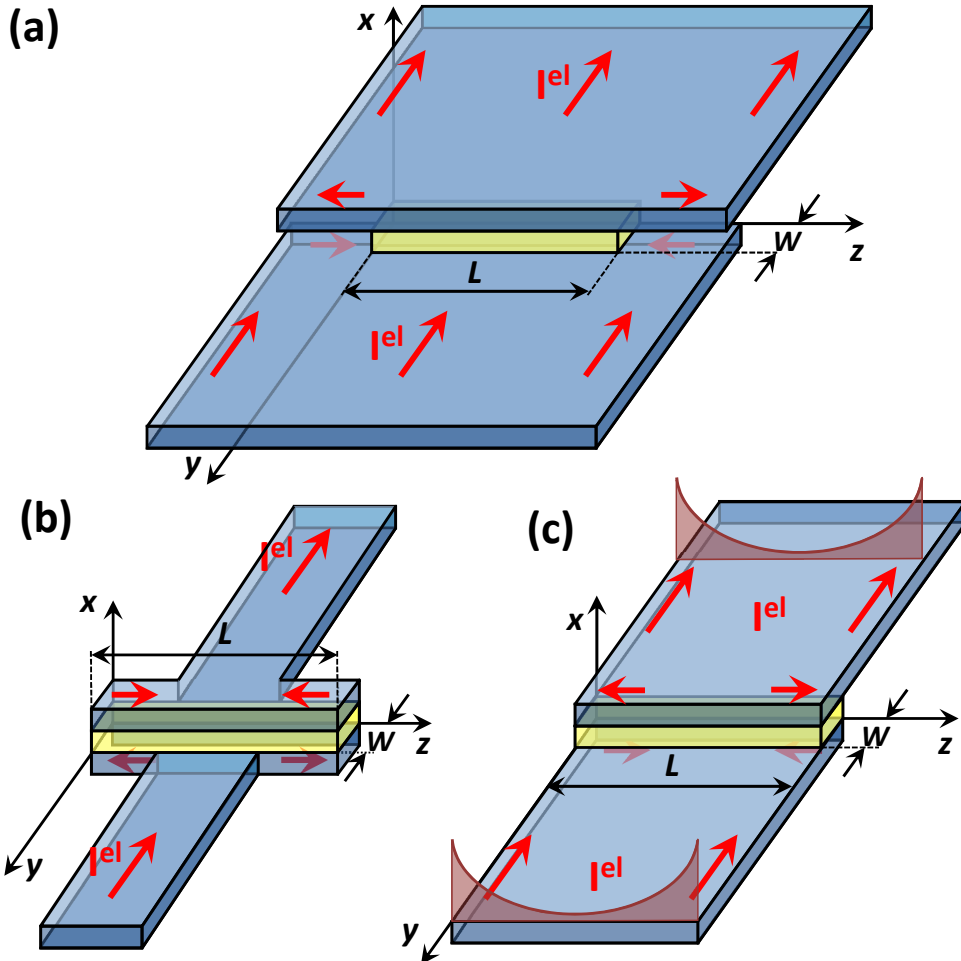


Figure 2.17: The geometry of mixed overlap and inline junctions. In (a) and (b) the width of the electrodes is larger and smaller than the junction length L , respectively, resulting in an electrode current parallel to the z -direction both in the bottom and top electrode. In (c) an electrode current density peaked at the electrode edges results in an electrode current parallel to the z -direction at the edges of the junction area.

with $\gamma \equiv I^{el}/I_c$. The boundary conditions are

$$\left. \frac{\partial \varphi}{\partial z} \right|_{z=0} = + \frac{2\pi t_B}{\Phi_0} \left(B_y^{ex} - s \frac{\mu_0 I^{el}}{2W} \right)_{z=0} \quad (2.3.47)$$

$$\left. \frac{\partial \varphi}{\partial z} \right|_{z=L} = + \frac{2\pi t_B}{\Phi_0} \left(B_y^{ex} + s \frac{\mu_0 I^{el}}{2W} \right)_{z=L} . \quad (2.3.48)$$

Grain Boundary Josephson Junctions

In grain boundary junctions the junction area is perpendicular to the direction of the electrode currents. This is different to overlap and inline junctions, where the junction area is parallel to the direction of the electrode currents. In contrast to the overlap junction for the grain boundary junction geometry we have to take into account the y -component of the magnetic field B^{el} due to the electrode currents:

$$B_y^{el} \simeq \pm \frac{\mu_0}{2} \frac{I^{el}}{L} . \quad (2.3.49)$$

For the overlap geometry this field was perpendicular to the junction area and had no effect on the gauge-invariant phase difference. In contrast, for the grain boundary junctions B_y^{el} is parallel to the junction area. The field component B_y^{el} results in a finite inline admixture. Writing B_y^{el} as

$$B_y^{el} \simeq \pm \frac{\mu_0}{2} \frac{W}{L} \frac{I^{el}}{W} = s \frac{\mu_0}{2} \frac{I^{el}}{W} \quad (2.3.50)$$

we see by comparison with (2.3.47) and (2.3.48) that the amount of inline admixture is just $s = W/L \ll 1$, since the length L of the grain boundary junction usually is much larger than the width W . Our analysis shows that the grain boundary junction can be considered as an overlap junction with a small inline admixture. Therefore, we can use the expression for the mixed overlap and inline geometry and the stationary Sine-Gordon equation can be written as

$$\frac{\partial^2 \varphi(z)}{\partial z^2} - \frac{1}{\lambda_J^2} \sin \varphi(z) = \left(1 - \frac{W}{L}\right) \frac{1}{\lambda_J^2} \gamma = (1-s) \frac{1}{\lambda_J^2} \gamma. \quad (2.3.51)$$

The boundary conditions are

$$\left. \frac{\partial \varphi}{\partial z} \right|_{z=0} = \frac{2\pi t_B}{\Phi_0} \left(B_y^{ex} + \frac{W}{L} \frac{\mu_0 I^{el}}{2W} \right)_{z=0} \quad (2.3.52)$$

$$\left. \frac{\partial \varphi}{\partial z} \right|_{z=L} = \frac{2\pi t_B}{\Phi_0} \left(B_y^{ex} - \frac{W}{L} \frac{\mu_0 I^{el}}{2W} \right)_{z=L}. \quad (2.3.53)$$

We note that for an electrode thickness larger than the London penetration depth λ_L the electrode current is peaked at the junction edges. This results in an additional inline admixture as already discussed above.

2.3.4 Additional Topic: Josephson Current Density Distribution and Maximum Josephson Current

After having found the stationary Sine-Gordon equation and the boundary conditions for the various junction types we can calculate the Josephson current distribution $J_s(y, z)$ in the junction as well as the maximum Josephson current. We perform this calculation only for a few simple cases assuming that the critical current density $J_c(y, z)$ is homogeneous across the junction. We start with the zero field case.

Overlap Junction: $\mathbf{B}^{ex} = 0$

We first consider an overlap junction with a spatially homogeneous electrode current distribution. For zero external magnetic field we have $\partial \varphi / \partial z = 0$ at both junction edges according to (2.3.38) and (2.3.39). Therefore, $\partial^2 \varphi / \partial z^2 = 0$ and we obtain the following trivial solution of the SSGE (2.3.36)

$$\varphi(z) = \arcsin(\gamma) + 2\pi n = const. \quad (2.3.54)$$

and hence for the Josephson current density

$$J_s(z) = J_c \sin \varphi(z) = const. \quad (2.3.55)$$

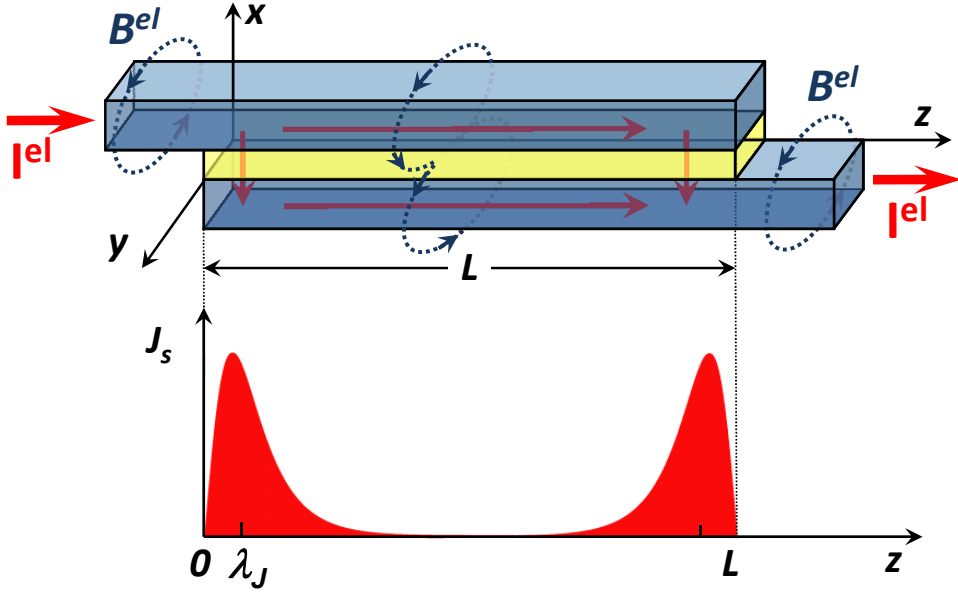


Figure 2.18: The geometry (a) and the Josephson current distribution of a long inline Josephson junction. The Josephson current density J_s is restricted to the boundaries of the junction thereby resulting in the Meißner state of the long inline Josephson junction.

The maximum Josephson current in this case is

$$I_s^m = \int_{A_i} J_s dA = J_c \cdot LW = J_c \cdot A_i . \quad (2.3.56)$$

Here, $A_i = LW$ is the junction area.

For the overlap junction we obtain the important result that for zero applied magnetic field the Josephson current density is constant across the junction area and the maximum Josephson current is increasing linearly with increasing junction area.

Inline Junction: $\mathbf{B}^{ex} = 0$

In contrast to the overlap junction, for the inline junction we have to take into account the magnetic field due to the electrode current. Qualitatively, we can find the current distribution by recalling that a superconducting system always wants to stay in the Meißner state, that is, it wants to expel the magnetic field. As shown in Fig. 2.18, in an inline junction the Meißner state can be achieved by restricting the Josephson current density to the left and right edge of the junction. Then, the electrode current flowing in the top and bottom electrode are the same along the junction and their magnetic fields cancel each other. In this way the inner of the junction resides in the Meißner state. This situation is similar to a bulk superconductor, where the supercurrent density flows only on the surface of the sample and decays exponentially away from the surface. There, the characteristic decay length is the London penetration depth λ_L . For a Josephson junction an exponential decay is obtained only in the linear approximation (compare (2.3.8) to (2.3.10)). However, due to the nonlinearity of the Sine-Gordon equation the Josephson current density is zero at the edges, increases to the maximum value J_c at a depth equal to about λ_J and then decays again so that the Josephson current density is restricted to an edge region with a length

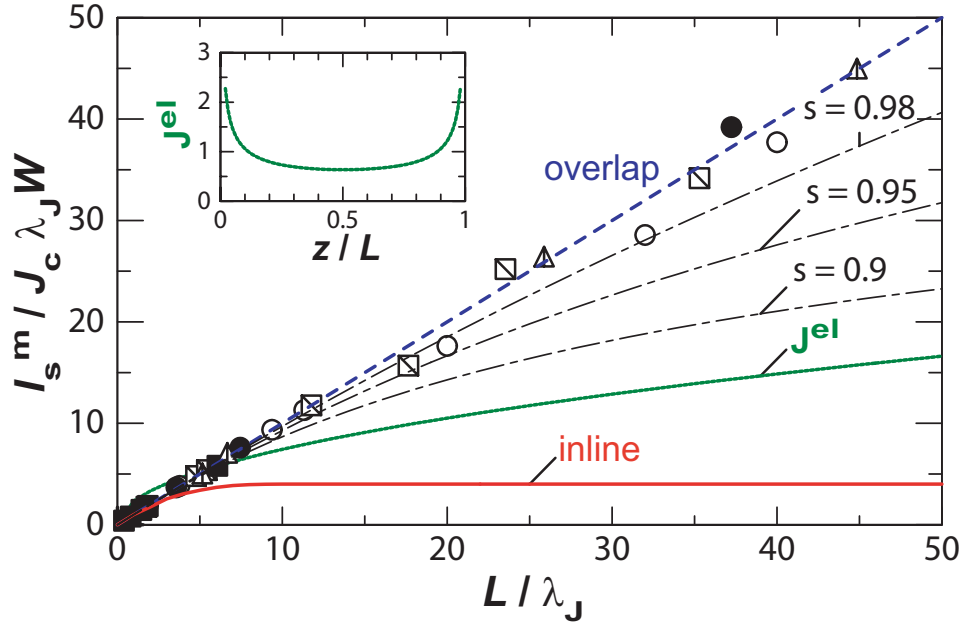


Figure 2.19: The maximum Josephson current I_s^m plotted as a function of the junction length for a pure overlap and inline geometry as well as for different amount s of an inline admixture to the pure overlap geometry. Also shown is the $I_s^m(L)$ dependence for an overlap junction with an inhomogeneous electrode current distribution $J_{el}(z)$ according to (2.3.58).

of about $2\lambda_J$. A detailed calculation shows that the integral maximum Josephson current is

$$I_s^m = \int_{A_i} J_s dA = J_c \cdot 4W\lambda_J . \quad (2.3.57)$$

That is, in contrast to the overlap junction, for which the maximum Josephson current increases linearly with the junction length, the maximum Josephson current of an inline junction is independent of the junction length L . This is evident from Fig. 2.18. Since the Josephson current density is restricted to the edges of the junction, an increase of the junction length above a value of about $L = 4\lambda_J$ does no longer increase the integral junction current.

Grain Boundary Junction: $\mathbf{B}^{ex} = 0$

For the grain boundary junction we have an overlap type geometry with a certain amount of inline admixture. If the thickness t of the electrodes of the grain boundary Josephson junction is smaller than the London penetration depth, the current distribution in the electrodes is quite homogeneous and, hence, the inline admixture is $s = W/L = t/L$ (compare (2.3.50) and Fig. 2.15). Since usually $t/L \ll 1$, the inline admixture is small and the maximum Josephson current is expected to increase linearly with increasing junction length.

As shown in Fig. 2.19 this has been indeed observed experimentally. The experimental data obtained for the grain boundary junctions follow the theoretical estimate for the overlap junction. Fig. 2.19 also shows that with increasing inline admixture the increase of the maximum Josephson current with increasing junction length L becomes more flat and finally vanishes for a pure inline junction.

In Fig. 2.19 we also show the effect of a spatially inhomogeneous current distribution in the junction electrodes. Assuming for an overlap junction an electrode current distribution

$$J^{el}(z) = \frac{L}{\pi\sqrt{z(L-z)}} , \quad (2.3.58)$$

which is peaked at the edges of the junction, we obtain

$$I_s^m(L) = 2.35 \sqrt{L} . \quad (2.3.59)$$

That is, the maximum Josephson current does no longer increase linearly with L but proportional to the square root of the junction length.

The Magnetic Field Dependence of the Maximum Josephson Current

The magnetic field dependence of the maximum Josephson current in the presence of an applied magnetic field has to be calculated numerically in most cases.^{23,24,25} A convenient way to calculate the local Josephson current density as well as the integral maximum Josephson current is the use of an iteration method as described in Appendix C.

Fig. 2.20a and b show the magnetic field dependence of the maximum Josephson current for a symmetric overlap junction with a reduced junction length $L/\lambda_J = 5$ and 10. Qualitatively, we can understand the $I_s^m(B^{ex})$ dependence of the symmetric junction as follows: For small applied fields the junction can screen the applied external field by a circulating screening current. This current flows in opposite direction at both junction edges and adds to the external applied transport current. Since the local Josephson current density cannot exceed J_c , the integral maximum Josephson current of the junction decreases, since at one junction edge the screening current flows in the same direction as the transport current. This is shown in Fig. 2.20d where we have plotted the $J_s(z)$ dependence of an overlap junction for increasing applied field. On the left junction edge the screening current is in the same direction as the applied current, whereas it is opposite on the right edge. It can be seen that with increasing applied field the screening current is increasing until it reaches the critical value at the right edge. Then vortices start to penetrate the junction resulting in an oscillating $J_s(z)$ dependence.

We can use Ampère's law $\partial B_y(z)/\partial z = -\mu_0 J_x(z)$ to estimate the maximum field value that can be screened by the junction. Assuming for simplicity an exponential decay of the applied field in the junction, $B_y^{ex}(z) \propto \exp(-z/\lambda_J)$ (linear approximation), we obtain $\partial B_y(z)/\partial z = -\frac{1}{\lambda_J} B_y^{ex}(z) = -\mu_0 J_x(z)$ and hence $J_x = \frac{1}{\lambda_J} \frac{B_y^{ex}}{\mu_0}$. Since $J_x \leq J_c$ we can estimate the maximum field value that can be screened by the junction to $B_c = \mu_0 J_c \lambda_J$. Within a factor of unity this rough estimate is equal to the lower critical field B_{c1} of a long Josephson junction (compare (2.3.27)). Indeed, for $B^{ex} \geq B_{c1} = \frac{4}{\pi} \mu_0 J_c \lambda_J$ a state with one vortex in the junction is energetically more favorable.

The state with no vortex in the junction is called the Meißner state of the junction. For fields larger than the lower critical field B_{c1} a state with one or more vortices inside the junction is more favorable. This can be seen in Fig. 2.20, where the symbols mark the maximum Josephson current values for the different vortex states. It can be seen that for a certain external field the 1-vortex solution has a higher maximum Josephson current than the Meißner state solution, that is, the 1-vortex solution is energetically more

²³see e.g. A. Barone and G. Paterno, *Physics and Application of the Josephson Effect*, John Wiley & Sons, New York (1982).

²⁴S. Pagano, B. Ruggiero and E. Sarnelli, Phys. Rev. B **43**, 5364 (1991).

²⁵S. Pagano, B. Ruggiero, M. Russo and E. Sarnelli, in *Nonlinear Superconductive Electronics and Josephson Devices*, G. Constabile, S. Pagano, N. F. Pedersen, and M. Russo eds., Plenum Press, New York (1991).

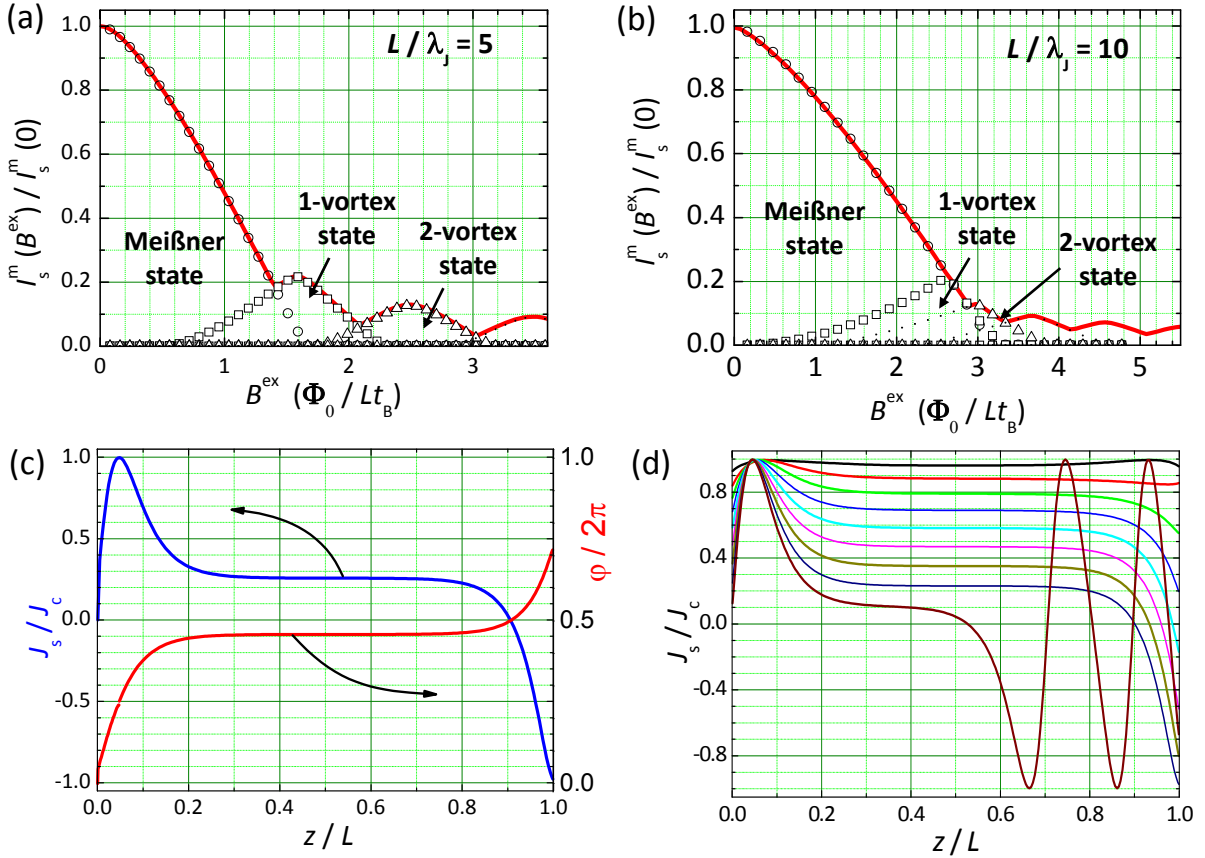


Figure 2.20: I_s^m plotted versus the applied magnetic field B^{ex} for a symmetric overlap junction with $L/\lambda_J = 5$ (a) und $L/\lambda_J = 10$ (b). The symbols mark the solutions for the different vortex states. The solid line shows the envelop of the different solutions. In (c) $J_s(z)$ as well as $\varphi(z)$ is shown along the junction for a magnetic field close to B_{c1} . In (d) the change of $J_s(z)$ with increasing applied magnetic field is shown. Only for the highest field vortices can penetrate the junction as can be seen by the oscillating $J_s(z)$ dependence.

favorable. Note that on increasing the magnetic field starting from zero, so that initially the junction is in its Meissner state, the penetration of vortices will start only at a field $B_{\max} > B_{c1}$. This relation can be understood in terms of vortex pinning at the sharp edges of the uniform junction. It can be shown that $B_{\max} = \frac{\pi}{2}B_{c1} = 2\mu_0 J_c \lambda_J$ for an infinitely long junction.²⁶

It is also important to note that for a large Josephson junction the variation of the gauge invariant phase difference along the junction is nonlinear (see Fig. 2.20c). This is in contrast to short junctions, where the phase difference was increasing linearly along the junction resulting in a sinusoidal variation of the Josephson current density. The reason for this behavior was the fact that we could neglect the magnetic field of the current and therefore had a spatially homogeneous total magnetic field $B = B^{ex}$. For long junctions, however, we have to take into account the field of the current what results in a spatially varying total field $B = B^{ex} + B^{el}$. Therefore, the spatial variation of $\varphi(z)$ along the junction and, in turn, of the Josephson current density $J_s(z) = J_c \sin \varphi(z)$ is more complicated.

In Fig. 2.21 we have plotted the magnetic field dependence of the maximum Josephson current for symmetric overlap and inline junctions as well as for an asymmetric inline junction. The junctions have a reduced length $L/\lambda_J = 10$. It can be seen that the overlap junction has the highest zero field Josephson current, since here the maximum Josephson current is proportional to the junction length, $I_s^m = J_c WL$. In contrast, as discussed above for the inline junction the maximum Josephson current saturates as a

²⁶ K. K. Likharev, *Dynamics of Josephson Junctions and Circuits*, Gordon and Breach Science Publishers, New York (1986).

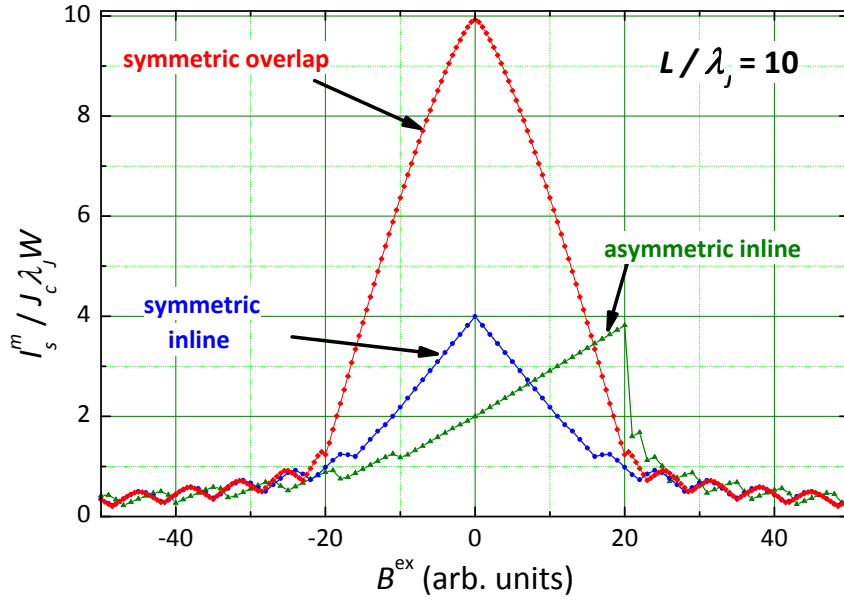


Figure 2.21: I_s^m plotted versus the applied magnetic field B^{ex} for a symmetric overlap and inline junction as well as for an asymmetric inline junction with $L/\lambda_J = 10$. T

$I_s^m = 4J_cW\lambda_J$. The asymmetric inline junction shows a highly asymmetric $I_s^m(B^{ex})$ dependence. This can be understood as follows (compare Fig. 2.16): The magnetic fields generated by the electrode currents flowing in the bottom and top electrode point in the same direction for the asymmetric inline junction. Now, this field direction can be parallel or anti-parallel to the external field. For anti-parallel orientation the external magnetic field is compensating the field of the electrode currents thereby causing a reduction of the total magnetic field. Therefore the maximum Josephson current is increasing with increasing applied field. In contrast, for parallel orientation the applied field is adding to the field of the electrode currents causing an increase of the total field and, hence, the maximum Josephson current is decreasing with increasing applied field.

2.3.5 The Pendulum Analog

In order to get some insight into the nature of the solutions for φ we recall that the stationary Sine-Gordon equation has the same form as the differential equation for a pendulum. If we make the transcriptions $z \rightarrow t$, $\varphi \rightarrow \theta$ and $1/\lambda_J^2 \rightarrow \omega_0^2 = g/L$, where θ is the angle of the pendulum measured from the top of its circular orbit, and ω_0 is its natural frequency. In terms of this transcription, the solutions for φ found by neglecting the effect of the electrode currents corresponds to the motion of the pendulum whirling around and around with so much kinetic energy that gravitational acceleration is negligible. In the Sine-Gordon equation this limit corresponds to $\lambda_J \rightarrow \infty$ so that $d^2\varphi/dz^2 = 0$ and $d\varphi/dz = \text{const}$ resulting in a sinusoidal variation of the Josephson current density.

If we consider now a pendulum moving with less energy, but still sufficient energy to have nonzero kinetic energy at the top of the circle, the motion of $\theta(t)$, which is equivalent to $\varphi(z)$, will be periodic but anharmonic. This leads to a non-sinusoidal, periodically reversing current distribution $J_s(z)$. Each cycle of the oscillating current contains one flux quantum. Unlike the sinusoidal case these Josephson vortices are actually localized entities, since they are spaced with a separation exceeding λ_J .

We finally discuss the Meißner limit of a junction of length L . The Meißner solution corresponds to a pendulum moving with an energy that is just sufficient to go over the top. In this case, starting with an

initial angular velocity $(d\theta/dt)_0$ from an initial angle $-\theta_0$ at the time t corresponding to $-L/2$, the pendulum decelerates nearly exponentially as it rises. It moves very slowly for a long time (corresponding to the interior length of the junction), while going over the top, and then exponentially accelerates down the other side, recovering the initial angular velocity at θ_0 (at a time t corresponding to $+L/2$).

If the angular velocity at the top is negligible compared to the initial value, then θ_0 and $(d\theta/dt)_0$ are connected by the conservation of energy and are not independent. Translating back to the junction problem we see that the corresponding initial condition is

$$\left(\frac{2\pi}{\Phi_0}B_y t_B\right)^2 = \left(\frac{d\varphi}{dz}\right)_0^2 = \frac{2}{\lambda_J^2} (1 - \cos \varphi_0) . \quad (2.3.60)$$

Solving this equation for $\cos \varphi_0$, we obtain

$$\cos \varphi_0 = 1 - \frac{1}{2} \left(\frac{B_y}{\mu_0 J_c \lambda_J}\right)^2 . \quad (2.3.61)$$

Thus, for small fields we can use the approximation $\cos x = 1 - \frac{1}{2}x^2$ and the phase difference φ_0 at the edges of the junction is given by

$$\varphi_0 = \frac{B_y}{\mu_0 J_c \lambda_J} . \quad (2.3.62)$$

If we want to estimate the strongest field that can be screened by the junction, we have to consider the case at which the pendulum is starting from the bottom, that is, $\varphi_0 = \pi$. Then we obtain

$$B_{\max} = 2\mu_0 J_c \lambda_J . \quad (2.3.63)$$

This field is just the highest field for which the Meißner solution is possible. Actually, the screening at B_{\max} is only metastable. The maximum value for which screening is thermodynamically stable has been derived above to $B_{c1} = 4\mu_0 J_c \lambda_J / \pi$ (compare (2.3.27)). Note that for fields close to B_{c1} screening is no longer exponential, but rather becomes so in the interior when φ has become small.

Summary

Short Josephson Junctions:

- We can distinguish between short and long Josephson junctions depending on whether their spatial dimensions (width, length) are smaller or larger than the Josephson penetration depth

$$\lambda_J \equiv \sqrt{\frac{\Phi_0}{2\pi\mu_0 t_B J_c}}$$

- The Josephson coupling energy is given by

$$E_J = \frac{\Phi_0 I_c}{2\pi} (1 - \cos \varphi) = E_{J0} (1 - \cos \varphi)$$

and can be viewed as a molecular binding energy of two weakly coupled superconductors.

- In an equivalent circuit, an ideal Josephson element can be represented by a nonlinear inductance

$$L_s = \frac{\Phi_0}{2\pi I_c \cos \varphi} = L_c \frac{1}{\cos \varphi} \quad \text{with} \quad L_c = \frac{\hbar}{2eI_c} .$$

- The potential energy of a current biased Josephson junction is given by the tilted washboard potential

$$E_{\text{pot}}(\varphi) = E_J(\varphi) - \frac{\Phi_0}{2\pi} I = E_{J0} \left[1 - \cos \varphi - \frac{I}{I_c} \varphi \right] .$$

- A magnetic field B_y applied parallel to the junction plane (yz -plane) results in a phase gradient

$$\frac{\partial \varphi}{\partial z} = \frac{2\pi}{\Phi_0} B_y t_B$$

in z -direction proportional to B_y and the magnetic thickness t_B . Due to this phase gradient the Josephson current density oscillates in space as

$$J_s(y, z, t) = J_c(y, z) \sin \left(\frac{2\pi}{\Phi_0} t_B B_y z + \varphi_0 \right) = J_c(y, z) \sin(kz + \varphi_0) .$$

The integral Josephson current is given by the modulus of the Fourier transform of $i_c(z)$ (the critical current density integrated along the field direction):

$$I_s^m(B_y) = \left| \int_{-\infty}^{\infty} i_c(z) e^{ikz} dz \right|$$

For a rectangular junction with homogeneous critical current density, i_c corresponds to the transmission function of a slit and $I_s^m(B_y)$ is given by a Fraunhofer diffraction pattern.

Long Josephson Junctions:

- The spatial distribution of the gauge invariant phase difference is given by the stationary Sine-Gordon equation (SSGE)

$$\frac{\partial^2 \varphi(y,z)}{\partial y^2} + \frac{\partial^2 \varphi(y,z)}{\partial z^2} = \frac{2\pi\mu_0 t_B J_c}{\Phi_0} \sin \varphi(y,z) = \frac{1}{\lambda_J^2} \sin \varphi(y,z) .$$

The solution of the SSGE requires the knowledge of the boundary conditions. Since the boundary conditions are determined by the flux density at the edges of the junction, which in turn depends on $\varphi(y,z)$, a self-consistent solution is required.

- Depending on the boundary conditions, three basic junction types can be distinguished: inline, overlap, and grain boundary junctions.
- A possible solution of the SSGE is the particular solution

$$\varphi(z) = \pm 4 \arctan \left\{ \exp \left(\frac{z-z_0}{\lambda_J} \right) \right\} + 2\pi n$$

describing a Josephson vortex.

Chapter 3

Physics of Josephson Junctions: The Voltage State

In Chapter 2 we have considered Josephson junctions, for which the current was less than the maximum Josephson current I_s^m . Then, the junction resides in the zero voltage state which is equivalent to the static state. In this chapter we generalize our discussion and treat the situation, where the junction current is larger than the maximum Josephson current and therefore only part of the total current can be carried by the Josephson current. That is, in addition to the Josephson current we have to include other current channels carrying the excess current. In this situation the Josephson junction resides in the finite voltage state, where the phase difference evolves in time. This state corresponds to the dynamic state of the junction. One additional current channel is the ***resistive channel***. At temperatures above zero temperature there is a finite probability for Cooper pairs to be broken up by thermal excitation thereby generating unpaired “normal” electrons. In the presence of a finite voltage across the junction these normal electrons contribute to the current. In contrast to the Josephson current this normal current channel is resistive. The second current channel is the ***capacitive channel*** due to the finite capacitance of the Josephson junction. For example, a tunneling type superconductor/insulator/superconductor junction just represents a parallel plate capacitor. In the present of a time varying junction voltage we have a finite displacement current across this capacitor. Finally, noise is taken into account by adding a fluctuation current.

In this chapter we first describe the additional current channels in the voltage state of a Josephson junction and then in section 3.2 discuss models for the description of the current-voltage characteristics. In particular, we discuss Josephson junctions driven by dc and ac sources and analyze the effect of thermal fluctuations. Initially, we describe the junction dynamics within a classical framework. Then, in section 3.5 we show that this classical treatment is no longer valid for Josephson junctions with small capacitance. We discuss the limits of the classical treatment and the relevance of secondary macroscopic quantum effects. Finally, in section 3.6 we extend our discussion from zero-dimensional Josephson junctions to extended junctions.

3.1 The Basic Equation of the Lumped Josephson Junction

If we want to derive the basic equation describing the Josephson junction in the voltage state, we have to consider the additional current channels relevant in the voltage state. In the following we will consider the resistive and capacitive channel as well as an additional channels due to fluctuations (noise). In our discussion we first consider lumped Josephson junctions that can be characterized by the integral current values. Extended junctions will be discussed later in section 3.6.

3.1.1 The Normal Current: Junction Resistance

At finite temperatures ($T > 0$) there is a finite density of normal electrons due to thermal break-up of Cooper pairs. The presence of the condensate of paired electrons makes the properties of these “normal excitations” somewhat different from those in the normal state. We call them *quasiparticles*.

In the zero-voltage state of a Josephson junction the quasiparticles do not contribute to the junction current. However, if the gauge-invariant phase difference changes in time resulting in a non-vanishing junction voltage V according to the second Josephson equation, $d\phi/dt = 2eV/\hbar$, then a quasiparticle component of the total current, the **normal current** I_N , is obtained. This current is a resistive current and therefore the **voltage-state** of a Josephson junction is also called the **resistive state**.

We briefly discuss the temperature and voltage dependence of the normal current. First, for temperatures close to the transition temperature ($T \lesssim T_c$) the energy $2\Delta(T)$ (Δ is the energy gap) required to break up a Cooper pairs is much smaller than $k_B T$. Therefore, almost all Cooper pairs are broken up and the concentration of quasiparticles is close to the electron density in the normal state. In this case we expect that the current-voltage characteristic (IVC) is close to the usual Ohm’s law

$$I_N = G_N V , \quad (3.1.1)$$

where $G_N = 1/R_N$ is the **normal conductance** of the Josephson junction.

Second, if the junction voltage is above the so-called **gap voltage**

$$V_g = \frac{\Delta_1(T) + \Delta_2(T)}{e} , \quad (3.1.2)$$

the external circuit provides sufficient energy eV to break up Cooper pairs. Here, $\Delta_1(T)$ and $\Delta_2(T)$ are the energy gaps in the two junction electrodes. A Cooper pair is broken up in one of the electrodes and the two newly formed quasiparticles pass to the other electrode. This process can set in only above the gap voltage because a minimum energy $\Delta_1(T) + \Delta_2(T)$ is required for this process. Hence, also for $|V| > V_g$ the IVC is expected to be close to an ohmic dependence independent of the temperature.

Third, for $T \ll T_c$ and $|V| < V_g$ there should be a vanishing normal current, since neither the thermal energy $k_B T$ nor the energy eV supplied by the external circuit are sufficient to break up Cooper pairs. That is, the quasiparticle density and hence the normal current is vanishingly small.

The IVC expected from our discussion is shown schematically in Fig. 3.1. For $T > T_c$ and $|V| > V_g$ an ohmic dependence is obtained. For $T \ll T_c$ and $|V| < V_g$ the IVC depends on the sweep direction and on the type of the external source (current or voltage source). Here, for a current source a hysteretic IVC is obtained. The detailed reason for that will be discussed later in section 3.2.1. We note that if the junction is driven by a current source, the total current through the junction, $I = I_s + I_N$ is constant. Since in the voltage state the supercurrent $I_s = I_c \sin \phi$ is varying in time due to the time evolution of ϕ , also

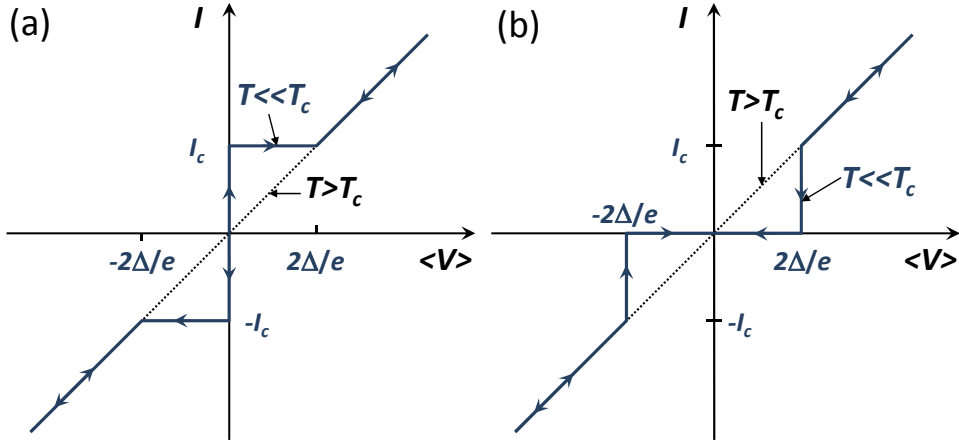


Figure 3.1: Current-voltage characteristics (IVC) of a Josephson junction driven by a constant current source. The voltage $\langle V \rangle$ represents the time-averaged voltage. Curve (a) is for increasing and curve (b) for decreasing driving current.

the normal current has to vary in time to keep the total current constant. Then, also the junction voltage $V = I_N/G_N$ is varying in time. The voltage shown in the IVCs of Fig. 3.1 is the time-averaged voltage $\langle V \rangle$.

Summarizing our discussion we see that in the voltage state of a Josephson junction we have to take into account the quasiparticle current. The quasiparticles are generated either by thermal excitation at finite temperature or due to breaking up of Cooper pairs by the junction voltage even at zero temperature. A circuit model that incorporates both the Josephson current and the normal current channel is shown in Fig. 3.2.

At $T = 0$, the equivalent conductance for the normal channel is given by

$$G_N(V) = \begin{cases} 0 & \text{for } |V| < 2\Delta/e \\ \frac{1}{R_N} & \text{for } |V| \geq 2\Delta/e \end{cases}. \quad (3.1.3)$$

At finite temperatures thermally excited quasiparticles can tunnel already at voltages smaller than the gap voltage resulting in a finite resistance $R_{sg}(T)$ called **sub-gap resistance**. The magnitude of the sub-gap resistance, or equivalently the sub-gap conductance, is determined by the amount of thermally excited quasiparticles and can be expressed as

$$G_{sg}(T) = \frac{1}{R_{sg}(T)} = \frac{n(T)}{n_{tot}} G_N. \quad (3.1.4)$$

Here, $n(T)$ is the density of excited quasiparticles at temperature T and n_{tot} is the total density of electrons in the normal state. Hence, at $T > 0$ we expect that the normal conductance channel can be characterized by the voltage and temperature dependent conductance

$$G_N(V, T) = \begin{cases} \frac{1}{R_{sg}(T)} & \text{for } |V| < 2\Delta(T)/e \\ \frac{1}{R_N} & \text{for } |V| \geq 2\Delta(T)/e \end{cases}. \quad (3.1.5)$$

Here, the fact that the energy gap and thereby the gap voltage is temperature dependent has been included. It is evident that the normal channel results in a **nonlinear conductance** $G_N(V, T)$ that depends on voltage and temperature.

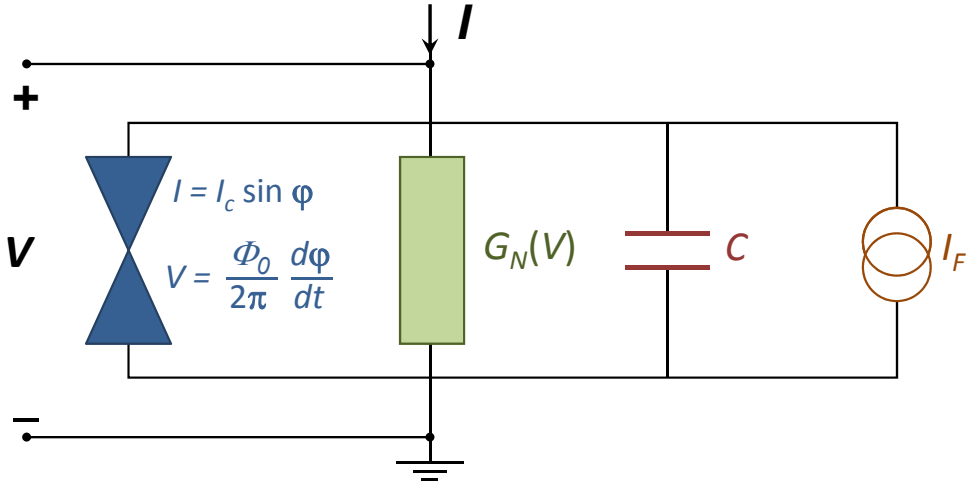


Figure 3.2: Equivalent circuit for a Josephson junction including the Josephson current as well as the normal current and the displacement current channel. Furthermore, noise is taken into account by a noise source providing a fluctuation current.

Our discussion shows that the equivalent circuit of the Josephson junction including the Josephson current and the normal current channel is characterized by a natural current scale I_c and a natural resistance R_N . Therefore, we can define a *characteristic voltage*

$$V_c \equiv I_c R_N = \frac{I_c}{G_N} , \quad (3.1.6)$$

which usually is called the $I_c R_N$ -product of the Josephson junction.

We close this subsection by noting that we did not take into account any frequency dependence of the normal conductance. Of course, at high frequency the normal electrons have to be accelerated resulting in an inductive component of the normal channel and hence in a frequency dependent conductance. However, in most cases the inductance of the superelectron channel dominates over that of the normal channel and therefore we only use a frequency independent conductance for modeling the normal current channel. Finally, we should emphasize that our discussion was focused on Josephson tunnel junctions and did not include other junction types where the Josephson coupling is achieved by a normal metal, a semiconductor, a micro-constriction, etc..

3.1.2 The Displacement Current: Junction Capacitance

In situations where not only V but also its time derivative dV/dt is nonzero, the displacement current I_D plays an important role. For most practical junctions the displacement current can be represented in the usual form

$$I_D = C \frac{dV}{dt} . \quad (3.1.7)$$

Here, C is the junction capacitance, which is the same in the normal and the superconducting state. The capacitance depends on the junction type and its size. For a planar tunnel junction with area A_i and an insulating barrier of thickness d the junction capacitance is just given by

$$C = \frac{\epsilon \epsilon_0 A_i}{d} , \quad (3.1.8)$$

where ϵ is the dielectric constant of the barrier material. The displacement current results in an additional current channel parallel to the Josephson and the normal current channel.

With $V = L_c \dot{I}_s$, $I_N = V G_N$ and $I_D = C \dot{V}$ we can compare the current values in the three different current channels at a given frequency. With $L_s = L_c / \cos \varphi \geq L_c$ and $G_N(V, T) \leq 1/R_N$ we have

$$I_s \leq \frac{V}{\omega L_c} \quad I_N \leq \frac{V}{R_N} \quad I_D \simeq \omega C V . \quad (3.1.9)$$

3.1.3 Characteristic Times and Frequencies

If we characterize the three different current channels in the equivalent circuit shown in Fig. 3.2 by the inductance L_c , the normal resistance R_N and the capacitance C , we immediately can define three characteristic time scales or, equivalently, frequencies. The first one is the **plasma frequency** of the junction defined as

$$\omega_p = \frac{1}{\tau_p} \equiv \frac{1}{\sqrt{L_c C}} = \sqrt{\frac{2eI_c}{\hbar C}} . \quad (3.1.10)$$

The plasma frequency scales proportional to $\sqrt{J_c/C_A}$, where $C_A = C/A$ is the specific junction capacitance. Evidently, for $\omega < \omega_p$ the displacement current is smaller than the Josephson current.

The second characteristic frequency is related to the L_c/R_N **time constant** of the circuit:

$$\omega_c = \frac{1}{\tau_c} \equiv \frac{R_N}{L_c} = \frac{2e}{\hbar} V_c = \frac{2\pi}{\Phi_0} V_c . \quad (3.1.11)$$

Here, $L_c = \frac{\hbar}{2eI_c}$ is the Josephson inductance (cf. eq. (2.1.22)) characterizing the superconducting transport channel. We see that ω_c is just the inverse relaxation time in a system consisting of a normal current and a supercurrent. Furthermore, it is seen from (3.1.11) that the characteristic junction frequency ω_c directly follows from the characteristic junction voltage V_c via the second Josephson equation. Therefore, ω_c is usually called the **characteristic frequency** of the Josephson junction. Evidently, the normal current is smaller than the critical junction current for $V < V_c$ or equivalently $\omega < \omega_c = R_N/L_c$.

The third characteristic frequency is defined by the $R_N C$ **time constant** of the equivalent circuit:

$$\omega_{RC} = \frac{1}{\tau_{RC}} \equiv \frac{1}{R_N C} = \frac{\omega_p^2}{\omega_c} \quad (3.1.12)$$

Evidently, the displacement current is smaller than the normal current for $\omega < 1/\tau_{RC}$.

In order to characterize the capacitance effect at all frequencies up to the frequency ω_c corresponding to the characteristic junction voltage $V_c = I_c R_N$ one can use the dimensionless parameter

$$\beta_C \equiv \frac{\omega_c^2}{\omega_p^2} = \frac{\omega_c}{\omega_{RC}} = \omega_c \tau_{RC} = \frac{2e}{\hbar} I_c R_N^2 C . \quad (3.1.13)$$

This parameter has been introduced by McCumber¹ and Stewart² and therefore is referred to as the ***Stewart-McCumber parameter***. It corresponds to the square of the quality factor

$$Q = \frac{RC}{\sqrt{LC}} = \frac{\omega_p}{\omega_{RC}} = \frac{\omega_c}{\omega_p} = \sqrt{\beta_C} \quad (3.1.14)$$

of a parallel *LRC* circuit. The quality factor Q compares the decay time constant of the amplitude of an oscillating physical system to its oscillation period. Junctions with $\beta_C \ll 1$ have small capacitance and/or small resistance. These junctions have small $R_N C$ time constants ($\tau_{RC} \omega_p \ll 1$) and therefore are highly damped. In contrast, junctions with $\beta_C \gg 1$ are those with large capacitance and/or large resistance and hence have a large $R_N C$ time constant ($\tau_{RC} \omega_p \gg 1$). These junctions are weakly damped.³

3.1.4 The Fluctuation Current

In many problems it is important to take into account fluctuations (noise). In most cases, this can be done by using the ***Langevin method***,^{4,5} that is, by including a random force in the system equation that describes the fluctuation sources. As we will see below, for Josephson junctions the system equation arises from summing up the different current contributions. Therefore, the random force is just some fluctuation current $I_F(t)$, which is represented by a current noise source in the equivalent circuit shown in Fig. 3.2.

Thermal Noise: There are three different types of fluctuations, namely thermal fluctuations, shot noise and $1/f$ noise. According to the Johnson-Nyquist formula^{6,7} for ***thermal noise*** the power spectral density of the current fluctuations are given by

$$S_I(f) = \frac{4k_B T}{R_N} . \quad (3.1.15)$$

We note that this expression only holds for an Ohmic resistor at⁸

$$k_B T \gg eV, \hbar\omega . \quad (3.1.16)$$

The relative intensity of the thermal noise current can be expressed by the dimensionless parameter given by the ratio of the thermal energy and the coupling energy of the Josephson junction

$$\gamma \equiv \frac{k_B T}{E_J} = \frac{2e k_B T}{\hbar I_c} . \quad (3.1.17)$$

¹D.E. McCumber, J. Appl. Phys. **39**, 3113 (1968).

²W.C. Stewart, Appl. Phys. Lett. **12**, 277 (1968).

³Note that for large R_N the conductance of the resistive channel is small and hence results in small damping due to a small normal current.

⁴P. Langevin, *Sur la theorie du mouvement brownien*, Comptes Rendus **146**, 604 (1908).

⁵Sh. Kogan, *Electronic Noise and Fluctuations in Solids*, Cambridge University Press (1996).

⁶H. Nyquist, *Thermal agitation of electric charge in conductors*, Phys. Rev. **32**, 110 (1928).

⁷J.B. Johnson, *Thermal agitation of electricity in conductors*, Phys. Rev. **32**, 97 97 (1928).

⁸The case $\hbar\omega \gg k_B T, eV$ is discussed in section 3.5.5. In this limit quantum fluctuations are dominant.

This equation can be rewritten into the form

$$\gamma \equiv \frac{I_T}{I_C} \quad \text{with} \quad I_T = \frac{2e}{\hbar} k_B T . \quad (3.1.18)$$

Here, I_T is the equivalent ***thermal noise current***. Inserting numbers we see that $I_T \simeq 0.15 \mu\text{A}$ at liquid helium temperature ($T = 4.2 \text{ K}$).

Shot Noise: If the voltage across the junction is large so that $eV \gg k_B T$ ($V > 0.5 \text{ mV}$ at 4.2 K), then ***shot noise*** is of major importance and we have to use the Schottky formula^{9,10} to express the power spectral density of the current fluctuations:

$$S_I(f) = 2eI_N \quad \text{at} \quad eV \gg k_B T, \hbar\omega . \quad (3.1.19)$$

Shot noise consists of random fluctuations of the electric current in an electrical conductor, which are caused by the fact that the current is carried by discrete charges (electrons). Shot noise is to be distinguished from current fluctuations in equilibrium, which happen without any applied voltage and without any average current flowing. These equilibrium current fluctuations are known as Johnson-Nyquist noise discussed above.

Shot noise is a Poisson process and the charge carriers which make up the current will follow a Poissonian distribution. The strength of the current fluctuations can be expressed by the variance

$$\Delta I^2 \equiv \langle (I - \langle I \rangle)^2 \rangle \quad (3.1.20)$$

of the current I , where $\langle I \rangle$ is the average current. However, the value measured in this way depends on the frequency range of fluctuations (bandwidth of the measurement): The measured variance of the current grows linearly with bandwidth. Therefore, a more appropriate quantity is the noise power, which is essentially obtained by dividing through the bandwidth (and, therefore, has the SI units A^2/Hz). It can be defined as the zero-frequency Fourier transform of the current-current correlation function:

$$S(f) = \int_{-\infty}^{+\infty} (\langle I(t)I(0) \rangle - \langle I(0) \rangle^2) dt . \quad (3.1.21)$$

We note that this expression is the total noise power, which includes the equilibrium fluctuations (Johnson-Nyquist noise).

1/f Noise: At low frequencies ***1/f noise*** often is the dominant noise source. In contrast to thermal or shot noise the physical nature of ***1/f noise*** is often not clear.^{11,12,13} Typically, for Josephson junctions ***1/f noise*** becomes dominant only below about 1 kHz . Therefore, in the following we will not consider the effect of ***1/f noise***, since its effect in most cases is negligible compared to the other noise sources.

⁹W. Schottky, *Über spontane Stromschwankungen in verschiedenen elektrischen Leitern*, Ann. Physik **57**, 541 (1918).

¹⁰W. Schottky, *Small-shot effect and flicker effect*, Phys. Rev. **28**, 74 (1926).

¹¹Sh. Kogan, *Electronic Noise and Fluctuations in Solids*, Cambridge University Press (1996).

¹²P. Dutta, P.M. Horn, Rev. Mod. Phys. **53**, 497 (1981)

¹³F.N. Hooge, T.G.M. Kleinpenning, L.K.J. Vandamme, Rep. Prog. Phys. **44**, 532 (1981).

3.1.5 The Basic Junction Equation

According to the discussion of the last subsections there are four essential components in the net current I flowing through the Josephson junction. Kirchhoff's law then requires that

$$I = I_s + I_N + I_D + I_F . \quad (3.1.22)$$

This equation together with the voltage-phase relation

$$\frac{d\varphi}{dt} = \frac{2e}{\hbar} V \quad (3.1.23)$$

forms the basic equation for the Josephson junction. From (3.1.22) and (3.1.23) we can calculate $I(t)$ provided that $V(t)$ is known and vice versa. In principle, after writing down this equation with concrete expressions for the different current contributions the solid-state physics part of the problem has been solved.

With the expressions derived above for the normal, the displacement and the fluctuation current we can express (3.1.22) as

$$I = I_c \sin \varphi + G_N(V)V + C \frac{dV}{dt} + I_F . \quad (3.1.24)$$

Using (3.1.23) we obtain

$$I = I_c \sin \varphi + G_N(V) \frac{\Phi_0}{2\pi} \frac{d\varphi}{dt} + C \frac{\Phi_0}{2\pi} \frac{d^2\varphi}{dt^2} + I_F . \quad (3.1.25)$$

This equation is nonlinear with nonlinear coefficients. Due to these nonlinearities concepts such as superposition fail. Furthermore, a nonintuitive behavior is obtained. For example, a dc driving current results in a time-dependent voltage. In general, the behavior of the Josephson junction in the voltage state is governed by a complex differential equation, which in most cases has to be solved numerically. In the following we will make some simplifying assumptions to arrive at simple solutions of (3.1.25).

3.2 The Resistively and Capacitively Shunted Junction Model

To gain some insight into the dynamics of the Josephson junction we simplify the model by taking the normal conductance to be constant. That is, we assume

$$G_N(V) = G = \frac{1}{R} = \text{const .} \quad (3.2.1)$$

We then arrive at the ***Resistively and Capacitively Shunted Junction*** (RCSJ) model. The equivalent circuit of this model is shown in Fig. 3.3. The Josephson junction is characterized by the Josephson inductance $L_s = L_c / \cos \varphi$ with $L_c = \hbar / 2eI_c$ and the resistance R is usually taken to be the normal resistance of the junction. However, more generally we can interpret R to be given by (3.1.5), so that the resistance is given by R_{sg} , if the average junction voltage is below the gap voltage, and is R_N , when the average voltage is above the gap voltage. Of course this description can only be approximate, since the junction voltage is time dependent. Nevertheless, the RCSJ-model will result in a still nonlinear but tractable differential equation. Rewriting (3.1.25) we obtain

$$\left(\frac{\hbar}{2e}\right)C \frac{d^2\varphi}{dt^2} + \left(\frac{\hbar}{2e}\right)\frac{1}{R} \frac{d\varphi}{dt} + I_c \left[\sin \varphi - \frac{I}{I_c} + \frac{I_F(t)}{I_c} \right] = 0 . \quad (3.2.2)$$

Multiply by $\frac{\hbar}{2e}$ and using the Josephson coupling energy $E_{J0} = \hbar I_c / 2e$ and the normalized currents

$$i = \frac{I}{I_c} \quad i_F(t) = \frac{I_F(t)}{I_c} \quad (3.2.3)$$

we obtain

$$\left(\frac{\hbar}{2e}\right)^2 C \frac{d^2\varphi}{dt^2} + \left(\frac{\hbar}{2e}\right)^2 \frac{1}{R} \frac{d\varphi}{dt} + \frac{d}{d\varphi} \{E_{J0} [1 - \cos \varphi - i\varphi + i_F(t)\varphi]\} = 0 . \quad (3.2.4)$$

In order to interpret this equation of motion we compare it to the equation of motion of a particle with mass M and damping η in the potential U :

$$M \frac{d^2x}{dt^2} + \eta \frac{dx}{dt} + \nabla U = 0 . \quad (3.2.5)$$

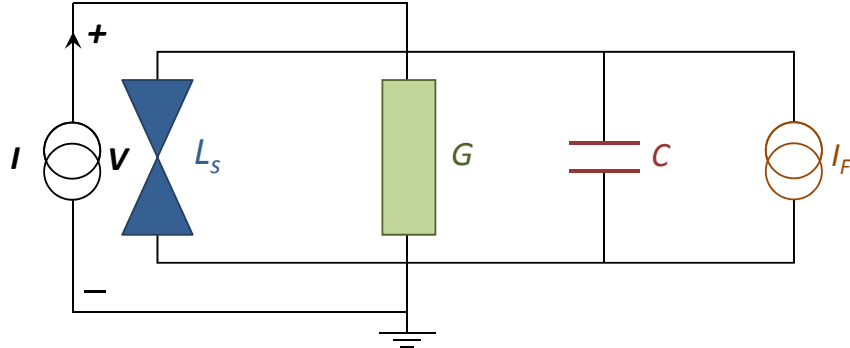


Figure 3.3: Equivalent circuit for the Resistively and Capacitatively Shunted Junction (RCSJ) Model. The Josephson junction can be characterized by the inductance $L_s = L_c / \cos \varphi$ with $L_c = \hbar / 2eI_c$, the resistive channel is approximated by a voltage independent conductance G .

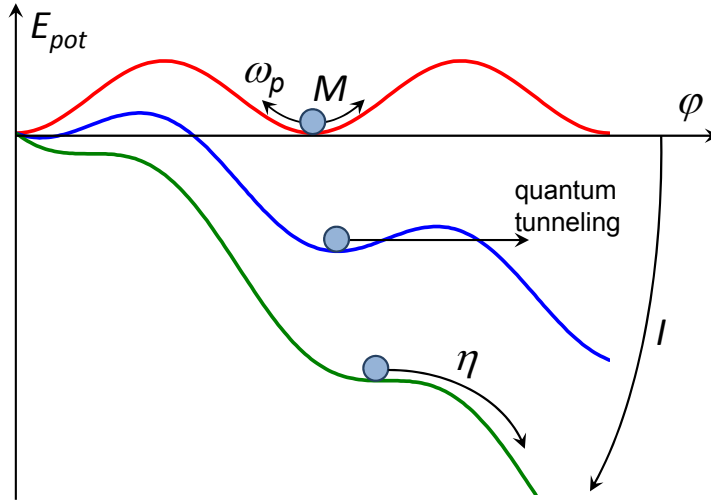


Figure 3.4: Analogy between the motion of the gauge-invariant phase difference of a Josephson junction and the damped motion of a particle of mass M in the tilt washboard potential. Note that the applied currents result in a tilt of the potential.

We immediately see that the equation of motion of the gauge-invariant phase difference of a Josephson junction is equivalent to the motion of a particle of mass M and damping η in a potential U with

$$M = \left(\frac{\hbar}{2e}\right)^2 C \quad (3.2.6)$$

$$\eta = \left(\frac{\hbar}{2e}\right)^2 \frac{1}{R} \quad (3.2.7)$$

$$U = E_{J0}[1 - \cos \varphi - i\varphi + i_F(t)\varphi] . \quad (3.2.8)$$

This situation is visualized in Fig. 3.4. We see that the mass of the particle is proportional to the capacitance and the damping proportional to $1/R$. Furthermore, the potential U is nothing else than the **tilt washboard potential** (cf. eq. (2.1.14)).

Equation (3.2.4) is often written in reduced units. By using the normalized time

$$\tau \equiv \frac{t}{\tau_c} = \frac{t}{2eI_c R / \hbar} \quad (3.2.9)$$

as well as the Stewart-McCumber parameter β_C (cf. (3.1.13)) we can write the basic equation (3.2.4) describing the Josephson junction within the RCSJ approximation as

$$\beta_C \frac{d^2\varphi}{d\tau^2} + \frac{d\varphi}{d\tau} + \sin \varphi - i - i_F(\tau) = 0 .$$

(3.2.10)

We can use the analogy between the motion of the phase and that of a particle to discuss the meaning of the plasma frequency.¹⁴ If we neglect damping and consider the case of zero driving current (horizontal potential in Fig. 3.4) and small amplitudes ($\sin \varphi \simeq \varphi$), we can write (3.2.10) as

$$\beta_C \frac{d^2\varphi}{d\tau^2} + \varphi = 0 . \quad (3.2.11)$$

¹⁴The expression plasma oscillation is used, since the oscillations show the same dispersion as plasma oscillations.

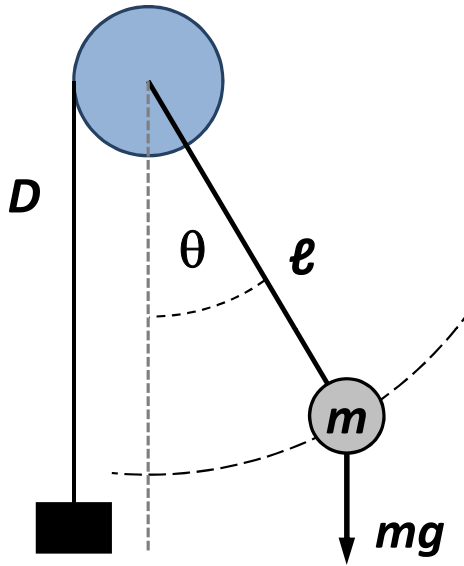


Figure 3.5: The pendulum analogue of a Josephson junction. The torque D deflecting the pendulum is represented by an unwinding mass.

The solution of this equation is

$$\varphi = c \cdot \exp\left(i \frac{\tau}{\sqrt{\beta_C}}\right) = c \cdot \exp\left(i \frac{t}{\sqrt{\beta_C} \tau_c}\right) = c \cdot \exp(i \omega_p t) . \quad (3.2.12)$$

That is, the plasma frequency represents the oscillation frequency of the particle around the potential minimum at small amplitudes.

We also note that there is a finite probability of the particle to tunnel through the potential well. This process is known as the macroscopic quantum tunneling of the gauge-invariant phase difference and has been observed experimentally. Furthermore, the phase particle can escape from the potential well by thermal activation. These processes will be discussed in sections 3.5.6 and 3.4, respectively.

The pendulum analogue

Besides the motion of a particle of mass M in the tilt washboard potential another mechanical analogue whose dynamics is described by an equation of the form (3.2.10) is the physical pendulum (see Fig. 3.5). We consider a pendulum of mass m and length ℓ that is deflected by an angle θ with respect to the normal by a torque D directed parallel to the rotation axis. The restoring torque is given by the length ℓ of the pendulum times the gravitational force $mg \sin \theta$. With these expressions we obtain the following equation of motion:

$$D = \Theta \ddot{\theta} + \Gamma \dot{\theta} + mg\ell \sin \theta . \quad (3.2.13)$$

Here, $\Theta = m\ell^2$ is the moment of inertia of the pendulum. The term $\Gamma \dot{\theta}$ describes the damping of the pendulum with the damping constant Γ .

If we compare (3.2.13) to (3.1.25) we immediately see that both equations are equivalent with the assignments $I \leftrightarrow D$, $I_c \leftrightarrow mg\ell$, $\Phi_0/2\pi R \leftrightarrow \Gamma$, and $C\Phi_0/2\pi \leftrightarrow \Theta$. The angle θ corresponds to the

gauge invariant phase difference φ . Hence, in order to analyze the dynamics of the Josephson junction we just can consider the dynamics of an oscillating or rotating pendulum. For example, for $D = 0$ we can consider the oscillations of the pendulum around its equilibrium position. The oscillation frequency is $\omega = \sqrt{mgl/\Theta} = \sqrt{g/l}$. This frequency of course corresponds to the plasma frequency $\omega_p = \sqrt{2\pi I_c/\Phi_0 C}$ of the Josephson junction what can be easily shown with the above assignments. A finite torque acting on the pendulum corresponds to a finite current applied to the Josephson junction. It results in a finite deflection angle θ_0 of the pendulum or, equivalently, a finite value φ_0 of the phase difference across the Josephson junction. If the torque is large enough to deflect the pendulum by 90° (corresponding to $J_s = J_c \sin \varphi = J_c$), any further increase of the torque results in a rotation of the pendulum. In this case the average angular velocity $\dot{\theta}$ is larger than zero. Equivalently, $\dot{\varphi} > 0$ corresponds to the finite voltage state of the Josephson junction.

3.2.1 Underdamped and Overdamped Josephson Junctions

The analogy between the motion of a “phase” particle in the tilt washboard potential and the motion of the gauge-invariant phase difference of a Josephson junction can be used to discuss the difference between underdamped and overdamped Josephson junctions. For underdamped Josephson junctions ($\beta_C = 2eI_c R^2 C / \hbar \gg 1$) the junction capacitance and/or the resistance are large. This means that the mass $M \propto C$ of the particle is large and/or the damping $\eta \propto 1/R$ is small. In contrast, for overdamped junctions ($\beta_C = 2eI_c R^2 C / \hbar \ll 1$) the junction capacitance and/or the resistance are small, that is, the mass M of the particle is small and/or the damping η is large.

Discussing the motion of the phase particle for this two limiting cases we start at an applied current larger than the critical current, that is, at a strong tilt of the potential so that the particle can move freely down the potential. Reducing the current we are reducing the tilt of the potential until at $I < I_c$ local minima are obtained. In the case of strong damping the particle will immediately stop its motion and will be trapped in one of the local minima. This is due to the small mass or equivalently small kinetic energy of the particle and the large damping. For the Josephson junction this means that the phase does no longer evolve in time and the junction switches into the zero voltage state as soon as the applied current is reduced below I_c (see Fig. 3.6a). The situation is completely different in the case of small damping. In this case the massive particle has sufficient kinetic energy and due to the small damping can easily move down the potential well even if there are local minima. In order to stop the particle, we have to bring the potential almost to the horizontal position. For the Josephson junction this means that we have to reduce the current almost to zero to achieve the zero voltage state of the junction (see Fig. 3.6b).

Starting from the zero voltage state at zero applied current and then increasing the current, both the under- and overdamped junction stay in the zero voltage state until the critical current is reached. In both cases the kinetic energy of the particle is zero and there is no reason why it should move down the potential well (we are neglecting thermally activated processes or quantum tunneling of the phase). However, above the critical current the behavior is different again. Whereas in the strongly damped case the particle is moving slowly (corresponding to small voltage) at currents slightly above I_c due to the strong damping, in the underdamped case the particle is immediately accelerating to an average velocity corresponding to the average slope of the potential and the amount of damping.

This different behavior results in different current-voltage characteristics of under- and overdamped Josephson junctions. Whereas for overdamped junctions the same IVC is obtained for increasing and decreasing current, for the underdamped junction the average voltage depends on whether one is decreasing or increasing the current. Decreasing the current the underdamped junction stays in the voltage state also below I_c due to the large kinetic energy and the small damping of the moving phase. Increasing the current from zero current the underdamped junction stays in the zero voltage state until the critical current, because now the particle has no kinetic energy and will therefore stay in the potential minimum

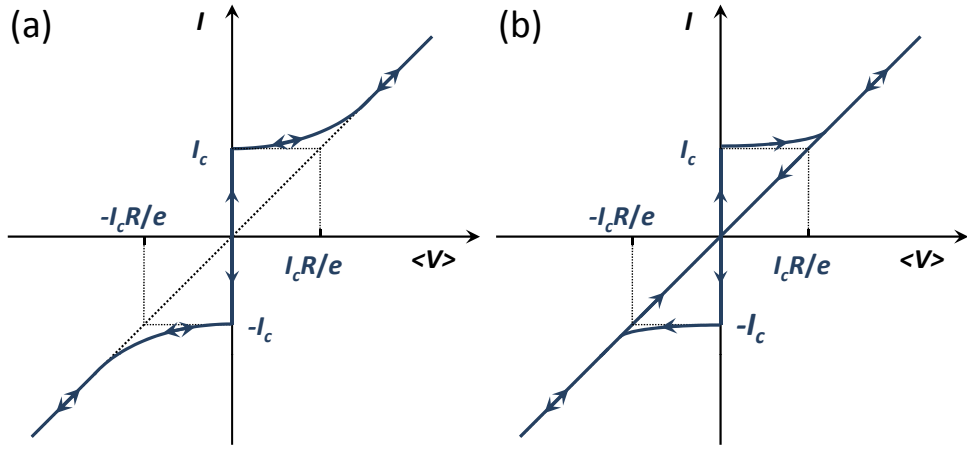


Figure 3.6: Current-voltage characteristics of an overdamped (a) and underdamped (b) Josephson junction. The arrows indicate the direction of the current variation.

even at small damping. In summary, this results in a hysteretic IVC of the underdamped Josephson junction as shown schematically in Fig. 3.6b. In contrast, for overdamped junctions the mass of the phase particle and, hence, its kinetic energy is small and/or the damping is large. Therefore, the motion of the phase particle is the same for increasing and decreasing the applied current. That is, overdamped junctions do not have hysteretic IVCs.

3.3 Response to Driving Sources

In the following subsections we will use the RCSJ-model to discuss the response of a Josephson junction to external driving sources quantitatively.

3.3.1 Response to a dc Current Source

We first discuss the response of a Josephson junction to a dc current source. Doing so we start to consider the time-averaged voltage of the junction in the presence of an applied dc current. We recall that in the voltage state we have an oscillating Josephson current. With the oscillation period T we can write

$$\langle V \rangle = \frac{1}{T} \int_0^T V(t) dt = \frac{1}{T} \int_0^T \frac{\hbar}{2e} \frac{d\varphi}{dt} dt = \frac{1}{T} \frac{\hbar}{2e} [\varphi(T) - \varphi(0)] = \frac{\Phi_0}{T}. \quad (3.3.1)$$

Here, we have used the fact that during one oscillation period the phase difference changes by 2π , that is, $\varphi(T) - \varphi(0) = 2\pi$. We see that the time-averaged voltage of the junction is determined by the flux quantum divided by the oscillation period.

We also have to recall that for a driving dc current source the total current of the junction has to be constant and equal to the driving current. That is, neglecting the fluctuation current we have to satisfy the condition

$$I = I_s(t) + I_N(t) + I_D(t) = I_c \sin \varphi(t) + \frac{V(t)}{R} + C \frac{dV(t)}{dt} = \text{const}, \quad (3.3.2)$$

where

$$\varphi(t) = \int_0^t \frac{2e}{\hbar} V(t') dt'. \quad (3.3.3)$$

We see, that for $I > I_c$ part of the current has to flow as normal or displacement current. This is only possible of course at a finite junction voltage. The finite junction voltage, in turn, results in a time varying Josephson current and, since the total current is fixed, in a temporal variation of the sum of the normal and displacement current. This results in a time varying voltage $V(t)$ and an even more complicated non-sinusoidal oscillation of the Josephson current. The oscillating voltage has to be calculated self-consistently. We immediately see that the oscillation period is $T = \Phi_0/\langle V \rangle$. The oscillation frequency is then $f = \langle V \rangle / \Phi_0$, which is just the Josephson frequency for a junction with an applied voltage equal to the average junction voltage. Of course the normal current has the same periodicity, since the sum of the currents is fixed by the applied current.

Fig. 3.7 shows the oscillating junction voltage for an applied current slightly above the critical current and for $I \gg I_c$. For $I \gtrsim I_c$, we have a highly non-sinusoidal oscillation with a long oscillation period. The time averaged voltage, which is proportional to $1/T$ is very low. In the case $I \gg I_c$, most of the current has to flow as a normal current resulting in a more constant junction voltage. That is, the relative oscillation of the junction voltage is small. Then, the oscillation of the Josephson current and, in turn, the normal current is almost sinusoidal resulting in an about sinusoidal variation of the junction voltage. Note that for a sinusoidal oscillation of the Josephson current the time-average of the Josephson current is zero. This results in a linear dependence of the time averaged voltage on the current, that is, in an ohmic IVC.

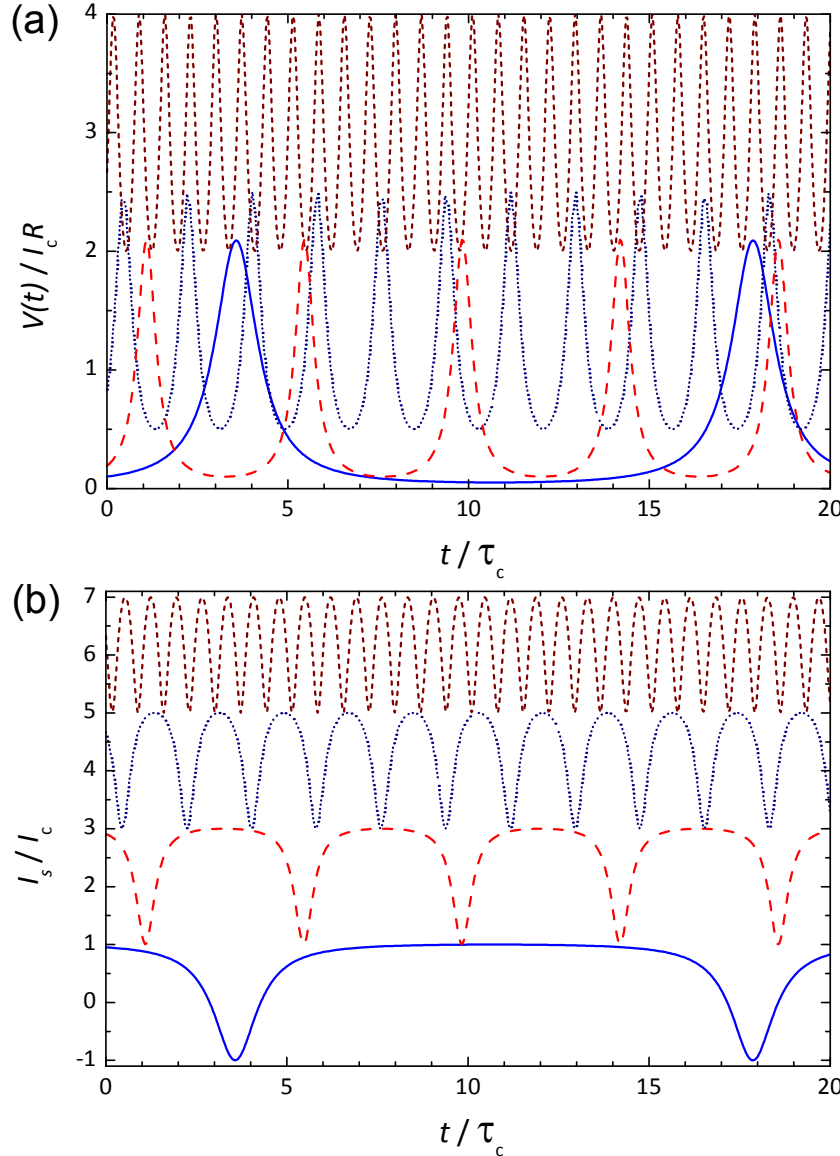


Figure 3.7: The variation of the junction voltage (a) and the Josephson current (b) with time for a current biased Josephson junction at different values of the applied current: $I/I_c = 1.05, 1.1, 1.5$, and 3.0 . The time is normalized to $\tau_c = \hbar/2eI_cR$. In (b) the curves for $I_s/I_c = 1.1, 1.5$, and 3.0 are displaced vertically by $2, 4$, and 6 , respectively.

Current-Voltage Characteristics

Strong Damping: For strong damping, $\beta_C \ll 1$, and neglecting the noise current we can rewrite (3.2.10) as

$$\frac{d\varphi}{d\tau} + \sin \varphi - i = 0 . \quad (3.3.4)$$

If $I \leq I_c$ (i.e. $i \leq 1$), we expect that all current is flowing as supercurrent. Indeed we see that

$$\varphi = \sin^{-1} i \quad \text{for } i \leq 1 \quad (3.3.5)$$

is a solution, since φ does not depend on time. The voltage-phase relation then implies that the junction is in the zero voltage state.

When $i > 1$, the current can no longer flow as a pure supercurrent. Some of the current has to flow through the resistive channel creating a finite junction voltage that will cause a temporal evolution of the phase. Then, the full time dependence of (3.3.4) is required. Equation (3.3.4) can be solved by rewriting it as

$$d\tau = \frac{d\varphi}{i - \sin \varphi} . \quad (3.3.6)$$

Integration results in a periodic function $\varphi(t)$ with period¹⁵

$$T = \frac{2\pi\tau_c}{\sqrt{i^2 - 1}} . \quad (3.3.7)$$

With $\langle V(t) \rangle = \frac{1}{T} \int_0^T V(t) dt = \frac{\Phi_0}{T}$ (cf. (3.3.1)) and using $\tau_c = \frac{\Phi_0}{2\pi} \frac{1}{I_c R}$, we obtain

$$\langle V(t) \rangle = I_c R \sqrt{\left(\frac{I}{I_c}\right)^2 - 1} \quad \text{for } \frac{I}{I_c} > 1 . \quad (3.3.8)$$

This current versus time-averaged voltage curve is shown in Fig. 3.8. For $I \leq I_c$, the gauge-invariant phase difference increases according to (3.3.5), but the voltage remains zero. As the applied current exceeds the critical current I_c , part of the current must flow as a normal current through the resistive channel thereby creating a nonvanishing voltage across the junction. This results in an oscillation of the Josephson current and, in turn, of the normal current, since the total current is fixed by the external circuit. In total this results in a complex oscillation of the junction voltage as shown in Fig. 3.7. The time-averaged junction voltage is just given by the flux quantum divided by the oscillation period T .

¹⁵From the table of integrals we know that for $a^2 > 1$ we have

$$\int \frac{dx}{a - \sin x} = \frac{2}{\sqrt{a^2 - 1}} \tan^{-1} \left(\frac{-1 + a \tan(x/2)}{\sqrt{a^2 - 1}} \right) .$$

Integration of (3.3.6) then yields

$$\tau - \tau_0 = \frac{2}{\sqrt{i^2 - 1}} \tan^{-1} \left(\frac{-1 + i \tan(\varphi/2)}{\sqrt{i^2 - 1}} \right) \quad \text{for } i > 1 .$$

Here, τ_0 is an integration constant. Recalling that $\tau = t/\tau_c$ and setting the integration constant equal to zero, we can solve this equation for the gauge-invariant phase difference:

$$\varphi(t) = 2 \tan^{-1} \left\{ \sqrt{1 - \frac{1}{i^2}} \tan \left(\frac{t\sqrt{i^2 - 1}}{2\tau_c} \right) + \frac{1}{i} \right\} .$$

Although this equation is quite complex we see that $\varphi(t)$ is periodic with a period

$$T = \frac{2\pi\tau_c}{\sqrt{i^2 - 1}} .$$

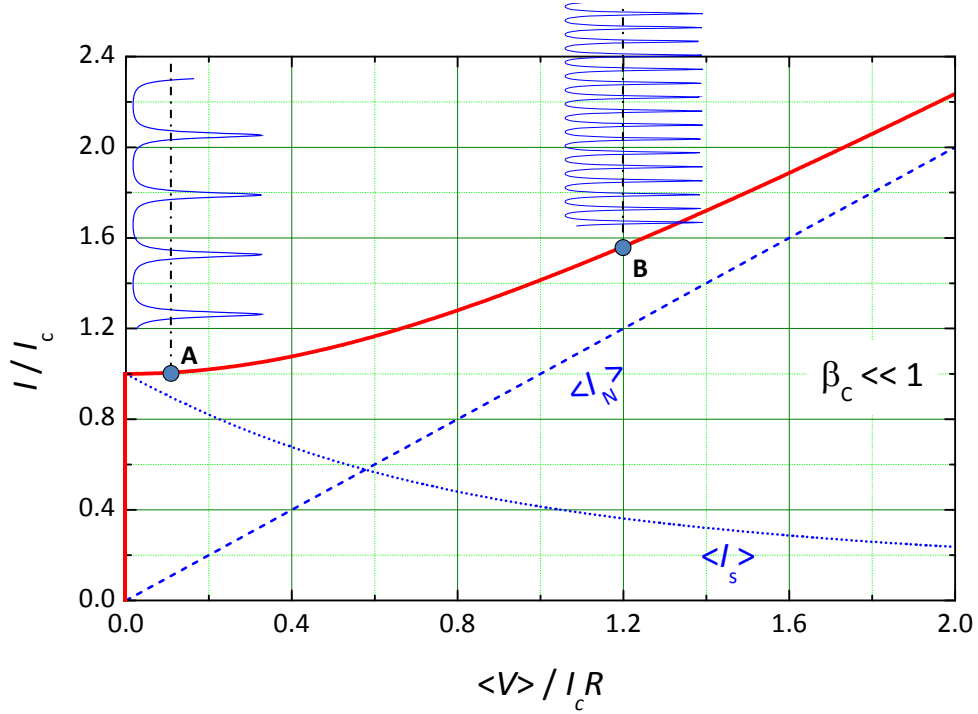


Figure 3.8: Current versus time-averaged voltage for an overdamped Josephson junction ($\beta_C \ll 1$). Also shown are the time-averaged components of the normal and the supercurrent as well as the time evolution of the junction voltage $V(t)$ for two bias points A and B on the IVC.

Weak Damping: In the underdamped case, $\beta_C \gg 1$, the characteristic frequency $\omega_{RC} = 1/R_N C$ is very small. Therefore, at almost all frequencies the large junction capacitance is effectively shunting the oscillating part of the junction voltage so that the junction voltage is almost constant: $V(t) \simeq \bar{V}$. Accordingly, the time evolution of the phase is almost linear

$$\varphi(t) = \frac{2e}{\hbar} \bar{V} t + const . \quad (3.3.9)$$

The almost linear time dependence of the gauge-invariant phase difference in turn results in an about sinusoidal oscillation of the Josephson current with a vanishing mean value

$$\overline{I_s(t)} = \overline{I_c \sin \left(\frac{2e}{\hbar} \bar{V} t + const \right)} \simeq 0 . \quad (3.3.10)$$

Thus, the total current has to be carried almost completely by the resistive channel and the IVC is given by an ohmic dependence

$$\bar{I} = I_N(\bar{V}) = \frac{\bar{V}}{R} \quad (3.3.11)$$

down to low voltages $\bar{V} \simeq \hbar \omega_{RC}/e \ll V_c = I_c R_N$. Since the related current is $\bar{I} \ll I_c$, this results in a hysteretic IVC as already discussed qualitatively above. Recall that for a real junction we have a voltage dependent normal resistance $R = R(V)$. Then, the IVC is determined by the voltage dependence of the normal resistance.

Additional Topic

Intermediate Damping: For $\beta_C \sim 1$, the calculation of the IVC cannot be carried out analytically even for the simplest model. Examples for numerical calculations can be found in literature.¹⁶ These calculations show that with increasing McCumber parameter the IVCs become more hysteretic (see Fig. 3.9a). The so-called **return-current** I_R , at which the junction switches back to the zero-voltage state is decreasing with increasing β_C . With finite damping, the return current is determined by the tilt of the washboard at which the energy dissipated in advancing the phase from one minimum to the adjacent exactly equals the work done by the drive current during this same motion. Using this criterion, we can calculate the normalized return current $i_R = I_R/I_c$ analytically for $\beta_C \gg 1$.

If the applied current I is close to I_R and thus for $\beta_C \gg 1$ much smaller than I_c , we can neglect both the normal current and the damping in zeroth order approximation. The junction equation then reads as $I = I_c \sin \varphi + C \frac{\phi_0}{2\pi} \frac{d^2\varphi}{dt^2}$. In this case the energy is conserved and is equal to the work $\int F dx$ (compare section 2.1.3) done by the drive current. Here, the generalized force is given by the current and the generalized coordinate x by $\frac{\phi_0}{2\pi} \varphi$. That is, the energy is given by the first integral of the junction equation:

$$\begin{aligned} E &= \frac{\phi_0}{2\pi} \int_0^\varphi I d\varphi' = \frac{\phi_0}{2\pi} \int_0^\varphi \left(I_c \sin \varphi' + C \frac{\phi_0}{2\pi} \frac{d^2\varphi'}{dt'^2} \right) d\varphi' \\ &= \frac{\Phi_0 I_c}{2\pi} \left[(1 - \cos \varphi) + \frac{1}{\omega_p^2} \int_0^t \frac{d^2\varphi}{dt'^2} \frac{d\varphi}{dt'} dt' \right] \\ &= E_{J0} \left\{ \frac{1}{2} \frac{1}{\omega_p^2} \left(\frac{d\varphi}{dt} \right)^2 + (1 - \cos \varphi) \right\}. \end{aligned} \quad (3.3.12)$$

Here, we have used $E_{J0} = \frac{\Phi_0 I_c}{2\pi}$ and $\omega_p^2 = \frac{2\pi I_c}{\Phi_0 C}$. Using this equation the energy dissipation can be expressed explicitly. Within the RCSJ model we obtain

$$\begin{aligned} W_{\text{diss}} &= \int_0^T I_N V dt = \int_0^T I_N \frac{\hbar}{2e} \frac{d\varphi}{dt} dt = \int_0^{2\pi} \frac{V}{R} \frac{\hbar}{2e} d\varphi = \int_0^{2\pi} \left(\frac{d\varphi}{dt} \right) \left(\frac{\hbar}{2e} \right)^2 \frac{1}{R} d\varphi \\ &= \frac{\Phi_0 V_p}{2\pi R} \int_0^{2\pi} \left\{ 2 \left(\frac{E}{E_{J0}} - 1 + \cos \varphi \right) \right\}^{1/2} d\varphi. \end{aligned} \quad (3.3.13)$$

Here, we have used $d\varphi/dt$ from (3.3.12) and the plasma voltage

$$V_p = \omega_p \frac{\Phi_0}{2\pi} = \omega_p \frac{\hbar}{2e} = \frac{V_c}{\sqrt{\beta_C}}. \quad (3.3.14)$$

The resistive state is only possible, if the minimum value of the junction kinetic energy is positive, that is, if $E \geq 2E_{J0}$. Thus, the limit $I = I_R$ corresponds to $E = 2E_{J0}$. In this limit the right hand side of (3.3.13) can be calculated resulting in

$$W_{\text{diss}} = 4 \frac{\Phi_0 I_c}{\pi} \frac{1}{\sqrt{\beta_C}} \quad (3.3.15)$$

¹⁶K. K. Likharev, *Dynamics of Josephson Junctions and Circuits*, Gordon and Breach Science Publishers, New York (1986).

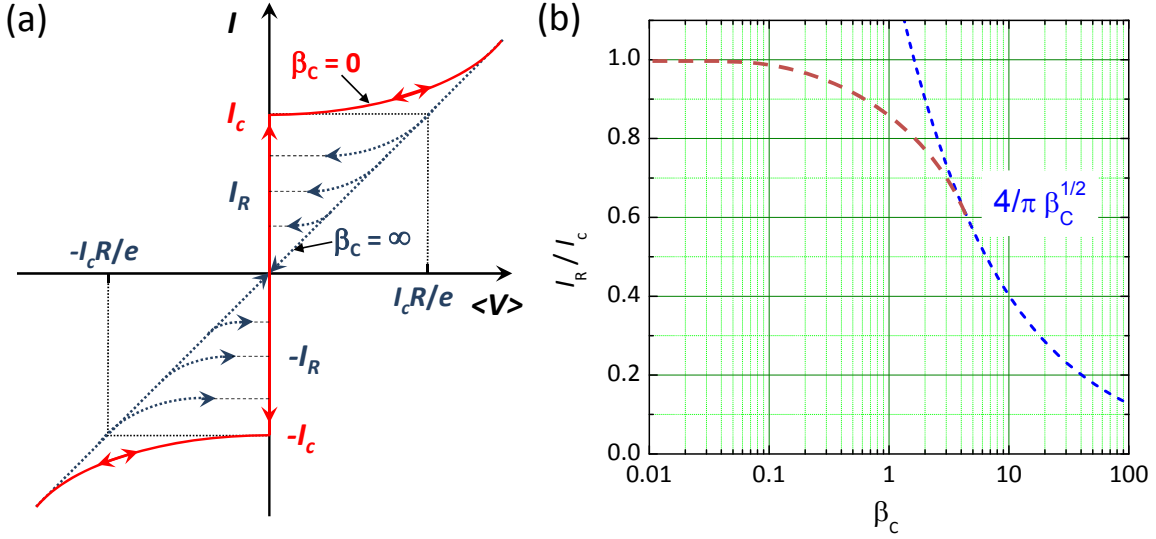


Figure 3.9: (a) RCSJ model IVCs at intermediate damping. The arrows mark the return current values I_R at which the junction jumps back to the zero-voltage state. (b) The normalized return current I_R/I_c plotted versus the Stewart-McCumber parameter β_C . The dashed line shows the large β_C approximation according to equation (3.3.16). The dotted line qualitatively shows the behavior at large damping (low β_C).

and hence in

$$\frac{I_R}{I_c} = \frac{4}{\pi} \frac{1}{\sqrt{\beta_C}} . \quad (3.3.16)$$

This result is plotted in Fig. 3.9b. Note that it is valid only for $\beta_C \gg 1$.

3.3.2 Response to a dc Voltage Source

If we drive the junction by a dc voltage source, the phase difference will evolve linearly in time as $\varphi(t) = \frac{2e}{\hbar} V_{dc} t + const$ and, in turn, the Josephson current $I_s(t) = I_c \sin \varphi(t)$ will oscillate sinusoidally. Then, the time average of the Josephson current is zero. Furthermore, since $dV/dt = 0$, also the displacement current is zero. Accordingly, the total current has to be carried by the normal current resulting in the IVC

$$I = \frac{V_{dc}}{R_N} . \quad (3.3.17)$$

That is, within the RCSJ model we obtain a simple ohmic dependence. In the more general case we have a voltage dependent resistance $R_N(V)$ and hence a nonlinear IVC.

3.3.3 Response to ac Driving Sources

In the previous section we have considered the response of a Josephson junction driven by a dc source. We now use the RCSJ model to analyze the dynamics of a Josephson junction driven both by an ac and dc source. We will see that the response of the supercurrent gives rise to constant-voltage **Shapiro steps**¹⁷ in the IVCs, whereas the **photon-assisted tunneling** response of the quasiparticles gives rise to shifted images of the energy gap structure in the IVCs.

¹⁷S. Shapiro, Phys. Rev. Lett. **11**, 80 (1963).

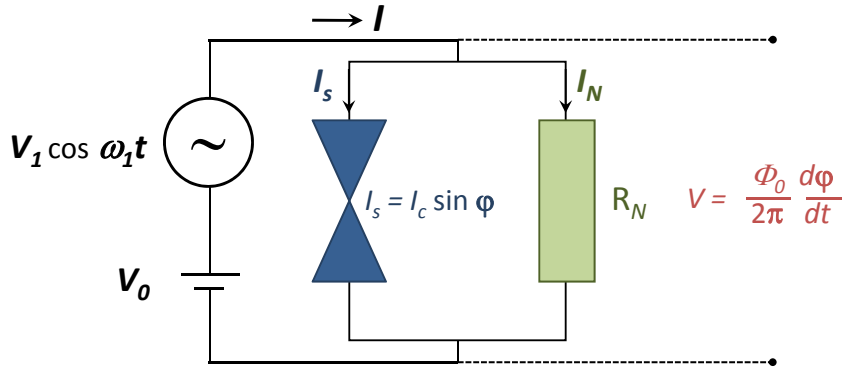


Figure 3.10: A dc and ac voltage source attached to an overdamped Josephson junction. The capacitance of the junction is assumed to be negligibly small (large damping, $\beta_C \ll 1$).

Response to an ac Voltage Source, Strong Damping

We first consider the most simple case of strong damping, $\beta_C \ll 1$, and an applied voltage

$$V(t) = V_{dc} + V_1 \cos \omega_1 t . \quad (3.3.18)$$

The equivalent circuit for this situation is shown in Fig. 3.10. From the integration of the voltage-phase relation we obtain

$$\varphi(t) = \varphi_0 + \frac{2\pi}{\Phi_0} V_{dc} t + \frac{2\pi}{\Phi_0} \frac{V_1}{\omega_1} \sin \omega_1 t , \quad (3.3.19)$$

where φ_0 is an integration constant. Inserting this into the current-phase relation we obtain

$$I_s(t) = I_c \sin \left\{ \varphi_0 + \frac{2\pi}{\Phi_0} V_{dc} t + \frac{2\pi}{\Phi_0} \frac{V_1}{\omega_1} \sin \omega_1 t \right\} . \quad (3.3.20)$$

We see that the frequency of the Josephson current is a superposition of the constant frequency $\omega_{dc} = \frac{2\pi}{\Phi_0} V_{dc}$ and a sinusoidally varying phase. Therefore, the frequency of the current is not the same as that of the driving ac voltage source. The reason for this is the fact that the nonlinear current-phase relation can couple different frequencies with the driving frequency.

In order to analyze the time dependence of the Josephson current we rewrite (3.3.20) as a Fourier series. In order to do so we use the Fourier-Bessel series identity

$$e^{ib \sin x} = \sum_{n=-\infty}^{+\infty} \mathcal{J}_n(b) e^{inx} . \quad (3.3.21)$$

Here, \mathcal{J}_n is the n^{th} order Bessel function of first kind. It is evident from (3.3.20) that the argument of the sine function is of the form $(a + b \sin x)$. Hence, in order to use the identity (3.3.21) we write

$$\sin(a + b \sin x) = \Im \left\{ e^{i(a + b \sin x)} \right\} . \quad (3.3.22)$$

The Fourier-Bessel series together with the fact that $\mathcal{J}_{-n}(b) = (-1)^n \mathcal{J}_n(b)$ allows us to write

$$e^{i(a + b \sin x)} = \sum_{n=-\infty}^{+\infty} \mathcal{J}_n(b) e^{i(a + nx)} = \sum_{n=-\infty}^{+\infty} (-1)^n \mathcal{J}_n(b) e^{i(a - nx)} . \quad (3.3.23)$$

Finally, the imaginary part of (3.3.22) then gives

$$\sin(a + b \sin x) = \sum_{n=-\infty}^{+\infty} (-1)^n J_n(b) \sin(a - nx) . \quad (3.3.24)$$

With $x = \omega_1 t$, $b = \frac{2\pi V_1}{\Phi_0 \omega_1}$ and $a = \varphi_0 + \omega_{dc} t = \varphi_0 + \frac{2\pi}{\Phi_0} V_{dc} t$, we can rewrite the current equation (3.3.20) as

$$I_s(t) = I_c \sum_{n=-\infty}^{+\infty} (-1)^n J_n\left(\frac{2\pi V_1}{\Phi_0 \omega_1}\right) \sin[(\omega_{dc} - n\omega_1)t + \varphi_0] . \quad (3.3.25)$$

We see that due to the nonlinear current-phase relation we obtain a current response, in which the frequency ω_{dc} couples to multiples of the driving frequency ω_1 .

The most interesting aspect of (3.3.25) is the fact that the ac voltage source driving the junction can result in a dc current (denoted as Shapiro steps), if the argument of the sine function becomes zero. That is, we obtain a dc current response for

$$\omega_{dc} = n\omega_1 \quad \text{or} \quad V_{dc} = V_n = n \frac{\Phi_0}{2\pi} \omega_1 . \quad (3.3.26)$$

For a specific n the amplitude of the average dc current is

$$|\langle I_s \rangle_n| = I_c \left| J_n\left(\frac{2\pi V_1}{\Phi_0 \omega_1}\right) \right| \quad (3.3.27)$$

with the detailed value depending on the initial value φ_0 (see inset of Fig. 3.11).

For all other voltages $V_{dc} \neq V_n$ we have a series of sinusoidally time dependent terms with a vanishing dc component. Thus, for $V_{dc} \neq V_n$ we have

$$\langle I \rangle = \frac{V_{dc}}{R_N} + \left\langle \frac{V_1}{R_N} \cos \omega_1 t \right\rangle = \frac{V_{dc}}{R_N} . \quad (3.3.28)$$

We see that all the current has to be carried by the normal current resulting in an ohmic behavior. Only for $V_{dc} = V_n$ an average dc Josephson current appears. With respect to the IVCs this means that we have an ohmic dependence with sharp current spikes at $V_{dc} = V_n$ (see Fig. 3.11). The amplitude of the current spikes is given by (3.3.27) and depends on the amplitude V_1 of the ac source. The appearance of current steps at fixed voltages V_n that already has been predicted by **B. Josephson** is due to the formation of higher harmonics of the signal frequency due to the nonlinearity of the Josephson junction. The n^{th} step corresponds to the phase locking of the junction oscillation by this n^{th} harmonic.

When we are applying for example an ac driving voltage source with $\omega_1/2\pi = 10$ GHz for various values of the applied dc voltage V_{dc} , a constant dc current will appear at $V_{dc} = 0$ and $V_n = n \frac{\Phi_0}{2\pi} \omega_1 \simeq n \cdot 20 \mu\text{V}$. That is, we obtain current steps in the IVCs, which have constant spacing $\delta V = \frac{\Phi_0}{2\pi} \omega_1 \simeq 20 \mu\text{V}$. Note that the spacing only depends on the frequency of the ac voltage source and on fundamental constants.

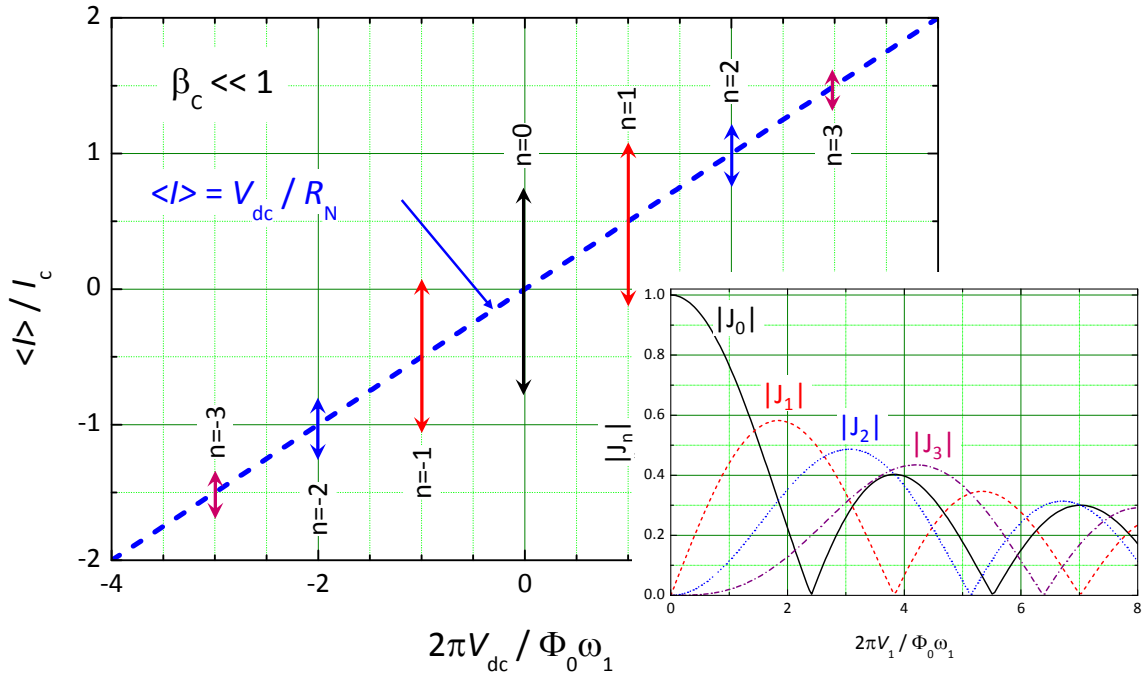


Figure 3.11: The dc component of the current plotted versus the applied dc voltage for a RCSJ model junction driven by a voltage source $V(t) = V_{dc} + V_1 \cos \omega_1 t$. At the voltages $V_n = n \frac{\Phi_0}{2\pi} \omega_1$ current steps appear. Their height has a Bessel function dependence on the amplitude V_1 of the ac voltage as shown in the inset.

Response to an ac Current Source, Strong Damping

In most experimental arrangements the external source has a larger impedance than the Josephson junction and therefore represents a current source. In this case Kirchhoff's law allows us to write

$$I_c \sin \varphi + \frac{1}{R_N} \frac{\phi_0}{2\pi} \frac{d\varphi}{dt} = I_{dc} + I_1 \sin \omega_1 t . \quad (3.3.29)$$

Here, we again have neglected the displacement current what is possible only in the limit of strong damping ($\beta_C \ll 1$) and we also did not take into account fluctuations.

The nonlinear differential equation (3.3.29) is difficult to solve. In order to understand what is going on we use the tilt washboard potential to perform a qualitative discussion (in the same way a qualitative discussion can be performed based on the pendulum analogue). We recall that the current tilts the washboard potential. Therefore, the dc current can be considered to result in a constant tilt angle, whereas the ac current results in oscillations around this tilt angle with the amplitude given by the amplitude I_1 of the ac current. If we increase I_{dc} from zero at a constant ac amplitude I_1 we expect that the junction stays in the zero voltage state as long as $I_{dc} + I_1 \leq I_c$ at all times. In this case the tilt angle is always small enough so that there is a local minimum in the tilted washboard potential.

As soon as $I_{dc} + I_1 > I_c$, the phase particle can leave the local minimum and move down the washboard potential. However, due to the ac current the total current varies between $I_{dc} + I_1 > I_c$ and $I_{dc} - I_1 < I_c$. Therefore, for some part of the ac cycle the phase particle can move, whereas for the rest of the cycle it is trapped again in a local minimum. In total the motion of the particle is complicated and therefore it is difficult to calculate the resulting time-averaged voltage. An interesting situation appears when the average junction voltage reaches the values $V_n = n \frac{\Phi_0}{2\pi} \omega_1$ (compare (3.3.26)). For these values the motion of the phase particle in the tilt washboard potential is synchronized by the ac driving current.

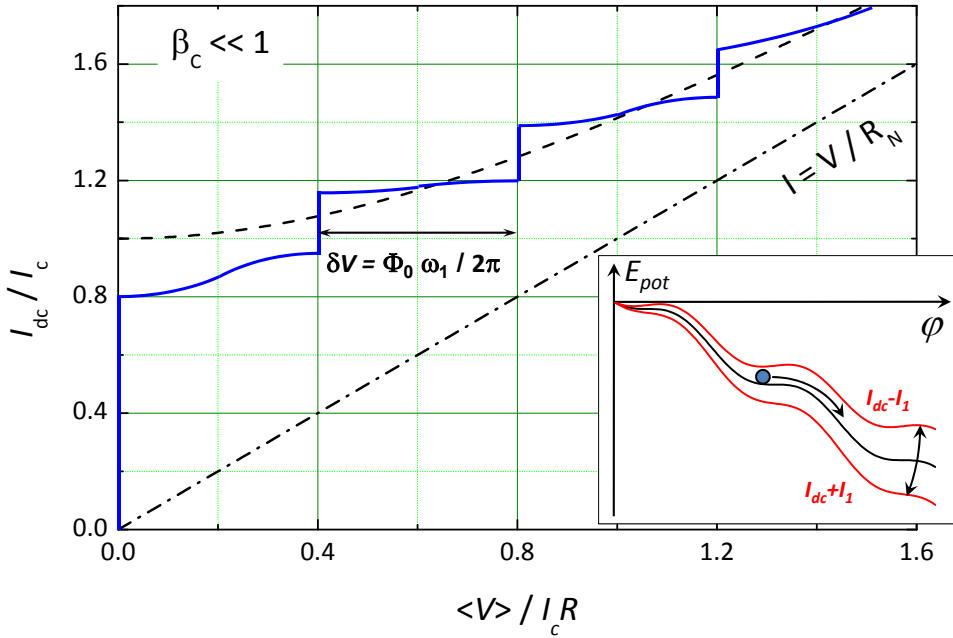


Figure 3.12: The time-averaged junction voltage plotted versus the applied dc current for an overdamped RCSJ model junction driven by a current source $I(t) = I_{dc} + I_1 \sin \omega_1 t$ (full line, $I_1/I_c \simeq 0.2$). The dashed line shows the RCSJ model IVC without ac driving current. Also shown is the ohmic line (dash dot). The inset shows the tilt washboard potential. Due to the finite ac amplitude the tilt angle varies during one rf cycle.

For example, if the phase particle moves from one local minimum to the adjacent one during each cycle $T = 2\pi/\omega_1$ of the ac source, there is a phase change $\phi/T = 2\pi/T = \omega_1$. This corresponds to an average voltage $\langle V \rangle = \frac{\Phi_0}{2\pi} \dot{\phi} = \frac{\Phi_0}{2\pi} \omega_1$. We see that this exactly corresponds to the voltage V_n of (3.3.26) for $n = 1$. We can generalize our discussion and assume that during each cycle of the ac source the phase particle is moving down n local minima. Then, the phase change is

$$\phi = n \frac{2\pi}{T} = n \omega_1 . \quad (3.3.30)$$

This results in an average dc voltage of

$$\langle V \rangle = n \frac{\Phi_0}{2\pi} \omega_1 = V_n . \quad (3.3.31)$$

We see that for the voltages V_n given by (3.3.26) the phase particle is moving down the potential well by a fixed number of minima during each cycle. That is we have a synchronization of the phase change with the external ac source. This synchronization is not only possible for a particular value of the dc current but for a complete interval of the dc current. The width of the dc current interval is proportional to the amplitude of the current spike according to (3.3.27).

The resulting IVC is shown schematically in Fig. 3.12 for an overdamped junction. Note that the appearance of the current steps occurs at precisely the values V_n given by (3.3.26). Experimental IVCs for an underdamped and overdamped Josephson junction are shown in Fig. 3.13.

Response to ac Driving Sources: Intermediate Damping

So far we have discussed only the effect of strong damping by neglecting the junction capacitance. The most visible effect of the junction capacitance on the IVCs is between the current steps rather than upon

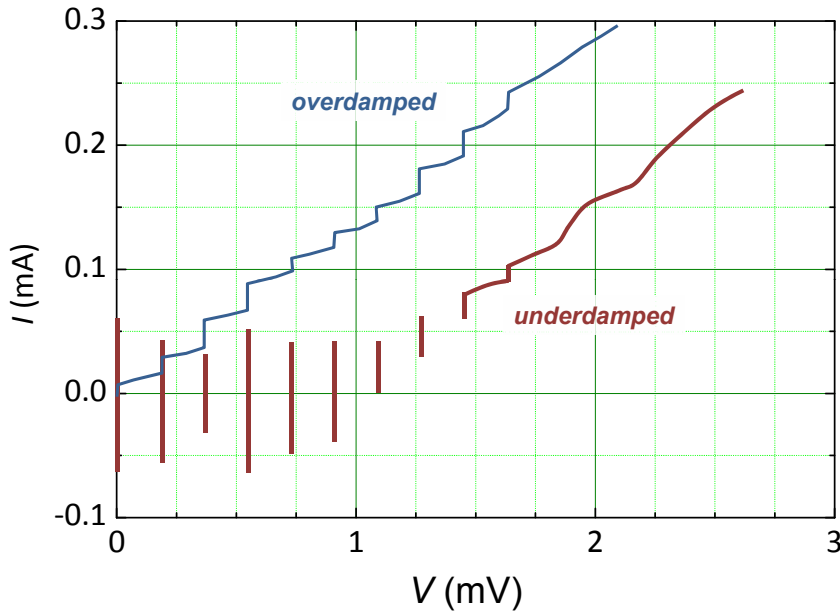


Figure 3.13: Experimental IVCs obtained for an underdamped and overdamped Nb Josephson junction under microwave radiation. The IVCs clearly show the constant voltage steps at $V_n = n \frac{\Phi_0}{2\pi} \omega_1$ (data from C.A. Hamilton, Rev. Sci. Instr. **71**, 3611 (2000)).

the steps themselves. With the increase of β_C the supercurrent contribution to the IVCs at $\langle V \rangle \neq V_n$ decreases, so that the IVCs become hysteretic in the vicinity of each step.¹⁸

3.3.4 Photon-Assisted Tunneling

In the discussion of the Shapiro steps we have approximated the normal resistance by an ohmic resistance R_N . However, in a superconducting tunnel junction the normal resistance $R(V)$ is highly nonlinear with a sharp step at the gap voltage $V_g = 2\Delta/e$ manifesting itself as a strong increase of the quasiparticle current at V_g . Therefore, instead of using the simple approximation $I = V/R_N$ it is more appropriate to use the quasiparticle tunneling current $I_{qp}(V)$. However, in the $I_{qp}(V)$ curve we have to take into account the effect of the ac source on the quasiparticle tunneling. This can be done by the method introduced by **P.K. Tien** and **J.P. Gordon**.¹⁹ They assumed that the effect of the rf driving voltage has no effect on the internal energy levels of the two electrodes but shifts these levels up or down in one electrode with respect to those in the other electrode as shown in Fig. 3.14. That means, that the energy of a quasiparticle becomes $E_{qp} + eV_1 \cos \omega_1 t$ so that the quantum mechanical phase factor $\exp(-iEt/\hbar)$ becomes frequency modulated. It can be written as

$$\exp\left(-\frac{i}{\hbar} \int (E_{qp} + eV_1 \cos \omega_1 t) dt\right) = \exp\left(-\frac{i}{\hbar} E_{qp} t\right) \cdot \exp\left(-i \frac{eV_1}{\hbar \omega_1} \sin \omega_1 t\right). \quad (3.3.32)$$

Using the Bessel function identity as discussed above we can write the factor containing V_1 as a sum of terms of the form $\mathcal{J}_n(eV_1/\hbar\omega_1) e^{-in\omega_1 t}$. This result can be interpreted as a splitting up of the quasiparticle levels into many levels at $E_{qp} \pm n\hbar\omega_1$ with probabilities given by the amplitude coefficient $\mathcal{J}_n(eV_1/\hbar\omega_1)$.

¹⁸see e.g. K. K. Likharev, *Dynamics of Josephson Junctions and Circuits*, Gordon and Breach Science Publishers, New York (1986).

¹⁹P.K. Tien, J.P. Gordon, Phys. Rev. **129**, 647 (1963).

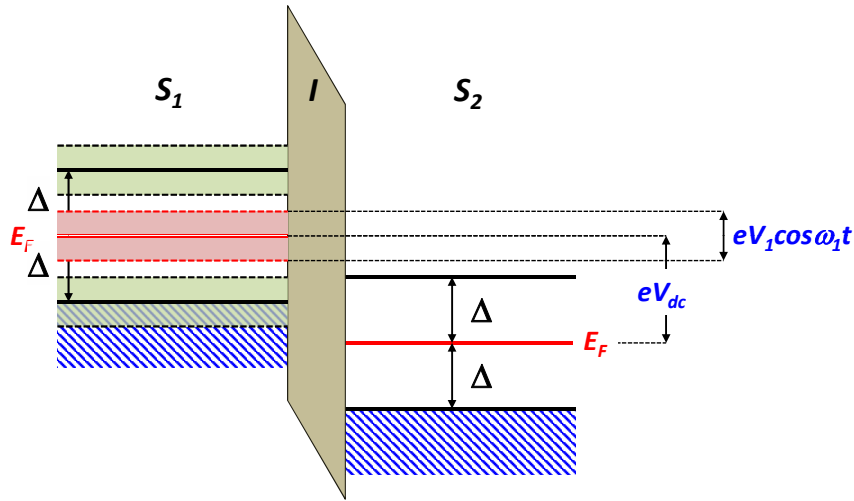


Figure 3.14: Illustration of the periodic shift of the quasiparticle levels of a superconducting tunnel junction due to an applied ac voltage of amplitude V_1 .

With this modified density of states the quasiparticle tunneling current is obtained to

$$I_{\text{qp}}(V) = \sum_{n=-\infty}^{+\infty} \mathcal{J}_n^2 \left(\frac{eV_1}{\hbar\omega_1} \right) I_{\text{qp}}^0(V + n\hbar\omega_1/e). \quad (3.3.33)$$

We see that the sharp increase of the quasiparticle tunneling current at the gap voltage is broken up into many steps of smaller current amplitude at the voltages $V_g \pm n\hbar\omega_1/e$. An experimental example is shown in Fig. 3.15.

Note that the steps in the quasiparticle tunneling curve resemble the Shapiro steps that occur at voltages

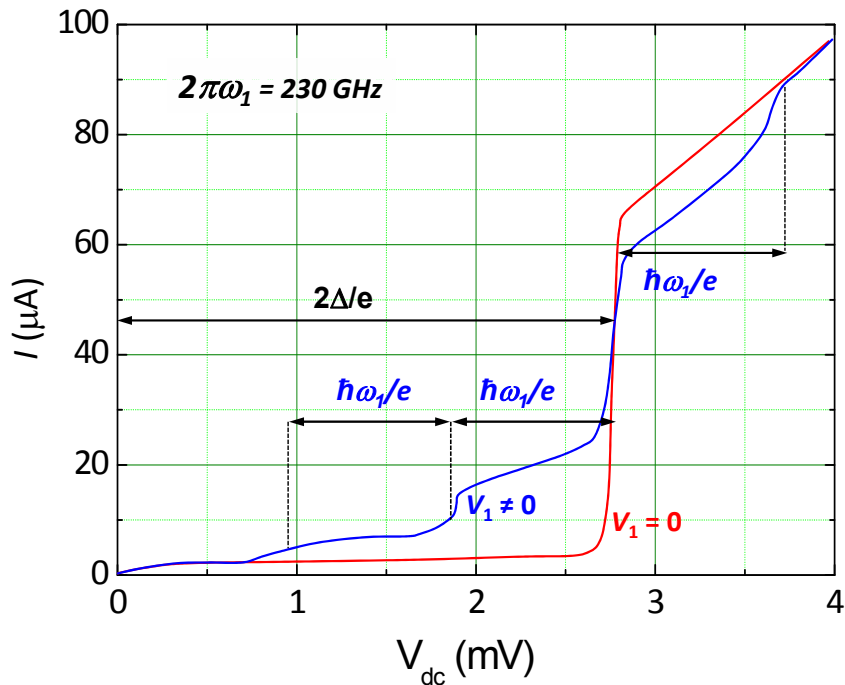


Figure 3.15: Quasiparticle current-voltage characteristics of a niobium SIS Josephson junction without and with microwave irradiation of frequency $2\pi\omega_1 = 230$ GHz corresponding to $\hbar\omega_1/e \approx 950$ μ V.

$V_n = n\hbar\omega_1/2e$. However, there are profound differences. First, the voltage separation of the quasiparticle steps is just twice of that of the Shapiro steps because e and not $2e$ appears in the denominator. Second, the steps have no constant voltage. The sharpness of the voltage is determined by the sharpness of the increase of the quasiparticle tunneling curve at the gap voltage. Third, their amplitude varies as the square of the Bessel function of the half argument.

3.4 Additional Topic: Effect of Thermal Fluctuations

In the previous subsections we have discussed the response of a RCSJ model Josephson junction to external voltage or current sources. However, in our discussion we did not take into account fluctuations. Therefore, in this section we analyze the effect of additional fluctuations. We will restrict our discussion to thermal fluctuations, which have a correlation function²⁰

$$\langle I_F(t)I_F(t+\tau) \rangle = \frac{2k_B T}{R_N} \delta(\tau) . \quad (3.4.1)$$

If the fluctuations are small, their effect are small phase fluctuations around the equilibrium value. Here, small means that the mean square of the phase fluctuations $\langle \bar{\varphi}^2 \rangle$ is much less than the width

$$\Delta\varphi = \tilde{\varphi}_n - \varphi_n = \pi - 2\arcsin(i) \quad (3.4.2)$$

of the potential well surrounding the point φ_n (compare (2.1.10) and Fig. 2.3 in section 2.1.3).

If the fluctuations become larger and $\langle \bar{\varphi}^2 \rangle$ becomes comparable to $(\Delta\varphi)^2$, there is a finite probability for the phase to escape from the local minimum of the potential well to one of the adjacent states $\varphi_{n\pm 1}$. This probability can be characterized by the rates $\Gamma_{n\pm 1}$ or the corresponding lifetimes $\tau_{n\pm 1} = \hbar/\Gamma_{n\pm 1}$. This is shown in Fig. 3.16. The escape of the phase to one of the adjacent minima results in a $\pm 2\pi$ change of the phase. Whereas for zero applied external current we have $\Gamma_{n+1} = \Gamma_{n-1}$ and therefore the time-averaged change of the phase difference, $\langle \dot{\varphi} \rangle$, is equal to zero, there is a net time-averaged change $\langle \dot{\varphi} \rangle \neq 0$ for $I \neq 0$, since now $\Gamma_{n+1} \neq \Gamma_{n-1}$. Once the phase has escaped from the potential minimum the further evolution of the phase difference strongly depends on the damping of the junction.

In order to quantify the effect of thermal fluctuations we have to calculate the rates $\Gamma_{n\pm 1}$ as a function of the applied bias current and the intensity of the fluctuations. The simplest result can be again obtained in the framework of the RCSJ model, when the Langevin equation has the form

$$I = I_c \sin \varphi + \frac{1}{R_N} \frac{\Phi_0}{2\pi} \frac{d\varphi}{dt} + C \frac{\Phi_0}{2\pi} \frac{d^2\varphi}{dt^2} + I_F . \quad (3.4.3)$$

As the general theory of Brownian motion^{21,22} shows, this equation is equivalent to the following **Fokker-Planck equation**:^{23,24,25,26,27}

$$\frac{1}{\omega_c} \frac{\partial \sigma}{\partial t} + \frac{\partial}{\partial \varphi} (\sigma v) + \frac{1}{\beta_C} \frac{\partial}{\partial v} (\sigma [f(\varphi) - v]) = \frac{\gamma}{\beta_C^2} \frac{\partial^2 \sigma}{\partial v^2} . \quad (3.4.4)$$

²⁰Note that according to the Wiener-Khintchine theorem the spectral density $S(f)$ of the fluctuations is twice the Fourier transform of the correlation function. That is, equation (3.4.1) is equivalent to $S(f) = 4k_B T/R_N$.

²¹H.A. Kramers, Physica **7**, 284 (1940).

²²S. Chandrasekhar, Rev. Mod. Phys. **15**, 1 (1943).

²³A.D. Fokker, *Die mittlere Energie rotierender elektrischer Dipole*, Ann. Phys. **43**, 810 (1914).

²⁴M. Planck, *Über einen Satz der statistischen Dynamik und seine Erweiterung in der Quantentheorie*, Preuss. Akad. Wiss. (1917), p.324

²⁵Yu.M. Ivanchenko, L.A. Zilberman, Sov. Phys. JETP **55**, 2395 (1968).

²⁶V. Ambegaokar, B.I. Halperin, Phys. Rev. Lett. **22**, 1364 (1969).

²⁷The Fokker-Planck equation has the form of a continuity equation in which the role of the flow in space is played by a quantity $J(\mathbf{r}, t)$ consisting of a drift and a diffusion flow. Depending on the meaning of the variable \mathbf{r} , it may be not only the diffusion in the configuration space but also diffusion in the space of velocities, diffusion of energy, diffusion of the phase of oscillation etc.

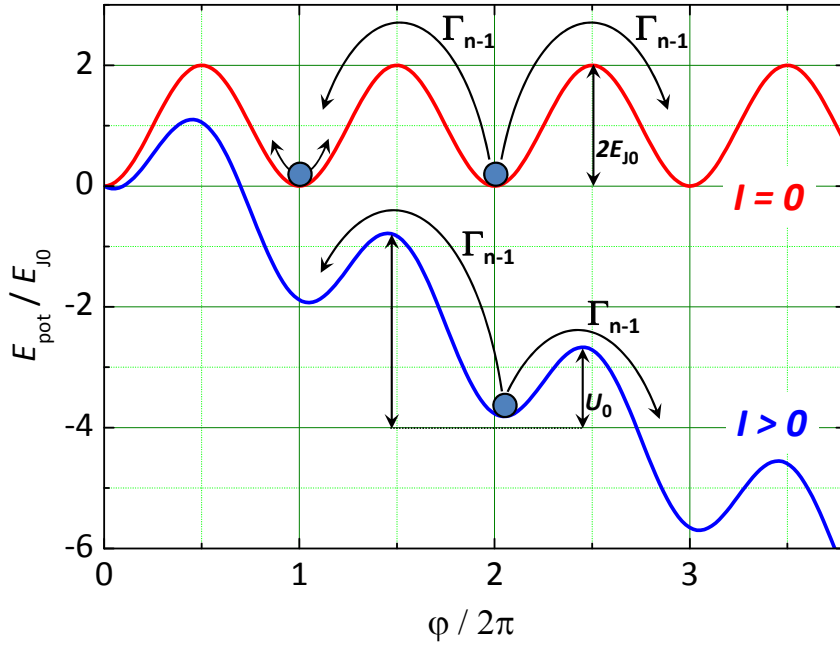


Figure 3.16: The thermally activated motion of the phase in the presence of thermal fluctuations for zero applied current and a finite applied current $I < I_c$. Small fluctuations result in fluctuations of the phase particle around the potential minimum. Large fluctuations result in a finite probability to escape into one of the adjacent phase states.

Here^{28,29}

$$f(\varphi) = -\frac{1}{E_{J0}} \frac{\partial U(\varphi)}{\partial \varphi} = \frac{I}{I_c} - \sin \varphi \quad (3.4.5)$$

is the effective normalized force,

$$\nu = \frac{d\varphi/dt}{\omega_c} = \frac{V}{I_c R_N} \quad (3.4.6)$$

the effective normalized momentum, and $\sigma(\nu, \varphi, t)$ is the probability density of finding the system at a specific point (φ, ν) in phase space at the time t . After σ is found from (3.4.4), the statistical average of every variable $X(\varphi, \nu, t)$ can be calculated as

$$\langle X \rangle(t) = \iint_{-\infty}^{+\infty} \sigma(\varphi, \nu, t) X(\varphi, \nu, t) d\varphi d\nu . \quad (3.4.7)$$

For small fluctuations (3.4.4) has the simple static ($d\sigma/dt = 0$) solution

$$\sigma(\nu, t) = \mathcal{F}^{-1} \exp \left(-\frac{G(\varphi, \sigma)}{k_B T} \right) \quad \text{with} \quad (3.4.8)$$

$$\mathcal{F} = \iint_{-\infty}^{+\infty} \exp \left(-\frac{G(\varphi, \sigma)}{k_B T} \right) d\varphi d\nu , \quad (3.4.9)$$

²⁸Yu. M. Ivanchenko, L.A. Zilberman, Sov. Phys. JETP **55**, 2359 (1968).

²⁹V. Ambegaokar, B.I. Halperin, Phys. Rev. Lett. **22**, 1364 (1969).

which is essentially the **Boltzmann distribution**. Here, $G = E - F \cdot x$ is the total energy with E the free energy. We see that we have a constant probability

$$p = \int_{-\infty}^{+\infty} dv \int_{\varphi \approx \varphi_n} \sigma(\varphi, v) d\varphi \quad (3.4.10)$$

to find the system in the n^{th} metastable state.

If the fluctuations are larger, the transition rate $\Gamma_{n\pm 1}$ to the adjacent phase states becomes significant and p can change in time. The corresponding law describing the amount of phase slippage is simply

$$\frac{dp}{dt} = (\Gamma_{n+1} - \Gamma_{n-1}) p , \quad (3.4.11)$$

if $\omega_A/\Gamma_{n\pm 1} \gg 1$. Here, ω_A is the so-called **attempt frequency**. In most cases $\Gamma_{n+1} \gg \Gamma_{n-1}$. Then, in the limit $\omega_A/\Gamma_{n+1} \gg 1$ an universal expression can be derived for Γ_{n+1} and ω_A :^{30,31}

$$\Gamma_{n+1} = \frac{\omega_A}{2\pi} \exp\left(-\frac{U_0}{k_B T}\right) \quad (3.4.12)$$

with^{32,33}

$$\omega_A = \begin{cases} \omega_0 = \omega_p(1-i^2)^{1/4} & \text{for } \omega_c \tau \gg 1, \\ \tau^{-1} = \omega_c(1-i^2)^{1/2} & \text{for } \omega_c \tau \ll 1 \end{cases} . \quad (3.4.13)$$

Here, U_0 is given by (2.1.15) and ω_0 and ω_c are the plasma frequency and the characteristic frequency in the washboard potential tilt by the applied current $i = I/I_c$, respectively. Note that at $I = 0$ the attempt frequency ω_A is given by the plasma frequency ω_p , since this frequency represents the characteristic frequency at which the phase oscillates back and forth in the potential well. In the presence of a finite current, the potential is tilted and hence the characteristic frequency is not exactly the plasma frequency but the frequency of small oscillations around the minimum of the tilted washboard potential. It is evident that unless I is close to I_c we have $\omega_A \simeq \omega_p$ in good approximation. Note that in the limit of strong damping ($\beta_C = \omega_c \tau_{RC} \ll 1$) one has to replace the undamped plasma frequency by the characteristic frequency of an overdamped oscillator, namely $\omega_A = \omega_p \sqrt{\beta_C} = \omega_p \sqrt{\omega_c R_N C} = \omega_c$ (compare (3.1.13) in section 3.1.2).

3.4.1 Underdamped Junctions: Reduction of I_c by Premature Switching

For $E_{J0} \gg k_B T$, the thermally activated escape from the potential minimum over the barrier height U_0 to the next minimum has a small probability $\propto \exp(-U_0(I)/k_B T)$ at each attempt. The dependence of the barrier height on the applied current, $U_0(I)$, can be approximated well by

$$U_0(I) \simeq 2E_{J0} \left(1 - \frac{I}{I_c}\right)^{3/2} . \quad (3.4.14)$$

³⁰H.A. Kramers, Physica 7, 284 (1940).

³¹S. Chandrasekhar, Rev. Mod. Phys. 15, 1 (1943).

³²Using the notation $i = I/I_c$, the minimum of the resulting potential occurs at $\varphi = \arcsin(i)$ (compare section 2.1.3). Here, the curvature of the potential is $d^2U/d\varphi^2 = (\hbar I_c/2e) \cos \varphi = (\hbar I_c/2e) \sqrt{1-i^2}$ using the relation $\arcsin x = \arccos \sqrt{1-x^2}$. The classical frequency of small oscillations about the minimum is $\omega_A = \omega_p(1-i^2)^{1/4}$.

³³If the McCumber parameter β_C is smaller than the critical value $\sqrt{(1-i^2)}$ the oscillation process in the potential well is aperiodic and the relaxation takes the time $\tau = 1/\omega_c \sqrt{1-i^2}$ (for a detailed discussion see K.K. Likharev, *Dynamics of Josephson Junctions and Circuits*, Gordon and Breach Science Publishers, New York (1986), section 3.2.)

We see that $U_0 = 2E_{J0}$ for $I = 0$ and $U_0 \rightarrow 0$ for $I \rightarrow I_c$.

Since the barrier height goes to zero on approaching the critical current, the escape probability increases exponentially from a very small value $\sim \frac{\omega_A}{2\pi} \exp(-2E_{J0}/k_B T)$ at $I \ll I_c$ up to a large value $\sim \omega_A/2\pi$ at $I \simeq I_c$. Note that for an underdamped junction the phase will accelerate down the tilt washboard potential until it reaches its average velocity determined by the damping $\sim 1/R_N$ of the junction. That is, after the phase has escaped from the potential well at the current I , the junction voltage switches to the value IR_N .

Since the escape is a stochastic process, the exact escape current I_M detected in an experiment will be different every time ramping up the current. That is, we will measure a distribution of current values I_M characterized by a width δI and a mean reduction $\langle \Delta I_c \rangle = I_c - \langle I_M \rangle$ below the critical current I_c obtained in the absence of any fluctuations. The determination of these values requires numerical calculations.³⁴ However, with the approximation (3.4.14) and the escape rate $\sim \frac{\omega_A}{2\pi} \exp(-U_0(I)/k_B T)$ the mean depression of I_c can be approximated by³⁵

$$\langle \Delta I_c \rangle = I_c - \langle I_M \rangle \simeq I_c \left[\frac{k_B T}{2E_{J0}} \ln \left(\frac{\omega_p \Delta t}{2\pi} \right) \right]^{2/3}. \quad (3.4.15)$$

Here, Δt is the time spent sweeping the applied current through the dense part of the distribution of observed critical current values. Since in experiments Δt is of the order of seconds and $\omega_p \sim 10^{10} \text{ s}^{-1}$, the logarithm typically is of the order of $\ln 10^{10} \simeq 23 \gg 1$. Since the logarithm is so large, it only weakly depends on the actual sweep rate of the applied current. Then, fluctuation effects cause a major reduction in I_c as soon as $k_B T$ is larger than about 5% of E_{J0} . One can further show that the width δI of the distribution is approximately given by the mean depression of I_c divided by the same logarithmic factor.

3.4.2 Overdamped Junctions: The Ambegaokar-Halperin Theory

When a thermal noise current is included into the driving term, **Ambegaokar** and **Halperin** showed³⁶ that the simple IVC for overdamped Josephson junctions, $V = R_N \sqrt{I^2 - I_c^2}$ for $I > I_c$ is fundamentally modified. In particular, they found that the finite amount of phase slippage results in a nonvanishing junction voltage even in the limit $I \rightarrow 0$. The corresponding resistance is the so-called phase slip resistance

$$R_p = \lim_{I \rightarrow 0} \frac{\langle V \rangle}{I}. \quad (3.4.16)$$

This resistance has been calculated by **Ambegaokar** and **Halperin** for strong damping ($\beta_C \ll 1$). They obtained

$$R_p(T) = R_N \left\{ \mathcal{J}_0 \left[\frac{\gamma_0(T)}{2} \right] \right\}^{-2} \quad (3.4.17)$$

with

$$\gamma_0(T) = \frac{2E_{J0}(T)}{k_B T} = \frac{\Phi_0 I_c(T)}{\pi k_B T}. \quad (3.4.18)$$

³⁴T. Fulton, L.N. Dunkelberger, Phys. Rev. **B9**, 4760 (1974).

³⁵For a detailed discussion see K. K. Likharev, *Dynamics of Josephson Junctions and Circuits*, Gordon and Breach Science Publishers, New York (1986), section 3.4.

³⁶V. Ambegaokar, B.I. Halperin, Phys. Rev. Lett. **22**, 1364 (1969).

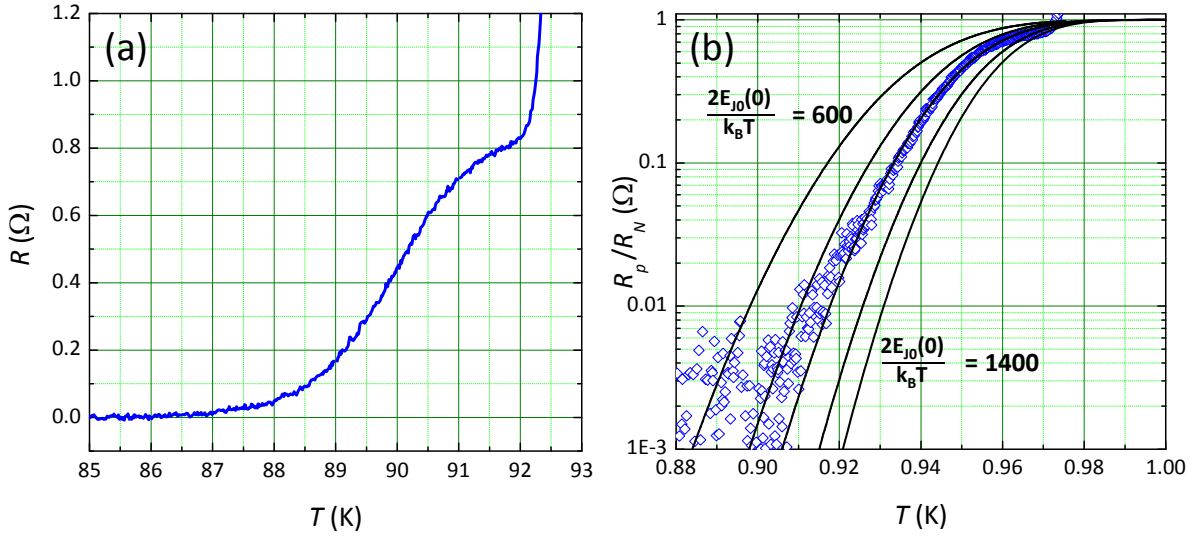


Figure 3.17: (a) Resistance versus temperature curve of a $\text{YBa}_2\text{Cu}_3\text{O}_7$ grain boundary Josephson junction showing the foot structure due to the thermally activated phase slippage. (b) Experimental $R_p(T)/R_N$ dependence (diamonds) as well as theoretical curves according to (3.4.17) and (3.4.18) for $\gamma_0(T) = \frac{\Phi_0 I_c(T)}{\pi k_B T} = \frac{2E_{J0}(0)}{k_B T} (1 - T/T_c)^2$ with $\frac{2E_{J0}(0)}{k_B T}$ ranging between 600 and 1400 (adapted from R. Gross *et al.*, Phys. Rev. Lett. **64**, 228 (1990)).

Here $\mathcal{J}_0(x) = \mathcal{J}_0(ix)$ is the modified Bessel function and we have used $U_0 = 2E_{J0}$ what is justified for $I \rightarrow 0$. For $E_{J0}/k_B T \gg 1$ the Bessel function dependence can be approximated by the exponential dependence $\mathcal{J}_0(x) = e^x/2\pi\sqrt{x}$ resulting in

$$\frac{R_p(T)}{R_N} \propto E_{J0} \exp\left(-\frac{2E_{J0}}{k_B T}\right) \quad \text{or} \quad (3.4.19)$$

$$\langle \dot{\phi} \rangle \propto \frac{2eI_c R_N}{\hbar} \exp\left(-\frac{2E_{J0}}{k_B T}\right) = \omega_c \exp\left(-\frac{2E_{J0}}{k_B T}\right). \quad (3.4.20)$$

We see that the attempt frequency is given by the characteristic junction frequency ω_c and not by the plasma frequency. As already discussed above, this is caused by the strong damping ($\beta_C = \omega_c \tau_{RC} \ll 1$). In this case one has to replace the undamped plasma frequency by the characteristic frequency of an overdamped oscillator, namely $\omega_A = \omega_p \sqrt{\beta_C} = \omega_p \sqrt{\omega_c R_N C} = \omega_c$.

In terms of the tilt washboard potential model the phase particle in an overdamped Josephson junction diffuses over the barriers in a continuous process rather than making a single escape as in the underdamped limit. This difference occurs, since the strong damping brings the phase particle back into equilibrium in the next local minimum before it can diffuse to the next barrier. Therefore, it has no chance to run away as it was the case for the underdamped junction. The phase diffusion results in an activated nonlinear resistance.

Fig. 3.17 shows the temperature dependence of the normalized junction resistance, R_p/R_N , due to thermally activated phase slippage. The data are obtained for an overdamped $\text{YBa}_2\text{Cu}_3\text{O}_7$ grain boundary Josephson junction.³⁷ The thermally activated phase slippage manifests itself as a foot structure in the $R(T)$ dependence of the Josephson junction. After the junction electrodes become superconducting below the transition temperature T_c of the electrode material there is still a measurable resistance due to the thermally activated phase slippage of the junction. This resistance becomes vanishingly small only at a

³⁷R. Gross, P. Chaudhari, D. Dimos, A. Gupta, G. Koren, *Thermally Activated Phase Slippage in High- T_c Grain Boundary Josephson Junctions*, Phys. Rev. Lett. **64**, 228 (1990).

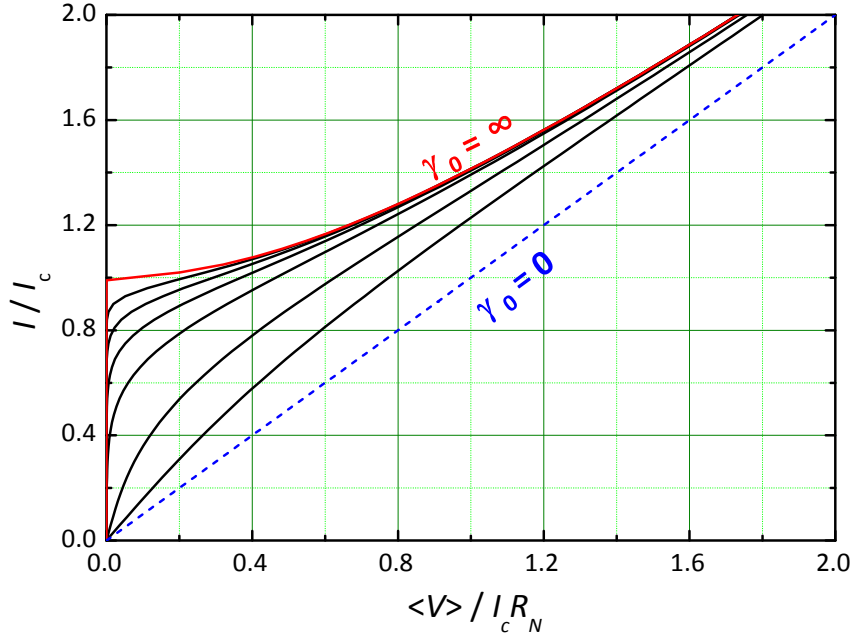


Figure 3.18: Current-voltage characteristics calculated according to (3.4.21) for a strongly overdamped Josephson junction ($\beta_C \ll 1$). The normalized barrier height was $\gamma_0 = 0, 1, 2, 5, 10, 20, 50$, and ∞ .

much lower temperature, at which the coupling energy $E_{J0}(T)$ has become sufficiently large to suppress the phase slippage. Also shown is a fit of the experimental data to equation (3.4.17). The fit can be used to determine the temperature dependence of the junction critical current $I_c(T)$ close to T_c as shown in Fig. 3.17 for a $\text{YBa}_2\text{Cu}_3\text{O}_7$ grain boundary Josephson junction. A direct measurement of $I_c(T)$ close to the critical temperature is difficult because of the finite slope of the IVCs due to thermally activated phase slippage (see Fig. 3.18). Hence, it is impossible to define I_c as the current flowing without measurable resistance.

Thermally activated phase slippage causes a rounding of the IVCs of Josephson junctions at $I \sim I_c$. This is evident, because already at current values $I < I_c$ the phase can move down the tilt washboard potential due to thermal activation resulting in a finite voltage. The IVCs in the presence of thermally activated phase slippage are shown in Fig. 3.18. Of course the rounding strongly decreases with increasing γ_0 , that is, with increasing barrier height. Note that the small linear resistance at low currents is the single junction analog of the so-called ***thermally activated flux-flow*** resistance in bulk superconductors, in which the activation energy is thought to be the energy to move a fluxon rather than the energy for a phase slip in a single junction.

According to Ambegaokar and Halperin, for strong damping ($\beta_C \ll 1$) the IVC can be calculated analytically giving

$$\langle V \rangle = \frac{2I_c R_N}{\gamma_0} \frac{e^{\pi\gamma_0 i} - 1}{e^{\pi\gamma_0 i}} \left\{ \int_0^{2\pi} d\varphi e^{-\gamma_0 i \varphi / 2} I_0 \left(\gamma_0 \sin \frac{\varphi}{2} \right) \right\}^{-1}, \quad (3.4.21)$$

where $i = \frac{I}{I_c}$.

We note that for small Josephson junctions ($L < \lambda_J$) the measurement of the resistance $R_p(T)$ also can be used to determine the magnetic field dependence of the critical current close to T_c . At constant

temperature the magnetic field dependence of $R_p(T)$ is obtained to^{38,39}

$$R_p(B) = R_N \left\{ I_0 \left[\frac{\gamma_0(B)}{2} \right] \right\}^{-2} \quad (3.4.22)$$

with

$$\gamma_0(B) = \frac{2E_{J0}(B)}{k_B T} = \frac{\Phi_0 I_c(B)}{\pi k_B T}. \quad (3.4.23)$$

³⁸Stephan Schuster, Diploma Thesis, University of Tübingen (1993).

³⁹B. Mayer, R. Gross, S. Schuster, A. Beck, L. Alff, Appl. Phys. Lett. **62**, 783 (1993).

3.5 Secondary Quantum Macroscopic Effects

3.5.1 Quantum Consequences of the Small Junction Capacitance

In our discussion so far we have treated the Josephson junction as a classical system. Both the gauge-invariant phase difference φ and its time derivative $\dot{\varphi}$, which is proportional to the charge $Q = CV = \frac{\hbar}{2e}C\dot{\varphi}$, have been treated as purely classical variables that in principle can be measured simultaneously with arbitrary precision. Within our classical description the dynamics of a Josephson junction was completely analogous to that of a classical particle of mass $M = (\hbar/2e)^2C$ moving in the tilt washboard potential or the motion of a pendulum (compare section 3.2).

In order to discuss the limits of this classical description let us consider a strongly underdamped junction. If the phase φ changes in time ($\dot{\varphi} \propto V \neq 0$), then the energy of the electric field is given by

$$K = \frac{1}{2}CV^2 = \frac{Q^2}{2C} = \frac{1}{2}C\left(\frac{\hbar}{2e}\right)^2\dot{\varphi}^2 = \frac{1}{2}E_{J0}\frac{\dot{\varphi}^2}{\omega_p^2} \quad (3.5.1)$$

with $Q \equiv CV = \int Idt$. We see that this energy is just the energy related to the extra charge Q on one junction electrode relative to the other due to the finite voltage V . With the energy contribution K of the electric field and the potential energy $U = E_{J0}(1 - \cos \varphi)$ (cf. eq. (2.1.8)) of the junction we can express the total energy of the junction as

$$E = K + U = E_{J0}\left(1 - \cos \varphi + \frac{1}{2}\frac{\dot{\varphi}^2}{\omega_p^2}\right) . \quad (3.5.2)$$

We see that it is very convenient to use φ as a principle variable (coordinate) of the system. In this case $U(\varphi)$ should be interpreted as the potential energy and $K \propto \dot{\varphi}^2$ as the kinetic energy. Note that for an overdamped junction equation (3.5.1) does not make sense, since such a junction is closely coupled to the environment through its normal current I_N and the energy is not conserved even over a short time scale.

Returning to the current-phase and voltage-phase relation describing the Josephson junction there is no doubt in their quantum nature. On the other hand, the structure of these equations contradicts basic quantum mechanical principles. We are assuming that all variables (observables) characterizing the state of the junction such as I , Q , V , φ , etc. can be measured simultaneously with arbitrary precision. Quantum mechanics, however, does not allow this and, in general, only the probability distribution of the variables can be calculated. From this we can conclude that the description of the Josephson junction by the current-phase and voltage-phase relation is at best an approximate description of a more precise quantum theory.

Following the recipes of quantum mechanics, we can just consider equation (3.5.2), $E = Q^2/2C + U(\varphi)$, as the Hamiltonian of the junction. We can rewrite the kinetic energy as

$$K = \frac{Q^2}{2C} = \frac{1}{2} \frac{1}{(\hbar/2e)^2C} \left(\frac{\hbar}{2e}Q\right)^2 . \quad (3.5.3)$$

This equation corresponds to the mechanical analogue $K = p^2/2M$. Hence, with the mass analogue $M = (\hbar/2e)^2C$ (cf. eq. (3.2.6)) the quantity $\frac{\hbar}{2e}Q$ corresponds to the momentum p . Therefore, we can make the operator replacement

$$\frac{\hbar}{2e}Q \rightarrow -i\hbar \frac{\partial}{\partial \varphi} , \quad (3.5.4)$$

that is, with the number $N = Q/2e$ of Cooper pairs we can write

$$Q = -i 2e \frac{\partial}{\partial \varphi} \quad N = -i \frac{\partial}{\partial \varphi} . \quad (3.5.5)$$

Then, the form of the Hamiltonian is

$$\begin{aligned} \mathcal{H} &= \frac{Q^2}{2C} + E_{J0}(1 - \cos \varphi) = -\frac{(2e)^2}{2C} \frac{\partial^2}{\partial \varphi^2} + E_{J0}(1 - \cos \varphi) \\ &= -4E_C \frac{\partial^2}{\partial \varphi^2} + E_{J0}(1 - \cos \varphi) . \end{aligned} \quad (3.5.6)$$

Here, $E_C = e^2/2C$ is the charging energy of the junction for a single electron charge.⁴⁰ Note that this Hamiltonian describes only the Cooper pairs neglecting the quasiparticle degrees of freedom, which however are unimportant as soon as we consider the case $T = 0$.

The commutation rule for the operators is obtained to

$$[\varphi, Q] = i 2e ; \quad [\varphi, N] = i \quad \text{or} \quad [\varphi, \frac{\hbar}{2e} Q] = i \hbar . \quad (3.5.7)$$

Here $N \equiv Q/2e$ is the deviation of the number of Cooper pairs in the junction electrodes from the equilibrium value. Equation (3.5.7) simply represents the uncertainty relation for the number of Cooper pairs and the phase difference:

$$\Delta N \cdot \Delta \varphi \geq 1 . \quad (3.5.8)$$

Note that this relation is completely analogous to the uncertainty relation between the number of photons and the phase of coherent light.

In many situations it is convenient to use the variable $\phi = \frac{\hbar}{2e}\varphi = \frac{\Phi_0}{2\pi}\varphi$ corresponding to a magnetic flux. In this case we have $\partial/\partial\varphi = \frac{\hbar}{2e}\partial/\partial\phi$ and obtain the Hamiltonian

$$\begin{aligned} \mathcal{H} &= \frac{Q^2}{2C} + E_{J0} \left(1 - \cos 2\pi \frac{\phi}{\Phi_0} \right) = -\frac{(2e)^2}{2C} \frac{\hbar^2}{(2e)^2} \frac{\partial^2}{\partial \phi^2} + E_{J0} \left(1 - \cos 2\pi \frac{\phi}{\Phi_0} \right) \\ &= -\frac{\hbar^2}{2C} \frac{\partial^2}{\partial \phi^2} + E_{J0} \left(1 - \cos 2\pi \frac{\phi}{\Phi_0} \right) \end{aligned} \quad (3.5.9)$$

and the commutator

$$[\phi, Q] = i \hbar . \quad (3.5.10)$$

That is, Q and ϕ are canonically conjugate variables just like coordinate x and momentum p .

⁴⁰Note that in some cases $E_C = (2e)^2/2C$, that is, the charging energy of a Cooper pair is used.

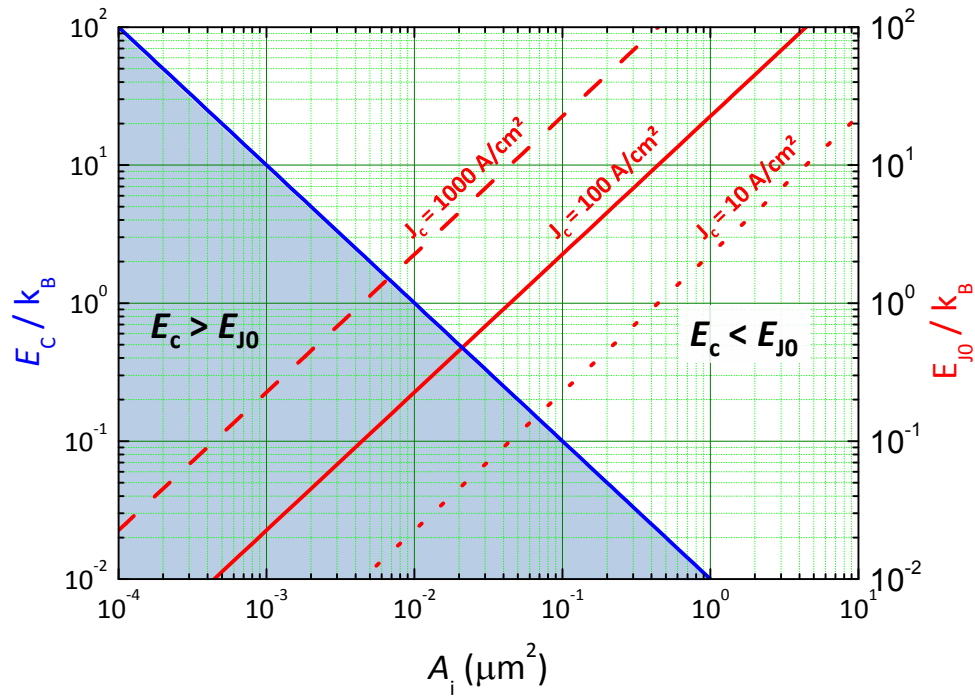


Figure 3.19: The Josephson coupling energy E_{J0} and the charging energy E_C plotted versus the junction area A_i for three different critical current densities J_c . Note that $E_{J0} \propto J_c \propto \exp(-2\kappa d)$ decreases exponentially with increasing thickness d of the tunneling barrier at constant junction area, whereas the charging energy $E_C \propto 1/C \propto d$ increases only linearly with increasing barrier thickness. We therefore have taken the charging energy the same for all three J_c values.

Equations (3.5.6) and (3.5.7) allow us to calculate the deviations of the junction properties from those predicted by the “classical” description. These deviations are called ***secondary macroscopic effects*** to be distinguished from the ordinary or primary effects like the Josephson effect itself.^{41,42}

The degree of deviation from the classical description can be estimated by considering again an isolated Josephson junction ($I = 0$) in the low damping limit. The potential energy is given by a cosine potential $E_{J0}(1 - \cos \varphi)$ with a depth determined by the characteristic energy E_{J0} . Approximating this potential close to a minimum by a parabolic potential, the Hamiltonian (3.5.6) reduces to that of a harmonic oscillator with frequency ω_p and level spacing $\hbar\omega_p$. It is obvious that the classical description holds as long as the level spacing is much smaller than the depth of the potential well, i.e. E_{J0} . That is, the degree of deviation from the classical description depends on the ratio of the two energies

$$\frac{\hbar\omega_p}{E_{J0}} = \sqrt{\frac{8E_C}{E_{J0}}} . \quad (3.5.11)$$

In order to get a feeling, in which cases the condition $\hbar\omega_p \ll E_{J0}$ or $E_C \ll E_{J0}$ holds for real Josephson junctions, we have to recall that $E_C \propto 1/C \propto 1/A$, whereas $E_{J0} \propto I_c \propto A$. We hence immediately see that we will enter the quantum regime ($E_C \gg E_{J0}$) on decreasing the junction area. In order to make an estimate we consider a planar tunnel junction of typical area $A_i = 10 \mu\text{m}^2$ with a tunneling barrier of thickness $d = 1 \text{ nm}$ and dielectric constant $\epsilon = 10$. The critical current density is $J_c \simeq 100 \text{ A/cm}^2$ giving a coupling energy $E_{J0} \simeq 3 \times 10^{-21} \text{ J}$. With $\epsilon_0 = 8.8 \times 10^{-12} \text{ F/m}$ we obtain the junction capacitance $C = \epsilon\epsilon_0 A_i/d \simeq 9 \times 10^{-13} \text{ F}$ and, hence, $E_C \simeq 1.6 \times 10^{-26} \text{ J}$. We see, that for this typical junction area and

⁴¹A.I. Larkin, K.K. Likharev, Yu.N. Ovchinnikov, Physica B **126**, 414 (1985).

⁴²A. Leggett, Suppl. Theor. Phys. **69**, 80 (1982).

current density the charging energy E_C is by about 5 orders of magnitude smaller than the Josephson coupling energy E_{J0} and also much smaller than $k_B T$ down to temperatures in the mK-regime. This is justifying our classical treatment of Josephson junctions in the previous sections. However, we see that the classical treatment is no longer possible for very small junctions or junctions with very small critical current density J_c . This is shown in Fig 3.19, where we have plotted the Josephson coupling energy and the charging energy as a function of the junction area for different values of the critical Josephson current density. For the typical current density $J_c = 100 \text{ A/cm}^2$ the charging energy becomes comparable to the coupling energy at a junction area of about $0.02 \mu\text{m}^2$ corresponding to a capacitance of about 1 fF . We also see that in order to observe the quantum phenomena we have to go to temperatures below about 100 mK in order to have $k_B T \ll E_C$.

3.5.2 Limiting Cases: The Phase and Charge Regime

In the following we discuss the two limiting cases $\hbar\omega_p \ll E_{J0}$ and $\hbar\omega_p \gg E_{J0}$ corresponding to $E_C \ll E_{J0}$ and $E_C \gg E_{J0}$, respectively. We will see that for the former the phase is a well defined quantity, whereas for the latter it is the charge. Hence, we denote the two limiting cases as the *phase regime* and the *charge regime*.

The Phase Regime: $\hbar\omega_p \ll E_{J0}, E_C \ll E_{J0}$

In this limit, the lowest energy levels of the system are localized near the bottom of the potential wells, that is, near the points $\varphi_n = 2\pi n$. For this case we can expand the $\cos \varphi$ in the potential energy U into a Taylor series with respect to small deviations $\delta\varphi = \varphi - \varphi_n$ and neglect all terms except $(\delta\varphi)^2/2 + \text{const}$. Then, as already discussed above the Hamiltonian is reduced to that of a harmonic oscillator with frequency ω_p and the energy eigenvalues

$$E_n = \hbar\omega_p \left(1 + \frac{1}{2} \right) . \quad (3.5.12)$$

Our discussion shows that for $\hbar\omega_p/E_{J0} \ll 1$ or, equivalently, $E_C/E_{J0} \ll 1$ the ground state of the system should be a narrowly peaked wave function centered at $\varphi = \varphi_n$ in order to minimize the dominating term $E_{J0} \cos \varphi$. That is, the fluctuations in the phase are very small and according to $\Delta Q \cdot \Delta\varphi \geq 2e$ those of the charge Q on the electrodes large. The physical reason for this is simple. The large fluctuations of the charge are possible due to the very small energy E_C required to add an extra Cooper pair to a junction electrode. That is, charge pairs can easily fluctuate back and forth resulting in a large uncertainty in the extra charge Q on the junction electrodes and, hence, due to $\Delta Q \cdot \Delta\varphi \geq 2e$ in a negligible uncertainty of φ . Then, the dynamics of the phase can be treated classically. Since the phase is well defined we denote the limit $\hbar\omega_p \ll E_{J0}$ as the phase regime.

In order to find the energy levels of the system we can use the Hamiltonian (3.5.6)

$$\mathcal{H} = -4E_C \frac{\partial^2}{\partial\varphi^2} + E_{J0}(1 - \cos \varphi) . \quad (3.5.13)$$

With the parameters $a = (E - E_{J0})/E_C$, $b = E_{J0}/2E_C$ and $z = \varphi/2$ we can rewrite this Hamiltonian to obtain the usual Mathieu equation

$$\frac{\partial^2\Psi}{\partial z^2} + (a + 2b \cos 2z) \Psi = 0 . \quad (3.5.14)$$

This differential equation is well known from the periodic potential problem in solid-state physics, leading to energy bands in crystals. The general solution is the superposition

$$\Psi(\varphi) = \sum_q c_q \psi_q \quad (3.5.15)$$

of the Bloch waves

$$\psi_q(\varphi) = u_q(\varphi) \exp(iq\varphi) \quad \text{with} \quad u_q(\varphi) = u_q(\varphi + 2\pi) . \quad (3.5.16)$$

Here, q is a “charge” or “pair number” variable and $u_q(\varphi)$ is a periodic function with period 2π . If only integer numbers of pairs are physically relevant, q is taking only integer values and Ψ would be 2π -periodic. However, q is a continuous variable, since it does not represent the total charge on an isolated piece of metal, but rather on the capacitor formed by the two junction electrodes. This charge can be varied continuously for example by a third gate electrode, which can change the charge in the junction region, although the tunnel current is restricted to the transfer of a discrete number of charges (e or $2e$ depending on whether one considers unpaired or paired electrons).

Since the problem under consideration is one-dimensional, it can be solved easily by numerical means. To get more insight into the physics we apply a variational approach to find an approximation for the ground state by using a trial function. For $E_C/E_{J0} \ll 1$, we use a Gaussian trial function

$$\Psi(\varphi) \propto \exp\left(-\frac{\varphi^2}{4\sigma^2}\right) , \quad (3.5.17)$$

where the rms spread σ in φ is chosen to minimize the expectation value of (3.5.6). For $E_C/E_{J0} \ll 1$, the minimum energy is

$$E_{\min} = E_{J0} \left(1 - \left[1 - \sqrt{\frac{2E_C}{E_{J0}}} \right]^2 \right) = E_{J0} \left(1 - \left[1 - \frac{\hbar\omega_p}{2E_{J0}} \right]^2 \right) . \quad (3.5.18)$$

That is, $E_{\min} \simeq 0$ for $\frac{\hbar\omega_p}{E_{J0}} \ll 1$. Fig. 3.20 shows the energy diagram of the Josephson junction for two different values of E_C/E_{J0} . In Fig. 3.20a we have sketched the situation for the phase regime for $E_C/E_{J0} = 0.1$ resulting in $E_{\min} \simeq 0.1E_{J0}$. We note that we have a periodic potential $E_{J0}(1 - \cos \varphi)$ and therefore always a finite tunneling coupling between the phase states in adjacent minima. However, the tunneling probability is proportional to $\exp[-(2E_{J0} - E)/\hbar\omega_p]$ (compare section 3.5.6) and therefore is very small in the phase regime ($\hbar\omega_p \ll E_{J0}$) and the lowest energy states ($(2E_{J0} - E) \sim 2E_{J0}$). Therefore, the tunneling splitting of the low lying phase states is exponentially small and becomes significant only for higher states with $(2E_{J0} - E) \ll 2E_{J0}$ as indicated by the broadening of the states in Fig. 3.20a.

The Charge Regime: $\hbar\omega_p \gg E_{J0}, E_C \gg E_{J0}$

In contrast, for the phase limit $E_C/E_{J0} \ll 1$ discussed above, now the term $E_C(\partial^2/\partial\varphi^2)$ is dominant. To minimize it in the ground state the wave function $\Psi(\varphi)$ should approach a constant. However, in this case all values of the phase are equally probable. That is, phase fluctuations are very large and in turn charge fluctuations small. The former are enabled by the small energy scale E_{J0} required for phase fluctuations by 2π and the latter are prevented by the large energy scale $4E_C$ for charge fluctuations by $2e$.

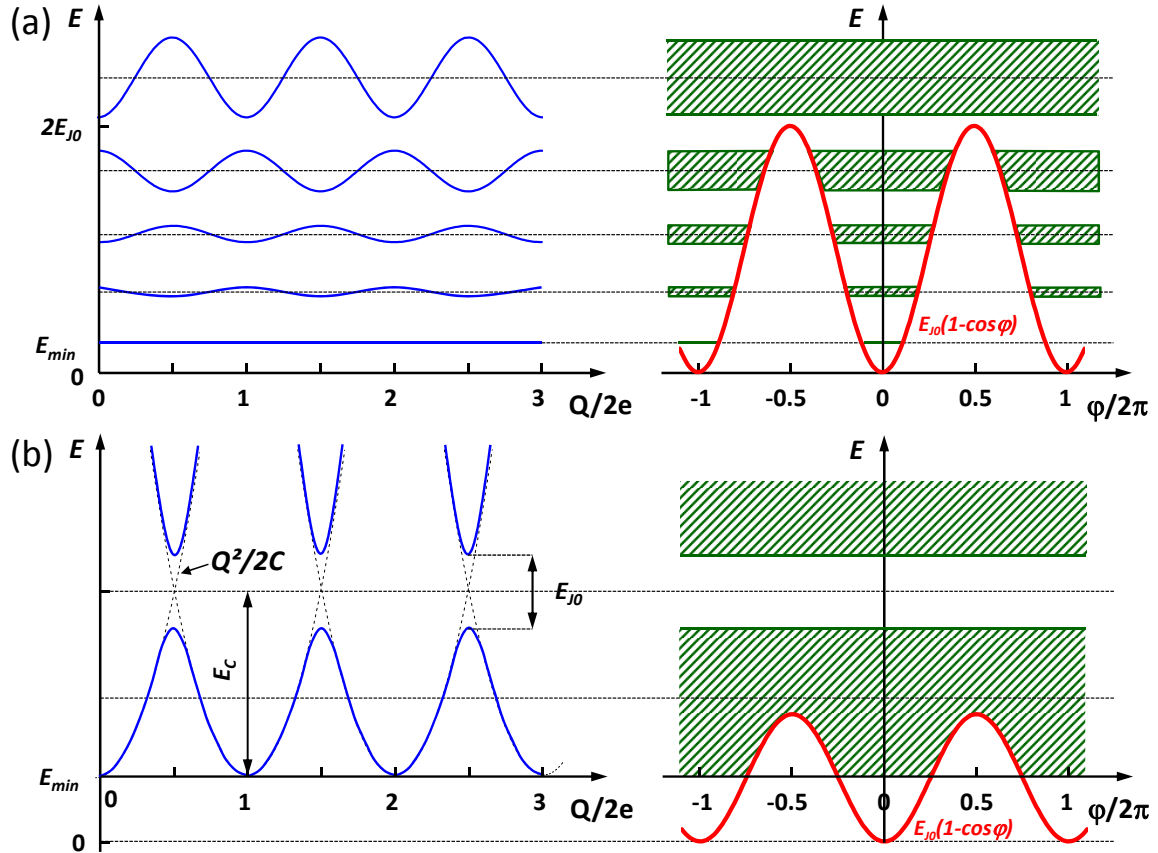


Figure 3.20: Sketch of the energy diagrams of an isolated Josephson junction ($I = 0$) in the case of low damping for (a) $E_C/E_{J0} = 0.1$ and (b) $E_C/E_{J0} = 2.5$.

In the charge limit, an appropriate trial function, which is periodic and satisfies the boundary conditions of zero slope at the edges of the cell, is

$$\Psi(\varphi) \propto (1 - \alpha \cos \varphi) , \quad (3.5.19)$$

which yields the approximate ground-state energy

$$E_{\min} \simeq E_{J0} \left(1 - \frac{E_{J0}}{8E_C} \right) . \quad (3.5.20)$$

We see that in the charge limit $\hbar\omega_p \gg E_{J0}$ or, equivalently, $E_C \gg E_{J0}$ the binding energy is of second order in E_{J0} , whereas it is of first order in the semi-classical limit of equation (3.5.18). In Fig. 3.20b we have sketched the situation for the charge regime for $E_C/E_{J0} = 2.5$ resulting in $E_{\min} \simeq 0.95E_{J0}$.

In the charge regime the periodic potential $E_{J0}(1 - \cos \varphi)$ is weak resulting in a strong coupling between neighboring phase states and, in turn, in broad bands. This is evident by considering equation (3.5.14): In the phase limit the factor $b = E_{J0}/2E_C$ is large, whereas it is small for the charge limit. This means that we have a strong periodic potential in the phase limit and only a weak one in the charge regime. We easily can compare this to the situation known for electrons moving in the periodic potential of a crystal. A strong periodic potential results in a localization of the charge carriers (well defined position, undefined momentum). This is equivalent to the phase regime, where we have a strong periodic potential resulting in exponentially narrow bands located at the points $E_n \simeq (n + \frac{1}{2})\hbar\omega_p$. In this case we have a

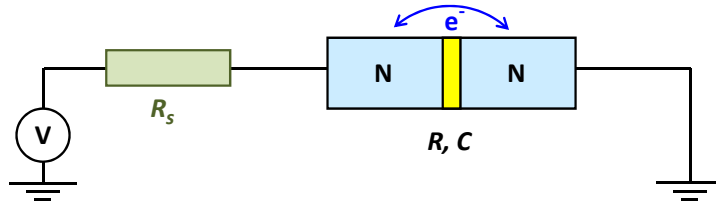


Figure 3.21: Coulomb blockade for a small normal metal tunnel junction with capacitance C und tunneling resistance R . The series resistor R_s must be sufficiently large to avoid the suppression of the Coulomb blockade effect by quantum fluctuations.

well defined phase but an undefined charge state. In contrast, a weak periodic potential results in broad energy bands and delocalized charge carriers with well defined momentum and undefined position. This situation is equivalent to the charge regime, where we have a weak periodic potential resulting in broad bands. In this case we have a well defined charge state but an undefined phase state.

3.5.3 Coulomb and Flux Blockade

Coulomb Blockade in Normal Metal Tunnel Junctions

In the charge regime the large energy E_C results in the phenomenon called **Coulomb blockade**. To discuss this phenomenon we consider a normal conducting tunnel junction with junction capacitance C (see Fig. 3.21). Suppose the voltage across the junction is V and the related charge and energy $Q = CV$ and $E = Q^2/2C$, respectively. Naively we could assume that there will be a finite tunneling current as soon as there is a finite voltage across the junction. However, if a single electron tunnels from one electrode to the other, the charge on the one electrode changes to $Q - e$. The electrostatic energy after the tunneling process is then $\tilde{E} = (Q - e)^2/2C$. Since the tunneling process is energetically allowed only if $\tilde{E} \leq E$, the tunneling current sets in only for $|Q| \geq e/2$ or, equivalently,

$$|V| \geq V_{CB} = \frac{e}{2C} . \quad (3.5.21)$$

We see that the tunneling process is only allowed above a certain threshold voltage. This effect is called Coulomb blockade.^{43,44} Of course the Coulomb blockade can be experimentally observed only if $E_C > k_B T$, i.e., if thermal fluctuations are small enough. This results in the condition $C < e^2/2k_B T$ for the capacitance ($C \lesssim 1 \text{ fF}$ at 1 K). For a tunnel junction with barrier thickness $d = 1 \text{ nm}$ and dielectric constant $\epsilon = 5$, the junction area has to be smaller than about $0.02 \mu\text{m}^2$ to observe the effect at a temperature of about 1 K .

We further have to consider quantum fluctuations. The effect of quantum fluctuations can be estimated using the uncertainty relation $\Delta E \cdot \Delta t \geq \hbar$. Since the tunnel junction has a finite tunneling resistance, charge fluctuations will decay with the characteristic time constant $\tau_{RC} = RC$. If we use $\Delta t = 2\pi RC$ and $\Delta E = e^2/2C$ we obtain $e^2 R \gtrsim \hbar$ or $R \geq \hbar/e^2 = R_K$. We see that the tunneling resistance must be larger than the quantum resistance $R_K = 24.6 \text{ k}\Omega$. For a junction area $A = 0.02 \mu\text{m}^2$ this results in a resistance times area product of above about $1 \mu\Omega\text{cm}^2$. This can be easily satisfied.

⁴³D.V. Averin, K.K. Likharev, J. Low Temp. Phys. **62**, 345 (1986).

⁴⁴T.A. Fulton, G.J. Dolan, Phys. Rev. Lett. **59**, 109 (1987).

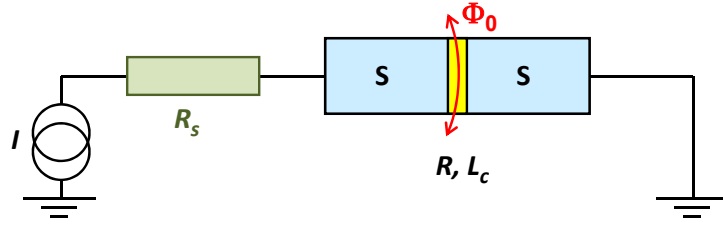


Figure 3.22: Phase blockade for a Josephson junction with Josephson inductance L_c und tunneling resistance R . The series resistor R_s must be sufficiently small to avoid the suppression of the phase blockade effect by quantum fluctuations.

Coulomb Blockade in Superconducting Tunnel Junctions

In the last paragraph we only have considered a normal conducting tunnel junction. We now switch to a superconducting tunnel junction. For simplicity we neglect the role of the unpaired quasiparticles and their interaction with the condensate in the following.⁴⁵ In our classical treatment of Josephson junctions we have seen that there is a finite supercurrent flowing between the electrodes at zero voltage. The magnitude of the supercurrent was determined by the phase difference of the macroscopic wave functions describing the two electrodes. Charging effects have been completely neglected in this treatment. However, we immediately see that for $Q^2/2C > k_B T, eV$ the flow of the Cooper pairs with charge $Q = 2e$ is prevented by the Coulomb blockade and charging effects play a dominant role.^{46,47} In analogy to the normal metal case we obtain the threshold voltage

$$|V| \geq V_{CB} = \frac{2e}{2C} = \frac{e}{C}. \quad (3.5.22)$$

The blockade of the pair transport means that the charge on both electrodes is fixed. Due to the uncertainty relation $\Delta Q \cdot \Delta \varphi \geq 2e$ this means that the phase is completely smeared out. As already discussed above, a well defined charge state results in an undefined phase and a loss of the Josephson effect. On the other hand, a well defined phase state results in an undefined charge state and the loss of the Coulomb blockade effect.

Phase or Flux Blockade in a Josephson Junction

In analogy to the Coulomb blockade in the charge regime we have a phase or flux blockade in the phase regime (see Fig. 3.22). Due to the large Josephson coupling energy $E_{J0} = \Phi_0 I_c / 2\pi$ the phase φ cannot be changed by applying a current across the junction, since it is trapped in one of the minima of the tilt washboard potential. Only if we exceed the critical current I_c , phase changes are possible. That is, in analogy to the Coulomb blockade in the charge regime we can speak about a **phase blockade** in the phase regime with the critical current I_c playing the role of the blockade voltage V_{CB} . Since a phase change of 2π is equivalent to moving a single flux quantum across a Josephson junction, we alternatively can denote the phenomenon as **flux blockade**. Note that the flux quanta are crossing the junction perpendicular to the current direction, whereas the charge carriers are tunneling in current direction.

⁴⁵For a discussion of this point see M. Tinkham, *Introduction to Superconductivity*, McGraw-Hill Book Company, New York (1996).

⁴⁶M.T. Touminen, J.M. Hergenrother, T.S. Tighe, M. Tinkham, Phys. Rev. Lett. **69**, 1997 (1992); Phys. Rev. **B 47**, 11599 (1993).

⁴⁷P. Joyez, P. Lafarge, A. Filipe, D. Esteve, M.H. Devoret, Phys. Rev. Lett. **72**, 2458 (1994).

With the Josephson inductance $L_c = \hbar/2eI_c$ we can write the Josephson coupling energy $E_{J0} = \hbar I_c/2e = \Phi_0^2/4\pi^2 L_c$ and we obtain the current value for the flux blockade to

$$I_{FB} \geq I_c = \frac{\Phi_0/2\pi}{L_c} = \frac{\overline{\Phi}_0}{L_c}. \quad (3.5.23)$$

Here, we have used $\overline{\Phi}_0 = \Phi_0/2\pi$. We immediately see the analogy to equation (3.5.22) by making the replacements $I \leftrightarrow V$, $e \leftrightarrow \overline{\Phi}_0$ and $C \leftrightarrow L$.

Of course the phase blockade effect can be observed only if $E_{J0} \gg k_B T$, what can be easily satisfied by using a sufficiently large junction area. The effect of quantum fluctuations can be estimated again using the uncertainty relation $\Delta E \cdot \Delta t \geq \hbar$. Since the tunnel junction has a finite tunneling resistance, phase or equivalently voltage fluctuations will decay with the characteristic time constant $\tau_{LR} = L_c/R$. If we use $\Delta t = 2\pi L_c/R$ and $\Delta E = 2E_{J0} = \hbar I_c/e$ we obtain $R \lesssim h/e^2 = R_K$. We see that in the phase regime the tunneling resistance must be smaller than the quantum resistance $R_K = 24.6 \text{ k}\Omega$.

3.5.4 Coherent Charge and Phase States

Coherent Charge States

In order to discuss the effect of finite Josephson coupling on the charge states in the charge regime, we consider the Cooper pair box sketched in the inset of Fig. 3.23. A Cooper pair box is a small superconducting island, which is coupled to a reservoir via a superconducting tunnel junction. The charge state of the island can be changed continuously by a gate electrode. Suppose the island is in the charge state $|0\rangle$ at $V_g = 0$. If we change the charge by $n \cdot 2e$, we switch the island into the charge state $|n\rangle$. If the different charge states would be completely independent, the energy of each state would correspond to a parabola $(Q - n \cdot 2e)^2/2C_\Sigma$ with $C_\Sigma = C + C_g$ (see Fig. 3.23). These parabolas are shown in Fig. 3.20b as dashed lines. However, the charge states are only independent of each other for $E_{J0} = 0$. For a small but finite Josephson coupling there will be an interaction of the charge state $|n\rangle$ and $|n+1\rangle$ at the crossing points of the corresponding parabolas at $Q = (n + \frac{1}{2}) \cdot 2e$. The resulting coherent superposition states are represented by the wave functions

$$\Psi_\pm = a|n\rangle \pm b|n+1\rangle, \quad (3.5.24)$$

where a and b are complex numbers. As a consequence, we obtain a splitting of the charge energy at the crossing points, which is called ***level anti-crossing***. The magnitude of the splitting is given by the Josephson coupling energy. A detailed discussion of the level anti-crossing for interacting quantum two-level systems is given in Appendix F.

Fig. 3.23 shows the expected average charge $\langle Q \rangle = 2e\langle N \rangle$ on the superconducting island as a function of the applied gate voltage V_g . Without interaction of neighboring charge states $|n\rangle$ and $|n+1\rangle$ a step-like behavior is expected with a step height of $2e$. However, in reality at the transition regions between the different charge states (crossing points of the parabolas shown in Fig. 3.20b) the steps are rounded due to the finite interaction resulting in a superposition of the adjacent charge states. In experiments the charge state of the superconducting island usually is measured using a single electron electrometer. The expected dependence shown in Fig. 3.23 has been confirmed in experiments.⁴⁸

The presence of a coherent quantum mechanical superposition of charge states has been measured recently by **Nakamura, Pashkin and Tsai**.⁴⁹ In their experiment they switched a Cooper pair box for a

⁴⁸V. Bouchiat, D. Vion, P. Joyez, D. Esteve, M.H. Devoret, Physica Scripta **T 76**, 165 (1998).

⁴⁹Y. Nakamura, Yu.A. Pashkin, J.S. Tsai, Nature **398**, 786 (1999); Physica **B 280**, 405 (2000); Phys. Rev. Lett. **87**, 246601 (2001); Physica **C 367**, 191 (2002).

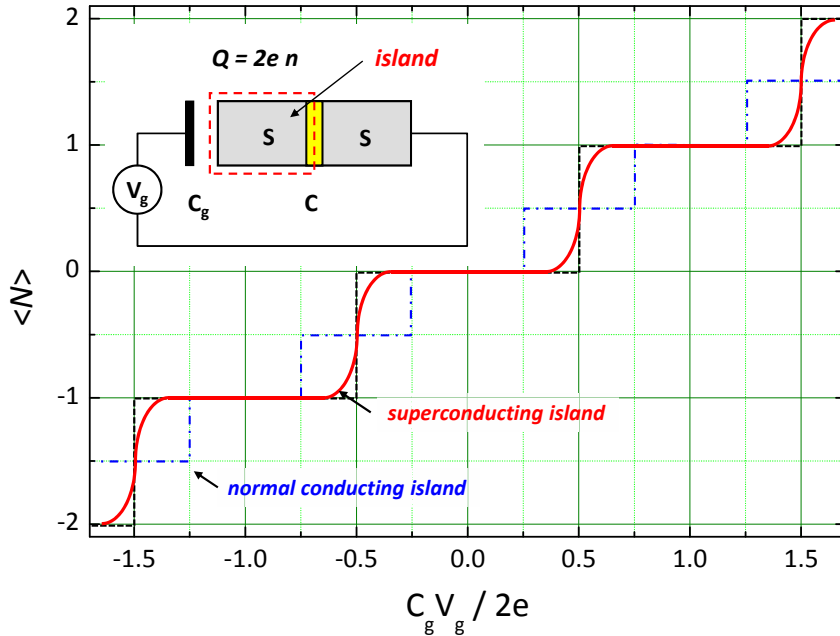


Figure 3.23: Average charge number $\langle N \rangle = \langle Q \rangle / 2e$ on a Cooper pair box as a function of the applied gate voltage. The Cooper pair box consists of a superconducting island coupled via a tunnel junction of capacitance C to a reservoir (see inset). The charge state of the island can be varied via a gate capacitor of capacitance C_g . For a superconducting island without any interaction of the different charge states a step-like dependence (dashed curve) is obtained. Due to the finite interaction between neighboring states $|n\rangle$ and $|n+1\rangle$ the steps are rounded (solid line). For comparison, also the dependence expected for a normal conducting island without interaction is shown (dash-dotted line).

short period Δt from $n = 0$ to $n = \frac{1}{2}$ by a pulsed gate. According to quantum mechanics, at $n = \frac{1}{2}$ the system is in a superposition state and coherently oscillates between the states $|0\rangle$ and $|1\rangle$ at a frequency $f = E_{J0}/\hbar$. The probability of finding the system in the charge state $|0\rangle$ after switching off the gate pulse at the time Δt , ranges between 0 and 1. It depends on the length Δt of the gate pulse. Varying the length of the gate pulse, a continuous oscillation of the probability between 0 and 1 is found. These oscillations are called **Rabi oscillations** (see Appendix F). A more detailed discussion of the quantum dynamics of coherent charge as well as phase states is given in Chapter 9.

Coherent Phase States

In the same way as we can generate coherent superposition states by the interaction of two adjacent charge states, we can obtain coherent phase states by the interaction of two adjacent phase states. This can be achieved for example by incorporating a single Josephson junction into a superconducting loop of inductance L (rf-SQUID, see section 4.2). To the potential energy of the Josephson junction we then have to add a term $(\Phi - \Phi_{\text{ext}})^2 / 2L = \frac{1}{2}LI_{\text{cir}}^2$ due to the magnetic energy of the flux in the ring generated by a circulating screening current I_{cir} (compare section 4). The total potential is then given by (compare (3.5.9))

$$U(\phi) = \frac{(\phi - \phi_{\text{ext}})^2}{2L} + E_{J0} \left(1 - \cos 2\pi \frac{\phi}{\Phi_0} \right). \quad (3.5.25)$$

Here, $\phi = \frac{\hbar}{2e}\phi = \frac{\Phi_0}{2\pi}\phi$ and the flux Φ in the loop is related to the phase difference across the junction by $\varphi = 2\pi \frac{\phi}{\Phi_0}$, i.e. $\Phi = \phi$. The potential (3.5.25) is shown in Fig. 3.24 for $\Phi_{\text{ext}} = \Phi_0/2$. We obtain

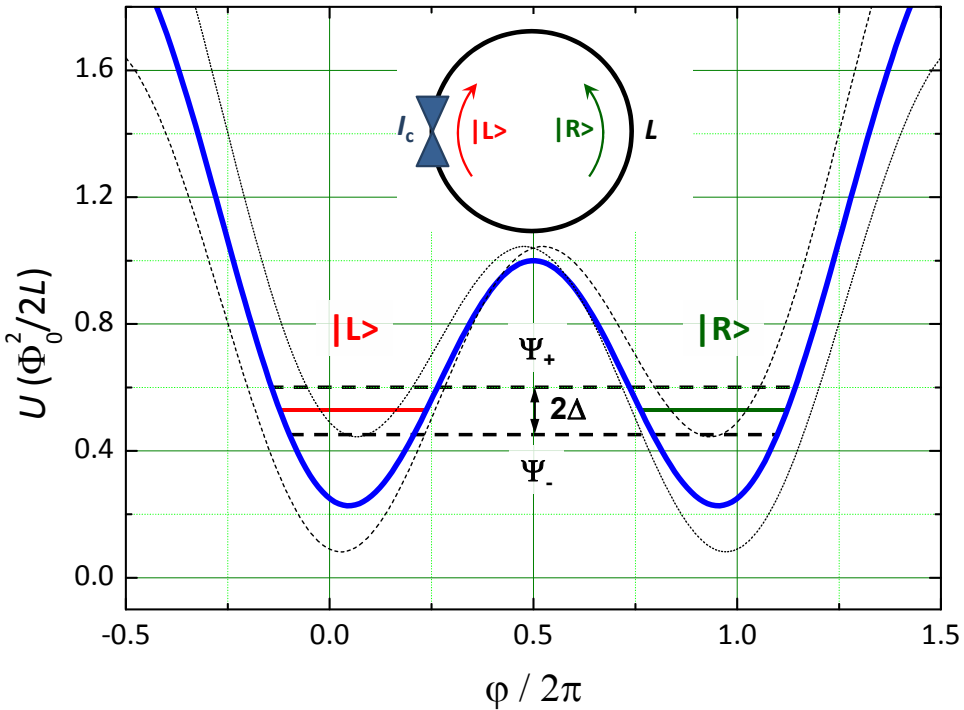


Figure 3.24: Double well potential for the generation of phase superposition states calculated according to (3.5.25) for $\Phi_{\text{ext}} = \Phi_0/2$ and $\beta_L = 2LI_C/\Phi_0 = 3$. Shown are the states $|L\rangle$ and $|R\rangle$ corresponding to clockwise and anticlockwise circulating currents (solid lines) and the superposition states Ψ_+ and Ψ_- (dashed line) split by 2Δ . The thin dashed and dotted lines show the potential for $\Phi_{\text{ext}} = 0.3\Phi_0$ and $0.7\Phi_0$, respectively.

a double well potential with two degenerate phase states $|L\rangle$ and $|R\rangle$ corresponding to a clockwise and anticlockwise circulating current, respectively. The two phase states are tunnel coupled resulting in the superposition states

$$\Psi_{\pm} = a|L\rangle \pm b|R\rangle \quad (3.5.26)$$

with energies $E_{\pm} = \varepsilon_0 \pm \Delta$ with ε_0 the energy of the degenerate phase states and Δ the tunnel splitting. If we move away with the external flux from the value $\Phi_0/2$, the double well potential is tilted to the left or the right lowering the $|L\rangle$ and $|R\rangle$ state, respectively.

Experimental evidence (e.g. Rabi oscillations) for the quantum coherent superposition states corresponding to macroscopic quantum states has been found recently.^{50,51,52} Meanwhile several experimental geometries appropriate for the realization of a double well potential similar to that shown in Fig. 3.24 have been studied.^{53,54} A detailed discussion of the quantum dynamics of the superposition state will follow in Chapter 9.

3.5.5 Quantum Fluctuations

Quantum mechanics shows that the classical theory of the harmonic oscillator coincides with the quantum one in all details but one: There is a finite motion of the quantum oscillator (quantum fluctuation) at the

⁵⁰J.E. Mooij, T.P. Orlando, L. Levitov, L. Tian, C.H. van der Wal, S. Lloyd, Science **285**, 1036 (1999).

⁵¹C.H. van der Wal, A.C.J. ter Haar, F.K. Wilhelm, R.N. Schouten, C.P.J.M. Harmans, T.P. Orlando, S. Lloyd, J.E. Mooij, Science **290**, 773 (2000).

⁵²J.R. Friedman, V. Patel, W. Chen, S.K. Tolpygo, J.E. Lukens, Nature **406**, 43 (2000).

⁵³I. Chiorescu, Y. Nakamura, C.J.P.M. Harmans, J.E. Mooij, Science **299**, 1869 (2003).

⁵⁴Y. Yu, S. Han, X. Chu, S.-I. Chu, Z. Wang, Science **296**, 889 (2002).

lowest energy level $n = 0$. In general, a quantum fluctuation is the temporary change in the amount of energy in a point in space, arising from Heisenberg's uncertainty principle $\Delta E \cdot \Delta t \geq \hbar$. That means that conservation of energy can appear to be violated, but only for small times. This allows the creation of virtual excitations.⁵⁵

The quantum fluctuations can be described in a convenient way by including a Langevin force I_F to the classical basic junction equation, which has the adequate statistical properties.^{56,57,58} If we assume that the junction environment is in thermal equilibrium, we can use the Callen-Welton fluctuation-dissipation theorem and write the spectral density of I_F as

$$S_I(f) = 2\pi S_I(\omega) = 4 \frac{E(\omega, T)}{R_N} . \quad (3.5.27)$$

Here, $E(\omega, T)$ is the average energy of the quantum oscillator with frequency ω at temperature T :

$$\begin{aligned} E(\omega, T) &= \frac{\hbar\omega}{2} + \hbar\omega \frac{1}{\exp\left(\frac{\hbar\omega}{k_B T}\right) - 1} \\ &= \frac{\hbar\omega}{2} \coth\left(\frac{\hbar\omega}{2k_B T}\right) . \end{aligned} \quad (3.5.28)$$

This expression describes the smooth transition from the **Johnson-Nyquist formula** (classical limit, compare (3.1.15)) at low frequencies ($\hbar\omega, eV \ll k_B T$) to a purely quantum noise at high frequencies ($\hbar\omega \gg k_B T, eV$).

In the classical limit ($\hbar\omega, eV \ll k_B T$) the argument of the coth-function is small and we can use the approximation $\coth x \simeq 1/x$ resulting in the classical Johnson-Nyquist formula

$$S_I(\omega) = \frac{1}{2\pi} \frac{4k_B T}{R_N} \quad (3.5.29)$$

In the quantum limit ($\hbar\omega \gg k_B T, eV$) the argument of the coth-function is large and we can use the approximation $\coth x \simeq 1$ resulting in

$$S_I(\omega) = \frac{1}{2\pi} \frac{2\hbar\omega}{R_N} . \quad (3.5.30)$$

3.5.6 Macroscopic Quantum Tunneling

One of the most convincing demonstrations of the quantum aspects of the Josephson effect is probably the observation of **macroscopic quantum tunneling** in an underdamped Josephson junction. The process of macroscopic quantum tunneling refers to the escape process of the “phase particle” from a minimum of the tilted washboard potential by tunneling through the barrier (see Fig. 3.25) rather than by thermal activation over the barrier as discussed in section 3.4. The process is called **macroscopic** because the tunneling quantity is not a single electron but the phase variable, which describes the collective state of a large, macroscopic number of electrons.

⁵⁵In the modern view, energy is always conserved, but the eigenstates of the Hamiltonian (energy observable) are not the same as (do not commute with) those of the particle number operators.

⁵⁶H.B. Callen, T.E. Welton, Phys. Rev. **83**, 34 (1951).

⁵⁷I.R. Senitzky, Phys. Rev. **124**, 642 (1961).

⁵⁸M. Lax, Phys. Rev. **145**, 110 (1966).

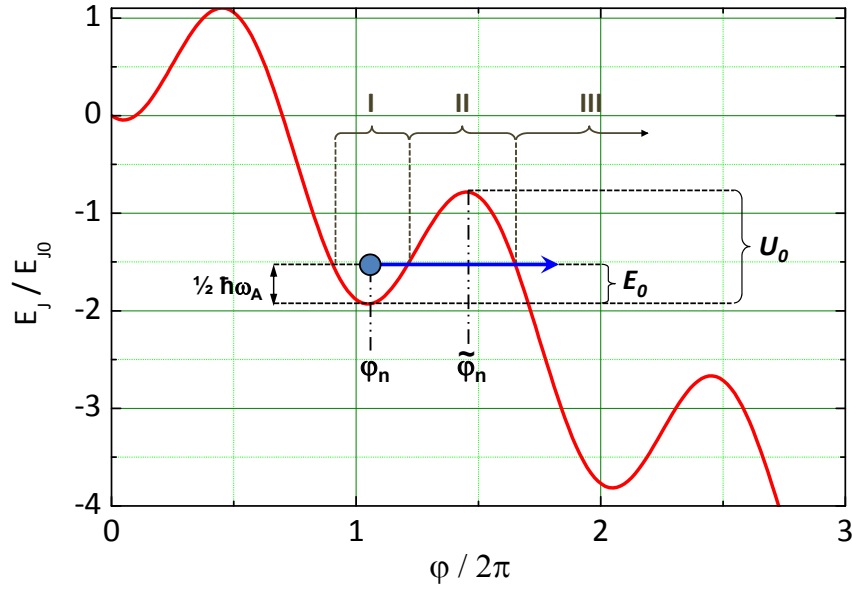


Figure 3.25: Macroscopic quantum tunneling of the gauge-invariant phase difference. U_0 is the barrier height and E_0 the energy of the “phase particle” with respect to the local minimum.

Quantum effects usually are difficult to be observed on a macroscopic scale, since they involve microscopic objects. Since in macroscopic quantum tunneling the system switches from the zero voltage state with the phase variable trapped in a minimum of the tilted washboard potential to the voltage state, where the phase variable is running down the potential, the study of macroscopic quantum tunneling is a particularly sensitive technique to reveal quantum effects. The two states are easily distinguishable. The only competing classical process is thermal activation over the barrier. However, this process can be frozen out by going to low enough temperatures. Another process preventing the observation of quantum effects is the presence of damping. It is reflected in the quantum Hamiltonian by coupling the phase degree of freedom to an environmental Hamiltonian with many degrees of freedom. In our discussion for simplicity we first neglect this coupling to the environment.

In the presence of a dc bias current, the Hamiltonian (3.5.6) is modified by the additional term $-\hbar I \varphi / 2e$. As already discussed before, the minimum of the resulting potential occurs at $\varphi = \arcsin i$ with $i = I/I_c$ (compare (2.1.9)). The curvature of the potential at the minimum is⁵⁹

$$\frac{\partial^2 U}{\partial \varphi^2} = E_{J0} \sqrt{1 - i^2} \quad (3.5.31)$$

and the classical frequency of small oscillations about the minimum is (compare (3.4.13))

$$\omega_A = \omega_p (1 - i^2)^{1/4}. \quad (3.5.32)$$

When solved quantum mechanically, the ground state wave function of a harmonic oscillator in such a potential minimum is approximately Gaussian, i.e. $\Psi \propto \exp(-c \cdot (\delta\varphi)^2)$, where $\delta\varphi$ is the deviation of the phase from the minimum value.⁶⁰ However, there is one important difference between the harmonic oscillator solution and that for the tilted washboard potential: In contrast to the harmonic oscillator

⁵⁹We use the relation $\arcsin x = \arccos \sqrt{1 - x^2}$.

⁶⁰The wave function of the ground state of a harmonic oscillator is

$$\Psi_0 = C_0 \left(\frac{\mu \omega_0}{\pi \hbar} \right)^{1/4} \exp \left\{ -\frac{\mu \omega_0}{2\hbar} (\delta\varphi)^2 \right\} e^{-i\omega_0 t/2}.$$

potential, for the tilted washboard potential the barrier is of finite width. Therefore, there is an exponentially small but finite tunneling amplitude through the barrier, which connects to an outgoing wave in the unbounded space. Therefore, the eigenstates are forming a continuum. However, only those states corresponding to the quasi-bound solutions have a high amplitude in the well of the potential. The energy width Γ of these states is given by \hbar/τ , where τ is the lifetime for the escape from the potential well.

In order to determine the wave function we have to solve the Schrödinger equation for the regions I to III in Fig. 3.25 and then match the solutions at the boundaries (wave matching method). However, since we are not interested in the detailed quantitative result, we disregard algebraic prefactors in the following and concentrate on the exponential factor, which dominates the transmission probability through the barrier. Within the WKB approximation method, in a one-dimensional situation the absolute square $|\Psi(x)|^2$ of the wave function of a particle with mass M and energy E decays in the barrier region as

$$|\Psi(x)|^2 \propto \exp \left\{ -\frac{2}{\hbar} \int_{\text{II}} \sqrt{2M[V(x) - E]} dx \right\}. \quad (3.5.33)$$

Here the integral extends over the region under the barrier (region II in Fig. 3.25). For a rough estimate we can use a constant average barrier height V_B of width Δx so that (3.5.33) becomes

$$|\Psi(x)|^2 \propto \exp \left\{ -\frac{2}{\hbar} \sqrt{2MV_B} \Delta x \right\}. \quad (3.5.34)$$

If $U(\varphi) \gg E_0 = \hbar\omega_A/2$ is satisfied, that is, if the ground state energy of the harmonic oscillator is much smaller than the barrier height, we can apply the quasi-classical WKB method to our problem. With respect to the Josephson junction problem we have to replace Δx by $\Delta\varphi$ and have to use $M = (\hbar/2e)^2 C$ (see (3.2.6)). Then we obtain

$$|\Psi(\varphi)|^2 \propto \exp \left\{ -\frac{2}{\hbar} \int_{\text{II}} \sqrt{2 \left(\frac{\hbar}{2e} \right)^2 C \left[U(\varphi) - \frac{\hbar\omega_A}{2} \right]} d\varphi \right\}. \quad (3.5.35)$$

With $U(\varphi) \gg \hbar\omega_A/2$ we can use the approximation $U(\varphi) - \frac{\hbar\omega_A}{2} \simeq U(\varphi)$. Again, for a rough estimate we can use a constant average barrier height U_0 of width $\Delta\varphi$ so that (3.5.35) becomes

$$|\Psi(\varphi)|^2 \propto \exp \left\{ -\sqrt{\frac{U_0}{E_C}} \Delta\varphi \right\} \quad (3.5.36)$$

with $E_C = e^2/2C$. This results in the decay rate

$$\Gamma = \frac{\omega_A}{2\pi} \exp \left\{ -\sqrt{\frac{U_0}{E_C}} \Delta\varphi \right\}. \quad (3.5.37)$$

For small tilt angles of the washboard potential we usually (except for very small junctions) have $U_0 \simeq 2E_{J0} \gg E_C$ and $\Delta\varphi \simeq 2\pi$. Therefore, the transmission probability is very small. However, with increasing bias current both U_0 and $\Delta\varphi$ become smaller as

$$U_0 \simeq 2E_{J0}(1 - i^2)^{3/2} \quad \text{and} \quad \Delta\varphi \simeq \pi\sqrt{1 - i^2} \quad (3.5.38)$$

and the transmission probability can become significant and can be measured.^{61,62,63}

In the following, we briefly give an estimate for the temperature T^* , at which the rate for macroscopic quantum tunneling becomes equal to that for thermal activation. Note that the rate for thermal activation is proportional to $\exp(-U_0/k_B T)$ and therefore also becomes exponentially large when increasing the bias current to the critical current. This already indicates that the temperature T^* should depend only weakly on the applied current. We start our discussion with $I \simeq 0$. In this limit, $U_0 \simeq 2E_{J0}$, $\hbar\omega_p = \sqrt{8E_{J0}E_C} \simeq 2\sqrt{U_0E_C}$. If we set $\Delta\varphi \simeq \pi$, with these approximations we can rewrite (3.5.37) as

$$\Gamma = \frac{\omega_p}{2\pi} \exp\left\{-2\pi\frac{U_0}{\hbar\omega_p}\right\} \quad (3.5.39)$$

and the rates for macroscopic quantum tunneling and thermal activation become equal at the temperature

$$k_B T^* \simeq \frac{\hbar\omega_p}{2\pi}. \quad (3.5.40)$$

For $I > 0$, we have to take into account the current dependent factors. We see that with $\sqrt{U_0} \propto (1 - i^2)^{3/4}$ and $\Delta\varphi \propto (1 - i^2)^{1/2}$ the exponent in (3.5.36) scales with $(1 - i^2)^{5/4}$, whereas the exponent in the Boltzmann factor $\exp(-U_0/k_B T)$ scales as $(1 - i^2)^{3/2}$. That is, they differ by $(1 - i^2)^{1/4}$, which exactly corresponds to the current dependence of the frequency ω_A for small oscillations around the minimum. Thus, for arbitrary currents below I_c we obtain the general result for the cross-over temperature⁶⁴

$$k_B T^* \simeq \frac{\hbar\omega_A}{2\pi} = \frac{\hbar\omega_p}{2\pi} (1 - i^2)^{1/4}. \quad (3.5.41)$$

For a typical plasma frequency of the order of 10^{11}s^{-1} we obtain $T^* \sim 100\text{ mK}$. This temperature is easily accessible with dilution refrigerators.⁶⁵

Additional Topic: Effect of Damping

In our previous discussion we have neglected the effect of damping. To account for damping in quantum tunneling we have to take into account the coupling of the system with the environment (heat bath). This

⁶¹R.F. Voss, R.A. Webb, Phys. Rev. Lett. **47**, 265 (1981).

⁶²J.M. Martinis, M.H. Devoret, J. Clarke, Phys. Rev. **B 35**, 4682 (1987).

⁶³J. Clarke, A.N. Cleland, M.H. Devoret, D. Esteve, J.M. Martinis, Science **239**, 992 (1988).

⁶⁴For the decay rate we obtain the result

$$\Gamma = \frac{\omega_A}{2\pi} \left(\frac{864\pi U_0}{\hbar\omega_A} \right)^{1/2} \exp\left\{-\frac{36U_0}{5\hbar\omega_A}\right\}.$$

See K. K. Likharev, *Dynamics of Josephson Junctions and Circuits*, Gordon and Breach Science Publishers, New York (1986).

⁶⁵We note that in a real experiments the rate for macroscopic quantum tunneling should also be large enough that a single event can be measured at least within the lifetime of the person doing the experiment. If a convenient rate required for an experiment is τ^{-1} , we also have to satisfy the criterion

$$\omega_A \exp\left\{-\sqrt{\frac{U_0}{E_C}} \Delta\varphi\right\} \geq \tau^{-1}.$$

With $\sqrt{U_B} \propto (1 - i^2)^{3/4}$ this can of course always be done by using $i \simeq 1$. However, since due to technical reasons one usually has to use $i \leq 0.99$, this sets an upper limit for E_{J0}/E_C . Therefore, in most experiments junctions with small critical currents (typically smaller than $10\mu\text{A}$) and, hence, small E_{J0} are used.

results in a much more complicated problem that has been solved by **Caldeira** and **Leggett** within the RCSJ model.^{66,67,68,69} According to this work the damping results in a multiplication of the decay rate by the factor $\exp(-2\pi CU_0\tau/\hbar) < 1$, where $C \simeq 1$ for $\omega_A\tau_{RC} \gg 1$ and $C = 3/2$ for $\omega_A\tau_{RC} \ll 1$. That is, damping strongly suppresses macroscopic quantum tunneling. Due to the strong suppression of quantum tunneling the damped system follows the classical thermal activation behavior to lower temperatures. The crossover temperature T^* in the presence of damping is no longer given by (3.5.41) but by a similar expression, where ω_A has been replaced by a damping dependent frequency $\omega_R = 1/\tau$:

$$k_B T^* \simeq \frac{\hbar\omega_R}{2\pi} \quad (3.5.42)$$

with

$$\omega_R = \omega_A \left\{ \sqrt{1 + \alpha^2} - \alpha \right\} . \quad (3.5.43)$$

Here, $\alpha = 1/2R_NC\omega_A$ is a dimensionless damping parameter. Obviously, for $\alpha = 0$ we recover the result (3.5.40). For $\alpha \gg 1$, we obtain $\omega_R \simeq \omega_A/2\alpha = \omega_A^2 R_N C \ll \omega_A$.⁷⁰ Hence, we obtain a much lower cross-over temperature T^* and the observation of macroscopic quantum tunneling is more difficult. The strong damping result can be understood by the fact that in the limit of strong damping one has to replace the undamped oscillation frequency ω_A around the minimum of the potential well by the characteristic frequency of an overdamped oscillator, namely by $\omega_A/2\alpha = \omega_A^2 R_N C = \omega_R$.

An experimental example is shown in Fig. 3.26, where the temperature dependence of the escape rate described by an effective temperature T_{esc} is plotted versus the sample temperature for a “quantum junction” and a “classical junction”. In the experiment the capacitance was chosen to put the sample into the lightly (quantum junction) and moderate damping regime (classical junction) in the presence of transmission line damping. Excellent agreement with theoretical predictions of the cross-over temperature was found. It is also seen that the escape temperature follows the sample temperature in the classical regime where thermal activation dominates. In the low temperature regime T_{esc} is a fictitious temperature, at which the classical thermal activation would yield the same escape rate as the actual quantum tunneling.

Phase Diffusion by Macroscopic Quantum Tunneling

An interesting situation occurs in the study of small junctions with small coupling energy and high resistance. In such junctions a finite resistance R_p is observed at low current, which is interpreted classically as resulting from phase diffusion. The temperature dependence of R_p is described at least qualitatively in terms of the classical thermally activated phase slippage (compare (3.4.17)). However, at very low temperature the data appear to bottom out at a finite, temperature independent phase slippage rate. Qualitatively this is what one would expect, if macroscopic quantum tunneling takes over below a certain cross-over temperature. Then a temperature independent value is expected for R_p determined by the rate of macroscopic quantum tunneling given by (3.5.36) with $U_0 = 2E_{J0}$ and $\Delta\varphi = \pi$. However, until now the validity of this interpretation is unclear.⁷¹

⁶⁶A.O. Caldeira, A. Leggett, Phys. Rev. Lett. **46**, 211 (1981).

⁶⁷A.O. Caldeira, A. Leggett, Ann. Phys. **149**, 374 (1983).

⁶⁸A.I. Larkin, Yu.N. Ovchinnikov, JETP Lett. **37**, 322 (1983).

⁶⁹H. Grabert, *Macroscopic Quantum Tunneling and Quantum Coherence in Josephson Systems*, in “Superconducting Quantum Interference Devices and their Applications”, H.-D. Hahlbohm and H. Lübbig eds., de Gruyter, Berlin (1985), p. 289.

⁷⁰We use the approximation $\sqrt{1 + \alpha^2} = \alpha\sqrt{1 + 1/\alpha^2} \simeq \alpha(1 + 1/2\alpha)$.

⁷¹For further discussion see M. Tinkham, *Introduction to Superconductivity*, McGraw-Hill Book Company, New York (1996).

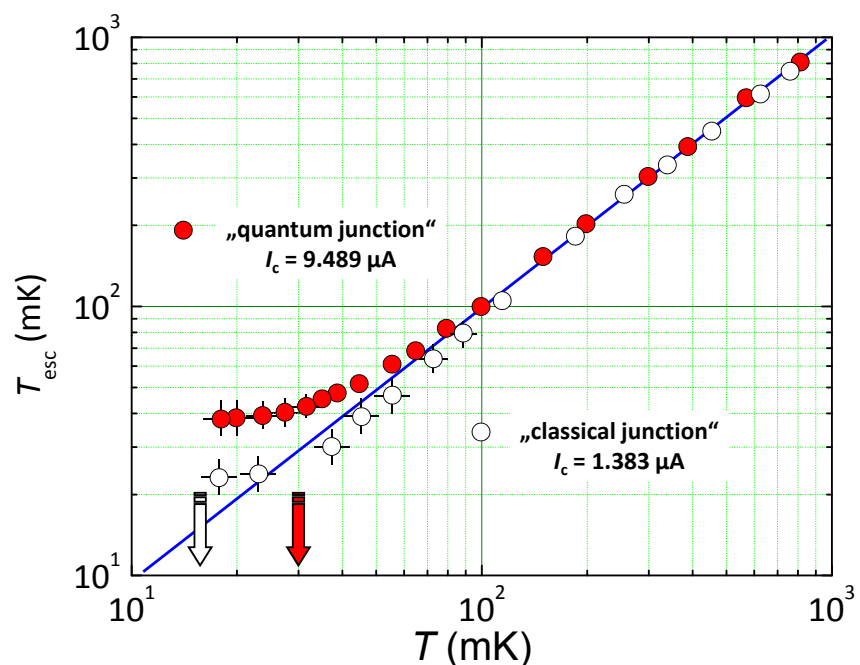


Figure 3.26: Temperature dependence of the escape rate described by an effective temperature for a “quantum junction” and a “classical junction”. The arrows mark the theoretically expected cross-over temperatures from thermal activation to macroscopic quantum tunneling (data after Martinis *et al.*, Phys. Rev. **B** **35**, 4682 (1987)).

3.6 Voltage State of Extended Josephson Junctions

In the previous sections we have assumed that the Josephson junction can be modeled as a lumped element. That is, we have described the junction by integral quantities such as its maximum Josephson current. Such a description is only possible for small Josephson junctions ($W, L < \lambda_J$) in the absence of an applied magnetic field. In this section we extend the discussion of extended Josephson junctions in the zero voltage state (see section 2.2 and 2.3) to the finite voltage state.

3.6.1 Negligible Screening Effects

As we have done for the zero voltage state (cf. section 2.2.6), for simplicity we first consider the case, where we can completely neglect the effect of the currents flowing in the junction electrodes. In this case the magnetic flux density in the junction is determined solely by the applied magnetic field: $\mathbf{B} = \mathbf{B}^{ex}$. Furthermore, the junction voltage V is given by the applied voltage V_0 throughout the junction. Then, the time dependence of the gauge-invariant phase difference is the same everywhere and given by the voltage-phase relation

$$\frac{\partial \varphi}{\partial t} = \frac{2e}{\hbar} V_0 = \omega_0 , \quad (3.6.1)$$

whereas the spatial variation (for the junction geometry of Fig. 2.4) is given by

$$\frac{\partial \varphi(z,t)}{\partial z} = \frac{2\pi}{\Phi_0} t_B B_y(z,t) . \quad (3.6.2)$$

Eqs. (3.6.1) and (3.6.2) are satisfied by a gauge-invariant phase difference given by

$$\varphi(z,t) = \varphi_0 + \omega_0 t + \frac{2\pi}{\Phi_0} B_y t_B \cdot z = \varphi_0 + \omega_0 t + k \cdot z . \quad (3.6.3)$$

This solution gives a periodic Josephson current distribution (compare discussion given in section 2.2.6)

$$J_s(z,t) = J_c \sin(\omega_0 t + k \cdot z + \varphi_0) \quad (3.6.4)$$

of exactly the same form as shown in Fig. 2.6. That is, the current distribution has the same form as the Josephson vortices in the zero voltage case except that in the case of a finite voltage these vortices are moving along the z -direction with a velocity (compare section 2.2.6 and Fig. 2.13)

$$v_z = \frac{\omega_0}{k} = \frac{V_0}{B_y t_B} . \quad (3.6.5)$$

This motion of Josephson vortices is completely analogous to the motion of Abrikosov vortices in a type II superconductor.

3.6.2 The Time Dependent Sine-Gordon Equation

We now take into account the effect of the Josephson currents on the time-dependent electromagnetic fields. We consider a Josephson junction as shown in Fig. 2.4. The barrier is in the yz -plane, the magnetic field is applied in y -direction resulting in phase variations along the z -direction. The applied current is flowing in the negative x -direction. The magnetic flux density in the junction results both from the externally applied field *and* the Josephson current density and must satisfy Ampère's law. With $\mathbf{B} = \mu_0 \mathbf{H}$ (we assume $\mu = 1$) and $\mathbf{D} = \epsilon \epsilon_0 \mathbf{E}$ we obtain

$$\nabla \times \mathbf{B} = \mu_0 \mathbf{J} + \epsilon \epsilon_0 \mu_0 \frac{\partial \mathbf{E}}{\partial t} . \quad (3.6.6)$$

Here, μ_0 and ϵ_0 are the permeability and permittivity in vacuum, respectively, and ϵ is the dielectric constant of the barrier material.

In contrast to section 2.2 and 2.3 we now have to take into account the term $\partial \mathbf{E} / \partial t$, which was zero in the zero voltage state of the junction. Then, for the geometry of Fig. 2.4 we obtain

$$\frac{\partial B_y(z,t)}{\partial z} = -\mu_0 J_x(z,t) - \epsilon \epsilon_0 \mu_0 \frac{\partial E_x(z,t)}{\partial t} . \quad (3.6.7)$$

Using (3.6.2) we obtain

$$\frac{\partial^2 \varphi(z,t)}{\partial z^2} = -\frac{2\pi}{\Phi_0} t_B \left\{ \mu_0 J_x(z,t) + \epsilon \epsilon_0 \mu_0 \frac{\partial E_x(z,t)}{\partial t} \right\} . \quad (3.6.8)$$

Then, with $E_x = -V/d$, $J_x = -J_c \sin \varphi$ and $\partial \varphi / \partial t = 2\pi V / \Phi_0$ we can rewrite (3.6.8) as

$$\frac{\partial^2 \varphi(z,t)}{\partial z^2} = -\frac{2\pi}{\Phi_0} t_B \left\{ \mu_0 J_c \sin \varphi(z,t) + \epsilon \epsilon_0 \mu_0 \frac{\Phi_0}{2\pi d} \frac{\partial^2 \varphi(z,t)}{\partial t^2} \right\} . \quad (3.6.9)$$

With the definition (2.3.6) of the Josephson penetration depth, $\lambda_J \equiv \sqrt{\frac{\Phi_0}{2\pi \mu_0 t_B J_c}}$, we can rearrange this equation and obtain a wave equation for the junction known as the ***time dependent Sine-Gordon equation***:

$$\frac{\partial^2 \varphi(z,t)}{\partial z^2} - \frac{1}{c^2} \frac{\partial^2 \varphi(z,t)}{\partial t^2} - \frac{1}{\lambda_J^2} \sin \varphi(z,t) = 0 . \quad (3.6.10)$$

Here,

$$\bar{c} = \sqrt{\frac{d}{\epsilon \epsilon_0 \mu_0 t_B}} = \frac{1}{\sqrt{\epsilon_0 \mu_0}} \sqrt{\frac{d}{\epsilon(2\lambda_L + d)}} = c \sqrt{\frac{1}{\epsilon(1 + 2\lambda_L/d)}} \quad (3.6.11)$$

is the velocity of the TEM mode in the transmission line formed by the two junction electrodes and the dielectric barrier named the ***Swihart velocity***.⁷² Since $\epsilon \sim 5 - 10$ and $2\lambda_L/d \sim 50 - 100$, the Swihart

⁷²J.C. Swihart, J. Appl. Phys. **32**, 461 (1961).

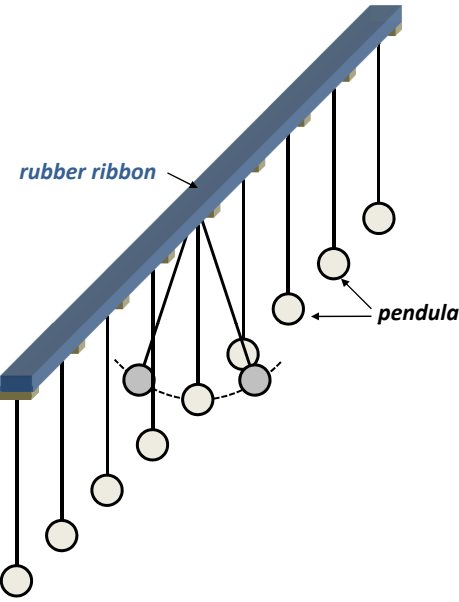


Figure 3.27: Chain of pendula attached to a twistable rubber ribbon as a mechanical analogue for the phase dynamics of a long Josephson junction. If one pendulum is deflected from its equilibrium position, the rubber ribbon is locally twisted and exerts a torque on the neighboring pendula, which in turn are also deflected (not shown).

velocity is usually by more than an order of magnitude smaller than the velocity of light in vacuum. Furthermore, the wavelength is significantly reduced compared to free space. For example, microwaves at $f = 10 \text{ GHz}$, which have a free-space wavelength of about 3 cm, would have a wavelength in the junction of only about 1 mm. This disparity of the wave velocities makes it difficult to couple electromagnetic energy in and out of the junction.

Using the expressions for \bar{c} and λ_J we obtain

$$\frac{\bar{c}}{\lambda_J} = \frac{\omega_p}{2\pi} = v_p \quad (3.6.12)$$

and we can rewrite the sine-Gordon equation as

$$\lambda_J^2 \frac{\partial^2 \varphi(z,t)}{\partial z^2} - \frac{4\pi^2}{\omega_p^2} \frac{\partial^2 \varphi(z,t)}{\partial t^2} - \sin \varphi(z,t) = 0 . \quad (3.6.13)$$

The mechanical analogue to the phase dynamics described by (3.6.10) or (3.6.13) is a chain of mechanical pendula, which are attached to a twistable rubber ribbon (see Fig. 3.27). If we would have a spatially homogeneous current density $J_x(z) = \text{const}$, the term $\frac{\partial^2 \varphi}{\partial z^2}$ would vanish and we obtain the result of the RCSJ model. For the pendulum analogue this would mean that we would establish a rigid connection between all pendula so that all pendula have to rotate synchronously. The term $\lambda_J^2 \frac{\partial^2 \varphi}{\partial z^2}$ can be interpreted within the pendulum model as the restoring torque, which is acting on a pendulum at position z by the neighboring pendula. Since the pendula are fixed at a twistable rubber ribbon, a finite restoring force is generated if the neighboring pendula are twisted against each other.

3.6.3 Solutions of the Time Dependent Sine-Gordon Equation

The time dependent Sine-Gordon equation is nonlinear and has many interesting types of behavior. We only address a few simple cases. We restrict ourselves to quasi-one-dimensional junctions having a

width $W \ll \lambda_J$. We call these junctions ***short*** and ***long***, if their length L is small and large compared to the Josephson penetration depth λ_J , respectively.

Short Junctions ($L \ll \lambda_J$), Low and Intermediate Damping

In the short junction limit ($L \ll \lambda_J$) we can neglect the z variation of φ so that the Sine-Gordon equation reduces to

$$\frac{\partial^2 \varphi(z, t)}{\partial t^2} + \frac{\omega_p^2}{4\pi^2} \sin \varphi(z, t) = 0 . \quad (3.6.14)$$

This equation is equivalent to the differential equation (compare section 3.2) found from the RCSJ model approximation for zero damping ($G_N = 0$) and zero bias current ($I = 0$). This is expected, since for $L \ll \lambda_J$ the behavior of the lumped junction modeled by the RCSJ model should be recovered. Note that the definition $\omega_p^2 = 2eI_c/\hbar C$ is equivalent to the ω_p^2 value in (3.6.14) with $C/A_i = \varepsilon\varepsilon_0/d$, $I_c/A_i = J_c$ and $c^2 = 1/\varepsilon_0\mu_0$. Of course, the Sine-Gordon equation in the same way as the RCSJ model can be generalized by the inclusion of a damping term which is proportional to $\partial\varphi/\partial t$.⁷³ However, we will not discuss the case of finite damping here. As already discussed in section 3.2, in the case of small amplitudes we can use the approximation $\sin \varphi \simeq \varphi$, that is, we can linearize the differential equation. In this case the solutions of (3.6.14) are plasma oscillations (compare (3.2.12)).

Long Junction Limit ($L \gg \lambda_J$), Solitons

The time dependent Sine-Gordon equation is invariant under the Lorentz transformation, in which \bar{c} plays the role of the velocity of light. This can be seen by its structure. An interesting type of solution for the (infinitely) long Josephson junction is the ***soliton*** or ***fluxon*** solution, which we already have discussed in section 2.3.2 for the stationary case. The solution has the form

$$\varphi(z, t) = 4 \arctan \left\{ \exp \left(\pm \frac{\frac{z-z_0}{\lambda_J} - \frac{v_z}{\bar{c}} t}{\sqrt{1 - \left(\frac{v_z}{\bar{c}}\right)^2}} \right) \right\} . \quad (3.6.15)$$

This solution maintains the value $\varphi = \pi$ at the moving point $z = z_0 + v_z t$ and goes from 0 to 2π as $[z - (z_0 + v_z t)]$ goes from $-\infty$ to $+\infty$ for the upper sign (“fluxon”) and vice versa for the lower sign (“anti-fluxon”). The solution represents a fluxon or anti-fluxon as shown in Fig. 2.14 moving with velocity v_z along the junction. In the pendulum analogue the fluxon corresponds to a local 360° twist of the rubber ribbon with the twist axis parallel to the ribbon.

Under the action of the Lorentz force due to the applied current the fluxon is moved along the junction. The fluxon behaves as a particle and suffers Lorentz contraction on approaching the Swihart velocity \bar{c} , which plays the role of the velocity of light. For example, if a fluxon moves along the z -direction, it becomes narrower proportional to $1/\sqrt{1 - v_z^2/\bar{c}^2}$. Furthermore, the moving fluxon causes a temporal change of the local phase difference which according to the 2. Josephson equation corresponds to a voltage. Hence, the moving fluxon corresponds to a voltage pulse, which is becoming sharper with increasing velocity due to Lorentz contraction in order to satisfy the condition $\int V dt = \Phi_0$.

⁷³D.W. McLaughlin, A.C. Scott, Phys. Rev. A **18**, 1652 (1978).

We also note that other solutions exist for the infinitely long lossless junction representing fluxon-fluxon collisions, fluxon-anti-fluxon collisions, bound states, plasma waves etc.. Most of these solutions, which will not be discussed here, have been observed experimentally.^{74,75,76}

The linearized Sine-Gordon Equation: Josephson Plasma

Another class of solutions can be studied by linearizing the Sine-Gordon equation. Let

$$\varphi(z,t) = \varphi_0(z) + \varphi_1(z,t) , \quad (3.6.16)$$

where $\varphi_0(z)$ is a time independent solution and $\varphi_1(z,t)$ is a small deviation from this solution, i.e. $\varphi_1 \ll \varphi_0$. Then, a good approximation is

$$\sin \varphi \simeq \sin \varphi_0 + \varphi_1 \cos \varphi_0 . \quad (3.6.17)$$

Substitution into the Sine-Gordon equation and keeping only linear terms in φ_1 yields

$$\frac{\partial^2 \varphi_0}{\partial z^2} + \frac{\partial^2 \varphi_1(z,t)}{\partial z^2} - \frac{1}{\bar{c}^2} \frac{\partial^2 \varphi_1(z,t)}{\partial t^2} - \frac{1}{\lambda_J^2} \sin \varphi_0 - \frac{1}{\lambda_J^2} \cos \varphi_0 \varphi_1(z,t) = 0 . \quad (3.6.18)$$

With $\frac{\partial^2 \varphi_0}{\partial z^2} = \frac{1}{\lambda_J^2} \sin \varphi_0$ (φ_0 has to satisfy the time independent Sine-Gordon equation) we obtain

$$\frac{\partial^2 \varphi_1(z,t)}{\partial z^2} - \frac{1}{\bar{c}^2} \frac{\partial^2 \varphi_1(z,t)}{\partial t^2} - \frac{1}{\lambda_J^2} \cos \varphi_0 \varphi_1(z,t) = 0 . \quad (3.6.19)$$

If we further assume that φ_0 varies slowly over the scale that φ_1 changes, we can assume $\varphi_0 \simeq const$. In this case the solution is

$$\varphi_1(z,t) = \exp(-i[kz - \omega t]) \quad (3.6.20)$$

and ω has to satisfy the dispersion relation

$$\omega^2 = \bar{c}^2 k^2 + \omega_{p,J}^2 . \quad (3.6.21)$$

Here, $\omega_{p,J}$ is the Josephson plasma frequency and is given by

$$\frac{\omega_{p,J}^2}{4\pi^2} = \frac{\bar{c}^2}{\lambda_J^2} \cos \varphi_0 . \quad (3.6.22)$$

Note that for frequencies below $\omega_{p,J}$ the wave vector k is imaginary so that no propagating solutions exist. However, for $\omega > \omega_{p,J}$ modes will propagate and at $\omega = \omega_{p,J}$ the wavelength will be infinitely long just as it is for the plasma frequency in a metal. With the typical values $\bar{c} \sim 0.05c$ and $\lambda_J \sim 100 \mu m$ for Nb Josephson junctions we obtain a Josephson plasma frequency of about 10 GHz.

In the pendulum analogue the Josephson plasma waves are obtained, if we deflect a single pendulum within a coupled chain of pendula and then let it relax. This results in a wavelike excitation that propagates along the chain. We note that the above discussion can be extended to the case of larger applied currents. In this case the plasma frequency $\omega_{p,J}$ has to be replaced by the current dependent frequency $\omega_{p,J}(1-i^2)^{1/4}$.

⁷⁴R.A. Fulton, R.C. Dynes, Solid State Commun. **12**, 57 (1973).

⁷⁵B. Duenholm, O.A. Levring, J. Mygind, N.F. Pedersen, O.H. Soerensen, M. Cirillo, Phys. Rev. Lett. **46**, 1299 (1981).

⁷⁶K. Nakajima, H. Mizusawa, Y. Sawada, H. Akoh, S. Takada, Phys. Rev. Lett. **65**, 1667 (1990).

Plane waves: If λ_J is very large or the driving current is very small, we can completely neglect the term $\sin \varphi / \lambda_J^2$ and the Sine-Gordon equation reduces to the familiar linear wave equation

$$\frac{\partial^2 \varphi(z,t)}{\partial z^2} - \frac{1}{\bar{c}^2} \frac{\partial^2 \varphi(z,t)}{\partial t^2} = 0. \quad (3.6.23)$$

The solutions of this equation are simply plane waves with velocity \bar{c} .

3.6.4 Additional Topic: Resonance Phenomena

So far we have discussed Josephson plasma waves and fluxons as possible solutions of the time-dependent sine-Gordon equation. The interaction of these excitations with the oscillating Josephson current results in interesting resonance phenomena appearing as structures in the current-voltage characteristics. In the following we will briefly address a few of them. We will do so, since some of these dynamic phenomena are not only interesting with respect to nonlinear dynamics but also are used in high-frequency applications of Josephson junctions.⁷⁷ We will come back to them in chapters 6 and 7.

Flux-Flow Steps and the Eck peak

For $B_{\text{ext}} > 0$, the Josephson current density is spatially modulated with a wave vector $k = \frac{2e}{\hbar} B_y t_B$. In the voltage state, this spatially modulated current density is moving along the junction at velocity $v_z = V/B_y t_B$. The oscillating Josephson current density can excite Josephson plasma waves. As for every driven oscillator we expect a resonant behavior, if both the wave vector and the frequency of the two excitations match.⁷⁸ That is, the electromagnetic waves are expected to strongly couple to the Josephson currents, if the wave velocity \bar{c} matches the velocity v_z of the moving vortex pattern. This occurs, when the junction voltage is

$$V_{\text{Eck}} = \bar{c} B_y t_B = \sqrt{\frac{d}{\epsilon \epsilon_0 \mu_0 t_B}} B_y t_B = \frac{\omega_p}{2\pi} \frac{\lambda_J}{L} B_y t_B L = \frac{\omega_p}{2\pi} \frac{\lambda_J}{L} \Phi_0 \frac{\Phi}{\Phi_0}, \quad (3.6.24)$$

where we have used $\bar{c} = \frac{\omega_p}{2\pi} \lambda_J$, and $\Phi = B_y t_B L$. The IVCs of Josephson junctions indeed show a current peak at the matching condition. This peak was first found by **R. E. Eck et al.**⁷⁹ and therefore is called the the **Eck peak**. The so-called **Eck voltage** corresponds to the frequency

$$\omega_{\text{Eck}} = \frac{2e}{\hbar} V_{\text{Eck}} = \omega_p \frac{\lambda_J}{L} \frac{\Phi}{\Phi_0}. \quad (3.6.25)$$

The Eck peak can be interpreted as the result of the nonlinear interaction of the current wave given by (3.6.4) with the traveling electromagnetic wave of the same velocity. In fact the traveling wave of current (3.6.4) excites only the traveling wave of the same direction. When damping is low, the electromagnetic wave reflected at the open end of the junction transmission line can travel back almost without any loss of amplitude. Hence, a standing wave is formed. The Eck peak is therefore observed only at **medium damping** and large junction length $kL \gg 1$ (with $k = \frac{2e}{\hbar} B_y t_B$ this is equivalent to $B_y t_B L \gg \Phi_0/2\pi$), where the backward wave is significantly damped after reflection.

⁷⁷For a detailed discussion of the dynamic behavior of long Josephson junctions see:
J. Bindslev-Hansen, P.E. Lindeloff, Rev. Mod. Phys. **56**, 431 (1981).

M. Darula, T. Doderer, S. Beuven, Supercond. Sci. Techn. **12**, R1 (1999).

K. K. Likharev, *Dynamics of Josephson Junctions and Circuits*, Gordon and Breach Science Publishers, New York (1986).

⁷⁸Note that we have to deal with a nonlinear oscillator, which may have a much more complicated behavior in particular for large driving amplitudes.

⁷⁹R.E. Eck, D. J. Scalapino, B.N. Taylor, Phys. Rev. Lett. **13**, 15 (1964).

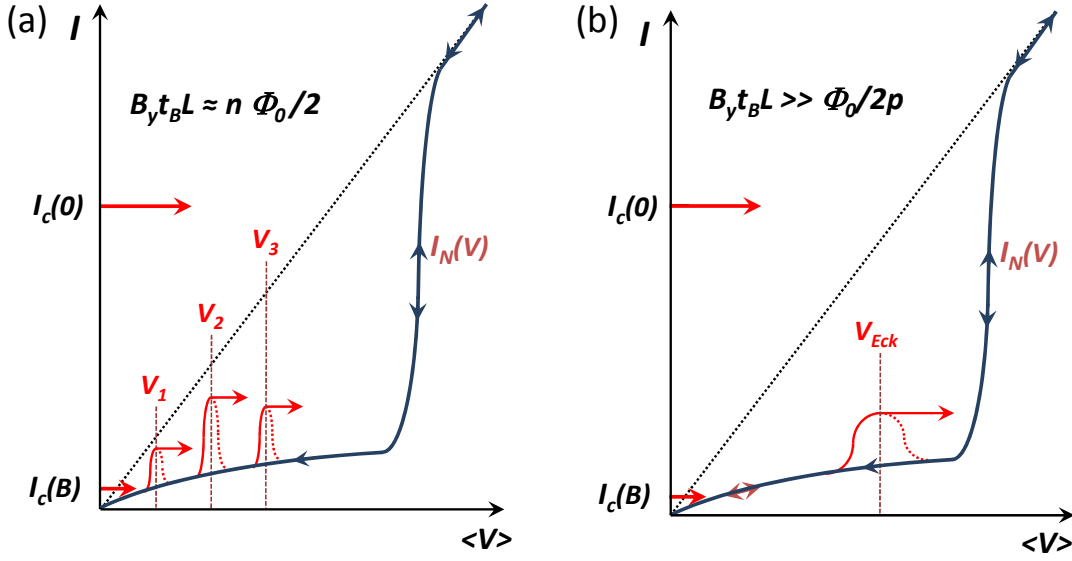


Figure 3.28: Schematic IVCs of a long Josephson tunnel junction at small damping and/or small magnetic field (a) showing the Fiske steps at voltages V_n and at medium damping and/or medium magnetic field (b) showing the Eck peak. Note that if the external source is a current source, there will be horizontal jumps in the IVCs as indicated by the arrows, since the current is fixed by the external source.

The appearance of the Eck peak can be interpreted also as the result of a maximum velocity for moving Josephson vortices. We already have discussed in section 3.6.1 that the Josephson vortices move under the action of the Lorentz force of an applied current at a velocity $v_z = V_{ff}/B_y t_B$ (compare (3.6.5)). Of course, the velocity v_z depends on the damping and a steady state motion is obtained, if the Lorentz force equals the friction force. We denote the resulting voltage as flux-flow voltage V_{ff} . If we increase the driving force, i.e. the applied current, we expect that v_z and hence V_{ff} is increasing. However, we have to take into account that the maximum velocity is bound to \bar{c} . That is, upon approaching \bar{c} a further increase of the current will no longer result in an increase of the velocity and the corresponding flux-flow voltage. Therefore, in the IVCs we obtain a so-called *flux-flow step* at the limiting voltage

$$V_{ffs} = \bar{c} B_y t_B = \bar{c} \frac{\Phi}{L} = \frac{\omega_p}{2\pi} \frac{\lambda_J}{L} \Phi_0 \frac{\Phi}{\Phi_0} . \quad (3.6.26)$$

The current step in the IVC is therefore also called *flow-flow step*. We see that V_{ffs} just corresponds to the Eck voltage.

Fiske steps

A related effect is the observation of steps in the IVCs as first found by **M. D. Fiske**.^{80,81} The *Fiske steps* occur at junction voltages V_n , where the frequency of the oscillating Josephson currents matches the frequencies

$$\omega_n = 2\pi f_n = 2\pi \frac{\bar{c}}{2L} n = \frac{\pi \bar{c}}{L} n \quad (3.6.27)$$

⁸⁰M.D. Fiske, Rev. Mod. Phys. **36**, 221 (1964).

⁸¹D.D. Coon, M.D. Fiske, Phys. Rev. **A 138**, 744 (1965).

of the electromagnetic cavity modes, which can be regarded as standing wave modes. Note that the two junction electrodes separated by the insulating barrier can be regarded as a cavity with the eigenfrequencies given by (3.6.27). The Fiske steps occur at the voltages

$$V_n = \frac{\hbar}{2e} \omega_n = \Phi_0 \frac{\bar{c}}{2L} n = \frac{\omega_p}{2\pi} \frac{\lambda_J}{L} \Phi_0 \frac{n}{2}. \quad (3.6.28)$$

For a typical long junction with $L \sim 100 \mu\text{m}$ the first Fiske step appears at a frequency of the order of 10 GHz. The corresponding voltage is of the order of several tens of μV , which is much less than the gap voltage (e.g. $V_g \sim 3 \text{ mV}$ for Nb).

The wave length $2\pi/k$ of the Josephson current density modulated along the z -direction is proportional to the applied magnetic field. The resonance condition $L = \frac{\bar{c}}{2f_n} n = \frac{\lambda}{2} n$ results in the condition $kL = n\pi$ or, equivalently, that the applied magnetic flux $\Phi = B_y t_B L$ should be equal to $n\frac{\Phi_0}{2}$. These are exactly the flux values for which the maximum Josephson current density of a short junction vanishes. At these flux values the spatial distribution of the Josephson current density (compare Fig. 2.6) matches the standing wave pattern in the junction allowing an effective nonlinear interaction between the oscillating current modes and the electromagnetic waves. If the oscillating Josephson current has excited a standing wave, it stays locked onto this standing wave for a certain current interval. In analogy to the Shapiro steps one obtains current steps in the IVC called Fiske steps.

We briefly discuss the shape of the IVCs of underdamped extended junctions shown in Fig. 3.28. For voltages that are not equal to V_{Eck} and V_n , the simple solution $J_s(z, t) = J_c \sin(\omega_0 t + k \cdot z + \phi_0)$ is a good approximation. This means that the time-average of the Josephson current vanishes, $\langle I_s \rangle = 0$, and that the IVCs are given by $I_N(V) = V/R_N(V)$. In the case of a tunnel junction the nonlinear quasiparticle IVC is obtained. However, at all dc voltages close to V_n the nonlinear interaction of the current waves (3.6.4) and the standing waves leads to narrow peaks (the Fiske steps) in the IVCs, whose height depends on the applied magnetic field and can be of the order of I_c (see Fig. 3.28). The Fiske modes appear at low damping. If the damping and/or the applied magnetic field is increasing, the width of the resonance peaks at V_n is increasing so that they are merging into a single Eck peak at V_{Eck} .

Zero field steps

Fluxons can be trapped in long Josephson junctions also in the absence of an applied magnetic field.⁸² The motion of these fluxons under the Lorentz force of an applied current results in so-called **zero field steps** in the IVCs of long Josephson junctions at zero external field. When a propagating fluxon reaches the end of the junction transmission line, it is reflected back as an anti-fluxon. In a junction of length L , a full period for moving back and forth takes the time $T = 2L/v_z$. The associated phase change is 4π , since the passage of a fluxon and the return of an anti-fluxon both change ϕ by 2π . Thus, in the relativistic limit ($v_z \rightarrow \bar{c}$) reached at large bias current (large driving force), the dc voltage across the junction will be

$$V_{\text{zfs}} = \dot{\phi} \frac{\hbar}{2e} = \frac{4\pi}{T} \frac{\hbar}{2e} = \frac{4\pi}{2L/\bar{c}} \frac{\hbar}{2e} = \frac{\hbar}{2e} \frac{\bar{c}}{L} = \frac{\omega_p}{2\pi} \frac{\lambda_J}{L} \Phi_0. \quad (3.6.29)$$

If n fluxons are present in the junction, the voltage will be n times larger:

$$V_{n,\text{zfs}} = \Phi_0 \frac{\bar{c}}{L} n = \frac{\omega_p}{2\pi} \frac{\lambda_J}{L} \Phi_0 n. \quad (3.6.30)$$

⁸²A.V. Ustinov *et al.*, Phys. Rev. Lett. **69**, 1815 (1992).

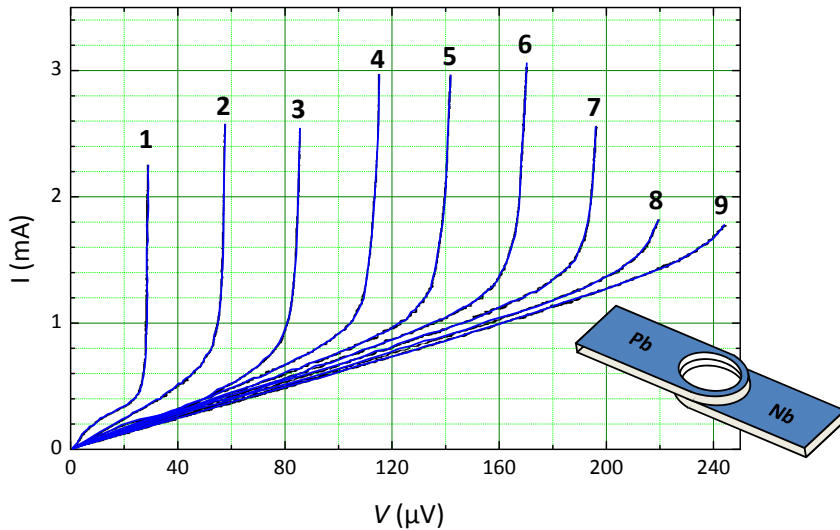


Figure 3.29: IVCs of an annular Nb/insulator/Pb Josephson junction containing a different number of trapped fluxons as indicated by the numbers. The geometry of the junction is shown in the inset. The ring diameter was about $100\text{ }\mu\text{m}$, the ring width about $10\text{ }\mu\text{m}$ (after A.V. Ustinov *et al.*, Phys. Rev. Lett. **69**, 1815 (1992)).

These constant voltage values are referred to as ***zero field steps***, because they are based on fluxons trapped in the junction in the absence of an external field. An experimental example is shown in Fig. 3.29. We see that $V_{n,zfs}$ is just twice the Fiske step voltage V_n . Comparing (3.6.28) and (3.6.30) we see that this is caused by the fact that for the Fiske steps the characteristic period for a 2π phase change is $\bar{c}/2L$, whereas it is \bar{c}/L for the zero field step. The reason for this is the fact that in the zero-field step case the fluxon has to move back and forth. We also see that $V_{ffs} = V_{n,zfs}$ for $\Phi/\Phi_0 = n$. This is obvious, since the introduction of n fluxons into the junction at zero field is equivalent to generating a flux $\Phi = n\Phi_0$ by applying a corresponding external field.

Interesting phenomena due to the motion and collision of fluxons can be observed in ring-shaped Josephson junctions. For example, if one introduces a fluxon and an anti-fluxon in such a junction, they circulate in opposite direction under the action of a finite driving current and collide during each round-trip. This collision has been observed by Low Temperature Scanning Electron Microscopy.⁸³ It was found that the collision zone shrinks with increasing speed of the fluxon and anti-fluxon due to Lorentz contraction.^{84,85,86}

Vortex-Cherenkov Radiation

Under certain conditions Josephson fluxons can move faster than \bar{c} , that is, faster than light.^{87,88,89} This is analogous to the motion of charged particles, which are moving in a medium at a velocity very close to the velocity of light. If their velocity is larger than the velocity of light in the medium, they emit electromagnetic radiation, which is called ***Cherenkov radiation***. Such radiation can for example be seen

⁸³R. Gross, D. Koelle, *Low Temperature Scanning Electron Microscopy of Superconducting Thin Films and Josephson Junctions*, Reports on Progress in Physics **57**, 651-741 (1994).

⁸⁴S. Keil, I. V. Vernik, T. Doderer, A. Laub, H. Preßler, R. P. Huebener, N. Thyssen, A. V. Ustinov, and H. Kohlstedt, Phys. Rev. **B 54**, 14948 (1996).

⁸⁵S. G. Lachenmann, T. Doderer, R. P. Huebener, D. Quenter, J. Niemeyer, and R. Pöpel, Phys. Rev. **B 48**, 3295 (1993).

⁸⁶A. Laub, T. Doderer, S. G. Lachenmann, R. P. Huebener, and V. A. Oboznov, Phys. Rev. Lett. **75**, 1372 (1995).

⁸⁷R.G. Mints, I.B. Snapiro, Phys. Rev. **B 52**, 9691 (1995).

⁸⁸V.V. Kurin, A.V. Yulin, I.A. Sheresheskii, N.K. Vdovicheva, Phys. Rev. Lett. **80**, 3372 (1998).

⁸⁹E. Goldobin, A. Wallraff, N. Thyssen, A.V. Ustinov, Phys. Rev. **B 57**, 130 (1998); see also Phys. Rev. Lett. **79**, 1365 (1997); Phys. Rev. **B 66**, 064527 (2001).

as a blue lightning in water surrounding a nuclear reactor. In the same way fast fluxons are emitting Josephson plasma waves called ***Vortex-Cherenkov radiation***.

Summary

Voltage State of Short Josephson Junctions:

- In the voltage state, the total current across a Josephson junction is given by the sum of the Josephson current I_s , the normal current I_N , the displacement current I_D and a fluctuation current I_F .
- In the RCSJ model the normal current channel is modeled by a voltage independent resistance R . The equation of motion of the phase difference φ is given by

$$\beta_C \frac{d^2\varphi}{d\tau^2} + \frac{d\varphi}{d\tau} + \sin \varphi - i - i_F(\tau) = 0$$

with $\tau = t/\tau_c = t/(2eI_cR/\hbar)$. The motion of φ is equivalent to the motion of a particle with mass $M = (\hbar/2e)^2C$ in the tilted washboard potential $U = E_{J0}[1 - \cos \varphi - (I/I_c)\varphi]$ at damping $\eta = (\hbar/2e)^2/R$.

The equivalent circuit is a parallel LCR oscillatory circuit with the nonlinear Josephson inductance $L_s = \hbar/2eI_c \cos \varphi = L_c/\cos \varphi$, the junction capacitance C and the junction normal resistance R . The oscillatory circuit is characterized by the characteristic frequencies

$$\omega_p = \sqrt{\frac{1}{L_c C}} = \sqrt{\frac{2eI_c}{\hbar C}} \quad \omega_c = \frac{R}{L_c} = \frac{2eI_c R}{\hbar} \quad \omega_{RC} = \frac{1}{RC}$$

and the quality factor

$$Q^2 = \beta_C \equiv \frac{2e}{\hbar} I_c R^2 C .$$

- Overdamped Josephson junctions ($\beta_C > 1$) have non-hysteretic IVCs, whereas underdamped junctions ($\beta_C < 1$) show hysteretic IVCs.
- The IVC of an overdamped Josephson junction driven by a dc current source is given by

$$\langle V(t) \rangle = I_c R \sqrt{\left(\frac{I}{I_c}\right)^2 - 1} \quad \text{for} \quad \frac{I}{I_c} > 1 .$$

- Driving a Josephson junction with a voltage $V(t) = V_{dc} + V_1 \cos \omega_1 t$ results in current steps (Shapiro steps) at voltages

$$V_n = n \frac{\Phi_0}{2\pi} \omega_1$$

with amplitudes

$$|\langle I_s \rangle_n| = I_c \left| \mathcal{J}_n \left(\frac{2\pi V_1}{\Phi_0 \omega_1} \right) \right| .$$

Secondary Quantum Macroscopic Effects:

- A classical description of the motion of φ is possible only in the phase regime ($\hbar\omega_p \ll E_{J0}$ or, equivalently, $E_C = e^2/2C \ll E_{J0}$). The phase regime is present for junctions with large area (typically $0.01 - 0.1 \mu\text{m}^2$) and hence small $E_C \propto A^{-1}$ and large Josephson coupling energy $E_{J0} \propto A$.
- For $\hbar\omega_p \sim E_{J0}$ or, equivalently, $E_C = e^2/2C \sim E_{J0}$, the motion of φ has to be described fully quantum mechanically. For Josephson junctions with negligible damping the adequate Hamiltonian is

$$\mathcal{H} = -4E_C \frac{\partial^2}{\partial \varphi^2} + E_{J0}(1 - \cos \varphi) .$$

The variables φ and $(\hbar/2e)Q = (\hbar/2e)^2 C \dot{\varphi}$ are canonically conjugate variables just like position and momentum and obey the commutation rule

$$[\varphi, \frac{\hbar}{2e} Q] = i\hbar ,$$

resulting in the uncertainty relation

$$\Delta N \cdot \Delta \varphi \geq 1$$

for the number of Cooper pairs $N = Q/2e$ and the phase difference φ .

- In the phase regime ($\hbar\omega_p \ll E_{J0}$ or, equivalently, $E_C = e^2/2C \ll E_{J0}$) we have $\Delta\varphi \rightarrow 0$ and $\Delta N \rightarrow \infty$, whereas in the charge regime ($\hbar\omega_p \gg E_{J0}$ or, equivalently, $E_C = e^2/2C \gg E_{J0}$) we have $\Delta N \rightarrow 0$ and $\Delta\varphi \rightarrow \infty$.
- In the charge regime, at $T = 0$ charge tunneling between the junction electrodes is possible only for $V_{CB} \geq e/C$ due to the Coulomb blockade effect. In the phase regime, fluxon motion along the junction is possible only for $I_{FB} \geq \Phi_0/L_c$ due to the flux blockade effect.
- At $I < I_c$ and $T > 0$, the phase difference can escape from a local minimum of the tilted washboard potential by thermal activation, resulting in a finite junction voltage by thermally activated phase slippage.
- The phase difference φ also can escape from a local minimum of the tilted washboard potential by tunneling through the potential barrier. This process is called macroscopic quantum tunneling, since the phase difference describing the collective state of a large number of electrons is tunneling.
- The cross-over temperature between thermal and tunnel escape from a local potential well is

$$k_B T^* \simeq \frac{\hbar\omega_A}{2\pi} = \frac{\hbar\omega_p}{2\pi} \left[1 - \left(\frac{I}{I_c} \right)^2 \right]^{1/4} .$$

Voltage State of Long Josephson Junctions:

- The equation of motion of the phase difference in long Josephson junctions is described by the time-dependent Sine-Gordon equation

$$\frac{\partial^2 \varphi(z,t)}{\partial z^2} - \frac{1}{\bar{c}^2} \frac{\partial^2 \varphi(z,t)}{\partial t^2} - \frac{1}{\lambda_J^2} \sin \varphi(z,t) = 0 ,$$

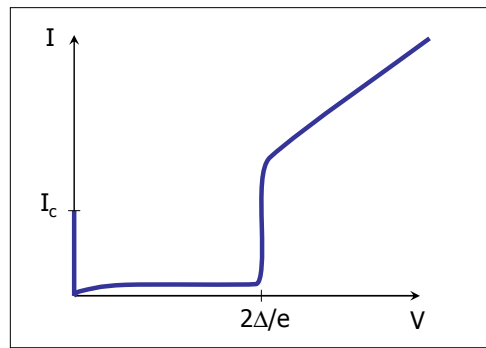
where the Swihart velocity \bar{c} is the propagation velocity of electromagnetic waves in the junction.

- Prominent solutions of the Sine-Gordon equation are plasma oscillations and solitons. The nonlinear interaction of these excitations with the oscillating Josephson current results in various resonant phenomena such as flux-flow steps, Fiske steps, or zero-field steps.

Part II

Applications of the Josephson Effect

Since the prediction of the Josephson effect and the first experimental realization of pair tunneling in superconductor/insulator/superconductor (SIS) systems, the technology of superconducting electronics has made tremendous progress. Superconducting electronics based on the Josephson effect covers a large number of both analog and digital applications. The properties of Josephson tunnel junctions and their typical current-voltage characteristics (IVC) immediately suggest the following applications:



1. The maximum Josephson current depends on externally applied magnetic fields (see chapter 2), i.e. $I_s^m = I_s^m(B)$. The magnetic field dependence $I_s^m(B)$ is used in magnetic field sensors based on Superconducting Quantum Interference Devices (SQUIDs) as discussed in detail in chapter 4.
2. In an underdamped Josephson tunnel junction with $\beta_C \gg 1$ there is a bistable voltage state for $I < I_s^m$, namely the superconducting or **zero voltage state** and the **voltage state** with $V \sim V_g$. This bistability can be exploited in fast switching devices usable for digital circuits in Josephson computers (see chapter 5). The energy dissipation per switching process is expected to be very low.
3. The nonlinear dependence of the supercurrent on the phase difference across a Josephson junction leads to structures in the IVC with an applied ac-source (eg. Shapiro steps). The relation between the ac frequency and the voltage/current steps can be utilized in voltage controlled oscillators (VCO) and in defining a voltage standard (see chapter 6).
4. The nonlinear IVC can be used in different kinds of mixers (Josephson- and QP-mixer) for frequencies up to several THz. Furthermore, the coupling of the oscillating Josephson current to resonant modes of the junction can be exploited in microwave oscillators (see chapter 7).
5. The macroscopic quantum behavior of Josephson junction circuits allows to use single Josephson junctions and loops containing one or more Josephson junctions as effective quantum two-level systems for the realization of superconducting quantum bits (see chapter 9).

The most important applications of Josephson junctions in analog and digital devices and circuits are discussed in the following chapters.

Chapter 4

Superconducting Quantum Interference Devices

The discussion of the magnetic field dependence of the maximum Josephson current I_s^m as a function of the applied magnetic field in Chapter 2 already showed that there is a strong modulation of I_s^m with the applied field. Therefore, in principle a simple Josephson junction already can be used as a magnetic field sensor. However, for practical applications the sensitivity of such a device is not high enough to compete with other techniques. The magnetic field dependence of the maximum Josephson current was found to have the shape of the diffraction pattern of a slit. The first minimum of the diffraction pattern is obtained, when the applied field generates one flux quantum in the junction area. Therefore, the sensitivity of the device is roughly $I_s^m/\Phi_0 = I_s^m/B_0 t_B L$, where $t_B L$ is the junction area threaded by the magnetic field. We immediately see, that we should increase the area $t_B L$ in order to increase the sensitivity. Then, one flux quantum is generated already at a much smaller applied magnetic field.

The easiest way to increase the area threaded by the magnetic field is to use not only a single Josephson junction but a superconducting loop or cylinder containing one or more Josephson junctions. We will see that in this case the relevant area is determined by the cross-sectional area of the ring or cylinder and not the junction area. Devices consisting of a superconducting loop interrupted by one or more Josephson junctions are denoted as ***Superconducting Quantum Interference Devices*** (SQUIDs). Hence, SQUIDs combine two physical phenomena, namely ***flux quantization in superconducting loops*** and the ***Josephson effect***. Today SQUIDs are the most sensitive detectors for magnetic flux available. In essence, a SQUID is a flux to voltage converter providing a flux dependent output voltage with a period of one flux quantum. We will see that SQUIDs are very versatile. They can measure all physical quantities that can be converted into magnetic flux, for example magnetic field, magnetic field gradients, current, voltage, displacement, or magnetic susceptibility.

In this chapter we will discuss the underlying physics, the performance limits and some practical applications of SQUIDs. In doing so we will focus on two kinds of SQUIDs. The first, the so-called ***direct current or dc-SQUID***,¹ consists of two junctions connected in parallel on a superconducting loop. It is named dc-SQUID, since it operates with a steady bias current. The second, ***radio frequency or rf-SQUID***,^{2,3} consists of a superconducting loop interrupted by a single junction. It operates with a radio-frequency flux bias. Historically, the dc-SQUID was used for magnetic measurements just after

¹R.C. Jaklevic, J. Lambe, A.H. Silver, J.E. Mercereau, *Quantum Interference Effects in Josephson Tunneling*, Phys. Rev. Lett. **12**, 159 (1964).

²J.E. Zimmermann, P. Thiene, J.T. Harding, *Design and Operation of Stable rf-biased Superconducting Point-contact Quantum Devices*, J. Appl. Phys. **41**, 1572 (1970).

³J.E. Mercereau, *Superconducting Magnetometers*, Rev. Phys. Appl. **5**, 13 (1970).

the first observation of macroscopic quantum interference in superconductivity.^{4,5} However, later in the late 1960s and early 1970s the rf-SQUID was preferred, mainly since it was easier to fabricate single junction interferometers using a simple point-contact. However, then in 1975 **J. Clarke** and co-workers showed that the energy sensitivity of dc-SQUIDs can be improved by using externally shunted junctions to values better than those of the rf-SQUID.⁶ This made the use of dc-SQUIDs preferable in applications requiring optimum resolution. Despite the improvement of rf-SQUIDs, their energy sensitivity is still worse than that of dc-SQUID at 4 K. However, at 77 K both types of SQUIDs are comparable making rf-SQUIDs again attractive for SQUIDs based on the high temperature superconductors.

⁴J. Clarke, Phil. Mag. **13**, 115 (1966).

⁵R.L. Forgacs, A. Warnick, Rev. Sci. Instr. **18**, 214 (1967).

⁶J. Clarke, W.M. Goubau, M.B. Ketchen, Appl. Phys. Lett. **27**, 155 (1976); J. Low Temp. Phys. **25**, 99 (1976).

4.1 The dc-SQUID

4.1.1 The Zero Voltage State

Two superconducting Josephson junctions can be combined in parallel as shown in Fig. 4.1 to obtain a superconducting quantum interference device known as the *direct current superconducting quantum interference device*. The two superconducting junctions, which we will consider as lumped elements, are connected in parallel and joined by a superconducting loop. The two junctions are assumed to have identical critical current I_c so that they are characterized by the current-phase relations $I_{s1} = I_c \sin \varphi_1$ and $I_{s2} = I_c \sin \varphi_2$. Applying Kirchhoff's law we obtain for the total current⁷

$$\begin{aligned} I_s &= I_{s1} + I_{s2} = I_c \sin \varphi_1 + I_c \sin \varphi_2 \\ &= 2I_c \cos\left(\frac{\varphi_1 - \varphi_2}{2}\right) \sin\left(\frac{\varphi_1 + \varphi_2}{2}\right). \end{aligned} \quad (4.1.1)$$

The gauge-invariant phase differences φ_1 and φ_2 can be found by considering the line integral along the contour shown in Fig. 4.1. We have to demand that the total phase change along the closed contour is $2\pi n$. Hence, in the same way as for the situation discussed in section 2.2.1 we obtain

$$\begin{aligned} \oint_C \nabla \theta \cdot d\mathbf{l} &= 2\pi n \\ &= (\theta_{Q_b} - \theta_{Q_a}) + (\theta_{P_c} - \theta_{Q_b}) + (\theta_{P_d} - \theta_{P_c}) + (\theta_{Q_a} - \theta_{P_d}) + 2\pi n \end{aligned} \quad (4.1.2)$$

Using $\nabla \theta = \frac{2\pi}{\Phi_0} (\Lambda \mathbf{J}_s + \mathbf{A})$ (compare (2.2.2)) and $\varphi = \theta_2 - \theta_1 - \frac{2\pi}{\Phi_0} \int_1^2 \mathbf{A} \cdot d\mathbf{l}$ (compare (2.2.3)) we obtain in analogy to section 2.2.1:

$$\theta_{Q_b} - \theta_{Q_a} = +\varphi_1 + \frac{2\pi}{\Phi_0} \int_{Q_a}^{Q_b} \mathbf{A} \cdot d\mathbf{l} \quad (4.1.3)$$

$$\theta_{P_d} - \theta_{P_c} = -\varphi_2 + \frac{2\pi}{\Phi_0} \int_{P_c}^{P_d} \mathbf{A} \cdot d\mathbf{l} \quad (4.1.4)$$

$$\theta_{P_c} - \theta_{Q_b} = \int_{Q_b}^{P_c} \nabla \theta \cdot d\ell = +\frac{2\pi}{\Phi_0} \int_{Q_b}^{P_c} \Lambda \mathbf{J}_s \cdot d\ell + \frac{2\pi}{\Phi_0} \int_{Q_b}^{P_c} \mathbf{A} \cdot d\mathbf{l} \quad (4.1.5)$$

$$\theta_{Q_a} - \theta_{P_d} = \int_{P_d}^{Q_a} \nabla \theta \cdot d\ell = +\frac{2\pi}{\Phi_0} \int_{P_d}^{Q_a} \Lambda \mathbf{J}_s \cdot d\ell + \frac{2\pi}{\Phi_0} \int_{P_d}^{Q_a} \mathbf{A} \cdot d\mathbf{l}. \quad (4.1.6)$$

Substitution of (4.1.3) – (4.1.6) into (4.1.2) yields

$$\varphi_1 - \varphi_2 = -\frac{2\pi}{\Phi_0} \oint_C \mathbf{A} \cdot d\ell - \frac{2\pi}{\Phi_0} \int_{Q_b}^{P_c} \Lambda \mathbf{J}_s \cdot d\ell - \frac{2\pi}{\Phi_0} \int_{P_d}^{Q_a} \Lambda \mathbf{J}_s \cdot d\ell. \quad (4.1.7)$$

⁷We use $\sin \alpha + \sin \beta = 2 \sin\left(\frac{\alpha+\beta}{2}\right) \cos\left(\frac{\alpha-\beta}{2}\right)$.

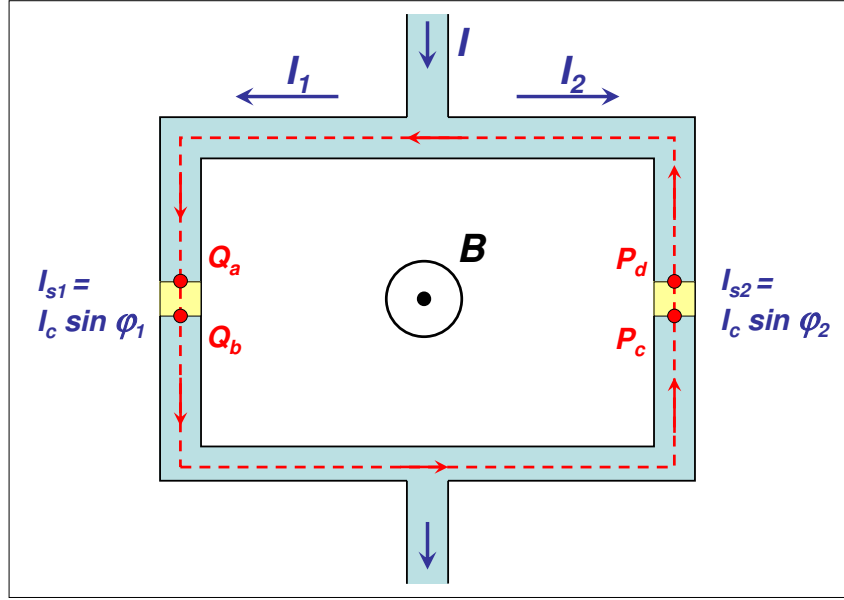


Figure 4.1: The dc-SQUID formed by two Josephson junctions intersecting a superconducting loop. The upper and the lower part of the loop can be represented by the macroscopic wave functions $\Psi_2 = \Psi_{20} \exp(i\theta_2)$ and $\Psi_1 = \Psi_{10} \exp(i\theta_1)$, respectively. The broken line indicates the closed contour path of the integration.

The integration of \mathbf{A} is around a closed contour and therefore is equal to the total flux Φ enclosed by the superconducting loop. The integration of \mathbf{J}_s follows the same contour C but excludes the integration over the insulating barrier. Furthermore, if the superconducting loop consists of a superconducting material with a thickness large compared to the London penetration depth λ_L , the integration path can be taken deep inside the superconducting material where the current density is negligible. Therefore, the two integrals involving the current density can be omitted and we obtain

$$\varphi_2 - \varphi_1 = \frac{2\pi\Phi}{\Phi_0} . \quad (4.1.8)$$

We see that the two phase differences across the junctions are not independent but are linked to each other via the boundary condition that we have to satisfy fluxoid quantization in the superconducting loop. Using expression (4.1.8) we can rewrite (4.1.1) as⁸

$$I_s = 2I_c \cos\left(\pi \frac{\Phi}{\Phi_0}\right) \sin\left(\varphi_1 + \pi \frac{\Phi}{\Phi_0}\right) . \quad (4.1.9)$$

If the flux Φ threading the loop would be given just by the flux Φ_{ext} due to the externally applied magnetic field, we would have solved the problem. Then, the maximum supercurrent of the parallel combination is just given by

$$I_s^m = 2I_c \left| \cos\left(\pi \frac{\Phi_{\text{ext}}}{\Phi_0}\right) \right| . \quad (4.1.10)$$

⁸Here, we use $(\varphi_1 + \varphi_2)/2 = [2\varphi_1 + (\varphi_2 - \varphi_1)]/2 = \varphi_1 + (\varphi_2 - \varphi_1)/2$.

However, in many cases we have to take into account the finite inductance L of the superconducting loop. Then, the flux Φ threading the loop is given by the sum

$$\Phi = \Phi_{\text{ext}} + \Phi_L \quad (4.1.11)$$

due to the applied magnetic field and the currents flowing in the loop. If we assume that the two sides of the loop are identical, we can write the currents flowing in the two arms of the loop as

$$I_{s1} = \tilde{I} + I_{\text{cir}} \quad (4.1.12)$$

$$I_{s2} = \tilde{I} - I_{\text{cir}} , \quad (4.1.13)$$

where

$$\tilde{I} = \frac{I_{s1} + I_{s2}}{2} \quad \text{and} \quad I_{\text{cir}} = \frac{I_{s1} - I_{s2}}{2} \quad (4.1.14)$$

are the average current common in both arms and the current circulating in the loop, respectively. Note that only the latter generates a net magnetic flux in the loop with the total flux then given by

$$\begin{aligned} \Phi &= \Phi_{\text{ext}} + LI_{\text{cir}} = \Phi_{\text{ext}} + \frac{LI_c}{2} (\sin \varphi_1 - \sin \varphi_2) \\ &= \Phi_{\text{ext}} + LI_c \sin\left(\frac{\varphi_1 - \varphi_2}{2}\right) \cos\left(\frac{\varphi_1 + \varphi_2}{2}\right) . \end{aligned} \quad (4.1.15)$$

Using (4.1.8), we can write the total flux threading the loop as a function of Φ_{ext} and φ_1 :⁹

$$\boxed{\Phi = \Phi_{\text{ext}} - LI_c \sin\left(\pi \frac{\Phi}{\Phi_0}\right) \cos\left(\varphi_1 + \pi \frac{\Phi}{\Phi_0}\right)} . \quad (4.1.16)$$

We see that we have now two equations, (4.1.9) and (4.1.16), which determine the behavior of the dc-SQUID. These two equations have to be solved self-consistently. The maximum current I_s^m that can be sent through the SQUID at a given Φ_{ext} has to be found by maximizing (4.1.9) with respect to φ_1 , however, with the constraint given by (4.1.16). This problem has been solved first by **R. de Bruyn Ouboter and A.Th.A.M. de Waele**.¹⁰

In order to analyze limiting cases we introduce the so-called *screening parameter* β_L defined as

$$\beta_L \equiv \frac{2LI_c}{\Phi_0} . \quad (4.1.17)$$

This parameter represents the ratio of the magnetic flux generated by the maximum possible circulating current $I_{\text{cir}} = I_c$ and $\Phi_0/2$. We also see that for $\beta_L = 1$ the coupling energy $2E_J = 2\hbar I_c/2e = \Phi_0 I_c/\pi$ of the two Josephson junctions is, apart from a factor $4/\pi$, equal to the magnetic energy $\Phi_0^2/8L$ due to the magnetic flux $\Phi_0/2$ stored in the superconducting loop.

⁹Here, we use $\sin(-\alpha) = -\sin \alpha$.

¹⁰ R. de Bruyn Ouboter, A.Th.A.M. de Waele, *Superconducting Point Contacts Weakly Connecting Two Superconductors*, Progress in Low Temp. Phys. VI, C.J. Gorter ed., Elsevier Science Publishers (1970).

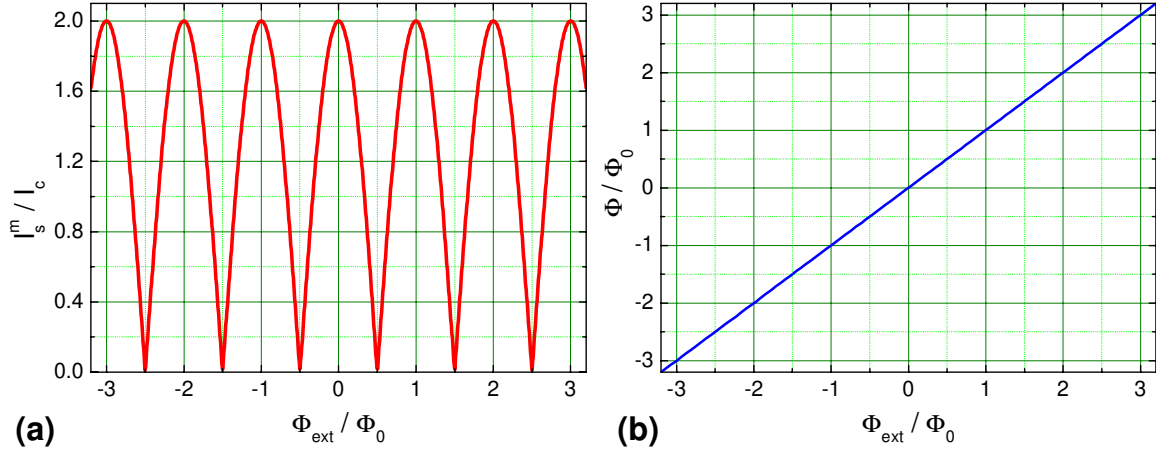


Figure 4.2: (a) The maximum supercurrent I_s^m plotted versus the applied magnetic flux Φ_{ext} for a dc-SQUID with two identical Josephson junctions in the limit $\beta_L \ll 1$. In (b) the flux threading the SQUID loop is plotted versus the applied flux Φ_{ext} .

Negligible Screening: $\beta_L \ll 1$

In the case $\beta_L \ll 1$ the flux generated by the circulating current is small compared to the flux quantum and therefore can be neglected compared to Φ_{ext} . At a given Φ_{ext} the maximum supercurrent of the dc-SQUID is found by maximizing (4.1.9) with respect to φ_1 . From the condition $dI_s/d\varphi_1 = 0$ we obtain

$$\cos\left(\varphi_1 + \pi \frac{\Phi_{\text{ext}}}{\Phi_0}\right) = 0. \quad (4.1.18)$$

Thus, at the maximum we have $\sin\left(\varphi_1 + \pi \frac{\Phi_{\text{ext}}}{\Phi_0}\right) = \pm 1$ and the maximum value of the supercurrent is found by taking the sign of the sine term. That is, we obtain the result

$$I_s^m \simeq 2I_c \left| \cos\left(\pi \frac{\Phi_{\text{ext}}}{\Phi_0}\right) \right|, \quad (4.1.19)$$

which is of course equivalent to (4.1.10). As shown in Fig. 4.2, I_s^m is a periodic function of the external flux. Note that for a loop area of 2 mm^2 an applied field of 1 nT results in $\Phi_{\text{ext}} = \Phi_0$, that is, the periodicity of the curve corresponds to the very small field of 1 nT , which is more than four orders of magnitude smaller than the earth magnetic field.

Large Screening: $\beta_L \gg 1$

For large inductance L we have $LI_c \gg \Phi_0$ and the circulating current tends to compensate the applied flux. The loop of the SQUID looks more and more like the single loop formed by a superconducting wire. This situation was discussed already in section 1.2 when we discussed flux quantization in multiply connected superconductors. Consequently, the total flux in the loop will tend to be quantized:

$$\Phi = \Phi_{\text{ext}} + LI_{\text{cir}} \simeq n\Phi_0. \quad (4.1.20)$$

Let us consider the case of large screening a bit more closely. The transport supercurrent through the SQUID is the sum of the currents passing junction 1 and 2:

$$I_s = I_c \sin \varphi_1 + I_c \sin \varphi_2. \quad (4.1.21)$$

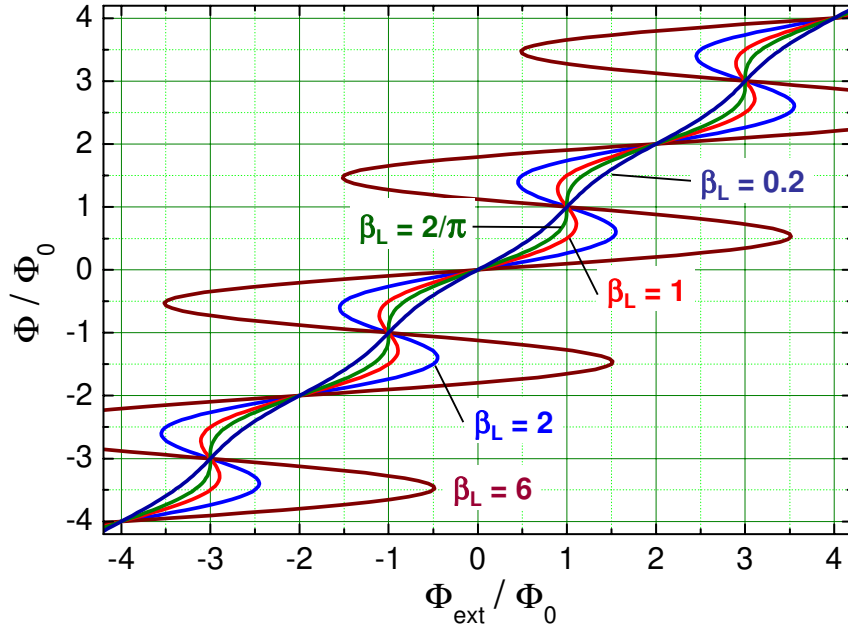


Figure 4.3: The total magnetic flux Φ plotted versus the applied magnetic flux Φ_{ext} for a dc-SQUID with two identical Josephson junctions for different values of the screening parameter β_L .

On the other hand, the circulating screening current is given by

$$I_{\text{cir}} = \frac{I_c}{2} (\sin \varphi_1 - \sin \varphi_2) . \quad (4.1.22)$$

Both (4.1.21) and (4.1.22) are constraint by the condition

$$\varphi_2 - \varphi_1 = \frac{2\pi\Phi}{\Phi_0} . \quad (4.1.23)$$

Note that here the magnetic flux is the sum of the external flux Φ_{ext} and the flux $\Phi_{\text{cir}} = LI_{\text{cir}}$ due to the screening current. Given the applied current I and the total flux Φ we have two equations for the two phase differences $\varphi_{1,2}$ and hence can solve for them and finally for Φ_{cir} and Φ_{ext} . For example, if $I \simeq 0$, we have $\sin \varphi_1 \simeq -\sin \varphi_2$ and obtain

$$\begin{aligned} \Phi_{\text{ext}} &= \Phi + LI_c \sin \left(\pi \frac{\Phi}{\Phi_0} \right) \quad \text{or} \\ \frac{\Phi_{\text{ext}}}{\Phi_0} &= \frac{\Phi}{\Phi_0} + \frac{\beta_L}{2} \sin \left(\pi \frac{\Phi}{\Phi_0} \right) . \end{aligned} \quad (4.1.24)$$

This relationship of course can be inverted to obtain Φ as a function of Φ_{ext} as shown in Fig. 4.3.

An interesting case occurs for $\Phi = n\Phi_0$, for which $\varphi_1 = \varphi_2 + n2\pi$, so that $I_{\text{cir}} = 0$ and $\Phi = \Phi_{\text{ext}}$. We see that the SQUID response to Φ_{ext} in integer multiples of Φ_0 is not affected by the screening. However, for practical applications it is often required that the relation between Φ and Φ_{ext} is single-valued and non-hysteretic. As shown by Fig. 4.3 this is possible only for small values of the screening parameter β_L . This results from the fact that the maximum possible value of Φ_{cir} is LI_c . Since roughly speaking a multivalued relationship between Φ and Φ_{ext} can be avoided only for $|\Phi_{\text{cir}}| \leq \Phi_0/2$, we immediately see that this is equivalent to $LI_c \leq \Phi_0/2$ or $\beta_L = 2LI_c/\Phi_0 \leq 1$. A more detailed analysis shows that a hysteretic $\Phi(\Phi_{\text{ext}})$ dependence can be avoided for $\beta_L \leq 2/\pi$.

We still have to discuss the dependence of the supercurrent on the applied magnetic flux. From (4.1.20) we obtain for large β_L

$$I_{\text{cir}} \simeq -\frac{\Phi_{\text{ext}} - n\Phi_0}{L} . \quad (4.1.25)$$

We see that $I_{\text{cir}} \rightarrow 0$ for large L . Then, the applied current divides about equally in the two SQUID arms. The maximum current is obtained to $I_s^m \simeq 2I_c$. When n is initially zero, a small screening current $I_{\text{cir}} \simeq -\Phi_{\text{ext}}/L$ will flow to screen the applied magnetic field. Therefore, the current I_1 will tend to decrease and I_2 to increase with increasing Φ_{ext} . However, since $I_2 \leq I_c$, it will be fixed at I_c as I_1 decreases as

$$I_1 \simeq I_c - \frac{2\Phi_{\text{ext}}}{L} . \quad (4.1.26)$$

With this expression for I_1 and $I_2 \simeq \text{const} \simeq I_c$ we obtain

$$I_s^m \simeq 2I_c - \frac{2\Phi_{\text{ext}}}{L} \quad \text{or} \quad (4.1.27)$$

$$\frac{I_s^m}{2I_c} \simeq 1 - \frac{2\Phi_{\text{ext}}}{\Phi_0} \frac{1}{\beta_L} . \quad (4.1.28)$$

We see that the modulation of the maximum supercurrent of the SQUID by the applied magnetic flux is strongly decreasing with increasing β_L roughly proportional to $1/\beta_L$.

4.1.2 The Voltage State

Practical dc-SQUIDs are not operated in the zero voltage state. They are operated at a constant bias current above the maximum supercurrent $I_s^m(0)$ at zero applied magnetic flux. That is, the SQUID is in the voltage state. We will show that in this situation the dc-SQUID produces an output voltage that is related to the applied magnetic flux.

Negligible screening: $\beta_L \ll 1$, strong damping: $\beta_C \ll 1$

In order to discuss the dependence of the SQUID voltage on the applied magnetic flux we start with the limit of negligible screening. In this case the total flux in the SQUID loop is just given by the applied flux. We further assume that the junction capacitance is negligible small, that is, we consider the case of strongly overdamped Josephson junctions ($\beta_C \ll 1$) and that the two junctions are identical. Then, we only have to consider the Josephson current and the resistive current giving

$$\begin{aligned} I &= I_c \sin \varphi_1 + I_c \sin \varphi_2 + \frac{V}{R_N} + \frac{V}{R_N} \\ &= 2I_c \cos \left(\pi \frac{\Phi}{\Phi_0} \right) \sin \left(\varphi_1 + \pi \frac{\Phi}{\Phi_0} \right) + 2 \frac{V}{R_N} . \end{aligned} \quad (4.1.29)$$

Here, we have used (4.1.1) and (4.1.8). Let us define the new phase

$$\varphi = \varphi_1 + \pi \frac{\Phi}{\Phi_0} \quad (4.1.30)$$

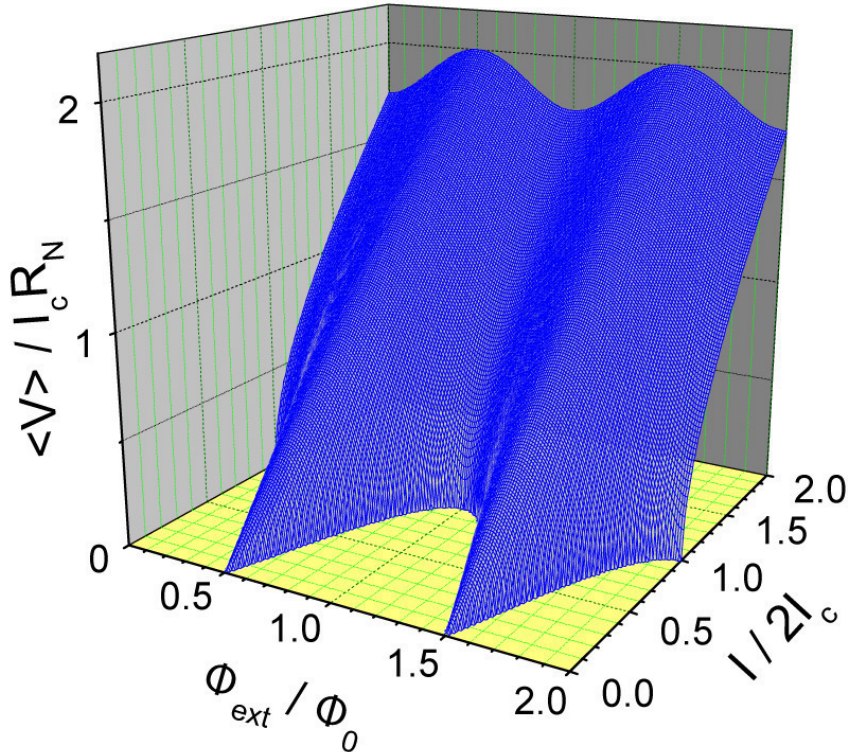


Figure 4.4: Current-voltage characteristics of a dc-SQUID in the limit $\beta_L \ll 1$, $\beta_C \ll 1$ for different values of the applied magnetic flux Φ_{ext} for a dc-SQUID with two identical Josephson junctions.

and note that due $\Phi \simeq \Phi_{\text{ext}} = \text{const}$ we have

$$\frac{d\varphi}{dt} = \frac{d\varphi_1}{dt} = \frac{2\pi}{\Phi_0} V(t) . \quad (4.1.31)$$

Then, we can rewrite (4.1.29) as

$$I = I_s^m(\Phi_{\text{ext}}) \sin \varphi + \frac{2}{R_N} \frac{2\pi}{\Phi_0} \frac{d\varphi}{dt} \quad (4.1.32)$$

with

$$I_s^m(\Phi_{\text{ext}}) = 2I_c \cos \left(\pi \frac{\Phi_{\text{ext}}}{\Phi_0} \right) . \quad (4.1.33)$$

We see, that equation (4.1.32) represents the equation of a single Josephson junction with a maximum Josephson current that depends on the external flux. For a single junction we have used the pendulum as a mechanical analog. In the same way we can use two pendula that are coupled to each other as the analogue for the dc-SQUID. In the case of negligible screening ($\beta_L \ll 1$) the coupling of the two pendula is rigid as can be seen from (4.1.30) and they move with the same angular velocity according to (4.1.31). Note that the rigid coupling is no longer true for significant screening ($\beta_L \geq 1$).

Due to the equivalence of the dc-SQUID with a single junction having a flux dependent maximum Josephson current, the current-voltage characteristic of the dc-SQUID is just given by the RSJ-model

result (3.3.8):

$$\langle V(t) \rangle = I_c R_N \sqrt{\left(\frac{I}{2I_c}\right)^2 - \left(\frac{I_s^m(\Phi_{\text{ext}})}{2I_c}\right)^2} = I_c R_N \sqrt{\left(\frac{I}{2I_c}\right)^2 - \left[\cos\left(\pi \frac{\Phi_{\text{ext}}}{\Phi_0}\right)\right]^2}. \quad (4.1.34)$$

The IVCs obtained according to this equation are shown in Fig. 4.4. It can be seen that the IVCs are periodic with the applied magnetic flux with the periodicity of a single flux quantum. Considering the time-averaged junction voltage as a function of the applied flux for different values of the bias current we see that these curves are also periodic with the same periodicity. Furthermore, the minima and maxima of the $\langle V \rangle(\Phi_{\text{ext}})$ always appear at the same flux values. Fig. 4.4 also shows the $\cos \pi \Phi_{\text{ext}} / \Phi_0$ dependence of the zero voltage supercurrent through the SQUID. Furthermore, it is seen that the maximum modulation of the time-averaged voltage with varying applied flux occurs for $I \simeq 2I_c$.

Finite screening: $\beta_L \sim 1$, **intermediate damping:** $\beta_C \sim 1$

For practical SQUIDs the inductance L of the loop containing the Josephson junctions must be taken into account. As already discussed above, the loop area should be made large in order to increase the flux threading the SQUID at a given field value. However, a large loop area can not be obtained without increasing the loop inductance. Furthermore, for typical Josephson junctions we cannot neglect the displacement current due to the finite junction capacitance as well as the fluctuating noise current. In this general case the dc-SQUID circuit is governed by a set of time-dependent nonlinear equations that must be solved numerically.

The phase differences across the two junctions have to satisfy the following equations:^{11,12,13}

$$V = \frac{\Phi_0}{4\pi} \left(\frac{d\varphi_1}{dt} + \frac{d\varphi_2}{dt} \right) \quad (4.1.35)$$

$$2\pi n = \varphi_2 - \varphi_1 - 2\pi \frac{\Phi_{\text{ext}}}{\Phi_0} - 2\pi \frac{LI_{\text{cir}}}{\Phi_0} \quad (4.1.36)$$

$$\frac{I}{2} = \frac{\hbar C}{2e} \frac{d^2\varphi_1}{dt^2} + \frac{\hbar}{2eR_N} \frac{d\varphi_1}{dt} + [I_c \sin \varphi_1 + I_{\text{cir}}] + I_{F1} \quad (4.1.37)$$

$$\frac{I}{2} = \frac{\hbar C}{2e} \frac{d^2\varphi_2}{dt^2} + \frac{\hbar}{2eR_N} \frac{d\varphi_2}{dt} + [I_c \sin \varphi_2 - I_{\text{cir}}] + I_{F2}. \quad (4.1.38)$$

Equation (4.1.35) relates the SQUID voltage to the rate of phase change. Note that for negligible screening we have $\frac{d\varphi_1}{dt} = \frac{d\varphi_2}{dt}$ and the usual voltage-phase relation is recovered. For finite screening this is no longer the case and we have $\frac{d\varphi_1}{dt} \neq \frac{d\varphi_2}{dt}$. Equation (4.1.36) expresses the fluxoid quantization in the superconducting loop. We see that in contrast to negligible screening (compare (4.1.8)) we have to take into account also the flux LI_{cir} due to the finite inductance of the loop. Equations (4.1.37) and (4.1.38) are Langevin equations coupled via I_{cir} . These coupled equations have to be solved numerically under the constraint given by (4.1.36) as a function of the screening parameter $\beta_L = 2LI_c/\Phi_0$, the Stewart-McCumber parameter $\beta_C = 2\pi I_c R_N^2 C / \Phi_0$ and the thermal noise parameter $\gamma = 2\pi k_B T / I_c \Phi_0$.

¹¹C.D. Tesche, J. Clarke, *dc-SQUID: Noise and Optimization*, J. Low Temp. Phys. **27**, 301 (1977).

¹²J.J.P. Bruines, V.J. de Waal, J.E. Mooij, J. Low Temp. Phys. **46**, 383 (1982).

¹³V.J. de Waal, P. Schrijner, R. Llurba, *Simulation and Optimization of a dc-SQUID with Finite Capacitance*, J. Low Temp. Phys. **54**, 215 (1984).

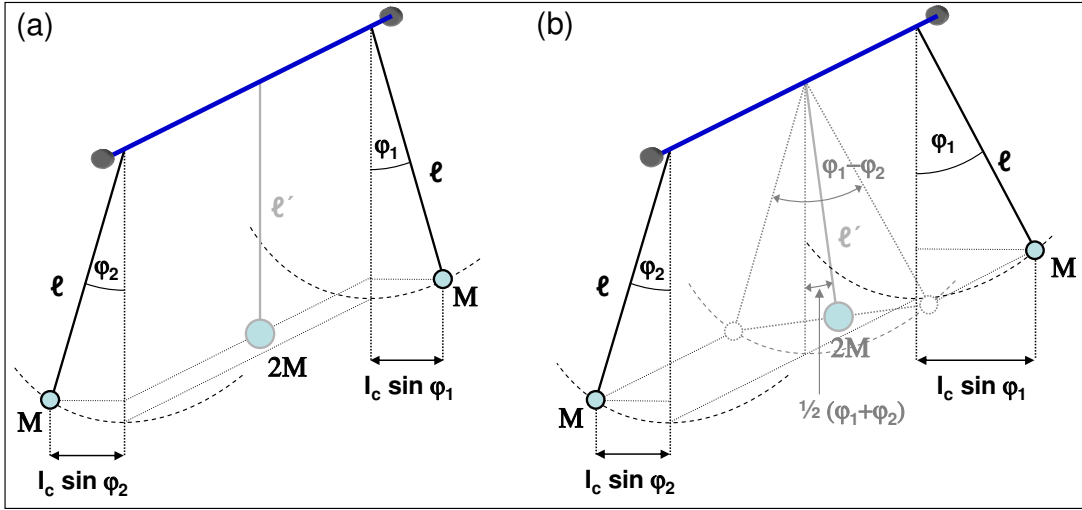


Figure 4.5: The pendulum analogue of a dc SQUID. The pendula are rigidly attached to the bar and the bar can rotate. At negligible screening ($\beta_L \ll 1$) the bar connecting the two pendula is rigid resulting in a combined pendulum with mass $2M$ at the center of mass. (a) Zero applied bias current and (b) finite bias current. The combined pendulum is shown in the center using grey lines.

Mechanical Analogue

We can gain insight into the equations of motion of a dc-SQUID by the pendulum analogue (see Fig. 4.5) already used for the single Josephson junction. The dc-SQUID formed by two identical junctions can be modeled by two pendula with the same mass M and length ℓ hanging from the same pivot point with the two pendula coupled via a twistable bar. The case of negligible screening ($\beta_L = 0$) corresponds to the case that the connecting bar is rigid. The relative angle $\varphi_1 - \varphi_2 = 2\pi\Phi_{\text{ext}}/\Phi_0$ is fixed by the external flux. That is, in effect we have to deal with a single combined pendulum with its full mass $2M$ located at the center of mass halfway between the two individual masses, which is at distance $\ell' = \ell \cos[\frac{1}{2}(\varphi_1 - \varphi_2)]$ from the pivot point. Alternatively, we can consider the net gravitational torque (corresponding to the net critical current) as the vector sum of those of the two pendula. In the absence of an applied torque (applied current) the combined pendulum hangs with the center of mass pointing down with the individual pendula at $\frac{1}{2}(\varphi_1 - \varphi_2)$ on either side (see Fig. 4.5a). Note that for $(\varphi_1 - \varphi_2) = \pi$ corresponding to $\Phi_{\text{ext}} = \Phi_0/2$ the center of mass is at the pivot point. As a torque (bias current) is applied this is rotating the combined pendulum (see Fig. 4.5b). The circulating current $I_{\text{cir}} = \frac{1}{2}(I_c \sin \varphi_1 - \sin \varphi_2)$ is half the difference of the horizontal projections of the two pendula.

In the case of finite screening ($\beta_L > 0$) the situation is a little bit more complicated, since now the bar connecting the two pendula is no longer rigid but flexible. We can regard it as a torsional spring on the rotation axis with a loose spring corresponding to a large loop inductance and hence a large screening effect. An applied flux again results in a finite angle $\varphi_1 - \varphi_2 = 2\pi\Phi/\Phi_0$, which is given now by the total flux $\Phi = \Phi_{\text{ext}} + L I_{\text{cir}}$. For a large inductance L the applied flux is well screened by the circulating current so that $\Phi \sim 0$. That means, that also $\varphi_1 - \varphi_2 \sim 0$ at zero bias current. This is evident from our mechanical analogue. A large inductance corresponds to a loose spring connecting the pendula. Hence, the applied flux tries to rotate the pendula in opposite directions but they will stay in their bottom position and twist the loose spring connecting them. Due to the loose spring the difference $\varphi_1 - \varphi_2$ is no longer constant as in the case of negligible screening and hence $\frac{d\varphi_1}{dt} \neq \frac{d\varphi_2}{dt}$. As the inductance becomes smaller the connecting spring becomes stiffer and finally rigid at $\beta_L \rightarrow 0$.

4.1.3 Operation and Performance of dc-SQUIDs

The principle of operation of a dc-SQUID is shown in Fig. 4.6. The two junctions, which are modeled by the RCSJ model, are connected in parallel in a superconducting loop with inductance L . In order to eliminate hysteretic IVCs, the Stewart-McCumber parameter of the junctions is restricted to $\beta_C \leq 1$. In practice, this is usually achieved by using external shunt resistors (see Fig. 4.11). The IVCs of the SQUID depend on the applied magnetic flux as shown in Fig. 4.4 for $\beta_C \ll 1$ and $\beta_L \ll 1$. In Fig. 4.6b only the IVCs with the largest ($\Phi_{\text{ext}} = n\Phi_0$) and the smallest critical current ($\Phi_{\text{ext}} = (n + \frac{1}{2})\Phi_0$) are shown. When the SQUID is biased at a constant current $I > 2I_c$, the time-averaged voltage $\langle V \rangle$ of the SQUID varies periodically with the applied flux with period Φ_0 as shown in Fig. 4.6c.

For practical applications the flux threading the loop has to be measured with high resolution. Therefore, the SQUID is operated at the steepest part of the $\langle V \rangle(\Phi_{\text{ext}})$ curve, where the *flux-to-voltage transfer coefficient*

$$H \equiv \left| \left(\frac{\partial V}{\partial \Phi_{\text{ext}}} \right)_{I=\text{const}} \right| \quad (4.1.39)$$

is a maximum. We see that the dc-SQUID can be considered as a flux-to-voltage transducer, which produces an output voltage in response to small variations of the input flux.

The resolution of the SQUID can be characterized by the *equivalent flux noise* $\Phi_F(t)$, which has the power spectral density

$$S_\Phi(f) = \frac{S_V(f)}{H^2} \quad (4.1.40)$$

at a given frequency f . Here, $S_V(f)$ is the power spectral density of the voltage noise across the SQUID at a fixed bias current. The flux noise power spectral density is inconvenient for comparing the noise in SQUIDs with different values of the loop inductance. A more convenient characterization of the noise is to use the *noise energy* $\varepsilon(f)$ associated with $S_\Phi(f)$:

$$\varepsilon(f) = \frac{S_\Phi(f)}{2L} = \frac{S_V(f)}{2LH^2}. \quad (4.1.41)$$

The noise energy of the dc-SQUID sets the energy resolution of the SQUID, which for practical applications should be as small as possible. For a given $S_V(f)$ we therefore have to maximize H and L . Using a plausibility consideration we see the following:

1. **Bias current I :** In order to maximize H we should choose a bias current just above $2I_c$, since here the modulation of the $\langle V \rangle(\Phi_{\text{ext}})$ curve is largest.
2. **Flux bias:** For optimum bias current the flux bias should be close to $(2n + 1)\Phi_0/4$, since here H is maximum.

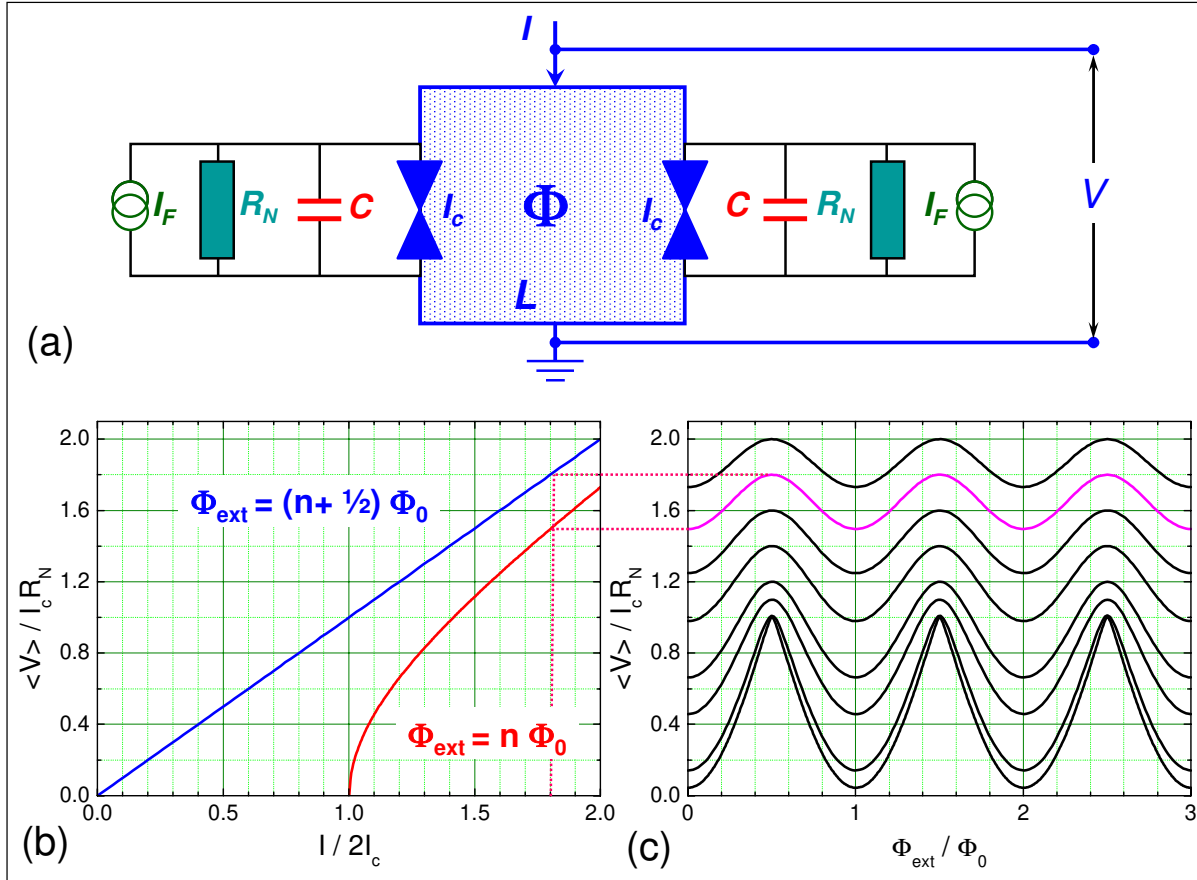


Figure 4.6: (a) The equivalent circuit of a dc-SQUID, (b) the current-voltage characteristics for two different values of the applied magnetic flux ($\Phi_{\text{ext}} = n\Phi_0$ and $\Phi_{\text{ext}} = (n + 1/2)\Phi_0$) and (c) the time-averaged voltage plotted versus the applied flux for different values of the bias current ($I/2I_c = 1.001, 1.01, 1.1, 1.2, 1.4, 1.6, 1.8$, and 2.0).

3. **Junction critical current I_c :** The junction critical currents should be much larger than the thermal noise current, or equivalently, the coupling energy $I_c\Phi_0/2\pi$ should be much larger than the thermal energy $k_B T$. In this way, noise rounding of the IVCs as shown in Fig. 3.18 is avoided, which would deteriorate H . Computer simulations show that¹⁴

$$\frac{1}{5} \cdot I_c \gtrsim I_{\text{th}} \equiv \frac{2\pi k_B T}{\Phi_0} \quad (4.1.42)$$

is sufficient. At 4.2 K this condition, which is equivalent to asking for a sufficient coupling of the phases of the superconducting wave functions across the two Josephson junctions, implies that $I_c \gtrsim 1 \mu\text{A}$.

4. **The loop inductance L :** The loop inductance should be as large as possible for optimum sensitivity. However, at a given temperature T the thermal energy $k_B T$ causes a root mean square thermal noise flux in the loop, $\langle \Phi_{\text{th}}^2 \rangle^{1/2} = \sqrt{k_B T L}$. This noise flux should be considerably smaller than Φ_0 giving an upper bound for L . We can define a thermal inductance L_{th} as the inductance value, for which the thermal noise current I_{th} generates just half a flux quantum in the loop, that is $L_{\text{th}} I_{\text{th}} = \Phi_0/2$ or $2L_{\text{th}} I_{\text{th}}/\Phi_0 = 1$. In order to keep the effect of thermal fluctuations small, the loop inductance L of the SQUID has to be sufficiently smaller than L_{th} . Again, computer simulations

¹⁴J. Clarke, R. Koch, *The Impact of High Temperature Superconductivity on SQUIDs*, Science **242**, 217 (1988).

show that

$$5 \cdot L \lesssim L_{\text{th}} \equiv \frac{\Phi_0}{2I_{\text{th}}} = \frac{\Phi_0^2}{4\pi k_B T} \quad (4.1.43)$$

is sufficient. This constraint, which is equivalent to asking for a sufficient coupling of the phase differences of the two junctions, implies that $L \lesssim 1 \text{ nH}$ at 4.2 K.

In analogy to the screening parameter β_L we can define the parameter

$$\beta_{\text{th}} = \frac{2I_{\text{th}}L}{\Phi_0} = \frac{L}{L_{\text{th}}} = \frac{I_{\text{th}}}{I_c} \beta_L = \gamma \beta_L \quad (4.1.44)$$

with $\gamma = I_{\text{th}}/I_c$ (compare (3.1.17)). This parameter is of crucial importance for the SQUID performance (see Fig. 4.7).

5. **The screening parameter β_L :** The screening parameter $\beta_L = 2I_c L / \Phi_0$ has to be smaller than unity to avoid hysteretic $\langle V \rangle(\Phi_{\text{ext}})$ curves. This condition can be easily satisfied by making L small. However, we already have seen that we should make L as large as possible to increase the SQUID sensitivity. Therefore, we should choose $\beta_L \simeq 1$, i.e. as large as possible. For $\beta_L \simeq 1$ and taking the smallest possible I_c value at 4.2 K ($\sim 1 \mu\text{A}$), we obtain $L \lesssim 1 \text{ nH}$, which is still compatible with the constraint given by (4.1.43).¹⁵
6. **The Stewart-McCumber parameter β_C :** The Stewart-McCumber parameter has to be smaller than unity in order to avoid hysteretic IVCs. For superconducting tunnel junctions, which intrinsically have large capacitance and hence $\beta_C \gg 1$, this is achieved by using an external shunt resistor smaller than the normal resistance of the junction (see Fig. 4.11). That is, in principle it is not a problem to satisfy the condition $\beta_C \leq 1$. However, using a small shunt resistor $R_{\text{shunt}} \ll R_N$ reduces the voltage amplitude of the $\langle V \rangle(\Phi_{\text{ext}})$ curves to $I_c R_{\text{shunt}} \ll I_c R_N$. Therefore, R_{shunt} should be as large as possible, that is, we have to choose $\beta_C \simeq 1$.

The detailed values of the parameters describing the performance of the SQUID have to be evaluated by numerical simulations.^{16,17,18,19} These simulations show that the noise energy of dc-SQUIDs has a minimum for $\beta_L \simeq 1$, $\beta_C \simeq 1$, for a flux bias close to $(2n+1)\Phi_0/4$ and for a bias current I , for which the voltage modulation of the $\langle V \rangle(\Phi_{\text{ext}})$ curves is largest. Since the maximum voltage modulation is about $I_c R_N$ we have

$$H \simeq \frac{I_c R_N}{\Phi_0/2} \simeq \frac{R_N}{L} \quad (4.1.45)$$

for $\beta_L \simeq 1$. In the white noise regime²⁰ the voltage noise of the SQUID can be estimated by splitting up the current noise power spectral density S_I into an in-phase part $S_I^{in} = 4k_B T / (R_N/2)$ and an out-of-phase

¹⁵Note that for high temperature superconductor dc-SQUIDs the operation temperature is about 20 times higher and therefore we have the constraint $I_c \gtrsim 20 \mu\text{A}$ and $L \lesssim 50 \text{ pH}$. Again, for $\beta_L \simeq 1$ we obtain with $I_c \simeq 20 \mu\text{A}$ an inductance value $L \lesssim 50 \text{ pH}$, which is compatible with the thermal constraint. However, due to the smaller inductance value it is in general more difficult to couple magnetic flux into the SQUID loop.

¹⁶C.D. Tesche, J. Clarke, *dc-SQUID: Noise and Optimization*, J. Low Temp. Phys. **27**, 301 (1977).

¹⁷D. Drung, W. Jutzi, IEEE Trans. Magn. **21**, 330 (1985).

¹⁸D. Kölle, R. Kleiner, F. Ludwig, E. Dantsker, J. Clarke, *High-transition-temperature superconducting quantum interference devices*, Rev. Mod. Phys. **71**, 631 (1999).

¹⁹J. Clarke, A.I. Braginski (eds.), *The SQUID Handbook*, Vol. 1: “Fundamentals and Technology of SQUIDS and SQUID Systems” Wiley-VCH, Weinheim (2004).

²⁰The low-frequency regime, where $1/f$ noise dominates is not discussed here.

part $S_I^{out} = 4k_B T / 2R_N$. Note that for the in-phase current fluctuations, which have the same direction in the two arms of the SQUID, the relevant resistance is $R_N/2$ due to the parallel connection of the two junction resistors. In contrast, for the out-of-phase part, which is in opposite direction in the two arms and results in a circulating current, the relevant resistance is $2R_N$ due to the series connection of the two junction resistors for the circulating current. In a small signal analysis the voltage noise power spectral density due to the in- and out-of-phase current fluctuations is given by^{21,22,23}

$$S_V(f) = S_I^{in}(f)R_d^2 + S_I^{out}(f)L^2H^2 = \frac{4k_B T}{R_N} \left[2R_d^2 + \frac{L^2 H^2}{2} \right], \quad (4.1.46)$$

where R_d is the differential resistance at the operation point. With the optimum values $H \sim R_N/L$ and $R_d \sim \sqrt{2}R_N$ obtained from numerical simulations we obtain

$$S_V(f) \approx \frac{4k_B T}{R_N} \left[4R_N^2 + \frac{R_N^2}{2} \right] = 18k_B T R_N. \quad (4.1.47)$$

The noise energy then can be estimated to

$$\epsilon(f) = \frac{S_V(f)}{2LH^2} \approx \frac{9k_B T L}{R_N} \approx \frac{9k_B T \Phi_0}{2I_c R_N} \quad \text{for } \beta_L \approx 1. \quad (4.1.48)$$

We see that the noise energy increases with temperature and decreasing $I_c R_N$ product of the Josephson junctions. If we eliminate R_N by using $\beta_C = 2\pi I_c R_N^2 C / \Phi_0 \approx 1$ and if we also eliminate L by using $\beta_L = 2I_c L / \Phi_0 \approx 1$ we obtain

$$\begin{aligned} \epsilon(f) &\approx 16k_B T \sqrt{\frac{LC}{\beta_C}} \\ &\approx 16\sqrt{\pi} k_B T \sqrt{\frac{\Phi_0 C_s}{2\pi J_c}} = \frac{16\sqrt{\pi} k_B T}{\omega_p} \quad \text{for } \beta_L \approx 1; \beta_C \approx 1. \end{aligned} \quad (4.1.49)$$

Here, $C_s = C/A$ is the specific junction capacitance and $J_c = I_c/A$ the critical current density of the junction. We see that we can improve the performance of the dc-SQUID by reducing the temperature as well as by decreasing the capacitance and by increasing the critical current density, i.e. by increasing the plasma frequency of the Josephson junctions. Today critical current densities above 10^3 A/cm^2 are used requiring junction areas of the order of $1 \mu\text{m}^2$ for realizing critical current values of a few μA . Until today, a large number of dc-SQUIDS has been studied and it was found that their performance agrees well with the predictions of the numerical simulations. Today it is common to quote the noise

²¹We note that in a more detailed analysis the voltage noise of a single Josephson junction at a measuring frequency f much smaller than the Josephson frequency f_J is given by

$$S_V(f) = \frac{4k_B T}{R_N} R_d^2 + \frac{4k_B T}{R_N} R_d^2 \frac{1}{2} \left(\frac{I_c}{I} \right)^2,$$

where the first term is the usual Nyquist noise and the second represents the Nyquist noise generated at frequencies $f_J \pm f$ mixed down to the measurement frequency by the Josephson oscillations due to the nonlinearity of the IVC. The factor $\frac{1}{2} \left(\frac{I_c}{I} \right)^2$ is the mixing coefficient, which vanishes at large bias currents $I \gg I_c$. Furthermore, at sufficiently high bias currents the Josephson frequency exceeds $k_B T/h$ and quantum corrections become important (compare section 3.5.5).

²²K.K. Likharev, V.K. Semonov, JETP Lett. **15**, 442 (1972).

²³R.H. Koch, D.J. van Harlingen, J. Clarke, Phys. Rev. Lett. **45**, 2132 (1980).

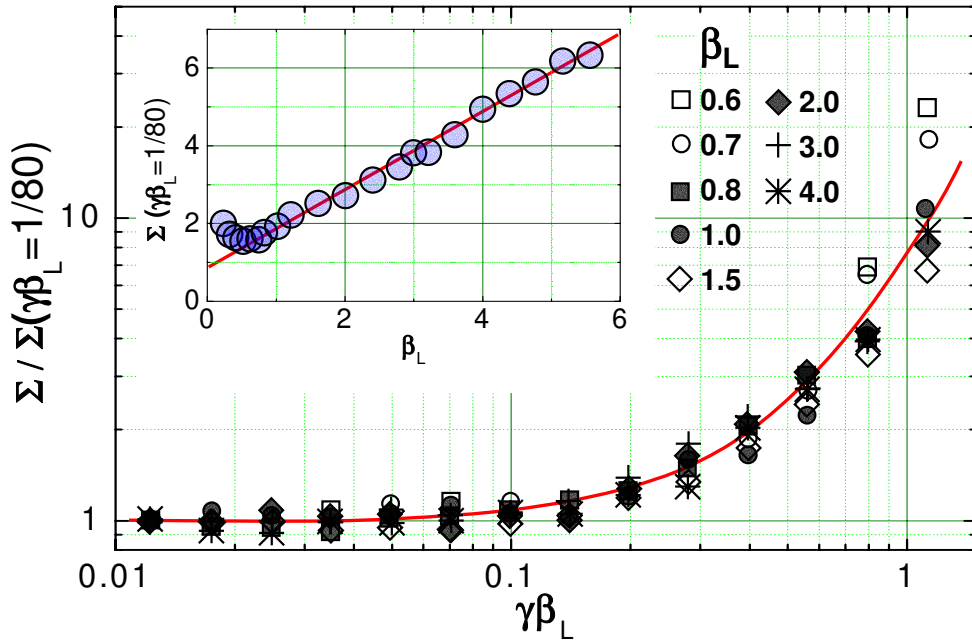


Figure 4.7: Calculated reduced energy resolution $\Sigma(\gamma\beta_L)$ normalized to $\Sigma(\gamma\beta_L = 1/80)$. Inset shows $\Sigma(\gamma\beta_L = 1/80)$ versus β_L (data from D. Kölle *et al.*, Rev. Mod. Phys. **71**, 631 (1999)).

energy of SQUIDs in units of $\hbar \simeq 10^{-34}$ Js. Optimized SQUIDs have a noise energy approaching the quantum limit \hbar . However, these SQUIDs have very low inductance and therefore are not useful for most applications requiring optimum magnetic field resolution. Best practical dc SQUIDs have reached an energy resolution of some $10\hbar$.²⁴

A recent result of a numerical simulation is shown in Fig. 4.7. Here, the reduced noise energy

$$\Sigma(f) = \frac{\epsilon(f)}{\frac{2\Phi_0 k_B T}{I_c R_N}} \quad (4.1.50)$$

is plotted versus the dimensionless parameter

$$\beta_{\text{th}} = \gamma\beta_L = \frac{2\pi k_B T}{I_c \Phi_0} \frac{2I_c L}{\Phi_0} = \frac{L}{\frac{\Phi_0^2}{4\pi k_B T}} \equiv \frac{L}{L_{\text{th}}} . \quad (4.1.51)$$

For $\gamma\beta_L \leq 0.2$ corresponding to $L \leq \frac{1}{5}L_{\text{th}}$, the reduced noise energy is almost constant, while for higher values of $\gamma\beta_L$ it increases rapidly. The rapid increase in noise energy arises from the rapid degradation of the transfer function with increasing $\gamma\beta_L = L/L_{\text{th}}$ due to thermal noise rounding of the IVCs.

4.1.4 Practical dc-SQUIDs

Practical dc-SQUIDs do not only consist of the SQUID loop discussed so far, but also of an antenna and a room temperature electronics as schematically shown in Fig. 4.8. The antenna has both to transfer the quantity that has to be measured into magnetic flux and to couple this flux effectively into the SQUID loop. The SQUID itself acts as a flux-to-voltage transducer. The room temperature electronics has to amplify the voltage signal as well as to provide the current and flux bias.

²⁴A.A. Jin, T.R. Stevenson, F.C. Wellstood, W.W. Johnson, IEEE Trans. Appl. Supercond. **AS-7**, 2742 (1997).

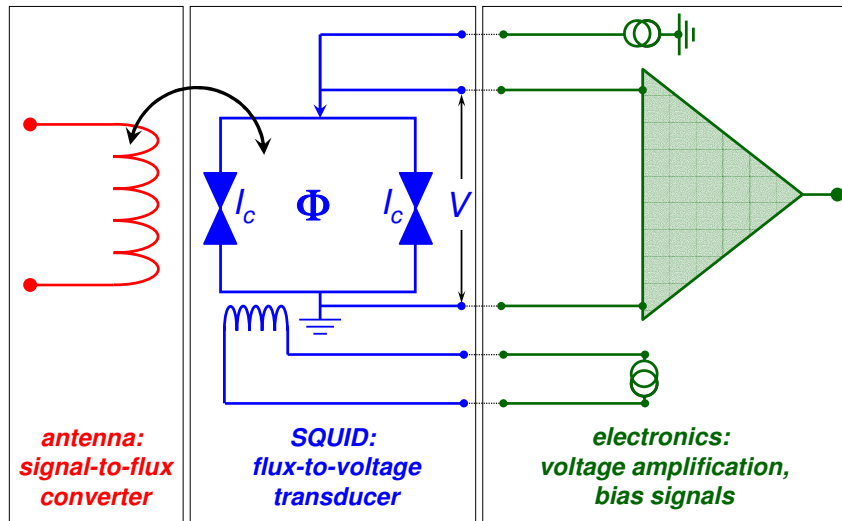


Figure 4.8: The practical dc-SQUID consisting of an antenna acting as a signal-to-flux converter, the SQUID loop acting as the flux-to-voltage transducer, and the room temperature electronics.

The Washer Type dc-SQUID

Obviously, a large area A of the SQUID loop is advantageous to increase the sensitivity of a SQUID, since small field changes ΔB then result in large flux changes $\Delta\Phi_{\text{ext}} = A \cdot \Delta B$. However, a large A also results in a large loop inductance L , which may deteriorate the SQUID performance as discussed above. Based on this conflicting requirements various SQUID designs have been developed. In the 1970ies and 1980ies, often three-dimensional loop geometries have been used for the realization of SQUIDs (e.g. by evaporation of a cylinder containing the Josephson junctions on a thin quartz thread).

Today dc-SQUIDs are based on thin film structures, which are patterned using optical and electron beam lithography. Here, a large effective loop area at small loop inductance can be achieved by making use of the perfect diamagnetism of superconductors. As shown in Fig. 4.9, instead of a narrow superconducting loop structure a broad “washer-type” structure can be used. Such geometries have been successfully used for high T_c dc-SQUIDs using grain boundary Josephson junctions.^{25,26,27} The washer design was first proposed by **M.B. Ketchen** and therefore these SQUID structures today are denoted as Ketchen-type SQUIDs.²⁸ This geometry also helps to overcome the problem of coupling the magnetic flux of the antenna system effectively to the SQUID loop of a thin film SQUID. In 1981 **M.B. Ketchen** and **J.M. Jaycox** introduced the idea of depositing a planar spiral input coil on a dc-SQUID in a square washer geometry.^{29,30} The thin film planar coil is separated from the SQUID washer only by a thin insulating layer. A typical washer type dc-SQUID is shown schematically in Fig. 4.11. The square washer forms the SQUID loop. It contains a narrow slit, which is closed by a superconducting line containing the two junctions, which are located at the outer rim of the washer.

For the washer geometry shown in Figs. 4.9 and 4.11, the loop currents circulate around the inner opening (hole or slit) of the washer, which then determines the inductance of the SQUID loop. **Jaycox** and **Ketchen** showed that a square washer with a hole of diameter D (without slit) and an outer edge W

²⁵R. Gross *et al.*, Appl. Phys. Lett. **57**, 727 (1990).

²⁶R. Gross *et al.*, Physica C **170**, 315 (1990).

²⁷D. Kölle *et al.*, Rev. Mod. Phys. **71**, 631 (1999).

²⁸M.B. Ketchen, IEEE Trans. Magn. **MAG-17**, 387 (1980).

²⁹M.B. Ketchen, J.M. Jaycox, *Ultra-low Noise Tunnel Junction dc-SQUID with a Tightly Coupled Planar Input Coil*, Appl. Phys. Lett. **40**, 736 (1982).

³⁰J.M. Jaycox, M.B. Ketchen, *Planar Coupling Scheme for Ultra-low Noise dc-SQUIDS*, IEEE Trans. Magn. **17**, 400 (1981).

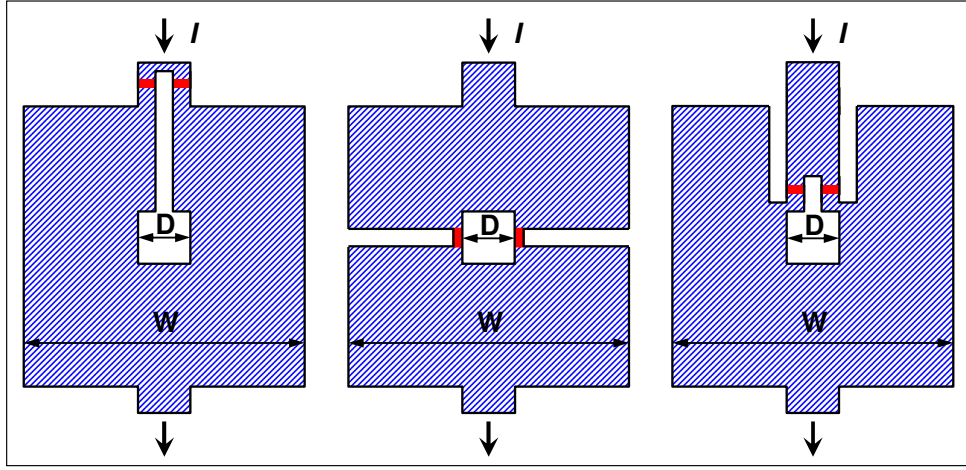


Figure 4.9: Sketch of various geometries for planar dc-SQUIDs with washer geometry.

has the inductance

$$L \simeq 1.25 \mu_0 D \quad (4.1.52)$$

in the limit $W \gg D$. That is, the loop inductance scales with the inner diameter D . In contrast, the effective area of the SQUID loop is³¹

$$A_{\text{eff}} \propto D \cdot W , \quad (4.1.53)$$

that is, it scales with the outer dimension of the washer. Of course, one cannot increase W arbitrarily, since for large W one starts to trap magnetic flux quanta in the washer area during cool down even in small magnetic fields. The thermally activated motion of these flux quanta generate disturbing $1/f$ -noise. An experimental example for the flux focusing effect is shown in Fig. 4.10 for a geometry shown in the inset. Here, A_{eff}/D^2 is plotted versus W^2/D^2 on a double logarithmic scale. In such plot a straight line with slope 1/2 is expected according to (4.1.53) in good agreement with the data.

We briefly address the inductance and the coupling of a spiral input coil that can be put on top of the washer as shown in Fig. 4.11. Neglecting the parasitic inductance associated with the Josephson junctions, the following expressions for the inductance L_i of the spiral input coil, the mutual inductance M_i and the coupling coefficient α^2 between the spiral and the SQUID loop are found:

$$L_i \simeq n^2 L + L_s \quad (4.1.54)$$

$$M_i \simeq \sqrt{n^2 L \cdot L} = nL \quad (4.1.55)$$

$$\alpha^2 \simeq \frac{1}{1 + L_s/n^2 L} . \quad (4.1.56)$$

Here, L_s is the stripline inductance of the spiral coil, n the number of turns of the spiral input coil and $n^2 L$ the geometric self-inductance of the input coil. For the estimate of M_i we have assumed that the flux due to a current flowing in the spiral input coil is perfectly coupled in the SQUID hole. The coupling coefficient α is obtained from the expression $\alpha = M_i / \sqrt{L_i L} = nL / \sqrt{(n^2 L + L_s)L}$. As an example, for $D = 20 \mu\text{m}$ we obtain $L \simeq 30 \text{ pH}$. For a 50 turn input coil we obtain $L_i \simeq 75 \text{ nH}$ ³² and $M_i \simeq 1.5 \text{ nH}$. The

³¹M.B. Ketchen, W.J. Gallagher, A.W. Kleinsasser, S. Murphy, J.R. Clem, in *SQUID'85*, H.D. Hahlbohm and H. Lübbig eds., Walther de Gruyter, Berlin (1985), p. 865.

³²The stripline inductance is usually negligible for a 50 turn coil.

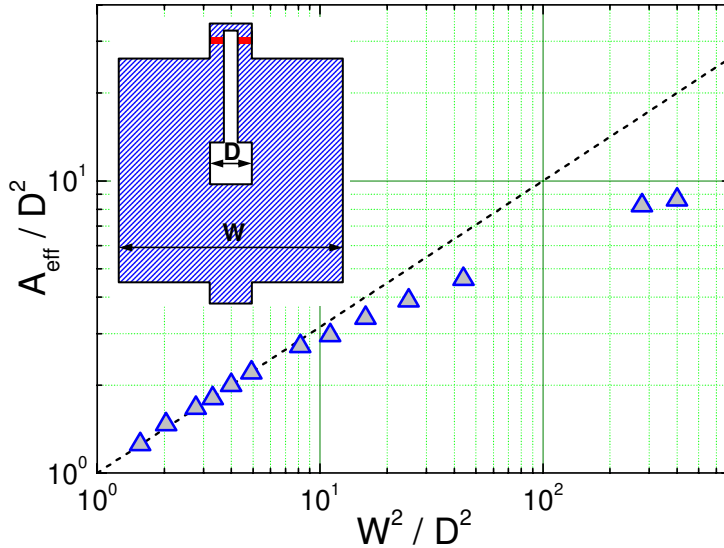


Figure 4.10: Flux focusing effect in a washer-type $\text{YBa}_2\text{Cu}_3\text{O}_{7-\delta}$ grain boundary junction dc SQUID measured at 77 K. The dashed line shows the theoretical dependence expected according to (4.1.53). The deviations at large W^2/D^2 values are caused by the finite slit inductance of the used washer geometry shown in the inset (data according to R. Gross *et al.*, Appl. Phys. Lett. **57**, 727 (1990)).

experimentally determined coupling coefficient typically ranges between 0.6 and 0.8. A specific problem of the washer-type dc SQUID geometry is the considerable capacitance between the spiral input coil and the square washer. This can result in *LC*-resonances. These resonances, in turn, result in structures in the IVCs, which can give rise to excess noise. The effect of the *LC*-resonances can be reduced by reducing the number of turns on the washer and thereby reducing the parasitic capacitance (in this case an intermediate superconducting transformer can be used to couple in the signal). On the other hand, the shunt resistance of the junctions can be decreased thereby increasing the damping.

Low- T_c dc-SQUIDs: Low- T_c dc SQUIDs are fabricated using standard multilayer thin film technology (cf. Fig. 4.11). In order to increase the energy sensitivity, Josephson junctions with a high plasma frequency have to be used. This is achieved by using high critical current density junctions, which allow to minimize the junction area and hence the junction capacitance. Although various materials combinations have been used so far, the most successful is the combination of niobium and aluminium. This combination is stable in time and not affected by thermal cycling. Furthermore, Nb/AlO_x/Nb tunnel junctions show a low level of $1/f$ noise due to critical current fluctuations compared to e.g. NbN/MgO/NbN junctions.

High- T_c dc-SQUIDs: Today high- T_c dc-SQUIDs are also fabricated using multilayer thin film technology. However, in contrast to low- T_c materials an heteroepitaxial growth of the different superconducting layers is required to avoid grain boundaries in the thin film structures. These are known to be responsible for a high level of $1/f$ -noise. A further problem in the fabrication of high- T_c dc-SQUIDs is the poor reproducibility of the junctions. Various junction types such as grain boundary junctions, ramp junctions or edge junctions have been used with different success.^{33,34}

Due to the problem of heteroepitaxial growth of multilayer structures the integration of the input coil

³³R. Gross, P. Chaudhari, *Status of dc-SQUIDS in the High Temperature Superconductors*, in *Principles and Applications of Superconducting Quantum Interference Devices*, pp. 419–479, A. Barone ed., World Scientific, Singapore (1992).

³⁴For a more recent review see D. Kölle *et al.*, Rev. Mod. Phys. **71**, 631 (1999).

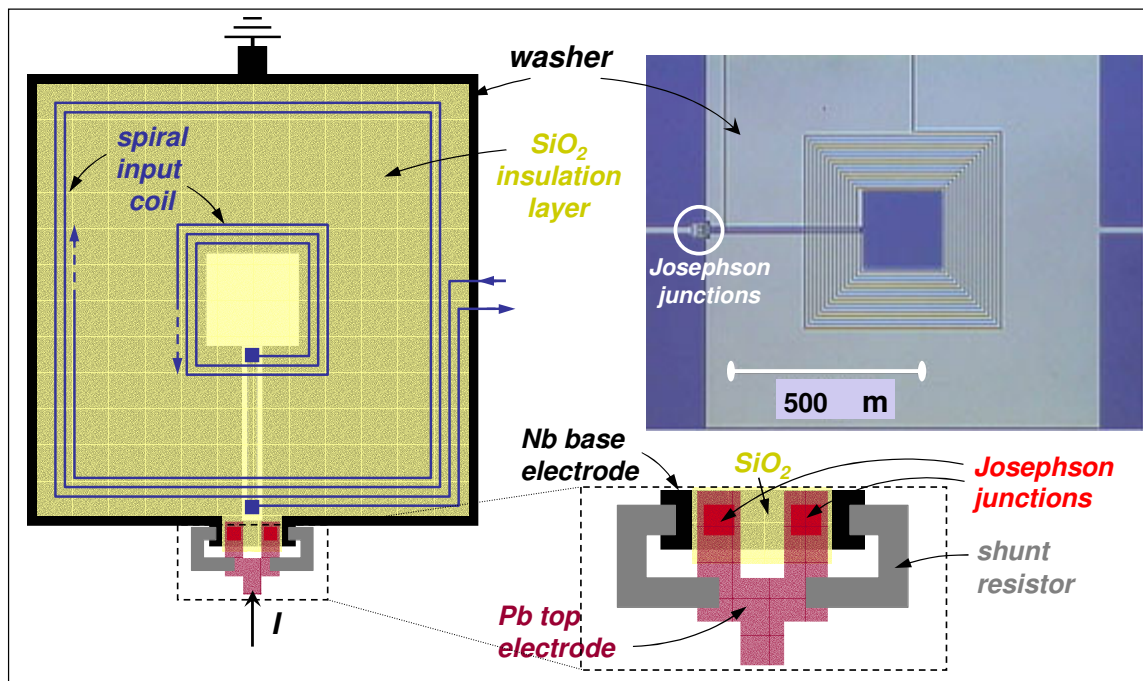


Figure 4.11: Sketch of a Nb/Pb dc-SQUID using a square washer geometry and a planar spiral input coil. The junction area is shown on an enlarged scale on the right. Also shown is an optical micrograph of a washer-type Pb/Nb dc-SQUID (by courtesy of J. Clarke).

on a washer structure is still a challenge for high- T_c SQUIDs.^{35,36} Therefore, often so-called flip-chip structures have been applied where the input coil is fabricated on a separate chip and then flip-chipped on the washer.³⁷

In order to avoid complicated multilayer structures it is also common to use directly coupled high- T_c dc-SQUIDs. Here, the SQUID loop is directly coupled to a parallel loop that acts as a signal pick-up loop. The big advantage of such directly coupled SQUIDs is the fact that only a single superconducting layer is required that can be grown with high quality on a single or bi-crystalline substrate. A schematic drawing of such a SQUID can be found in Fig. 4.22). For such directly coupled dc-SQUIDs field sensitivities down to $20 \text{ fT}/\sqrt{\text{Hz}}$ have been obtained in the white noise regime at 77 K.³⁸

4.1.5 Read-Out Schemes

The Flux-Locked Loop Operation

The $\langle V \rangle(\Phi_{\text{ext}})$ curves of the dc-SQUID are nonlinear. Therefore, a linear relation between an input signal and the output voltage is obtained only in the small signal limit. This problem can be solved by using the SQUID in a feedback circuit as a null-detector for magnetic flux.³⁹ One simply applies an oscillating magnetic flux with a peak-to-peak amplitude of about $\Phi_0/2$ and a frequency f_{mod} in the 100 kHz regime as shown in Fig. 4.12. If the quasistatic flux is exactly $n\Phi_0$, the resulting ac voltage is a rectified version

³⁵J.W.M. Hilgenkamp, G.C.S. Brons, J.G. Soldevilla, R.P. Ijsselstein, J. Flokstra, H. Rogalla, Appl. Phys. Lett. **64**, 3497-3499 (1994).

³⁶B. David, D. Grundler, J.P. Krumme, O. Doessel, IEEE Trans. Appl. Supercond. **AS-5**, 2935-2938 (1995).

³⁷P.A. Nilsson, Z.G. Ivanov, E.A. Stephanov, H.K. Hemmes, J.W.M. Hilgenkamp, J. Flokstra, Inst. Phys. Conf. Ser. **148**, 1537-1540 (1995), D. Dew-Hughes ed., Institute of Physics, Bristol.

³⁸D. Kölle, A.H. Micklich, F. Ludwig, E. Dantsker, D.T. Nemeth, J. Clarke, Appl. Phys. Lett. **63**, 2271-2273 (1993).

³⁹J. Clarke, W.M. Goubau, M.B. Ketchen, J. Low. Temp. Phys. **25**, 99 (1976).

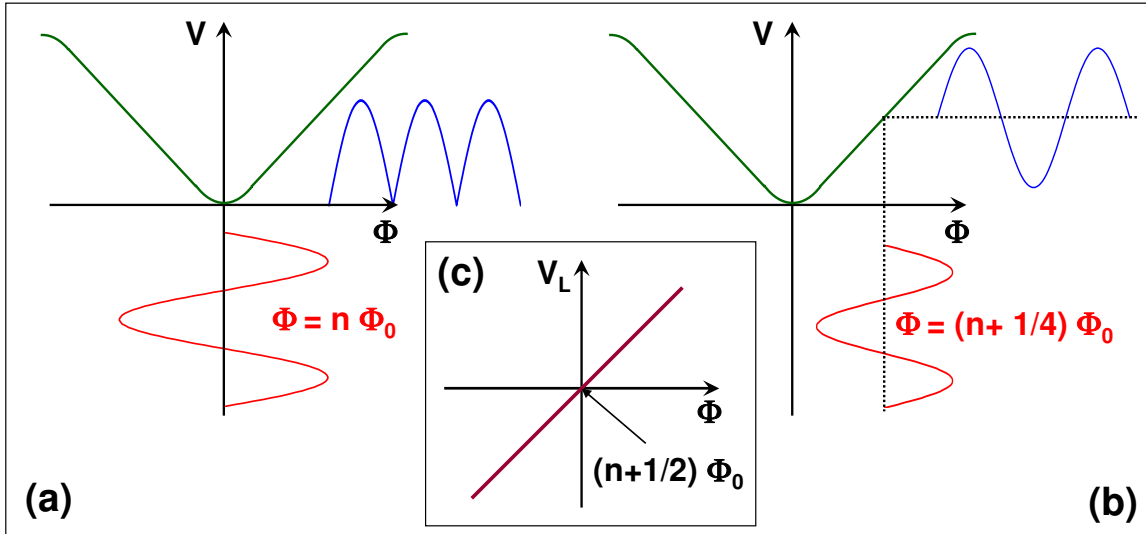


Figure 4.12: Flux modulation scheme for a dc-SQUID showing the voltage across the SQUID for (a) $\Phi = n\Phi_0$ and (b) $\Phi = (n + \frac{1}{4})\Phi_0$. In (c) the output signal V_L of the lock-in amplifier is plotted versus the applied flux.

of the input signal. That is, it contains only a $2f_{\text{mod}}$ frequency component. If this signal is detected by a lock-in amplifier referenced to the fundamental frequency f_{mod} , the resulting output voltage is zero. In contrast, if the quasistatic flux is $(n + \frac{1}{4})\Phi_0$, the voltage across the SQUID is at f_{mod} and the output signal from the lock-in amplifier will be maximum. Thus, increasing the flux from $n\Phi_0$ to $(n + \frac{1}{4})\Phi_0$ the lock-in output signal will increase, whereas it will increase in the negative direction on decreasing the flux from $n\Phi_0$ to $(n - \frac{1}{4})\Phi_0$. Instead of a sinusoidal a square-wave flux signal can be used. Then, for the operation point $\Phi = n\Phi_0$ and a peak-to-peak amplitude of $\Phi_0/2$ the SQUID is biased at the points of maximum slope of the $\langle V \rangle(\Phi_{\text{ext}})$ curve for each half-wave of the square-wave signal.

The ac voltage across the SQUID is usually coupled to a low noise preamplifier via a cooled transformer, which results in an increase of the low SQUID impedance from R_d to $N^2 R_d$, where R_d is the differential resistance of the SQUID at the operation point and N the turns-ratio of the transformer. One also can use a cooled LC series resonant circuit, which provides an impedance $Q^2 R_d$, where Q is the quality of the tank circuit. The values of N or Q are chosen to obtain an optimum impedance match between the SQUID and the room temperature preamplifier.

Fig. 4.13 shows the equivalent circuit of a dc-SQUID operated in the **flux-locked loop**. An oscillator applies a modulating flux to the SQUID and also serves as the reference for the lock-in amplifier. After amplification, the ac voltage signal from the SQUID is phase sensitively detected by the lock-in amplifier. The output voltage V_L of the lock-in amplifier is sent to an integrator. The output voltage of the integrator is decreasing and increasing for negative and positive V_L , respectively. The output signal of the integrator is connected to the SQUID via a resistor R_f to the feedback coil L_f . If we are applying a small flux change $+\delta\Phi$ to the SQUID, the lock-in will generate a positive output voltage proportional to $\delta\Phi$. The positive output signal will cause an increase of the integrator output voltage, which in turn is causing an increase of the current through the feedback coil. The integrator voltage will increase until the current through the feedback coil is sufficient to compensate the small applied flux change. Then, the total flux coupled to the SQUID and, in turn, the lock-in signal is zero and the integrator output voltage stays constant. We see that the SQUID is operating as a null detector.

The change δV_{in} of the integrator output voltage is directly proportional to the flux change $\delta\Phi$. With the change of the feedback current $\delta I_f = \delta V_{\text{in}}/R_f$ and the flux induced by the feedback current, $\delta\Phi_f = k^2 L_f \delta I_f$ (here k^2 is the coupling constant between the feedback coil and the SQUID loop), we obtain

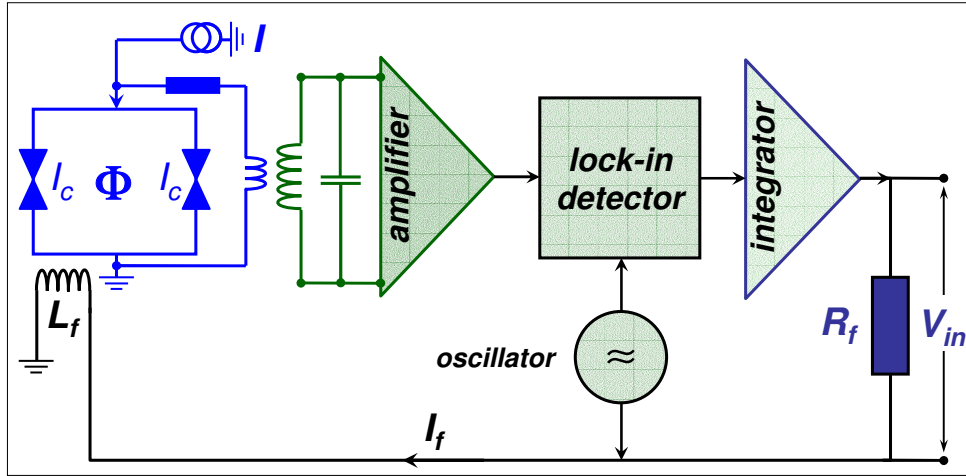


Figure 4.13: The modulation and feedback circuit of a dc-SQUID.

from the condition $|\delta\Phi_f| = |\delta\Phi|$

$$\delta V_{in} = \frac{R_f}{k^2 L_f} \delta\Phi . \quad (4.1.57)$$

We see that the output signal increases with increasing feedback resistance. Furthermore, the output signal is linear with $\delta\Phi$ even if the flux change is several Φ_0 .

The typical modulation frequency of the flux-locked loop circuit is from 100 kHz to several MHz. Using suitable electronics a very high dynamic range above 140 dB and a signal bandwidth of up to 100 kHz can be achieved. An important quantity is the slew rate, which gives the speed at which the feedback circuit can compensate for rapid flux changes at the input. State of the art SQUID electronics has slew rates of up to $10^7 \Phi_0/\text{s}$.

Bias Current Reversal: For dc-SQUIDs based on high temperature superconductors often the bias current is modulated in addition to the flux. The reason for that is that Josephson junctions based on high temperature superconductors usually show large low-frequency fluctuations of the critical current.^{40,41,42,43} These fluctuations can be eliminated by a periodic reversal of the bias current.^{44,45} Since the fluctuations of the critical current of the two junctions are independent, they can be separated in a symmetric and antisymmetric part. The symmetric part results in a shift of the $V(\Phi_{ext})$ curves along the voltage axis. This shift is eliminated by the flux modulation technique discussed above, since only the modulated signal at f_{mod} is detected by the lock-in amplifier. In contrast, the asymmetric part corresponds to a circulating current, which induces magnetic flux fluctuations and hence results in a shift of the $V(\Phi_{ext})$ curve along the flux axis. By a periodic reversal of the bias current at a frequency f_{rev} much larger than the low-frequency I_c -fluctuations one obtains a periodic shift of the $V(\Phi_{ext})$ curve in opposite directions. Then, by averaging over several periods also the asymmetric fluctuations can be eliminated.

⁴⁰R. Gross, P. Chaudhari, M. Kawasaki, A. Gupta, M. B. Ketchen, IEEE Trans. Magn. **MAG-27**, 2565 (1991).

⁴¹R. Gross, *Grain Boundary Josephson Junctions in the High Temperature Superconductors*, in *Interfaces in High- T_c Superconducting Systems*, S. L. Shinde and D. A. Rudman eds., Springer Verlag, New York (1994), pp. 176-210

⁴²A. Marx, L. Alff, R. Gross, IEEE Trans. Appl. Supercond. **7**, 2719 (1997).

⁴³A. Marx, R. Gross, Appl. Phys. Lett. **70**, 120 (1997).

⁴⁴R.H. Koch, J. Clarke, W. M. Goubau, J. M. Martinis, C. M. Pegrum, and D. J. Van Harlingen, J. Low Temp. Phys. **51**, 207 (1983).

⁴⁵V. Foglietti, W. J. Gallagher, M. B. Ketchen, A. W. Kleinsasser, R. H. Koch, S. I. Raider, and R. L. Sandstrom, Appl. Phys. Lett. **49**, 1393 (1986).

The application of both flux modulation and bias current reversal is called double modulation technique. It can reduce the low-frequency $1/f$ -noise of SQUIDs based on high temperature superconductors by several orders of magnitude.^{46,47}

Additional Positive Feedback: An important reason for the use of the flux modulation technique is the fact that the voltage changes $\delta V(\Phi_{\text{ext}})$ (typically less than $100 \mu\text{V}/\Phi_0$) and the SQUID impedance (typically a few Ω) are small. This is inadequate for semiconductor devices. Applying the flux modulation, the SQUID impedance can be increased by a step-up transformer and matched to the room temperature semiconductor electronics. An alternative way is to use the *additional positive feedback* (APF) technique, in which part of the bias current is used to obtain an asymmetric $V(\Phi_{\text{ext}})$ dependence with a steep slope and hence larger value for $\partial V/\partial\Phi$. In this case a direct read-out of the SQUID signal with low noise room temperature semiconductor electronics is possible.^{48,49}

Additional Topic: Digital Read-Out Schemes

Fujimaki et al.⁵⁰ and **Drung et al.**^{51,52} have developed schemes in which the output from the SQUID is digitized and fed back to the SQUID as an analog signal to flux-lock the loop. Fujimaki *et al.* used Josephson digital circuits to integrate their feedback system on the same chip as the SQUID. Drung *et al.* obtained a flux resolution of about $10^{-6}\Phi_0/\sqrt{\text{Hz}}$ in a 50 pH SQUID. They were also able to reduce the $1/f$ noise by using a modified bias current modulation scheme. In general, the cryogenic digital feedback schemes have the advantage that they are compact, offer wide flux-locked bandwidth and produce digitized output signals for transmission to room temperature.

Additional Topic: The Relaxation Oscillation Scheme

Mück and Heiden have operated a dc SQUID with hysteretic junctions in a relaxation oscillator.⁵³ Here, the SQUID is shunted by a series connection of an inductor and resistor. The circuit performs relaxation oscillations at a frequency depending on the flux in the SQUID. The oscillation frequency has a minimum for $(n + \frac{1}{2})\Phi_0$ and a maximum for $n\Phi_0$ with a typical frequency modulation of about 100 kHz at an oscillation frequency of about 10 MHz. The advantage of this scheme is that it produces a large voltage across the SQUID so that no matching network to the room temperature electronics is required. The room temperature electronics is allowed to be simple and compact. A flux resolution of about $10^{-5}\Phi_0/\sqrt{\text{Hz}}$ for a 80 pH SQUID operated at 4.2 K has been achieved. The so-called double relaxation oscillation SQUID (DROS) is briefly addressed in section 4.3.1.

⁴⁶R.H. Koch, W. Eidelloth, B. Oh, R. P. Robertazzi, S. A. Andrek, and W. J. Gallagher, *Appl. Phys. Lett.* **60**, 507 (1992).

⁴⁷A.H. Micklich, D. Koelle, E. Dantsker, D. T. Nemeth, J. J. Kingston, R. F. Kroman, and J. Clarke, *IEEE Trans. Appl. Supercond.* **3**, 2434 (1993).

⁴⁸D. Drung, *Physica C* **368**, 134 (2001).

⁴⁹D. Drung, in *SQUID Sensors: Fundamentals, Fabrication and Applications*,

NATO Science Series E: Applied Sciences, Vol. 329, Kluwer Academic Publishers, Dordrecht, Boston, London (1996).

⁵⁰N. Fujimaki, H. Tamura, T. Imamura, S. Hasuo, ISSCC San Francisco, (1988), pp. 40-41.

⁵¹D. Drung, *Cryogenics* **26**, 623-627 (1986).

⁵²D. Drung, E. Crocoll, R. Herwig, M. Neuhaus, W. Jutzi, *IEEE Trans. Magn.* **MAG-25**, 1034-1037 (1989).

⁵³M. Mück, C. Heiden, *IEEE Trans. Magn.* **MAG-25**, 1151-1153 (1989).

4.2 Additional Topic: The rf-SQUID

In contrast to the dc SQUID the rf-SQUID is formed by a superconducting loop containing only a single Josephson junction. Although it is still widely used today, it has seen less development in recent years compared to the dc SQUID. Whereas the dc SQUID is operated by applying a dc current and measuring the time-averaged voltage, the rf-SQUID is operated by applying an rf current via a tank circuit inductively coupled to the SQUID loop and measuring the time-averaged rf-voltage of the tank circuit. This makes the choice of names obvious. The advantage of the rf-SQUID compared to the dc SQUID is the fact that it requires only a single Josephson junction and no dc current has to be applied. Therefore, no current leads have to be attached which guarantees safe operation and good protection against current spikes. However, as we will see below, at 4.2 K the energy resolution of the rf-SQUID is limited by the read-out electronics and therefore is worse than that of dc-SQUIDs. However, at 77 K, the commonly used operation temperature of SQUIDs based on high temperature superconductors, this problem is relaxed. Although less sensitive than the dc-SQUID, the rf-SQUID is entirely adequate for a large variety of applications and is until today more widely used than the dc SQUID.

4.2.1 The Zero Voltage State

We consider the rf-SQUID shown in Fig. 4.14. In the same way as for the dc SQUID the total phase change along a closed contour line is $2\pi n$:

$$\oint_C \nabla\theta \cdot d\mathbf{l} = 2\pi n = (\theta_{Q_b} - \theta_{Q_a}) + (\theta_{Q_a} - \theta_{Q_b}) + 2\pi n \quad (4.2.1)$$

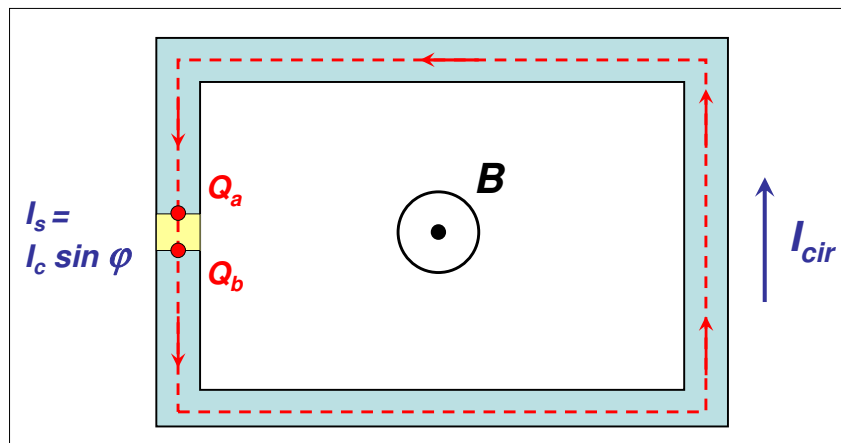


Figure 4.14: The rf-SQUID formed by a single Josephson junction intersecting a superconducting loop. The broken line indicates the closed contour path of the integration.

Using $\nabla\theta = \frac{2\pi}{\Phi_0}(\Lambda\mathbf{J}_s + \mathbf{A})$ (compare (2.2.2)) and $\varphi = \theta_2 - \theta_1 - \frac{2\pi}{\Phi_0} \int_1^2 \mathbf{A} \cdot d\mathbf{l}$ (compare (2.2.3)) we obtain

$$\theta_{Q_b} - \theta_{Q_a} = +\varphi + \frac{2\pi}{\Phi_0} \int_{Q_a}^{Q_b} \mathbf{A} \cdot d\mathbf{l} \quad (4.2.2)$$

$$\theta_{Q_a} - \theta_{Q_b} = \int_{Q_a}^{Q_b} \nabla\theta \cdot d\mathbf{l} = +\frac{2\pi}{\Phi_0} \int_{Q_a}^{Q_b} \Lambda\mathbf{J}_s \cdot d\mathbf{l} + \frac{2\pi}{\Phi_0} \int_{Q_a}^{Q_b} \mathbf{A} \cdot d\mathbf{l} . \quad (4.2.3)$$

Substitution these expression into (4.2.1) yields

$$\varphi = -\frac{2\pi}{\Phi_0} \oint_C \mathbf{A} \cdot d\mathbf{l} - \frac{2\pi}{\Phi_0} \int_{Q_a}^{Q_b} \Lambda\mathbf{J}_s \cdot d\mathbf{l} . \quad (4.2.4)$$

The integration of \mathbf{A} around the close contour is equal to the total flux Φ enclosed by the superconducting loop. The integration of \mathbf{J}_s follows the same contour C but excludes the integration over the insulating barrier. Furthermore, if the superconducting loop consists of a superconducting material with a thickness large compared to the London penetration depth λ_L , the integration path can be taken deep inside the superconducting material where the current density is negligible. Therefore, the integral involving the current density can be omitted and we obtain

$$\boxed{\varphi = -\frac{2\pi\Phi}{\Phi_0}} . \quad (4.2.5)$$

The phase difference across the junction determines the supercurrent

$$I_s = I_c \sin\left(-\frac{2\pi\Phi}{\Phi_0}\right) = -I_c \sin\frac{2\pi\Phi}{\Phi_0} . \quad (4.2.6)$$

The total flux Φ threading the loop is given by the sum of the flux Φ_{ext} due to an externally applied magnetic field B_{ext} and the flux LI_{cir} due to the circulating current I_{cir} . With $I_{\text{cir}} = I_s$ we obtain

$$\Phi = \Phi_{\text{ext}} + LI_{\text{cir}} = \Phi_{\text{ext}} - LI_c \sin\frac{2\pi\Phi}{\Phi_0} . \quad (4.2.7)$$

Introducing the screening parameter $\beta_{L,\text{rf}} = 2\pi LI_c/\Phi_0$ we can rewrite this expression and obtain⁵⁴

$$\boxed{\frac{\Phi}{\Phi_0} = \frac{\Phi_{\text{ext}}}{\Phi_0} - \frac{\beta_{L,\text{rf}}}{2\pi} \sin\left(2\pi\frac{\Phi}{\Phi_0}\right)} . \quad (4.2.8)$$

The variation of Φ with Φ_{ext} is shown in Fig. 4.15 for two different values of $\beta_{L,\text{rf}}$. The regions with positive slope are stable, whereas those with negative slope are not. Regions with negative slope only appear for $\beta_{L,\text{rf}} > 1$. Most practical rf-SQUIDs are operated in this regime.

⁵⁴Note that the screening parameter deviates from that defined for the dc SQUID by a factor of π .

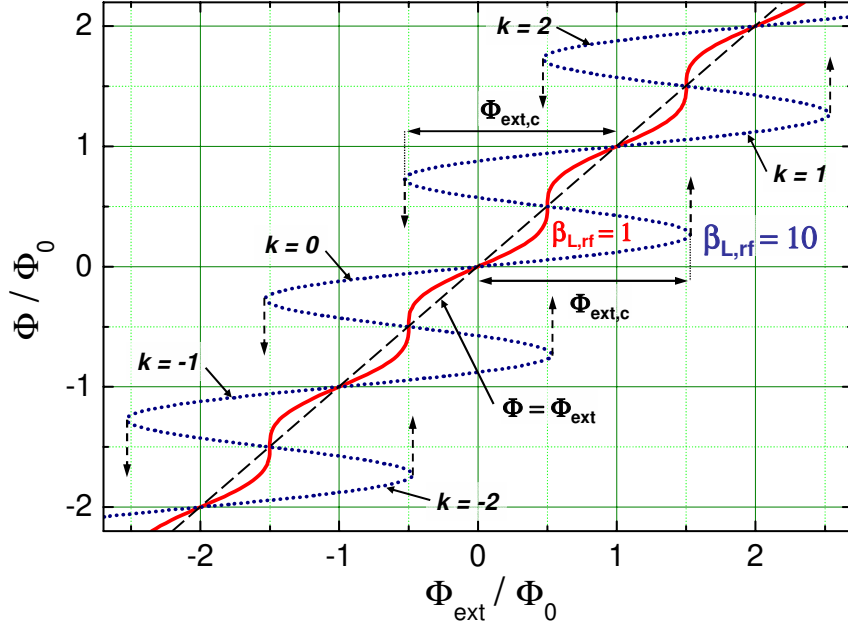


Figure 4.15: Total flux Φ versus applied flux Φ_{ext} for a rf-SQUID for $\beta_{L,\text{rf}} = 1$ (solid line) and 10 (dotted line). The dashed line shows the dependence for $\beta_{L,\text{rf}} = 0$.

If we are slowly increasing Φ_{ext} , the total flux Φ increases less rapidly than Φ_{ext} , since the flux due to the shielding current opposes Φ_{ext} . However, when I_s reaches I_c , this shielding behavior cannot be continued, since the critical current of the Josephson junction is reached. Therefore, at a critical value $\Phi_{\text{ext},c}$ the junctions momentarily switches into the voltage state and a flux quantum can penetrate the loop. The SQUID switches from the $k = 0$ to the $k = 1$ quantum state. If we subsequently reduce the applied flux again, the SQUID remains in the $k = 1$ state until $\Phi_{\text{ext}} = \Phi_0 - \Phi_{\text{ext},c}$ is reached. At this point I_s again exceeds I_c and the SQUID returns to the $k = 0$ state. That is, in sweeping back and forth the applied flux a hysteresis loop is traced out.

4.2.2 Operation and Performance of rf-SQUIDs

Operation of rf-SQUIDs

As already mentioned the rf-SQUID is operated at radio frequencies. The SQUID loop is inductively coupled to the coil of an LC resonant circuit called tank circuit with a quality factor $Q = R_T / \omega_{\text{rf}} L_T$ as shown in Fig. 4.16. Here, $\omega_{\text{rf}} = 1 / \sqrt{L_T C_T}$ is the resonance frequency of the tank circuit, L_T , C_T and R_T are the inductance, capacitance and the damping resistance of the tank circuit. The mutual inductance between the inductance L of the SQUID loop and L_T of the tank circuit is $M = \alpha \sqrt{L_T L}$. The tank circuit is excited by a rf-current $I_{\text{rf}} \sin \omega_{\text{rf}} t$, which results in a rf-current $I_T = Q I_{\text{rf}}$ in the tank circuit. The rf-voltage is amplified by a high impedance preamplifier.

For the case of $\beta_{L,\text{rf}} < 1$ the $\Phi(\Phi_{\text{ext}})$ curves are non-hysteretic and the rf-SQUID behaves as a nonlinear inductor, which is modifying the resonance frequency $1 / \sqrt{L_{T,\text{eff}} C_T}$ of the tank circuit periodically with the applied flux. Here, $L_{T,\text{eff}}$ is the effective inductance of the tank circuit, which deviates from L_T due to the coupling to the SQUID loop.⁵⁵ If the resonant circuit is operated close to its resonance frequency, the

⁵⁵We can write the total flux through L_T as $\Phi_T = L_T I_T - M I_{\text{cir}}$, where M is the mutual inductance and I_{cir} the circulating current in the SQUID loop. On the other hand we can write the flux through the SQUID loop as $\Phi = \alpha \Phi_T$, where α is the coupling coefficient between L and L_T . With $\Phi = L I_{\text{cir}}$ we obtain $I_{\text{cir}} = \alpha \Phi_T / L = \alpha L_T I_T / L$. Then we obtain $\Phi_T =$

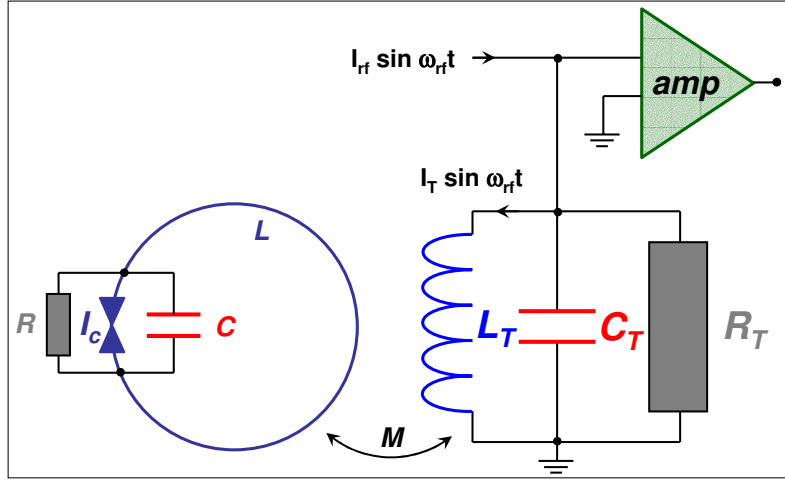


Figure 4.16: The rf-SQUID inductively coupled to the resonant tank circuit.

change of the resonance frequency causes a strong change of the rf-current and hence of the rf-voltage of the tank circuit.

For $\beta_{L,\text{rf}} > 1$, the situation is different, since we have to deal with hysteretic $\Phi(\Phi_{\text{ext}})$ curves. The total applied flux to the SQUID is

$$\Phi_{\text{ext}} = \Phi_s + \Phi_{\text{rf}} \sin \omega_{\text{rf}} t . \quad (4.2.9)$$

It is composed of a low frequency (static) signal flux Φ_s and a rf-flux Φ_{rf} coupled to the SQUID via the tank circuit. Here,

$$\Phi_{\text{rf}} = M \cdot I_T = M \cdot Q I_{\text{rf}} \quad (4.2.10)$$

is determined by the applied rf-current I_{rf} , the Q factor of the tank circuit and the mutual inductance M . As soon as $\Phi_s + \Phi_{\text{rf}}$ exceeds the critical flux value $\Phi_{\text{ext,c}}$, a hysteresis loop is traced out in the $\Phi(\Phi_{\text{ext}})$ curve. This results in an energy loss proportional to the area of the hysteresis loop and hence in a damping of the tank circuit. It is obvious from Fig. 4.15 that the damping is minimum, if the signal flux is close to $n \cdot \Phi_0$, whereas it is maximum, if the signal flux is close to $\frac{2n+1}{2} \cdot \Phi_0$. This shows that also for the case $\beta_{L,\text{rf}} > 1$ the tank voltage is a periodic function of the applied flux.

In order to discuss how the tank voltage V_T depends on the signal flux Φ_s and the rf-flux Φ_{rf} we discuss the situations $\Phi_s = n\Phi_0$ and $\Phi_s = (n + \frac{1}{2})\Phi_0$. We first consider the case $\Phi_s = n\Phi_0$ with $n = 0$. On increasing I_{rf} the tank voltage V_T initially increases linearly with I_{rf} as long as the resulting rf-flux $\Phi_{\text{rf}} = M Q I_{\text{rf}}$ does not exceed the critical value $\Phi_{\text{ext,c}}$. The corresponding critical rf-current is $I_{\text{rf,c}} = \Phi_{\text{ext,c}}/M$ and the tank voltage is

$$V_T^{(0)} = \omega_{\text{rf}} L_T I_{\text{rf,c}} = \omega_{\text{rf}} L_T \frac{\Phi_{\text{ext,c}}}{M} . \quad (4.2.11)$$

Here, the superscript 0 indicates $\Phi_s = n\Phi_0$ with $n = 0$. If we further increase the rf-current resp. rf-flux a jump to the $k = +1$ or $k = -1$ branch of the $\Phi(\Phi_{\text{ext}})$ curve occurs and a hysteresis loop is traced out

$(L_T - \alpha M L_T/L) I_T$. That is, we have the effective inductance $L_{T,\text{eff}} = L_T (1 - \alpha M/L)$. With $M = \alpha \sqrt{L_T L}$ we finally obtain $L_{T,\text{eff}} = L_T (1 - \alpha^2 \sqrt{L_T L}/L)$. For $\alpha = 0$ we obtain the obvious result $L_{T,\text{eff}} = L_T$, for $\alpha = 1$ the tank circuit inductance is reduced to the effective value $L_{T,\text{eff}} = L_T (1 - \sqrt{L_T/L})$.

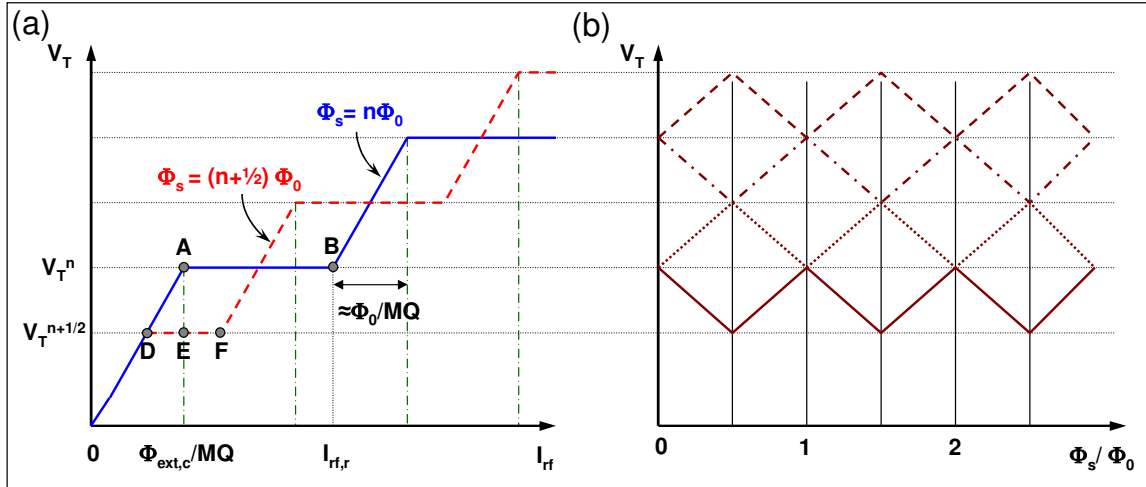


Figure 4.17: (a) Tank voltage V_T plotted versus rf-current I_{rf} for $\Phi_s = n\Phi_0$ and $\Phi_s = (n + \frac{1}{2})\Phi_0$. (b) Tank voltage V_T plotted versus signal flux Φ_s for constant rf-current values marked in (a) by the vertical dash-dotted lines.

(see Fig. 4.15). This is associated with an energy loss ΔE extracted from the tank circuit. Because of this loss, the rf-current amplitude in the tank circuit and, in turn, the rf-flux coupled into the SQUID loop is reduced below $\Phi_{ext,c}$ in the next cycle. That is, no hysteresis loops are traversed until the tank circuit has recovered what usually takes several cycles. A further increase of the rf-current would result in the same jumps to the $k = +1$ or $k = -1$ branches at the same current resp. flux value. That is, the transitions occur at the same rf-current amplitude $I_{rf,c}$ corresponding to the same voltage V_T^0 given by (4.2.11). The only difference is that the tank circuit recovers faster due to the larger I_{rf} and hence the transitions occur at a higher rate. Hence, on increasing I_{rf} the tank voltage stays constant at V_T^0 and we obtain a horizontal branch from point A to B in the $V_T(I_{rf})$ curve (see Fig. 4.17a). The horizontal branch extends until $I_{rf,r}$. At this value the rf-current amplitude is large enough to compensate for the energy loss within a single rf-cycle. Then, a transition is induced in each rf-cycle and the tank voltage V_T increases linearly again until the next critical rf-value is reached, where transitions from the $k = \pm 1$ to the $k = \pm 2$ states become possible. Here, the energy loss increases suddenly, so that the next horizontal branch in the $V_T(I_{rf})$ curve is obtained by the same reason as discussed above.

In order to see how the $V_T(I_{rf})$ curves depend on the signal flux we discuss the case $\Phi_s = (n + \frac{1}{2})\Phi_0$ with $n = 0$. The flux loops traced out during a rf-cycle are now shifted by $\Phi_0/2$. Therefore, during the positive cycle transitions to the $k = +1$ branch occur at the flux $\Phi_{ext,c} - \Phi_0/2$, whereas during the negative cycle transitions occur at $-(\Phi_{ext,c} + \Phi_0/2)$. As a result, when we increase I_{rf} we observe the first horizontal part in the $V_T(I_{rf})$ curve already at

$$V_T^{(1/2)} = \omega_{rf} L_T \frac{\Phi_{ext,c} - \Phi_0/2}{M}. \quad (4.2.12)$$

The horizontal part extends to the rf-current value, which is large enough to compensate for the energy loss within a single rf-cycle. On further increasing I_{rf} we obtain a linear part again until I_{rf} reaches the next critical value corresponding to a peak flux value of $-(\Phi_{ext,c} + \Phi_0/2)$. Then transitions to both the $k = +1$ and $k = -1$ branch are allowed. In total, we observe a series of horizontal branches and linear risers for $\Phi_s = \Phi_0/2$ interlocking those obtained for $\Phi_s = 0$ (see Fig. 4.17a). $V_T(I_{rf})$ curves for intermediate flux values are situated between the two curves obtained for $\Phi_s = \Phi_0/2$ and $\Phi_s = 0$. The $V_T(\Phi_s)$ curves for constant I_{rf} are triangular as shown in Fig. 4.17b.

The change of V_T on increasing the signal flux from 0 to $\Phi_0/2$ is obtained to $\omega_{rf} L_T \Phi_0 / 2M$ by subtracting (4.2.12) from (4.2.11). Thus, for small flux changes near $\Phi_s = \Phi_0/4$ we find the flux-to-voltage transfer

function (compare Fig. 4.17b)

$$H = \left(\frac{\partial V_T}{\partial \Phi_s} \right)_{I_{\text{rf}}=\text{const}} = \frac{\omega_{\text{rf}} L_T}{M} . \quad (4.2.13)$$

This expression suggests that we can increase H arbitrarily by reducing $M \propto \alpha$. However, then we would completely decouple the SQUID loop from the tank circuit and can no longer perform any measurement. That is, there must be a lower bound for α . The lower bound results from the fact that we must be able to choose a specific value of I_{rf} that intersects the first step of the $V_T(I_{\text{rf}})$ curves for all signal flux values. According to Fig. 4.17a, this means that point F has to lie to the right of point E or, equivalently, that \overline{DF} has to exceed \overline{DE} . We can estimate \overline{DF} by noting that the power dissipation at D is zero and $E_0 \omega_{\text{rf}} = I_c \Phi_0 \omega_{\text{rf}} / 2\pi$ at F. This means that $\frac{1}{2}(I_{\text{rf}}^F - I_{\text{rf}}^E)V_T^{1/2} = I_c \Phi_0 \omega_{\text{rf}} / 2\pi$. Furthermore, from Fig. 4.17a we see that $I_{\text{rf}}^E - I_{\text{rf}}^D = \Phi_0 / 2MQ$. Using $LI_c \simeq \Phi_0$ and $V_T^{1/2}$ from (4.2.12) the condition $I_{\text{rf}}^E > I_{\text{rf}}^D$ can be written as

$$\alpha^2 Q \gtrsim \frac{\pi}{4} . \quad (4.2.14)$$

If we use the approximation $\alpha^2 \sim 1/Q$ we obtain the transfer function

$$H \approx \frac{\omega_{\text{rf}} L_T}{\alpha \sqrt{L_T L}} = \omega_{\text{rf}} \sqrt{Q \frac{L_T}{L}} . \quad (4.2.15)$$

During practical operation of a rf-SQUID one adjusts I_{rf} so that the SQUID stays biased on the first step for all values of Φ_s . The rf-voltage across the tank circuit is amplified and demodulated to produce a signal that is periodic in Φ_s as shown in Fig. 4.17b. Then, in the same way as the dc SQUID a flux locked loop operation is performed by applying a modulating flux at typically 100 kHz and amplitude $\Phi_0/2$. The voltage produced by this modulation is lock-in detected and fed back into the modulation coil to flux-lock the SQUID.

Additional Topic:

Noise in rf-SQUIDs

Noise in the rf-SQUID results from the fact that the switching from the $k = 0$ to the $k = 1$ state at $\Phi_{\text{ext},c}$ shows stochastic fluctuations due to thermal activation. These fluctuations have two consequences. First, noise is introduced on the step voltage V_T resulting in an equivalent flux noise^{56,57}

$$S_\Phi \approx \frac{(LI_c)^2}{\omega_{\text{rf}}} \left(\frac{2\pi k_B T}{I_c \Phi_0} \right)^{4/3} . \quad (4.2.16)$$

Second, the noise causes a finite slope of the horizontal branches of the $V_T(I_{\text{rf}})$ curves. **Jackel** and **Buhrman** introduced a slope parameter $\eta = \Delta V_{T,\text{step}} / \Delta V_{T,0}$, where $\Delta V_{T,\text{step}}$ is the increase of the tank voltage along the length of the step and $\Delta V_{T,0}$ is the voltage separation of two adjacent steps. They showed that η is related to S_Φ by the relation⁵⁸

$$\eta^2 \approx \frac{S_\Phi \omega_{\text{rf}}}{\pi \Phi_0^2} . \quad (4.2.17)$$

⁵⁶J. Kurkijärvi, W.W. Webb, in *Proceedings of the Applied Superconductivity Conference*, Annapolis, Maryland (1972), pp. 581-587.

⁵⁷J. Kurkijärvi, *J. Appl. Phys.* **44**, 3729 (1973).

⁵⁸L.D. Jackel, R.A. Buhrman, *J. Low. Temp. Phys.* **19**, 201 (1975).

This relation has been verified in many experiments.

Beyond the intrinsic noise of the rf-SQUID one has to take into account the finite noise temperature T_{amp} of the rf-amplifier. Furthermore, part of the coaxial line connecting the tank circuit to the preamplifier is at room temperature. Since the capacitance of the line and the preamplifier contribute a significant part to the total capacitance of the tank circuit, part of the resistive damping of the tank circuit is well above the operation temperature of the SQUID. This adds additional noise which can be included into the preamplifier noise by assuming an effective noise temperature $T_{\text{amp}}^{\text{eff}}$. The noise energy by the extrinsic circuit is given by $2\pi\eta k_B T_{\text{amp}}^{\text{eff}}/\omega_{\text{rf}}$.⁵⁹ Together with the intrinsic noise (4.2.16) this results in an energy resolution of

$$\varepsilon \simeq \left(\frac{\pi\eta^2\Phi_0^2}{2L} + 2\pi\eta k_B T_{\text{amp}}^{\text{eff}} \right) \frac{1}{\omega_{\text{rf}}} . \quad (4.2.18)$$

We see that the energy resolution of the rf-SQUID scales as $1/\omega_{\text{rf}}$. Therefore, it is obvious to increase the tank frequency. However, one has to bear in mind that also T_{amp} increases with increasing frequency. The energy resolution of rf-SQUIDs operated at typical frequencies of a few 10 MHz is a few 10^{-29}J/Hz . This sensitivity has been improved by using higher resonance frequencies^{60,61} and cold preamplifiers.^{62,63} For systems operating at frequencies up to 3 GHz and using high electron mobility transistors energy sensitivities down to $3 \times 10^{-32}\text{J/Hz}$ have been obtained.⁶⁴

Comparing (4.2.18) to (4.1.48) we see that the intrinsic energy resolution of the rf-SQUID can be roughly approximated by $\varepsilon \sim k_B T / \omega_{\text{rf}}$, whereas that of the dc SQUID is roughly $\varepsilon = k_B T / \omega_c$. Here, $\omega_c = 2\pi I_c R_N / \Phi_0$ is the characteristic frequency, which typically ranges in the 100 GHz regime. This shows that the better intrinsic energy resolution of the dc SQUID is mainly related to the fact that $\omega_c \gg \omega_{\text{rf}}$.

4.2.3 Practical rf-SQUIDs

Low T_c rf-SQUIDs

RF-SQUIDs based on metallic low temperature superconductors are commercially available since the early 1970s (notably from Biomagnetic Technologies (BTi) – formerly S.H.E. Corporation, Quantum Design, and Tristan Technologies Inc.). The early rf-SQUIDs had a toroidal configuration machined from Nb. These devices are operated at a few 10 MHz and typically have a white noise energy of $5 \times 10^{-29}\text{J/Hz}$ and a $1/f$ noise of roughly 10^{-28}J/Hz at 0.1 Hz. Today rf-SQUIDs are fabricated in the same way as dc-SQUIDs using thin film technology. Energy sensitivities down to a few 10^{-32}J/Hz have been achieved in the white noise regime.

High T_c rf-SQUIDs

After the discovery of the high temperature superconductors rf-SQUIDs based on the cuprate superconductors have been developed operating at 77 K. In order to increase the operation frequency conventional

⁵⁹R.P. Giffard, J.C. Gallop, B.N. Petley, Prog. Quantum Electr. **4**, 301 (1976).

⁶⁰A. Long, T.D. Clark, R.J. Prance, M.G. Richards, Rev. Sci. Instrum. **50**, 1376 (1979).

⁶¹J.N. Hollenhorst, R.P. Giffard, IEEE Trans. Magn. **15**, 474 (1979).

⁶²H. Ahola, G.H. Ehnholm, B. Rantala, P. Ostman, J. Low. Temp. Phys. **35**, 313 (1979).

⁶³M. Mück, Th. Becker, Ch. Heiden, Appl. Phys. Lett. **66**, 376 (1995).

⁶⁴J. Clarke, IEEE Trans. Electron. Devices **27**, 1896 (1980).

washer-type rf-SQUIDs have been incorporated into a superconducting $\lambda/2$ microstrip resonator, which serves as the tank circuit (see Fig. 4.18).^{65,66} In this way a flux noise level of $10\mu\Phi_0/\sqrt{\text{Hz}}$ could be obtained for a 50 pH rf SQUID operated at 150 MHz. This noise was found to be independent of frequency down to 1 Hz.

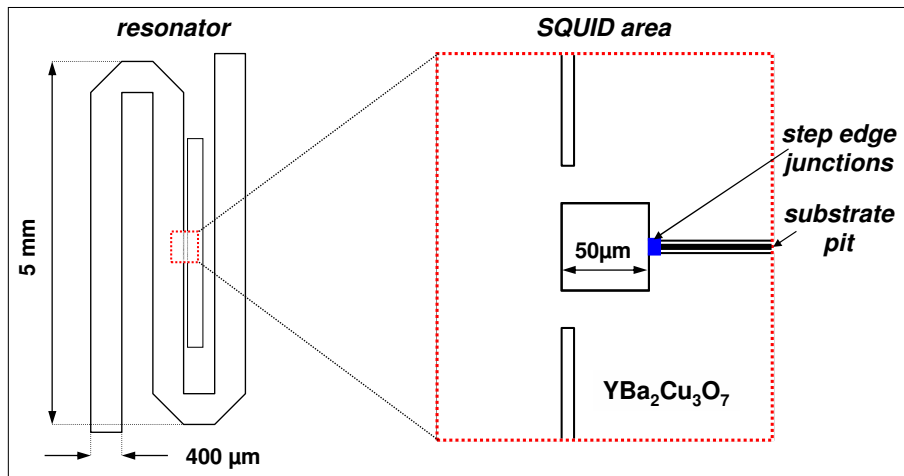


Figure 4.18: Schematic drawing of a high- T_c rf-SQUID integrated into a $\lambda/2$ resonator. The right hand side shows a magnified view of the SQUID area (after Y. Zhang, M. Mück, A.I. Braginski, H. Töpfer, Supercond. Sci. Technol. **77**, 269 (1994)).

⁶⁵Y. Zhang, M. Mück, A.I. Braginski, H. Töpfer, Supercond. Sci. Technol. **77**, 269 (1994).

⁶⁶A.I. Braginski, in *SQUID Sensors: Fundamentals, Fabrication and Applications*, H. Weinstock ed., NATO Science Series E: Applied Sciences, Vol. 329, Kluwer Academic Publishers, Dordrecht, Boston (1996).

4.3 Additional Topic: Other SQUID Configurations

Over the years many other SQUID configurations besides the dc- and rf-SQUID have been developed. A few of them are briefly addressed in the following.

4.3.1 The DROS

To simplify the readout electronics of SQUIDs, the flux-to-voltage transfer coefficient should be large enough such that direct readout of the SQUID output voltage by standard room-temperature preamplifiers is possible. Compared with the standard dc SQUIDs, the **Double Relaxation Oscillation SQUID** (DROS) provides very large flux-to-voltage transfer and large modulation voltage, and thus simple flux-locked loop electronics can be used for SQUID operation.^{67,68,69}

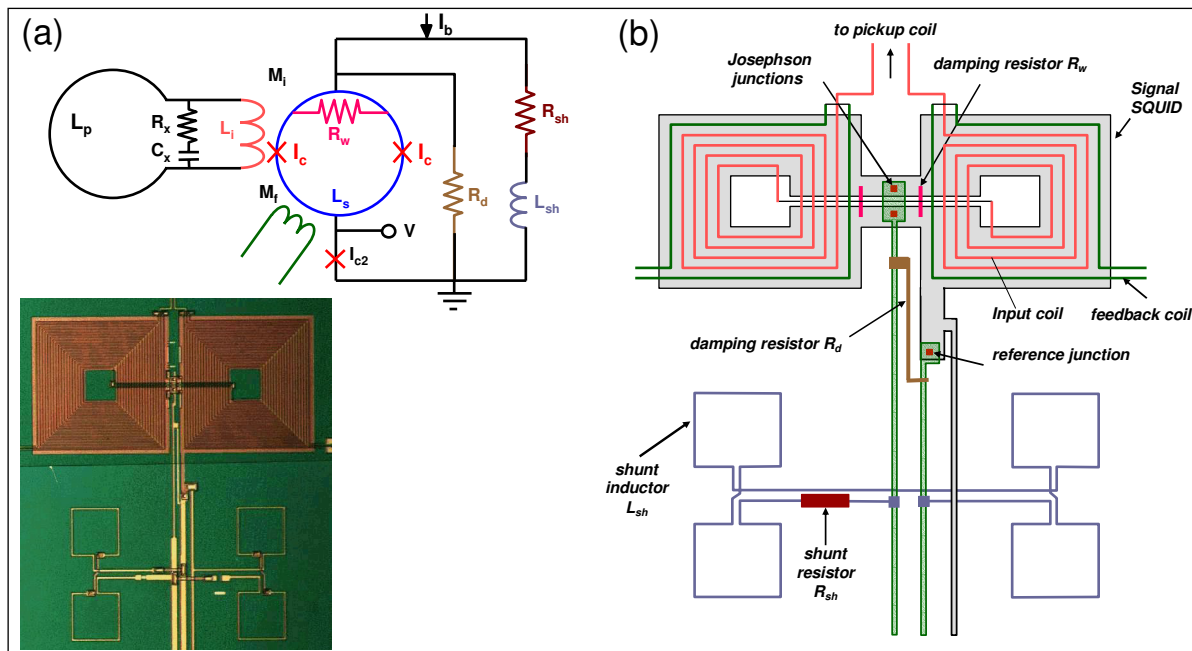


Figure 4.19: (a) Schematic circuit drawing of a double relaxation oscillation SQUID sensor and (b) close-up view of the DROS. I_b is the bias current, $2I_c$ is the critical current of the signal SQUID, L_s is the inductance of the signal SQUID, R_{sh} and L_{sh} are the resistance and inductance of the relaxation circuit, respectively, R_d and R_w are damping resistors, M_i and M_f are the mutual inductances between the SQUID and the input coil L_i and the feedback coil, respectively, R_x and C_x are used to damp the input coil resonance. The output voltage V is measured across the reference junction I_{c2} . Also shown is an optical micrograph of the SQUID sensor (after Y. H. Lee, J. M. Kim, H. C. Kwon, Y. K. Park, J. C. Park, D. H. Lee, and C. B. Ahn, Progress in Supercond. Vol. 2, 20-26 (2000)).

The DROS consists of a hysteretic ($\beta_C > 1$) dc SQUID (the signal SQUID) and a hysteretic junction (the reference junction), shunted by a relaxation circuit of an inductor and a resistor. In this way the system

⁶⁷D. J. Adelerhof, H. Nijstad, F. Flokstra and H. Rogalla, *(Double) relaxation oscillation SQUIDs with high flux-to-voltage transfer: Simulations and experiments*, J. Appl. Phys. **76**, 3875-3886 (1994).

⁶⁸M.J. van Duuren, Y.H. Lee, D.J. Adelerhof, J. Kawai, H. Kado, J. Flokstra, H. Rogalla, IEEE Trans. Appl. Supercond. **AS-6**, 38-44 (1996).

⁶⁹D. Drung, *Advanced SQUID readout electronics*, in *SQUID Sensors: Fundamentals, Fabrication and Application*, H. Weinstock ed., Dordrecht, Kluwer Academic Publishers (1996), pp. 63-116.

performs relaxation oscillations (cf. section 4.1.5). Instead of the reference junction also a reference SQUID can be used. However, the reference junction has the advantage to be less susceptible for flux trapping than the reference SQUID and to eliminate the lines needed for the adjustment of a reference flux.

The schematic circuit drawing of the DROS planar gradiometer and the close-up view of the DROS are shown in Fig. 4.19a and b, respectively. In an adequate bias current range, the DROS functions as a comparator of the two critical currents, namely the signal critical current and the reference critical current. Thus, the voltage output of the DROS behaves like a square-wave function as the signal flux changes, resulting in a very large flux-to-voltage transfer coefficient when the two critical currents are equal.

As an example, in Fig. 4.19b a gradiometer-type signal SQUID is shown with two square-shaped washers connected in parallel. A reference junction is used instead of the reference SQUID. The high flux-to-voltage transfer coefficient of typically $3 \text{ mV}/\Phi_0$ enables direct readout by simple room temperature electronics with a modest voltage noise. By integrating a pickup coil consisting of two planar coils (typical size: $10 \times 10 \text{ mm}^2$, baseline length: a few cm) connected in series on the same chip a planar gradiometer with a field gradient noise of a few $\text{fT}/\text{cm Hz}$ in the white noise regime can be obtained.

4.3.2 The SQIF

For the realization of SQUIDs also interferometer structures consisting of more than two junctions can be used. As we have seen, for $\beta_L \ll 1$ the dependence of the maximum Josephson current of a dc SQUID on the external flux corresponds to the diffraction pattern of a double slit configuration. In analogy to optics it is evident that we can achieve an even steeper $I_s^m(\Phi_{\text{ext}})$ dependence by using a structure corresponding to an optical grid. Such a structure is obtained by putting N junctions in parallel. The problem in the realization of such structures is the requirement to fabricate a large number of identical Josephson junctions and loops separating them. If the junction and loop parameters vary considerably, the resulting interference pattern is very irregular and hardly useful. However, recently it was pointed out that also irregular configurations are useful. Such arrays have been named *Superconducting Quantum Interference Filters* (SQIFs).

By using an irregular parallel array of Josephson junctions as shown in Fig. 4.20a, the resulting interference pattern, i.e. the $I_s^m(\Phi_{\text{ext}})$ dependence of the array shows a sharp peak at zero flux followed by a very steep decrease. A similar result is obtained for the array voltage $V(\Phi_{\text{ext}})$ at constant bias current (see Fig. 4.20b). The idea then is to use the peak in the maximum Josephson current to realize a sensitive flux sensor. Typically, a SQIF device consists of a parallel array of several 10 Josephson junctions. Devices with both low- T_c and high- T_c Josephson junctions have been realized.^{70,71} Compared to dc SQUIDs the SQIF shows a considerably higher flux-to-voltage transfer coefficient. Beyond irregular parallel arrays also series configurations of dc SQUIDs with varying loop size and two-dimensional structures have been studied.⁷²

4.3.3 Cartwheel SQUID

In so-called cartwheel SQUIDs the SQUID loop consists of several loops forming a cartwheel. The loops are parallel to each other thereby reducing the total inductance of the SQUID loop. Cartwheel SQUIDs

⁷⁰J. Oppenländer, Ch. Häussler, T. Träuble, N. Schopohl, Physica C **368**, 119 (2002).

⁷¹V. Schultze, R.I. Ijsselstein, H.-G. Meyer, J. Oppenländer, Ch. Häussler, N. Schopohl, IEEE Trans. Appl. Supercond. **AS-13**, 775 (2003).

⁷²J. Oppenländer, P. Caputo, Ch. Häussler, T. Träuble, J. Tomes, A. Friesch, N. Schopohl, Appl. Phys. Lett. **83**, 969 (2003); IEEE Trans. Appl. Supercond. **AS-13**, 771 (2003).

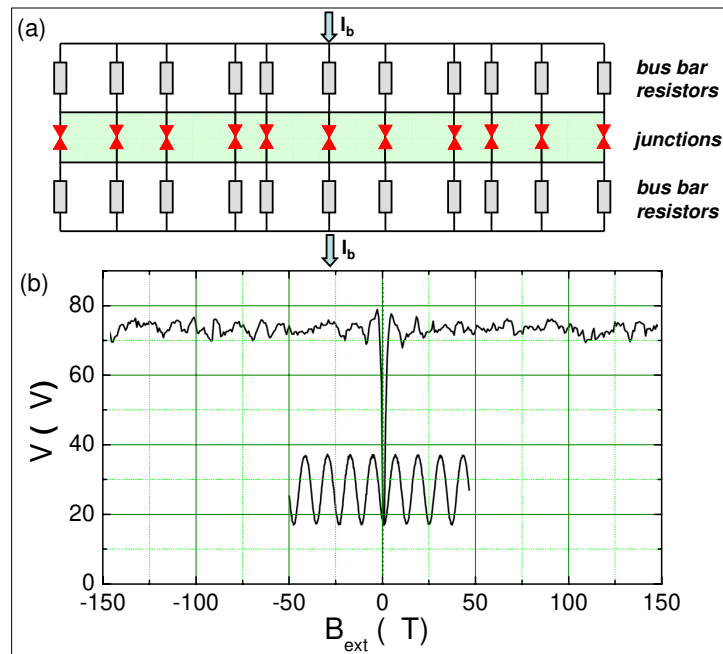


Figure 4.20: (a) Schematic diagram of a parallel Superconducting Quantum Interference Filter (SQIF) circuit. The different array loops have different areas. The bias current I_b is fed into the array through bus bar resistors. (b) Voltage response of a parallel SQIF plotted vs. the magnetic applied field B_{ext} (upper curve). The lower curve shows a part of the voltage response of a conventional two junction SQUID (after J. Oppenländer, Ch. Häussler, T. Träuble, N. Schopohl, Physica C **368**, 119 (2002)).

have been fabricated both from low- T_c and high- T_c materials. With a high- T_c version field sensitivities down to $18 \text{ fT}/\sqrt{\text{Hz}}$ have been achieved in the white noise regime.⁷³ A more detailed description of the cartwheel SQUID is given in section 4.4.1 in our discussion of SQUID magnetometers (see also Fig. 4.22d and e).

⁷³F. Ludwig, E. Dansker, R. Kleiner, D. Kölle, J. Clarke, S. Knappe, D. Drung, H. Koch, N. Alford, T.W. Button, Appl. Phys. Lett. **66**, 1418-1420 (1995).

4.4 Instruments Based on SQUIDS

In principle, a SQUID can sense any kind of signal that can be converted into a flux coupled into the SQUID loop. Therefore, both dc- and rf-SQUIDs are used as sensors in a broad assortment of instruments. In the following we briefly discuss some of them. Each SQUID instrument involves a specific antenna attached to the input of the SQUID. This antenna determines the quantity that is measured by the SQUID as shown in Fig. 4.21.

In using the SQUID in different applications involving different antenna at the input we should recognize that the presence of an input circuit influences both the signal and the noise properties of the SQUID. On the other hand, the SQUID reflects a complex impedance into the input. Furthermore, the SQUID represents a nonlinear device. Therefore, a full description of the interactions is complicated and we will not go into the details here. We only will concentrate on one important aspect that already was recognized in 1971 by **J.E. Zimmerman**.⁷⁴ Suppose we are connecting a pick-up loop of inductance L_p to the input coil of the SQUID with inductance L_i to form a magnetometer as shown in Fig. 4.21. It can be shown that the SQUID inductance L is thereby reduced to the value

$$L' = L - \frac{M^2}{L_i + L_p} = L \left(1 - \frac{\alpha^2 L_i}{L_i + L_p} \right), \quad (4.4.1)$$

where α^2 is the coupling coefficient between L and L_i , which determines the mutual inductance $M_i = \alpha\sqrt{L_i L}$ between L and L_i . Here, we have neglected any stray inductances in the leads connecting L_i and L_p . The reduction in L tends to increase the transfer function ($H \sim R_N/L$ for the dc-SQUID) of the SQUID.

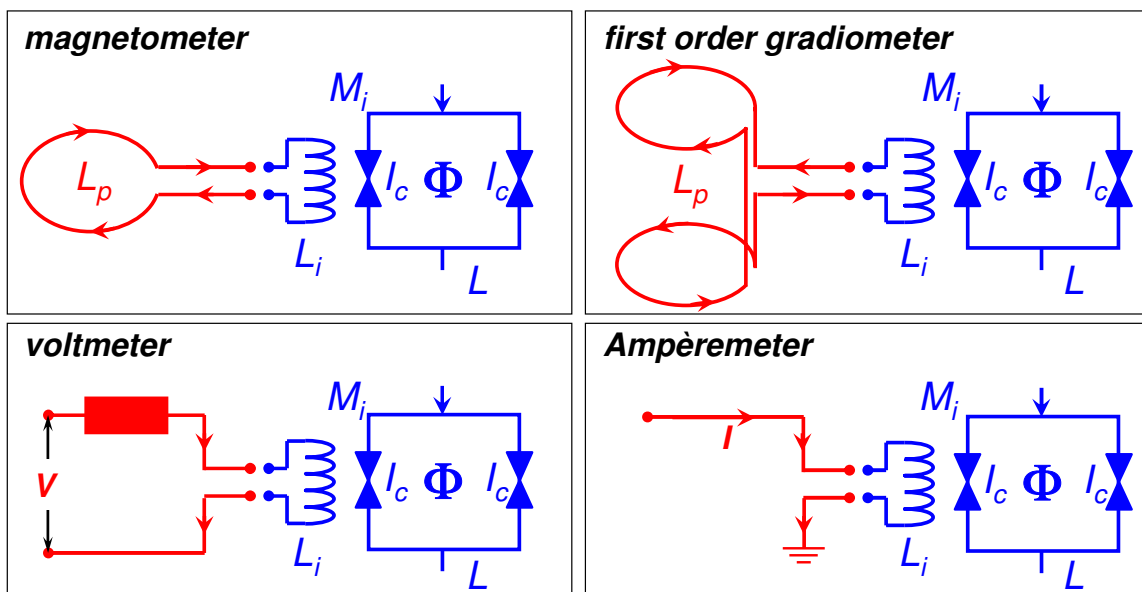


Figure 4.21: Different types of input antenna for superconducting quantum interference devices used in different applications. The input antenna converts the quantity to be measured into magnetic flux.

⁷⁴J.E. Zimmerman, *Sensitivity enhancement of SQUIDs through the use of fractional turn loops*, J. Appl. Phys. **42**, 4483 (1971).

4.4.1 Magnetometers

The probably most simple and straightforward SQUID instrument is the SQUID magnetometer. Here, a pick-up loop with inductance L_p is connected to the input coil of the SQUID forming a superconducting flux transformer. That is, a small flux change $\delta\Phi^p = N_p A_p \delta B_{\text{ext}}$ applied to the pick-up loop is causing a shielding current I_{sh} flowing through both the pick-up and the input coil. Here, A_p and N_p are the area and turn number of the pick-up loop. The current through the input coil generates a magnetic flux that is coupled into the SQUID loop. Flux quantization requires that

$$\delta\Phi^p + (L_i + L_p)I_{\text{sh}} = N_p A_p \delta B_{\text{ext}} + (L_i + L_p)I_{\text{sh}} = 0 . \quad (4.4.2)$$

We have neglected the effects of the SQUID on the input circuit. The flux coupled into the SQUID operated in the flux locked loop is

$$\delta\Phi = M_i |I_{\text{sh}}| = M_i \frac{\delta\Phi^p}{L_i + L_p} = \frac{\alpha \sqrt{L_i L}}{L_i + L_p} \delta\Phi^p = \frac{\alpha \sqrt{L_i L}}{L_i + L_p} N_p A_p \delta B_{\text{ext}} , \quad (4.4.3)$$

where $M_i = \alpha \sqrt{L_i L}$ is the mutual inductance between L_i and L .

In order to find the minimum detectable value of $\delta\Phi^p$, we equate $\delta\Phi$ to the equivalent flux noise of the SQUID. Defining S_Φ^p as the spectral density of the flux noise referred to the pick-up loop, we find

$$S_\Phi^p = \frac{(L_i + L_p)^2}{M_i^2} S_\Phi = \frac{(L_i + L_p)^2}{\alpha^2 L_i L} S_\Phi . \quad (4.4.4)$$

Introducing the equivalent noise energy referred to the pick-up loop, we obtain

$$\epsilon^p = \frac{S_\Phi^p}{2L_p} = \frac{(L_i + L_p)^2}{L_i L_p} \frac{S_\Phi}{2\alpha^2 L} = \frac{(L_i + L_p)^2}{L_i L_p} \frac{\epsilon}{\alpha^2} . \quad (4.4.5)$$

Analyzing (4.4.5) we see that it has the minimum value

$$\epsilon^p(f) = \frac{4\epsilon(f)}{\alpha^2} \quad (4.4.6)$$

for $L_i = L_p$. Thus, a maximum fraction $\alpha^2/4$ of the energy in the pick-up loop is transferred to the SQUID, if we match L_p and L_i . Here, we have neglected the noise currents in the input circuit and the fact that the input circuit reduces the SQUID inductance.

With the optimum flux resolution for $L_p = L_i$ we can give the corresponding magnetic field resolution $S_B^p(f) = S_\Phi^p(f)/(\pi r_p^2)^2$, where r_p is the radius of the pick-up loop. With $S_\Phi^p = 8\epsilon L_p/\alpha^2$ we obtain

$$S_B^p(f) = \frac{8L_p}{\alpha^2(\pi r_p^2)^2} \epsilon(f) . \quad (4.4.7)$$

The inductance of the superconducting pick-up coil made from a wire with radius r_0 is given by $L_p = \mu_0 r_p [\ln(8r_p/r_0) - 2]$ and can be approximated by $L_p \approx 5\mu_0 r_p$ over a wide range of values r_p/r_0 . Therefore, we obtain $S_B^p(f) \approx 4\mu_0 \epsilon / \alpha^2 r_p^3 \propto 1/A_p^{3/2}$. This shows that we can increase the magnetic field resolution by increasing the radius of the pick-up loop while keeping $L_p = L_i$. In practice, of course there is a limitation due to the finite size of the cryostat used for cooling down the system. Furthermore, a spatially varying signal is averaged over the area of the pick-up loop. Taking $\epsilon \approx 10^{-28} \text{ J/Hz}$, $\alpha = 1$ and $r_p = 25 \text{ mm}$, we calculate $\sqrt{S_B^p} \approx 5 \times 10^{-15} \text{ T}/\sqrt{\text{Hz}}$. This is a much better value than that achieved with non-superconducting magnetometers.

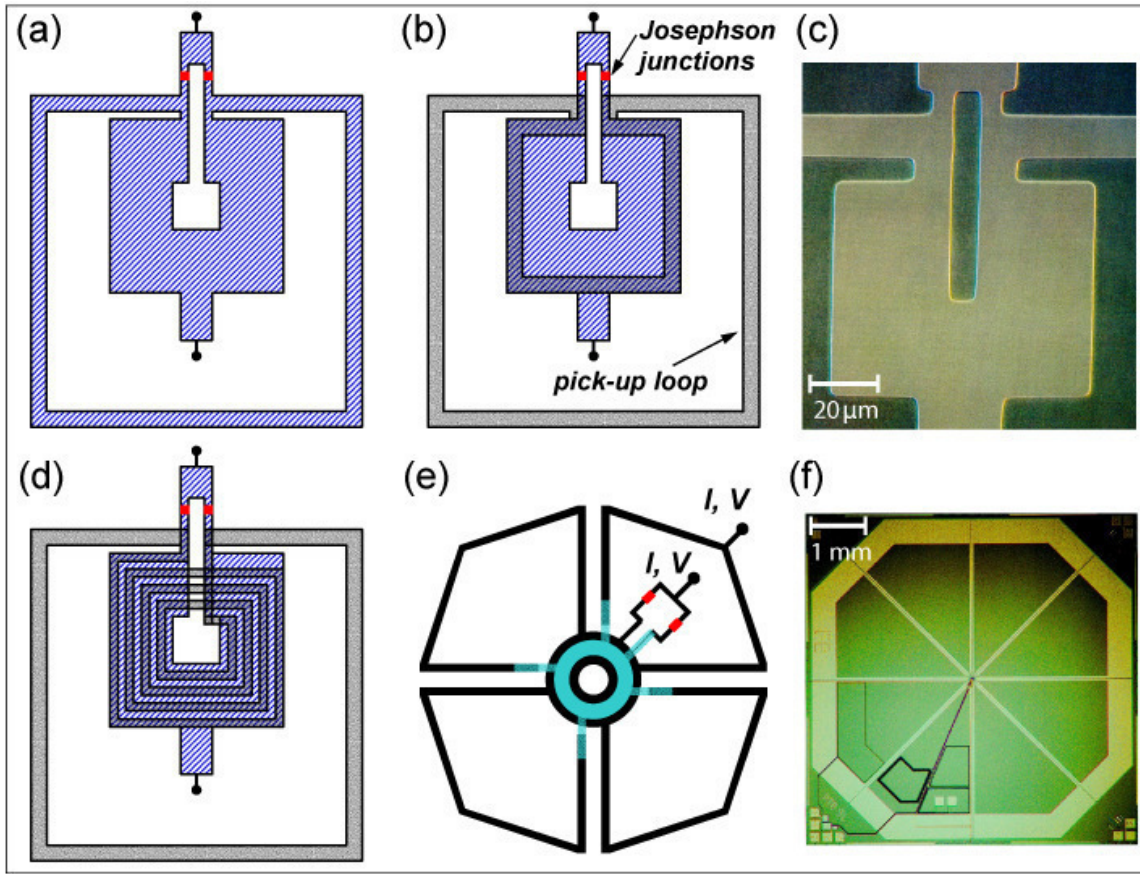


Figure 4.22: Various types of thin film SQUID magnetometers: (a) directly coupled SQUID magnetometer (single layer structure), (b) flip-chip magnetometer with single-turn input coil, (c) optical micrograph of a directly coupled YBCO grain boundary junction dc SQUID (by courtesy of D. Kölle), (d) flip-chip magnetometer with multi-turn input coil, (e) multi-loop magnetometer (the inner part consists of a trilayer structure), and (f) optical micrograph of an 8-loop Nb SQUID magnetometer (by courtesy of PTB Braunschweig).

Thin Film Magnetometers

SQUIDs operated at 4.2 K or below can make use of wire wound flux transformers. The wire wound flux transformer is then connected to the planar multi-turn thin film input coil positioned on top of the SQUID washer. Note that the contact between the input coil and the flux transformer must be superconducting. Unfortunately, for high temperature superconductors there exists no highly flexible superconducting wire that could be connected via a superconducting contact to the input coil. Therefore, no wire-wound flux transformers can be used and thin film flux transformers have to be applied. A solution to the problem is the directly coupled SQUID (see Fig. 4.22a).^{75,76} It consists of a large pick-up loop of inductance L_p and area A_p directly connected to the SQUID body of inductance $L \ll L_p$. A magnetic field B_{ext} applied to the pickup loop induces a screening current $I_{\text{sh}} = B_{\text{ext}}A_p/L_p$, which in turn links a flux $(L - L_J)I_{\text{sh}}$ to the SQUID. Here, L_J is the parasitic inductance of the striplines incorporating the junctions, to which the current does not couple. The effective area is $A_{\text{eff}} = (L - L_J)A_p/L_p \pm A_s$, where $A_s \ll A_{\text{eff}}$ is the effective area of the bare SQUID and the sign of A_s depends on the relative senses of the SQUID and the pickup loop. We note that the direct coupling of the flux transformer and the SQUID body can be avoided by coupling the SQUID loop in a flip-chip arrangement to a single-layer flux transformer (see Fig. 4.22b)

⁷⁵M. Matsuda, Y. Murayama, S. Kiryu, N. Kasai, S. Kashiwaya, M. Koyanagi, and T. Endo, IEEE Trans. Magn. **MAG-27**, 3043 (1991).

⁷⁶D. Koelle, A. H. Miklich, F. Ludwig, E. Dantsker, D. T. Nemeth, and J. Clarke, Appl. Phys. Lett. **63**, 2271 (1993).

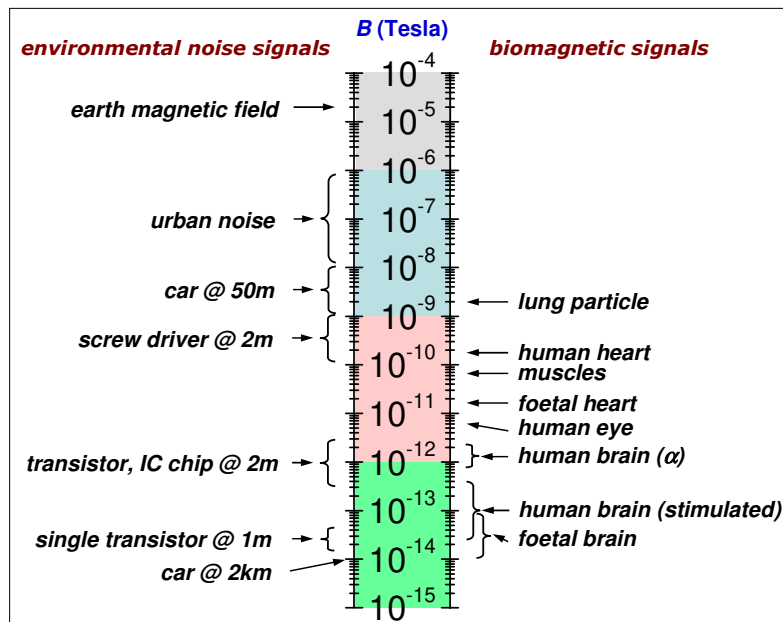


Figure 4.23: Signal strength of some magnetic noise signals compared to that of biomagnetic signals.

fabricated on a separate substrate.⁷⁷

A general problem of using single turn flux transformers as shown in Fig. 4.22a and b is the bad coupling due to $N_p = N_i = 1$. In order to improve the situation, multi-turn input coils have been used (see Fig. 4.22c). The fabrication of such structures, however, already requires multi-layer thin film technology, which is complicated for the high temperature superconductors due to the requirement of heteroepitaxial growth.

A completely different concept for achieving large effective areas is the multi-loop magnetometer (see Fig. 4.22e). It was originally proposed and demonstrated by **J.E. Zimmerman** in 1971.⁷⁸ The essential idea is to connect N loops in parallel, thus reducing the total inductance to a level acceptable for a SQUID, while keeping the effective area large. In the thin-film multiloop magnetometer, shown schematically in Fig. 4.22d, N loops are connected in parallel with the connection made at the center via coplanar lines. The two Josephson junctions connect the upper and lower superconducting films of the central trilayer structure. Today sensitive multiloop SQUID magnetometers are fabricated using niobium thin-film technology. For example, with eight parallel loops and a diameter of 7.2 mm these devices have a typical magnetic field sensitivity of $1.5 \text{ fT}/\sqrt{\text{Hz}}$ down to a few Hz at 4.2 K.⁷⁹ These devices have been used successfully for multichannel biomagnetic studies.^{80,81}

4.4.2 Gradiometers

Since SQUIDs are very sensitive magnetic field sensors, they are susceptible to all kind of perturbing magnetic field fluctuations caused by the environment. Fig. 4.23 shows a collection of perturbing signals compared to interesting biomagnetic signals. For example, a screw driver placed about 5 m from

⁷⁷D. Koelle, A. H. Miklich, E. Dantsker, F. Ludwig, D. T. Nemeth, J. Clarke, W. Ruby, and K. Char, *Appl. Phys. Lett.* **63**, 3630 (1993).

⁷⁸J.E. Zimmerman, *J. Appl. Phys.* **42**, 4483 (1971).

⁷⁹D. Drung, in *SQUID Sensors: Fundamentals, Fabrication and Applications*, NATO ASI Series, edited by H. Weinstock (Kluwer Academic, Dordrecht), p. 63 (1996).

⁸⁰D. Drung, R. Cantor, M. Peters, H.-J. Scheer, and H. Koch, *Appl. Phys. Lett.* **57**, 406 (1990).

⁸¹D. Drung, S. Knappe, and H. Koch, *IEEE Trans. Appl. Supercond.* **3**, 2019 (1995).

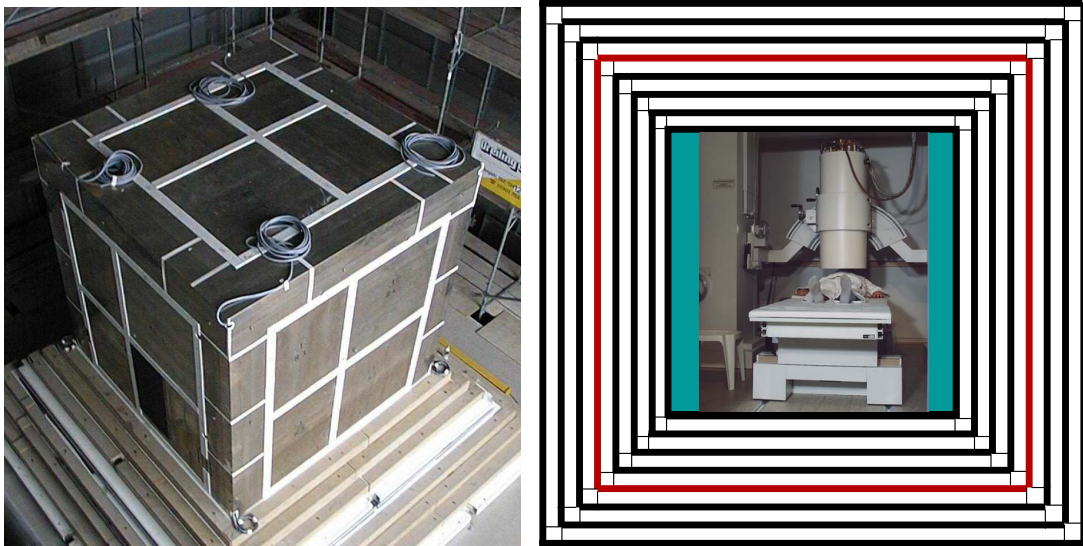


Figure 4.24: Magnetically shielded room at the PTB in Berlin. Left: Photograph of the shielded room with a diameter of 2.9 m. Right: Cross-sectional view showing the seven μ -metal and the single Al layer as well as a photograph of the multi-channel SQUID system positioned inside the room (by courtesy of PTB Berlin).

the SQUID sensor is generating a magnetic field strength above the signal originating from our heart activity. Signals originating from our brain activity are even much smaller. They are of the same order of magnitude as those of a car passing at a distance of about 2 km.

In order to do biomagnetic measurements one has to reduce the perturbing magnetic fields of the environment. First of all, the SQUID set-up has to be made from non-magnetic materials. Furthermore, one can use μ -metal shields to reduce static and low-frequency perturbing magnetic fields by about three to four orders of magnitude. A convenient but expensive way is the use of magnetically shielded rooms. One of the most effective magnetically shielded rooms is presently used by the PTB in Berlin (see Fig. 4.24). The walls of the room consist of 7 μ -metal shields and an additional Al-layer for shielding of high-frequency electromagnetic fields. In addition, an active magnetic field reduction is used. In this way a shielding factor of 2×10^6 and 2×10^8 is achieved at a frequency of 0.01 and 5 Hz, respectively.

In many situations magnetic shielding is too expensive or one simply cannot shield perturbing signals. This is for example the case, when one is interested in the measurement of brain signals, which are superimposed by the much stronger heart signals (compare Fig. 4.23). In this case the use of gradiometers is useful. Ideal gradiometers of n^{th} order are susceptible only to gradients of n^{th} and higher order. Since signals of remote sources appear almost constant at the sensor position, they are strongly suppressed by gradiometers. For example, the signals generated by the heart are almost constant at a sensor placed on the head of a person for the measurement of the brain signals. Therefore, the heart signals are strongly suppressed by the use of gradiometers. In contrast, the brain signals are very close to the sensor and have strong gradients.

Figs. 4.25a and b show a few axial gradiometer configurations, which can be realized by winding a superconducting wire on a suitable support structure. Such gradiometers are widely used in SQUID sensors applied in magneto encephalography. For a first order gradiometer a constant magnetic field is generating shielding currents flowing in opposite directions in the two coils. Hence, there is no net flux and no net shielding current flowing to the SQUID input coil. In contrast, for a gradient $dB_z/dz \neq 0$ the shielding currents in the two sub-coils are different. Hence there is a net flux and shielding current. In the same way, for a second order gradiometer, a constant field gradient is causing no net flux and shielding current. For a third order gradiometer this is the case for a second order gradient and so on.

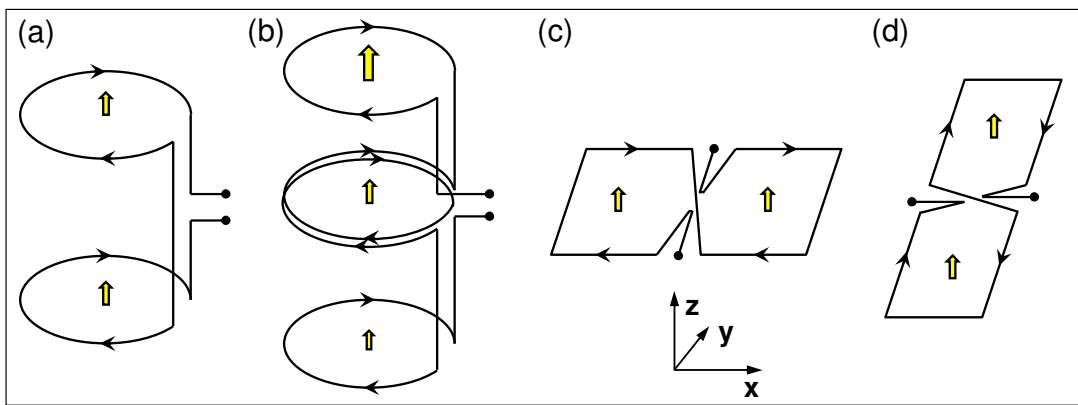


Figure 4.25: (a) First and (b) second order axial gradiometer detecting dB_z/dz and d^2B_z/dz^2 . (c) and (d) show planar first order gradiometers for dB_z/dx and dB_z/dy . The big arrows mark the direction of the magnetic field, the small arrows that of the shielding currents.

Beyond axial gradiometers one also can design various planar gradiometers. For example, a first order planar gradiometer has the shape of a “8”. If the axis of the “8” is along the y -direction and the direction perpendicular to it is the z -direction, the gradiometer is measuring the gradient dB_z/dy . In the same way gradiometers for other gradients can be constructed.⁸² We also note that beyond the so-called hardware gradiometers shown in Fig. 4.25 also software gradiometers can be used. Here, for example the signals of two magnetometers can be combined to realize a first order gradiometer by means of a suitable software. By combining a larger number of magnetometers or low-order gradiometers various higher order gradiometers can be realized.

4.4.3 Susceptometers

SQUID susceptometers are used today in many laboratories for measuring the magnetic properties of materials. The susceptibility can be measured by a first order gradiometer as shown in Fig. 4.25a. The sample to be studied and the gradiometer are brought into a static homogeneous magnetic field. The sample is positioned in one of the pick-up loops of the gradiometer. If the sample would be non-magnetic, there would be no output signal from the gradiometer provided that the magnetic field is perfectly homogeneous and the gradiometer perfectly balanced. However, for a magnetic sample with a nonvanishing susceptibility χ an additional flux is generated in one of the pick-up loops of the gradiometer. This results in a finite shielding current that is coupling flux to the SQUID via the SQUID input coil connected to the gradiometer.

Today sophisticated SQUID susceptometers are commercially available.⁸³ In these systems usually the sample is moved along an axial second order gradiometer. The resulting signal is measured as a function of the position and fitted to a theoretically expected curve. These susceptometers allow to measure the susceptibility in the temperature range between 1.8 and 400 K in fields up to 7 T at a resolution of about 10^{-8} emu.

For even more sensitive measurements of very small samples one can use miniature SQUID susceptome-

⁸²Note that for the measurement of the gradients dB_z/dz , dB_y/dy and dB_x/dx three-dimensional gradiometer configurations are required, whereas the other gradients can be measured by planar configurations.

⁸³For example: Magnetic Property Measurement System (MPMS), Quantum Design, 6325 Lusk Boulevard, San Diego, CA 92121-3733, USA.

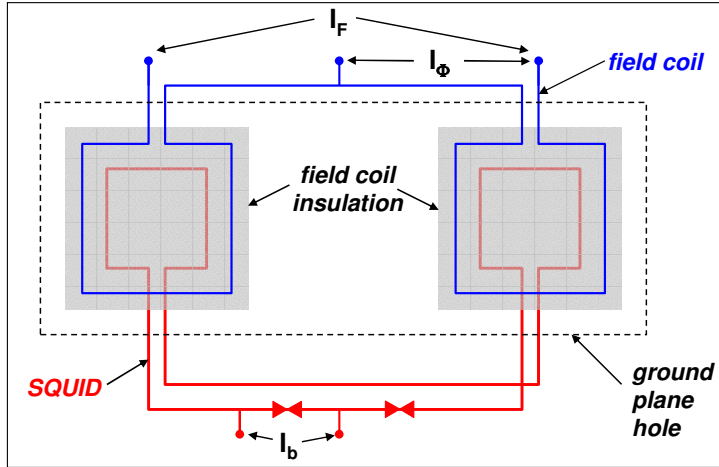


Figure 4.26: Thin film miniature SQUID susceptometer. The SQUID consisting of two series connected pick-up loops wound in opposite sense are placed on a superconducting ground plane to minimize the inductance due to the connecting lines. The hole in the ground plane is indicated by the dashed line.

ters, which have been pioneered by **Ketchen** and coworkers.^{84,85,86} An example for a miniature SQUID susceptometer is shown in Fig. 4.26. The SQUID loop is formed by two pick-up loops that are wound in opposite sense and connected in series. The pick-up loops are deposited on a superconducting ground plane in order to minimize the inductance of the whole device. The SQUID is flux biased at the position of maximum transfer function H by applying a control current I_Φ to one of the pick-up loops. Furthermore, a magnetic field can be applied to both loops via the field current I_F . By passing part of this current into the center connector one can obtain a high degree of balance between the two loops. The sample to be measured is placed over one of the loops. The output of the SQUID, when the field is applied, is then proportional to the magnetization of the sample. The sensitivity of the miniature SQUID susceptometer is impressive. It is capable of detecting the magnetization of about 3000 electron spins.

4.4.4 Voltmeters

As shown in Fig. 4.21 a SQUID can be used for the detection of small voltages. The voltage to be measured is transformed to a current via an input resistor. The current flowing into the input coil is coupling flux to the SQUID loop, which generates an output signal that is proportional to the voltage at the input. The use of SQUIDs as sensitive voltmeters was proposed by **J. Clarke** already in 1966.⁸⁷ In practical voltmeters the SQUID voltage output signal from the flux-locked loop is fed back to the known input resistor to realize a null-balancing measurement of the voltage. The resolution of the SQUID voltmeter is limited by the Nyquist noise in the input circuit, which varies from about $10^{-12}\text{V}/\sqrt{\text{Hz}}$ for an input resistance of 0.01Ω to about $10^{-10}\text{V}/\sqrt{\text{Hz}}$ for 100Ω . That is, SQUID voltmeters are superior to semiconductor amplifiers, which have a typical voltage input noise of several $10^{-10}\text{V}/\sqrt{\text{Hz}}$ for low impedance samples. Typical applications are the measurement of thermoelectric voltages, the measurement of the transport properties of low resistance metallic nanostructures, the study of low-frequency $1/f$ noise in Josephson junctions and SQUIDS, or the study of nonequilibrium phenomena in superconductors such as quasiparticle charge imbalance.

⁸⁴M.B. Ketchen, D.D. Awschalom, W.J. Gallagher, A.W. Kleinsasser, R.L. Sanstrom, J.R. Rozen, B. Bumble, IEEE Trans. Magn. **MAG-25**, 1212-1215 (1989).

⁸⁵M.B. Ketchen, T. Kopley, H. Ling, Appl. Phys. Lett. **44**, 1008-1010 (1984).

⁸⁶D.D. Awschalom, J. Warnock, IEEE Trans. Magn. **MAG-25**, 1186-1192 (1989).

⁸⁷J. Clarke, A superconducting galvanometer employing Josephson tunneling, Phil. Mag. **13**, 115-127 (1966).

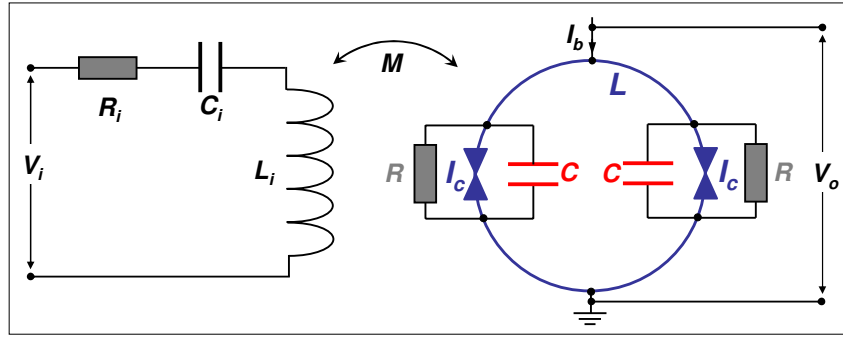


Figure 4.27: Schematic circuit diagram of a tuned radio-frequency amplifier based on a dc SQUID.

4.4.5 Radiofrequency Amplifiers

Over the last years SQUIDs have been used to develop low-noise amplifiers for frequencies up to 100 MHz.⁸⁸ As shown in Fig. 4.27 one can realize a tuned amplifier by connecting an input circuit consisting of a series connection of an input inductance L_i , an input capacitor C_i and an input resistor R_i to the SQUID. The presence of this input circuit modifies the SQUID parameters and the magnitude of the noise spectral density.⁸⁹ Furthermore, the SQUID reflects back an impedance $\omega^2 M^2 / Z$ into the input circuit, where Z is the input impedance of the SQUID.⁹⁰ Fortunately, if the coupling coefficient α between the input inductance and the SQUID inductance is small enough, one can neglect the mutual influence of the SQUID and the input circuit.

For a signal frequency f generated by a source with resistance R_s the optimum noise temperature of the amplifier is given by⁹¹

$$T_N^{\text{opt}} = \frac{\pi f}{k_B H} (S_V S_I - S_{VI}^2)^{1/2}. \quad (4.4.8)$$

Here, H is the flux-to-voltage transfer coefficient of the SQUID, S_V and S_I the voltage and current noise spectral density of the SQUID, respectively, and S_{VI} is the cross-spectral density. The latter arises from the correlations between S_V and S_I , because the asymmetric part of the current noise generates a flux noise, which in turn contributes to the total voltage noise for $H \neq 0$ (compare section 4.1.3). Simulations show that $S_I \approx 11k_B T / R_N$ and $S_{VI} \approx 12k_B T$ for a SQUID with $\beta_L = 1$, $\gamma = 0.05$ and $\Phi = (2n+1)\Phi_0 / 4$.⁹²

The minimum noise temperature is actually obtained off-resonance. If one wants to operate the amplifier at the resonance frequency of the input circuit, the noise temperature is increased to

$$T_N^{\text{res}} = \frac{\pi f}{k_B H} (S_V S_I)^{1/2}. \quad (4.4.9)$$

The corresponding power gain is $G \approx H/\omega$. Note that expressions (4.4.8) and (4.4.9) do not contain the Nyquist noise of the input resistor R_i which may be significant and exceeds the noise of the amplifier. **Hilbert** and **Clarke** fabricated several amplifiers and achieved $G = 18.6$ and $T_N = 1.7 \pm 0.5$ K at 93 MHz. The theoretically expected values were 17 dB and 1.1 K.

⁸⁸C. Hilbert, J. Clarke, *dc-SQUIDS as radiofrequency amplifiers*, J. Low Temp. Phys. **61**, 263-280 (1985).

⁸⁹C. Hilbert, J. Clarke, J. Low Temp. Phys. **61**, 237-262 (1985).

⁹⁰J.M. Martinis, J. Clarke, J. Low Temp. Phys. **61**, 227-236 (1985).

⁹¹J. Clarke, *SQUIDS: Principles, Noise and Applications*, in *Superconducting Devices*, S.T. Ruggiero and D.A. Rudman, eds., Academic Press Inc., Boston (1990), pp. 51-100.

⁹²C.D. Tesche, J. Clarke, J. Low Temp. Phys. **37**, 397-403 (1979).

At $T = 0$ the Nyquist noise has to be replaced by the quantum expression taking into account zero point fluctuations. It was shown by **Koch** *et al.* that in the quantum limit the noise temperature of a tuned amplifier is given by⁹³

$$T_N^{\text{quantum}} = \frac{hf}{k_B \ln 2} . \quad (4.4.10)$$

This is the result for any quantum limited amplifier.

⁹³R.H. Koch, D.J. van Harlingen, J. Clarke, Appl. Phys. Lett. **38**, 380-382 (1981).

4.5 Applications of SQUIDS

Due to their exceptional sensitivity and the fact that SQUID sensors are sensitive to all kind of signals that can be converted to a magnetic flux signal by the input antenna, SQUIDs have found widespread applications. In this section we describe a few of them.

4.5.1 Biomagnetism

Non-invasive medical investigations utilizing the detection of magnetic signals originating from the human body are termed biomagnetic methods. Over the last decades, **biomagnetic imaging** has been developed as a new modality for functional diagnosis providing valuable new insight into a broad variety of problems. The basic idea is that every activity of the brain is connected with neuronal ionic currents and every beat of the heart is generated by ionic depolarization currents. These currents create magnetic fields that can be measured non-invasively outside the body. By measuring the field strength and direction at many positions, a field map can be constructed that allows the calculation of the location of the source inside the body. The electrical potentials at the surface are well known signals in medical diagnosis (EEG: electroencephalography, ECG: electrocardiography). However, since the human body consists of different tissues with different electrical conductivities, it is usually very difficult to determine the location of a current source from the measurement of the potentials on the surface. In contrast, very simple volume conductor models are adequate to interpret the magnetic field distribution for the localization of sources (MEG: magnetoencephalography, MCG: magnetocardiography).⁹⁴ Over the last decades a remarkable success has been achieved in applying SQUID systems to magnetoencephalography and magnetocardiography.^{95,96,97,98} These achievements in biomagnetic imaging are closely related to the high level of development of SQUID instrumentation. On the one hand, biomagnetism has been the major driving force for improvements in SQUID system development. However, on the other hand, better SQUID systems opened up new perspectives and applications and produced better results in biomagnetism.

The magnetic fields to be measured in biomagnetism are extremely small (see Fig. 4.23) and range from the 100 fT (brain) to the 10 pT regime (heart).⁹⁹ Therefore, highly sensitive SQUID magnetometers are a prerequisite for the detection of biomagnetic signals. In particular, the SQUID sensors should have very low $1/f$ noise, since the typical frequency range of biomagnetic signals is between 1 and 100 Hz. Note that the field strength of a single neuron is only about 0.1 fT and would not be sufficient to be detected. What is measured is the combined action of some 10 000 neurons.

The aim of an MCG or MEG measurement is to determine the spatio-temporal magnetic field distribution in a measurement plane just above the thorax or the head. Thus, in the ideal case, the magnetic field signals should be detected simultaneously by a set of SQUID sensors covering this plane with a spatial sampling frequency which allows all relevant features to be detected. Real SQUID systems are, of course, a compromise. In order to reduce system costs, one approach is to use single measurement

⁹⁴M. Hämäläinen, R. Hari, R.J. Ilmoniemi, J. Knuutila, O.V. Lounasmaa, *Magnetoencephalography – theory, instrumentation and applications to noninvasive studies of the working human brain*, Rev. Mod. Phys. **65**, 413-492 (1993).

⁹⁵C. Baumgartner, L. Deecke, G. Stroink, and S. J. Williamson, eds., *Biomagnetism: Fundamental Research and Clinical Applications*, Proc. 9th Int. Conf. Biomagnetism, in Studies in Applied Electromagnetics and Mechanics, vol. **7**, IOS Press, Amsterdam (1995).

⁹⁶C.J. Aine, Y. Okada, G. Stroink, S. Swithenby, and C. C. Wood, eds., Biomag 96, Proc. 10th Int. Conf. Biomagnetism, vol. **1** and **2**, Springer, New York (2000).

⁹⁷T. Yoshimoto, M. Kotani, S. Kuriki, H. Karibe, and N. Nakasato, eds., *Recent Advances in Biomagnetism*, Proc. 11th Int. Conf. Biomagnetism, Tohoku University Press, Sendai (1999).

⁹⁸J. Nenonen, R.J. Ilmoniemi, T. Katila (eds.), Biomag 2000, Proc. 12th Int. Conf. Biomagnetism, Helsinki University of Technology, Espoo, Finland (2001).

⁹⁹J.P. Wikswo Jr., IEEE Trans. Appl. Supercond. **5**, 74 (1995).

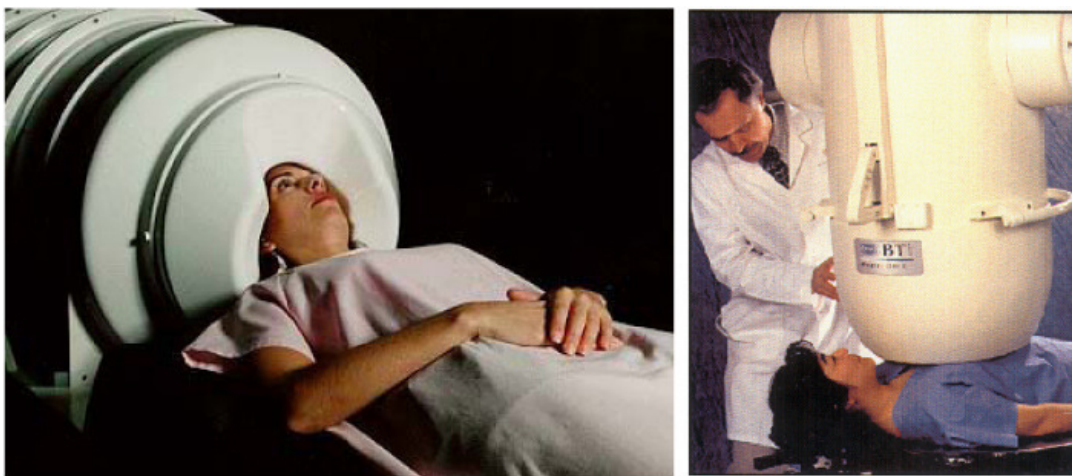


Figure 4.28: Multichannel SQUID systems for magnetoencephalography (left, CTF Systems Inc., Vancouver, Canada) and magnetocardiography (right, Biomagnetic Technologies, San Diego, USA)

position SQUID systems and to scan these systems over several measurement sites to carry out a measurement of the spatio-temporal magnetic field distribution. Another approach is to use a SQUID system with many SQUIDs that measure simultaneously the magnetic field signals at the sites according to the positional configuration of the SQUID sensors. Today in most cases complex multichannel SQUID systems are used consisting of a large number of channels (up to several hundred).^{100,101} Fig. 4.28 shows two multichannel systems used for magnetoencephalography (left) and magnetocardiography (right). Unfortunately, the specification of multichannel SQUID systems often is confusing, since usually no distinction is made between the number of SQUIDs in a system, the number of signal output channels and the number of measurement sites. For example, a number of SQUIDs is frequently used for gradiometry or other purposes and only a subtotal of all SQUIDs is involved in the measurement itself. From the point of view of cardiology only the number of measurement sites is relevant. For example, a sophisticated single measurement position SQUID sensor for unshielded operation may well contain up to more than 10 SQUIDs, that is, the system would require more than 1 000 SQUIDs for 100 measuring sites.

The magnetic signals generated by the human brain are of the order of 100 fT and therefore much smaller than the environmental noise signals (see Fig. 4.23). Hence, today almost all multichannel SQUID systems are operated in magnetically shielded rooms consisting of several layers of μ -metal (see Fig. 4.24). Unfortunately, these shielded rooms have a typical weight of several tons and cost about EUR 500 000. There is an ongoing discussion whether or not it is possible to perform biomagnetic measurements of high quality also in an unshielded environment. Active shielding has been proposed as well as systems that carry out software corrections using several additional magnetometers and gradiometers that measure the environmental noise.^{102,103} In any case gradiometer configurations have to be used for the detection of brain signals to suppress the much stronger signals generated by the heart. Today both wirewound and thin-film gradiometers are used.^{104,105}

¹⁰⁰J. Vrba, S.E. Robinson, *Supercond. Sci. Techn.* **15**, R51 (2002).

¹⁰¹V. Pizella, S. Della Penna, C. Del Gratta, G.L. Romani, *Supercond. Sci. Techn.* **14**, R79 (2001).

¹⁰²H.J.M. ter Brake, N. Janssen, J. Flokstra, D. Veldhuis, and H. Rogalla, *IEEE Trans. Appl. Supercond.* **AS-7**, 2545 (1997); *Meas. Sci. Technol.* **8**, 927 (1997); *Supercond. Sci. Technol.* **10**, 512 (1997).

¹⁰³B. David, O. Dössel, V. Doermann, R. Eckart, W. Hoppe, J. Krüger, H. Laudan, and G. Rabe, *IEEE Trans. Appl. Supercond.* **AS-7**, 3267 (1997).

¹⁰⁴J. Vrba, in *SQUID Sensors: Fundamentals, Fabrication and Applications*, NATO ASI Series, H. Weinstock ed., Kluwer Academic, Dordrecht (1996), p. 117.

¹⁰⁵J. Borgmann, P. David, G. Ockenfuß, R. Otto, J. Schubert, W. Zander, and A. I. Braginski, *Rev. Sci. Instrum.* **68**, 2730 (1997).

Signal Reconstruction

The magnetic field distribution measured by the SQUID system is caused by currents flowing in the human body. Unfortunately, it is impossible to calculate the current distribution from the measured field distribution even if we could measure the field distribution with arbitrary precision. The reason for that is the fact that the so-called inverse problem of electrodynamics has no unique solution.¹⁰⁶ That is, many different current distributions can create similar field patterns. Fortunately, not all of these current distributions are physiologically meaningful. Therefore, making additional model assumptions based on medical background knowledge the inverse problem can be solved. All models have in common that the current distribution is assumed to be the sum of elementary physiological sources that can be modeled as current dipoles. Current dipoles consist of short localized conductor segments and broad volume currents flowing back through the surrounding tissue closing the circuit. Both the short current path and the volume current contribute to the magnetic field. Obviously, a detailed description of the volume currents depends on the geometry and conductivity of the surrounding tissue. Often simplifying assumptions are made as e.g. a homogeneous spherical or half-space model.

By measuring the field distribution by a multichannel SQUID system the orientation and position of the current dipoles can be determined. For example, in this way the coordinates of the brain regions responsible for an epileptic attack can be determined. These regions in turn can be superimposed with a three-dimensional image of the brain obtained by magnetic resonance imaging.

Magnetocardiography

The heart signals are of the order of 100 pT and therefore by about three orders of magnitude larger than the brain signals. However, fine structures with signal amplitudes of only a few pT are clinically relevant. In MCG the goal is to determine the sources of pathological signals with high precision in three dimensions. Therefore, all three vector components of the magnetic field have to be measured. In Fig. 4.29a a common measurement configuration in MCG is illustrated. The instantaneous heart action is modeled by a current dipole associated with a magnetic field threading the sensor plane. The planar sensor loops detect B_z , the z -component of the field. Thus, for this configuration, some sensors yield positive and others negative values of the instantaneous field component B_z . From the measured distribution of B_z values a so-called field map can be derived for every instant during the heart beat. Doing so one is interpolating between the values obtained in the different measuring channels. Common representations of such maps are by iso-contour lines or by false color scaling as shown in Fig. 4.29b and c. Since such maps can be constructed for each instant during a heart beat, a video sequence of such maps can be constructed to give the medical doctor a valuable impression of the spatio-temporal dynamics of the evolution of the magnetic field associated with the heart function.

Two magnetic field map sequences (MFMS) covering a whole heart beat are shown in Fig. 4.29b and c. The sequence on the left is that of a volunteer with a healthy heart, whereas on the right the map sequence of a patient is shown who suffered from ventricular tachycardia. The differences in field distributions are considerable. It should be noted that a great variety of MFMS exists due to the biological variability. Each heart-healthy individual and each patient has its own finger print of an MFMS that may even vary in time and circumstances for a particular person. The art of interpreting these patterns is to identify the signatures in these varying patterns that are clinically relevant indications of typical pathologies.

While shielded rooms offer excellent conditions for basic biomagnetic research, unshielded operation of SQUID systems is the ultimate goal from the commercial point of view. This is in particular true for MCG applications. However, this goal is very hard to achieve and requires state-of-the-art noise suppression

¹⁰⁶J. Sarvas, Phys. Med. Biol. **32**, 11 (1987).

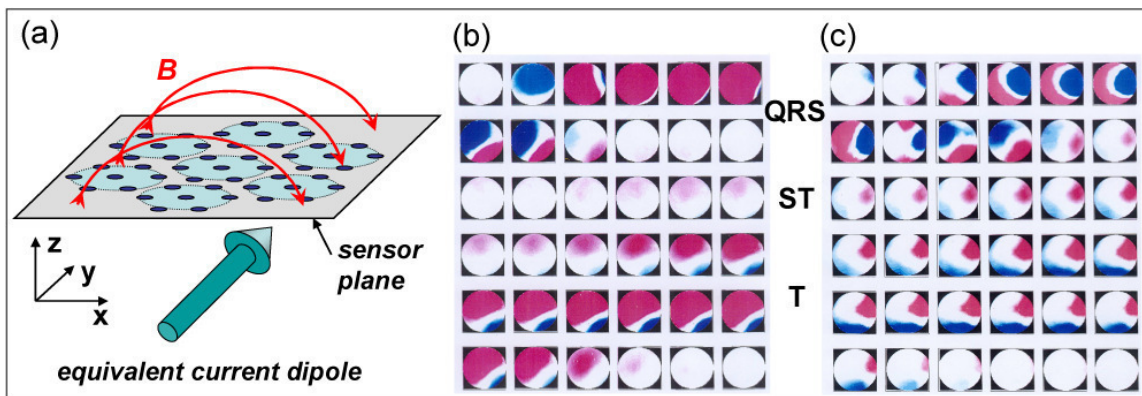


Figure 4.29: (a) Typical measurement configuration for MCG. (b) Magnetic field map sequences (false color representation) of a heart-healthy volunteer and (c) of a patient with a high risk for sudden heart death (according to H. Koch, IEEE Trans. Appl. Supercond. **AS-11** 49-59 (2001)).

techniques by sophisticated gradiometer approaches. In recent years considerable progress has been made as far as ever better noise suppression techniques are concerned, and combinations of hardware and software gradiometers produced impressive results.¹⁰⁷ An example is shown in Fig. 4.30 where the magnetic field distribution during the R-peak above the thorax of a healthy volunteer is shown in an arrow field representation. The field distribution was measured with a SQUID configuration consisting of 11 SQUID chips positioned at the sides of two cubes placed on top of each other.¹⁰⁸ Thus the vector components B_x , B_y and B_z of two planes could be approximated by composing the signals from the individual SQUIDs according to $B_x \sim (B_{x1} + B_{x2})/2$. The acquired field distribution is surprisingly smooth and simple and it is straightforward to derive the corresponding current distribution generating the measured magnetic field pattern. Improved vector magnetometer systems containing modules with an even larger number of SQUIDs allow the measurement of the magnetic field vectors in three planes at many measurement sites. Then, by exploitation of redundancies and vector analytical relations (such as curl and div), a comprehensive picture of the biomagnetic field is obtainable.

Magnetoencephalography

Magnetoencephalography (MEG) is a completely noninvasive, non-hazardous technology for functional brain mapping. It provides a spatial resolution of about 2 mm and an excellent temporal resolution on the order of 1 ms, during the localization and characterization of the electrical activity of the central nervous system by measuring the associated magnetic fields emanating from the brain. MEG measures the intercellular currents of the neurons in the brain giving a direct information on the spontaneous or stimulated brain activity. Since MEG takes its measurements directly from the activity of the neurons themselves, its temporal resolution is comparable with that of intracranial electrodes. Since the first MCG-SQUID experiments in 1970,¹⁰⁹ a large number of different MEG-system solutions have been introduced, which we will not address here. MEG has particularly profitted from advances in computing algorithms and SQUID sensor hardware. Due to the small signals SQUID sensors with optimum field resolution are required. Furthermore, the suppression of noise signals is an important aspect in MEG.

¹⁰⁷J. Vrba, *SQUID gradiometers in real environments*, in *SQUID Sensors: Fundamentals, Fabrication and Applications*, H. Weinstock, ed., NATO ASI Series E: Applied Sciences, Vol. 329, pp. 117-178, Kluwer Academic Publishers, Dordrecht (1996).

¹⁰⁸M. Burghoff, H. Schleyerbach, D. Drung, L. Trahms, and H. Koch, *A vector magnetometer module for biomagnetic application*, IEEE Trans. Appl. Supercond. **AS-9**, 4069-4072 (1999).

¹⁰⁹D. Cohen, E. A. Edelsack, and J.E. Zimmerman, *Magnetocardiograms taken inside a shielded room with a superconducting point-contact magnetometer*, Appl. Phys. Lett. **19**, 278-280 (1970).

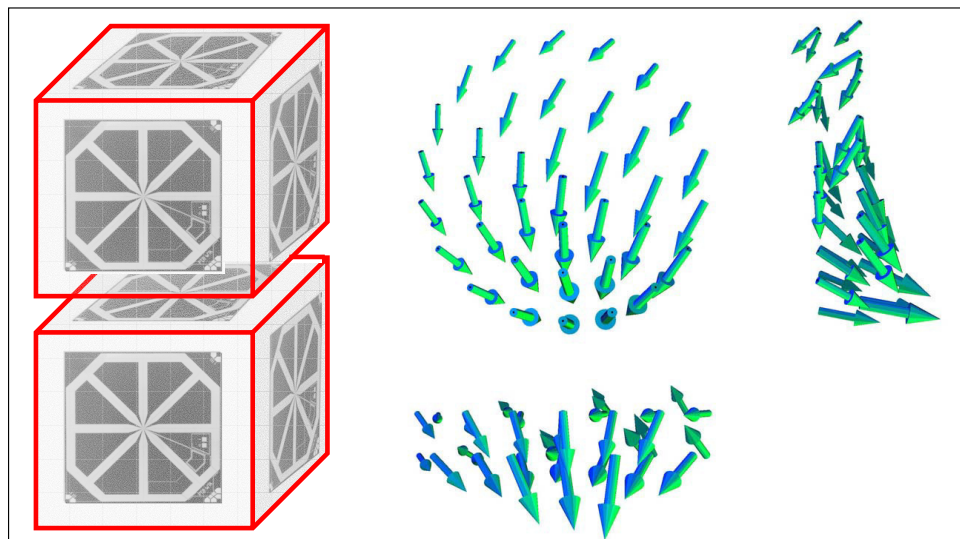


Figure 4.30: Magnetic vector field during the R peak measured sequentially at 37 positions with an 11 SQUID chip configuration as shown on the left. Displayed are the top view and two side views of an arrow representation of the field distribution (courtesy of PTB Berlin).

The information provided by MEG is entirely different from that provided by Computer Tomography (CT) or Magnetic Resonance Imaging (MRI). Whereas these techniques provide structural/anatomical information, MEG provides functional information. That is, MEG is a functional imaging technique complementary to the anatomical imaging methods MRI and CT. Of course, the two modalities can be combined into a composite image containing information on function *and* anatomy. It is obvious that the combination of MEG and MRI techniques has considerable clinical potential.

Of course, SQUID based MEG has to compete with various other functional imaging techniques such as Positron Emission Tomography (PET) and functional MRI (fMRI), which are weakly invasive and measure signals caused by changes of blood flow. At present, the time resolution of MEG (about 1 ms) is far superior to that of the other techniques, while the spatial resolution is similar. In general, MEG's strengths complement those of other brain activity measurement techniques such as electroencephalography (EEG), PET and fMRI. Here particular advantages of MEG are that the measured biosignals are not distorted by the body as in EEG (unless ferromagnetic implants are present) and that it is completely non-invasive, as opposed to PET and possibly MRI/fMRI. The clinical uses of MEG are in detecting and localizing epileptiform spiking activity in patients with epilepsy, and in localizing eloquent cortex for surgical planning in patients with brain tumors or intractable epilepsy. In research, MEG's primary use is the measurement of time courses of activity, which cannot be measured using fMRI.

4.5.2 Nondestructive Evaluation

An interesting field of application of SQUID sensors is **nondestructive evaluation** (NDE). NDE is the noninvasive identification of structural or material flaws in a specimen. Examples are the imaging of surface and subsurface cracks or pits due to corrosion or fatigue in aging aircraft and reinforcing rods in concrete structures.^{110,111} Of course, there are several competing methods for NDE such as acoustic, thermal, and electromagnetic techniques. However, these methods are often not entirely adequate for detecting flaws at an early enough stage, usually because of a lack of spatial or depth resolution. Since

¹¹⁰J.P. Wikswor Jr., IEEE Trans. Appl. Supercond. **AS-5**, 74 (1995).

¹¹¹G.B. Donaldson, A. Cochran, R.M. Bowman, *More SQUID Applications*, in *The New Superconducting Electronics*, H. Weinstock, R.W. Ralston (eds.), Kluwer Academic Publishers, Dordrecht (1993), pp. 181-220.

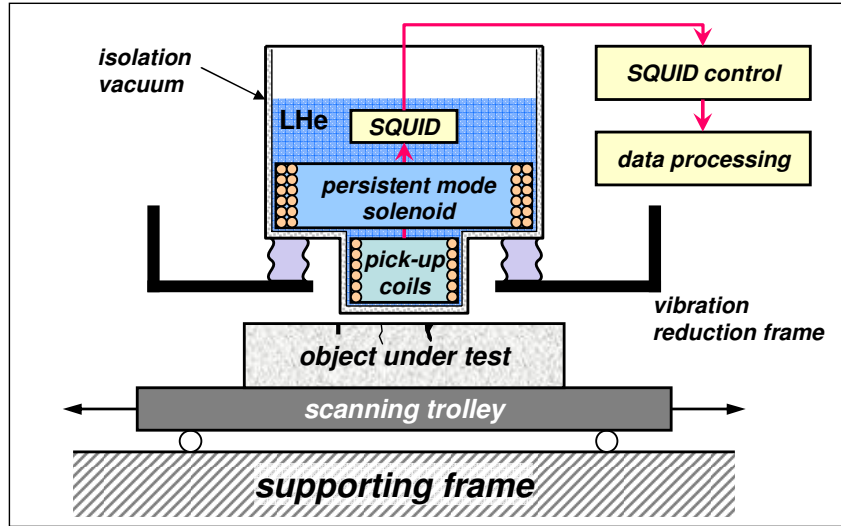


Figure 4.31: Typical experimental set-up for SQUID based NDE. For high- T_c SQUIDs liquid nitrogen or cryocoolers instead of liquid helium is used for cooling. The sample motion is controlled by a motorized motion control and linear encoders.

the object to be studied usually is at room temperature and an important parameter is the lateral spatial resolution, which is of the order of the distance between the sensor and the object under study, the distance between the inner cold wall and the outer warm wall of the SQUID measuring systems must be as small as possible. Therefore, SQUIDs based on high temperature superconductors operated at 77 K are advantageous for NDE applications. In this case the required dewars or cryocoolers are simpler and more compact.

Fig. 4.31 shows a typical experimental set-up for SQUID based NDE. A magnet is used to magnetize the object under study, which is placed below the pick-up coil of a SQUID sensor. Cracks in the plate or variations in the magnetic properties will disturb the magnetic field pattern and the resulting flux change is detected by the SQUID sensor. The advantage of the SQUID sensor is that the flux changes can be measured with unchanged sensitivity in rather high background fields. This method of detection is also called remote magnetometry.

An important application of SQUIDs in NDE is the detection of subsurface damage in metallic structures such as aircraft parts by eddy current techniques. Here, an alternating magnetic field produced by a drive coil is applied and the fields generated by the induced eddy currents in the structure are lock-in detected. The eddy currents are diverted by structural flaws resulting in distortions of the magnetic field. Since the eddy currents flow over a skin depth, which is inversely proportional to the square root of the frequency, deep defects require correspondingly low frequencies. Here, the flat frequency response of SQUIDs is a distinct advantage over the response of currently used coil systems, which fall off with decreasing frequency. Demonstrations of eddy-current NDE using high- T_c SQUIDs have been reported by a number of groups.^{112,113,114,115,116} One should note however that the better sensitivity of SQUID systems has to be retained in a mobile unit capable of operating in the magnetically unfriendly environment such as an

¹¹²Y. Tavrin, H.-J. Krause, W. Wolf, V. Glyantsev, J. Schubert, W. Zander, and H. Bousack, *Cryogenics* **36**, 83 (1995).

¹¹³M. Mück, M., M. v. Kreutzbruck, U. Baby, J. Tröll, and C. Heiden, *Physica C* **282-287**, 407 (1997).

¹¹⁴M. v. Kreutzbruck, J. Tröll, M. Mück, C. Heiden, and Y. Zhang, *IEEE Trans. Appl. Supercond.* **AS-7**, 3279 (1997).

¹¹⁵R. Hohmann, H.-J. Krause, H. Soltner, Y. Zhang, C. A. Copetti, H. Bousack, and A. I. Braginski, *IEEE Trans. Appl. Supercond.* **AS-7**, 2860 (1997).

¹¹⁶H.-J. Krause, Y. Zhang, R. Hohmann, M. Grüneklee, M. I. Faley, D. Lomparski, M. Maus, H. Bousack, and A. I. Braginski, in *Proceedings of the EUCAS'97*, Ueldhoven Institute of Physics Conference Series No. 158, H. Rogalla and D. H. A. Blank eds., Institute of Physics, Philadelphia (1997), p. 775.

aircraft maintenance hangar or a factory.

NDE with SQUIDs can also be used for the detection of magnetic fields generated by specimens containing magnetized components.¹¹⁷ Furthermore, by scanning samples of steel one can explore the correlation between mechanical stress and magnetic-field distribution. This represents a unique probe of the mechanical or thermal stress to which a sample has been subjected. For example, it was shown that SQUID sensors based on second-order electronic gradiometers can be used to detect ferrous inclusions in the disks of turbine engine rotors.¹¹⁸ In an other application a dc SQUID magnetometer was used to detect fine magnetic particles in a rapidly moving copper wire. The nitrogen-cooled SQUID was surrounded by a magnetic shield and the wire was pulled through holes in the shield about 15 mm below the SQUID sensor at speeds of 10 to 500 m/min. Iron particles as small as 50 μm in diameter could be detected. The goal of this technique is to locate impurities that make the wire brittle, causing it to break. Fortunately, most NDE applications do not require the highest sensitivity of SQUID sensors, since the Nyquist noise generated by the sample can be of the order of $1 \text{ pT}/\sqrt{\text{Hz}}$. However, this noise level is still much lower than that of coil systems conventionally used for eddy current NDE. Thus, NDE applications based in particular on high- T_c SQUIDs are very promising.

4.5.3 SQUID Microscopy

Scanning SQUID microscopy (SSM) is a modern technique capable of imaging the magnetic field distribution in close proximity across the surface of a sample under investigation with high sensitivity and modest spatial resolution. It is based on a thin-film SQUID sensor. Initially, scanning SQUID microscopes were based on low- T_c dc-SQUIDs and have been used to image static magnetic fields with a combination of high field and spatial resolution.^{119,120} Shortly afterwards, high- T_c SQUID microscopes have been developed, in which the sample could be either at 77 K or at room temperature.^{121,122,123,124} Most often, the sample is moved over the SQUID in a two-dimensional scanning process and the magnetic signal is plotted versus the coordinate to produce an image. The frequency at which the image is obtained ranges from near zero, where simply the static magnetic field produced by the sample is measured, to beyond 1 GHz. Today SQUID microscopes with cold samples have a spatial resolution of about 5 μm , while those with room temperature samples have a resolution ranging between 30 and 50 μm . A recent innovation has dramatically improved the spatial resolution for cold samples, albeit at the price of reduced magnetic field sensitivity. A soft magnetic tip is used to focus the flux from the sample into the SQUID resulting in a spatial resolution of the order of 0.1 μm .¹²⁵

Fig. 4.32 shows a SQUID microscope, in which the sample is kept at room temperature. The SQUID is mounted in vacuum at the upper end of a sapphire rod (cold finger), the lower end of which is cooled by liquid nitrogen. Superinsulation surrounding the rod ensures that the temperature gradient along the rod is negligible. The SQUID is separated from the room temperature part and atmospheric pressure by a thin window, which may be either a 75 μm thick sapphire disk or a 3 μm thick Si_xN_y window fabricated

¹¹⁷G.B. Donaldson, S. Evanson, M. Otaka, K. Hasegawa, T. Shimizu, and K. Takaku, Br. J. Non-Destr. Test. **32**, 238 (1990).

¹¹⁸Y. Tavrin, M. Siegel, and J. Hinzen, 1999, IEEE Trans. Appl. Supercond. **AS-9**, 3809 (1999).

¹¹⁹A. Mathai, D. Song, Y. Gim, and F. C. Wellstood, IEEE Trans. Appl. Supercond. **AS-3**, 2609 (1993).

¹²⁰C.C. Tsuei, J. R. Kirtley, C. C. Chi, L. S. Yu-Jahnes, A. Gupta, T. Shaw, J. Z. Sun, and M. B. Ketchen, Phys. Rev. Lett. **73**, 593 (1994).

¹²¹R.C. Black, A. Mathai, F. C. Wellstood, E. Dantsker, A. H. Miklich, D. T. Nemeth, J. J. Kingston, and J. Clarke, Appl. Phys. Lett. **62**, 2128 (1993).

¹²²R.C. Black, F. C. Wellstood, E. Dantsker, A. H. Miklich, D. Kölle, F. Ludwig, and J. Clarke, IEEE Trans. Appl. Supercond. **AS-5**, 2137 (1995).

¹²³T.S. Lee, E. Dantsker, and J. Clarke, Rev. Sci. Instrum. **67**, 4208 (1996).

¹²⁴T.S. Lee, Y. R. Chemla, E. Dantsker, and J. Clarke, IEEE Trans. Appl. Supercond. **AS-7**, 3147 (1997).

¹²⁵P. Pitzius, V. Dworak, and U. Hartmann, in *Extended Abstracts of the 6th International Superconductive Electronics Conference (ISEC'97)*, H. Koch and S. Knappe eds., Physikalisch-Technische Bundesanstalt, Berlin, Vol. 3, (1997), p. 395.

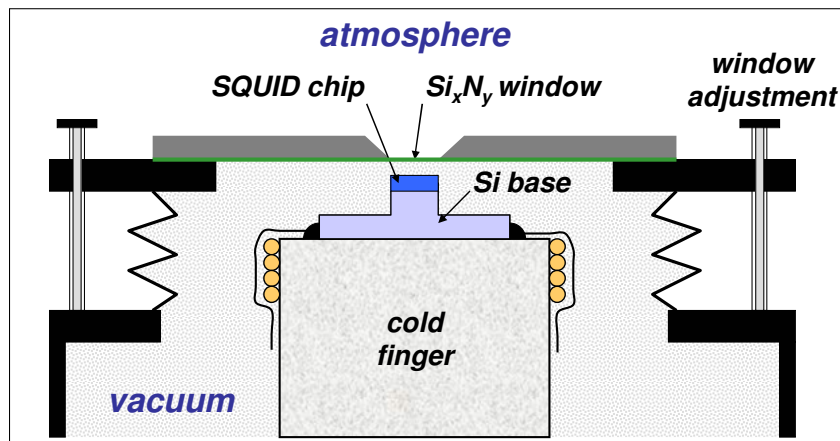


Figure 4.32: Cross-sectional view of a scanning SQUID microscope. The distance between the SQUID sensor and the Si_xN_y window can be adjusted by adjustment screws.

on a Si chip. In the first case, the SQUID-to-sample separation is typically $150 \mu\text{m}$, whereas in the latter, the separation can be as low as $15 \mu\text{m}$. Note that the smaller the SQUID-to-sample distance the better the spatial resolution. The entire system is surrounded by a μ -metal shield to exclude spurious magnetic field fluctuations.

For low-frequency operation (typically less than 1 kHz) the SQUID is operated in the flux lock loop. Here, a typical application is the study of the magnetic properties of superconducting thin-film structures as well as the diagnostics of superconducting integrated circuits or highly sensitive bolometers. In such application the sample is usually at the same temperature as the SQUID sensor. Two typical examples are shown in Fig. 4.33. Furthermore, SSM can be applied to study magnetic properties of the ultra-thin magnetic films. The distribution of stray magnetic fields produced by the remnant magnetization or the induced magnetization of the film can be visualized. The domain structures, the orientation of the magnetic moment and the value of the magnetization can be determined. Moreover, SSM has the potential to image the magnitude of a magnetic field normal component over the surface of magnetic recording media. It also can be applied to the analysis of chips or wafers in microelectronics^{126,127} or the study of magnetically active bacteria.¹²⁸ For higher-frequency operation (typically 1 kHz to 1 MHz) the SQUID is operated open loop and a drive coil is used to apply a sinusoidal magnetic field to induce eddy currents in the sample and modulate the flux in the SQUID.¹²⁹ The magnetic response of the sample is determined by measuring the amplitude and phase of the output from the SQUID: the out-of-phase component corresponds to the eddy current in the sample. The imaging frequency has further been extended from 1 MHz to 1 GHz by applying a rf-field to the sample, which, in turn, couples an rf-flux into the SQUID.¹³⁰

There are many other techniques for imaging magnetic fields at surfaces: decoration techniques,¹³¹ magneto-optical imaging,¹³² magnetic force microscopy,¹³³ scanning Hall probe microscopy,¹³⁴ scan-

¹²⁶S. Chatraphorn, E.F. Fleet, F.C. Wellstood, *J. Appl. Phys. Lett.* **92**, 4731 (2002).

¹²⁷J. Beyer, H. Matz, D. Drung, Th. Schurig, *Appl. Phys. Lett.* **74**, 2863 (1999).

¹²⁸T.S. Lee, Y.R. Chemla, E. Dantsker, J. Clarke, *IEEE Trans. Appl. Supercond.* **AS-7**, 3147 (1997).

¹²⁹R.C. Black, F. C. Wellstood, E. Dantsker, A. H. Miklich, J. J. Kingston, D. T. Nemeth, and J. Clarke, *Appl. Phys. Lett.* **64**, 1 (1994).

¹³⁰R.C. Black, F. C. Wellstood, E. Dantsker, A. H. Miklich, D. T. Nemeth, D. Koelle, F. Ludwig, and J. Clarke, *Appl. Phys. Lett.* **66**, 1267 (1995).

¹³¹D. J. Bishop, P. L. Gammel, D. A. Huse, and C. A. Murray, *Science* **255**, 165 (1992).

¹³²S. Gotoh and N. Koshizuka, *Phys. C* **176**, 300 (1991).

¹³³D. Rugar, H. J. Mamin, P. Guethner, S. E. Lambert, J. E. Stern, I. McFadyen, and T. Yogi, *J. Appl. Phys.* **68**, 1169 (1990).

¹³⁴A. M. Chang, H. D. Hallen, L. Harriott, H. F. Hess, H. L. Kao, J. Kwo, R. E. Miller, R. Wolfe, and J. van der Ziel, *Appl.*

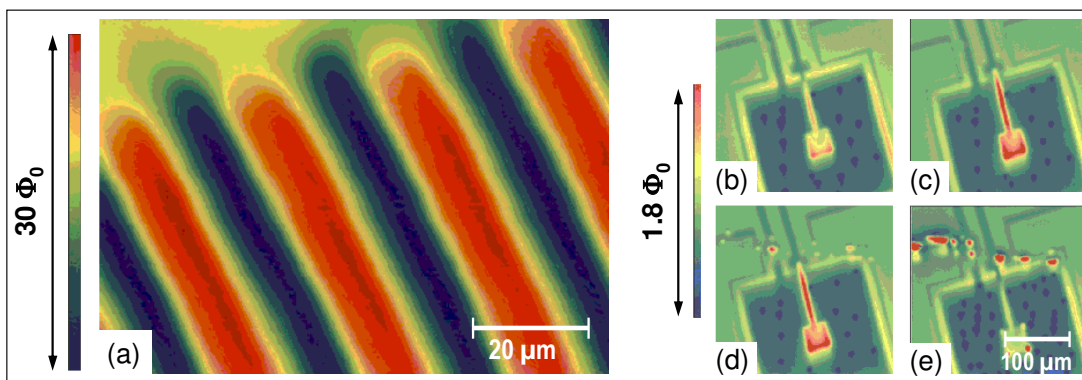


Figure 4.33: (a) Scanning SQUID microscopy image showing the magnetic field distribution above the alignment track on a 5.25 in floppy disk. The color code gives the flux range threading the $10 \mu\text{m}$ diameter SQUID loop oriented normal to the disk surface. (b) to (e) Images of the normal component of the field above a high- T_c YBCO washer SQUID with a scratch running from the upper left to the middle right. (a) Washer cooled in low field, then (b) cycled to 0.6 G , and (c) to 2.2 G at 4.2 K , and finally (d) cycled to 2.4 G at 77 K . Flux traps first along the scratch, and then at inside corners of the SQUID (according to J. R. Kirtley, M. B. Ketchen, C. C. Tsuei, J. Z. Sun, W. J. Gallagher, Lock See Yu-Jahnes, A. Gupta, K. G. Stawiasz, S. J. Wind, IBM J. Res. Develop. **39**, 655 (1995)).

ning electron microscopy with polarization analysis (SEMPA),¹³⁵ and electron holography.¹³⁶ Each of these techniques has its own advantages: For example, the magneto-optical techniques are relatively simple and provide the possibility for time-resolved studies, and the electron microscope techniques have very good spatial resolution.¹³⁷ The advantage of the scanning SQUID microscope is its very high sensitivity. Roughly speaking, the scanning SQUID microscope is orders of magnitude more sensitive to magnetic fields than the other techniques. In addition, it gives an easily calibrated absolute value for the local magnetic fields. A disadvantage of SSM is its relatively poor spatial resolution. Whereas for SSM a resolution of only $5 \mu\text{m}$ has been demonstrated, SEMPA, for example, has a spatial resolution of 30-50 nm. Nevertheless, there are many possible applications of SSM, which do not require submicron spatial resolution.

4.5.4 Gravity Wave Antennas and Gravity Gradiometers

SQUID systems are used in a number of experiments designed for measuring gravitational forces. Important topics in this area are inertial navigation, general relativity verification, the analysis of deviations from the $1/r^2$ law and the detection of gravitational waves. Gravitational waves are emitted by bodies when the mass distribution varies non-spherically (e.g. collapsing star or rotating double star). To detect gravitational waves one can look for the expansion and contraction oscillations caused by the gravitational wave. A simple version of such a setup is called a **Weber bar** – a large, solid piece of metal with electronics attached to detect any vibrations.^{138,139} However, the expected length change $\Delta\ell/\ell$ is extremely small and typically below 10^{-19} . Therefore, highly sensitive detectors are required having a resolution down to 10^{-21} .

A typical experimental setup is shown in Fig. 4.34. The vibrations of the large bar are amplified by a

Phys. Lett. **61**, 1974 (1992).

¹³⁵M. R. Scheinfein, J. Unguris, M. H. Kelley, D. T. Pierce, and R. J. Celotta, Rev. Sci. Instrum. **61**, 2501 (1990).

¹³⁶K. Harada, T. Matsuda, J. Bonevich, M. Igarashi, S. Kondo, G. Pozzi, U. Kawabe, and A. Tonomura, Nature **360**, 51 (1992).

¹³⁷L. N. Vu and D. J. Van Harlingen, IEEE Trans. Appl. Supercond. **AS-3**, 1918 (1993).

¹³⁸S.L. Shapiro, R.F. Stark, S.J. Teukolsky, Am. Sci. **73**, 248-257 (1985).

¹³⁹J.C. Price, R.C. Taber, Science **237**, 150-157 (1987).

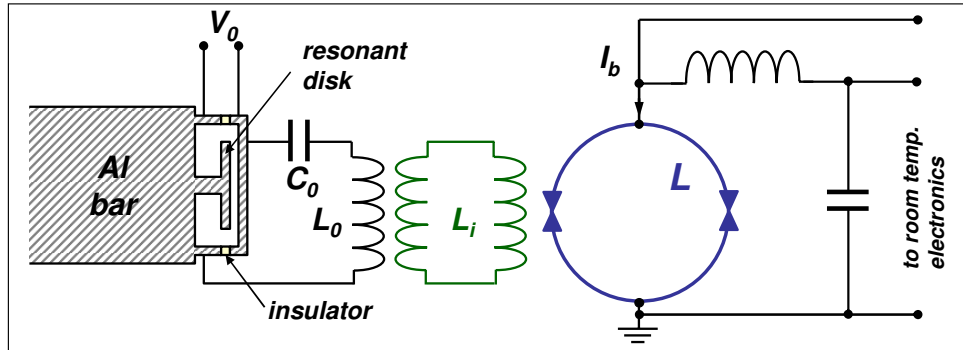


Figure 4.34: Typical setup for the detection of gravity waves. An Al-bar of several tons has a resonant transducer connected to the end of the bar. The small displacement of the disk is detected by a SQUID sensor via a capacitive coupling of the disk-to-flux transformer circuit.

resonant mass transducer and the displacement induces a current in a flux-transformer which is coupled to the input coil of a SQUID sensor. The antenna has to be cooled down to the mK-regime to reduce the mechanical noise and it further needs a very high quality factor. The resolution is then determined only by the bar's zero point motion. Since the typical resonance frequencies range in the 1 kHz regime one has to cool down below $\hbar\omega_{\text{ant}}/k_B \simeq 50 \text{ nK}$. However, one can make the effective noise temperature of the antenna much higher by increasing the bar's resonant quality factor Q . If a gravitational signal in the form of a pulse of length τ interacts with the antenna that has a decay time Q/ω_{ant} , the effective noise temperature is given by $T_{\text{eff}} = T \frac{\tau}{Q/\omega_{\text{ant}}}$, that is by the antenna temperature multiplied by the ratio of the signal pulse length and the antenna decay time. To achieve the quantum limit, where the bar energy $\hbar\omega_{\text{ant}}$ is larger than the effective thermal energy $k_B T_{\text{eff}}$, one has to cool down below $T = Q\hbar/k_B\tau$. For $Q = 2 \times 10^6$ and $\tau = 1 \text{ ms}$ this is roughly 20 mK what is achievable with standard dilution refrigerators. Of course, a quantum limited sensor is required for the detection of the motion of the quantum-limited antenna. That is, the sensitivity of the SQUID has to approach the quantum limit. At present, a number of gravity wave antennas with $\Delta\ell/\ell$ sensitivities in the 10^{-18} regime have been fabricated and are in use since a few years. However, until now no detection of gravity waves has been reported. There are plans to build spherical detectors with a diameter of 3 m and an sensitivity of about 10^{-21} .

Gravity gradiometers are in principle also displacement sensors.^{140,141} A typical configuration is shown in Fig. 4.35. The gradiometer consists of two superconducting test masses, which are fixed by springs so that they can move along their common axis. A single layer wire-wound spiral coil is attached to the surface of one of the masses so that the surface of the wire is very close to the opposing surface of the other mass. The induction of the coil depends on the separation of the two test masses, which in turn depends on the gravity gradient. The coil is connected to a second coil which is coupled to the input coil of a SQUID sensor via a superconducting flux transformer. The gravity gradient is a tensor and is expressed in Eötvös ($1 \text{ Eötvös} = 10^{-9} \text{ s}^{-2}$). Until today sensitivities of a few Eötvös have been achieved. Gravity gradiometers can be used for mapping the earth's gravity gradient and have the potential for testing the inverse square law. A further application is inertial navigation. Several space-born instruments with sensitivities of a few to 0.001 Eötvös down to the mHz-regime have been proposed.

¹⁴⁰H.J. Paik, in *SQUID Applications to Geophysics*, H. Weinstock and W.C. Overton (eds.), Soc. of Exploration Geophysicists, Tulsa, Oklahoma (1981), pp. 3-12.

¹⁴¹E.A. Mapoles, in *SQUID Applications to Geophysics*, H. Weinstock and W.C. Overton (eds.), Soc. of Exploration Geophysicists, Tulsa, Oklahoma (1981), pp. 153-157.

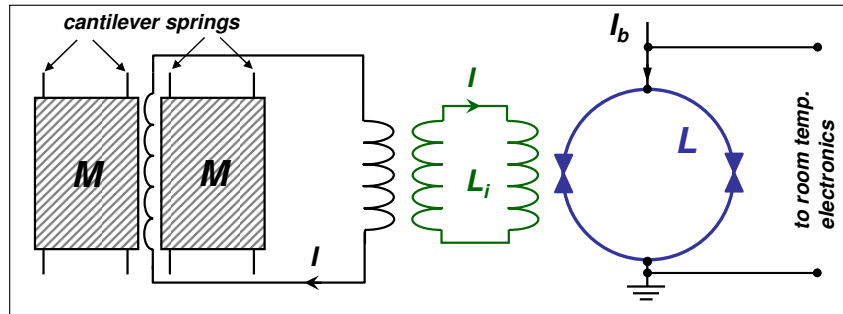


Figure 4.35: Gravity gradiometer consisting of two test masses M on either side of a planar spiral coil.

4.5.5 Geophysics

SQUID systems play an important role in determining the magnetic properties of the earth. This concerns both the characterization of specific earth samples (rock magnetometry) and the mapping of the earth magnetic field as well as its electromagnetic impedance. Particularly, high- T_c SQUID magnetometers are promising for geophysical surveying such as for example, magnetotellurics, controlled-source electromagnetics, and cross-borehole sounding.¹⁴² In magnetotellurics, the fluctuating horizontal components of the electric and magnetic fields at the earth's surface are measured simultaneously. These fluctuating fields originate in the magnetosphere and ionosphere. From these frequency-dependent fields the impedance tensor of the ground can be calculated allowing to estimate the spatial variation of the resistivity of the ground. The interesting frequency range is about 10^{-3} to 10^2 Hz corresponding to a skin depth between about 50 km and 150 m (assuming a resistivity of $10\Omega\text{m}$). An important problem is the elimination of local noise sources. This can be achieved by cross-correlating the fluctuating fields with those measured by a remote (several km away) reference magnetometer. Applications of magnetotellurics include surveying for oil and gas, mineral and geothermal sources, and locating subsurface fault lines.

Currently, magnetic measurements in geophysics are mostly made with induction coils. However, the availability of high- T_c based liquid nitrogen-cooled magnetometers has renewed interest in the use of SQUID sensors. Below about 1 Hz, the spectral density of the noise in coils increases as $1/f^3$, whereas that of SQUIDs increases only as $1/f$, giving the latter magnetometer a substantial advantage at low frequencies. Furthermore, coils for use below 1 Hz can be as long as 1.5 m, and the deployment of three such coils orthogonally, buried in the ground for stability, is a tedious undertaking. Obviously, a three-axis high- T_c magnetometer in a compact dewar with a long hold time becomes competitive.^{143,144} The sensitivity required for magnetotellurics is about $20\text{-}30 \text{ fT}/\sqrt{\text{Hz}}$ in the white noise regime and a $1/f$ knee of 1 Hz.

¹⁴²J. Clarke, T. D. Gamble, W. M. Goubau, R. H. Koch, and R. F. Miracky, *Geophys. Pros.* **31**, 149 (1983).

¹⁴³D. Drung, T. Radic, H. Matz, H. Koch, S. Knappe, S. Menkel, and H. Burkhardt, *IEEE Trans. Appl. Supercond.* **AS-7**, 3283 (1997).

¹⁴⁴E. Dantsker, D. Kölle, A. H. Miklich, D. T. Nemeth, F. Ludwig, J. Clarke, J. T. Longo, and V. Vinetskiy, *Rev. Sci. Instrum.* **65**, 3809 (1994).

Summary

dc-SQUID:

- A dc-SQUID is formed by a superconducting loop of inductance L intersected by two Josephson junctions with critical currents I_c .
- For negligible screening parameter $\beta_L = 2LI_c/\Phi_0 \ll 1$, the magnetic flux $\Phi = \Phi_{\text{ext}} + LI_{\text{cir}}$ threading the SQUID loop is about equal to the external flux, $\Phi \simeq \Phi_{\text{ext}}$, and the maximum supercurrent of the SQUID varies as

$$I_s^m = 2I_c \left| \cos \left(\pi \frac{\Phi_{\text{ext}}}{\Phi_0} \right) \right| .$$

- For large screening parameter $\beta_L = 2LI_c/\Phi_0 \gg 1$, the magnetic flux $\Phi = \Phi_{\text{ext}} + LI_{\text{cir}}$ threading the SQUID loop is about equal to $\Phi \simeq n\Phi_0$, and the maximum supercurrent of the SQUID varies as

$$I_s^m = 2I_c - \frac{2\Phi_{\text{ext}}}{L} = 2I_c \left(1 - \frac{2\Phi_{\text{ext}}}{\Phi_0} \frac{1}{\beta_L} \right) .$$

- For intermediate screening the $I_s^m(\Phi_{\text{ext}})$ dependence has to be determined self-consistently from the $\Phi(\Phi_{\text{ext}})$ and $I_s^m(\Phi)$ dependences.
- For negligible screening ($\beta_L \ll 1$) and strong damping ($\beta_C \ll 1$), the IVC of the dc-SQUID is given by

$$\langle V(t) \rangle = I_c R_N \sqrt{\left(\frac{I}{2I_c} \right)^2 - \left[\cos \left(\pi \frac{\Phi_{\text{ext}}}{\Phi_0} \right) \right]^2} .$$

- The mechanical analogue of the dc-SQUID are two pendula attached to a twistable rubber bar. For $\beta_L \ll 1$, the rubber bar is rigid, for $\beta_L \gg 1$ the rubber bar is soft. The relative angle of the pendula is determined by the applied magnetic flux: $\varphi_1 - \varphi_2 = 2\pi\Phi_{\text{ext}}/\Phi_0$.
- The performance of the dc-SQUID is determined by the flux-to-voltage transfer function

$$H = \left| \left(\frac{\partial V}{\partial \Phi_{\text{ext}}} \right)_{I=const} \right|$$

and the equivalent flux noise or noise energy

$$S_\Phi(f) = \frac{S_V(f)}{H^2} \quad \varepsilon(f) = \frac{S_\Phi(f)}{2L} = \frac{S_V(f)}{2LH^2} .$$

The noise energy sets the energy resolution of the dc-SQUID, which should be as small as possible for practical applications.

- For optimum operation parameters ($\beta_L \simeq 1$, $\beta_C \simeq 1$) the noise energy of the dc-SQUID is given by

$$\varepsilon(f) \simeq 16k_B T \sqrt{\frac{LC}{\beta_C}} \simeq \frac{16\sqrt{\pi}k_B T}{\omega_p} .$$

Best dc-SQUIDs have a noise energy of only a few \hbar .

- Since the $V(\Phi_{\text{ext}})$ dependence of dc-SQUIDs is nonlinear and periodic, the SQUID usually is operated in a flux-locked-loop, acting as a null detector.

RF-SQUID:

- A rf-SQUID is formed by a superconducting loop of inductance L intersected by a single Josephson junction with critical current I_c .
- The variation of the flux Φ threading the SQUID loop as a function of the applied flux Φ_{ext} is given by

$$\frac{\Phi}{\Phi_0} = \frac{\Phi_{\text{ext}}}{\Phi_0} - \frac{\beta_{L,\text{rf}}}{2\pi} \sin\left(2\pi\frac{\Phi}{\Phi_0}\right) .$$

- The rf-SQUID is operated by inductively coupling it to a resonant tank circuit and measuring the voltage V_T of the tank circuit (with inductance L_T , resonance frequency ω_{rf} , quality factor Q) as a function of the external flux Φ_{ext} .
- The performance of the rf-SQUID is determined by the flux-to-voltage transfer function

$$H \equiv \left| \left(\frac{\partial V_T}{\partial \Phi_{\text{ext}}} \right)_{I_{\text{rf}}=\text{const}} \right| \simeq \frac{\omega_{\text{rf}} L_T}{M}$$

and the equivalent flux noise or noise energy

$$S_\Phi \approx \frac{(LI_c)^2}{\omega_{\text{rf}}} \left(\frac{2\pi k_B T}{I_c \Phi_0} \right)^{4/3}$$

$$\varepsilon \approx \left(\frac{\pi \eta^2 \Phi_0^2}{2L} + 2\pi \eta k_B T_{\text{amp}}^{\text{eff}} \right) \frac{1}{\omega_{\text{rf}}} .$$

In order to make the noise energy small one has to increase the tank frequency ω_{rf} . Best rf-SQUIDs have a noise energy of the order of $100\hbar$.

- Since the $V_T(\Phi_{\text{ext}})$ dependence of rf-SQUIDs is nonlinear and periodic, the SQUID is usually operated in a flux-locked-loop, acting as a null detector.

SQUID Based Instruments:

- SQUID based instruments usually consist of an antenna transferring an input signal into a magnetic flux threading the SQUID loop, the autonomous SQUID acting as a flux-to-voltage converter, and the read out electronics.
- Depending on the antenna, SQUIDs can be used as magnetometers, gradiometers of different order, susceptometers, voltmeters, ammeters, or rf-amplifiers.
- The magnetic field resolution of best SQUID magnetometers are of the order of a few $\text{fT}/\sqrt{\text{Hz}}$ at a frequency of 1 Hz.
- First and higher order gradiometers are used for suppression of perturbing magnetic field fluctuations caused by the environment.

Applications of SQUIDs:

- In medical technology important applications of SQUIDs are magnetocardiography and magnetoencephalography. Multichannel SQUID systems are used to measure the magnetic field distribution due to currents flowing inside the body.
- SQUID sensors can be used for nondestructive evaluation of materials, in particular for the detection of structural or material flaws deep inside of a specimen.
- SQUID microscopy allows the imaging of the distribution of weak magnetic fields in various materials and devices such as superconducting and magnetic films and electronic circuits with a spatial resolution of a few μm .
- Further fields of application of SQUID systems are gravity wave detection and geophysics.

Chapter 5

Digital Electronics

The main purpose of digital electronics is to process and store binary signals. That is, two basic elements are required for any digital computing technology: a fast switching device and a memory element for bit storage. For semiconductor digital electronics the transistor is the switch and the memory is predominantly realized by storing charge on a capacitor. In analogy, in superconducting digital electronics the Josephson junction is the switch and the memory is realized by storing magnetic flux in an inductor realized by a superconducting loop.

After addressing the basic advantages and disadvantages of superconducting devices in digital electronics in section 5.1, we discuss the foundations and technical implementation of the ***Voltage State Josephson Logic*** and the ***Rapid Single Flux Quantum Logic*** in sections 5.2 and 5.3, respectively. As an important and promising application of superconducting digital devices and circuits, in section 5.4 we discuss ***Superconducting Analog-to-Digital Converters***.

5.1 Superconductivity and Digital Electronics

There are only a few basic requirements for any digital technology. Firstly, the processing, which is realized by elementary logic gates, should be fast, error free and low power. Secondly, in the same way the storage of data into a memory as well as the read-out should be fast, error free and low power. Thirdly, since digital electronics requires a large number of gates and memory cells, the fabrication process of the required devices should be reproducible and cheap. Finally, it should be possible to integrate a large number of devices into a small volume. Compared to semiconductor electronics the main advantages of superconducting digital electronics are its lower power consumption and higher speed.¹ Until today, clock frequencies above 100 GHz have been realized for superconducting digital circuits.^{2,3} Furthermore, the power consumption of the competing semiconductor digital electronics becomes an increasingly important problem and already today limits the further increase of clock frequency and integration level. Therefore, the main focus of digital applications of the Josephson effect is high-speed low power consumption computer systems.^{4,5,6}

Today, the applications of superconducting circuits in digital electronics are still under development because the scale/amount of technology required is much larger than that of analog applications. However, superconducting digital circuit technology always has been the driving technology for other applications such as SQUIDs, mixers, etc.. The fabrication technology for high-quality, reproducible Josephson junctions with low parameter spread and the required integration technology have been developed mainly for digital applications. In turn, these technologies have greatly improved the performance of analog Josephson devices such as integrated SQUID sensors, digital-to-analog converters, etc.. Digital electronics is certainly a huge and attractive but also very competitive market. In order to make it to the market place and to compete with the established semiconductor electronics, superconducting digital electronics must show up with significant advantages over semiconducting electronics in order to compensate for several disadvantages implied by the superconducting state:

- Cooling to low temperatures is required: Since complicated integrated superconducting circuits at least at present require Nb-technology, cooling to well below the transition temperature of Nb (9.2 K) is necessary. This requires cooling by liquid helium or expensive cryocoolers. Higher operation temperatures allowing for the use of liquid nitrogen or less expensive closed cycle refrigerators would be desirable. However, up to now there is no established technology for high temperature superconductor (HTS) that would allow the reproducible fabrication of a large number of Josephson junctions and other circuit elements within the required margins of yield and parameter spread. It should be noted, however, that the disadvantage related to the required cooling of superconducting circuits becomes less severe as the competing semiconductor circuits require an increasing effort for removing the large amount of dissipated heat.
- The change-over to a new technology (e.g. from semiconductor to superconductor technology) involves huge financial investments for fabrication equipment and the development of the fabrication technology.
- New technologies for logic elements, packaging, power supply, ... have to be developed causing again significant costs.

¹D.G. McDonald, R.L. Petersen, C.A. Hamilton, R.E. Harris, R.L. Kautz, IEEE Trans. El. Dev. **ED-27**, 1945-1965 (1980).

²K.K. Likharev, V.K. Semenov, IEEE Trans. Appl. Supercond. **AS-1**, 3 (1991).

³W. Chen, V. Rylyakov, V. Patel, J.E. Lukens, K.K. Likharev, IEEE Trans. Appl. Supercond. **AS-9**, 3212 (1999).

⁴S. Hasuo, T. Imamura, Proc. IEEE **77**, 1177 (1989).

⁵H. Hayakawa, Computing, in *Superconducting Devices*, Steven T. Ruggiero, David A. Rudman (eds.), Academic Press Inc., San Diego (1990).

⁶S. Hasuo, *Josephson Processors*, in *The New Superconducting Electronics*, H. Weinstock ed., Kluwer Academic Publishers, Dordrecht (1993).

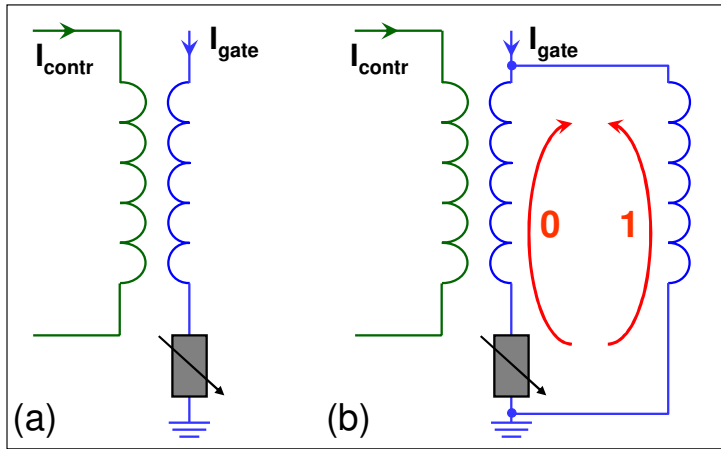


Figure 5.1: Illustration of the switching element (a) and the memory element (b) for the cryotron. The magnetic field of the control current switches the gate line into the resistive normal state represented in the equivalent circuit by the switchable series resistor.

5.1.1 Historical development

In this subsection we briefly address the historical development of superconducting digital circuits. Many ideas are quite old and never made it to the market place due to the dominating semiconductor technology.

1. *Cryotron* (1956):

In 1956 the *cryotron* was suggested.⁷ Here, the transition between the superconducting and normal state in a superconducting thin film was used for switching a current path. As shown in Fig. 5.1, the cryotron consists of two superconducting lines, where the control line has a higher critical magnetic field H_c than the gate line. This can be realized by using different materials. The control current generates a magnetic field that exceeds H_c of the gate line driving it into the normal state. With appropriate design parameters this normal gate can switch enough current to control another gate. Combining these cryotrons various logic gates can be realized. The memory cell was essentially a closed superconducting loop that could store magnetic flux of either sign (corresponding to 0 or 1) by a persistent current circulating in opposite directions. If part of the loop is also a cryotron gate, flux can be transferred into or out of the loop by driving this part into the normal state with the control current. This allows to write in or read out the stored bit.

The major drawback of this device was the low switching speed of ~ 10 ns limited by the L/R time. Furthermore, local self-heating in the normal state resulted in an increased time for the return into the superconducting state. Already in the early 1960s it was clear that this technology could not compete with the upcoming semiconductor integrated circuits.

2. *Josephson Switching Device* (1966):

J. Matisoo of IBM realized the first Josephson switching device in 1966 with sub-nanosecond switching speed soon after the Josephson effect has been discovered.⁸ As shown in Fig. 5.2, in this *Josephson cryotron* the critical current of a Josephson junction was suppressed by a magnetic field that was typically orders of magnitude smaller than the critical field of a superconductor. An even much smaller field is required to suppress the critical current of a dc SQUID. Hence, much smaller control currents and smaller inductances were required to drive the Josephson junction or

⁷D.A. Buck, Proc. IRE **44**, 482 (1956).

⁸J. Matisoo, Appl. Phys. Lett. **9**, 167 (1966).

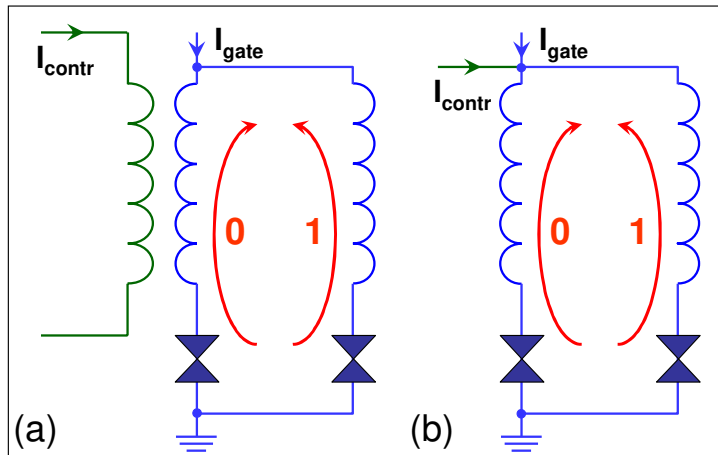


Figure 5.2: Schematic illustration of the Josephson cryotron switching and memory element. (a) Inductively and (b) directly coupled switching or memory element. The Josephson element acts as the switchable resistor.

the SQUID into the resistive state. This resulted in smaller L/R and in turn shorter switching times. A loop containing Josephson junctions also could be used to store magnetic flux via a circulating current. The flux is entering and leaving the loop via one of the Josephson junctions. The more sensitive control permits the use of the natural binary bit of a superconducting loop, namely the flux quantum Φ_0 . The proper choice of the circuit parameters allows to switch the SQUID between zero and a single flux quantum in the loop. Of course, the large sensitivity to even small magnetic fields created also the problem that ambient magnetic fields lead to the presence of accidentally trapped magnetic flux in the circuit. This requires very good magnetic shielding by e.g. several μ -metal shields. In addition, thin film Josephson circuits have been fabricated with so called magnetic moats, slots in the superconducting ground plane of the circuit, where any residual magnetic flux was trapped away from the sensitive parts of the circuit.⁹

Following the initial work on the Josephson cryotron IBM conducted a large program for developing a Josephson computer.¹⁰ This program was stopped in 1983. In the course of this program essential computer components including logic and memory circuits and systems have been developed as well as fabrication and packaging technologies. There were two major reasons why IBM stopped the project. Firstly, the use of Pb-alloy technology did not allow to fabricate Josephson junctions with a sufficiently small spread of the critical current. Furthermore, the Pb-alloy junctions were not stable enough to withstand repeated thermal cycling. Secondly, the IBM program was focusing on latching logic gates based on underdamped Josephson junctions. This latching logic, where the current bias has to be switched off to return to the zero voltage state, has several disadvantages discussed below and did not allow for clock speeds well above 1 GHz. The former problem nowadays has been solved through the Nb-technology, the latter by using the non-latching ***Rapid Single Flux Quantum (RSFQ)*** logic.

Stimulated by the IBM activities, major Japanese computer companies and government agencies (ETL, NEC, Hitachi, Fujitsu, NTT) started the ***Japanese High Speed Computer project*** in 1981, in which the Josephson junction device was selected as one possible candidate (together with GaAs and HEMT) for the realization of future high-speed computer systems. These efforts continued even after the IBM project has been stopped and led to much progress in junction fabrication

⁹M. Jeffery, T. Van Duzer, J.R. Kirtley, and M.B. Ketchen, *Magnetic Imaging of Moat-Guarded Superconducting Electronic Circuits*, Appl. Phys. Lett. **67**, 1769 (1995).

¹⁰W. Anacker, *Josephson Computer Technology*, IBM J. Res. Develop. **24**, 107 (1980).

and integration technology, device concepts and systems.^{11,12,13,14} With respect to technology the most important progress was the fabrication of Nb/Al₂O₃/Nb tunnel junctions instead of Pb-alloy junctions.¹⁵ These so-called “refractory” junctions even allow the construction of circuits with large scale integration (LSI) complexity. The Nb-technology also had a large impact on the further development of other Josephson applications (sensors, mixer, AD converter, . . .).

3. *Rapid Single Flux Quantum (RSFQ) Logic* (1985):

After the failure of the IBM project significant progress was achieved by the suggestion of the *RSFQ (Resistive or Rapid Single Flux Quantum) logic*.¹⁶ In RSFQ overdamped Josephson junctions are used. In this non-latching logic information is represented in a totally different way from that used in the latching voltage logic based on underdamped Josephson junctions. If an overdamped junction is biased with a current slightly larger than the critical current, the Josephson current has the form of short pulses with the pulse duration being of the order of $\Phi_0/I_c R_N$ (compare Fig. 3.7 in section 3.3). For a typical $I_c R_N$ product of 1 mV the pulse duration is only 2 ps. During a single pulse the phase difference across the Josephson junction evolves by 2π . According to the 2. Josephson equation ($\dot{\phi}/2\pi = V/\Phi_0$) this means that the phase change results in a short voltage pulse with $\int V dt = \Phi_0$. The idea of the RSFQ logic is to use these voltage pulses for the realization of logic circuits. Following the first ideas by Likharev^{17,18} as well as Nakajima and coworkers^{19,20} the first logic element, a T-flip-flop, has been proposed by Silver in 1978.²¹ Today a large variety of RSFQ circuits has been implemented^{22,23} with the ultimate speed of an RSFQ device ever measured experimentally being 770 GHz.²⁴ Major advantages of the RSFQ logic are (i) low power consumption, (ii) intrinsic memory, and (iii) very high speed.

5.1.2 Advantages and Disadvantages of Josephson Switching Devices

Before discussing the foundations of latching Josephson switching gates in section 5.2 and non-latching RSFQ circuits in section 5.3, we briefly address several basic advantages and disadvantages of Josephson junction based devices compare to semiconductor devices.

¹¹T. Nishino, Supercond. Sci. Techn. **10**, 1 (1997).

¹²S. Kotani, A. Inoue, H. Suzuki, S. Hasuo, T. Takenouchi, K. Fukase, F. Miyagawa, S. Yosida, T. Sano, Y. Kamioka, IEEE Trans. Appl. Supercond. **AS-1**, 164 (1991).

¹³M. Hosoya, T. Nishino, W. Hioe, S. Kominami, K. Takagi, IEEE Trans. Appl. Supercond. **AS-5**, 3316 (1995).

¹⁴H. Kroger, *Josephson devices and technology*, in Japanese Assessment, Noyes Data Corporation, Park Ridge, NJ (1986) pp. 250-306.

¹⁵H. Nakagawa, I. Kurosawa, M. Aoyagi, S. Kosaka, Y. Hamazaki, Y. Okada, S. Takada, IEEE Trans. Appl. Supercond. **AS-1**, 37-47 (1991).

¹⁶K.K. Likharev, V.K. Semenov, *RSFQ Logic/Memory Family: A New Josephson Junction Technology for sub-THz Clock Frequency Digital Systems*, IEEE Trans. Appl. Supercond. **AS-1**, 3 (1991).

¹⁷K.K. Likharev, *Properties of a superconducting ring closed with a weak link as a device with several stable states*, Radio Eng. and Electron. Phys. **19**, 109-115 (1974).

¹⁸K.K. Likharev, O.A. Mukhanov, V.K. Semenov, in *Resistive Single Flux Quantum Logic for the Josephson Junction Digital Technology*, in *SQUID 85*, H.-D. Hahlbohm, H. Lübbig eds., Walther de Gruyter, Berlin (1985), pp. 1103-1108.

¹⁹K. Nakajima, Y. Onodera, and Y. Ogawa, *Logic design of Josephson network*, J. Appl. Phys. **47**, 1620-1627 (1976).

²⁰K. Nakajima and Y. Onodera, *Logic design of Josephson network - II*, J. Appl. Phys. **49**, 2958-2963 (1978).

²¹A.H. Silver, *Superconductivity in Electronics*, IEEE Trans. Appl. Supercond. **AS-7**, 69 (1997).

²²T. Van Duzer, *Superconductor Electronics*, IEEE Trans. Appl. Supercond. **AS-7**, 98 (1997).

²³K.K. Likharev, Czech. J. Phys. **46**, 3331 (1996).

²⁴W. Chen, V. Rylyakov, V. Patel, J.E. Lukens, K.K. Likharev, IEEE Trans. Appl. Supercond. **AS-9**, 3212 (1999).

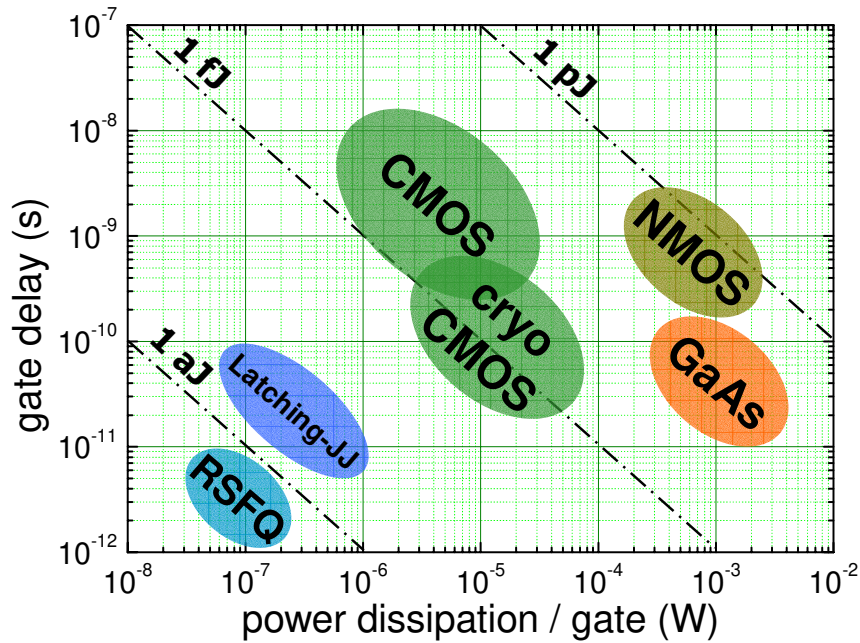


Figure 5.3: Comparison of device performance based on the delay-power relation for various devices. “Latching-JJ” stands for Josephson latching circuits, “RSFQ” represents RSFQ-based gates. Josephson devices are superior in both propagation delay and power dissipation to any semiconducting device.

Pros:

- Josephson junctions can switch very fast between the zero voltage and the voltage state with low power dissipation. In Fig. 5.3 the delay-power characteristics of Josephson devices are compared with various semiconductor devices. The switching delay times of Josephson devices are scattered below 10 ps, what is about one order of magnitude shorter than for semiconductor devices.
- The power dissipation per gate is $P_{\text{diss}} \sim V^2/R_N$ with $V = \max[I_c R_N, \hbar \omega_p/e]$ and typically ranges between 0.1 and 1 μW (see section 5.2.2). This is by two to three orders of magnitude less than for semiconductor devices. Low power dissipation is crucial for large scale integration, which in turn is important for reducing the wiring length and thus reducing the gate delay times. The dissipated energy per gate cycle is typically in the range of $10^{-18} - 10^{-17} \text{ J}$ and hence by several orders of magnitude lower than for semiconductor devices.

In the following table we show the product $P_{\text{diss}} \cdot \tau$ of the power dissipation per gate and the gate delay for a logic circuit consisting of 10^6 switching elements. For a Josephson logic circuit the energy dissipation is only $\sim 10^6 \times 10^{-18} = 1 \text{ pJ}$ resulting in a power dissipation of 1 mW and 1 W for a single user at a clock speed of 1 GHz and 1 THz, respectively. For a Si based circuit these numbers are by a factor of about 1000 larger. For 10^7 users the power dissipation of the Si circuits would be already 10 MW and 10 GW for a clock speed of 1 GHz and 1 THz, respectively. In the latter case this would correspond to the power of several nuclear power stations. This is demonstrating the demand for low power logic circuits, if we want to further increase the computing power by either increasing the clock speed or the number of switching elements. It also should be noted that the lower power dissipation of superconducting devices is inherently related to the low temperature operation. If they could be operated at higher temperature, higher power consumption would be required to overcome the thermal noise and guarantee error free operation.

		1 user		10^7 users	
		dissipated power at clock speed		dissipated power at clock speed	
$P_{\text{diss}} \cdot \tau$		1 GHz	1 THz	1 GHz	1 THz
Si	1 nJ	1 Watt	1000 Watt	10^7 Watt	10^{10} Watt
Josephson	1 pJ	1 mWatt	1 Watt	10^4 Watt	10^7 Watt

- Superconducting matched striplines can be used for wiring chips and packaging. These transmission lines are capable of transferring picosecond waveforms up to frequencies corresponding to the gap energy $\omega \sim 2\Delta/\hbar$ over virtually any interchip distance with a speed approaching that of light, and low attenuation and dispersion.^{25,26,27} The wave impedance Z of a microstrip line is given by (cf. section 8.1)

$$Z [\Omega] = 60 \frac{\sqrt{t_I t_M}}{W \sqrt{\epsilon}} , \quad t_M = t_I + 2\text{Re}\delta \quad (5.1.1)$$

and can readily be made close to the Josephson junction resistance (which is of the order of its normal resistance). With a typical width $W \simeq 1 \mu\text{m}$ and an insulator thickness $t_I \simeq 0.3 \mu\text{m}$ a value $Z \simeq 10 \Omega$ can be realized. The character of signal propagation in these lines is ballistic rather than diffusive and the contribution τ_i to the delay per gate is quite small (typically $\tau_i \simeq 10 \text{ ps}$ for lines as long as 1 mm). The absence of notable dispersion up to frequencies of 10^{12} Hz makes them the only means to transfer ps-pulses along a chip. It is also very important that these lines can be quite densely laid out (since spacing between the lines and their width are limited only by the available patterning technology), while having low crosstalk.

- Refractory Josephson junctions can nowadays be fabricated reproducibly with small parameter spread using the Nb technology.

Cons:

- At present there are no feasible transistor-like three-terminal devices with high gain such as semiconductor transistors. This causes problems to realize a high fan-out, the ability of a single logic gate to trigger a large number of consecutive gates.
- Due to the lack of transistor like devices providing gain, integrated Josephson electronic circuits usually require a small parameter spread of the Josephson junctions.

²⁵R.L. Kautz, *Miniaturization of normal-state and superconducting microstrip lines*, J. Res. of NBS **84**, 247-259 (1979).

²⁶E.B. Ekhholm, S.W. McKnight, *Attenuation and dispersion for high- T_c superconducting microstrip lines*, IEEE Trans. on Microwaves Theory and Technol. **38**, 387-395 (1990).

²⁷V.P. Andratsky, V.S. Bobrov, *Propagation of single flux pulse on superconducting transmission line*, Cryogenics **30**, 1109-1112 (1990).

5.2 Voltage State Josephson Logic

In this section we discuss the use of underdamped Josephson junctions as switching gates in a voltage state Josephson logic. As already discussed in chapter 3, for current values ranging between the critical current I_c and the return current I_R there are two possible voltage states, namely the zero and finite voltage state. These states can be assigned to the logical states “0” and “1”. Voltage-state logic is a natural emulation of semiconductor technology in that data is encoded by steady voltage levels. This is a very significant advantage. Since Josephson junction voltage-state logic resembles semiconductor logic, the entire and elaborate edifice of digital circuit design tools and concepts used for semiconductor integrated circuits can be rather directly applied to develop superconducting circuits. The design infrastructure for the RSFQ logic discussed in 5.3 is much less well-developed, although the semiconductor experience is still highly relevant.

5.2.1 Operation Principle and Switching Times

Fig. 5.4 illustrates the switching of an underdamped Josephson junction from the “0” ($V = 0$) state along the load line to the “1” ($V = V_g$) state. The load line is defined by the load resistance R_L . Initially, the junction is biased with a current $I_{\text{gate}} < I_c$. If an input current I_{contr} is added to I_{gate} so that $I_{\text{contr}} + I_{\text{gate}}$ exceeds I_c , the junction switches into the voltage state. The load resistor R_L is chosen to be much smaller than the sub-gap resistance R_{sg} of the junction. Therefore, almost all of the current through the junction is transferred to the load after the junction switches.

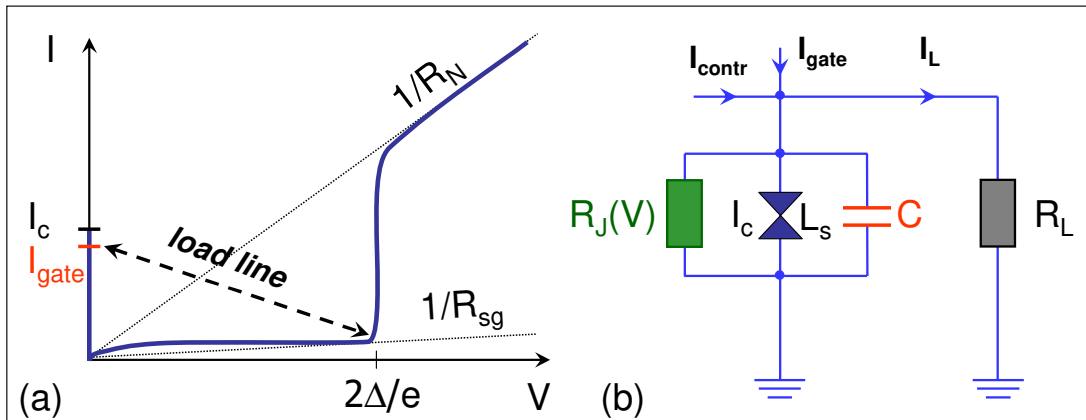


Figure 5.4: (a) Schematic illustration of the switching process of a Josephson tunnel junction along the load line. (b) Equivalent circuit for the Josephson junction switching device. The Josephson junction is represented by an ideal junction with critical current I_c and kinetic Josephson inductance L_s , which is shunted by the junction capacitance C and the voltage dependent normal resistance $R_J(V)$. The switching is along the dashed line defined by the load resistance R_L .

As shown by the equivalent circuit for the Josephson junction switch in Fig. 5.4b the Josephson element can be replaced by the Josephson inductance (compare section 2.1.4)

$$L_s = \frac{\Phi_0}{2\pi I_c \cos \varphi(t)} = \frac{L_c}{\cos \varphi(t)} \quad \text{with} \quad L_c = \frac{\Phi_0}{2\pi I_c} = \frac{\hbar}{2eI_c}, \quad (5.2.1)$$

which is shunted by a capacitance C and a voltage dependent resistance $R_J(V)$.

Characteristic Time Scales

In order to estimate the characteristic times we consider the equivalent circuit of the Josephson junction switch in Fig. 5.4b. Due to the nonlinearity of the Josephson junction ($L_s = L_c / \cos \varphi$, $R_J = R_J(V)$) we have to deal with a nonlinear LCR circuit with the total R given by the parallel connection of the junction resistance R_J and the load resistance R_L . For getting rough estimates we can approximate the circuit by a linear LCR oscillator by simply replacing L_s by L_c and $1/R(V) = 1/R_L + 1/R_J(V)$ by either $1/R_L + 1/R_{sg}$ or $1/R_L + 1/R_N$ depending on whether $V < 2\Delta/e$ or for $V > 2\Delta/e$. Considering the switching process of the Josephson junction device we then have to consider the following three characteristic time constants (compare sections 3.1.1 and 3.1.2):

$$\tau_{RC} = RC \quad (5.2.2)$$

$$\tau_{RL} = \frac{L_c}{R} = \frac{\Phi_0}{2\pi I_c R} \quad (5.2.3)$$

$$\tau_{LC} = \sqrt{L_c C} = \sqrt{\tau_{RC} \tau_{RL}} = \left(\frac{\Phi_0 C}{2\pi I_c} \right)^{1/2} \quad (5.2.4)$$

It is expected that the switching speed of the Josephson junction is limited by the slower of the time constants τ_{RC} and τ_{RL} . The time constant τ_{LC} is the geometric mean of these two time constants and therefore always ranges between them. Since we are considering underdamped Josephson junctions with hysteretic IVCs, the McCumber parameter must satisfy $\beta_C = \tau_{RC}/\tau_{RL} > 1$. Therefore, the time constants order as

$$\tau_{RC} > \tau_{LC} > \tau_{RL} \quad (5.2.5)$$

and the switching time is expected to be limited by $\tau_{RC} = RC$. Note that $1/R = 1/R_L + R_{sg}$ for $V < 2\Delta/e$ and $1/R = 1/R_L + 1/R_N$ for $V > 2\Delta/e$ resulting in different time constants τ_{RC} and τ_{RL} in both regimes.

The switching process of a junction is shown in Fig. 5.5. The switching delay mainly consists of two components: the so-called **turn-on** delay τ_t , which is required to increase the junction current from $I_{gate} < I_c$ to I_c , and the **rise-time** τ_r , which is required to increase the junction voltage after exceeding I_c to about the gap voltage $V_g = 2\Delta/e$. The latter is mainly the time required for charging the junction capacitance.

Turn-on Delay τ_t

In order to switch the junction we have to increase the junction current from $I_{gate} < I_c$ by ΔI so that $I_{gate} + \Delta I > I_c$. Initially, this current is not flowing through the junction (due to its kinetic inductance L_c) but through the capacitance C and the resistance R . Therefore, τ_t is the characteristic time required for redirecting this current through the junction. It is given by

$$\tau_t = \sqrt{\frac{\Phi_0}{2\pi} \frac{C}{\Delta I}} = \tau_{LC} \sqrt{\frac{I_c}{\Delta I}} \quad (5.2.6)$$

We see that τ_t is proportional to $\sqrt{C}/\sqrt{\Delta I}$. Therefore a small junction capacitance and a high overdrive current ΔI decrease τ_t .

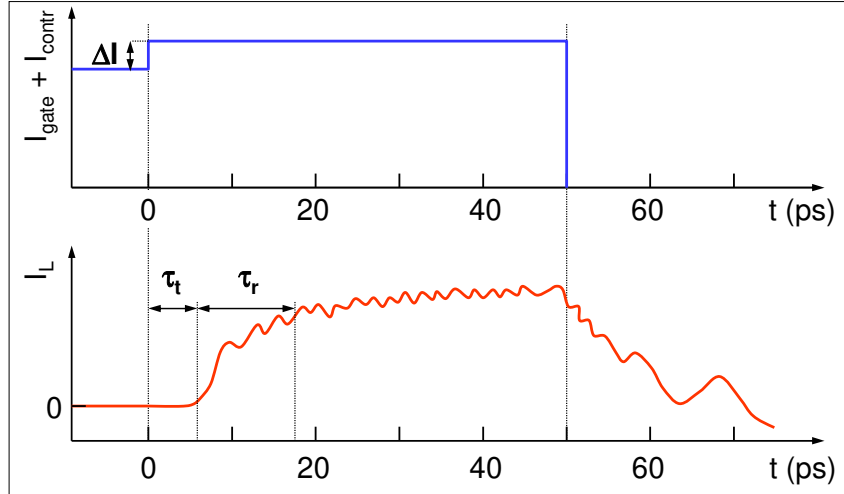


Figure 5.5: Output current waveform $I_L(t)$ when the junction switches to the voltage state. The total switching delay is composed of two components: turn-on delay τ_t and rise time τ_r . The data are obtained with a computer simulation for a junction with critical current $I_c = 100 \mu\text{A}$, a sub-gap resistance $R_{sg} = 150 \Omega$, normal resistance $R_N = 15 \Omega$, capacitance $C = 1 \text{ pF}$, and load resistance $R_L = 10 \Omega$. The bias current is stepped from I_c to $I_c + \Delta I = 1.1 \cdot I_c$.

Rise Time τ_r :

The rise time is the time required to charge the junction capacitance. It is given by²⁸

$$\tau_r = RC , \quad (5.2.7)$$

where R is the total resistance given by $1/R = 1/R_J(V) + 1/R_L$. In order to transfer a large current to the load, R_L is usually chosen much smaller than the junction sub-gap resistance, so that $\tau_r = R_L C$. Furthermore, R_L is chosen that $I_c R_L \simeq V_g = 2\Delta/e$ in order to make use of the maximum voltage swing (see Fig. 5.4a). Then, the rise time can be written as

$$\tau_r = R_L C = \frac{2\Delta C}{e I_c} . \quad (5.2.8)$$

Fig. 5.5 shows a characteristic switching waveform obtained by computer simulation.

Typical values for Nb junctions are $J_c = 10^3 \text{ A/cm}^2$, $C/A \simeq 5 \mu\text{F/cm}^2$, $\Delta I/I_c \simeq 0.1$, and $2\Delta/e \simeq 3 \text{ mV}$. This results in $\tau_t \simeq 4 \text{ ps}$ and $\tau_r \simeq 10 \text{ ps}$ comparable to the simulation results in Fig. 5.5. The total delay for Nb Josephson switching devices would then typically be $\tau = \tau_t + \tau_r \simeq 14 \text{ ps}$. Both τ_t and τ_r depend on the ratio C_s/J_c of the specific junction capacitance, $C_s = C/A$, and the critical current density, $J_c = I_c/A$. Smaller delay times and faster switching can therefore be obtained by reducing this ratio, i.e., by increasing the plasma frequency $\omega_p = \sqrt{2eJ_c/\hbar C_s}$. This can be achieved by reducing the thickness t_I of the tunneling barrier. Although the specific junction capacitance increases proportional to $1/t_I$, this is by far overcompensated by the exponential increase of the critical current density.

We note, however, that on increasing J_c we are at the same time decreasing the resistance times area product $\rho_N = R_N A$, since $J_c \rho_N \sim 2\Delta/e$ stays about constant for superconducting tunnel junctions. Then, we are also decreasing $\beta_C \propto J_c \rho_N^2 C_s$ and we are finally entering the overdamped case. However, for

²⁸Note that for overdamped junctions with $\beta_C < 1$ the smallest time constant is τ_{RL} and the rise time is determined by $\tau_r = L_c/R_L = e\Phi_0/4\pi\Delta$.

$\beta_C < 1$ the switching speed is determined by τ_{RL} , which is now the largest time constant. For $\beta_C = 1$ all characteristic times τ_{RL} , τ_{RC} and τ_{LC} are the same. It is easy to show that in this case the switching speed, which is set by the larger of τ_{RL} and τ_{RC} is minimum.

Steering time

The steering time τ_{st} is required to redistribute the current in a circuit with an inductance L . With the typical voltage scale given by $2\Delta/e$ we obtain from $V = 2\Delta/e = L\dot{I}$ with $\dot{I} = I_{\text{gate}}/\tau_{st}$

$$\tau_{st} = \frac{LI_{\text{gate}}}{2\Delta/e} . \quad (5.2.9)$$

Usually LI_{gate} is chosen to be much larger than Φ_0 . For $LI_{\text{gate}}/\Phi_0 \sim 10$ the steering time $\tau_{st} \simeq 10 \text{ ps}$ is obtained for Nb junctions.

Conclusions on Delay Times

Summarizing our discussion on delay times we can state the following:

- The characteristic times τ_t , τ_r , and τ_{st} of Josephson switching devices are of the order $\simeq 1 - 10 \text{ ps}$ for Josephson junction based on Nb technology.
- Since $\tau_t \propto \sqrt{C_s/J_c}$ and $\tau_r \propto C_s/J_c$, it is advantageous to use junctions with low specific capacitance $C_s = C/A$ and high critical current density $J_c = I_c/A$, that is, with large plasma frequency $\omega_p = \sqrt{2eJ_c/\hbar C_s}$.

5.2.2 Power Dissipation

The power dissipated when a Josephson junction switches from the superconducting state to the voltage state as shown in Fig. 5.4 is given by

$$P_{\text{diss}} = \frac{V_g^2}{R_{sg}} , \quad (5.2.10)$$

where R_{sg} is the sub-gap resistance of the junction. For a Nb junction with a $R_{sg} \simeq 30 \Omega$ one obtains $P_{\text{diss}} \simeq 3 \times 10^{-7} \text{ Watt}$, which amounts to an energy dissipation per switching cycle $E = P_{\text{diss}} \cdot \tau \simeq 3 \times 10^{-18} \text{ J}$ (compare latching-JJ in Fig. 5.3). This value has to be compared to values obtained for semiconducting or expected for high-temperature superconducting (HTS) devices:

material	$P_{\text{diss}} \cdot \tau$ (Joule)
Si	$10^{-8} - 10^{-10}$
GaAs	$10^{-8} - 10^{-10}$
HEMT	$10^{-10} - 10^{-11}$
HTS	3×10^{-15}

For RSFQ logic (cf. section 5.3) $P_{\text{diss}} \cdot \tau \simeq 10^{-18}$ Joule is obtained, which would yield a power dissipation per area of 1 W/cm² at an integration density of 10⁷ gates/cm². Such power density can be easily removed by liquid helium. Note that for the same integration density the power density of semiconductor circuits is by several orders of magnitude larger giving severe problems with heat removal.

At a typical operation temperature $T/T_c \simeq 0.5$ of Josephson junction circuits the sub-gap resistance is determined by thermally activated quasiparticles resulting in $R_{sg} \simeq 10R_n$. The device application determines the minimum critical current I_c^{th} , which is needed for a reliable device operation²⁹. Since the $I_c R_n$ product for SIS junction is a material parameter with $I_c R_n \simeq \Delta/e = V_g$, we obtain

$$R_{sg}^{th} \lesssim \frac{V_g}{I_c^{th}} \times 10 \simeq 30 \Omega \quad (5.2.11)$$

for $T = 4.2$ K, $I_c^{th} = 100 \mu\text{A}$, and $V_g = 3$ mV.

5.2.3 Switching Dynamics, Global Clock and Punchthrough

Switching Dynamics

The switching dynamics of Josephson junction digital circuits strongly depends on whether the junctions are under- or overdamped. For the voltage state Josephson logic underdamped junctions are required, whereas for the RSFQ logic discussed below overdamped junctions are used. Let us first discuss the switching behavior of an underdamped junction with $\beta_C \gg 1$. The IVC of such a junction is strongly hysteretic. The switching behavior can be discussed qualitatively by considering Fig. 5.5. If the bias current is increased from $I < I_c$ to $I > I_c$ (or equivalently if the critical current is suppressed below I_{gate}) the junction switches into the resistive state and the current is redirected to the load resistor R_L . The junction voltage is obtained by multiplying the current I_L shown in Fig. 5.5 by the load resistor R_L . It is obvious that due to its hysteretic IVC the junction latches into the voltage state. The rise time of the junction voltage is determined by the RC time constant as discussed above. Furthermore, the junction voltage shows small (plasma) oscillations typical for the underdamped limit with the oscillation period given by $2\pi\tau_{LC}$ (about 2 ps in Fig. 5.5). In order to reset the junction to the zero voltage state, the current has to be switched off. The junction then returns to the zero voltage state with the time constant given by τ_{RC} . Due to the underdamping the decay of the junction voltage is not smooth but accompanied by characteristic oscillations.

Global Clock

In order to operate a latching voltage state Josephson logic circuit the bias current has to be switched on and off periodically. The rf-power required per gate is well beyond that which can be produced by a similar gate. Thus, the clock signals must be generated externally, so that the latching circuits are restricted to external (global) timing. Obviously, the use of a global clock system, where the power is cycled on and off once each cycle, is an adequate choice for a latching logic Josephson circuit.³⁰ In a complex circuit with a large number of junctions the current bias could be distributed to the junctions in parallel using a voltage bias and a resistor network. In any case the development of a power supply operating in the GHz regime is a technical challenge. In particular, the rf-currents necessary to drive

²⁹ I_c^{th} is given by the requirement that thermally induced switching to the voltage state should be negligibly small (compare section 3.4).

³⁰S. Hasuo, T. Imamura, Proc. IEEE 77, 1177 (1989).

a VLSI circuit would be very high and cause considerable crosstalk. Note that the requirement of an ac-power supply is completely different to semiconductor technology, where a dc-power supply is used.

Of course, an implicit requirement of a global biasing scheme is that the output value of a given gate is stored during the off time. This requires a latch between each gate, where the latch accepts the data during the turn-off period and transmits it again during the next turn-on. The latch may be based on a persistent current in a SQUID loop. The loop can store a binary bit even in the absence of the bias current.

Two different types of power supplies have been suggested: (i) a single-phase bipolar power system³¹ and (ii) a 2- or 3-phase unipolar power system. For the single-phase system, logical operations are performed on both the positive and negative portion of the power current and the transition period between the positive and negative branch is used to reset the gates. However, for this operation the so-called punchthrough phenomenon discussed below is a serious problem and limits the clock frequency. The multiphase power supply has the advantage that it does not require a latch, since the data can be read out to the next circuit operated by the next phase power cycle.

Punchthrough

For any global clock system the goal is to run the systems at the highest possible clock frequency. This however means that we have to consider an underdamped Josephson junction with a time-varying current source. As we have seen in section 3.3 this results in current steps in the IVC at constant voltages $V_n = n \cdot \Phi_0 f_1$, where f_1 is the frequency of the ac current source and n an integer. These current steps can even cross the current axis (zero current steps) and are used for the Josephson voltage standard (see chapter 6). Therefore, upon switching off the bias current, the junction cannot only return to the zero voltage state but also to one of the voltages V_n of the current-axis crossing current steps. Furthermore, using a bipolar power supply, the junctions may not reset to the zero voltage state during the transition from the positive to the negative branch of the cycle but switch through to the negative voltage branch. This phenomenon is known as the **punchthrough effect**.^{32,33} If one would switch on and off the power supply, the junction may return to the voltage state when the bias current is switched on again after a too short period, since it performs small plasma oscillations for a certain time after switching off the bias current.³⁴ The only way to avoid this problem and to guarantee save return to the zero voltage state is to reduce the clock frequency or to increase the damping. The former is reducing the performance of the digital circuit. Actually, the maximum clock frequency of Josephson voltage state logic circuits was limited to a few GHz what is much to low to compete with semiconductor circuits. The latter results in smaller β_C and in turn larger return currents $I_R \propto I_c / \sqrt{\beta_C}$ (compare (3.3.16)). Then the junction no longer safely stays in the voltage state.

In a more general view the notation “punchthrough” has been used for the maximum speed errors of the Josephson voltage-state logic in analogy with certain errors in transistor operation. This name gives the impression that these errors are due to the device structure and hence could be eliminated with better technology. This is not correct. In fact, the errors are intrinsic since they are directly related to the topology of the phase space of a Josephson junction. As we have already seen, the fundamental parameters for the Josephson effect are the current I and the phase difference φ , not I and V . The Josephson equation $V = (\hbar/2e)\dot{\varphi}$ states that if the voltage is constant the phase is increasing rapidly, i.e. it is essentially undefined in the voltage state. The Josephson equation $I_s = I_c \sin \varphi$ on the other hand states that the phase must be well defined in the zero-voltage state. Therefore, in order to reset a

³¹H.C. Jones, T.R. Gheewala, IEEE J. Solid State Circuits **17**, 1201 (1982).

³²R.E. Jewett, T. Van Duzer, IEEE Trans. Magn. **MAG-17**, 599 (1981).

³³E.P. Harris, W.H. Chang, *Punchthrough in Josephson Logic Devices*, IEEE Trans. Magnetics **MAG-17**, 603 (1981).

³⁴Q.P. Herr, M.J. Feldman, *Error Rate of a Superconducting Circuit*, Appl. Phys. Lett. **69**, 694 (1996).

Josephson junction from finite voltage to zero voltage ***the phase must be recaptured***. We can use this picture to calculate the minimum error rate of voltage-state logic as a function of operating speed. The conclusion is that the bit error rate due to phase recapture is too large for an integrated circuit operating at 10 GHz.

The Pendulum Analogue: We can intuitively understand the punchthrough phenomenon in the pendulum analogue often used in chapter 3. An underdamped junction corresponds to a pendulum with large mass and small damping. Once the pendulum is rotating (corresponding to the voltage state) it goes on to rotate for a considerable time even if the driving torque (corresponding to the applied current) is switched off and then performs oscillations around the bottom before it finally settles down. If the driving torque, i.e. the bias current, is switched on again during the oscillation period, the pendulum may start to rotate again. That is, if we do not wait for a sufficiently long period in the off state (corresponding to a decrease of the frequency of the global clock), the junction may prematurely switch into the resistive state again.

The pendulum analogue makes clear that the only way to get rid of the punchthrough effect is to increase the damping. Then, however, we can no longer use the voltage state logic requiring hysteretic IVCs with two well-defined voltage states for the same current. In general, depending on the damping we can distinguish two major classes of Josephson logic circuits. In the voltage state or latching logic based on underdamped junctions the “off-state” is the $V = 0$ state, while the “on-state” corresponds to the $V \neq 0$ state with $V \simeq 2\Delta/e$. Due to the hysteretic nature of the IVCs the junction stays in the “on-state” until it is reset (latching logic). In contrast, the flux state logic discussed in section 5.3 is based on overdamped junctions. Here, the binary logic states are realized by the rapid passage of a single flux quantum (RSFQ pulse). This represents a nonlatching logic, since the junction automatically resets into the zero voltage state. We will see that the RSFQ circuits can operate at much higher clock frequencies but require a more complicate timing associated with the motion of the RSFQ pulses.

5.2.4 Josephson Logic Gates

Although the voltage state Josephson logic cannot be used for ultrafast speed due to the reasons discussed above, many technical accomplishments were first demonstrated using voltage state logic. Therefore, in this section we briefly describe the key elements of voltage state logic circuits based on hysteretic junctions. The newer non-latching RSFQ logic is then discussed in section 5.3.

In order to realize logic operations various logic gates have to be designed. The general requirements for practical logic gates are:

- high ***fan out***: a single switching gate should be capable of triggering N consecutive gates
- large operating margins for stable operation
- small size allowing for very large scale integration (VLSI)
- short switching time allowing for high clock frequency
- low power dissipation allowing for high integration density
- sufficient input – output isolation allowing for directionality of logic signals

Note that the Josephson switching device shown in Fig. 5.4 cannot be used in logic circuits because there is no input-output isolation. Therefore, it is very difficult to get directionality of the logic signal in the

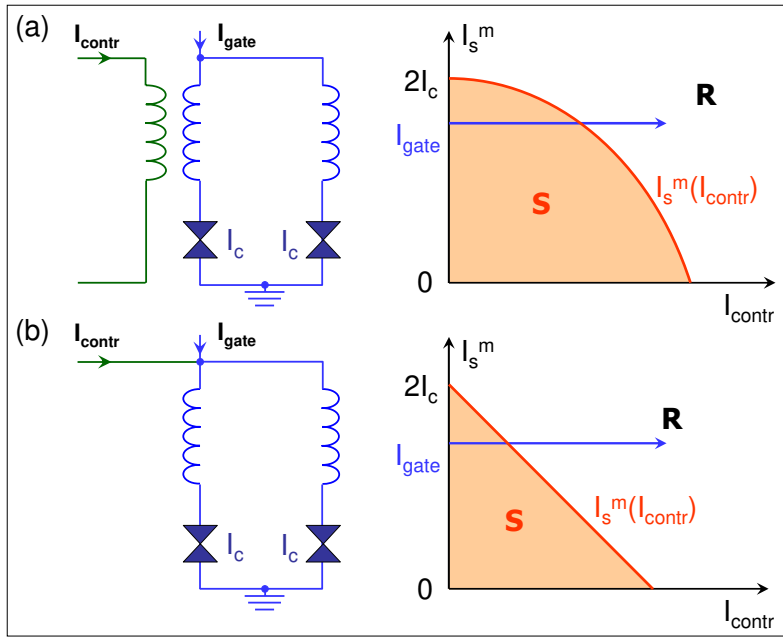


Figure 5.6: Sketch of the equivalent circuit and the threshold characteristics $I_s^m(I_{\text{contr}})$ for (a) a magnetically coupled gate and (b) a directly coupled gate.

circuit. It is evident that the current switched from one gate can flow in both forward and backward direction.

Until today a large number of different devices have been suggested, which can be classified into two types according to the way they are controlled: (i) magnetically coupled gates and (ii) directly coupled gates. These basic gate types together with their threshold characteristics are shown in Fig. 5.6. The threshold characteristic corresponds to the dependence of the maximum supercurrent I_s^m on the control current I_{contr} . The threshold curve $I_s^m(I_{\text{contr}})$ separates the superconducting or zero voltage regime from the resistive or finite voltage regime. For the magnetically controlled gate the maximum supercurrent I_s^m of a single junction or a dc-SQUID is reduced by the magnetic field generated by the control current I_{contr} below the applied gate current I_{gate} and the device switches from the superconducting (S) into the resistive (R) state. The corresponding threshold characteristics are about a Fraunhofer diffraction pattern or a $|\cos(I_{\text{contr}})|$ dependence for the single junction and the dc-SQUID, respectively. For the directly coupled gate the control current is directly injected and the threshold characteristic takes the form $I_s^m = 2I_c - I_{\text{contr}}$.

Magnetically coupled gates

A typical magnetically coupled gate is the **3-Junction Interferometer Logic (JIL) gate**,³⁵ which is shown in Fig. 5.7 together with its threshold characteristic. When the control current I_{contr} applied to the control line is large enough, the gate switches to the voltage state. Three junction SQUIDs are used because of their wider operating margins. By choosing the SQUID critical currents $I_{c1} = I_{c3} = I_{c2}/2$ the side lobes between the main lobes in the threshold characteristics are suppressed and a wider operating window for the control current switching the gate into the voltage state is obtained. Note that LC resonances, which may be excited in the circuit by the switching process, are suppressed by damping resistors R_d .

Another important gate is the Current Injection Device (CID),³⁶ which is also based on a SQUID as

³⁵M. Klein, D.J. Herrel, IEEE J. Solid-State Circuits **13**, 593 (1978).

³⁶T. R. Gheewala, IBM J. Res. Dev. **24**, 130 (1980).

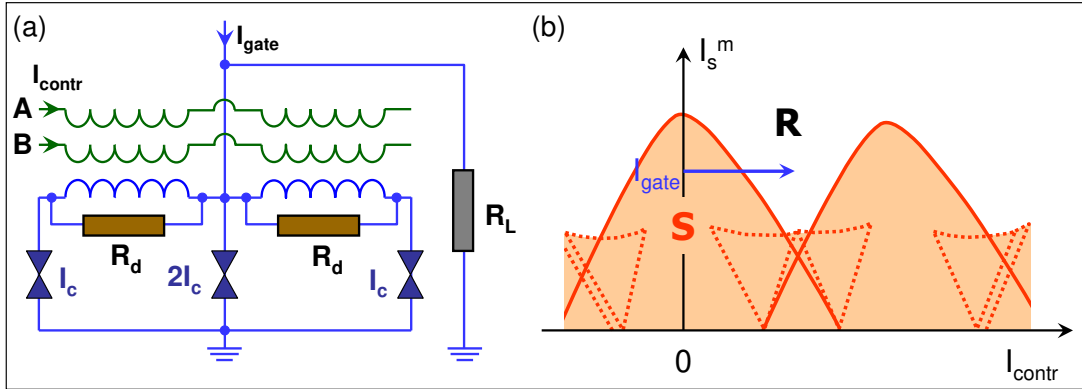


Figure 5.7: (a) Equivalent circuit of a 3-Junction Interferometer Logic (JIL) gate with two inputs A and B. The resistors R_d are damping resistors to damp out LC resonances (the junction capacitances parallel to the ideal Josephson elements are not shown for simplicity). (b) Threshold characteristic $I_s^m(I_{\text{contr}})$. The shaded region indicates the superconducting (S) state.

shown in Fig. 5.8. The CID is operated by direct current injection into the SQUID loop. The threshold characteristics can be made symmetric in the two input currents I_A and I_B by a proper choice of the circuit parameters. The CID gate switches to the voltage state with a broad operating window, if both input currents are applied simultaneously. Therefore, the CID can be used as a simple AND gate. However, the CID has no current isolation. A JIL gate in front of a CID gate could be used as current isolation gate.

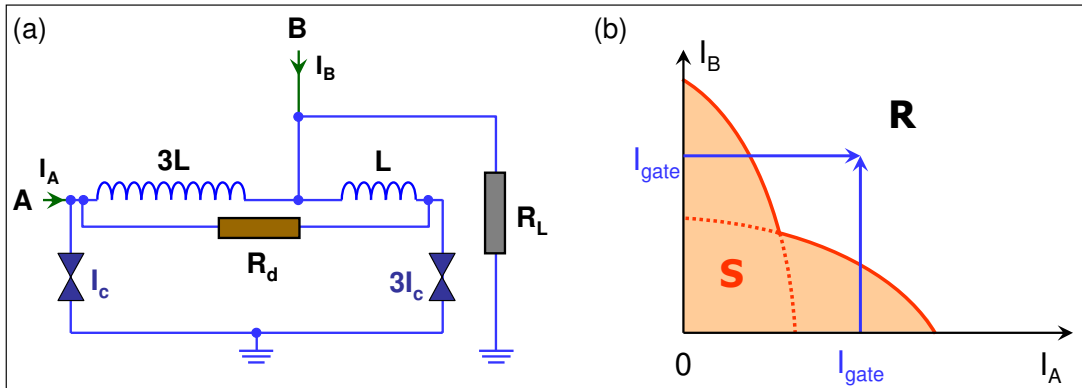


Figure 5.8: (a) Equivalent circuit of the Current-Injection Device (CID). (b) Threshold characteristic $I_A(I_B)$, which is symmetric to the characteristic $I_B(I_A)$. That is, the threshold characteristics is symmetric in the two input currents I_A and I_B . No gate current is required.

The operation of JIL and CID gates depends on rather large loop inductances. Therefore, the required areas of these gates are also rather large preventing a high integration density and hence large scale integration of these devices.

Directly Coupled Gates

Directly coupled gates are controlled by direct injection of the input currents. Note that in the CID described above the magnetic field generated by the injected currents is used to operate the gate. That is why the CID is classified as a magnetically coupled gate. A main advantage of directly coupled devices is the fact that inductances can be eliminated and the devices can be made small.

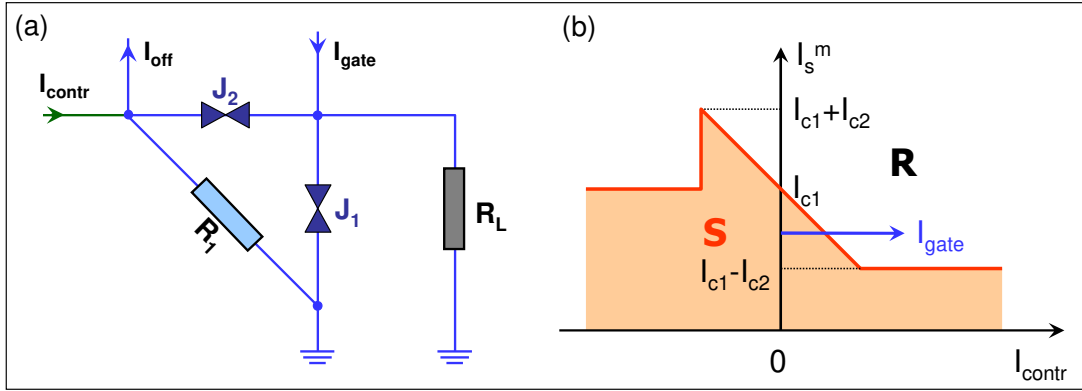


Figure 5.9: (a) Equivalent circuit of the Josephson Atto Weber Switch (JAWS) gate. (b) Threshold characteristic of the JAWS. The input-output current isolation is achieved by the junction J_2 and the resistor R_1 . I_s^m is the maximum current that can be applied via the gate line without switching junction J_1 into the voltage state.

An important issue in directly coupled gates is the realization of the current isolation functions. The first device satisfying this requirement is the **Josephson Atto Weber Switch (JAWS)**.³⁷ As shown in Fig. 5.9, the JAWS consists of two Josephson junctions and a resistor. The gate is biased with a current I_{gate} below the critical current I_{c1} of junction J_1 , i.e. the current flows through J_1 and the gate stays in the superconducting state. An input current I_{contr} through junction J_2 increases the current through J_1 to $I_{\text{gate}} + I_{\text{contr}}$, which switches J_1 to the voltage state. After J_1 has switched, I_{gate} flows through J_2 and a small resistor R_1 to the ground and J_2 also switches to the voltage state. As a result, I_{gate} is transferred to a load resistor R_L and I_{contr} flows through R_1 to the ground thus providing the current isolation.

Another current isolated gate is the **Directly Coupled Logic (DCL) gate**³⁸ shown in Fig. 5.10. The operating principle is similar to that of the JAWS gate. For both the JAWS and DCL gate the threshold curves separating the superconducting from the voltage state have a slope $\Delta I_{\text{gate}}/\Delta I_{\text{contr}} = -1$. For higher slopes ($|\Delta I_{\text{gate}}/\Delta I_{\text{contr}}| > 1$) a higher sensitivity is obtained.

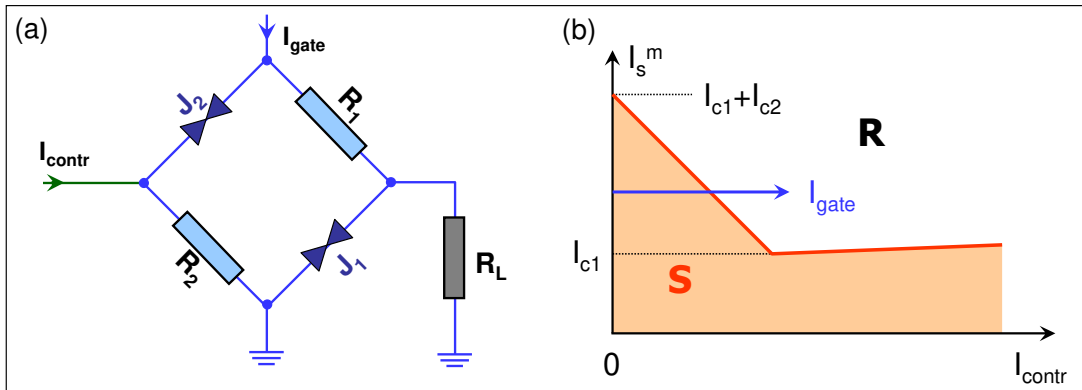


Figure 5.10: (a) Equivalent circuit of the Directly Coupled Logic (DCL) gate. (b) Threshold characteristic of the DCL gate. I_s^m is the maximum current that can be applied via the gate line without switching junction J_1 into the voltage state.

The gates shown in Fig. 5.11 have a higher sensitivity or gain compared to the JAWS or DCL gates by inserting an additional Josephson branch. These gates are called **Resistor Coupled Josephson Logic**

³⁷T. A. Fulton, S.S. Pei, L.N. Dunkleberger, Appl. Phys. Lett. **34**, 1876 (1979).

³⁸T. R. Gheewala, A. Mukherjee, in Tech. Digest International Electron Device Meeting (IEDM), p. 482 (1979).

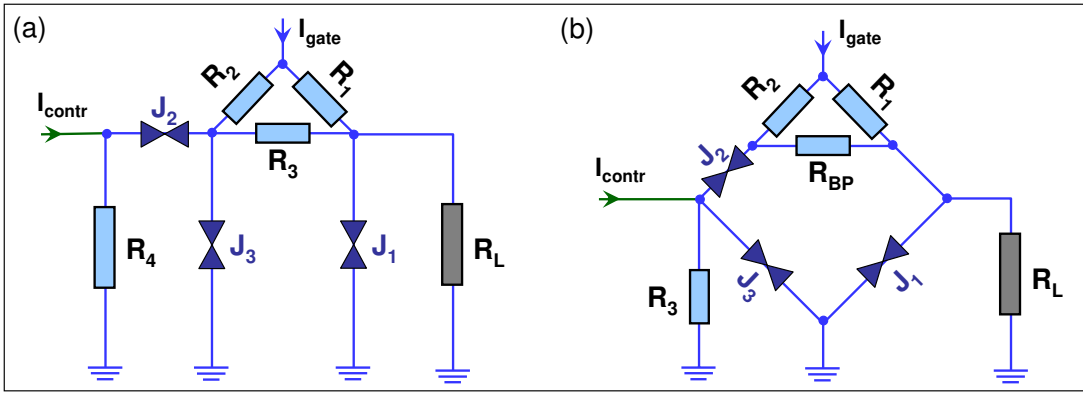


Figure 5.11: Equivalent circuits of (a) the Resistor Coupled Josephson Logic (RCJL) and (b) the Resistor Coupled Logic (RCL) gate. An additional Josephson branch (J_3) enhances the sensitivity or gain compared to the JAWS and DCL gates.

(RCJL)³⁹ and **Resistor Coupled Logic (RCL)**⁴⁰. We note that also modified versions of the RCJL and RCL gates shown in Fig. 5.11 with improved threshold characteristics have been designed.

The **4 Junction Logic (4JL) gate**⁴¹ shown in Fig. 5.12 is constructed of 4 Josephson junctions, which are coupled together in a loop. The essential feature of the 4JL gate is that the geometric loop inductance can be made as small as possible and therefore the threshold curve depends entirely on the phase differences across the junctions. The current isolation is realized by introducing a small resistor R_i at the input terminal and by making junction J_1 to switch at the final stage of the switching sequence. Based on this 4JL concept an AND gate was realized.

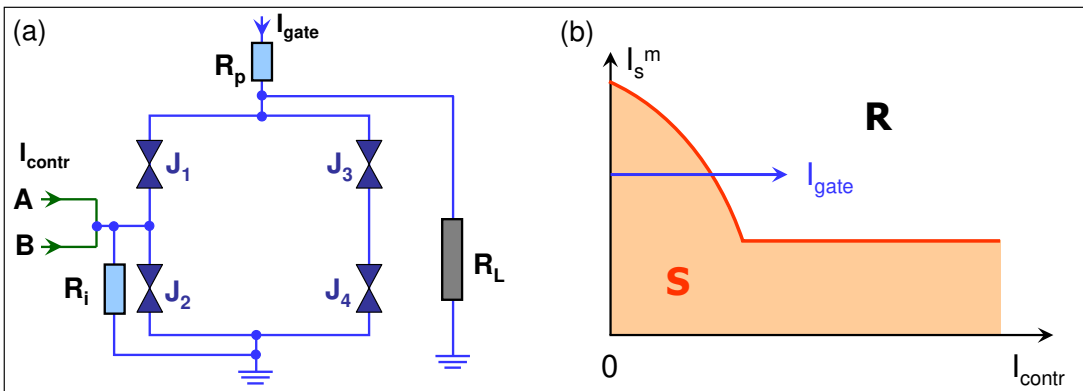


Figure 5.12: (a) Equivalent circuit and (b) threshold characteristic of the 4 Junction Logic (4JL) gate.

The advantage of direct coupled gates over magnetically coupled gates is the elimination of the loop inductance. The 4JL gates for example have been realized with a size of $1200 \mu\text{m}^2$, whereas a JIL gate based on the same design rules has an area of $4400 \mu\text{m}^2$.

Hybrid devices with both magnetic and direct coupled gates have also been investigated. In the **Modified Variable Threshold Logic (MVTL)**⁴² the input current is first fed into a SQUID control line and then injected into the SQUID directly resulting in a very high sensitivity of the device.

³⁹J. Sone, T. Yoshida, H. Abe, Appl. Phys. Lett. **40**, 886 (1982).

⁴⁰K. Hohkewa, M. Okada, A. Ishida, Appl. Phys. Lett. **39**, 653 (1981).

⁴¹S. Takada, S. Kosada, H. Hayakawa, Jpn. J. Appl. Phys. Suppl. **19-1**, 601 (1981).

⁴²N. Fujimaki, S. Kotani, S. Hasuo, T. Yamaoka, Jpn. J. Appl. Phys. **24**, L1 (1985).

Switching Delay of Logic Gates

In Table 5.1 the logic delays and the power dissipation measured for several gates are listed. The shortest delay of 2.5 ps was obtained for the MVTL fabricated with $1.5\text{ }\mu\text{m}$ Nb/AlO_x/Nb Josephson junctions. However, this should not suggest the superiority of the MVTL, because most of the experiments with the other gate types have been made at an early stage when only the Pb-alloy junction technology was available. Gate delays could be significantly shorter for devices fabricated with modern Nb-technology.

Table 5.1: Switching delay and power dissipation for various types of logic gates.

gate	linewidth (μm)	switching time (ps)	power dissipation (μW)	junction technology	Ref.
CIL	2.5	13	2	Pb-alloy	^a
JAWS	5	13		Pb-alloy	^b
RCJL	5	10.3	11.7	Pb-alloy	^c
RCL	2	4.2		Pb-alloy	^d
4JL	2.5	7	4	Pb-alloy	^e
DCL	1.5	5.6	4	NbN/Pb-In	^f
MVTL	1.5	2.5	4	Nb/AlO _x /Nb	^g

^aT.R. Gheewala, A. Mukherjee, in *Tech. Digest International Electron Device Meeting (IEDM)*, p. 482 (1979).

^bS.S. Pei, *Appl. Phys. Lett.* **40**, 739 (1982).

^cJ. Sone, T. Yoshida, S. Tahara, H. Abe, *Appl. Phys. Lett.* **41**, 886 (1982).

^dJ. Nakano, Y. Mimura, K. Nagata, Y. Hasumi, T. Waho, in *Ext. Abstr. of 16th Conf. Solid State Dev. and Mat.*, Kobe (1984), p. 636.

^eH. Nakagawa, T. Odake, E. Sogawa, S. Takada, H. Hayakawa, *Jap. J. Appl. Phys.* **22**, L297 (1983).

^fY. Hatano, T. Nishino, Y. Tarutani, U. Kawabe, *Appl. Phys. Lett.* **44**, 1095 (1984).

^gS. Kotani, T. Imamura, H. Hasuo, in *IEEE IEDM Techn. Digest*, p. 865 (1987).

Logical Operations

The gates described above can be used for the realization of basic gate operations such as AND, OR and NOT. It is a well known theorem of binary logic that any arbitrary complex logical operation can be expressed in terms of the basic operations AND, OR and NOT. If the control current applied to one of the two control lines A and B is able to reduce the maximum supercurrent I_s^m below the applied gate current, the JIL gate acts as an OR gate. The device switches to the resistive (R) state, if a control signal is present either at input A or B or at both A and B. Only if no control signal is present at both input channels, the device stays in the superconducting (S) state. If only the sum of the control currents at both input channels is able to reduce I_s^m below the applied gate current, the JIL gate acts as an AND gate. Then, the device stays in the S state, if no input signal is present in both or a single input channel. Switching to the R state occurs only, if input signals are present in both channels. The realization of the NOT operation is not as simple. The NOT operation requires that an input with $V \neq 0$ (finite control current) would generate an output $V = 0$ and vice versa. In order to realize this operation the ***dual-rail logic*** can be used, in which both the binary signal and its complement are carried in parallel throughout the entire set of logic operations. Using the dual rail system one can construct a unit cell consisting of two OR and a single AND gate that allows to implement all the required basic gate operations.⁴³

⁴³H. Hayakawa, *Computing*, in *Superconducting Devices*, Steven T. Ruggiero, David A. Rudman (eds.), Academic Press Inc., San Diego (1990).

5.2.5 Memory Cells

Memories are essential components of any computing system. Most digital systems require memory elements that can store and retrieve binary information on the same time scale as the operation of the logic gates. Such memory is acting as the fast cache memory of a computer system. Semiconducting memories rely on electrical charge stored on capacitors with the logical “0” and “1” corresponding to zero and finite charge, respectively. Here, finite charge means typically a few 1000 electrons on a sub- μm^2 capacitor. In superconducting devices it is natural to use persistent currents or magnetic flux stored in superconducting loops for binary information storage.⁴⁴ Again, the logical “0” and “1” correspond to zero and finite flux in the loop. Usually, in superconducting circuits only a single flux quantum in the loop is representing the logical “1”. In addition to the superconducting loop, READ and WRITE gates are required for fast read out and write in the binary information. Just as for logic circuits, Josephson gates based on hysteretic Josephson junctions can be used to implement a complete memory cell with READ and WRITE gate.⁴⁵

The various memory cells can be divided into ***Non-Destructive Read-Out (NDRO)*** and ***Destructive Read-Out (DRO)*** memory cells. The information stored in non-destructive memory cells can be retrieved without changing the cell state. The NDRO cell is useful to realize cache memories that communicate directly with a central processing unit (CPU). For such application the speed is important, since the memory cell must be capable to store and retrieve binary information at the clock speed of the CPU.

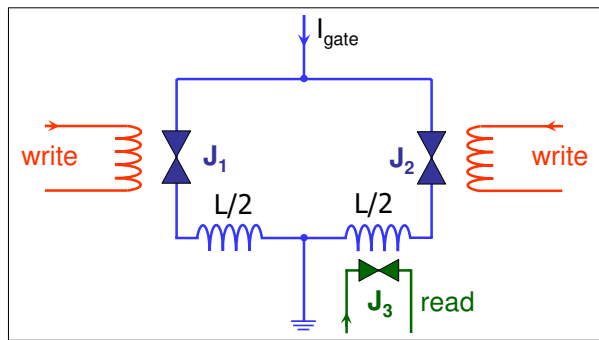


Figure 5.13: Equivalent circuit of the Non-Destructive Readout (NDRO) memory cell.

The earliest NDRO memory cell was suggested in 1969 by **Anacker**⁴⁶ and implemented by **Zappe**.⁴⁷ Fig. 5.13 shows the operation principle of a NDRO cell. Information is represented as magnetic flux enclosed in the loop (e.g. “0”: no flux in the loop, “1”: a single or several flux quanta in the loop). In order to discuss the operation principle we start with a loop containing no magnetic flux. If we are biasing the cell by a current I_{gate} , due to the symmetry of the cell the current through each of the junctions J_1 and J_2 is $I_{\text{gate}}/2$ for zero writing current. That is, no flux is written into the loop. This corresponds to the “0” state of the loop. If we are now applying a finite writing current to the WRITE gate, we are coupling magnetic flux into the loop. Of course the loop tries to shield this magnetic flux by a circulating current. However, if the write current I_w is large enough, this circulating current exceeds the critical current I_c of the junctions and magnetic flux is entering the loop. If we are now switching off the write current again, the loop keeps the magnetic flux trapped, if the product LI_c of the loop inductance and the critical current of the junctions is larger than Φ_0 . Depending on the magnitude of the screening parameter $\beta_L = 2LI_c/\Phi_0$ (compare section 4.1) and the applied write current a single or several flux quanta are trapped in the loop. The state represents the logical “1”.

⁴⁴J. Matisoo, *Overview of Josephson Technology Logic and Memory*, IBM J. Res. Develop. **24**, 113 (1980).

⁴⁵Y. Wada, *The Josephson Memory Technology*, Proc. IEEE **77**, 1194 (1989).

⁴⁶W. Anacker, IEEE Trans. Magn. **5**, 968 (1969).

⁴⁷H.H. Zappe, IEEE J. Solid State Circuits **10**, 12 (1975).

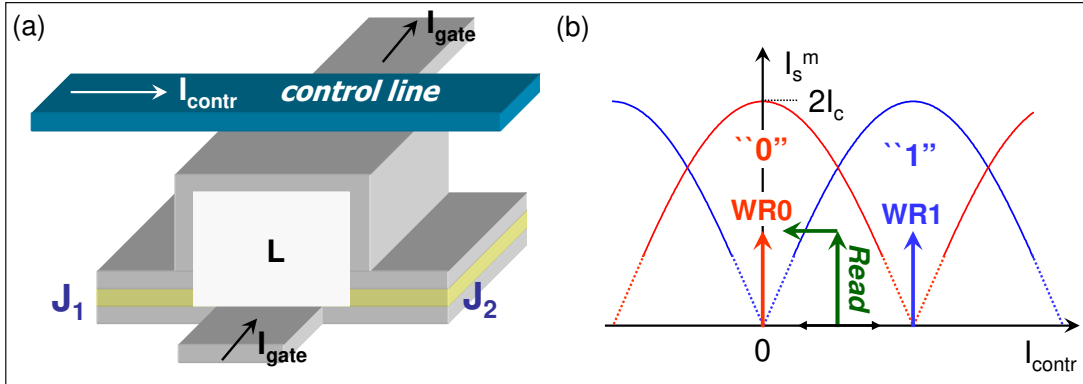


Figure 5.14: (a) Sketch of a Destructive Read-Out (DRO) memory cell and (b) its threshold characteristic. The two-junction SQUID loop has inductance $L = \Phi_0/2I_c$.

The circulating current in the loop can be used as the control current of a READ gate. In Fig. 5.13 the READ gate consists of junction J_3 . This junction is biased at a current smaller than its critical current. Then, without any circulating current, i.e. no flux in the loop, the junction J_3 is in the superconducting or zero-voltage state. However, if there is flux stored in the loop, the corresponding circulating current suppresses the maximum Josephson current of junction J_3 to a value below the bias current forcing this junction to switch into the voltage state. The information in the cell can be read out repeatedly without affecting the magnetic flux. That is, the cell acts as a NDRO cell.

An alternative, more compact memory cell is obtained by using only a single two-junction SQUID but in a different operation mode. Fig. 5.14 shows the equivalent circuit and the threshold characteristics of such a Destructive Read-Out (DRO) memory cell⁴⁸. It consists of a symmetrically biased SQUID with two identical junctions with critical currents I_c and loop inductance L . The loop inductance is chosen that $2LI_c = \Phi_0$, i.e. $\beta_L = 1$. In this case the two-junction SQUID has a threshold characteristic with overlapping regions of vortex modes where either of the states is stably maintained. For $\Phi = 0$, i.e. no flux in the loop, the threshold characteristic is peaked at $I_{\text{contr}} = 0$. For $\Phi = \Phi_0$, i.e. a single flux quantum in the loop, the threshold curve is peaked at a I_{contr} value corresponding to an applied flux of one flux quantum.

In the DRO shown in Fig. 5.14 information is stored in a single flux quantum by using the mode overlapping region. When the operating point moves across the curve there are two different kinds of transitions: the flux transition and the voltage transition. When the operating point crosses the dashed lines in Fig. 5.14 (flux transition) the flux mode is changed without generating a voltage (only a voltage spike is generated). When the operating point moves across the solid lines the cell generates a voltage. To write a “1” the currents I_{contr} and I_{gate} are used to move the operating point across the vortex transition along the arrow WR1 to the $n = 1$ state. To write “0” the operating point must be moved along WR0 to the $n = 0$ state. To read the cell the operating point is moved across the voltage transition line as depicted in Fig. 5.14. Only if the cell had been in the “1” state a voltage is generated. By reading out the cell the information stored in the cell is erased. Therefore, the cell content needs to be refreshed after each read-out process.

We note that the memory cells described above are idealized simple examples. Those memory cells (e.g. the variable threshold memory cells⁴⁹) that have been used in real digital systems are more complex.

⁴⁸H. H. Zappe, Appl. Phys. Lett. **25**, 424 (1974).

⁴⁹I. Kurosawa, A. Yagi, H. Nakagawa, H. Hayakawa, Appl. Phys. Lett. **43**, 1067 (1983).

Table 5.2: Josephson 4 kbit RAM characteristics (organization: 4096 word \times 1 bit, NEC).

access time	380 ps
power dissipation	9.5 mW
bit yield	99.8 %
Josephson junctions	Nb/AlO _x /Nb
number of junctions	21.000
critical current density	3.3 kA/cm ²
minimum junction size	2 μ m \times 2 μ m
minimum line width	1.5 μ m
cell size	55 μ m \times 55 μ m
RAM size	4.5 mm \times 4.5 mm

Performance of Josephson Memory

The performance of the Josephson memory cells has been improved considerably over the years. Particularly noteworthy are the refinements in Josephson RAM at NEC. The use of moats to control flux trapping and careful attention to the fabrication process has enabled the increase in size to 4 kbit organization and a reduction in critical path access time to below 400 ps. The memory is based on $55 \times 55 \mu\text{m}^2$ vortex transition cells. Table 5.2 summarizes the status of the NEC memory work. This size, however, is still inadequate for most applications. Using a shrink of design rules to submicron features, NEC also has demonstrated an $8.5 \times 11.5 \mu\text{m}^2$ cell which the researchers project to $1 \text{ Mb}/\text{cm}^2$ density.⁵⁰ Nevertheless, much effort remains to solve the memory deficiency of superconductive technology.

5.2.6 Microprocessors

Different elements such as logic gates, memory cells, address latches, decoders, power supply schemes, timing control circuits have to be functionally integrated to demonstrate the feasibility of Josephson computer systems. Fig. 5.15 shows the block diagram of an early 4 bit Josephson microprocessor,⁵¹ which is representative of a realistic computer model. The circuit consisting of 64 bit NDRO RAM, ALU, and control circuit was realized through 1841 gates using 2.5 μm Nb technology. A typical operation, a carry signal processed in the ALU transferred to the RAM, was performed with a maximum clock frequency of 770 MHz. Table 5.3 summarizes the performance of various logic circuits that have been realized in the 1980s using Josephson latching logic.

Until the end of the 1990s voltage state Josephson logic circuits were continuously improved mainly within the Japanese Josephson Computer Project (participation by the Electrotechnical Laboratory (ETL) and the Central Research Laboratories of Fujitsu, Hitachi, and NEC). The accomplishments included (i) the reduction to practice and exploitation of the trilayer Josephson junction process, (ii) the demonstration of GHz clock speed for a 8-bit DSP chip with 23 000 junctions and (iii) the fabrication of 380 ps 1 kbit and 4 kbit memories. Particularly noteworthy is the Fujitsu effort that produced 3000-gate (24 000-junction) microprocessor circuits with 1.5 μm diameter junctions and demonstrated functionality at a 1.1 GHz clock speed. Other examples are somewhat less complex microprocessors at Hitachi and ETL, as well as random access memory (RAM) of 1-4 kbit at ETL, Fujitsu, and NEC. Fabricated memories were as fast as 380 ps. Late in the project, work was initiated at ETL to combine multiple chips into a high-speed package, and at Fujitsu an innovative through-the-Dewar-wall packaging scheme was demonstrated for

⁵⁰H. Numata, S. Nagasawa, S. Tahara, IEEE Trans. Appl. Supercond. **AS-7**, 2282-2287 (1996).

⁵¹S. Kotani, IEEE ISSCC Digest of Technical Papers, p. 150 (1988).

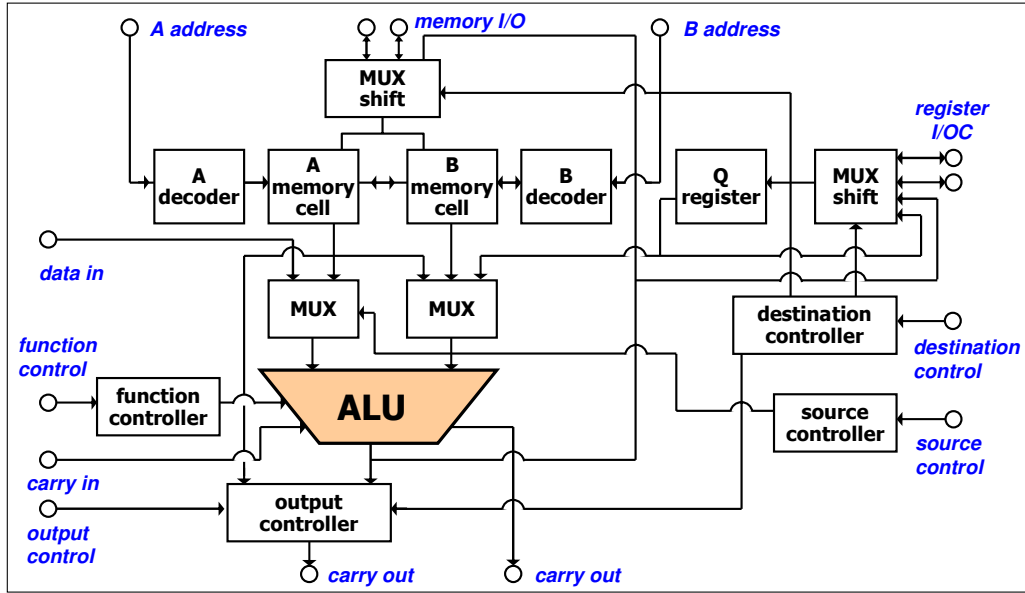


Figure 5.15: Block diagram of the 4 bit Josephson microprocessor (after H. Hayakawa, in *Superconducting Devices*, Steven T. Ruggiero, David A. Rudman (eds.), Academic Press Inc., San Diego (1990)).

high-speed operation. After the discovery of the high temperature superconductors in 1986 the activities on low- T_c digital Josephson electronics was reduced considerably also in Japan.

Table 5.3: Performance of various logic gates

circuit	gate family	junction type	# of gates	performance	Ref.
8 bit adder	4JL	Pb-alloy	300	add time 300 ps	^a
8 bit adder	4JL	NbN/Oxide/NbN	364	add time 700 ps	^b
4 bit adder	RCJL	Pb-alloy	56	add time 172 ps	^c
4 bit multiplier	4JL	NbN/Oxide/NbN	652	mult. time 1 ns	^d
4 bit multiplier	RCJL	Pb-alloy	249	mult. time 280 ps	^e
4 bit multiplier	JTHL	Nb/AlO _x /Nb	104	mult. time 210 ps	^f
16 bit multiplier	MVTL	Nb/AlO _x /Nb	828	mult. time 1.1 ns	^g

^aH. Nakagawa, in “Extended Abstracts of 15th Conf. on Solid-State Devices and Materials”, p. 137 (1983).

^bS. Kosaka, IEEE Trans. Magn. **21**, 102 (1985).

^cJ. Sone, in “Technical Digest Int. Electron Device Meeting (IEDM)”, p. 765 (1982).

^dS. Kosaka, IEEE Trans. Magn. **21**, 102 (1985).

^eJ. Sone, IEEE Solid-State Circuits **20**, 1056 (1985).

^fH. Hatano, in “ISSCC Digest of Tech. Papers”, p. 196 (1986).

^gS. Kotani, IEEE J. Solid-State Circuits **22**, 98 (1987).

5.2.7 Problems of Josephson Logic Gates

Although the Josephson logic gates and memory cells based on underdamped Josephson junctions can be used to built a Josephson microprocessor, the voltage state Josephson logic suffers several problems that so far prevented their practical use:

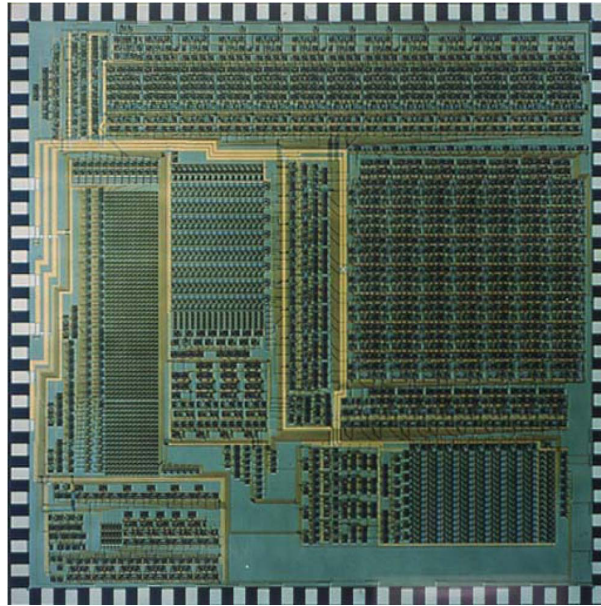


Figure 5.16: Optical micrograph of a Josephson microprocessor.

- The first attempts of IBM to fabricate logic gates were based on unreliable Pb-alloy technology (large parameter spread, unstable against repeated thermal cycles). This problem has been solved by the more appropriate Nb-technology, which provided a significant improvement for the junction quality and reproducibility.
- The voltage state Josephson logic is a latching logic, i.e. switching the junction back to the $V = 0$ state can not be achieved by switching off the control current but requires to switch off the gate current. As discussed above this results in the following complications:
 - an ac power supply is needed,
 - the punchthrough phenomenon limits clock frequencies to ~ 1 GHz,
 - a global timing scheme is needed,
 - the junctions switch to the voltage state very fast (“0” \rightarrow “1”: 1-10 ps), however, switching back is slow (“1” \rightarrow “0”: ~ 1 ns).
- There is no transistor-like 3-terminal device providing significant amplification.

5.3 RSFQ Logic

To overcome the limitations of the Josephson latching logic based on underdamped Josephson junctions the ***Resistive*** or ***Rapid Single Flux Quantum (RSFQ) logic*** has been proposed.^{52,53,54} This nonlatching logic family is based on overdamped Josephson junctions. Since these junctions do no longer have hysteretic IVCs, the information can no longer be encoded in different voltage states of the junctions. In contrast, a totally different representation of information based on single flux quantum (SFQ) pulses is used. The specific properties of the RSFQ logic are:

- nonlatching logic,
- clock frequencies above 100 GHz,
- requirement of overdamped Josephson junctions,
- low power consumption: $P_{\text{diss}} \tau \simeq 10^{-18} \text{ J per bit}$.

In order to see the basic difference between the latching and nonlatching Josephson logic we consider Fig. 5.17. In Fig. 5.17a we have sketched the simplest logic gate, the buffer stage, used in latching logic. It employs an underdamped Josephson junction and thus exhibits a hysteretic IVC shown in Fig. 5.17b. The junction is biased at $I_{\text{gate}} < I_c$ so that the junction initially is in its superconducting state ($V = 0$, logical “0”). A control current I_{contr} drives the total junction current beyond I_c and triggers its switching to its resistive state ($V = 2\Delta/e$, logical “1”), so that a considerable part of the current is steered into the load R_L (typically, through a microstrip line). The latter current serves as an output signal. As we have discussed above, the “0” \rightarrow “1” switching process can be very fast (a few ps). However, due to the latching nature of the logic the reset (“1” \rightarrow “0” switching) cannot be achieved by just turning off I_{contr} but requires to switch off the bias current I_{gate} . Unfortunately, this operation mode has severe drawbacks as discussed above.

As a result of these drawbacks, no prospects have been found to increase clock frequencies of latching-logic circuits beyond a few GHz. This speed is only comparable to that of semiconductor digital circuits which do not require helium refrigeration. Hence, the only advantage of superconducting voltage state digital circuits would be their smaller power consumption. However, this advantage is not sufficient to warrant commercial introduction of this digital technology. This is why much attention was turned to the alternative ***flux-state*** or ***Single-Flux-Quantum (SFQ)*** logic, which uses coding of the binary information not by the dc voltage, but by single quanta of magnetic flux ($\Phi_0 = h/2e = 2.07 \times 10^{-15} \text{ Vs}$). SFQ devices are based on overdamped Josephson junctions with non-hysteretic IVCs (see Fig. 5.17c). Here, the states corresponding to the logical “0” and “1” are those without and with the emission of single flux quantum pulses.

SFQ devices can be divided into two groups, defined by the method used to pass the information between logic circuits. First, in ***static SFQ circuits*** the information is passed in the form of dc flux (or supercur-

⁵²K. K. Likharev, O.A. Mukhanov, V.K. Semenov, *Resistive single flux quantum logic for the Josephson-junction technology*, in SQUID’85, W. de Gruyter, Berlin (1985), pp. 1103-1108.

⁵³K.K. Likharev, V.K. Semenov, *RSFQ logic/memory family: A new Josephson-junction technology for sub-THz-clock-frequency digital systems*, IEEE Trans. Appl. Supercond. **AS-1**, 3-28 (1991).

⁵⁴K.K. Likharev, *Rapid Single Flux Quantum (RSFQ) Logic*, in *Encyclopedia of Materials: Science and Technology*, Elsevier, Amsterdam (2001).

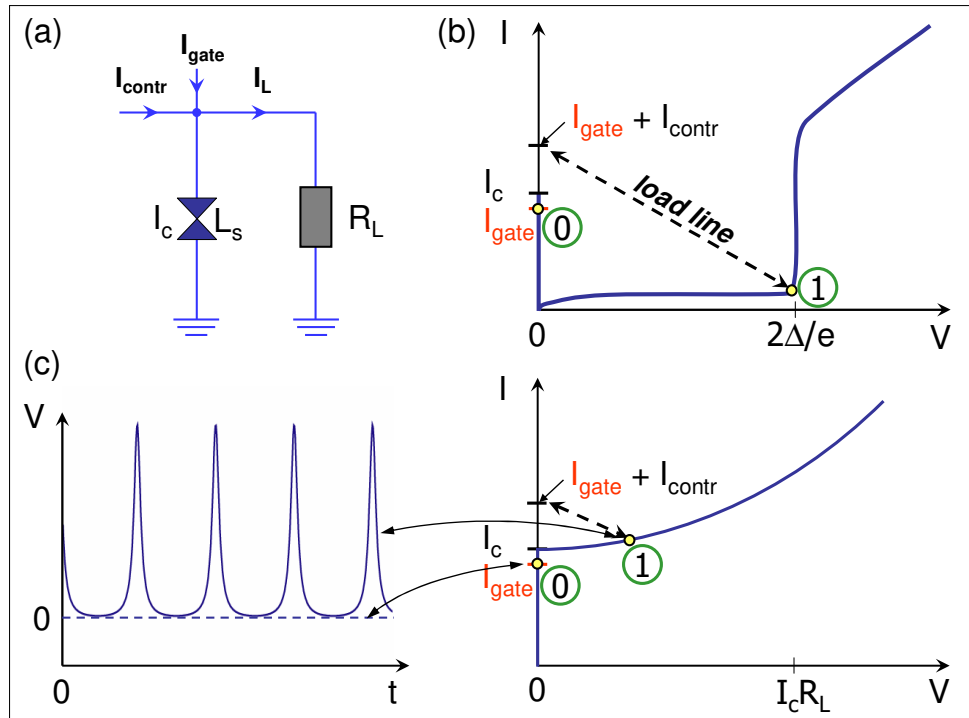


Figure 5.17: (a) Sketch of the buffer stage, the simplest latching logic gate. (b) IVC of an underdamped Josephson junction used for the latching logic. (c) IVC of an overdamped Josephson junction used for the non-latching logic. The states corresponding to the logical "0" and "1" are those without and with the emission of single flux quantum pulses.

rent).^{55,56,57,58,59,60} Although these devices are of a high fundamental interest because of their capability to implement the reversible processing of digital information, in static circuits the intergate distance is severely limited (practically, to the nearest neighbors) by the inductance of the interconnects. A further disadvantage of this approach is the need for an rf-supply/clock with similar limitations on speed as for the voltage-state logic. Finally, a detailed analysis shows that parameter tolerances in static SFQ circuits are very low.

In **dynamic SFQ circuits**^{61,62,63,64,65} information between logic devices is passed ballistically, along either passive microstrip lines or active Josephson transmission lines, in the form of very short (picosecond)

⁵⁵C.J. Anderson, M. Klein, M.B. Ketchen, *Transmission of high speed electrical signals in a Josephson package*, IEEE Trans. Magn. **MAG-19**, 1182-1185 (1983).

⁵⁶T.A. Fulton, L.N. Dunkleberger, *Experimental flux shuttle*, Appl. Phys. Lett. **22**, 232-233 (1973).

⁵⁷K.K. Likharev, *Dynamics of some single flux quantum devices. I. Parametric quantron*, IEEE Trans. Magn. **MAG-13**, 242-244 (1976).

⁵⁸J.P. Hurrell, A.H. Silver, *SQUID digital electronics*, in B.S. Deaver Jr. *et al.* (eds.), *Future Trends in Superconductive Electronics*, AIP, New York (1978), pp. 437-447.

⁵⁹K.K. Likharev, *Classical and quantum limitations on energy consumption in computation*, Int. J. Theor. Phys. **21**, 311-326 (1982).

⁶⁰K.K. Likharev, S.V. Rylov, and V.K. Semenov, *Reversible Conveyor Computation in Array of Parametric Quantrons*, IEEE Trans. Magn. **MAG-21**, 947-950 (1985).

⁶¹K. Nakajima, Y. Onodera, and Y. Ogawa, *Logic design of Josephson network*, J. Appl. Phys. **47**, 1620-1627 (1976).

⁶²K. Nakajima and Y. Onodera, *Logic design of Josephson network - II*, J. Appl. Phys. **49**, 2958-2963 (1978).

⁶³C.A. Hamilton, F.L. Lloyd, *100 GHz binary counter based on dc SQUIDs*, IEEE Electron. Dev. Lett. **3**, 335-338 (1982).

⁶⁴A.H. Silver, R.P. Phillips, R.D. Sandell, *High speed nonlatching SQUID binary ripple counter*, IEEE Trans. Magn. **MAG-21**, 204-207 (1985).

⁶⁵K. Nakajima, G. Oya, Y. Sawada, *Fluxoid motion in phase mode Josephson switching system*, IEEE Trans. Magn. **MAG-19**, 1201-1204 (1983).

quantized voltage pulses $V(t)$ associated with a 2π -change of the phase difference across a Josephson junction. According to the Josephson relation $V = \frac{\hbar}{2e}\dot{\phi}$ it is obvious that the 2π -change results in a voltage pulse of fixed area

$$\int V dt = \int \frac{\hbar}{2e} d\phi = \frac{\hbar}{2e} = \Phi_0 = 2.07 \times 10^{-15} \text{ Vs} \quad (5.3.1)$$

The essence of this idea is that these SFQ pulses can be quite naturally generated, reproduced, amplified, memorized, and processed by elementary circuits comprised of overdamped Josephson junctions. This unique ability, fully realized quite early in some analog devices based on the Josephson effect, was virtually neglected in latching logic. Moreover, in the latching logic circuits the SFQ pulse generation is an inherent reason for the punchthrough effect, which limits operation speed.

Until the mid-1980s, several suggestions on how to use SFQ pulses for processing of digital information and analog-to-digital (A/D) conversion were put forward.^{66,67,68,69,70} However, it was only in 1985-86 that a complete family of dynamic SFQ circuits, with the nickname **Rapid Single-Flux-Quantum (RSFQ)** was suggested by the group around **K.K. Likharev** at the Moscow State University.^{71,72} Until the early 1990s a few circuits containing several of the simplest basic components of the RSFQ family have been fabricated and tested. These components were demonstrated to work at clock frequencies in excess of 100 GHz.^{73,74} Simultaneously, numerical simulations had shown that the speed could be increased beyond 300 GHz going from a 5 to a 1 μm technology. Since the early 1990s the RSFQ idea has been adopted by several groups worldwide.

We also would like to mention that an alternate family of dynamic SFQ devices was suggested under the name **Phase Mode Josephson System** by **K. Nakajima** and coworker at Tohoku University, Japan.^{75,76}

5.3.1 Basic Components of RSFQ Circuits

Generation of SFQ Pulses

SFQ pulses are most simply generated by biasing an overdamped Josephson junction slightly above its critical current I_c . As we have discussed in section 3.3, the Josephson current I_s in this case flows in form of short pulses across the junction with the pulse duration being of the order of $\Phi_0/2I_cR$ (see Fig. 5.18).

⁶⁶T.D. Clark, J.P. Baldwin *Superconducting memory device using Josephson junctions*, Electron. Lett. **3**, 178-179 (1967).

⁶⁷W. Anacker, H.H. Zappe, *Superconducting memory array using weak links*, U.S. Patent No.: 3705393, filed June 30, 1970; published Dec. 5, 1972.

⁶⁸W.J. Lum, H.W.K. Chan, T. Van Duzer, *Memory and logic circuits using semiconductor-barrier Josephson junctions*, IEEE Trans. Magn. **MAG-13**, 48-51 (1977).

⁶⁹H.H. Zappe, *A single flux quantum Josephson junction memory cell*, Appl. Phys. Lett. **25**, 424-426 (1974).

⁷⁰H.H. Zappe, *A subnanosecond Josephson tunneling memory cell with nondestructive readout*, IEEE J. on Solid State Circuits **10**, 12-19 (1975).

⁷¹K. K. Likharev, O.A. Mukhanov, V.K. Semenov, *Resistive single flux quantum logic for the Josephson-junction technology*, in SQUID'85, W. de Gruyter, Berlin (1985), pp. 1103-1108.

⁷²O.A. Mukhanov, V.K. Semenov, K.K. Likharev, *Ultimate performance of RSFQ logic circuits*, IEEE Trans. Magn. **MAG-23**, 759-762 (1987).

⁷³V.K. Kaplunenko, M.I. Khabipov, V.P. Koshelets, K.K. Likharev, O.A. Mukhanov, V.K. Semenov, I.L. Serpuchenko, A.N. Vystavkin, *Experimental study of the RSFQ logic elements*, IEEE Trans. Magn. **MAG-25**, 861-864 (1989).

⁷⁴L.V. Fillipenko, V.K. Kaplunenko, M.I. Khabipov, V.P. Koshelets, K.K. Likharev, O.A. Mukhanov, V.K. Semenov, I.L. Serpuchenko, A.N. Vystavkin, *Experimental implementation of analog-to-digital converter based on the reversible ripple counter*, IEEE Trans. Magn. **MAG-27**, 2464-2467 (1991).

⁷⁵K. Nakajima, H. Mizusawa, H. Sugahara, Y. Sawada, *Phase mode Josephson computer system*, IEEE Trans. Appl. Supercond. **AS-1**, 29-36 (1991).

⁷⁶K. Nakajima, *Single Flux Quantum Electronics*, in *Handbook of Applied Superconductivity*, Vol. **2**, B. Seeger ed., IOP Publishing, Bristol (1998), pp. 1795-1812.

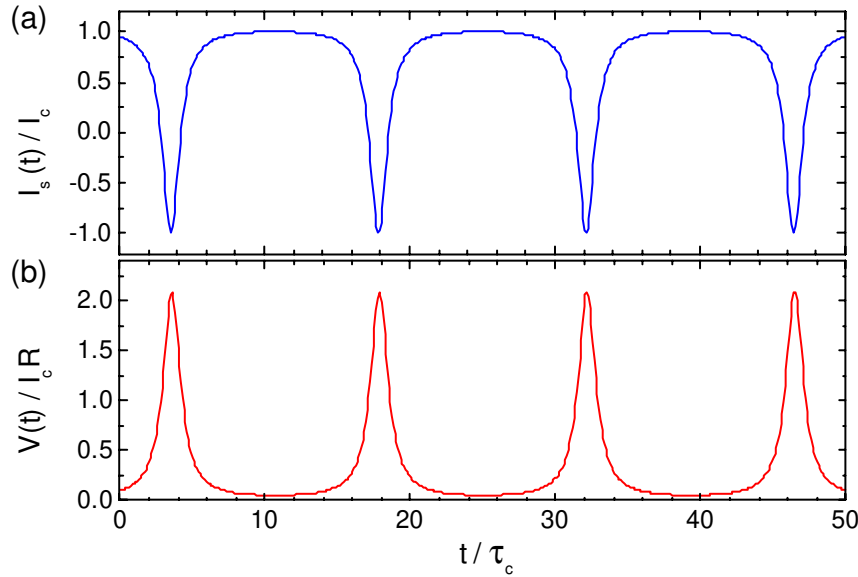


Figure 5.18: Time variation of (a) the Josephson current I_s and (b) the junction voltage V for an overdamped Josephson junctions biased at $I/I_c = 1.05$. The time is normalized to $\tau_c = \Phi_0/2\pi I_c R$.

Here, $1/R = 1/R_N + 1/R_L$ is the total resistance in parallel to the ideal Josephson element. In the best case, $R \sim R_N$ and the pulse duration is given by $\Phi_0/2I_c R_N$, which is about 1 ps for $I_c R_N \sim \Delta/e \sim 1$ mV. Note that superconducting tunnel junctions are usually intrinsically underdamped and have to be brought to the overdamped regime by a small shunt resistance. Then, $I_c R < I_c R_N$ resulting in a longer pulse duration and smaller pulse height. We see that the typical SFQ pulse is smaller in voltage and shorter in time than the typical pulses obtained in voltage state logic.

In order to generate individual SFQ pulses the circuit shown in Fig. 5.17a can be used. A single quantized SFQ pulse may be generated by feeding the Josephson junction by a short non-quantized current pulse I_{contr} arriving from e.g. a semiconductor electronic device. A disadvantage of this circuit is that the pulse should be very short (a few picoseconds), and its duration should be within certain limits.

A less demanding way to generate SFQ pulses is to use a Josephson junction in parallel with the superconducting inductor L , that is an rf-SQUID with a screening parameter $\beta_{L,\text{rf}} = 2\pi I_c L / \Phi_0$ ranging somewhere between 3 and 10 (compare section 4.2). A slightly modified version is shown in Fig. 5.19a. In order to generate a single SFQ pulse, the interferometer may be fed by a usual dc current pulse, with amplitude (but not length) within certain limits. For example, a periodic train of SFQ pulses can be generated by using an external microwave signal for I_{contr} , which can be sent from room temperature via coaxial lines at least up to several 10 GHz. A single SFQ pulse is generated every rf-cycle when the rf-current exceeds the current value I_1 . The generated pulse train can be distributed to the various gates of a circuit via transmission lines acting as a clock for the circuit. Of course a train of SFQ pulses can be generated also by biasing an overdamped Josephson junction slightly above the critical current as shown in Fig. 5.18b.

Fig. 5.19d shows a more advanced version of such a **dc to SFQ converter**. If its input current I_{gate} is increased beyond a certain threshold value I_{high} , the critical state of the junction J_3 is achieved, and the SFQ pulse is generated across it. Simultaneously, the three-junction interferometer (J_1-J_3 , L_1-L_3) is switched into another flux state. In order to reset the interferometer into its initial state, the current should then be decreased below a value I_{low} at which sequential 2π -jumps are triggered in the junctions J_1 and J_2 . The reset is accompanied by the generation of SFQ pulses across these junctions.

We note that also the inverse of a dc to SFQ converter, a SFQ to dc converter can be implemented.

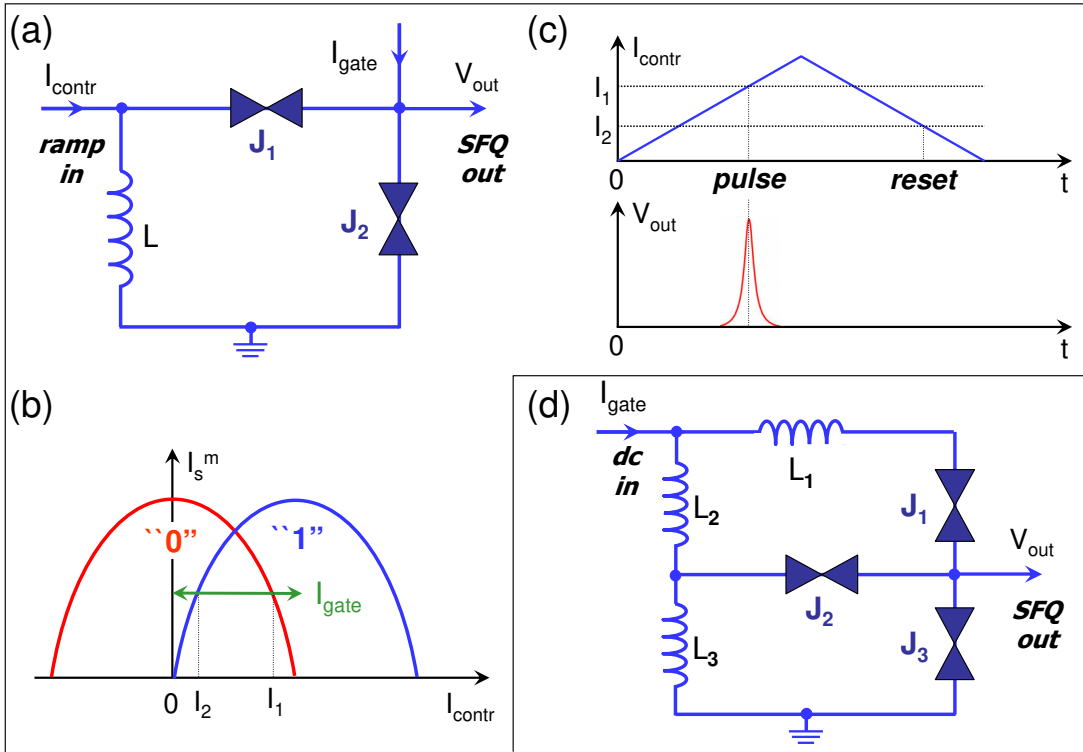


Figure 5.19: (a) Circuit and (b) approximate threshold characteristic of a SFQ pulse generator. I_1 and I_2 mark the current values for the “0” → “1” and the return transition, respectively. (c) shows the current ramp used for I_{contr} and the resulting SFQ output pulse. In (d) another possible structure of a dc to SFQ converter is shown that requires only a dc input signal.

Reproduction, Amplification and Transfer of SFQ Pulses

We have seen that if the dc bias current I_{gate} is not too far from the critical value I_c , a SFQ pulse can be triggered by an incoming short control pulse, with either the nominal or a somewhat different amplitude. This means that the simple circuit shown in Fig. 5.19a can reproduce SFQ pulses, bringing their area $\int V(t)dt$ to the nominal value Φ_0 , i.e. providing a moderate voltage gain if necessary. On the other hand, if the input pulse is too weak (e.g. a weak noise signal due to parasitic crosstalk between the signal transfer lines) it is not reproduced by the circuit, so that the circuit also serves as a noise discriminator.

Josephson Transmission Line: Key elements of RSFQ circuits are Josephson transmission lines (JTL, see Fig. 5.20a) comprising several Josephson junctions connected in parallel by superconducting strips of a relatively low inductance $L \sim \Phi_0/I_c$, and dc-current biased to their sub-critical state ($I_{\text{gate}} < I_c$). If the inductance would be much smaller, then a fluxon in the JTL would be spread out over several junctions. On the other hand, if L would be much larger, then several flux quanta could be in a single loop. Upon triggering a 2π -jump of the Josephson phase in the left junction J_1 by the input signal A, the resulting SFQ pulse developed across J_1 will trigger a 2π -jump in J_2 , and so on. This is equivalent to a flux quantum moving from left to right. That is, the SFQ pulse is transferred along the Josephson transmission line. It has been shown that 5 ps SFQ pulses can be transferred over distances up to 1 cm without noticeable attenuation. JTLs can also be used to amplify SFQ pulses (or, more exactly, to provide their current/power gain while conserving their voltage area). For that, the critical currents of the junctions and the corresponding dc bias currents should grow in the direction of the pulse propagation, with the proportional decrease of the inductances.

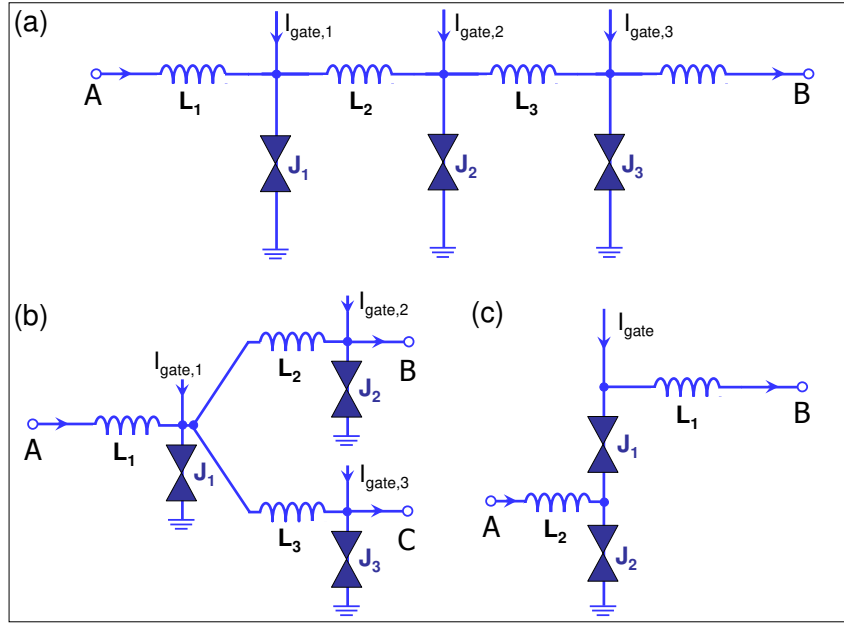


Figure 5.20: Some basic elements of RSFQ circuits: (a) Discrete Josephson transmission line for active SFQ pulse transfer, (b) SFQ pulse splitter, and (c) buffer stage.

Alternatively, a purely passive superconducting transmission line can be used for transmitting SFQ pulses with low loss or dispersion. The impedance of this line should be close to that of the shunt resistor R_L for good matching. However, the nonlinear active transmission line shown in Fig. 5.20a has the advantage that it automatically filters out low-level noise and also regenerates the SFQ pulse.

SFQ Pulse Splitter: As shown in Fig. 5.20b, an evident generalization of the JTL can be used to provide splitting of the SFQ pulse, i.e., reproduction of the input pulse A at each of its two outputs B and C, without noticeable decrease of the pulse voltage amplitude. That is, the JTL can be split into two or more lines so that one SFQ pulse can give rise to many such pulses. Note that the pulse splitter is symmetric among its three ports and an SFQ pulse incident from any of these ports will yield an SFQ pulse out along the two others. Again, a splitter also can be achieved by splitting a passive transmission line. However, in this case one has more stringent requirements for the matching condition at the intersection to avoid reflections.

Buffer Stage: Unfortunately transmission lines and splitters transmit pulses equally well in both directions and cannot be used for isolation. That is, we need a buffer stage as shown in Fig. 5.20c. The junctions are dc-current biased below their critical currents. If a short pulse arrives at A, it induces a 2π switching of the Josephson phase of junction J_2 . This switching produces the standard SFQ pulse at the output terminal B. The input pulse may be weaker than the standard pulse, so that the circuit provides some amplification. On the other hand, if the pulse arrives at terminal B, junction J_1 generates a 2π pulse because of its lower critical current. Thus, no SFQ pulse passes to the input A of the circuit, i.e. it performs the function of a one-directional buffer.

SFQ Memory Cell

Fig. 5.21 shows the SFQ memory cell also known as the RS flip-flop and DRO register. This standard RSFQ latch essentially consists of a two-junction (J_1 and J_2) superconducting quantum interferometer

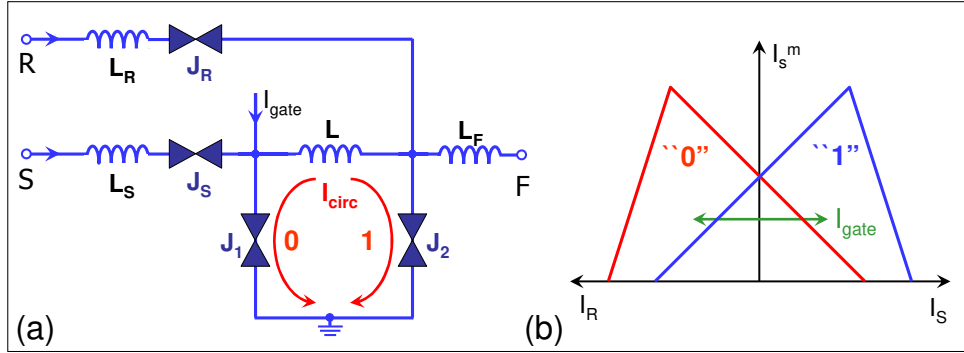


Figure 5.21: (a) Circuit diagram of the SFQ memory cell also known as RS flip-flop. (b) Approximate critical current threshold characteristic for the RS flip-flop showing the zero voltage regime for the “0” and the “1” state as a function of the control currents at the S and the R inputs.

(dc-SQUID) with two input lines each with a buffering series junction (J_S and J_R). It stores information in form of quantized flux trapped in the superconducting loop. If the inductance L of the interferometer is chosen so that the screening parameter $\beta_L = 2I_c L / \Phi_0 \sim 3$ and the dc bias current $I_{\text{gate}} \sim 0.8 I_c$, the circuit has two symmetric stable stationary states, which differ with respect to the direction of the persistent current $I_{\text{circ}} = \Phi_0 / 2L$ circulating in the loop. In other words, one of these states corresponds to an additional single flux quantum trapped in the superconducting loop of the interferometer.

Let us suppose that the SQUID is initially in the “0” state with zero flux in the loop. If the bias current I_{gate} is switched on to a value below the critical current of the SQUID, most of the current will flow through the left junction J_1 due to the large inductance L . Actually, this corresponds to a counterclockwise circulating current with $I_1 = I_{\text{gate}}/2 + I_{\text{circ}} < I_c$ and $I_2 = I_{\text{gate}}/2 - I_{\text{circ}}$. If now a SFQ pulse arrives at the input S, it triggers a 2π -jump in junction J_1 , which is biased close to I_c , but not in J_2 , which carries a lower dc current $I_2 = I_{\text{gate}}/2 - I_{\text{circ}}$. This corresponds to a fluxon crossing J_1 and entering the loop. As a result, the cell is switched to its opposite state 1 with the clockwise circulation of the persistent current I_{circ} . It is evident that now the reset (the “1” \rightarrow “0” switching) can be triggered by the SFQ pulse arriving at the R terminal. Simultaneously, an SFQ pulse $V(t)$ is developed across J_2 , which can serve as an output signal F. This corresponds to a flux quantum leaving the loop through junction J_2 . The auxiliary junctions J_S and J_R defend the SFQ pulse sources from the back reaction of the interferometer in the case of a “wrong” signal, for example, the S (set) pulse arriving during the state 1. In this case, junction J_S (rather than J_1) switches. That is, the incoming single flux quantum drops out of the circuit through J_S , if the interferometer loop is unable to accept it. In the same way, if the circuit is in the 0 state, then a readout pulse into the R input will not trigger J_2 , since the effective bias current is quite small, but rather the right buffer junction J_R . Therefore, no output signal will be generated. One can see that for SFQ pulses the circuit works exactly as a standard RS flip-flop (latch): SFQ pulses can be trapped by this circuit, so that the information about their arrival can be conveniently stored there in the form of static magnetic flux, and released when necessary in SFQ pulse form.

At present the absence of large Josephson junction memories is a major problem for the successful application of RSFQ circuits (compare also section 5.2.5). Demonstrated RAM chips had shown a decent access time of the order of a few 100 ps, but only of a few 10 kbit size. However, there is no inherent problem with the implementation of high-density Josephson junction RAMs. But of course their development would require a large investment of effort and money. Right now these resources are not in sight.

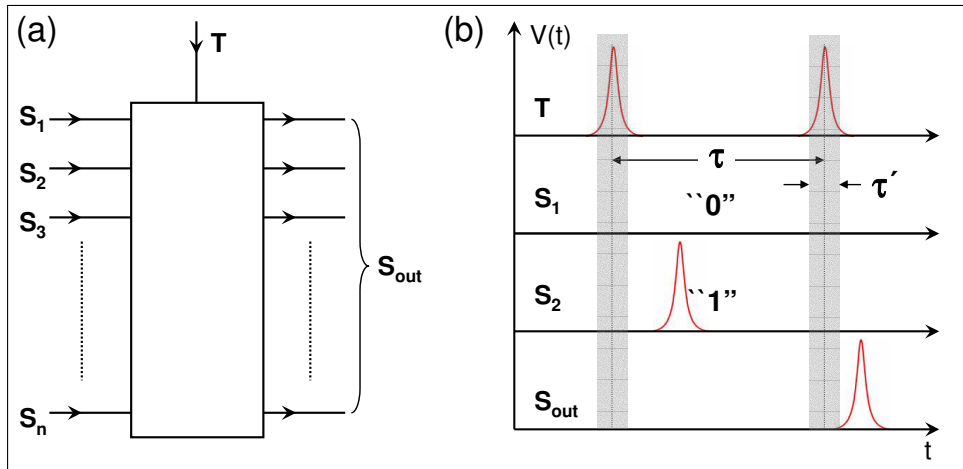


Figure 5.22: Representation of binary units in the RSFQ logic circuits. The signal pulses S are allowed to arrive during the whole clock period τ except some close vicinity τ' of the clock pulses (after Likharev *et al.*, IEEE Trans. Appl. Supercond. **AS-1**, 3-28 (1991)).

5.3.2 Information in RSFQ Circuits

In order to perform digital operations with signals as unusual as picosecond SFQ pulses, an explicit definition of what digital information is in RSFQ circuits is required. Such a definition was probably the most important conceptual step made by **Likharev** and coworkers.⁷⁷

According to this concept, any RSFQ circuit may be considered as consisting of **elementary cells** or **timed gates** operating as shown in Fig. 5.22. Each cell has two or more stable flux states. The cell is fed by SFQ pulses, which can arrive from signal lines S_1, S_2, \dots, S_n and a clock or timing line T . Each clock pulse marks a boundary between two adjacent clock periods by setting the cell into its initial state "1". During the new period, an SFQ pulse can arrive (or not arrive) at each of the cell inputs S_i (see Fig. 5.22b). Then information can be transferred generally through two lines, one carrying short (quasi)periodic clock pulses T , while the other carries the bit pulses S_i . The logical value "1" of the signal S_i is characterized by the arrival of a single pulse at terminal S_i between two consecutive T pulses, whereas the absence of a pulse denotes a "0". In Josephson junction circuits this representation is very natural, if single flux quantum (SFQ) pulses of the form $\int V dt = \Phi_0$ are used in both the S and T line. As shown above, such pulses can be readily generated and reproduced/amplified either by single overdamped Josephson junctions or by simple circuits consisting of such junctions.

The convention for representing information in RSFQ circuits does not require the exact coincidence of SFQ pulses in time, nor is a specified time sequence of the various input signals needed. Each pulse can either change or not change the internal state of the cell, but it can not produce any immediate reaction at its output terminal(s) S_{out} . Only the clock pulse T is able to fire out the pulse(s) S_{out} corresponding to the internal state of the cell, predetermined by the input signal pulses which have arrived during this period. The same clock pulse terminates the clock period by resetting the cell into its initial state. Thus, an elementary cell of the RSFQ family is equivalent to a usual asynchronous logic circuit coupled with a latch (flip-flop) storing its output bit(s) until the end of the clock period.

⁷⁷K. K. Likharev, O.A. Mukhanov, V.K. Semenov, *Resistive single flux quantum logic for the Josephson-junction technology*, in SQUID'85, W. de Gruyter, Berlin (1985), pp. 1103-1108.

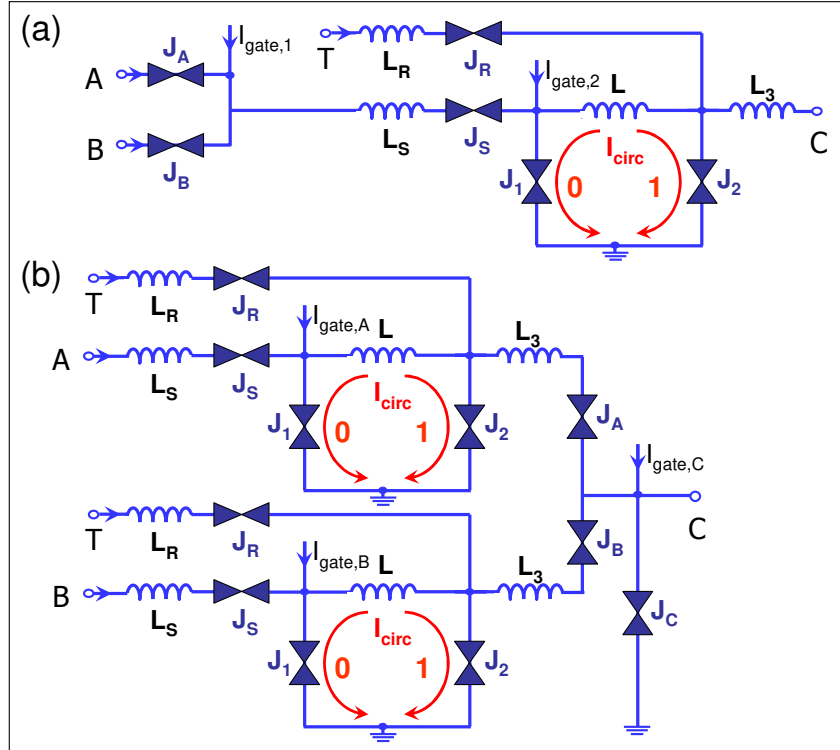


Figure 5.23: Circuit diagram of (a) the triggered OR gate and (b) the triggered AND gate.

5.3.3 Basic Logic Gates

YES Gate: In addition to being a basic RSFQ memory cell, the RS flip-flop can also function as a latch for a logic state. We consider the RS flip-flop shown in Fig. 5.21a. We suppose that the input S is fed from a signal line, while the clock pulses are fed into input R. The clock cycle starts from the clock pulse, resetting the system back into its state “0”. If no signal pulse S arrived during the current clock cycle, then the new clock pulse R would trigger the SFQ pulse across J_R rather than J_2 . That is, no output signal appears at F. However, if this concluding clock pulse was preceded by the signal pulse S (switching the interferometer to state “1”), then the clock pulse would trigger the SFQ pulse across J_2 , which will serve as the output signal. Simultaneously, the flip-flop is reset into state “0”. We see that the RS flip-flop in this case works in accordance with the above definition of an RSFQ elementary cell, performing the function YES, i.e. reproducing the input signal S, with its time delay until arrival of the clock pulse. In other words, this circuit works as a 1-bit stage of a shift register. Such RSFQ registers have been tested successfully at frequencies up to 60 GHz with parameter margins up to $\pm 30\%$.⁷⁸

OR Gate: We next consider a simple triggered OR gate shown in Fig. 5.23a. It consists of a so-called confluence buffer with its output connected to the input S of an RS flip-flop. For the confluence buffer the bias current of junction J_1 partly act as bias for the buffer junctions J_A and J_B . A voltage pulse coming in will generate a current that subtracts from the bias current and therefore will not switch the buffer junctions. In contrast, a pulse going out will add to this bias and switch the junction. If two SFQ pulses enter at A and B at different times, only the first fluxon will be stored in the SQUID loop. The second pulse will leave the line across the buffer junction J_S . When the timing pulse T is sent, only a single SFQ pulse is generated at the output. It is evident that this circuit functions as an OR gate. Note that four

⁷⁸O.A. Mukhanov, Rapid single flux quantum (RSFQ) shift register family, IEEE Trans. Appl. Supercond. **AS-3**, (1993).

out of the six junctions are buffer junctions and only two form the latch. Of course more complicated OR gates with optimized performance, allowing for large parameter spread of the junctions, have been fabricated.^{79,80}

AND Gate: Fig. 5.23b shows a triggered AND gate, which has an RS flip-flop before each input of a confluence buffer. If the input pulses A and B come in at different times, the input latches serve to store them until they are released simultaneously by the trigger pulse T. This in turn triggers the nearby junction J_C , which provides an output pulse only when both inputs were “1”. Note that for the AND gate as well as for the OR gate there are several closed superconducting loops, which would be more evident if all the ground lines would be connected. This makes RSFQ circuits sensitive for trapped magnetic flux. That is, sufficient magnetic shielding and the use of moats keeping trapped flux away from the circuits are required.

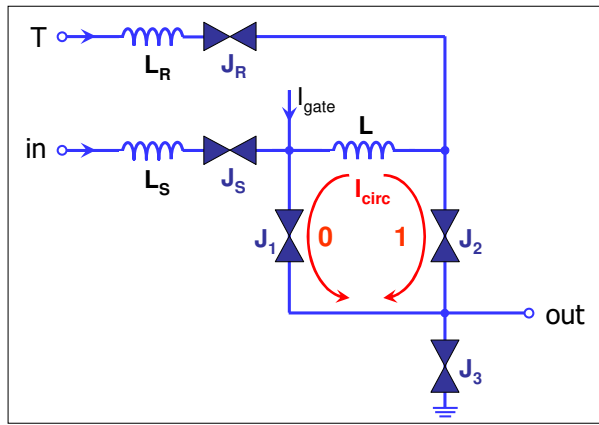


Figure 5.24: Circuit diagram of the RSFQ NOT gate.

NOT Gate: Fig. 5.24 shows a possible implementation of an RSFQ inverter. This circuit is also built around a single interferometer (J_1, L, J_2), but also includes an additional Josephson junction J_3 . In the initial state “0” the higher current is flowing through J_1 , while J_2 carries virtually no current. This means that in the absence of an input pulse S_1 , the next clock pulse would trigger the SFQ pulse in J_3 rather than in J_2 , and this pulse would appear at the circuit output J_3 . That is, an input “0” provides an output “1”. If in contrast a signal pulse S_1 arrives, it would switch the interferometer into the state “1”, with a higher current in J_2 . In this case, the next clock pulse would trigger the SFQ pulse across J_2 rather than J_3 . That is, the circuit would be reset, and no output pulse developed. In total, an input “1” yields an output “0”.

Shift Register: We can arrange a large number of RS flip-flops as shown in Fig. 5.25 to obtain a shift register. Here, the bottom row of linked SQUIDs ($\beta_L \sim 3$) represents a series of binary bits. Each cell contains either no (logical state “0”) or a single flux quantum (logical state “1”). The upper row of SQUIDs do not store fluxons but rather form a Josephson transmission line that transmits the trigger/reset pulses entering from the right. The shift register operates as a first-in, first-out (FIFO) memory. If the trigger pulse enters, it shifts the contents of the cells a single cell to the right. Then, a new data bit can be inserted at the input on the left.

⁷⁹S.V. Polonsky, V.K. Semenov, P.I. Bunyk, A.F. Kirichenko, A. Yu. Kidiyarova-Shevchenko, O.A. Mukhanov, P.N. Shevchenko, D.F. Schneider, D.Yu. Zinoviev, K.K. Likharev, *New RSFQ circuits*, IEEE Trans. Appl. Supercond. **AS-3** 2566-2577 (1993).

⁸⁰Y.K. Kwong, V. Nandakumar, *Experimental evaluation of some rapid single flux quantum cells*, IEEE Trans. Appl. Supercond. **AS-3**, (1993).

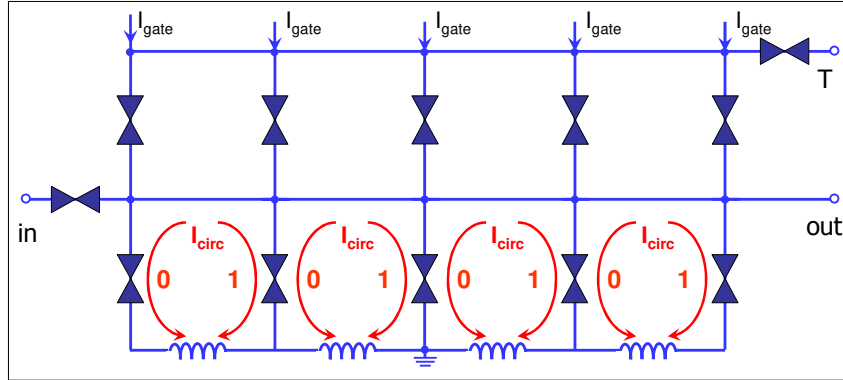


Figure 5.25: RSFQ shift register formed by a series array of RS flip-flops.

5.3.4 Timing and Power Supply

At the very high speed of RSFQ circuits timing becomes an issue of primary importance. It is obvious that the use of a global clock is problematic. In particular, external (global) synchronization of VLSI circuits, as it is common practice up to now, at frequencies beyond 100 GHz is relatively impractical, since the small relative time differences necessary for this clocking procedure can no longer be guaranteed over larger distances. In distributing the global clock signal varying delay times may appear that can result in a clock skew. Furthermore, the signal pulses themselves may have different delays. Fortunately, clock pulses for RSFQ cells are physically identical to the signal pulses, and hence can be generated inside RSFQ circuits. Thus, the external global synchronization can be complemented and sometimes replaced by very convenient *local self-timing*.

A number of asynchronous clocking schemes have been proposed⁸¹ but have not yet been implemented in complex circuits. Data-driven self timing was tested with success for the data exchange between two shift registers at data rates up to 20 Gbit/s.⁸² Furthermore, in projects aiming at high speed data switches, a clock recovery circuit⁸³ has been tested successfully at frequencies up to 35 GHz. In the same project, an underdamped long Nb/AlO_x/Nb junction was tested as soliton oscillator SFQ clock achieving a linewidth of 38 kHz at 12 GHz⁸⁴.

In contrast to the latching voltage state logic the non-latching RSFQ logic does not require an ac power supply. As for semiconductor logic, a much more simple dc power supply is sufficient.

5.3.5 Maximum Speed

The probably most impressive figure of merit of RSFQ cells is their extremely high operation speed. Discussing the maximum speed we have to consider the logic delay of RSFQ circuits. For timed circuits such as RSFQ elementary cells, the logic delay is defined as the minimum value of the clock period for which the cell operates correctly. Numerical simulations show that for a typical RSFQ cell, this delay is of the order of $6\pi\tau_{RL}$ with (compare (5.2.3))

$$\tau_{RL} = \frac{\Phi_0}{2\pi I_c R} . \quad (5.3.2)$$

⁸¹K. Gaj, Proc. of ISEC 1997, Vol. 2, p. 299 (1997).

⁸²Z. J. Deng, Proc. of ISEC 1997, Vol. 2, p. 332 (1997).

⁸³V. Kaplunenko, V. Borzenets, N. Dubash, and T. Van Duzer, *Superconducting single flux quantum 20 Gb/s clock recovery circuit*, Appl. Phys. Lett. **71**, 128 (1997).

⁸⁴Y. M. Zhang, V. Borzenets, V. K. Kaplunenko, and N. B. Dubash, *Underdamped long Josephson junction coupled to overdamped single-flux-quantum circuits*, Appl. Phys. Lett. **71**, 1863 (1997).

Here, R is the total normal resistance given by the parallel connection of the shunt resistance R_L and the normal resistance of the junction. We have to take into account that the McCumber parameter

$$\beta_C = \frac{2\pi}{\Phi_0} I_c R^2 C = \frac{2\pi}{\Phi_0} J_c R^2 C_s \quad (5.3.3)$$

can be unity at maximum to have an overdamped junction. With $\beta_C = 1$ we obtain

$$\tau_{RL} = \frac{\Phi_0}{2\pi I_c} \sqrt{\frac{\Phi_0 I_c C}{2\pi}} \propto \sqrt{\frac{C}{I_c}}. \quad (5.3.4)$$

Because I_c is determined by thermal fluctuation stability of the RSFQ circuits requiring $I_c \sim 100 \mu\text{A}$ at $T = 4.2 \text{ K}$, τ_{RL} is determined solely by C . Since both C and I_c scale with the junction area, one can reduce C by reducing the junction area. In order to keep I_c at the required value of about $100 \mu\text{A}$ at the same time one has to increase the current density of the junctions. We see that we need high current density Josephson junctions with small junction area.

For standard niobium trilayer technology the characteristic time $2\pi\tau_{RL}$ expressed in ps roughly coincides with the linear size of Josephson junctions expressed in μm . This means that for a $3 \mu\text{m}$ technology $2\pi\tau_{RL} \sim 3 \text{ ps}$ and a typical elementary cell can operate at clock frequencies of the order of 100 GHz . If submicron technology is employed, external shunting of the junctions may become unnecessary, and the operation frequency may approach 500 GHz . At the end, the limiting frequency is the gap frequency \hbar/Δ corresponding to about 0.5 ps for Nb.

5.3.6 Power Dissipation

The power dissipation of RSFQ switches is similar to that of the Josephson switches discussed in section 5.2.2. The energy dissipated per switching process can be estimated to $E_{diss} \simeq \int I_c V dt$. With $I_c \simeq 100 \mu\text{A}$ and $\int V dt = \Phi_0 = 2 \times 10^{-15} \text{ Vs}$ we obtain the very small value of $E_{diss} \simeq 2 \times 10^{-19} \text{ J}$.

We note however, that the power consumption of real RSFQ cells is determined not by the energy dissipation inside the Josephson junctions, but by the dissipation in dc supply resistors used for the biasing network. This power dissipation is of the order of $1 \mu\text{W}$ per gate. Nevertheless, this value is also slightly lower than that for latching Josephson logic cells.

5.3.7 Prospects of RSFQ

There are several potential applications of RSFQ circuits that will be only briefly addressed in the following. Table 5.4 contains a list of possible applications of superconductor digital circuits with the estimated number of required junctions giving the complexity of the circuits.

Analog-to-Digital Converters

The simplest and hence the most immediate application of RSFQ technology is analog-to-digital conversion. The reasons for this is obvious: The extremely high switching speed of the Josephson junctions can provide a very short aperture time τ_a and hence a very high resolution $\varepsilon = 1/2^n = (\pi f_N \tau_a)^{-3/2}$ of the AD converter.⁸⁵ Here, f_N is the Nyquist frequency (compare section 5.4.1).

⁸⁵V.K. Semenov, *Digital to analog conversion based on processing of the SFQ pulses*, IEEE Trans. Appl. Supercond. **AS-3**, (1993).

Table 5.4: Possible applications of superconductor digital circuits (source: SCENET 2001).

application	no. of JJs	estimated market size
integrated SIS receivers with correlator	10^6	small
digital multichannel SQUID arrays	10^5	medium
dc voltage standards	10^4	small
ac voltage standards digital synthesizer	10^5	medium
A/D converters	10^4	large
D/A converters	10^3	medium
dc/ac quantum voltmeters	10^5	large
time-digital converters	10^3	medium
digital SFQ test circuits for rf-metrology	10^3	medium
frequency dividers, digital frequency meters	500	medium
transient recorders	10^4	medium
TeraFLOP workstation	10^6	medium
PetaFLOP computer	10^9	??

Digital SQUIDs

The effective digital filtering described above can be also used for the development of digital SQUIDS which can combine the high sensitivity of analog SQUIDS with a much higher slew rate, linearity and a virtually unlimited dynamic range.⁸⁶ Also, the sensitivity is somewhat improved because of the lower noise contribution of the readout electronics. The advantages of the digital SQUID are essential for portable and open environment sensor systems, e.g. for medical diagnostics and imaging, for non-destructive testing (NDE) of materials and for geophysical surveying. Furthermore, digital SQUIDS will certainly relax constraints regarding system design for other applications (e.g. MEG, where shielding is a significant part of the costs). The digital interface with room-temperature electronics will also make digital SQUIDS attractive for gradiometry involving a large baseline or operating at some distance from the ground, in e g geophysical surveying or oil prospecting.

Digital Signal Processing

A further promising application of RSFQ circuits is digital signal processing, because many algorithms in this field can be implemented with relatively small on-chip memory. A typical example of such processing is digital filtering.⁸⁷ In general, RSFQ circuits could extend the well-known complex methods of digital signal processing from acoustic frequencies (tens of kHz) to radio-frequencies (tens and hundreds of MHz) typical for bandwidths of radar, TV, and communication systems.

Computing

In contrast to digital signal processing, an universal von Neumann-type computer represents a difficult system to be improved by RSFQ technology. The reason is that such a system relies on frequent data

⁸⁶S.V. Rylov, *Analysis of high-performance counter-type A/D converters using RSFQ logic/memory elements*, IEEE Trans. Magn. **MAG-27**, 2431-2434 (1991).

⁸⁷VLSI and Modern Signal Processing, S.Y. Kung, H.J. Whitehouse, T. Kailath, eds., Prentice-Hall, Englewood Cliffs, New York (1985).

Table 5.5: Performance of various RSFQ based circuits.

circuit type	circuit metric(s)
toggle flip flop	144 GHz
4-bit shift register	66 GHz
6-bit flash ADC	20 GHz
1:8 demultiplexor (synchronous)	20 Gb/s
1-bit half-adder	23 GHz
$8 \times N$ bit serial multiplier	16 GHz
128-bit auto-correlator	16 GHz
2-bit counter	120 GHz
1-kbit shift register	19 GHz
6-bit transient digitizer	16 Gb/s
1:2 demultiplexor	95 Gb/s
2-bit full-adder	13 GHz
14-bit digital comb filter	20 GHz
time-to-digital converter	31 GHz

exchange between the processor and the memory. Here, the exchange rate is limited by at least the speed of light (delay time of about 100 ps for a distance of 1 cm) and by today's chip packaging technologies (about 1 ns for data transfer to/from the chip). Direct implementation of such a computer using the RSFQ logic and an existing superconductor memory would probably give a system some 10 times faster than those achievable with semiconductor technologies. It is of course questionable, whether this advantage is sufficient to switch to superconductor technology with its necessity for helium refrigeration. The key problem for superconducting circuits will always be the advancing semiconducting competition. Here, the challenge for superconducting circuits is the fact that a new technology not only has to match the current semiconductor performance but rather has to greatly surpass the performance that may be anticipated for the next 5 to 10 years.

However, there is a general demand from telecommunication and computer area for above 100 GHz systems. For traditional three-terminal semiconducting transistor devices a cutoff frequency approaching 1 THz is needed to achieve a throughput of the order of 100 GHz for small application specific ICs (ASICs). Such performance requirements are beginning to reach the limits of the physical properties of semiconductors^{88,89}. Furthermore, it has been noted that the rate of innovation in semiconductor materials and devices has dramatically slowed down with very marginal improvements in device speed.⁹⁰ RSFQ technology, based on low-temperature superconductors, has the potential to leapfrog the performance of traditional silicon and III-V compound semiconductors. Simple circuits have been demonstrated with speeds in excess of 750 GHz,^{91,92} and complex medium-scale integrated circuits (ICs) operated at 30 GHz^{93,94} with performance up to 200 GHz projected in the not-too-distant future.⁹⁵ These achieve-

⁸⁸M. Schulz, *The end of the road for silicon?*, Nature **399**, 729 (1999).

⁸⁹P.A. Packan, *Device Physics: Pushing the Limits*, Science **285**, 2079 (1999)

⁹⁰See for example *The International Technology Roadmap for Semiconductors*, Semiconductor Industry Association (1999).

⁹¹W. Chen, A. V. Rylyakov, V. Patel, J. E. Lukens, and K. K. Likharev, *Rapid single flux quantum T-flip-flop operating up to 770 GHz*, IEEE Trans. Appl. Supercond. **AS-9**, 3212-3215 (1999).

⁹²W. Chen, A. V. Rylyakov, Vijay Patel, J. E. Lukens, and K. K. Likharev, *Superconductor digital frequency divider operating up to 750 GHz*, Appl. Phys. Lett. **73**, 2817 (1998)

⁹³D. K. Brock, *RSFQ technology: Circuits and systems*, Int. J. High Speed Electron. Syst. **11**, 307-362 (2001).

⁹⁴A. F. Kirichenko, S. Sarwana, D. Gupta, I. Rochwarger, and O. A. Mukhanov, *Multi-channel time digitizing system*, IEEE Trans. Applied Supercond. **AS-13**, 454-458 (2003).

⁹⁵A. M. Kadin, C. A. Mancini, M. J. Feldman, and D. K. Brock, *Can RSFQ logic circuits be scaled to deep submicron*

ments represent faster demonstrated electronic circuit speeds than any other technology has predicted to date, even through computer simulations. Prototype RSFQ circuits made with modest research-grade 2-3 μm linewidth niobium (Nb) fabrication processes have demonstrated circuits such as those shown in Table 5.5.

PetaFLOP supercomputers are a class of massively parallel processing computer architectures, in which RSFQ processors, an RSFQ-based crossbar switch core and Josephson transmission line (JTL) interconnects are essential enabling technology components. One million 1 GHz processors are needed to work in parallel, accessing each other and a large semiconductor memory bank (in the order of 30 terabytes) through a very fast central crossbar switch structure. The task of building a computer capable of 10^{15} floating point operations per second (FLOPS) would be virtually impossible without RSFQ technology for, above all, power consumption reasons.

On the long run RSFQ circuits may be the ideal readout and operation circuits for **superconducting quantum computers**. Cooling to liquid Helium temperatures in such cases can be tolerated, since the quantum performance needs such cooling anyway.

5.3.8 Fabrication Technology

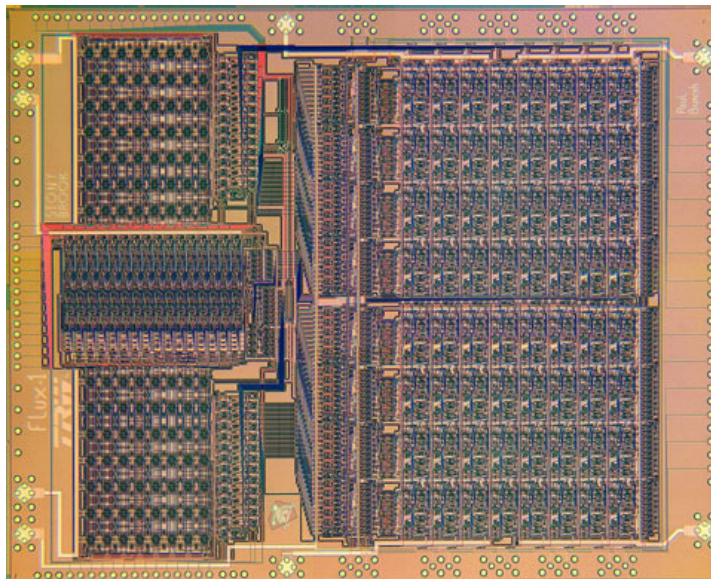


Figure 5.26: First superconducting 20 GHz 8-bit RSFQ microprocessor built in 1.75 μm Nb-technology designed at SUNY Stony Brook and fabricated using TRW's Nb-trilayer technology ("FLUX-1"). The MPU which uses 16 word instruction memory is fabricated from 70,000 Josephson junctions, consumes 14 mW and is designed to operate at 20 – 22 GHz.

As discussed above the delay time of RSFQ gates is proportional to $\sqrt{C/I_c}$. Since for I_c there is a lower bound of about 100 μA due to thermal fluctuation problems, one is trying to increase the critical current density J_c of the Josephson junctions. This allows to reduce the junction area and hence the capacitance at the same I_c value. However, increasing the critical current density to values above 10^4 A/cm^2 requires very thin tunneling barriers and usually results in an increased I_c spread due to problems with pinholes.

Until today RSFQ circuits with a complexity of $> 1\,000$ Nb/AlO_x/Nb junctions have been realized for digital filter and correlator circuits.⁹⁶ A-to-D and D-to-A converters with a complexity of about 2 000

dimensions?, IEEE Trans. Appl. Supercond. **11**, 1050-1055 (2001).

⁹⁶S.V. Polonsky, Proc. of ISEC 1997, H. Koch and S. Knappe (eds.), Vol. **1** (1997) p. 125.

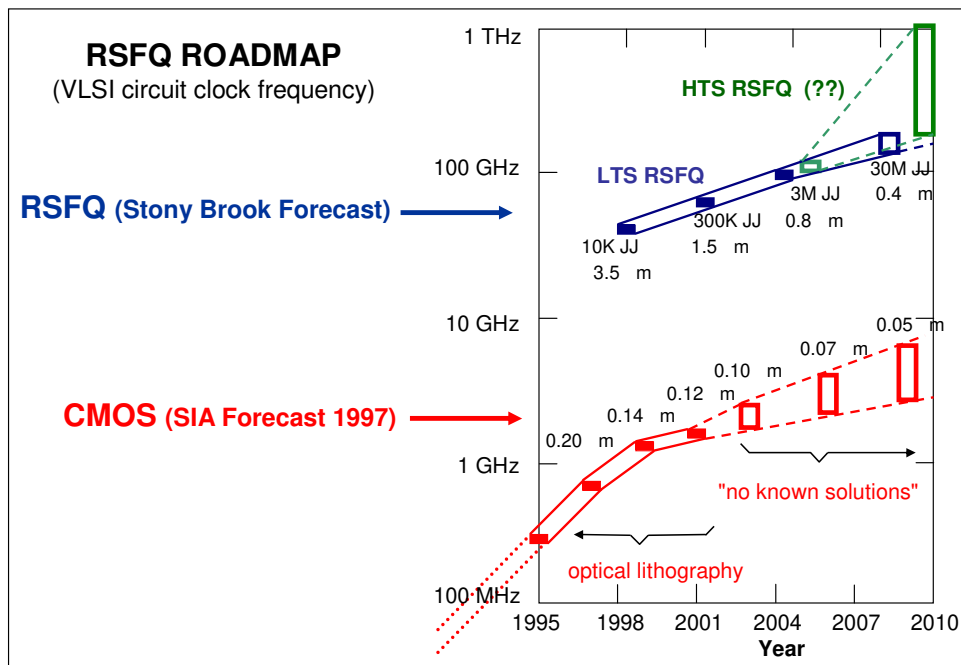


Figure 5.27: Roadmap for RSFQ digital electronics (as projected by K. K. Likharev, SUNY Stony Brook) compared to the SIA forecast for semiconducting CMOS electronics. The numbers below the symbols denote the technology linewidth. The major obstacle for advancing semiconducting electronics above several GHz is the high power dissipation.

junctions have been realized with performance that challenges the best semiconductor converters. One of the most complex RSFQ circuits fabricated so far is an RSFQ microprocessor consisting of about 70 000 Josephson junctions (see Fig. 5.26). Design methods developed for metallic superconductors and cuprate superconductor based RSFQ circuits, for Nb circuits even cell libraries, permit simulations of fairly complex circuits.

Novel developments in the Nb junction technology provide the shunt resistance for the shunting required to overdamp the junction without extra need of chip area thus paving the way for a VLSI integration level.^{97,98} To obtain internally shunted Josephson junctions the use of SNS or SINIS type junctions instead of SIS junctions seems to be advantageous. RSFQ shift registers based on SINIS junction technology already have been fabricated and tested.

5.3.9 RSFQ Roadmap

The projected potential of RSFQ circuits and their eventual superiority over semiconductor devices is illustrated in the roadmap for RSFQ digital electronics in Fig. 5.27 (as projected by K. K. Likharev, SUNY Stony Brook). Note that the major obstacle for advancing semiconductor electronics above several GHz is the high power dissipation.

⁹⁷H. Kohlstedt, Proc. of ISEC 1997, H. Koch and S. Knappe (eds.), Vol. 1, p. 254.

⁹⁸M. Maezawa, A. Shoji, *Overdamped Josephson junctions with Nb/A_xO_y/Al/A_xO_y/Nb structure for integrated circuit application*, Appl. Phys. Lett. **70**, 3603 (1997).

5.4 Analog-to-Digital Converters

Analog-to-Digital Converters (ADCs) are known to have widespread applications in consumer as well as professional electronics such as digital tape recorders, digitizing oscilloscopes, voltmeters, transient recorders etc.. Today, mostly semiconductor ADCs are used. The relentless quest for higher performance of analog-to-digital converters (ADCs) is fundamental to progress in communications, radar, high-speed instrumentation, and sensor applications. For many applications, ADCs are the critical elements that define the architecture and the performance capabilities of the entire system. The present relatively slow progress in ADCs based on conventional silicon technology is no longer capable of matching the current rate of advancements in digital circuits. The ever increasing demand for speed and resolution brought superconducting devices into play. For example, for advanced radar systems 16-bit ADCs with a bandwidth of 10 MHz are required. This performance is very difficult to be achieved with semiconductor ADCs, although these devices are improving steadily. On the other hand, superconductor technology exhibits a set of characteristics uniquely suitable for the implementation of analog-to-digital conversion. It simultaneously includes high switching speed (providing a very short aperture time τ_a and hence a very high speed and resolution for ADCs), low power, natural quantization, quantum accuracy, high sensitivity, and low noise. Superconductor ADCs have already demonstrated superior performance in the laboratory,^{99,100} and are now being developed into high-speed and precision instrumentation and communication systems.¹⁰¹ The first proposals for a Josephson ADC were made by **Klein** and **Zappe** already in the mid 1970s.^{102,103}

Superconducting ADCs are based on the principle of flux quantization in a closed superconducting loop and the fast switching of Josephson junctions.^{104,105} Together, these naturally occurring quantum phenomena set the current circulating around a closed superconducting loop with Josephson junctions to be fundamentally periodic in the analog magnetic flux applied to it. That is, the threshold spacing of a superconductive loop is determined with the accuracy of fundamental constants. This natural relationship of analog and digital forms makes superconductor technology especially suitable for ADC implementation. In a practical device the input signal to be measured (e.g. a current or voltage) is converted into a magnetic flux Φ in the same way as we already have discussed for SQUID sensors in chapter 4 and the corresponding circuit has to determine the integer m satisfying the relation

$$(m-1)\Phi_0 \leq \Phi \leq m\Phi_0 . \quad (5.4.1)$$

In this way the input signal is determined within an accuracy of $\Phi_0/2$. An important fact is that the quantization process relies on a fundamental physical constant and therefore has an inherent precision that is not known for semiconductor devices. Of course there exist various ways to determine the number m and related types of ADCs.

⁹⁹S. B. Kaplan, P. D. Bradley, D. K. Brock, D. Gaidarenko, D. Gupta, W.-Q. Li, and S. V. Rylov, *A superconductor flash digitizer with on-chip memory*, IEEE Trans. Appl. Supercond. **AS-9**, 3020-3025 (1999).

¹⁰⁰O. A. Mukhanov, V. K. Semenov, W. Li, T. V. Filippov, D. Gupta, A. M. Kadin, D. K. Brock, A. F. Kirichenko, Y. A. Polyakov, and I. V. Vernik, *A superconductive high-resolution ADC*, IEEE Trans. Appl. Supercond. **AS-11**, 601-606 (2001).

¹⁰¹O.A. Mukhanov, D. Gupta, A.M. Kadin, V.K. Semenov, *Superconductor Analog-to-Digital Converters*, Proceedings IEEE **92**, 1564-1585 (2004).

¹⁰²M. Klein, *Analog-to-digital converter using Josephson junctions*, in *Digest of Tech. Papers*, Int. Solid-State Circuits Conference, Vol. XX (1977), pp. 202-203.

¹⁰³H.H. Zappe, *Ultrasensitive analog-to-digital converter using Josephson junctions*, IBM Tech. Disclosure Bull. **17**, 3053-3054 (1975).

¹⁰⁴A. M. Kadin, O. A. Mukhanov, *Analog-to-digital converters*, in *Handbook of Superconducting Materials*, D. Cardwell and D. Ginley eds., Institute of Physics, Bristol, UK (2002), pp. 1815-1824.

¹⁰⁵J. X. Przybysz, *Josephson analog-to-digital converters*, in *The New Superconducting Electronics*, H. Weinstock ed., Kluwer, Dordrecht, The Netherland (1992), pp. 329-361.

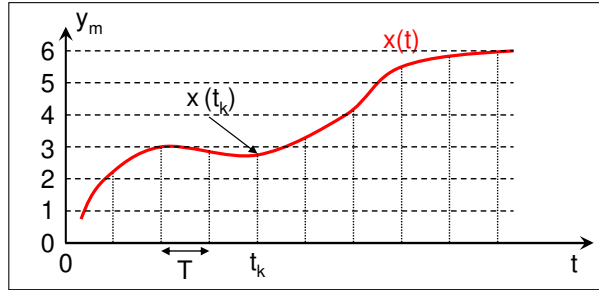


Figure 5.28: Principle of operation of an analog-to-digital converter. The analog signal is sampled at times $t_k = kT$ and the value $x(t_k)$ is mapped onto an integer $y_m = m$.

5.4.1 Additional Topic: Foundations of ADCs

Principle of Operation

An ADC has to convert an analog signal $x(t)$ into a digital signal. The first operation transforms the time-continuous signal $x(t)$ into a time-discrete signal $x_k = x(t_k)$, where t_k are the points in time at which the signal is sampled. Usually the time intervals between two successive sampling processes are equidistant as shown in Fig. 5.28 and we can write $t_k = kT$. Here, k is an integer and T the sampling period. So far the time-discrete signal is still continuous in amplitude and may be represented by a real number. The second operation now transforms this real number into a set of discrete numbers y_m , which most conveniently are represented by a set of integer numbers $y_m = m$. For example, this may be achieved by mapping $x \in [0, 0.5]$ onto $y_0 = 0$, $x \in [0.5, 1.5]$ onto $y_1 = 1$, $x \in [1.5, 2.5]$ onto $y_2 = 2$, and so on. For this particular mapping the spacing between the output bins is just 1. The quantization error ε is the difference between the input and the output signal, i.e. $\varepsilon \in [-0.5, 0.5]$.

For an ADC used for digitizing a voltage signal the output level spacing may be for example $1 \mu\text{V}$. The smallest step in the quantization process is denoted as the **least significant bit (LSB)**. The quantization error may then be equivalently written as $\varepsilon = \pm 0.5 \text{ LSB}$. A graphical representation of the mapping process is sketched in Fig. 5.29.

Resolution

In practice both the range of the input signal x and the number of output values y_m is limited. Furthermore, the number of output values is usually given as a power of 2. If the power is n , the ADC is denoted as an n -bit converter and the integer numbers 0 to $2^n - 1$ are used (the example shown in Fig. 5.29 represents an 3-bit converter). We can now represent an arbitrary integer number within this range as $x = x_0 2^0 + x_1 2^1 + x_2 2^2 + \dots + x_{n-1} 2^{n-1}$, where the coefficient x_0, x_1, x_2, \dots are either 0 or 1. Furthermore, we can scale and offset the input signal in the analog domain so that $x' = ax + b$ (see Fig. 5.29b). If the input signal ranges in the interval $x_{\min} \leq x \leq x_{\max}$ the scaling is used to transform this interval to the range $0 \leq x' \leq 2^n - 1$ and subsequently map this onto the integer numbers 0 to $2^n - 1$. In this way we are taking care about negative signal values.

The resolution of an ADC is given by the number of discrete values it can produce. It is usually expressed in bits. For example, an ADC that encodes an analog input to one of 256 discrete values has a resolution of eight bits, since $2^8 = 256$. If we are digitizing for example a voltage signal, the resolution can also be defined electrically, and expressed in volts. The voltage resolution of an ADC is equal to its overall voltage measurement range divided by the number of discrete values. For example, if the full scale

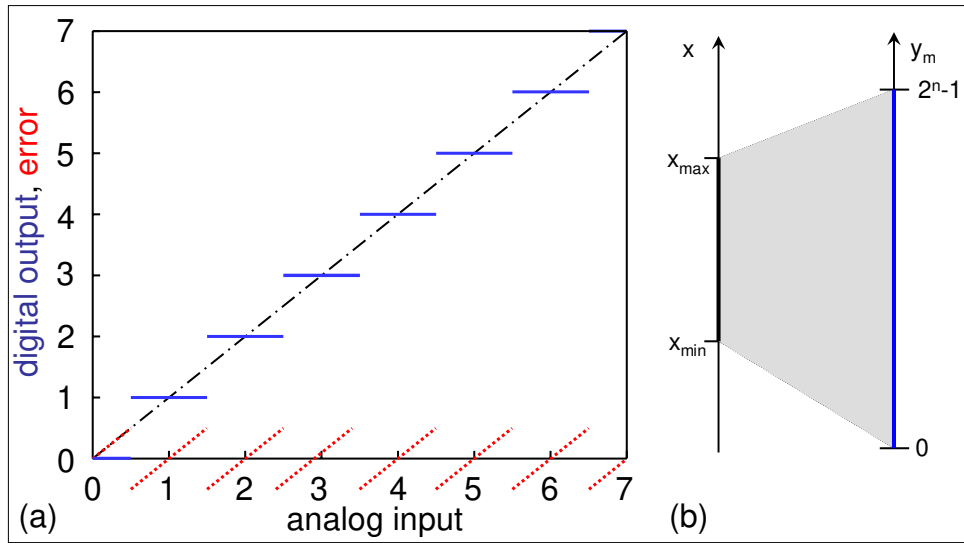


Figure 5.29: (a) Sketch of the analog-to-digital conversion process assuming 8 available output levels. The full lines represent the output signal, the dash-dotted line the input signal, and the dotted line the quantization error. (b) Mapping of the input signal range onto the available range of digits.

measurement range is 0 to 10 V and the ADC resolution is 12 bits ($2^{12} = 4096$ quantization levels), then the ADC voltage resolution is: $(10 - 0)/4096 = 0.00244 \text{ V} = 2.44 \text{ mV}$. If the full scale measurement range is -10 to +10 V and the ADC resolution is 14 bits ($2^{14} = 16384$ quantization levels), then the ADC voltage resolution is: $[10 - (-10)]/16384 = 20/16384 = 0.00122 \text{ V} = 1.22 \text{ mV}$.

The resolution of the ADC may be limited by the signal-to-noise ratio of the signal in question. If there is too much noise present in the analog input, it will be impossible to accurately resolve beyond a certain number of bits of resolution, the so-called **effective number of bits (ENOB)**. While the ADC will produce a result, the result is not accurate, since its lower bits are simply measuring noise. The S/N ratio should be $20 \log_{10} 2 = 6.02 \text{ dB}$ per bit of resolution required.

Accuracy

Accuracy depends on the error in the conversion. This error is measured in a unit called the LSB. For example, for a 8 bit ADC, an error of one LSB is 1/256 of the full signal range, or about 0.4%. The quantization error is due to the finite resolution of the ADC, and is an unavoidable imperfection in all types of ADC. The magnitude of the quantization error at the sampling instant is between zero and half of one LSB.

The instances t_i of the sampling process are determined by the sampling period T . In the general case, the original signal is much larger than one LSB. When this happens, the quantization error is not correlated with the signal, and has a uniform distribution. Then, the quantization error can be treated as white noise.

Its root mean square (rms) value is the standard deviation of this distribution, given by¹⁰⁶

$$\varepsilon_{\text{rms}} = \frac{1}{\sqrt{12}} \text{LSB} \simeq 0.289 \text{ LSB} . \quad (5.4.2)$$

Signal-to-Noise Ratio: For an n -bit converter the peak-to-peak amplitude is $A_{\text{pp}} = 2^n - 1$. If we assume a sinusoidal input signal, then the rms value of its amplitude is given by $A_{\text{rms}} = A_{\text{pp}}/2\sqrt{2}$. The signal to noise ratio (SNR) for an ADC is defined as the so-called dynamic range of the ADC and is equal to $A_{\text{rms}}/\varepsilon_{\text{rms}}$. Usually, the SNR is expressed in decibels. For $n > 5$, we can use $2^n - 1 \simeq 2^n$ and obtain

$$\text{SNR}_{\text{ADC}}(\text{dB}) = 20 \log_{10} \left(\frac{A_{\text{rms}}}{\varepsilon_{\text{rms}}} \right) \simeq 20 \log_{10} \left(2^n \sqrt{3/2} \right) = 6.02 n + 1.76 . \quad (5.4.3)$$

Putting in some numbers we obtain a dynamic range of 98.1 dB for a 16-bit ADC, which is often used in consumer electronics such as compact-disc players. Of course, besides the quantization error there may be additional errors arising from the analog part of the converter (inaccuracy of the scaling constants a and b).

Sampling Rate

The analog signal is continuous in time and it is necessary to convert this to a flow of digital values. It is therefore required to define the rate at which new digital values are sampled from the analog signal. The rate of new values is called the *sampling rate* or *sampling frequency* of the ADC. A continuously varying bandlimited signal $x(t)$ can be sampled. That is, the signal values at intervals of time T (the sampling time) are measured and stored. Then, the original signal can be exactly reproduced from the discrete-time values by an interpolation formula. The accuracy is, however, limited by quantization errors. The successful reproduction is only possible if the sampling rate is higher than twice the highest frequency of the signal. This is essentially what is embodied in the *Shannon-Nyquist sampling theorem*¹⁰⁷ also known as

¹⁰⁶The quantization noise $\varepsilon(n)$ is treated as a random variable in the interval $[-q/2, +q/2]$. It therefore has the probability density function $p_\varepsilon(x) = 1/q$ for $|x| \leq q/2$ and $p_\varepsilon(x) = 0$ for $|x| > q/2$. Thus, the probability that a given roundoff error $\varepsilon(n)$ lies in the interval $[x_1, x_2]$ is given by

$$\int_{x_1}^{x_2} p_\varepsilon(x) dx = \frac{x_2 - x_1}{q}$$

with x_1 and $x_2 \in [-q/2, +q/2]$. We can now calculate the variance of the random variable $\varepsilon(n)$ which we assume to be uniformly distributed on $[-q/2, +q/2]$. We obtain

$$\sigma_\varepsilon^2 = \int_{-q/2}^{q/2} x^2 \frac{1}{q} dx = \frac{1}{q} \frac{x^3}{3} \Big|_{-q/2}^{q/2} = \frac{q^2}{12} .$$

Since in our case $q = 1$ we obtain the variance $1/12$. For sampled processes the sample variance is proportional to the average power in the signal. Finally, the square root of the sample variance (the rms level) is sometimes called the standard deviation of the signal. However, this notation is only correct if the random variable has a Gaussian probability density function.

¹⁰⁷The WKS theorem was formulated by Claude Elwood Shannon in 1948 as the starting point for his theory on the maximum bit rate in a frequency limited transmission channel. He was using results of Harry Nyquist (1928) on the transmission of number series by trigonometric polynomials and the theory of the cardinal functions by Edmund Taylor Whittaker (1915) and his son John Macnaughten Whittaker (1929). Independently, the sampling theorem was introduced by the Russian scientist Vladimir Alexandrovitsch Kotelnikow in 1933. However, this was noticed in the western literature only in the 1950s. The sampling theorem says that a continuous signal with minimum frequency 0 and maximum frequency f_{max} has to be sampled by a frequency larger than $f_{\text{sam}} > 2f_{\text{max}}$ in order to be reconstructed from the time-discrete signal without loss of information. The Nyquist-Shannon sampling theorem is relevant for digitizing. The characteristic frequency $f_N = \frac{1}{2}f_{\text{sam}}$ is denoted as the Nyquist frequency.

Nyquist-Shannon-Kotelnikov, Whittaker-Shannon-Kotelnikov, Whittaker-Nyquist-Kotelnikov-Shannon, WKS, etc.^{108,109,110,111}

As the input signal $x(t)$ varies in time, a sample of it is taken at a certain moment t_s . However, in practice the sampling process takes a finite amount of time given by the so-called aperture time t_a or acquisition time for sample & hold. This aperture time has to incorporate the aperture times of the different comparators as well as of the spread in sampling times. In practice, an input circuit called a sample and hold performs this task (in most cases by using a capacitor to store the analog voltage at the input, and using an electronic switch or gate to disconnect the capacitor from the input). Many ADC integrated circuits include the sample and hold subsystem internally.

Obviously, if the input signal changes by more than one LSB during the aperture time, the error in the conversion process would exceed the resolution of the ADC. In order to avoid this we directly obtain an upper limit for the bandwidth of the ADC, which is directly related to the aperture time. For a harmonic signal $S = \sin 2\pi f t$ with frequency f and amplitude 1 the maximum slew rate is $2\pi f \cos 2\pi f t = 2\pi f$. The analog signal needs the minimum time $1/(2^n - 1)\pi f$ to slew by an amount equal to the LSB.¹¹² This time must be larger than the aperture time. Hence, the frequency of the input signal must satisfy the condition

$$f \leq f_B = \frac{1}{(2^n - 1) \pi t_a} \quad (5.4.4)$$

to ensure that the error does not exceed ± 0.5 LSB. Here, f_B is the input bandwidth of the ADC. Expression (5.4.4) immediately shows that the product $2^n f_B \simeq 1/t_a$, that is, the aperture time is limiting the performance of the ADC. If we want to increase the bit resolution, we have to reduce the bandwidth and vice versa. We also see that the performance of an ADC is the better the shorter the aperture time.

We note that even in the case of zero aperture time, errors may arise if the input bandwidth is too high. If the signal with frequency f is sampled at a frequency f_{sam} , mixing products at $f_{\text{sam}} \pm f$, $2f_{\text{sam}} \pm f$, etc. appear in the output spectrum. Therefore, the input bandwidth f_B is not allowed to exceed $f_{\text{sam}}/2$. If a signal is sampled at twice the input bandwidth we say that it is sampled at the *Nyquist rate* $f_{\text{sam}} = 2f_N = 2f_B$.¹¹³

We can summarize our discussion by stating that there are two distinct aspects of the analog-to-digital conversion process: *sampling* and *quantization*, which deal with discretization in time and in magnitude,

¹⁰⁸Claude Elwood Shannon, *Communication in the Presence of Noise*, Proc. IRE, Vol. **37**, No. 1 (1949), see also Proc. IEEE, Vol. **86**, No. 2, (1998).

¹⁰⁹J. M. Whittaker, *The Fourier theory of the cardinal functions*, Proc. Edinburgh Math. Soc. **1** (1929).

¹¹⁰V. A. Kotelnikow *On the transmission capacity of ether and wire in electrocommunications*, Izd. Red. Upr. Svyazzi RKKA (1933).

¹¹¹Harry Nyquist, *Certain Topics in Telegraph Transmission Theory*, Trans. Amer. Inst. Elect. Eng. **47**, 617-644 (1928); see also Proc. IEEE, Vol. **90**, No. 2 (2002).

¹¹²Here we have taken into account that the peak-to-peak amplitude of a harmonic signal with amplitude 1 is just 2.

¹¹³The Nyquist frequency f_N is half the sampling frequency for a signal. It is sometimes called the critical frequency. The sampling theorem tells us that aliasing can be avoided if the Nyquist frequency is at least as large as the bandwidth of the signal being sampled (or the maximum frequency, if the signal is a baseband signal).

In principle, a Nyquist frequency equal to the signal bandwidth is sufficient to allow perfect reconstruction of the signal from the samples. However, this reconstruction requires an unrealizable filter that passes some frequencies unchanged while suppressing all others completely. When realizable filters are used, oversampling is necessary to accommodate the practical constraints on anti-aliasing filters. Even with oversampling, the Nyquist frequency is half the sampling frequency.

For example, audio CDs have a sampling frequency of 44,100 Hz. The Nyquist frequency is therefore 22 050 Hz, which represents the highest frequency the data can produce (again if the anti-aliasing filter is perfect). For example, if the chosen anti-aliasing filter (a low-pass filter in this case) has a transition band of 2 000 Hz then the cut-off frequency should be at 20 050 Hz to yield a signal with no power at frequencies of 22 050 Hz and greater. Again, because realizable filters are not perfect, the frequencies greater than 22 050 will still have power except the aliasing they will produce is minimal.

respectively. The quantization process introduces some error or “quantization noise” into the system. Of course, this is in addition to any noise present in the signal, as well as other noise sources, such as jitter in the sampling clock. Even if the quantization is precise, the clock frequency will limit the bandwidth of a signal in the digital domain. According to the Nyquist sampling theorem, a signal that is sampled at a frequency can accurately represent an analog signal with bandwidth up to the Nyquist frequency $f_N = f_{\text{sam}}/2$.

Aliasing

All ADCs work by sampling their input at discrete intervals of time. Their output is therefore an incomplete picture of the input signal. By looking at the output, there is no way of knowing what the input was doing between one sampling instant and the next. If the input is known to be changing slowly compared to the sampling rate, then it can be assumed that the value of the signal between two sample instants was somewhere between the two sampled values. If, however, the input signal is changing fast compared to the sample rate, then this assumption is no longer valid.

If the digital values produced by the ADC are, at some later stage in the system, converted back to analog values, it is desirable that the output of the digital to analog converter (DAC) is a faithful representation of the original signal. If the input signal is changing much faster than the sample rate, then this will not be the case, and spurious signals called *aliases* will be produced at the output of the DAC. The frequency of the aliased signal is the difference between the signal frequency and the sampling rate. For example, a 10 kHz sinewave being sampled at 9 kHz would be reconstructed as a 1 kHz sinewave. This problem is called aliasing. To avoid aliasing, the input to an ADC must be low-pass filtered to remove frequencies above half the sampling rate. This filter is called an *anti-aliasing filter*.

Oversampling

The fabrication of ADCs with a large number of bits requires high precision components in order to define the transition points between the bits in an adequate way. Therefore, a variety of clever tricks to reduce the number of high precision components and thereby the costs have been developed.¹¹⁴ We only briefly address the oversampling technique.

The term oversampling is used, if the sampling rate is larger than the Nyquist rate f_N . The oversampling rate is defined as

$$\text{OSR} = \frac{f_{\text{sam}}}{f_N}. \quad (5.4.5)$$

For example, if an audio signal of 20 kHz bandwidth is sampled at a rate of 160 kHz we have with $f_N = 2f_B$ an OSR of four. The obvious advantage is that one can significantly reduce the requirement for the anti-alias filter leading to a significant cost reduction.

A further advantage is the reduction of quantization noise within the input bandwidth. Usually, signals are sampled at the minimum rate required, for economy, with the result that the quantization noise introduced is white noise spread over the whole pass band of the converter. If a signal is sampled at a rate much higher than the Nyquist frequency and then digitally filtered to limit it to the signal bandwidth, the signal-to-noise ratio due to quantization noise will be lower than in the case where the whole available band had been used. With this technique, it is possible to obtain an effective resolution larger than that provided by the converter alone by randomizing the quantization noise over a larger bandwidth. The

¹¹⁴D.F. Hoeschele, *Analog-to-digital and digital-to-analog conversion techniques*, Wiley, New York (1994).

power $\varepsilon_{\text{rms}}^2$ of the quantization noise is now spread over the bandwidth $f_{\text{sam}}/2$ instead of only f_B . This leads to a reduction of a factor $\sqrt{\text{OSR}}$ in the quantization noise of the ADC and the SNR is increased by $10\log(\text{OSR})$ dB. At 4-times oversampling this leads to an improvement of 6.02 dB or equivalently we gain an extra bit of dynamic range. An interesting aspect is to use a one-bit converter to arrive at a dynamic range of 16 bit. The advantage of a one-bit ADC would be that it is highly linear and hardly requires any costly components. The only penalty we have to pay is the increase of the sampling rate, the complexity of the digital part and processing speed. For example, digital filtering is required to remove the noise not lying in the input bandwidth. Of course, the physics behind oversampling is just signal averaging. If for example the sampling frequency is 16 times the Nyquist frequency, one can measure 16 times as often in the same time window. This improves the SNR by $16/\sqrt{16} = 4$ and one gains two bits in dynamic range.

5.4.2 The Comparator

A key element of any ADC is the comparator, which compares the analog input signal to some reference signal. If the input signal is smaller than the reference signal it generates a “0”, if it is larger than the reference signal, it generates a “1”. The reference signal value is set just at one of the transition points $x = 0.5, 1.5, 2.5, \dots$ (see Fig. 5.29). It is evident that there is some uncertainty in the comparison process just around the transition point due to noise. That is, in a small interval around the reference signal level the output is undetermined. This sets a lower bound for the resolution of the ADC, since two neighboring quantization levels can no longer be distinguished if they are too close.

Semiconductor Comparator

A semiconductor comparator is nothing else than a high gain amplifier with a clipped output (cf. Fig. 5.30a). If the input signal is larger or smaller than the reference signal, the small difference is amplified by such a high factor that the resulting output signal effectively is given by the clipped low or high level signal.

Superconductor Comparator

In a superconductor comparator flux quantization in a superconducting loop is used. In the one-junction comparator shown in Fig. 5.30b the input signal is compared to the maximum supercurrent I_s^m of a circuit consisting of a superconducting loop with inductance L and a quantizer Josephson junction J_Q with critical current I_c . If the input signal is smaller than the maximum supercurrent I_s^m , the circuit stays in the superconducting state and the output signal is zero. In this case most of the current is flowing across the junction and not the inductor, since this would generate too much flux and result in a lower I_s^m . This state can be represented by an equal current through the junction and the inductor plus a clockwise circulating current I_{circ} . If in contrast the input signal is increased above I_s^m , the junction will switch into the voltage state. A flux quantum enters the loop and a SFQ voltage pulse is generated at the output due to the 2π phase slip of the quantizer junction. As a result of the counter-clockwise circulating current associated with the trapped flux quantum the effective current across the junction is reduced below I_s^m again and the circuit again resides in the superconducting state. That is, the circuit generates a single SFQ voltage pulse of height $I_c R_N$ and duration $\Phi_0/I_c R_N$ at the output, if the signal current exceeds the reference value. Increasing the current further, the next flux quantum will enter at the next threshold value resulting in a further SFQ pulse. If the output pulses are fed into a counter, a so-called counting ADC is achieved. Here, an additional output pulse corresponds to a change by a discrete amount in the analog signal.

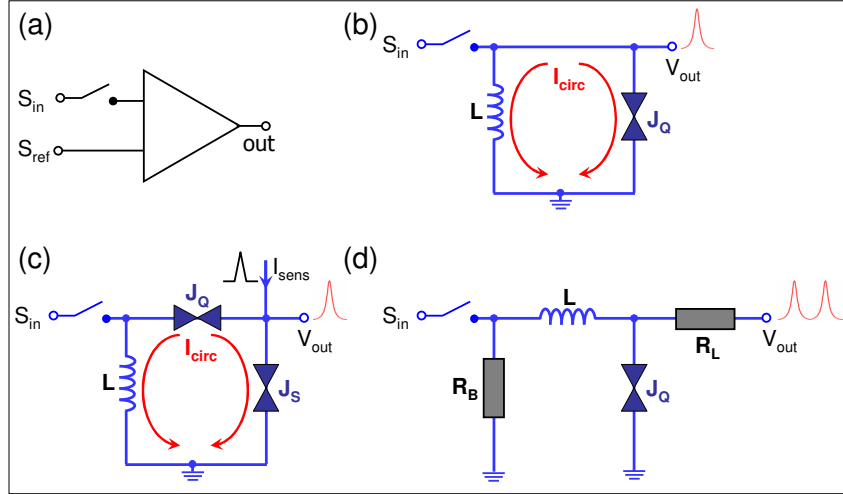


Figure 5.30: (a) Semiconductor comparator. (b) Superconducting one-junction SQUID comparator. Depending on the flux state of the loop the circulating current is clockwise or counterclockwise. (c) Superconducting quasi-one-junction SQUID comparator (QOS). (d) Voltage to frequency quantizer.

Instead of the output SFQ pulses, the direction of the circulating loop current I_{circ} may be sensed. In order to do so an extra sense junction J_S is introduced as shown in Fig. 5.30c. In this way a quasi-one-junction SQUID (QOS) may be obtained.¹¹⁵ The critical current of the sense junction must be larger than that of the quantizer junction, since it should not switch if the input signal is applied. The direction of the loop current is sensed by applying a sensing current pulse I_{sens} to the circuit. If $I_{\text{sens}} + I_{\text{circ}} > I_{c,S}$, a SFQ voltage pulse is generated at the output. For $I_{\text{sens}} + I_{\text{circ}} < I_{c,S}$ nothing happens. That is, the presence or absence of an output voltage pulse indicates whether the circulating current is clockwise or anti-clockwise. Note that the use of a sense junction is a prerequisite if the circuit is used in a parallel converter scheme. Here, the status of several comparators has to be sensed at exactly the same time. The simple one-junction comparator does not satisfy this condition, since the output pulse is generated as soon as the input signal exceeds the reference signal. In the QOS the result is stored in the loop and then asked for by the sensing current pulse at some specific time.

A further type of counting ADC can be realized by the quantizer circuit shown in Fig. 5.30d. The circuit is used to generate discrete voltage pulses in response to an input signal. In contrast to the circuit of Fig. 5.30b, now a train of pulses is generated at a rate proportional to the signal amplitude. We already have seen that a voltage biased Josephson junction acts as a voltage controlled oscillator with $V/f = 483.6 \text{ MHz}/\mu\text{V}$. Because the Josephson junction has a low impedance, it needs a bias resistor R_B of the order of $\text{m}\Omega$ in order for the analog signal to voltage bias the junction. The inductance L is required to block the produced pulses from draining into R_B . Instead the pulses pass to the counter through the resistance R_L which damps the junction ($\beta_C < 1$). The ADC is capable to measure a dc voltage. The resolution increases with increasing counting time. However, the accuracy cannot be increased arbitrarily due to the finite linewidth of the Josephson frequency. With the thermal voltage noise $S_V = \delta V^2/\Delta f = 4k_B T R_B$ of the small bias resistor and the 2. Josephson equation ($f = 2eV/h$ or $\Delta f = 2e\delta V/h$) the limit of the linewidth is obtained to

$$\Delta f = \left(\frac{2e}{h} \right)^2 4k_B T R_B . \quad (5.4.6)$$

For $R_B = 1 \text{ m}\Omega$ we obtain $\Delta f \sim 100 \text{ kHz}$ at 4 K. The maximum bit accuracy is then $\log_2(F/\Delta f)$, where F is the maximum counting rate. For $F = 50 \text{ GHz}$ we would obtain a bit accuracy of about 16 bit. We note

¹¹⁵H. Ko, T. Van Duzer, A new high speed periodic threshold comparator for use in a Josephson ADC, IEEE J. Solid-State Circuits **23**, 1017-1021 (1988).

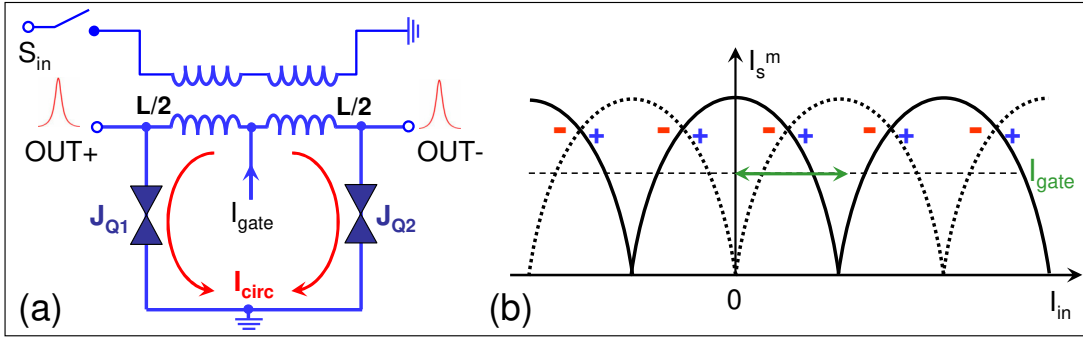


Figure 5.31: (a) Circuit diagram of an incremental quantizer. (b) Threshold characteristic of the incremental quantizer. Whenever the input signal I_{in} increases sufficiently to cross the right-hand side of a mode boundary, the phase of J_{Q2} changes by 2π and a SFQ pulse is sent out at OUT-. In the same way, whenever I_{in} decreases sufficiently to cross the left-hand side of a mode boundary, the phase of J_{Q1} changes by 2π and a SFQ pulse is sent out at OUT+.

that the V/f type counting ADC has an extreme nonlinearity close to $V = 0$ due to the strong nonlinearity of the IVC of an overdamped Josephson junction.

One also can implement an incremental comparator by the circuit shown in Fig. 5.31. If the analog signal increases or decreases, the threshold characteristic is crossed in the one or the other direction to a different flux state. This is equivalent to flux quanta entering or leaving the superconducting loop via the quantizer Josephson junctions J_{Q+} and J_{Q-} resulting in SFQ voltage pulses at the outputs OUT+ and OUT-, respectively. One can now use different counters for the two outputs and can determine the incremental change of the input signal in the one or the other direction from the counting rates. The incremental ADC theoretically has a very high linearity, although in practice the linearity will be limited by stray magnetic flux suppressing the critical current of the junctions.

5.4.3 The Aperture Time

We already have mentioned that a particular advantage of Josephson junction based ADCs is the very fast switching speed of Josephson junctions. The width of the SFQ pulse is $\Phi_0/I_c R_N \sim 2$ ps for an $I_c R_N$ product of 1 mV, which is in principle achievable e.g. for junctions based on Nb technology. From this we could conclude that for Josephson junction based ADC a bandwidth well above 100 GHz should be possible.

In general the speed and accuracy of any ADC is given by its aperture time

$$t_a = \frac{1}{(2^n - 1) \pi f_B} . \quad (5.4.7)$$

With the optimum estimate that t_a is set by the switching time of a Josephson junction (~ 2 ps) it would be possible to obtain a bandwidth of more than 1 MHz for a 16 bit ADC. Unfortunately, there are other limitations reducing the performance of Josephson junction based ADCs below this fantastic value. However, superconducting ADCs have at least exceeded the performance of the best semiconductor ADCs with further improvement anticipated.^{116,117} For example, in an effort to realize a true software-defined radio recently ultra-high-performance superconducting ADCs have been developed that directly convert

¹¹⁶T. Van Duzer, *Superconductor Electronics*, IEEE Trans. Appl. Supercond. **7**, 98 (1997).

¹¹⁷T. Van Duzer, *Digital Signal Processing*, in *Superconducting Devices*, S.T. Ruggiero, D.A. Rudman eds., Academic Press Inc., San Diego (1990).

RF signals from the antenna to digital baseband with an exceptionally high signal-to-noise ratio (SNR) and spurious-free dynamic range (SFDR). The expected performance is 14 to 16 effective bits with an SFDR of over 100 dB and an SNR of 90 dB at 14 bits.

At present the fast switching speed of Josephson junctions cannot be fully used due to several technical hurdles. Firstly, since the junctions are embedded into complex circuits, the actual switching speed of the junction may be larger due to parasitic capacitances and inductances. Secondly, the SFQ pulses do not arrive exactly at the intended moment. This is obvious, if several comparators have to work in parallel and not all sampling pulses arrive simultaneously or not all output pulses will be available at the same time. Another effect that limits the bandwidth is the dynamic hysteresis of the comparator. These hysteresis effects result from the charging and discharging of capacitors and inductors. Note that we have not shown the junction capacitance and parasitic capacitances in Figs. 5.30 and 5.31.

5.4.4 Different Types of ADCs

All superconductor ADCs generally fall into two categories: Nyquist-sampling ADCs and oversampling ADCs. An ideal Nyquist ADC samples a bandwidth-limited signal at a sampling rate $f_{\text{sam}} = 2f_N$ and provides an accurate digital representation of that signal, with the only error associated with the quantization noise. Most commonly, this Nyquist ADC is composed of a large number of separate quantizers (single-bit comparators), each defining a single quantization level. In practice, the performance of such an ADC is limited by the precision of the quantization levels, which are often determined by resistor values in resistor networks.

In the alternative oversampling ADC approach, the signal is sampled at a frequency $f_{\text{sam}} \gg 2f_N$ using a single quantizer. Then feedback techniques and digital filtering are used to decrease the quantization noise and enhance the effective dynamic range. Oversampling ADCs are built using a “delta” or more often a “delta- Σ ” modulator (sometimes called “sigma-delta”).¹¹⁸ Here, Δ refers to difference and Σ to sum, the discrete analogues of differentiation and integration.

Superconducting Nyquist ADCs: Flash Converters

A well-known representative of Nyquist ADCs is the flash converter (see Fig. 5.32). A flash ADC has a comparator that fires for each decoded voltage range. The comparator bank feeds a logic circuit that generates a code for each voltage range. Direct conversion is very fast, but usually has only small number of bits. For example, 8 bits of resolution requires 256 comparators and hence a large, expensive circuit.

We note, however, that a superconductor flash ADC based on SQUID comparators provides a unique solution for a strong reduction of circuit complexity and, at the same time, allows faster sampling. Utilizing the periodicity of a SQUID’s transfer characteristics in units of Φ_0 , an n -bit superconductor flash ADC uses only n clocked SQUID comparators.¹¹⁹

Fig. 5.32 shows the schematic of a flash ADC. The input signal is successively divided by factors of two and applied to a set of identical comparators, each with periodic thresholds. The output of the first comparator is the most significant bit (MSB) and that of the last comparator is the least significant bit (LSB). In an n -bit ADC, the first comparator gets $2^n - 1$ times the current applied to the last comparator. As the input signal increases, each comparator goes through multiple thresholds.

¹¹⁸S. R. Norsworthy, R. Schreier, and G. C. Temes, *Delta- Σ Data Converters: Theory, Design, and Simulation*, IEEE, New York (1997).

¹¹⁹P. Bradley and H. Dang, *Design and testing of quasi-one junction SQUID-based comparators at low and high speed for superconductor flash A/D converters*, IEEE Trans. Appl. Supercond. **AS-1**, 134-139 (1991).

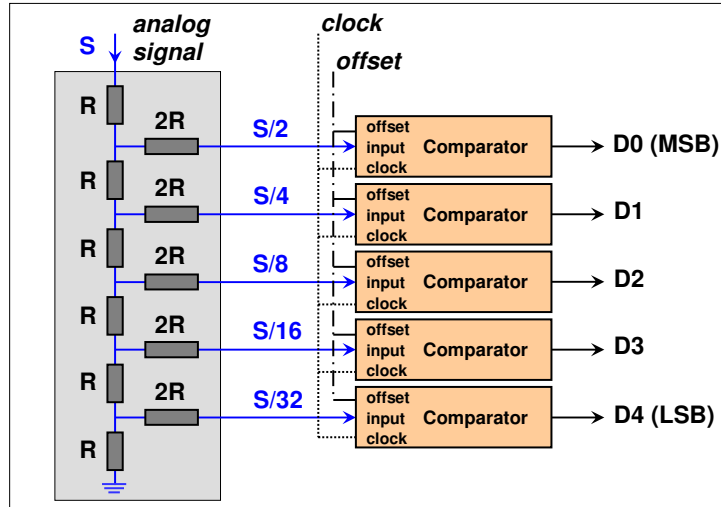


Figure 5.32: Schematic diagram of a 5 bit flash ADC with $n = 5$ SQUID comparators. The $R/2R$ resistor ladder serves for dividing the signal.

Like all multi-comparator ADCs, the superconductor flash ADC is susceptible to mismatched circuit components and other problems such as the resistor ladder, delays in clock and signal paths, and in differences in local magnetic environment. Component mismatches depend on the quality of the IC fabrication process. For correct operation, the analog signal and the sampling clock must be applied simultaneously at each comparator, requiring precise transmission line designs on the signal and clock paths as they travel from the LSB comparator to the MSB comparator. Otherwise, the aperture time would strongly increase resulting in a reduction in the input bandwidth. This can limit the number of bits for a high-speed flash ADC. Based on Nb/AlO_x/Nb junctions 6 bit flash-type ADCs have been fabricated and an effective 4 bit resolution has been demonstrated at 5 GHz.¹²⁰ Furthermore, 3 effective bits at 20 GHz have been experimentally demonstrated for junctions with $J_c = 2.5 \text{ kA/cm}^2$.¹²¹

Counting Converters

Historically, the first Josephson ADCs^{122,123} were based on the voltage-to-frequency (V/f) conversion utilizing the ac Josephson effect. In this type of ADC, the processes of quantization and sampling are separated. A single Josephson junction acts as a voltage-controlled oscillator (VCO) and produces an SFQ pulse train at a rate proportional to the applied analog voltage as $f = V/\Phi_0$. This is a process of signal magnitude quantization. As shown in Fig. 5.30d, a very small shunt resistor R_B converts input current to a voltage bias across the junction. It is worth noting that there is an inductance (often omitted in diagrams) between the junction and the resistor which prevents the generated SFQ pulses from being shunted. This inductor also forms a SQUID loop (a resistive single-junction interferometer) allowing the realization of implicit feedback and integration functions. The signal sampling process is performed by counting the number of generated SFQ pulses over a time interval (cf. Fig. 5.33), which is controlled by a sampling gate. Overall, this analog-to-digital conversion is equivalent to a low-pass first-order

¹²⁰P. Bradley, A 6 bit Josephson flash A/D converter with GHz input bandwidth, IEEE Trans. Appl. Supercond. **AS-3**, 2550-2557 (1993).

¹²¹S. B. Kaplan, P. D. Bradley, D. K. Brock, D. Gaidarenko, D. Gupta, W.-Q. Li, and S. V. Rylov, A superconductor flash digitizer with on-chip memory, IEEE Trans. Appl. Supercond. **AS-9**, 3020-3025 (1999).

¹²²J. P. Hurrell, D. C. Pridmore-Brown, and A. H. Silver, A/D conversion with unlatched SQUID's, IEEE Trans. Electron Devices **27**, 1887-1896 (1980).

¹²³C. A. Hamilton and F. L. Lloyd, 100 GHz binary counter based on dc SQUIDs, IEEE Electron Device Lett. **3**, 335-338 (1982).

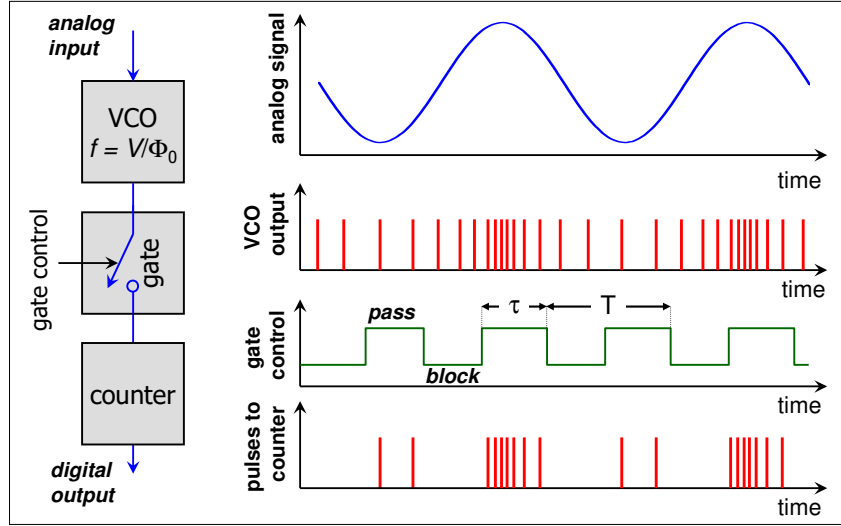


Figure 5.33: Block diagram, input signal, SFQ pulse output of voltage-to-frequency converter (VCO), gate control signals with counting and sampling time intervals (τ and T) controlled by a fast RSFQ logic gate, and resulting SFQ pulses sent to ripple counter (according to M. W. Johnson *et al.*, IEEE Trans. Appl. Supercond. **AS-11**, 607-611 (2001)).

sigma-Delta modulation. The pulse counting process is done using toggle flip-flops forming a ripple counter, which are the fastest elements in RSFQ technology. As a result, the digitized voltage averaged over the sampling period is read out from the counter.¹²⁴ In order to avoid strong nonlinearities of such a VCO at low input signal, it is necessary to operate the VCO at some input offset. This offset also helps to accommodate positive and negative signals.

In order to increase the sensitivity of the V/f counting-type ADC, one can replace the quantizer junction in Fig. 5.30d by a dc SQUID with a sensitive input transformer biased into the voltage state as a pulse generator.^{125,126} This transformer magnetically couples the input signal current (or flux) to a SQUID, which is biased above its critical current. The resultant flux in the SQUID loop produces modulation of the SQUID voltage. Once again, the SQUID produces an SFQ pulse stream, at a frequency that is exactly proportional to the voltage.

In another counting ADC design (flux quantizing or tracking ADC design) the input signal current is coupled into a SQUID loop, which generates one SFQ pulse for each change in flux. Similarly to the V/f ADC, these SFQ pulses can be counted using superconductor digital circuits to reconstruct the signal. This scheme can also be extended to obtain an incremental counting ADC as shown in Fig. 5.31.

Delta and Sigma-Delta Converters

A so-called delta-encoded ADC has an up-down counter that feeds a digital to analog converter (DAC). The input signal and the DAC both go to a comparator. The comparator controls the counter. The circuit uses negative feedback from the comparator to adjust the counter until the DAC's output is close enough to the input signal. The number is read from the counter. Delta converters have very wide ranges, and high resolution, but the conversion time is dependent on the input signal level.

¹²⁴ A. Iwata, N. Sakimura, M. Nagata, and T. Morie, *An architecture of delta sigma A-to-D converters using a voltage controlled oscillator as a multi-bit quantizer*, in Proc. IEEE Int. Symp. Circuits and Systems **1** 389-392 (1998).

¹²⁵ O. A. Mukhanov, S. Sarwana, D. Gupta, A. F. Kirichenko, and S. V. Rylov, *Rapid single flux quantum technology for SQUID applications*, Physica C **368**, 196-202 (2002).

¹²⁶ S. Sarwana, D. Gupta, A. Kirichenko, T. Oku, C. Otani, H. Sato, and H. Shimizu, *High-sensitivity high-resolution dual-function signal and time digitizer*, Appl. Phys. Lett. **80**, 2023-2025 (2002).

A Sigma-Delta ADC oversamples the desired signal by a large factor and filters the desired signal band. Generally a smaller number of bits than required are converted using a flash ADC after the filter. The resulting signal, along with the error generated by the discrete levels of the flash ADC is fed back and subtracted from the input to the filter. This negative feedback has the effect of noise shaping the error due to the flash ADC so that it does not appear in the desired signal frequencies. A digital filter (decimation filter) follows the ADC which reduces the sampling rate, filters off unwanted noise signal and increases the resolution of the output. Both superconducting delta and sigma-delta ADCs have been successfully implemented.¹²⁷

¹²⁷O.A. Mukhanov, D. Gupta, A.M. Kadin, V.K. Semenov, *Superconductor Analog-to-Digital Converters*, Proceedings IEEE **92**, 1564-1585 (2004).

Chapter 6

The Josephson Voltage Standard

The realization of Josephson voltage standard is one of the successful applications of the Josephson effect. It is based on the voltage-frequency relation $V = \frac{h}{2e}f = \Phi_0 f$. Therefore, defining the unit 1 V on the basis of the Josephson effect reduces the calibration of a voltage to the determination of a frequency and the knowledge of the ratio $h/2e$ of the Plank's constant and twice the elementary charge. Since the frequency can be determined with extreme accuracy by the standard of an atomic caesium clock, only a convention for the value of $\Phi_0 = h/2e$ is needed to obtain a very good reproducibility of the voltage calibration. Based on this idea the development of a Josephson voltage standard was started already in the 1970s. After overcoming some technical difficulties the Josephson effect based voltage standards are used as primary standards in the national calibration laboratories since 1990. Meanwhile even industrial companies are using these standards. Since the Josephson voltage standards have no competitors in semiconductor electronics, they represent a successful application of the Josephson effect.

6.1 Voltage Standards

6.1.1 Standard Cells and Electrical Standards

For a long period electrochemical cells were used for establishing reference voltages. Initially, these cells were mainly used to provide reliable sources of electrical current. For example, following the ideas of **Galvani**,¹ **Volta** built the first practical electrochemical cell in 1794. These cells had been the only reliable sources for electrical current for more than 50 years.²

Only after the introduction of the **Zn-Cu Daniell cell** in 1836,^{3,4} electrochemical cells were used as stable voltage sources for maintaining and disseminating the unit volt. There was a large effort in the late 19th and the early 20th century to establish a standard for electromotive force (emf) based on electrochemical reactions within chemical cells. For example, the first legal unit of voltage for the United States was based on the **Zn-Hg Clark cell**, developed by **Latimer Clark** in 1872, with its output assigned a value of 1.434 international volts by the 1893 International Electric Congress. Public Law 105, passed by the U.S. Congress in 1894, made this the legal standard of voltage in the U.S. During the years between 1893 and 1905, the standard cell devised by **Edward Weston**⁵ ($\text{Cd}(\text{Hg})/\text{CdSO}_4(\text{aq}), \text{Hg}_2\text{S}_4/\text{Hg}$ battery, see Fig. 6.1) was found to have many advantages over the Clark cell.⁶ The **Cd-Hg Weston cell** consists of a cadmium amalgam anode and a mercury-mercurous sulfate cathode with a saturated cadmium sulfate solution as the electrolyte. It has a much better long-term stability, a smaller temperature coefficient and less hysteresis. Furthermore, its output voltage of 1.0186 V was a better approximation to 1 V. In 1908, at the London International Conference on Electrical Units and Standards, the Weston cell was officially adopted for maintaining the volt. Due to the improved electrochemical cells in 1910 the Rayleigh Committee recommended a more precise value for the maintenance of the volt. Similar improvements had been adopted for the ampère and the ohm at the London Conference two years earlier. The newly recommended units were called **International Units**.

The Weston standard cell is sensitive to external parameters such as motion during transport, change in temperature or a small electrical current. When at times it was necessary to eliminate cells – due to changes in emf of a cell relative to the mean of the group – new cells could be added. In 1965 the National Reference Group of standard cells⁷ included 11 cells made in 1906, seven cells made in 1932, and 26 cells made in 1948. Long-term stability of the volt reference was also maintained by comparisons of neutral and acid cells, preparing and characterizing new cells, and through international comparisons and absolute ampère and ohm experiments.⁸ The use of the Weston cell as the national standard of voltage was supported by a considerable amount of research in electrochemistry and related fields. However, there were still problems with the standard cells. In the late 1960s the relative deviation of the output voltages of the individual national standards could be determined with an accuracy of less than 1 μV . However, the values deviated from each other by more than 10 μV . This clearly demonstrated

¹L. Galvani, *De Virebus Electricitatis in Motu Musculari Commentarius* (1791).

²W. Ostwald, *Elektrochemie, ihre Geschichte und Lehre* (1896).

³**John Frederic Daniell**, British chemist and meteorologist, born March 12, 1790 in London, England; died March 13, 1845 in London, England.

⁴J.F. Daniell, *Philosophical Transactions of the Royal Society* (1986).

⁵**Edward Weston**, born May 9, 1850, died August 20, 1936, English chemist noted for his achievements in electroplating and his development of the battery, named the Weston cell, for the voltage standard.

⁶F. B. Silsbee, *Establishment and Maintenance of the Electrical Units*, NBS Circular 475, National Bureau of Standards, Washington, DC (1949).

⁷Walter J. Hamer, *Standard Cells – Their Construction, Maintenance, and Characteristics*, NBS Monograph 84, National Bureau of Standards, Washington, DC (1965).

⁸R. L. Driscoll and P. T. Olsen, *Application of nuclear resonance to the monitoring of electrical standards*, in *Precision Measurement and Fundamental Constants*, D. N. Langenberg and B. N. Taylor (eds.), NBS Special Publication 343, National Bureau of Standards, Washington, DC (1971), pp. 117-121.



Figure 6.1: The Weston cell. Weston invented and patented the saturated cadmium cell in 1893. It had the advantage of being less temperature sensitive than the previous standard, the Clark cell. It also had the advantage of producing a voltage very near to one volt: 1.0183 V.

the necessity of a new voltage standard providing better accuracy and less deviations between of the various national standards.

We note that in 1948 the ***International Units*** were replaced by the ***Absolute Units – meter, kilogram, second, ampère (MKSA)***. In this system, the voltage is a derived quantity and its unit must be determined by an experiment, for example, by a voltage balance, which links it to the MKSA system. Accordingly, a standard cell became a laboratory realization of the unit volt. The system of absolute units was adopted unchanged by the ***Système International (SI)***, which was introduced by the Conférence Générale des Poids et Mesures in 1960.

In the late 1950s, research in solid-state physics stimulated the growth of the semiconductor industry. A new type of voltage standard based on a solid-state device, the **Zener diode**, appeared in the early 1960s. **W. G. Eicke** at NBS first reported the possibility of using Zener diodes as transport standards.⁹ In the following years, after several manufacturers started making commercial Zener voltage standards, these references began to replace standard cells in commercial use. Although Zener voltage standards exhibit higher noise characteristics than standard cells and are affected by environmental conditions such as temperature, atmospheric pressure, and relative humidity, they are now widely used in many metrology laboratories because of their robust transportability.

6.1.2 Quantum Standards for Electrical Units

The realization of physical units by systems like the standard cells implies a number of problems such as (i) damaging by improper handling, (ii) dependence on external parameters, and (iii) difficult comparison due to transport problems. In contrast, devices based on quantum effects could reduce the realization of a physical unit to the determination of fundamental constants, which are – as far as we know – independent of time and space. In the case of a quantum representation of a physical unit, the calibration can be decentralized because the unit can be reproduced with fundamental accuracy in every laboratory. Then, a regular comparison of standards is no longer necessary.

Due to the obvious advantages of quantum standards, there have been considerable efforts over the past decades to realize the physical units by quantum devices. For example, much progress has been made in the laser supported realization of the unit of length and the realization of the electrical units on the basis of the following quantum effects:

⁹W. G. Eicke, *Commentaires sur l'utilisation des diodes de zener comme étalons de tension*, Comité Consultatif d'Électricité, 11e Session, BIPM, Paris, France (1963), pp. 1874-1877.

- **Josephson Effect**¹⁰
- **Quantum Hall Effect**^{11,12}
- **Single Charge Tunneling Effect**^{13,14}

According to the second Josephson equation

$$V = \frac{h}{2e} f = \Phi_0 f , \quad (6.1.1)$$

the Josephson effect reduces the determination of a voltage V to the precise counting of the number of flux quanta Φ_0 crossing the junction. To ensure that all standard laboratories can take full advantage of the small uncertainty in the realization of the “quantum volt”, the **Consultive Committee of Electricity (CCE)**, recommended the following value for the Josephson constant in 1989¹⁵

$$K_{J-90} \equiv \left(\frac{h}{2e} \right)^{-1} = \frac{1}{\Phi_0} = 483\,597.9 \text{ GHz/V} . \quad (6.1.2)$$

This value is in use since January 1990. In the same way, according to

$$I = e f \quad (6.1.3)$$

the single charge tunneling effect reduces the determination of a current to the precise counting of single electrons tunneling from one electrode to the other. Although the determination of a current by counting electrons is studied intensively since about 1990, this method still suffers from the difficulties in fabricating the required nano-circuits.

Based on the quantum Hall effect also the ohm can be established based on a quantum effect. The von Klitzing constant $R_K = \frac{h}{e^2}$ was defined by the CCE in 1990 to

$$R_{K-90} \equiv \frac{h}{e^2} = 25\,812.802 \Omega . \quad (6.1.4)$$

The Quantum Triangle for Electrical Units

The relations between the electrical units according to the quantum definition are shown in Fig. 6.2. They are interrelated by the so-called **quantum mechanical triangle**. We note that the analogy between the determination of voltage and current – the counting of flux and charge quanta – results from the fact

¹⁰B.D. Josephson, *Possible new effects in superconducting tunneling*, Phys. Lett. **1**, 251-253 (1962).

¹¹K. von Klitzing, G. Dorda, M. Pepper, *New method for high accuracy determination of the fine-structure constant based on quantized Hall resistance*, Phys. Rev. Lett. **45**, 494-497 (1980).

¹²K. von Klitzing, *The quantized Hall effect*, Rev. Mod. Phys. **58**, 519-531 (1986).

¹³L.J. Geerlings *et al.*, *Frequency locked turnstile device for single electrons*, Phys. Rev. Lett. **64**, 2691-2694 (1990).

¹⁴K.K. Likharev, *Correlated discrete transfer of single electrons in ultra-small tunnel junctions*, IBM J. Res. Develop. **32**, 144-158 (1988).

¹⁵T.J. Quinn, *News from the BIPM*, Metrologia **26**, 69-74 (1989).

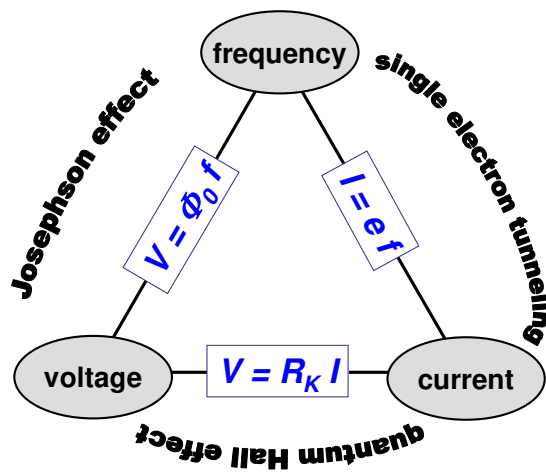


Figure 6.2: The metrological triangle for the electrical units. Josephson effect and single electron tunneling effect relate the units for voltage and current with that of the frequency. Voltage and current are linked via the quantum Hall effect.

that magnetic flux and electric charge are dual quantities from the viewpoint of quantum mechanics.¹⁶ Fig. 6.2 demonstrates that it would be important to close the triangle experimentally by the precise determination of the current via charge counting. This could be important for the redefinition of the international system of physical constants and might result in the clarification of discrepancies in the determination of the fine structure constant.^{17,18}

¹⁶ A.J. Leggett, *Macroscopic Quantum Systems and the Quantum Theory of Measurement*, Suppl. Theor. Phys. **69**, 80-100 (1980).

¹⁷ B.N. Taylor, *The possible role of the fundamental constants in replacing the kilogram*, IEEE Trans. Instrum. Meas. **IM-40**, 86-91 (1991).

¹⁸ B.N. Taylor, E.R. Cohen, *How accurate are the Josephson and quantum Hall effects and QED*, Phys. Lett. **153 A**, 308-312 (1991).

6.2 The Josephson Voltage Standard

6.2.1 Underlying Physics

The physics underlying the Josephson voltage standard already has been discussed in Chapter 3. As we have seen in section 3.3, the dynamics of the phase difference φ across a Josephson junction can be locked to an external oscillator. In this case the supercurrent is forced to oscillate at the frequency $f_1 = 2\pi\omega_1$ of the external oscillator or at higher harmonics nf_1 over a considerable range of the applied dc current. This effect results in a series of constant voltage steps in the current-voltage characteristics (IVCs) of the junction, the so-called Shapiro steps,¹⁹ at the voltages (compare (3.3.26) in section 3.3.3)

$$V_n = n \frac{h}{2e} f_1 = n \Phi_0 f_1 \quad n = 1, 2, 3, \dots . \quad (6.2.1)$$

For a specific n the dc current range $|\langle I_s \rangle_n|$ of the n^{th} voltage step is given by the n^{th} order Bessel function \mathcal{J}_n (compare (3.3.27) in section 3.3.3)

$$|\langle I_s \rangle_n| = I_c \left| \mathcal{J}_n \left(\frac{2eV_1}{hf_1} \right) \right| . \quad (6.2.2)$$

Here, V_1 is the amplitude of the external high-frequency voltage source. The maximum current width of the n^{th} step can be obtained by properly choosing the argument that maximizes the Bessel function, i.e. the amplitude V_1 of the microwave radiation. The dependence $\mathcal{J}_n \left(\frac{2eV_1}{hf_1} \right)$ has been shown in Fig. 3.11.

Equation (6.2.1) for V_n forms the physical basis of the Josephson voltage standard. It has been proven experimentally with very high precision.^{20,21,22} Fig. 6.3 shows a sketch of an underdamped planar SIS-type Josephson junction together with the IVCs under microwave radiation. It is seen that the constant voltage steps are crossing the voltage axis leading to the so-called zero-current constant voltage steps.

6.2.2 Development of the Josephson Voltage Standard

Single Junction Standards

Soon after the prediction of the Josephson effect the voltage-frequency relation $V = \Phi_0 f$ was experimentally confirmed with high precision. One of the early issues was whether this relationship was material independent. In 1968 **Clarke** as well as **Parker, Langenberg, Denenstein, and Taylor** compared, via a potentiometer, the Josephson voltages of junctions consisting of five different superconducting materials and various combinations of thin-film tunnel junctions or point contacts with 1.018 V Weston saturated

¹⁹S. Shapiro, Phys. Rev. Lett. (1963).

²⁰R.L. Kautz, L. Lloyd, *Precision of series array Josephson voltage standards*, Appl. Phys. Lett. **51**, 2043-2045 (1987).

²¹J. Niemeyer, L. Grimm, C.A. Hamilton, R.L. Steiner, *High precision measurement of a possible resistive slope of Josephson array voltage steps*, IEEE Electron Dev. Lett. **EDL-7**, 44-46 (1986).

²²J.-S. Tsai, A.K. Jain, J.E. Lukens, *High precision test of the universality of the Josephson voltage-frequency relation*, Phys. Rev. Lett. **51**, 316-318 (1983).

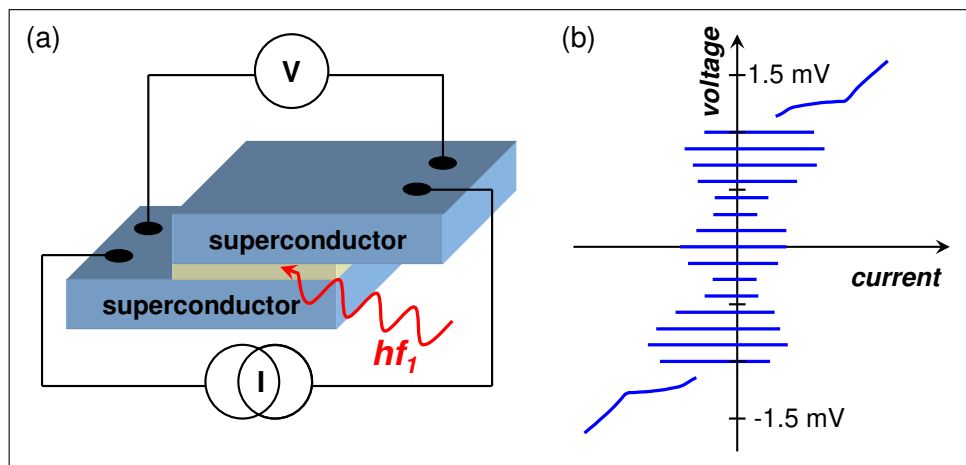


Figure 6.3: (a) Sketch of a planar SIS-type Josephson junction. (b) IVC of an underdamped Josephson junction under microwave irradiation ($f_1 = 35$ GHz). The Shapiro steps cross the voltage axis resulting in zero current constant voltage steps.

standard cells.^{23,24,25} They obtained a value of $2e/h$ with a one-standard-deviation fractional uncertainty of 3.6×10^{-6} . The use of SQUID null detectors in the early 1970s allowed this to be tested to a few parts in 10^9 , and thus the Josephson effect had obvious potential for use as a voltage standard.²⁶

As indicated by Fig. 6.3, the maximum available voltage of the current steps is of the order of 1 mV for a single Josephson junction. Therefore, precise voltage dividers have to be developed to compare the Josephson voltage standard to the electrochemical standard cells. By the early 1970s, the mV-range Josephson junction voltages could be compared with 1.018 V standard cells to a few parts in 10^8 .^{27,28} International comparisons in 1971-72 among national metrology institutes found that the measured values of $2e/h$ agreed with each other to within 2×10^{-7} .²⁹ These results suggested the course of adopting a value of $2e/h$ for use in maintaining units of voltage. Consequently, in 1972 the CCE suggested to use a value of $K_{J-72} = 2e/h = 483\,594.0$ GHz/V for voltage comparison.³⁰ This value was corrected to $K_{J-90} = 483\,597.9$ GHz/V in 1990. Since that time the national voltage standards have been controlled by single Josephson junction voltage standards and the role of the Weston cell as the primary standard for the volt has ended. Besides the relative insensitivity against environmental influences, the new Josephson voltage standard had a better reproducibility of only a few parts in 10^8 , which resulted in a considerable reduction of the spread of the standard voltages of the different national laboratories (cf. Fig. 6.4).³¹

²³J. Clarke, *Experimental comparison of the Josephson voltage-frequency relation in different superconductors*, Phys. Rev. Lett. **21**, 1566-1569 (1968).

²⁴W. H. Parker, D. N. Langenberg, A. Denenstein, and B. N. Taylor, *Determination of e/h using macroscopic quantum phase coherence in superconductors: I. Experiment*, Phys. Rev. **177**, 639-664 (1969).

²⁵T.D. Bracken, W.O. Hamilton, *Comparison of the microwave induced constant voltage steps in Pb and Sn Josephson junctions*, Phys. Rev. **B 6**, 1603-2609 (1972).

²⁶B. N. Taylor, W. H. Parker, D. N. Langenberg, and A. Denenstein, *On the use of the ac Josephson effect to maintain standards of electromotive force*, Metrologia **3**, 89-98 (1967).

²⁷F. K. Harris, H. A. Fowler, and P. T. Olsen, *Accurate Hamon-pair potentiometer for Josephson frequency-to-voltage measurements*, Metrologia **6**, 134-142 (1970).

²⁸B. F. Field, T. F. Finnegan, and J. Toots, *Volt maintenance at NBS via $2e/h$: a new definition of the NBS volt*, Metrologia **9**, 155-166 (1973).

²⁹Woodward G. Eicke and Barry N. Taylor, *Summary of international comparisons of as-maintained units of voltage and values of $2e/h$* , IEEE Trans. Instrum. Meas. **IM-21**, 316-319 (1972).

³⁰J. Terrien, *New from the Bureau International des Poids et Mesures*, Metrologia **9**, 40-43 (1973).

³¹B.W. Petley, *Quantum metrology and electrical standards: the measurement of $2e/h$* , Quantum Metrology and Fundamental Physical Constants, NATO ASI Series B, Vol. **98**, P.H. Cutler and A.A. Lucas eds., Plenum, New York (1983).

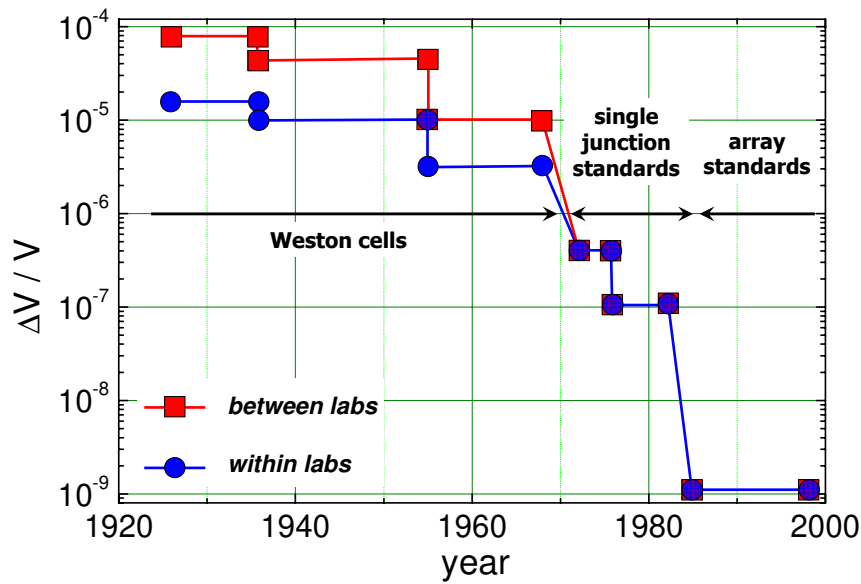


Figure 6.4: Results of the international voltage comparisons between 1920 and 2000 performed by several national laboratories. The relative accuracy $\Delta V/V$ has been improved from about 10^{-4} to 10^{-9} going from Weston cells to series array Josephson voltage standards (data from H. Bachmair, PTB Bericht E-24, 1 (1988), and C. A. Hamilton and Y. H. Tang, Metrologia 36, 53-58 (1999)).

Series Array Standards

Despite the fact that the Josephson junctions provided undoubtedly better references than standard cells, some problems remained. The typical 5 mV to 10 mV reference output from early Josephson devices made from a few junctions required both very low-level voltage balances and scaling by a factor of 100, both of which seriously limited the accuracy of measuring 1.018 V standard cells. To overcome these difficulties attempts to use series arrays of Josephson junctions were made to obtain larger reference voltages.³² However, that time the junction fabrication was not reliable enough to guarantee parameter spreads that would have allowed to bias a large series array of junctions with a single current source. Nevertheless, reference voltages up to 100 mV with an uncertainty of a few parts in 10^9 have been obtained.

Then in 1977, M.T. Levinson and colleagues showed that unbiased Josephson junctions spontaneously develop quantized dc voltages when irradiated with microwaves. Using the zero current steps, arrays can tolerate much larger spread in the junction parameters because they can be operated at zero current, where all the junctions have steps.³³ Stable 1 V zero-crossing arrays were operating at National Bureau of Standards (NBS)³⁴ and the Physikalisch-Technische Bundesanstalt (PTB)³⁵ by 1985, using about 1500 junctions and rf fields of 70 GHz to 90 GHz. Arrays with output voltages at the level of 1 V soon were used worldwide.³⁶ Note that for an operation frequency of 70 GHz Shapiro steps at multiples of about $145 \mu\text{V}$ are obtained. That is, in order to obtain a total output voltage of 1 V, about 7 000 junctions are

³²T. Endo, M. Koyanagi, A. Nakamura, *High accuracy Josephson potentiometer*, IEEE Trans. Instrum. Meas. **IM-32**, 267-271 (1983).

³³M.T. Levinson, R.Y. Chiao, M.J. Feldman, B.A. Tucker, *An inverse ac Josephson effect voltage standard*, Appl. Phys. Lett. **31**, 226-228 (1977).

³⁴C. A. Hamilton, R. L. Kautz, R. L. Steiner, and Frances L. Lloyd, *A Practical Josephson Voltage Standard at 1 V*, IEEE Electron Device Lett. **EDL-6**, 623-625 (1985).

³⁵J. Niemeyer, L. Grimm, W. Meier, J. H. Hinken, and E. Vollmer, *Stable Josephson reference voltages between 0.1 and 1.3 V for high-precision voltage standards*, Appl. Phys. Lett. **47**, 1222-1223 (1985).

³⁶Richard L. Steiner and Bruce F. Field, *Josephson array voltage calibration system: operational use and verification*, IEEE Trans. Instrum. Meas. **38**, 296-301 (1989).

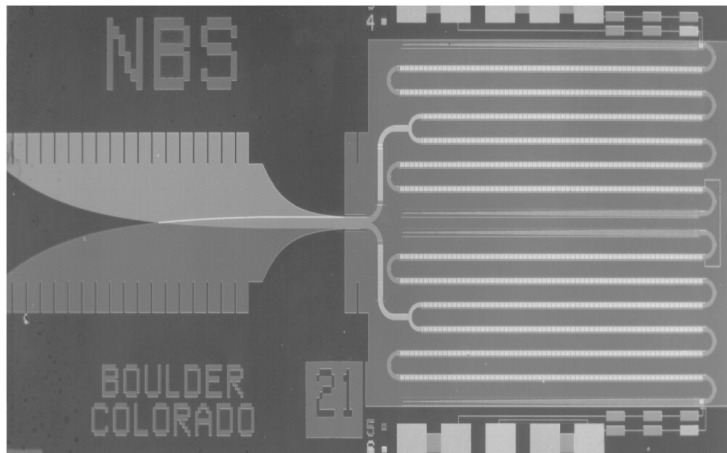


Figure 6.5: One-Volt Josephson junction array consisting of 3020 Josephson junctions (courtesy of NIST, Boulder).

required, if the junctions are operated at $n = 1$ Shapiro step. For $n = 5$, still about 1 400 junctions are required. Fig. 6.5 shows an optical micrograph of a 1 V series array consisting of 3020 junctions. The difficulties that have to be solved in the realization of series array Josephson voltage standards are the following:

- ***Fabrication of a large number of Josephson junctions with almost identical parameters***

If there is for example a too large spread of the critical current values $I_{c,i}$ of the Josephson junctions, there is a certain probability that not all junctions are operated at the same Shapiro step, since they are biased with the same dc current resulting in different values for $I_{\text{bias}}/I_{c,i}$. This problem has been solved by both improving the fabrication process, by optimizing the junction parameters (see section 6.2.3) and by using zero-current steps in arrays of underdamped junctions.

Voltage standard chips are typically fabricated on silicon or glass substrates with the integrated circuit consisting of eight levels: (1) a 300 nm thick Nb ground plane, (2) a 2 μm layer of SiO_2 that forms the microstripline dielectric, (3) a 200 nm Nb film that forms the lower electrode of the Josephson junctions, (4) a 3 nm metal oxide layer that forms the Josephson tunneling barrier, (5) a 100 nm Nb junction counterelectrode, (6) a 300 nm SiO_2 film with windows for contacts to the counterelectrode, (7) a 400 nm film of Nb that connects the junction counterelectrodes, and (8) a 100 nm resistive film that forms the stripline terminations. This structure is shown in Fig. 6.6, however, with the superconducting groundplane on top instead at bottom.

- ***Homogeneous microwave irradiation***

Each Josephson junction in the series array should be irradiated by the same microwave power. Therefore, the proper design of the microwave circuit is an important aspect of series array Josephson voltage standards. Usually, the Josephson junctions are arranged in a series array that is incorporated into a superconducting microwave stripline as shown in Fig. 6.6. In this way an effective and uniform coupling of the microwave to the single junctions could be obtained and large arrays with more than 15 000 junctions for reference voltages above 10 V could be realized.^{37,38} Due to the finite damping of the microwave signal along the microwave stripline sketched in Fig. 6.6, a homogeneous microwave irradiation is still difficult to achieve for large series arrays of several

³⁷F.L. Lloyd, C.A. Hamilton, J.A. Beall, D. Go, R.H. Ono, R.E. Harris, *A Josephson array voltage standard at 10 V*, IEEE El. Dev. Lett. **EDL-8**, 449-450 (1987).

³⁸R. Pöpel, J. Niemeyer, R. Frommknecht, W. Meier, L. Grimm, *1- and 10-V series array Josephson voltage standard in Nb/ AlO_x /Nb technology*, J. Appl. Phys. **68**, 4294-4303 (1990).

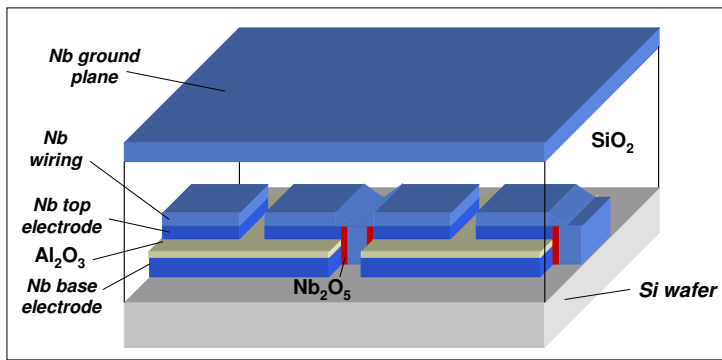


Figure 6.6: Sketch of a small part of a Josephson series array embedded into a microwave stripline.

thousands of junctions. This problem has been solved by using a meander-shaped design of the array. For the microwave signal, the different parts of the array are in parallel, whereas for the dc signal they are still in series. The microwave design and an optical micrograph of a chip with a series array Josephson voltage standard is shown in Fig. 6.7. A fin-line taper inserted into a slit in a waveguide is often used as microwave antenna. The antenna structure is then connected to a microwave divider and blocking capacitors. Each microwave path is terminated by a lossy line to prevent microwave reflections from the end, which would cause a standing wave pattern and hence an inhomogeneous microwave distribution. With respect to the dc connections, the four lines in Fig. 6.7a are connected in series. With some variations this design is used by most manufacturers worldwide.^{39,40}

In the 1980s series arrays with a continuously growing number of junctions have been developed mainly at NIST, Boulder, and PTB, Braunschweig.^{41,42} With arrays containing about 15 000 Josephson junctions about 150 000 quantized voltage values spanning the range from -10 V to +10 V could be realized. By 1989, all of the hardware and software for a complete voltage metrology system were commercially available. The widespread use of Josephson junction arrays in national standards laboratories, and better SI determinations of $2e/h$, led the CCE to recommend a new exact conventional value for the Josephson constant: $K_{J-90} = 483\,597.9 \text{ GHz/V}$, which is fractionally larger by 8×10^{-6} than the 1972 conventional value. The new value was adopted worldwide on January 1, 1990. This definition of K_{J-90} is the present volt representation, based on an ideal Josephson voltage standard. The conventional value was assumed by the CCE to have a relative standard uncertainty of $0.4 \mu\text{V/V}$. By convention, this uncertainty is not included in the uncertainties of the representation of the volt, since any offset from the SI volt will be consistent among different laboratories using the Josephson effect standard. Today, there are Josephson array voltage standards in more than 50 national, industrial, and military standards laboratories around the world. A program of international comparisons carried out by the Bureau International des Poids et Mesures (BIPM) has measured differences between a traveling Josephson standard and those of the National Measurement Institutes that are typically less than 1 part in 10^9 .^{43,44,45,46}

³⁹C.A. Hamilton, C.J. Burroughs, R.L. Kautz, *The performance and reliability of the NIST 10 V Josephson array*, IEEE Trans. Instrum. Meas. **IM-44**, 233-241 (1995).

⁴⁰S.B. Kaplan, *Technology transfer and the Josephson voltage standard*, Supercond. Industry **8**, 25-30 (1995).

⁴¹C.A. Hamilton, *Josephson voltage standards*, Rev. Sci. Instrum. **71**, 3611-3623 (2000).

⁴²J. Niemeyer, PTB Mitteilungen **110**, 169 (2000).

⁴³D. Reymann and T. J. Witt, IEEE Trans. Instrum. Meas. **42**, 596 (1993).

⁴⁴J. P. Lo-Hive, D. Reymann, and G. Geneve's, IEEE Trans. Instrum. Meas. **44**, 230 (1995).

⁴⁵D. Reymann, T. J. Witt, G. Eklund, H. Pajander, and H. Nilsson, IEEE Trans. Instrum. Meas. **46**, 220 (1997).

⁴⁶D. Reymann, T. J. Witt, G. Eklund, H. Pajander, H. Nilsson, R. Behr, T. Funck, and F. Müller, IEEE Trans. Instrum. Meas. **48**, 257 (1999).

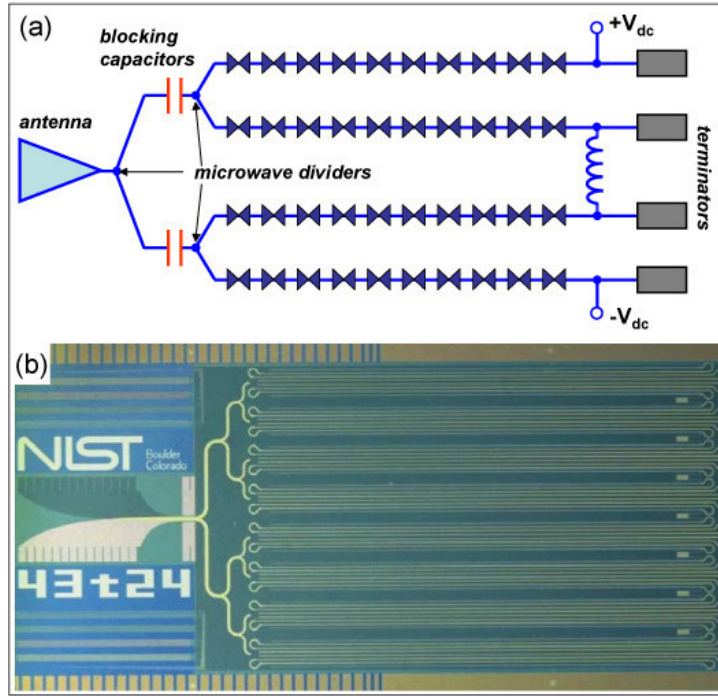


Figure 6.7: (a) Schematics of the microwave design of a series array Josephson voltage standard. (b) Optical micrograph of a NIST series array Josephson voltage standard for 10 V. The array consist of 20 208 Josephson junctions operated at 75 GHz. On the left the fin-line taper is seen. The series array on the right is split up into 16 parallel parts with 1 263 junctions each (courtesy of NIST, Boulder).

6.2.3 Junction and Circuit Parameters for Series Arrays

The idea of using series arrays for the realization of Josephson voltage standards with higher reference voltage is simple. By the use of N junctions in series the output voltage can be increased to N times the value available for a single junction. However, a prerequisite for the generation of stable zero current steps is that the phase lock of the phase dynamics of the nonlinear Josephson junction and the external microwave oscillator must be maintained during the calibration process. This condition must now be satisfied for a large series array and not only a single junction. In order to achieve this goal, reduction of external noise sources is required and one also has to avoid to operate the Josephson junctions in a regime where chaotic phenomena can occur.

The parameter regime of single Josephson junctions where optimum phase locking is guaranteed has been analyzed by **Kautz** as well as **Nöldeke** and coworkers.^{47,48} They found the following conditions for the frequency $f_1 = 2\pi\omega_1$ of the external microwave oscillator:

$$\omega_1 \gg \omega_p = \sqrt{\frac{2eI_c}{\hbar C}} = \sqrt{\frac{2eJ_c}{\hbar C_s}} . \quad (6.2.3)$$

Here, ω_p is the plasma frequency, $J_c = I_c/A$ is the critical current density and $C_s = C/A$ the specific junction capacitance. We see that one has to use junctions with low plasma frequency, i.e. low critical current density and large specific capacitance and/or high microwave frequencies.

⁴⁷R.L. Kautz, *Noise, chaos and the Josephson effect*, Rep. Prog. Phys. **59**, 935-992 (1996).

⁴⁸Ch. Noeldeke, R. Gross, M. Bauer, G. Reiner, H. Seifert, *Experimental Survey of Chaos in the Josephson Effect*, J. Low Temp. Phys. **64**, 235 (1986).

In order to obtain a homogeneous distribution of the rf current and in order to avoid large junction effects, the junction length L and width W must satisfy the conditions:

$$L < \frac{3}{\omega_1} \frac{1}{\sqrt{n\mu_0 C_s(t+2\lambda_L)}} = L_{\max} \quad (6.2.4)$$

$$L, W < \frac{\pi}{\omega_1} \frac{1}{\sqrt{\mu_0 C_s(t+2\lambda_L)}} = W_{\max} . \quad (6.2.5)$$

Here, t is the thickness of the tunneling barrier, λ_L the London penetration depth of the electrode material and n the number of the constant voltage step.⁴⁹

Detailed simulations have shown that the microwave frequency ω_1 should be larger than about $3\omega_p$ in order to avoid the regime of chaotic phase dynamics. This results in an upper limit of

$$J_{c,\max} = \frac{9\omega_1^2 \hbar C_s}{2e} . \quad (6.2.6)$$

Together with the limitations on the junction length and width this leads to a maximum value of the critical current $I_{c,\max} = J_{c,\max} W_{\max} L_{\max}$ and thus according to (6.2.2) to a maximum width of the constant voltage steps, over which a stable operation of the voltage standard can be achieved. For the commonly used Nb/AlO_x/Nb junction technology we have $C_s \simeq 6 \mu\text{F/cm}^2$ and $\lambda_L \simeq 80 \text{ nm}$. At $f_1 = 70 \text{ GHz}$ this results in $J_{c,\max} \simeq 40 \text{ A/cm}^2$, $W_{\max} \simeq 65 \mu\text{m}$, $L_{\max} \simeq 20 \mu\text{m}$, and hence $I_{c,\max} \simeq 500 \mu\text{A}$. The maximum step width for the 7th voltage step is then about $350 \mu\text{A}$.⁵⁰

⁴⁹R.L. Kautz, G. Costabile, *A Josephson voltage standard using a series array of 100 junctions*, IEEE Trans. Magn. **MAG-17**, 780-783 (1981).

⁵⁰J. Niemeyer, *Josephson voltage standards*, in *Handbook of Applied Superconductivity 2*, B. Seeger ed., Institute of Physics Publishing, Bristol (1998), pp.1813-1834.

6.3 Programmable Josephson Voltage Standard

In the previous section we have discussed Josephson voltage standards based on zero-current voltage steps. These steps are obtained for series arrays or single underdamped junctions. It is obvious from Fig. 6.3 that a particular problem with these steps is their strong overlapping making the rapid switching between the steps problematic. This problem is sketched in Fig. 6.8. In order to access a certain Shapiro step, that is a specific output voltage V_{out} , one could simply think of applying a dc voltage $V_b \simeq V_{\text{out}}$ using e.g. a battery. However, due to the finite resistance of the leads to the chip, the voltage is split up between the array and the leads following the loadline as shown in Fig. 6.8. Since the loadline is crossing several Shapiro steps, it is difficult to select a specific step in a well defined way. It is evident that there are different ways of splitting up the voltage between the leads and the array. Once a specific step is adjusted, the step voltage has to be measured by a voltmeter that has an accuracy sufficient to distinguish between neighboring steps (about $145 \mu\text{V}$ for 70 GHz).

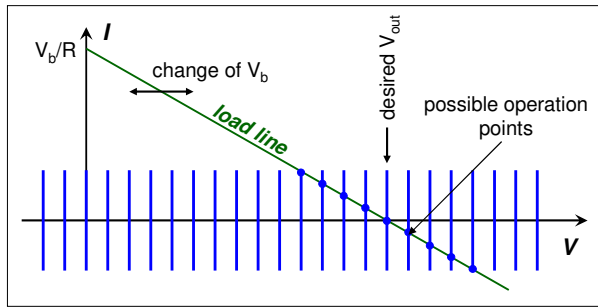


Figure 6.8: Sketch of the adjustment procedure for the quantized Shapiro step voltages in a series array of underdamped Josephson junctions. The external battery voltage V_b can be distributed along the load line V_b/R in different ways on the leads and the series array.

The problem sketched in Fig. 6.8 can be avoided by using overdamped Josephson junctions. In principle, overdamped Josephson junctions can be obtained by shunting underdamped SIS-type junctions with an external resistor. However, this makes the fabrication process more complicated. More appropriate are SNS-type (superconductor/normal/superconductor) or SINIS-type (superconductor/insulator/normal/insulator/superconductor) Josephson junctions. As shown by Fig. 6.9, in these overdamped junctions the steps do not overlap and one can rapidly select a specific step by adjusting the bias current.

Series arrays of overdamped junctions can be used to realize programmable Josephson voltage standards. Such systems use a series array of nonhysteretic junctions with IVCs as shown in Fig. 6.9, which are divided into a binary sequence as schematically shown in Fig. 6.10. The microwave excitation for each junction is set to roughly equalize the amplitude of the $n = 0$ and $n = 1$ constant voltage steps. Each segment of the array can be set to the $n = 1, 0$, or $+1$ steps by applying a bias current ($-I_1, I_0 = 0, +I_1$) corresponding to the middle of the corresponding steps (cf. Fig. 6.9). The combined step number N for the whole array can thus be set to integer values between $-M$ and $+M$, where M is the total number of junctions in the array.^{51,52,53} The rapid settling time, the inherent step stability, and the large operating current margins of the Josephson voltage standard sketched in Fig. 6.10 make it superior to a conventional Josephson voltage standard for many dc measurements. The improved performance of

⁵¹C.A. Hamilton, C.J. Burroughs, and R.L. Kautz, *Josephson D/A Converter with Fundamental Accuracy*, IEEE Trans. Instrum. Meas. **44**, 223-225 (1995).

⁵²C.A. Hamilton, C.J. Burroughs, R.L. Kautz, *Digital-to-Analog Converter with Voltage defined by Josephson Frequency Voltage Relation*, U.S. Patent No. 5565866, Oct. 1996.

⁵³C.A. Hamilton, C.J. Burroughs, S.P. Benz, and J.R. Kinard, *AC Josephson Voltage Standard: A Progress Report*, IEEE Trans. Instrum. Meas. **46**, 224-227 (1997).

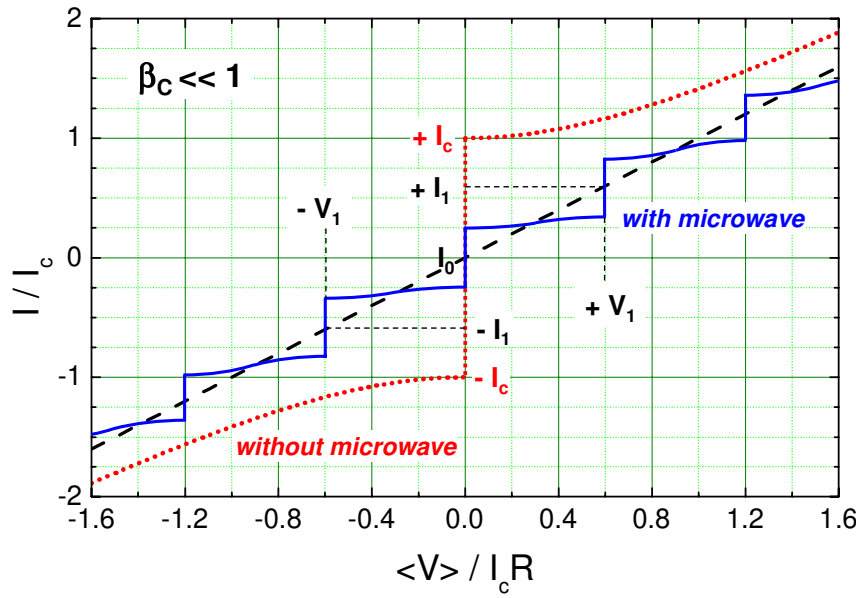


Figure 6.9: IVC of an overdamped ($\beta_c \ll 1$) Josephson junction with (solid line) and without (dotted line) microwave irradiation. The dashed curve shows the ohmic line.

programmable Josephson voltage standards has been made possible by a new integrated-circuit technology using intrinsically shunted SNS- or SINIS-type Josephson junctions. These junctions have been fabricated by extending the Nb/A_xO/Nb technology. However, also intrinsically overdamped junctions of the high temperature superconductors could be used, although at present the parameter spread of these junctions is still too large.⁵⁴ An important fact is that the overdamped junctions operate at lower excitation frequencies (10 to 20 GHz)⁵⁵ than those of Josephson voltage standards based on hysteretic SIS junctions and have about 100 times larger step amplitudes (typically 2 to 4 mA).⁵⁶ The only disadvantage of the programmable Josephson voltage standard is the required larger number of Josephson junctions, because only the first voltage step is contributing to the sum voltage. Typically, the number of junctions must be increased by a factor of five to seven.

For a microwave frequency of 20 GHz the voltage generated by each step is $V = f/K_{J-90} \simeq 41.3 \mu\text{V}$. Then, about 24 000 junctions are required to achieve a total output voltage of about 1 V. For example, a binary array consisting of segments from 2^0 to 2^{14} junctions would consist of $2^{15} - 1 = 32\,367$ individual junctions and would yield a maximum output voltage of about 1.35 V at a driving frequency of 20 GHz. Programmable voltage standards for the 1 V level have been successfully fabricated by NIST, Boulder, using Josephson junctions with a normal conducting barrier of AuPd alloy,⁵⁷ and by PTB using Josephson junctions with a superconductor-insulator-normal conductor-insulator-superconductor (SINIS) structure.⁵⁸

Since the Zener reference secondary voltage standards commonly used provide reference voltages of 1 and 10 V, there is a demand for an intrinsically stable and rapidly programmable voltage standard for the 10 V level. If microwaves in the frequency range of 70 GHz are used, a series array of about 70 000 junctions is required, which must be fabricated with low parameter spread and small defect rate. The

⁵⁴A.M. Klushin, S.I. Borovitskii, C. Weber, E. Sodtke, R. Semerad, W. Prusseit, V.D. Gelikonova, H. Kohlstedt, *Appl. Supercond.* **158**, 587 (1997).

⁵⁵R.L. Kautz, *Quasipotential and the stability of phase lock in nonhysteretic Josephson junctions*, *J. Appl. Phys.* **76**, 5538-5544 (1994).

⁵⁶S.P. Benz, *Superconductor-normal-superconductor Junctions for Programmable Voltage Standards*, *Appl. Phys. Lett.* **67**, 2714-2716 (1995).

⁵⁷S.P. Benz, C.A. Hamilton, C.J. Burroughs, T.E. Harvey, and L.A. Christian, *Appl. Phys. Lett.* **71**, 1866 (1997).

⁵⁸R. Behr, H. Schulze, F. Müller, J. Kohlmann, and J. Niemeyer, *IEEE Trans. Instrum. Meas.* **48**, 270 (1999).

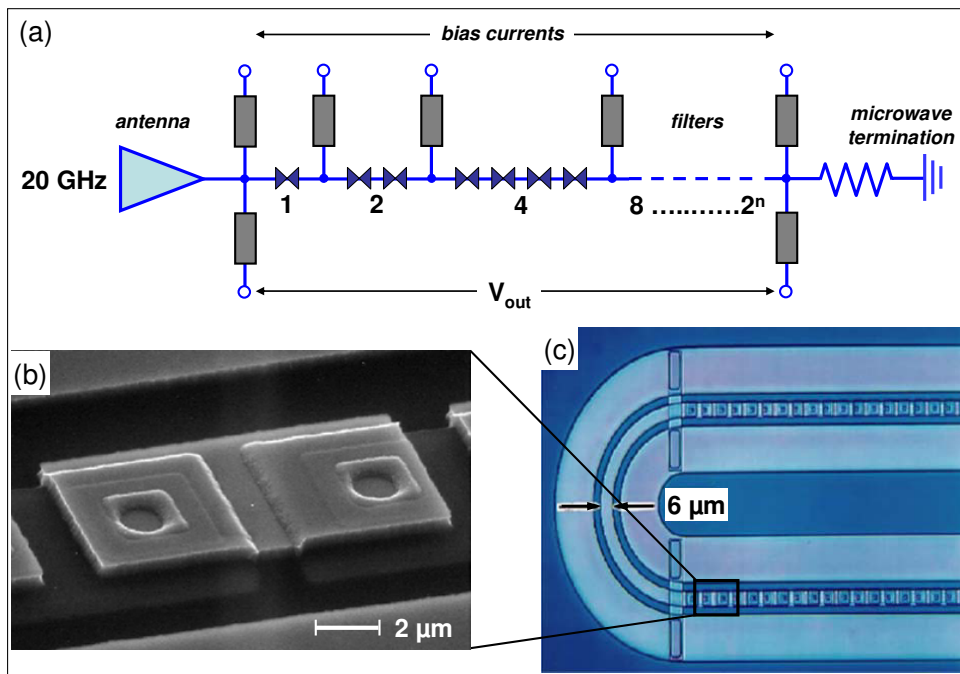


Figure 6.10: (a) Sketch of the arrangement and bias schematic of a programmable Josephson voltage standard. (b) Scanning electron microscopy image showing the $2 \times 2 \mu\text{m}^2$ Nb/PdAu/Nb Josephson junctions of a 32 768 Josephson junction series array. The series array is arranged in several segments connected with coplanar waveguides. In (c) a small section of the coplanar waveguide with the distribution of junctions along the center conductor is shown (images by courtesy of NIST, Boulder).

whole array must be fed homogeneously with sufficient microwave power. Due to the larger number of junctions required to obtain 10 V using programmable voltage standard arrays, a higher integration density is required to avoid an increase in the chip size. This can be achieved by moderate reduction of the junction area and by a modified microwave design, which is possible because of the different microwave properties of SINIS arrays. Chips with 69 120 SINIS-type Josephson junction series arrays for a programmable 10 V Josephson dc voltage standard have been successfully fabricated and operated with 70 GHz microwave irradiation. The current-voltage characteristics exhibits non-hysteretic voltage steps with a step width of $200 \mu\text{A}$.^{59,60}

6.3.1 Pulse Driven Josephson Arrays

Although the programmable Josephson voltage standards are quite useful in several applications, binary programmable arrays have not been very successful in the synthesis of ac wave forms because the undefined voltage during transitions between steps adds an unacceptable level of uncertainty. To solve this problem, **Benz** and **Hamilton** have developed another approach that biases the array with pulses.⁶¹ So far we only discussed to program the voltage of a Josephson array by changing the step number n resulting in a different voltage $V_n = nf\Phi_0$. It is clear that the same result might be achieved by changing f . Unfortunately, in the case of a sine-wave excitation, the step amplitudes collapse rapidly to zero as the

⁵⁹H. Schulze, R. Behr, J. Kohlmann, F. Müller, and J. Niemeyer, *Design and fabrication of 10 V SINIS Josephson arrays for programmable voltage standards*, Supercond. Sci. Technol. **13**, 1293-1295 (2000).

⁶⁰Yonuk Chong, C. J. Burroughs, P. D. Dresselhaus, N. Hadacek, H. Yamamori, and S. P. Benz, *Practical High-Resolution Programmable Josephson Voltage Standards Using Double- and Triple-Stacked MoSi₂-Barrier Junctions*, IEEE Trans. Appl. Supercond. **AS-15**, 461-464 (2005).

⁶¹S. P. Benz and C. A. Hamilton, Appl. Phys. Lett. **68**, 3171 (1996).

frequency decreases. This means that it is practical to control the voltage via the frequency only over a range of frequency within about a factor of 2 of the optimum frequency $f_c = I_c R / \Phi_0$. However, simulations show that if the sine-wave excitation is replaced with a pulse excitation, then the step amplitude is independent of the pulse repetition frequency for all frequencies below f_c .^{62,63,64} The optimum pulse width is $\tau = 1/\omega_c = 1/2\pi f_c$.

A programmable voltage source based on this idea consists of a single large array of N junctions distributed along a transmission line with wide bandwidth. A pulse train at frequency f propagating down the line generates an average voltage $Nf\Phi_0$ across the ends of the array. A complex output wave form can be generated by modulating the pulse train with a digital word generator. For example, using a clock frequency of $f_c = I_c R / \Phi_0 = 10$ GHz, the pulse sequence 11111000001111100000 creates an output square wave with amplitude $Nf_c\Phi_0$ and frequency 1 GHz.

⁶²R. Monaco, J. Appl. Phys. **68**, 679 (1990).

⁶³S. P. Benz, C. A. Hamilton, and C. J. Burroughs, IEEE Trans. Appl. Supercond. **AS-7**, 2653 (1997).

⁶⁴F. Liefink, G. de Jong, P. Teunissen, J. W. Heimeriks, A. Roystet, A. A. Dyrseth, H. Schulze, R. Behr, J. Kohlmann, E. Volmer, and J. Niemeyer, Proc. BEMC (1999).

Chapter 7

Superconducting Photon and Particle Detectors

Superconducting devices can be used for the sensitive detection of various quantities. We already have seen in Chapter 4 that SQUIDs can be used for the detection of magnetic flux at an accuracy below $10^{-6}\Phi_0$ and all other quantities that can be converted into a magnetic flux signal using a suitable antenna structure. In this Chapter we discuss the application of Josephson junctions as detectors for photons ranging from the microwave to the x-ray regime as well as for particles such as electrons, atoms, molecules etc.. With respect to the detection of microwave radiation the detection principle is based on the interaction of the microwave signal with the Josephson current resulting in Shapiro steps or the photon assisted tunneling process of quasiparticles. For radiation in the optical to x-ray regime both thermal detectors and nonthermal detector are used. The former are based on the sensitive measurement of the temperature rise induced by the incident radiation making use of the strong temperature dependence of the resistance or inductance of a superconducting thin film. The latter are based on the counting of excess quasiparticles generated in a superconductor due to the absorption of photons or particles.

In general, superconducting detectors can be classified in the following three categories

detector class	range	f_s (Hz)	λ (μm)	example	mechanism
modulation	radio, microwave	$< 10^{12}$	> 1000	heterodyne detector, direct detector	coherent incoherent
thermal	infrared	$10^{11} - 10^{15}$	$1 - 1000$	bolometer	incoherent
photon	visible, UV, x-ray	$> 10^{14}$	< 1	tunnel junction photon detector	incoherent

In the low frequency regime up to microwave frequencies, a **modulation detector** is fast enough to follow the incoming electromagnetic signal directly. In the intermediate regime, typically the infrared regime, the detector can no longer follow the signal directly so that modulation detectors do not work. Furthermore, the photon energy is too small to allow single photon detection. In this regime often **thermal detectors** are used, which measure the thermal response due to a larger number of absorbed photons. In the high frequency regime, typically from the visible to the x-ray regime, the detector is sensitive enough to measure the response due to the absorption of a single photon or particle. In this regime superconducting detectors can be used as single photon or particle detectors.

7.1 Superconducting Microwave Detectors: Heterodyne Receivers

Heterodyne receivers are modulation detectors used for the detection of high frequency signals in telecommunication systems and microwave instrumentation ranging from the radio to the mobile phone, television and satellite systems. The high frequency signal to be received is mixed with a so-called local oscillator signal thereby generating an intermediate frequency signal at the much lower difference frequency, which is processed further. One distinguishes between the *heterodyne receiver*, where the signal frequency f_s and the local oscillator frequency f_{lo} are different and the *homodyne receiver*, where f_s and f_{lo} are the same.

The development of low-noise superconducting heterodyne receivers was strongly stimulated by radio astronomy dealing with the observation of molecules and atoms in interstellar clouds. Most molecules are observed through their rotational emission lines. After the discovery of the spectral emission of carbon monoxide in 1970,¹ millimeter-wave radio astronomy became one of the most important branches of observational astronomy. Usually the associated signals are very weak corresponding about 10^6 microwave photons per second in a frequency interval of several 10 MHz. For the electronic processing of such weak signals with frequencies ranging from about 100 GHz to several THz amplifiers with sufficiently low noise temperatures do not exist. Therefore, heterodyne receivers have to be used for signal detection. Here, due to their superior noise performance receivers based on superconducting mixers play a dominating role.^{2,3,4}

7.1.1 Noise Equivalent Power and Noise Temperature

Before discussing the functional principle of superconducting heterodyne receivers, we introduce the quantities *Noise Equivalent Power (NEP)* and *noise temperature T_N* of detectors. As already discussed in Chapter 3, there are various sources of fluctuations of physical quantities that can be characterized by a noise power spectral density $S(f)$. Depending on the frequency dependence and the physical origin of the noise we distinguish between *Nyquist noise* and *shot noise* with white frequency spectrum, or $1/f$ *noise* (cf. section 3.1.4).

In order to detect a signal, the *signal-to-noise ratio (SNR)* must be larger than one, that is, the signal has to be larger than the noise floor. In this context, one can define the NEP of a detector as the equivalent signal power resulting in a SNR of one. That is, the NEP is equivalent to the signal power within a bandwidth $B = 1 \text{ Hz}$, which generates the same signal in the detector as the noise within the same bandwidth. In order to give an example we consider a detector, in which an incident signal power P_s generates a current response I_s . If the current noise power spectral density of this detector is $S_I(f) = \langle \Delta I^2 \rangle / B$, then the NEP in $\text{W}/\sqrt{\text{Hz}}$ can be written as

$$\text{NEP} = \sqrt{S_I(f)} \frac{P_s}{I_s} = \sqrt{\frac{\langle \Delta I^2 \rangle}{B}} \frac{P_s}{I_s}. \quad (7.1.1)$$

¹R.W. Wilson, K.B. Jefferts, A.A. Penzias, *Carbon monoxide in the Orion nebula*, *Astrophysics J.* **116**, L43 (1970).

²J.E. Carlstrom, J. Zmuidzinas, *Millimeter and sub-millimeter techniques*, *Reviews of Radio Sciences* **1993-1995**, W.R. Stone ed., Oxford University Press, Oxford (1996).

³R. Blundell and C.-Y. E. Tong, *Sub-millimeter receivers for radio astronomy*, *Proc. IEEE* **80**, 1702 (1992).

⁴T. Noguchi, S.-C. Shi, *Superconducting heterodyne receivers*, *Handbook of Applied Superconductivity Vol. 2*, B. Seeger ed., Institute of Physics Publishing, Bristol (1998).

We can divide the NEP by Boltzmann's constant and \sqrt{B} to obtain the noise temperature

$$T_N = \sqrt{\frac{S_I(f)}{B}} \frac{P_s}{k_B I_s} = \frac{\sqrt{\langle \Delta I^2 \rangle}}{B} \frac{P_s}{k_B I_s} . \quad (7.1.2)$$

A further common quantity is the ***detectivity*** $D = 1/\text{NEP}$ or the ***specific detectivity*** $D^* = D/\sqrt{A}$, where A is the detector area. In order to compare different detectors often the energy resolution in units of J/Hz is used. This quantity we already have used to characterize SQUID detectors in Chapter 4. It gives the energy per bandwidth of 1 Hz, which is associated with the detector noise.

Quantum Limit

In the ideal case the energy resolution or the noise temperature are limited only by quantum fluctuations, which can be obtained from quantization of the external circuit. The energy resolution or noise temperature due to quantum fluctuations represents the limiting value that can be reached under optimum conditions. According to (3.5.28) the average energy $E(\omega, T)$ of a quantum oscillator with frequency ω at temperature T is

$$E(\omega, T) = \frac{P_N^q}{B} = \frac{\hbar\omega}{2} \coth\left(\frac{\hbar\omega}{2k_B T}\right) . \quad (7.1.3)$$

At $T = 0$ this gives a minimum noise power $\hbar\omega B/2$ due to quantum fluctuations. We now can define a noise temperature T_N^q by setting $\hbar\omega B/2$ equal to $k_B T_N^q B$. This results in⁵

$$T_N^q = \frac{\hbar\omega}{2k_B} = \frac{hf}{2k_B} . \quad (7.1.4)$$

Putting in numbers we obtain $T_N^q \simeq 0.025 \text{ K/GHz}$, i.e. a quantum limited noise temperature of about 2.5 K at $f = 100 \text{ GHz}$.

7.1.2 Operation Principle of Mixers

The operation principle of a heterodyne receiver is shown in Fig. 7.1. The key element of a heterodyne receiver is a frequency mixer, which is a nonlinear circuit or device (e.g. a Schottky diode or a Josephson junction) which mixes the weak (e.g. astronomical) signal at the frequency f_s with a stronger signal from a local oscillator (LO) at the frequency f_{lo} . The resulting intermediate frequency (IF) $f_{IF} = |f_s - f_{lo}|$ is amplified by a broadband IF amplifier within a bandwidth Δf_{IF} of typically less than 1 GHz around a center frequency typically ranging between 1.5 and 4 GHz. For this frequency regime amplifiers with noise temperatures below 10 K are available. The output of the IF amplifier is then analyzed by a spectrum analyzer or a filter spectrometer. The resulting spectrum obtains information on the signal in a frequency range determined by the bandwidth of the IF amplifier.

⁵This result also can be obtained by the following qualitative arguments: If we are measuring a signal for the period $\tau = 1/\Delta f$, according to the energy-time uncertainty relation the energy uncertainty must be at least $\Delta E/\Delta f = \hbar/2$. If we are detecting a radiation field of frequency ω within this bandwidth, this corresponds to minimum noise energy of $\hbar\omega/2$.

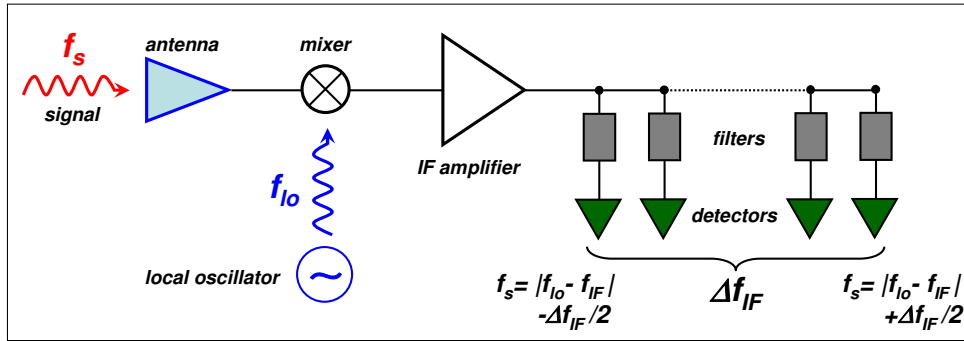


Figure 7.1: Block diagram of a heterodyne receiver with a backend filter spectrometer.

An ideal mixer consists of a switch that can be opened and closed at frequency f_{lo} without dissipation. Then, as it is evident from the equivalent circuit shown in Fig. 7.2a, we obtain a signal at the intermediate frequency $f_{IF} = |f_s - f_{lo}|$. This phenomenon is well known from the stroboscopic illumination at frequency f_{lo} of an object rotating at frequency f_s . Of course, for a proper operation of the mixer the closing period of the switch must be smaller than $1/f_{lo}$. That is, a very fast switch is required for the realization of mixers for high signal frequencies. As has been discussed already in Chapter 5, Josephson junctions are such fast switches with switching times in the ps regime. Fig. 7.2b illustrates how a switch can be realized using the nonlinear quasiparticle IVC of a superconducting tunnel junction. During one half-period of the local oscillator signal the switch is open ($R = R_{sg} \rightarrow \infty$), whereas during the other half-period of the LO signal the switch is closed ($R = R_N$). The resulting mixing device is the SIS mixer discussed below.

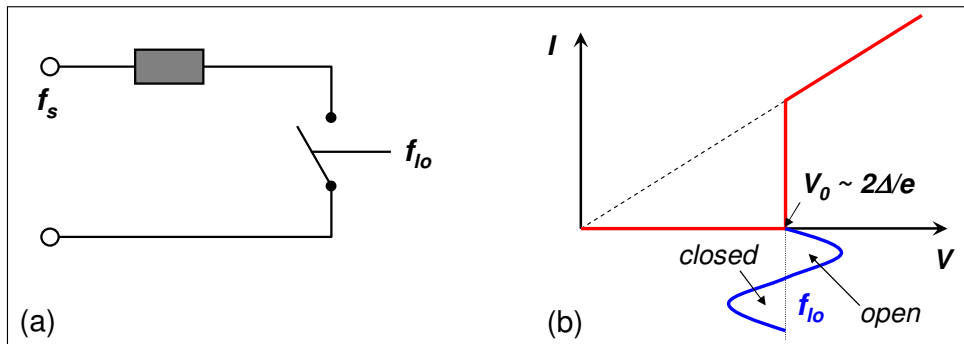


Figure 7.2: (a) Realization of an ideal mixer by a switch that is opened and closed at frequency f_{lo} . (b) Realization of the switch by the nonlinear IVC of a superconducting SIS junction.

More mathematically, a mixer is a nonlinear circuit or device that accepts as its input two different frequencies and presents at its output (i) a signal equal in frequency to the sum of the frequencies of the input signals, (ii) a signal equal in frequency to the difference between the frequencies of the input signals, and, if they are not filtered out, (iii) the original input frequencies. If the two frequencies that are to be mixed are e.g. sinusoidal voltage waves, they can be represented as:

$$v_s(t) = a_s \cos(2\pi f_s t) = a_s \cos(\omega_s t) \quad (7.1.5)$$

$$v_{lo}(t) = a_{lo} \cos(2\pi f_{lo} t) = a_{lo} \cos(\omega_{lo} t) , \quad (7.1.6)$$

where v_s and v_{lo} represent the two varying voltages, a_s and a_{lo} the respective voltage amplitudes, and f_s and f_{lo} their frequencies (e.g. the signal and the LO frequency), respectively. If we can find a way to multiply these two signals by each other at each instant in time, we could apply the trigonometric identity

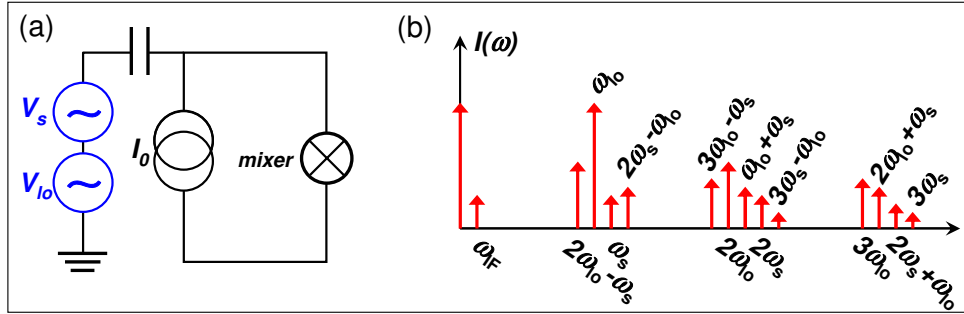


Figure 7.3: (a) Schematic circuit diagram and (b) spectrum of current response of a heterodyne mixer. Usually only the IF frequency $\omega_{IF} = \omega_s - \omega_{lo}$ is amplified and the other components are filtered out.

$\cos(A) \cdot \cos(B) \equiv \frac{1}{2} [\cos(A - B) + \cos(A + B)]$ and get

$$v_s(t) \cdot v_{lo}(t) = \frac{a_s a_{lo}}{2} \{ \cos([\omega_s - \omega_{lo}]t) + \cos([\omega_s + \omega_{lo}]t) \} . \quad (7.1.7)$$

That is, we obtain the sum ($\omega_s + \omega_{lo}$) and difference ($\omega_s - \omega_{lo}$) frequencies as required.

The next question is, how are we going to achieve this multiplication? In order to see this we assume that the mixer is a device with a nonlinear $I(V)$ dependence (IVC). For not too large voltage amplitudes we can express the current response by a power series (Taylor series)

$$I(t) = I_0 + \frac{\partial I}{\partial V} \Big|_{I=I_0} V + \frac{1}{2} \frac{\partial^2 I}{\partial V^2} \Big|_{I=I_0} V^2 + \frac{1}{6} \frac{\partial^3 I}{\partial V^3} \Big|_{I=I_0} V^3 + \dots . \quad (7.1.8)$$

If $V(t) = a_s \cos \omega_s t$, the linear term is proportional to $\cos \omega_s t$ and the quadratic proportional to $\cos^2 \omega_s t = \frac{1}{2}[1 - \cos 2\omega_s t]$. That is, the quadratic term yields a static contribution to I as well as a contribution at $2\omega_s$. The cubic term yields contributions at ω_s and $3\omega_s$ etc.. We see that the nonlinear terms yield higher harmonics of the incoming signal.

If we now use as input signal the sum of two voltage signals at frequencies ω_s and ω_{lo} , the quadratic term results in a contribution of the form $\cos \omega_s t \cos \omega_{lo} t$ given by (7.1.7). For $\omega_s \simeq \omega_{lo}$ we obtain $\omega_{IF} = |\omega_s - \omega_{lo}| \ll \omega_s$ and we say that the signal is downconverted to the intermediate frequency. In the same way, the higher order terms in (7.1.8) yields frequency components at $|2\omega_s - \omega_{lo}|$, $|2\omega_{lo} - \omega_s|$, $|3\omega_{lo} - \omega_s|$, etc.. We also see that the prefactor of the contribution resulting from the quadratic term is proportional to the second derivative of the IVC. Therefore, the nonlinearity of the IVC should be large in order to give a large value of $\frac{\partial^2 I}{\partial V^2}$. Fig. 7.3 shows the schematic circuit of a heterodyne mixer and the spectrum a current responses.

Single and Double Side Band Detection

The basic goal of a mixer is to effectively convert the signal at frequency $f_s = \omega_s/2\pi$ down to the intermediate frequency f_{IF} without adding much noise. In this process both the signal frequency $f_s = f_{lo} + f_{IF}$ and its mirror frequency $f_s = f_{lo} - f_{IF}$ can contribute. Depending on whether both frequencies are accepted or whether one of them is filtered out we distinguish between **Double Side Band (DSB)** or **Single Side Band (SSB)** receivers.

For most heterodyne receivers response is obtained from both sidebands $\omega_s = \omega_{lo} \pm \omega_{IF}$. Therefore, care must be taken in obtaining the noise temperature of SSB receivers from the measured DSB. When $\omega_{IF} \ll \omega_s$, the receiver response is fairly flat in frequency so that $T_N(\text{SSB}) \simeq 2T_N(\text{DSB})$.

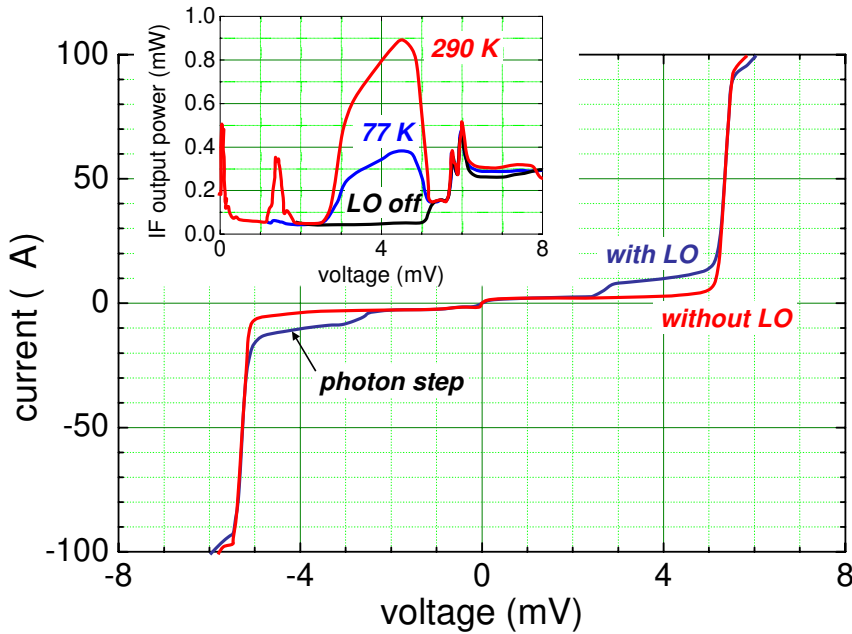


Figure 7.4: IVCs of an Nb/AlO_x/Nb SIS mixer (two junctions in series) with the LO switched on and off. The photon step corresponding to the LO frequency of 332 GHz is clearly seen. The curves in the lower-right-hand corner show the IF output power versus the bias voltage (according to H. Rothermel *et al.*, J. Physique IV C6, 267 (1994)).

Conversion Loss

An important quantity of a mixer is the ***conversion loss***

$$L_M = \frac{P_s}{P_{\text{IF}}} = \frac{\text{signal power available at input}}{\text{IF power coupled to IF amplifier}} . \quad (7.1.9)$$

Generally, mixers have a conversion loss, i.e. $L_M > 1$ for DSB and $L_M > 2$ for SSB. However, some mixers also can produce conversion gain so that $L_M(\text{DSB}) < 1$ and $L_M(\text{SSB}) < 2$. The signal conversion is the larger the more nonlinear the mixer IVC. The ideal case would be a step-like change of the conductance as it is the case for an ideal switch shown in Fig. 7.2.

Figure 7.4 shows the IVCs of two series connected Nb junctions without and with LO power injection at 332 GHz. Note the low leakage current below and the sharp current onset at the gap voltage. Also shown are the IF output power curves for hot (290 K) and cold (77 K) loads, i.e. 290 and 77 K black body radiation. The receiver noise temperature determined for this receiver was 80 K.⁶

7.1.3 Noise Temperature of Heterodyne Receivers

Although there are various kinds of heterodyne receivers, they all fulfill the Dicke⁷ radiometer equation.⁸ If T_N is the noise temperature of the heterodyne receiver, according to the Dicke radiometer equation the

⁶H. Rothermel, K.H. Gundlach, and M. Voß, J. Physique IV C6, 267 (1994).

⁷**Robert Henry Dicke**, born May 6, 1916, died March 4, 1997, was an American experimental physicist, who made important contributions to the fields of astrophysics, atomic physics, cosmology and gravity. Robert Dicke is also responsible for developing the lock-in amplifier, which is an indispensable tool in the area of applied science and engineering.

⁸J.D. Kraus, *Radio Astronomy*, 2nd edition, Powell, OH, Cygnus-Quasar (1986).

temperature corresponding to the minimum detectable input signal is

$$T_s^{\min} = \frac{T_N}{\sqrt{\Delta f \cdot \tau}} . \quad (7.1.10)$$

Here, τ is the observation time in a frequency channel of bandwidth Δf . It is evident that by increasing the observation time we can reduce T_s^{\min} by signal averaging. For a signal strength just corresponding to T_s^{\min} we have SNR=1. Taking into account not only the noise of the receiver but also the contributions due to the atmosphere (T_{atm}) and the antenna system (T_{ant}) we can write the SNR as

$$\text{SNR} = \frac{T_S \sqrt{\Delta f \cdot \tau}}{T_N + T_{\text{atm}} + T_{\text{ant}}} . \quad (7.1.11)$$

For radiotelescopes, under good conditions $T_{\text{atm}} + T_{\text{ant}}$ is 40-50 K at about 100 GHz and an altitude of 2500 m. Hence, the receiver noise should be below about 30-50 K in order not to dominate the noise of the complete system. Whereas this is achieved for the 100 GHz regime, the situation is different at THz frequencies and high altitudes, where $T_{\text{atm}} + T_{\text{ant}} \ll T_N$.⁹ Then according to (7.1.11) the observation time τ decreases proportional to T_N^2 on reducing the noise temperature of the receiver.

Referring to the block diagram shown in Fig. 7.1, the receiver noise temperature may be written as

$$T_N = T_{\text{in}} + L_{\text{in}} T_M + L_{\text{in}} L_M T_{\text{IF}} . \quad (7.1.12)$$

Here, T_{in} , T_M , and T_{IF} are the noise temperatures of the receiver input section, the mixer and the IF amplifier, respectively. The input section has the loss L_{in} and the mixer conversion loss $L_M = P_s/P_{\text{IF}}$ is the ratio of the signal power P_s at the mixer input to the power P_{IF} coupled to the IF amplifier.

Eq.(7.1.12) reveals the sensitivity of the receiver noise to the mixer performance. The mixer should not only have a low noise temperature but also a low conversion loss. A mixer with conversion loss enhances, and a mixer with conversion gain reduces the IF amplifier noise contribution to the receiver noise temperature. Although for some mixers conversion gain is possible, practical receivers usually operate at $L_M(\text{DSB}) \approx 1$ and $L_M(\text{SSB}) \approx 2$, since conversion gain can lead to instabilities in the IF output. It has been shown by **Barber** that $T_M \approx 0$ can be achieved if the conductance waveform of a mixer consists of a series of narrow pulses, which can be realized by a switch with a small pulse-duty ratio t/t_{lo} where $t_{\text{lo}} = f_{\text{lo}}$.¹⁰

Before the development of superconducting SIS mixers, heterodyne receivers for radioastronomical and atmospheric observation were commonly based on Schottky diode mixers.^{11,12} Typical receiver noise temperatures in the 690 and 830 GHz atmospheric window are above 2000 K DSB. Therefore, the reduction of the receiver noise to achieve shorter observation time, which is limited for example by weather conditions, was the motivation to look for other mixers. A further important limitation for Schottky mixers is the high LO power requirement for optimal mixing. This power usually ranges up to a few mW above 600 GHz, which is difficult to generate with sufficient frequency and amplitude stability.¹³

⁹In radioastronomy ground based observations are restricted to the so-called atmospheric frequency windows, where the atmospheric water vapor does not absorb the signals of interest. Therefore, especially in the lower THz range, astronomical measurements must be made from very high mountains, high flying aircrafts, balloons or from satellites. A project (ALMA, Atacama Large Millimetre Array) is under discussion to set up an array of 64 antennae at an altitude of 5000 m in Chile. The KAO (Kuiper Airborne Observatory), flying at an altitude of 14 km, was in use for many years. The successor will be SOFIA (Stratospheric Observatory For Infrared Astronomy), for which a telescope with the receivers will be mounted in a modified Boeing 747. Another project is the satellite FIRST (Far InfraRed and Submillimeter Space Telescope). The latter two projects aim for frequencies up to 2.5 THz.

¹⁰M.R. Barber, IEEE Trans. Microwave Theory Techniques **15**, 629 (1967).

¹¹J. Zmuidzinas, A. Betz, and D.M. Goldhaber, Astrophys. J. **L75**, 307 (1986).

¹²A.I. Harris, D.T. Jaffe, J. Stutzki, and R. Genzel, Int. J. Infrared Millimeter Waves **8**, 857 (1987).

¹³K.F. Schuster, A.I. Harris, and K.H. Gundlach, Int. J. Infrared Millimeter Waves **14**, 1867 (1993).

7.1.4 SIS Quasiparticle Mixers

The desired switching type behavior required for an ideal mixer can be obtained with the quasiparticle tunneling IVC of an SIS junction shown schematically in Fig. 7.2b, because for $T \rightarrow 0$ the subgap conductance should go to zero. Biasing the junction just below the gap voltage $V_g = 2\Delta/e$, already a small local oscillator signal is sufficient to periodically switch the junction between the high- and low-conductance state. Note that the Josephson current has to be suppressed to zero by applying a magnetic field parallel to the junction.

It was, however, soon realized that this classical picture for frequency mixing is too simple because SIS junctions exhibit photon-assisted tunneling when exposed to radio frequency (RF) irradiation. As discussed in section 3.3.4, the absorption/emission of n local oscillator photons by a quasiparticle provides/costs the energy $n\hbar\omega_{lo}$ thereby opening an additional photon assisted path for tunneling at the bias voltages

$$V_n = \frac{2\Delta \pm n\hbar\omega_{lo}}{e} . \quad (7.1.13)$$

This quantum effect leads to steps of the width $\hbar\omega_{lo}/e$ in the IVC (cf. Fig. 3.15 or 7.4).

The quantum theory of quasiparticle SIS mixers was developed by **Tucker**^{14,15} and thereafter analyzed in detail by **Richards et al.**,¹⁶ **Shen et al.**,¹⁷ **Hartfuß and Tutter**,¹⁸ **Tucker and Feldman**,¹⁹ **Winkler**²⁰ and others. Although the quantum theory of SIS mixers is quite complicated, the essential results can be summarized as:

1. the mixer can have conversion gain.
2. the mixer noise temperature can reach the quantum limit $T_N^q = \hbar\omega/2k_B$.²¹
3. the optimum local oscillator power is relatively small. If the mixer operates in the middle of the first photon step below the gap voltage, the optimum local oscillator power is²²

$$P_{lo}^{\text{opt}} = \frac{2(\hbar\omega_{lo})^2}{e^2 R_N} . \quad (7.1.14)$$

With a junction normal resistance $R_N = 50\Omega$ this gives $P_{lo}^{\text{opt}} \simeq 0.4 \mu\text{W}$ at 750 GHz as compared to a few mW required for Schottky mixers at the same frequency.

Danchi and Sutton²³ found that quasiparticle SIS mixers can, in principle, be used up to twice the gap frequency $f_{2g} = 4\Delta/eh$. However, **Feldman**²⁴ predicted that the noise of an optimized receiver increases

¹⁴J.R. Tucker, *Quantum limited detection in tunnel junction mixers*, IEEE J. Quantum Electron **15**, 1234-1258 (1979).

¹⁵J.R. Tucker, Appl. Phys. Lett. **36**, 477 (1980).

¹⁶P.L. Richards, T.M. Shen, R.E. Harris, and F.L. Lloyd, *Quasiparticle heterodyne mixing in SIS tunnel junctions*, Appl. Phys. Lett. **34**, 345-347 (1979).

¹⁷T.M. Shen, P.L. Richards, R.E. Harris, and F.L. Lloyd, Appl. Phys. Lett. **36**, 777 (1980).

¹⁸H.J. Hartfuß and M. Tutter, Int. J. InfraRed Millimetre Waves **5**, 717 (1984).

¹⁹J.R. Tucker and M.J. Feldman, *Quantum detection at millimeter wavelength*, Rev. Mod. Phys. **57**, 1055 (1985).

²⁰D. Winkler, PhD Thesis, University of Göteborg (1987).

²¹M.J. Feldman, IEEE Trans. Magn. **MAG-23**, 1054 (1987).

²²K.H. Gundlach, *Principles of direct and heterodyne detection with SIS junctions*, in *Superconducting Electronics*, Nato ASI Series, Springer, Berlin (1989), p. 259-284.

²³W.C. Danchi and E.C. Sutton, J. Appl. Phys. **60**, 3967 (1984).

²⁴M.J. Feldman, Int. J. InfraRed Millimetre Waves **8**, 1287 (1987).

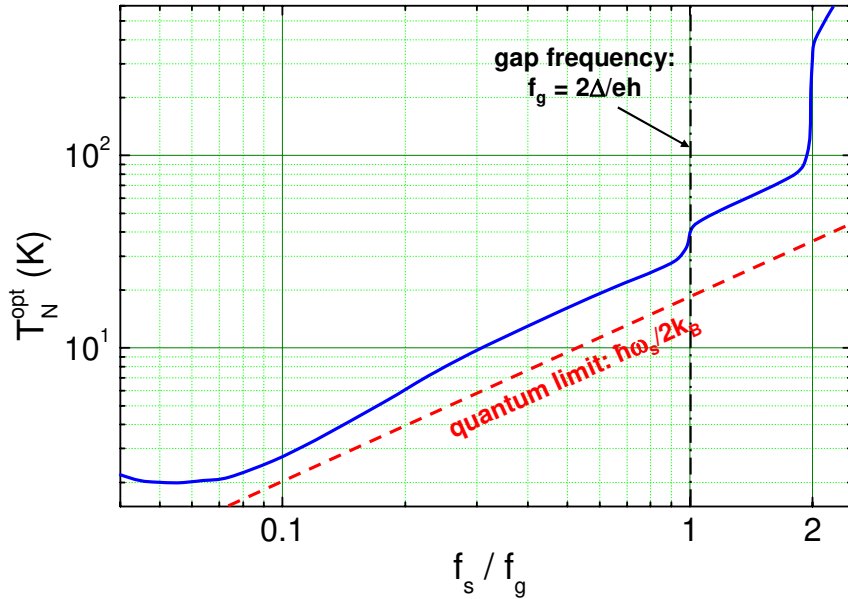


Figure 7.5: Calculated optimum noise temperature T_N^{opt} of a SIS quasiparticle mixer plotted versus the signal frequency f_s normalized to the gap frequency f_g . Also shown is the quantum limit for $f_g = 700 \text{ GHz}$ (Nb).

strongly when the signal frequency reaches $f_g = 2\Delta/eh$ but remains still reasonably low up to f_{2g} , above which the mixer performance drops very sharply. This result is summarized in Fig. 7.5. It is seen that over a wide frequency range the noise temperature of SIS quasiparticle mixers approaches the quantum limit. Practical devices do not reach the calculated optimum noise temperature. For example, mixers based on Nb junctions and an integrated Al matching circuit reach noise temperatures ranging between 680 and 1 700 K at frequencies ranging between 800 GHz and 1 THz.²⁵ A summary of experimentally determined noise temperatures is given in Fig. 7.6.

Frequency Limitations

As shown by Fig. 7.5 the energy gap of the superconducting material sets fundamental frequency limits for the mixing process and, moreover, for the surface resistance of the embedding circuit, which usually also contains a planar antenna. The gap frequency is about 700 GHz for Nb, 1.2 THz for NbN and several THz for high temperature superconductors.

Whereas Nb junctions with Nb embedding circuits are the first choice for frequencies below about 700 GHz, since Nb technology is well understood and presently provides lowest receiver noise temperatures, for frequencies above about 700 GHz Nb should be replaced by NbN. However, so far it is difficult to fabricate good tunnel junctions for this materials. Reasonable results have been obtained with NbTiN/MgO/NbTiN or Nb/Al-AlN_x/NbTiN structures.^{26,27,28} These junctions could be used up to about 1 THz. An alternative material is the recently discovered superconductor MgB₂. However, it is not known whether tunnel junctions of sufficient quality can be made from this material. The high temperature superconductors are not used for SIS mixer. Due to the $d_{x^2-y^2}$ symmetry of the order parameter, for

²⁵for a recent review see K.H. Gundlach, *SIS and bolometer mixers for terahertz frequencies*, Supercond. Sci. Techn. **13**, R171-R187 (2000).

²⁶M. Schicke, PhD Thesis, University of Hamburg, Germany (1998).

²⁷J.W. Kooi, J.A. Stern, G. Chattopadhyay, H.G. LeDuc, B. Bumble, and J. Zmuidzinas, Proc. 9th Int. Symp. on Space Terahertz Technol., Pasadena, CA (1998), p. 283.

²⁸B. Bumble, H.G. Leduc, and J.A. Stern, Proc. 9th Int. Symp. on Space Terahertz Technol., Pasadena, CA (1998), p. 295.

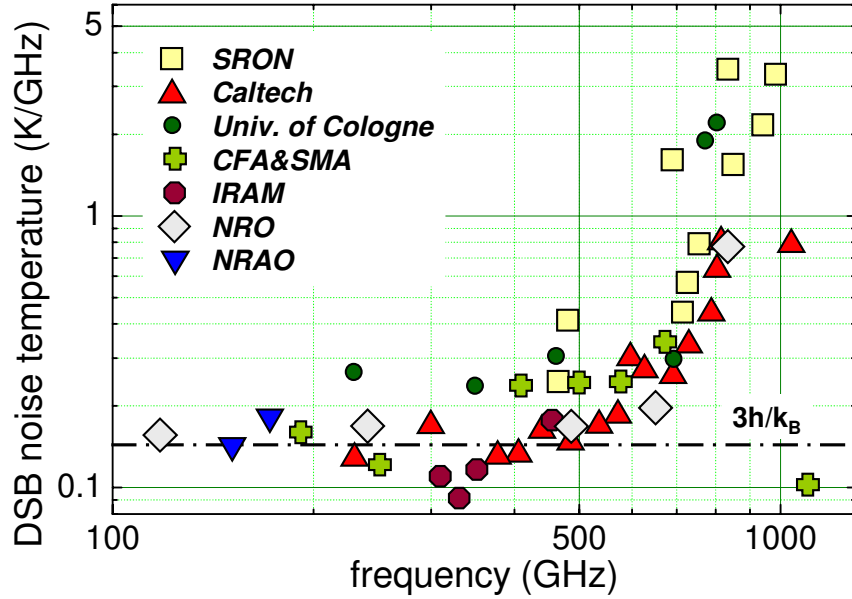


Figure 7.6: Measured DSB noise temperature of Nb based SIS quasiparticle mixers developed at different laboratories. The receiver noise temperatures fall in the range of $3 - 5\hbar\omega_s/k_B$ in the frequency range between 100 and about 600 GHz.

these junctions no sharp quasiparticle IVCs with negligible subgap conductance and a sharp increase of conductance at the gap voltage can be obtained.

A further frequency limitation is related to the junction capacitance. The geometrical capacitance of the SIS junction tends to short circuit the high frequency signal. The junctions are therefore usually embedded in a tuning circuit, which compensates for the SIS capacitance C and performs impedance transformation if required. Nevertheless, the large specific capacitance increasingly poses problems with increasing signal frequency.

The parallel-plate capacitor formed by the SIS junction is treated as an element of the embedding RF circuit. For its capacitance one has to find a compromise. To short circuit higher harmonics in the mixing process C should be sufficiently large. However, if C is too large it cannot be tuned out over the desired signal frequency bandwidth. Empirically, one came to the conclusion that optimized receivers must be designed with

$$\omega_s R_N C \simeq 2 - 4 . \quad (7.1.15)$$

Inserting $R_N \simeq 4/\omega_s C$ into the BCS expression $J_c \simeq \frac{\pi}{4} \frac{2\Delta}{e} \frac{1}{R_N A}$ for the critical current density, we arrive at the expression

$$J_c \simeq \frac{\pi}{16} \frac{2\Delta}{e} \frac{C}{A} \omega_s . \quad (7.1.16)$$

The specific capacitance $C_s = C/A = \epsilon \epsilon_0 A/t$, where A is the junction area, ϵ the relative dielectric constant and t the thickness of the tunnel barrier, only varies proportional to $1/t$, whereas J_c depends exponentially on t . Therefore, in first order approximation C_s can be assumed constant and J_c has to increase linearly with increasing signal frequency. Furthermore, the normal resistance R_N is constrained to be in a narrow range around 50Ω to ensure proper impedance matching at the mixer input and output. Then, keeping R_N constant the junction area A has to decrease as $1/\omega_s$. That is, going to higher frequencies smaller junctions with higher current densities are required. However, this goal is difficult

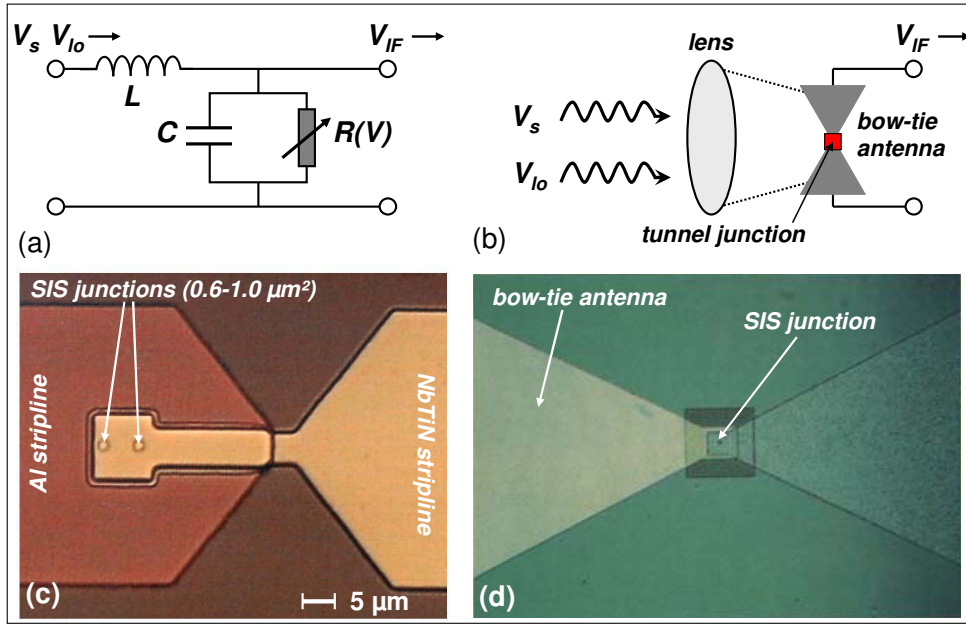


Figure 7.7: High frequency coupling schemes for SIS mixers. (a) A waveguide is used to couple in the signal and the local oscillator. (b) Quasi-optical coupling through a lens to a wide-band bow-tie antenna with the SIS tunnel junction located in the center. (c) and (d) Optical micrographs of two mixer chips showing the area around the junctions with a stripline structure (c) and a bow-tie antenna (d).

to achieve, because the junction quality usually decreases with increasing current density (e.g. larger subgap conductance due to pinholes in the very thin tunneling barrier). Furthermore, for lower junction quality the optimum noise temperature may be by almost an order of magnitude larger than the optimum noise temperature plotted in Fig. 7.5. For example, for Nb we have $I_c R_N \simeq \pi \Delta / 2e \simeq 2 \text{ mV}$, which gives $I_c \simeq 40 \mu\text{A}$ for $R_N \simeq 50 \Omega$. At $f_s = 500 \text{ GHz}$ the condition $\omega_s R_N C \simeq 4$ results in $C \simeq 25 \text{ fF}$. With the specific capacitance of Nb/AlO_x/Nb junctions of about $50 \text{ fF}/\mu\text{m}^2$, the required junction area is about $A \simeq 0.5 \mu\text{m}^2$ and, in turn, the required current density is as high as $J_c \simeq 8000 \text{ A/cm}^2$.

High Frequency Design

An important aspect for the design of high frequency receivers is the coupling structure for the high frequency radiation. Since the junction size is much smaller than the free-space wavelength (3 mm at 100 GHz), a carefully designed waveguide and antenna structure is required (see Fig. 7.7). Waveguides are intrinsically relatively narrow band and become more difficult to work with as the wavelength moves into the submillimeter regime. In this regime, a thin film antenna structure is preferable including bow-tie and spiral antennas.²⁹ These antennae can be fabricated lithographically using the same material as for the junctions or using a material with a larger energy gap to reduce the surface resistance. The radiation may be focused on the antenna quasi-optically using a lens made out of an appropriate material (e.g. quartz or Teflon).

²⁹M.J. Wengeler, Submillimeter wave detection with superconducting tunnel diodes, Proc. IEEE **80**, 1810 (1992).

7.1.5 Josephson Mixers

A mixer also can be realized by using the nonlinear IVC of a strongly overdamped Josephson junction. At this point we make a few remarks on the Josephson mixer.³⁰ The Josephson mixer can also have conversion gain³¹ and needs little local oscillator power. Experimental and theoretical results indicate that the best noise temperature of Josephson mixers is of the order of 40 times the larger of either the physical temperature or the quantum limit $hf_s/2k_B$.^{32,33} The noise is partly related to the fact that the Josephson junction is a nonlinear oscillator, which downconverts many high frequency noise components. Despite a variety of experiments, and some results which surpassed the above mentioned noise figures, up to now experimental Josephson mixers are not competitive with the quasiparticle mixers, if lowest noise temperatures are required. Note that in the quasiparticle mixer the Josephson currents and effects related to it, such as the return voltage V_r (cf. section 3.3) and Shapiro steps, can conflict with the optimal operation of the quasiparticle mixer. To avoid or reduce these effects pair tunneling is suppressed by an external magnetic field.

Of course, the high temperature superconductors can be used for the fabrication of Josephson mixers. However, the noise temperature of the best high- T_c Josephson mixers is also still considerably higher than that of corresponding low- T_c SIS mixers (Harnack et al 1998). Nevertheless, high- T_c Josephson mixers can be of interest for the THz frequency range because their upper frequency limit is set by the Josephson characteristic frequency $\omega_c = 2eI_cR_N/\hbar$ with $I_cR_N \simeq \pi\Delta/2e$ and therefore is about a factor of 10 above the low- T_c mixers. Recently, the Josephson mixer theory has been re-examined and it was found that under appropriate conditions (e.g. device parameters $I_cR_N \simeq 10$ mV, $R_N \simeq 50\Omega$) the noise temperature can be as low as about five times the physical temperature T for $\hbar\omega_{lo} < k_BT$ and 10 times the quantum noise for $\hbar\omega_{lo} > k_BT$. These promising new predictions have not yet been confirmed by experiments.

³⁰P.L. Richards, *The Josephson junction as a detector of microwave and far-infrared radiation*, in *Semiconductors and Semimetals*, R. C. Willardson and A. C. Beer eds., Vol. **12**, Academic, New York (1977), pp. 395-440.

³¹J. Taur, J. Claassen, and P.L. Richards, Appl. Phys. Lett. **24**, 101 (1974).

³²J.R. Tucker and M.J. Feldman, *Quantum detection at millimeter wavelength*, Rev. Mod. Phys. **57**, 1055 (1985).

³³J.H. Claassen and P.L. Richards, J. Appl. Phys. **49**, 4117 (1987).

7.2 Superconducting Microwave Detectors: Direct Detectors

A further modulation detector is the quasiparticle direct detector, which is also called square-law detector. This detector uses the nonlinearity of the quasiparticle tunneling IVC of SIS junctions to rectify an high-frequency signal.³⁴ In this case the incoming signal of power P_s is converted into a change ΔI of the dc current. Classically, the current to voltage conversion factor of such detector can be obtained form the Taylor's expansion (7.1.8) with the input signal $v_s(t) = a_s \cos(\omega_s t)$. We obtain

$$I(t) = I_0 + \frac{\partial I}{\partial V} \Big|_{I=I_0} a_s \cos(\omega_s t) + \frac{1}{2} \frac{\partial^2 I}{\partial V^2} \Big|_{I=I_0} [a_s \cos(\omega_s t)]^2 + \dots . \quad (7.2.1)$$

Neglecting higher order terms the current response ΔI is the time average of the third term on the right hand side (the time average of the second term vanishes), which is

$$\Delta I = \langle \overline{I(t)} \rangle - I_0 = \frac{1}{4} \frac{\partial^2 I}{\partial V^2} \Big|_{I=I_0} a_s^2 . \quad (7.2.2)$$

The time average of the power absorbed by the junction is

$$\alpha P_s = \frac{a_s^2}{2R_d} = \frac{1}{2} \frac{\partial I}{\partial V} \Big|_{I=I_0} a_s^2 . \quad (7.2.3)$$

Here, $\alpha \leq 1$ is a constant and R_d is the differential resistance at $I = I_0$. With (7.2.3) and (7.2.2) we obtain the current-to-power conversion factor $\eta_c = \Delta I / P_s$ of the junction to

$$\boxed{\eta_c = \frac{\alpha}{2} \frac{\frac{\partial^2 I}{\partial V^2} \Big|_{I=I_0}}{\frac{\partial I}{\partial V} \Big|_{I=I_0}} .} \quad (7.2.4)$$

This result obtained by a purely classical treatment is a good approximation as long as the onset of the quasiparticle current at the gap voltage is not too sharp. If not, a quantum mechanical treatment is required yielding^{35,36}

$$\boxed{\eta_q = \alpha \frac{e}{\hbar \omega_s} \frac{I(V_0 + \hbar \omega_s/e) - 2I(V_0) + I(V_0 - \hbar \omega_s/e)}{I(V_0 + \hbar \omega_s/e) - I(V_0 - \hbar \omega_s/e)} .} \quad (7.2.5)$$

We see that the derivatives in the classical expression (7.2.4) are now replaced by the second difference of the unpumped IVC computed for the three points $V = V_0$ and $V = V_0 \pm \hbar \omega_s/e$, divided by the first difference computed between $V = V_0 \pm \hbar \omega_s/e$. If the current changes slowly on the voltage scale $\hbar \omega_s/e$, then the (classical) differential expression is a good approximation. For a tunnel junction with a sharp

³⁴H.J. Hartfuß and K.H. Gundlach, *Video detection of mm-waves via photon assisted tunneling between two superconductors*, Int. J. Infrared and Millimeter Waves **2**, 809 (1981).

³⁵J. Tucker, *Quantum limited detection in tunnel junction mixers*, IEEE J. Quantum Electronics **15**, 1234-1258 (1979).

³⁶J.R. Tucker and M.J. Feldman, *Quantum detection at millimeter wavelength*, Rev. Mod. Phys. **57**, 1055 (1985).

onset of the quasiparticle current we can use the approximations $I(V_0) = I(V_0 - \hbar\omega_s/e) \simeq 0$. Then with $\alpha = 1$ we obtain the quantum limit of the current-to-power response to

$$\eta_q = \frac{e}{\hbar\omega_s} . \quad (7.2.6)$$

This corresponds to about 2500 A/W at a frequency of 100 GHz in good agreement with experiments.³⁷

We also could derive the quantum result by a qualitative discussion of the quantum nature of the detection process. To see this we note that for a purely classical detector the signal amplitude can be arbitrarily small resulting in a smooth change of the IVC due to the incoming signal. However, quantum effects become important, when the amplitude ea_s of the energy per electron is small and becomes comparable to the photon energy $\hbar\omega_s$. In the picture of photon assisted tunneling described in section 3.3.4, we obtain steps in the IVC at voltages $V_n = (2\Delta \pm n\hbar\omega_s)/e$. For large rf signals or small signal frequency ω_s , multi-photon events are likely and we obtain a series of voltage steps near the gap voltage which well approximate the rounded dc average obtained from classical theory. In contrast, for small signal amplitude and/or large photon energy only a single step is obtained since the multi-photon events are of higher order. Then, in the IVC only a single step would appear what is no longer in good agreement with the smooth classical IVC. That is, the classical result is a good approximation only for large signal amplitudes and/or small photon energy. Moreover, if the rise of the IVC at the gap voltage would be more gradual, also the series of discrete photon assisted steps would be smeared out making a classical treatment more appropriate. We finally note that the discrete steps are not a particular feature of SIS tunnel junctions. The special feature is only their observability due to the sharpness of the gap structure in the IVC.

7.2.1 NEP of Direct Detectors

The sensitivity of the detector can be described by the noise equivalent power

$$\text{NEP} = \sqrt{S_I(f)} \frac{P_s}{\Delta I} = \sqrt{\frac{\langle \Delta I^2 \rangle}{B}} \frac{1}{\eta_q} , \quad (7.2.7)$$

where $S_I(f)$ is the current noise power spectral density in A²Hz. At low temperature the Nyquist noise $S_I = 4k_B T/R$ usually can be neglected due to the small T and large R in the subgap regime of the SIS junction. The dominating noise source is shot noise $S_I(f) = 2eI$. With $S_I(f) = 2e(I_0 + I_s)$, where I_0 is the dark current and I_s the additional current due to the detected signal, we obtain

$$\text{NEP} = \sqrt{2e(I_0 + I_s)B} \frac{\hbar\omega_s}{e} = \sqrt{2(N_0 + N_s)B} \hbar\omega_s . \quad (7.2.8)$$

Here, $(N_0 + N_s)B = (I_0 + I_s)/e$ is the number of electrons flowing through the junction per time $\Delta t = 1/B$. For $I_0 \rightarrow 0$ the NEP approaches the value $\sqrt{2N_s B} \hbar\omega_s$. For example, for $N_s B = 1/\text{s}$ we obtain $\text{NEP} \simeq 9 \times 10^{-23} \text{W}/\sqrt{\text{Hz}}$ at $f_1 = \omega_1/2\pi = 100 \text{GHz}$. However, the experimentally measured values only range in the low $10^{-16} \text{W}/\sqrt{\text{Hz}}$ regime for several 10 GHz.³⁸ That is, we require more than 10^{12} photons/s to

³⁷P.L. Richards, T.-M. Shen, R.E. Harris, F.L. Lloyd, *Superconductor-insulator-superconductor quasiparticle junctions as microwave photon detectors*, Appl. Phys. Lett. **36**, 480-482 (1980).

³⁸Qing Hu and P.L. Richards, *Quasiparticle mixers and Detectors*, in *Superconducting Devices*, Steven T. Ruggiero and David A. Rudman (eds.), Academic Press Inc., San Diego (1990).

achieve SNR=1. Evidently, we are far from single photon detection. The obvious reason is the fact that we cannot operate the detector at $I_0 \simeq 0$ but require a finite bias current that introduces shot noise.

We also can estimate the optimum achievable NEP for SIS direct detectors. Doing so we point out that a specific advantage of SIS direct detectors is the fact that the current density in the subgap regime, i.e. the dark current, decreases exponentially with temperature due to the freeze out of thermally excited quasiparticles. For a dark current as small as 1 pA corresponding to about 10^7 electrons/s the sensitivity limit would be $\text{NEP} \simeq 3 \times 10^{-19} \text{W}/\sqrt{\text{Hz}}$ at 100 GHz. However, one has to take into account that the dark current of a SIS detector increases with the detector area A . In order to get orders of magnitude we consider a Nb based SIS junction with $I_c R_n \simeq 2 \text{ mV}$. For $A = 100 \times 100 \mu\text{m}^2$ we obtain a normal resistance $R_n \simeq 2 \Omega$ at a low current density $J_c \simeq 10 \text{ A/cm}^2$. For a very high quality junction at low temperature the subgap resistance R_{sg} may be by a factor of about 1000 larger. Then, the dark current is $I_0 \simeq 2 \text{ mV}/2000 \Omega = 1 \mu\text{A}$. The corresponding shot noise limited sensitivity would be $\text{NEP} \simeq 2 \times 10^{-16} \text{W}/\sqrt{\text{Hz}}$ at 100 GHz.

7.3 Thermal Detectors

As the frequency of the incoming signal is increasing, we arrive at a situation where the detector can no longer follow the electromagnetic wave directly. Furthermore, in this regime, which is including the entire infrared regime, the signal due to individual photons is smaller than the noise floor making the detection of single photon events impossible. The detectors measure the average number of photons absorbed per unit of time, that is, the average power dissipated by the radiation. The simplest way to do this is with a thermometer, which determines the temperature rise δT in the detector due to the incoming radiation. Such detector is then denoted as *thermal detector*. In some cases thermal equilibrium is not strictly reached in the detector and we have to deal with some effective temperature. In this case we usually speak about *quasi-thermal detectors*. The most simple superconducting thermal detector is a superconducting transition edge bolometer, which uses the sharp change of the resistance of a superconducting film close to the critical temperature T_c . Thin film bolometers based on the metallic superconductors have been developed for sensitive infrared detection. With the discovery of the high temperature superconductors the superconducting bolometers have found renewed interest due to the relaxed cryogenic requirements for operation temperatures above 77 K.

7.3.1 Principle of Thermal Detection

The principle of thermal detection is sketched in Fig. 7.8. An incoming electromagnetic radiation of power P_s is absorbed by an absorber mass M , which has large absorptivity determined by its surface emissivity ε . The absorbed power heats up the complete sensor with the temperature rise determined by the heat capacity C of the sensor and P_s . Of course the sensor has to get rid again of the absorbed energy. This happens by the following processes:

- radiation emission with the emitted power proportional to $\varepsilon A \sigma T^4$. Here, T is the detector temperature, A the area and $\sigma = 5.67 \times 10^{-8} \text{W/m}^2\text{K}^4$ the Stefan-Boltzmann constant.
- direct thermal coupling to a heat sink of temperature T_S with the transferred heat being proportional to the thermal conductance G and the temperature difference $\delta T = T - T_S$.

If we take into account that the sensor is also heated up by the incident thermal radiation $P_b = bA\sigma T_b^4$ (b is a geometry dependent constant) from the background of temperature T_b , we can write down the heat balance equation as

$$\varepsilon(P_s + P_b) = C \frac{d(\delta T)}{dt} + G \delta T + a\varepsilon A \sigma T^4 . \quad (7.3.1)$$

Here, a is also a geometry dependent constant. Knowing the boundary conditions and the quantities C , G , and ε we can solve for δT , the quantity detected in an experiment, e.g. by the resistance change $\delta R = \frac{\partial R}{\partial T} \delta T$ of a superconducting film.³⁹

For sufficient input power P_s we can usually neglect P_b and the radiative power emitted by the detector. However, one has to keep in mind that these powers introduce a certain amount of background noise. Assuming that the incoming power has a steady part P_0 and a time varying part $P_1 e^{i\omega t}$ we obtain from (7.3.1)

$$\varepsilon(P_0 + P_s e^{i\omega t}) = i\omega C \delta T e^{i\omega t} + \tilde{G} \delta T_0 + G \delta T e^{i\omega t} . \quad (7.3.2)$$

³⁹P.L. Richards, *Bolometers for infrared and millimeter waves*, J. Appl. Phys. **76**, 1-24 (1994).

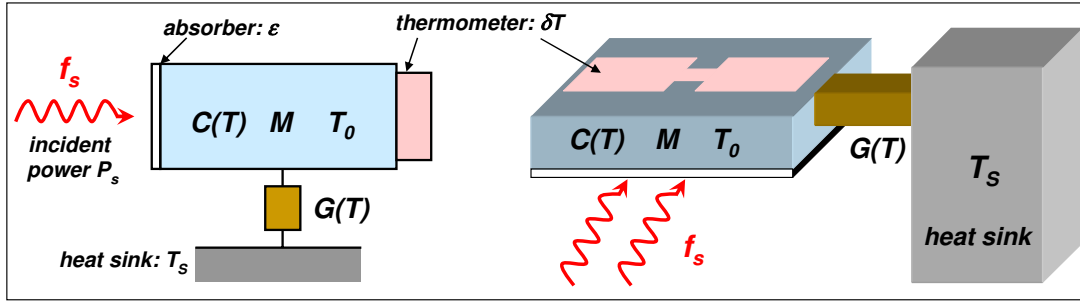


Figure 7.8: (a) Sketch of the general configuration of a thermal detector for electromagnetic radiation and (b) possible realization by weakly attaching a small mass to a heat sink.

Here, \tilde{G} is the heat conductance $\Delta P/\Delta T$ and G the dynamic heat conductance dP/dT . Equating the time independent terms gives the steady state heat flow equation that determines the average operation temperature T_0 of the bolometer

$$\delta T_0 = T_0 - T_S = \frac{\varepsilon P_0}{\tilde{G}} . \quad (7.3.3)$$

Equating the time varying terms yields

$$\frac{\delta T}{P_s} = \frac{\varepsilon}{G + i\omega C} = \frac{\varepsilon}{G(1 + i\omega\tau_{\text{th}})} \quad (7.3.4)$$

with the thermal time constant $\tau_{\text{th}} = C/G$.

Bolometers and Antenna-Coupled Microbolometer

Depending on whether the dissipative layer is larger or smaller than the wavelength of the incident radiation we can distinguish two different detector types. On the one hand, for infrared radiation the dissipative layer usually is much thicker than the wavelength. The radiation is absorbed completely by a layer of high absorptivity ε close to one. If the thermometer is a temperature-dependent resistance, we call this detector a **bolometer**.

On the other hand, for far-infrared or sub-millimeter radiation, the dissipative layer is usually much thinner than the wavelength. The radiation power is collected via a dipole, bow-tie, logarithmic spiral or log-periodic antenna with efficiency η and the radiation induced electric power is dissipated in a few micrometer-sized thermal active element. This type of detector is called **antenna-coupled microbolometer**.

Thermal Time Constants

In order to obtain a large detector response $\delta T/P_s$, the thermal conductance G , i.e. the coupling to the heat sink, should be small. However, a small G also results in a large thermal time constant $\tau_{\text{th}} = C/G$. This immediately shows that in order to obtain a large sensitivity and a reasonably fast response one has to reduce C to a minimum. For example, this can be achieved by fabricating the detector element on a very thin substrate such as a membrane.

In order to give an example we estimate the thermal time constant of a YBCO microbolometer. For a 100 nm thick YBCO film with area $10 \mu\text{m}^2$ we have a heat capacity of $C \simeq 10^{-11} \text{ J/K}$ at 90 K. If the

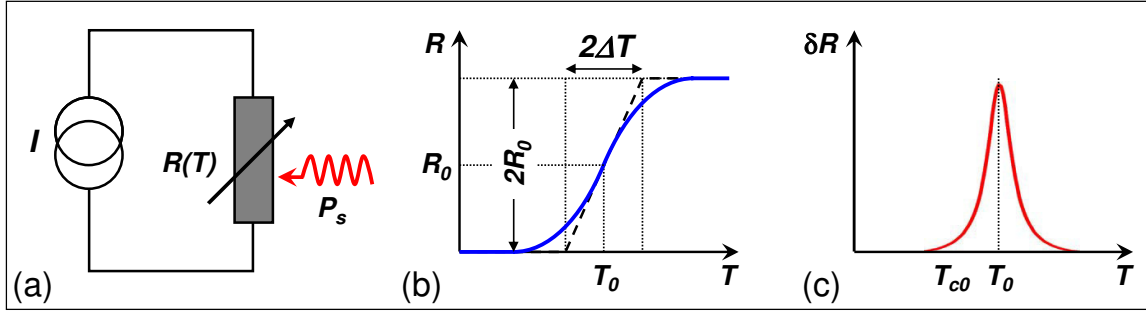


Figure 7.9: Operation principle of superconducting transition edge bolometer. (a) Circuit diagram of current biased superconducting strip. (b) Resistance vs. temperature curve (the dashed line shows the simplest approximation) and (c) typical response $\delta R(T)$.

thermal link is formed by four YBCO microbridges of length $10 \mu\text{m}$ and width $1 \mu\text{m}$, we have $G \simeq 10^{-7} \text{W/K}$ resulting in $\tau_{\text{th}} \simeq 100 \mu\text{s}$. This demonstrates that small bolometers can have fast response times. Note however, that in our simple estimate we have neglected substrate contributions. The situation in real thermal detectors is likely to be more complicated.

7.3.2 Bolometers

The operation principle of a superconducting transition edge bolometer is shown in Fig. 7.9. At T_0 the superconducting film has a resistance R_0 and a slope dR/dT . Usually, the temperature T_0 is chosen to have maximum slope dR/dT at T_0 . Upon irradiation we obtain a temperature rise δT . However, the temperature rise also increases the resistance of the film. This results in an increase of the heat dissipation due to the external circuit (current source) equal to $I^2(R_0 + \delta R) = I^2R_0 + I^2(dR/dT)\delta T e^{i\omega t}$. The heat balance equation for the time-varying terms gives then

$$\varepsilon P_s + I^2 \delta R = C \frac{d(\delta T)}{dt} + G \delta T \quad (7.3.5)$$

and further with $\delta R = (dR/dT)\delta T$

$$\varepsilon P_s = \delta T \left(G - I^2 \frac{dR}{dT} + i\omega C \right) . \quad (7.3.6)$$

With this expression we can obtain the **responsivity** S (in V/W) of the bolometer

$$S = I \frac{\delta R}{P_s} = \frac{I}{P_s} \frac{dR}{dT} \delta T = \frac{dR}{dT} \frac{\varepsilon I}{G - I^2(dR/dT) + i\omega C} . \quad (7.3.7)$$

We see that we need a large dR/dT and small G and C to obtain a large responsivity. We can introduce the effective thermal conductance

$$G_{\text{eff}} = G - I^2 \frac{dR}{dT} = G - I^2 R_0 \beta , \quad (7.3.8)$$

where

$$\beta = \frac{1}{R_0} \frac{dR}{dT} \simeq \frac{1}{\Delta T} \quad (7.3.9)$$

is the temperature coefficient of the resistance R_0 . For superconducting materials we have $\beta > 0$ and $G_{\text{eff}} < G$ and we obtain

$$|S| = \frac{dR}{dT} \frac{\varepsilon I}{G_{\text{eff}}(1 + \omega^2 \tau_{\text{eff}}^2)^{1/2}} = \frac{\varepsilon I R_0 \beta}{G_{\text{eff}}(1 + \omega^2 \tau_{\text{eff}}^2)^{1/2}} \quad (7.3.10)$$

with the effective thermal time constant $\tau_{\text{eff}} = C/G_{\text{eff}}$. We see that we have to limit the bias current to

$$I^2 \lesssim K G \frac{dT}{dR} \quad \text{or} \quad I \lesssim \sqrt{\frac{K G \Delta T}{R_0}} \quad (7.3.11)$$

with typically $K \simeq 0.3 - 0.5$ in order to avoid a value G_{eff} too close to zero. For example, for $K = 0.3$ we have $G_{\text{eff}} = 0.7G$ and $\tau_{\text{eff}} = 1.43\tau$.

Noise Equivalent Power

In order to estimate the noise equivalent power (NEP) of bolometers we have to discuss the following noise contributions:

- **Photon Noise:**

The photon noise originates from the quasi-random emission of photons. Neglecting the fluctuations due to radiation emitted by the sensor, the NEP is determined by the total radiative power fluctuations. The square of the NEP is proportional to the detector area and the sum of the two terms due to contributions of the background (e.g. 300 K radiation through the detector field of view) and the cold shields. Both terms are proportional to T^5 . The associated NEP is usually denoted as NEP_{BLIP} (BILP: Background Limited Infrared Photodetector).⁴⁰ A more detailed treatment of photon noise is given in Appendix D.

- **Thermal Fluctuation Noise:**

This noise results from thermodynamic energy fluctuations in the detector due to the random exchange of phonons (or electrons) through the thermal link which connects the detector to the heat sink at temperature T_0 . It is usually referred to as phonon noise. The corresponding noise equivalent power is⁴¹

$$\text{NEP}_{\text{th}} = \frac{\sqrt{4k_B T_0^2 G}}{\varepsilon} . \quad (7.3.12)$$

⁴⁰P.L. Richards, *Bolometers for infrared and millimeter waves*, J. Appl. Phys. **76**, 1-24 (1994).

⁴¹We use the thermal equilibrium mean square energy fluctuations $\langle \Delta u^2 \rangle = k_B T_0^2 C$ in the system. In the bolometer there is a thermometer which reads out the fluctuation as $\Delta T = \Delta u/C$. The mean square temperature fluctuation can be written as an integral over the temperature spectral density $S_T(f)$ such that

$$\langle (\Delta T)^2 \rangle = \frac{k_B T_0^2}{C} = \int_0^\infty S_T(\omega) \frac{d\omega}{2\pi} .$$

We now use (7.3.4) (omitting for simplicity the thermal feedback due to the bias current) to relate the power fluctuations S_P to the temperature spectral density as $S_T = \varepsilon^2 S_P / (G^2 + \omega^2 C^2)$. From the above integral we obtain $S_P(\omega) = 2k_B T_0^2 G / \pi \varepsilon^2$ or $S_P(f) = 4k_B T_0^2 G / \varepsilon^2$.

- **Nyquist Noise:**

This noise is introduced by the voltage fluctuations with power spectral density $S_V = 4k_B T_0 R_0$ (cf. section 3.1.4 and 3.5.5) in an ohmic resistor caused by the random motion of the charge carriers. In order to refer this voltage noise in the thermometer resistance to the detector input we can use the responsivity S . The corresponding noise equivalent power is

$$\text{NEP}_{\text{Nyquist}} = \frac{\sqrt{4k_B T_0 R_0}}{|S|} . \quad (7.3.13)$$

For $G_{\text{eff}} \sim G$ and $\tau_{\text{eff}} \sim \tau$ we obtain

$$\text{NEP}_{\text{Nyquist}} = \frac{G \Delta T}{\varepsilon I} \left(\frac{4k_B T_0}{R_0} (1 + \omega^2 \tau^2) \right)^{1/2} \quad (7.3.14)$$

resulting in

$$\frac{\text{NEP}_{\text{th}}}{\text{NEP}_{\text{Nyquist}}} = \frac{|S|^2 T_0 G}{\varepsilon^2 R_0} . \quad (7.3.15)$$

We see that thermal noise dominates for large $|S|$, T_0 and G . This is for example the case for bolometers based on the high temperature superconductors operating at $T_0 > 70$ K.

- **$1/f$ Noise:**

Low frequency $1/f$ noise originating from various sources (e.g. flux motion, trapping of charge carries in defects, etc.) causes fluctuations δR_f of the film resistance. The corresponding noise equivalent power is

$$\text{NEP}_{1/f} = I \frac{\delta R_f}{|S|} = \frac{\delta R_f \Delta T}{\varepsilon R_0} G (1 + \omega^2 \tau^2)^{1/2} . \quad (7.3.16)$$

- **Amplifier Noise:**

Amplifier noise usually is small and can be neglected.

If all the different noise sources are uncorrelated, the total NEP is obtained to

$$\begin{aligned} \text{NEP} &= \left(\text{NEP}_{\text{BLIP}}^2 + \text{NEP}_{\text{th}}^2 + \text{NEP}_{\text{Nyquist}}^2 + \text{NEP}_{1/f}^2 \right)^{1/2} \\ &= \left(\text{NEP}_{\text{BLIP}}^2 + \widetilde{\text{NEP}} \right)^{1/2} . \end{aligned} \quad (7.3.17)$$

For small enough bias current we can use $G_{\text{eff}} \sim G$ and $\tau_{\text{eff}} \sim \tau$ and obtain for the equivalent noise power contributed by the nonradiative effects as

$$\widetilde{\text{NEP}} = \frac{1}{\varepsilon} \left(4k_B T_0^2 G + \frac{4k_B T_0}{I^2 R_0} (G \Delta T)^2 (1 + \omega^2 \tau^2) + \frac{\delta R_f^2}{R_0^2} (G \Delta T)^2 (1 + \omega^2 \tau^2) \right)^{1/2} . \quad (7.3.18)$$

This expression shows the important influence of the thermal conductance. In order to have high responsivity and low NEP, G should be as small as possible. However, this also increases the response time,

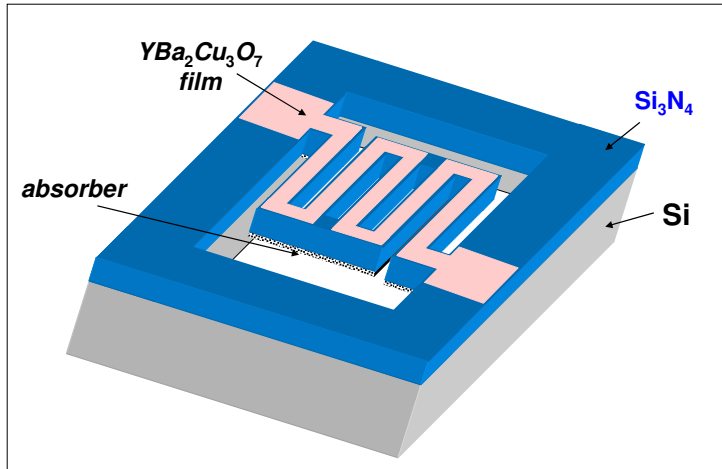


Figure 7.10: Sketch of a high temperature superconducting bolometer consisting of a meander shaped $\text{YBa}_2\text{Cu}_3\text{O}_{7-\delta}$ film deposited on a $\text{Si}/\text{Si}_3\text{N}_4$ substrate. Between the film and the Si_3N_4 usually a thin YSZ buffer layer is deposited. The SI substrate is removed below the bolometer area after the deposition process to achieve a free-standing structure with small heat capacity and small thermal coupling to the heat sink.

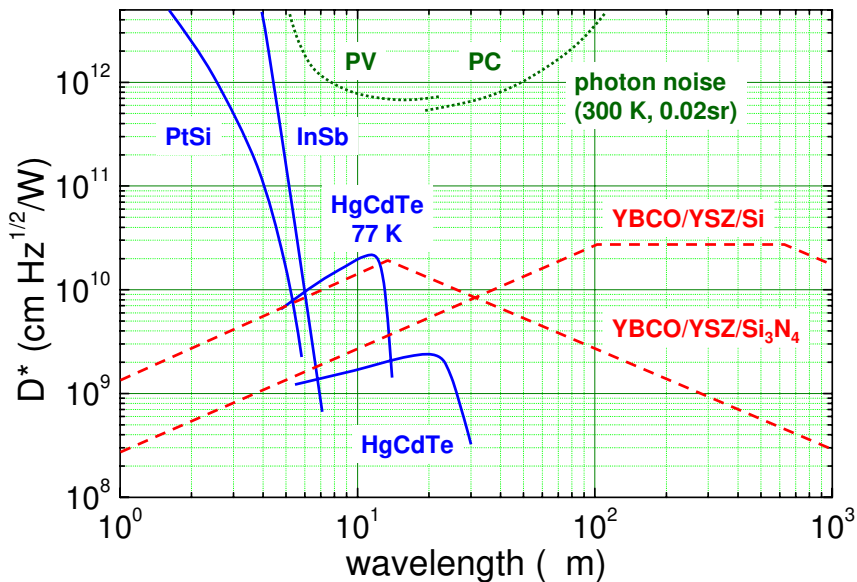


Figure 7.11: Specific detectivity D^* as a function of wavelength. The dashed lines show the predicted D^* for the high- T_c bolometers on silicon and Si_3N_4 membranes using YBCO thermometers. These lines were calculated using estimates for the minimum achievable heat capacity and thermal conductance and using measurements of the voltage noise of high- T_c thermometers. Typical values of D^* for InSb, PtSi, and HgCdTe detectors in two-dimensional staring arrays operated at 77 K are shown for comparison. Also shown are the photon noise limits for photovoltaic (PV) and photoconductive (PC) detectors, which view 300 K radiation in a 0.02 sr field of view (according to P.L. Richards, J. Appl. Phys. **76**, 1 (1994)).

which can be kept small by making C as small as possible. That is, both G and C should be as small as possible to achieve good detector performance.

In general, different detectors are compared with respect to their specific detectivity $D^* = \sqrt{A}/\text{NEP}$. Superconducting transition edge bolometer with $D^* \simeq 10^{14} \text{ cm}\sqrt{\text{Hz}}/\text{W}$ at a wavelength of $500 \mu\text{m}$ and a temperature of 1.27 K have been fabricated using superconducting aluminium films on sapphire suspended

by threads.⁴² For microbolometers based on high temperature superconductors $D^* \sim 10^{10} \text{ cm}\sqrt{\text{Hz}}/\text{W}$ and $\text{NEP} \sim 10^{-12} \text{ W}/\sqrt{\text{Hz}}$ have been achieved at about 70-90 K. This detectivity is significantly better than $D^* \sim 10^8 \text{ cm}\sqrt{\text{Hz}}/\text{W}$ achieved for room temperature detectors. For instance, $\text{YBa}_2\text{Cu}_3\text{O}_{7-\delta}$ meander-shaped films (see Fig. 7.10) have been deposited on micrometer thick Si_3N_4 membranes with intermediate yttria-stabilized zirconia (YSZ) buffer layers.^{43,44} Typical values obtained for various detectors are summarized in Fig. 7.11 including some cooled semiconductor detectors.⁴⁵

Nonequilibrium Effects

So far we have assumed that the detector element always is in thermal equilibrium at an elevated temperature T . However, this is true only on sufficiently long time scales that allow for establishing thermal equilibrium. Fig. 7.12 illustrates the various interaction processes going on in a solid after the absorption of electromagnetic radiation. If the frequency of the incoming radiation is small, the energy usually is directly coupled to the electronic system and results in Joule heating of the electronic system. The heating only results in a change of energy distribution within a single band. If however the frequency is larger the absorption of a single photon can result in band to band transitions. The resulting high energy electronic excitations relax down to lower energies on a very short time scale τ_{ee} of the order of ps via electron-electron interactions. In this process a large number of low energy excitations is generated. This process again results in heating up the electronic system to an effective temperature $T_{\text{eff}}^{\text{el}}$. That is, after a very short time scale only the electronic system has established thermal equilibrium but there is no thermal equilibrium between electrons and phonons. Therefore, we can attribute an effective temperature $T_{\text{eff}}^{\text{el}}$ only to the electronic systems but not to the sample as a whole. The value of $T_{\text{eff}}^{\text{el}}$ is given by the radiation power and the heat capacity of the electronic system.

In a second step the electronic systems establishes equilibrium with the phonon system by electron-phonon interaction. This process occurs on a much longer time scale $\tau_{ep} \sim 100 \text{ ps}$. After this thermal equilibrium is established within the sample and we can assign an effective temperature T_0 to the whole sample, which is of course above the temperature T_S of the heat sink. T_0 is determined by the total heat capacity of the sample. Finally, the excess heat is transferred to the heat sink of temperature T_S by thermal conduction. If the coupling to the heat sink is via an insulator, only the phonons contribute to this process and the characteristic time scale is given by the so-called phonon escape time τ_{es} . At low temperature this time depends on the temperature (roughly proportional to $1/T^3$) and the acoustic mismatch between the different materials. Typically, the phonon escape time is more than an order of magnitude larger than τ_{ep} . It becomes small for very thin films as discussed in section 7.3.3. Summarizing the discussion of the relaxation processes we can state that in most cases we have a three step process with $\tau_{ee} \ll \tau_{ep} \ll \tau_{es}$. A simple description of the relaxation processes going on after the absorption of the incoming radiation can be given by rate equation.^{46,47}

⁴²J. Clarke, G.I. Hoffer, P.L. Richards, N.H. Yeh, *Superconductive bolometers for submillimeter wavelengths*, J. Appl. Phys. **48**, 4865-4879 (1977).

⁴³S. Verghese, P.L. Richards, K. Char, D.K. Fork, T.H. Geballe, *Feasibility of infrared imaging arrays using high- T_c superconducting bolometers*, J. Appl. Phys. **71**, 2491-2498 (1992).

⁴⁴S.J. Berkowitz, A.S. Hirahara, K. Char, E.N. Grossman, *Low noise high temperature superconducting bolometers for infrared imaging*, J. Appl. Phys. **69**, 2125-2127 (1996).

⁴⁵P.L. Richards, *Bolometers for Infrared and Millimeter Waves*, J. Appl. Phys. **76**, 1 (1994).

⁴⁶R. Gross, M. Koyanagi, *Effect of Electron Beam Irradiation on Superconducting Films*, J. Low Temp. Phys. **60**, 277 (1985).

⁴⁷A.M. Kadin, A.M. Goldman, *Dynamical effects in nonequilibrium Superconductors*, in *Nonequilibrium Superconductivity*, D.N. Langenberg ed., North-Holland, Amsterdam (1986).

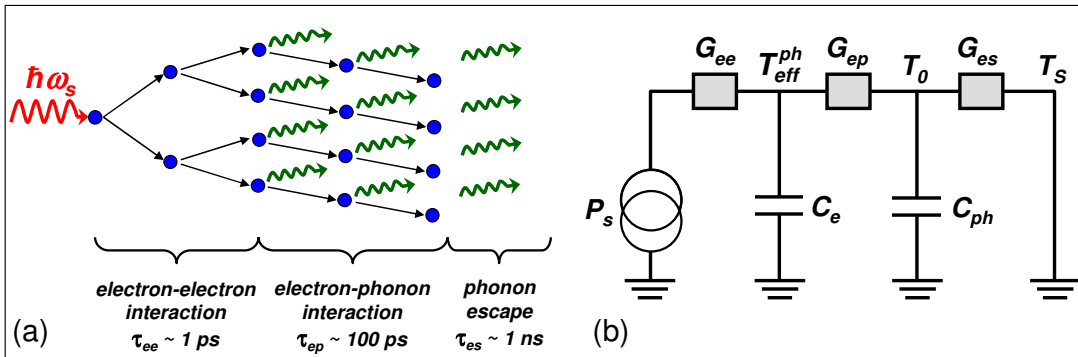


Figure 7.12: (a) Schematic illustration of the relaxation processes in a superconducting film deposited on a substrate after the absorption of electromagnetic radiation. (b) Equivalent circuit for the relaxation processes. The effective conductances are related to the relaxation times as $G_i = C_i/\tau_i$.

7.3.3 Antenna-Coupled Microbolometers

Antenna-coupled microbolometers are used for the thermal detection of far-infrared or millimeter radiation or the realization of so-called hot electron bolometers used for the direct detection and heterodyne detection of the same radiation. The typical configuration of an antenna-coupled microbolometer is shown in Fig. 7.13. The radiation is collected via an antenna structure (e.g. log-periodic or spiral antenna). Then the radiation induced electrical power is dissipated by a micrometer-sized thermometer such as a transition edge bolometer, a SIS junction, an inductance thermometer etc..

Transition-edge Microbolometers

For transition edge microbolometers the thermally active element is superconducting film positioned at the center of the antenna structure, which thermalizes the currents induced by the detected electromagnetic radiation. The impedance of the detector (about 80Ω) has to match the broadband antenna structure, which may be either normal or superconducting. A typical example is a high temperature superconducting microbolometer coupled to a log-periodic antenna as shown in Fig. 7.13. The thermally active element is for example an $\text{YBa}_2\text{Cu}_3\text{O}_{7-\delta}$ microbridge with width and length in the micrometer regime, which is suspended on a YSZ air-bridge. The free-standing YSZ structure is obtained by anisotropic chemical etching of the Si substrate. In this way a small thermal conductance between the bolometer and the substrate is established. At a temperature of about 85 K a responsivity of 1070 V/W was obtained for such structure and the estimated NEP was $3.2 \times 10^{-12} \text{ W}/\sqrt{\text{Hz}}$.⁴⁸ Due to the small size and suspended structure both a small thermal conductance and small heat capacity could be realized resulting in a small thermal time constant of about $2\mu\text{s}$.

Hot Electron Microbolometers

A hot electron microbolometer consists of a superconducting antenna, a thin strip of normal metal acting as antenna load and a thermometer to measure the electron temperature in the piece of normal metal. Such structure is advantageous at very low operation temperatures and can act as sensitive detector for far-infrared and millimeter wave radiation.

At low operation temperatures the thermal insulation of the dissipative element (normal metal) as well as its temperature rise due to the detected radiation is enhanced due to the following reasons. Firstly, the

⁴⁸M. Nahum, Qing Hu, P.L. Richards, S.A. Sachtn, N. Newman, B.F. Cole, *Fabrication and measurement of high- T_c superconducting microbolometers*, IEEE Trans. Magn. **MAG-27**, 3081-3084 (1991).

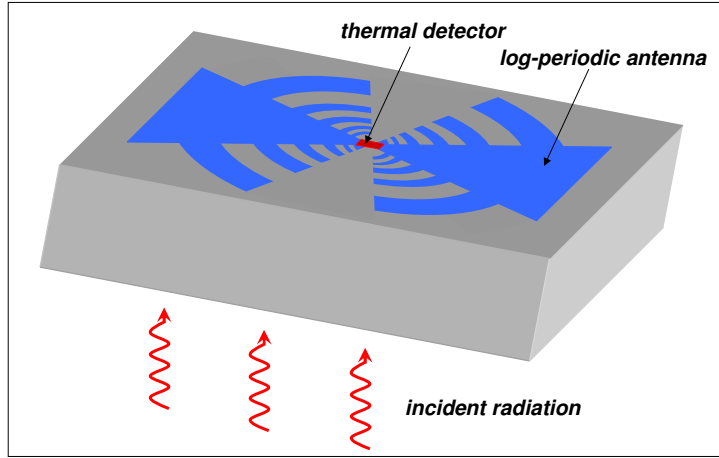


Figure 7.13: Schematic illustration of an antenna-coupled microbolometer. The thermal detector in the center of the antenna structure can be fabricated on a suspended structure (cf. Fig. 7.10) in order to realize a small heat capacity and thermal conductance and hence short thermal time constant.

thermal conductivity of insulators varies as T^3 and further the thermal conductance between the active element and the substrate varies roughly as T^3 (Kapitza thermal boundary resistance). This allows for a very efficient thermal decoupling of the absorber element from the environment going to low temperatures. Secondly, going to low temperatures the electron-phonon scattering time increases roughly as $1/T^3$ and reaches $\tau_{ep} \gtrsim 10\mu s$ at $T < 0.1$ K for copper.⁴⁹ Due to the large τ_{ep} the electron system effectively decouples from the lattice. That is, only a small amount of the detected radiation power is going into the lattice and mainly results in an increased electron temperature. Due to the decoupling between electron and phonons we can speak about hot electrons. Thirdly, if the active element is a normal conductor which is surrounded by superconducting material, the electronic excitations in the normal metal are trapped there due to Andreev reflection.⁵⁰ We see, that both the electrons and the phonons are trapped for a long time in the active detector area.

As a thermometer for the increased electron temperature T_{eff}^{el} of the normal metal absorber a superconductor-insulator-normal metal (SIN) type junction is used. The normal electrode of this junction is just the absorber element. The electron temperature in the N layer can be measured via the quasiparticle tunneling current through the insulator. For such kind of microbolometer an extremely low NEP of a few $10^{-19}W/\sqrt{Hz}$ and a high responsivity of a few $10^9V/W$ is expected for an operation temperature of 0.1 K and a normal metal volume of about $1\mu m^3$. The thermal conductance G between the electron and phonon systems is expected to be as low as about $10^{-13}W/K$ in this case. In experiments a responsivity of $10^9V/W$ was measured for $G = 2 \times 10^{-13}W/K$ and a normal metal (copper) volume of about $1.5\mu m^3$. The measured noise of $3 \times 10^{-18}W/\sqrt{Hz}$ was amplifier limited.⁵¹

Hot Electron Bolometer Mixer

The lack of SIS mixer technology for frequencies higher than about 1 THz (cf. section 7.1.4) initiated the search for alternatives. At present the most promising solution appears to be the **hot electron bolometer (HEB) mixer** shown in Fig. 7.14. It predominantly uses Nb or NbN microbridges as sensitive elements and offers the following advantages:

⁴⁹M. Nahum, P.L. Richards, C.A. Mears, *Design analysis of novel hot electron microbolometers*, IEEE Trans. Appl. Supercond. **AS-3**, 2124-2127 (1993).

⁵⁰An electron that wants to enter the superconducting material from the normal metal side cannot do so for energies smaller than the gap energy, since there are no available states in the superconductor below the gap energy.

⁵¹M. Nahum, J.M. Martinis, *Ultrasensitive hot electron microbolometers*, Appl. Phys. Lett. **63**, 3075-3077 (1993).

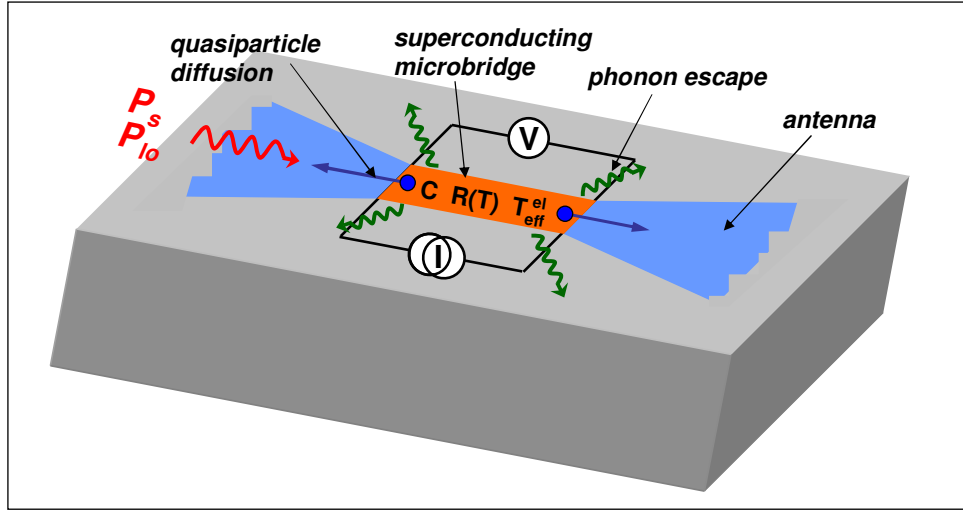


Figure 7.14: Schematic illustration of the hot electron bolometer mixer. The signal power P_s and the local oscillator power P_{lo} are detected by an antenna structure and transmitted through a superconducting microbridge operated as a transition edge bolometer. The heat is removed from the active area by phonon escape to the substrate and diffusion of hot electrons into the leads.

- the maximum signal frequency is not limited by the energy gap of the superconductor, enabling mixing up to several THz.
- the required local oscillator power is very low (about 20-1000 nW) and does not increase with frequency as for SIS mixers.
- for $f_s > 2\Delta(T)/h$ the rf impedance is expected to be essentially resistive and frequency independent. There are no harmonics of the LO and signal frequency because the thermal response of the bolometer is too slow. These two properties simplify the rf circuit design.
- a magnetic field to suppress Josephson currents is not required.

In contrast to diodes or SIS junctions with strongly nonlinear IVCs, the HEB is not switched by the local oscillator between high- and low-conductance states. The switching model mentioned in section 7.1.2 is therefore not appropriate for HEB mixers. The dissipated rf power coupled via the antenna into the microbridge can be written as

$$P(t) = \frac{1}{R} [v_{lo} \cos(\omega_{lo}t) + v_s \cos(\omega_s t)]^2 . \quad (7.3.19)$$

Due to the finite thermal time constant, the bolometer is too slow to follow the power variation at f_{lo} , f_s , and higher frequencies, but it should be fast enough to instantaneously respond to a power variation at the desired IF frequency $f_{IF} = |f_{lo} - f_s|$ of several GHz. We therefore obtain

$$P(t) = P_{lo} + P_s + 2\sqrt{P_{lo}P_s} \cos(\omega_{IF}t) \quad (7.3.20)$$

with $P_{lo} = v_{lo}^2/2R$ and $P_s = v_s^2/2R$. The IF voltage amplitude can be written as

$$v_{IF} = S \cdot 2\sqrt{P_{lo}P_s} = \frac{dR}{dT} \frac{I}{G_{eff}} \frac{2\sqrt{P_{lo}P_s}}{(1 + \omega_{IF}^2 \tau_{eff}^2)^{1/2}} \quad (7.3.21)$$

with the responsivity S given by (7.3.10).

For hf_S and $hf_{lo} > 2\Delta$, the superconductor behaves nearly as a normal conductor and $R \simeq R_N$ in good approximation. Note that in the SIS mixer absorption of photons occurs by photon assisted tunneling. The absorber itself, the SIS junction, stays at the bath temperature. In contrast, in the HEB the absorption of photons results in a considerable increase in the electron temperature. Consequently, mixing is not limited by the energy gap and good performance is expected up to tens of THz. Equation (7.3.21) is misleading in the sense that an infinite increase of the LO power induces an infinite increase of the IF output voltage. This is in principle correct, but other effects not included in (7.3.21) limit the LO power level for bolometers. For the transition-edge bolometer the LO power must remain below the level at which it would heat the electron gas in the microbridge above T_c . Usually the temperature of the heat sink is chosen well below T_c and the LO power adjusted to a value that heats up the electron gas close to T_c .

A few conditions have to be satisfied to achieve the desired high intermediate frequency of several GHz. Firstly, only the electron gas but not the lattice should be heated. As discussed above, this can be achieved, if the electron-electron scattering time τ_{ee} is much shorter than the electron-phonon scattering time τ_{ep} . Then the the electronic system reaches thermal equilibrium within a short time scale without the energy leaking into the phonon system. At low temperature, short τ_{ee} between 10^{-10} and 10^{-12} s is obtained for very thin films in the dirty limit. Such films have large sheet resistance $R_{sh} = \rho/d$, where ρ is the resistivity and d the film thickness. In good approximation we can express τ_{ep} as^{52,53}

$$\tau_{ee} \sim \frac{10^{-8} [\text{s}]}{R_{sh}[\Omega/\square] T_c[\text{K}]} \quad (7.3.22)$$

For 10 nm thick Nb films sheet resistances between 12 and $28\Omega/\square$ have been reported.^{54,55} These films typically have $T_c \simeq 5$ K. For 10 nm thick NbN films, $R_{sh} \simeq 70\Omega/\square$ and $T_c \simeq 14$ K.⁵⁶ Fig. 7.15 shows optical micrographs of HEB mixers consisting of a NbN superconducting bridge with submicron dimensions contacted by thick gold pads.

The hot electrons can be cooled down by phonon emission, which escape into the substrate, and/or by the diffusion of hot electrons into normal metal contact pads. Depending on the dominating mechanism one speaks about **phonon** or **diffusion cooling**.

Phonon Cooling: For phonon cooling we have an effective thermal time constant

$$\tau_{eff} = \tau_{ep} + \tau_{es} \ll \tau_{ee} . \quad (7.3.23)$$

For Nb the electron-phonon scattering time can be expressed as⁵⁷

$$\tau_{ep} \sim \frac{10^{-8} [\text{s}]}{T_{ph}^2 [\text{K}^2]} , \quad (7.3.24)$$

⁵²P. Santhanam and D. Prober, Phys. Rev. **B 29**, 3733 (1984).

⁵³E.M. Gershenson, M.E. Gershenson, G.N. Gol'tsman, A.M. Lyul'kin, A.D. Semenov, and A.V. Sergeev, Sov. Phys. Tech. **34**, 195 (1989); see also Sov. Phys. JETP **3**, 505 (1990).

⁵⁴R.J. Schoelkopf, P.J. Burke, D.E. Prober, B. Karasik, A. Skalare, W.R. McGrath, M.C. Gaidis, B. Bumble, and H.G. LeDuc, IEEE Trans. Appl. Supercond. **AS-7**, 3576 (1997).

⁵⁵M. Frommberger, M. Schicke, P. Sabon, K.H. Gundlach, and K.F. Schuster, Proc. 4th Eur. Conf. on Appl. Supercond. **Vol 2**, 667 (1999).

⁵⁶S. Cherednichenko, P. Yagoubov, K. Il'in, G. Gol'tsman, and E. Gershenson, Proc. 8th Int. Symp. on Space Terahertz Technol., Harvard University, Cambridge, MA (1997), p. 245.

⁵⁷D.E. Prober, Appl. Phys. Lett. **62**, 2119 (1993).

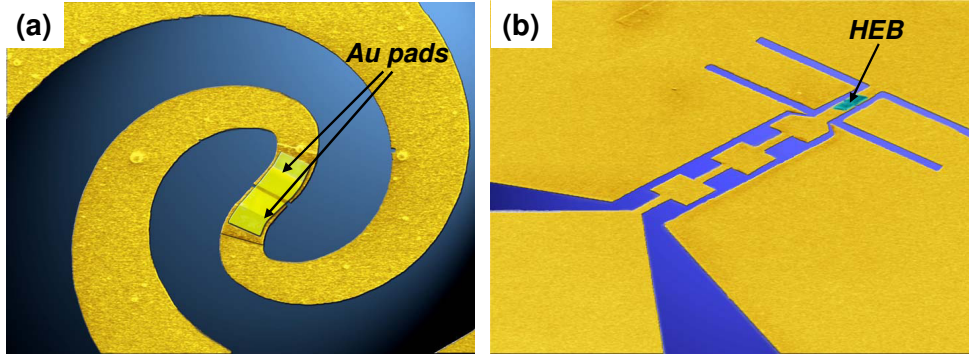


Figure 7.15: Optical micrographs of hot electron bolometer mixers consisting of a NbN superconducting bridge with submicron dimensions (not resolved in the micrograph) contacted by thick gold pads. (a) Spiral antenna and (b) twin slot antenna (micrographs courtesy of SRON, The Netherlands).

where T_{ph} is the phonon temperature. The escape time of phonons into the substrate can be written as⁵⁸

$$\tau_{\text{es}} \sim \frac{4d}{\gamma v_{\text{ph}}} , \quad (7.3.25)$$

where d is the film thickness, v_{ph} the sound velocity in the bolometer material and γ the transmission coefficient of phonons at the bolometer/substrate interface, which includes acoustic mismatch.

To obtain effective phonon cooling the phonons generated in the microbridge by hot electrons should escape as fast as possible into the substrate and not feed back energy into the electron system. This requires $\tau_{\text{es}} \ll \tau_{\text{ep}}, \tau_B$. Here, τ_B is the pair breaking time of phonons with energy larger than 2Δ . These phonons can break up Cooper pairs and feed back their energy into the electron system. According to (7.3.25), $\tau_{\text{es}} \ll \tau_{\text{ep}}$ can be obtained by using very thin films. Then, $\tau_{\text{eff}} \simeq \tau_{\text{ep}}$, i.e. the electron-phonon scattering time determines the speed of the HEB, which in turn determines the IF bandwidth $1/2\pi\tau_{\text{ep}}$ of the mixer. For Nb we have $\tau_{\text{ep}} \simeq 1 \text{ ns}$ giving $1/2\pi\tau_{\text{ep}} \simeq 160 \text{ MHz}$. This is too narrow for radio astronomy applications. Better results are expected for NbN. Here, $\tau_{\text{ep}} \simeq 15 \text{ ps}$ for $d < 5 \text{ nm}$ giving $1/2\pi\tau_{\text{ep}} \simeq 10 \text{ GHz}$.

The SSB conversion gain $1/L_M = P_{\text{IF}}/P_s$ has been calculated from (7.3.21). Assuming that the IF power is coupled into the matched load we obtain⁵⁹

$$\frac{1}{L_M} = \left(\frac{dR}{dT} \frac{I}{G_{\text{eff}}} \right)^2 \frac{P_{\text{lo}} P_s}{2R_L} \frac{1}{1 + \omega_{\text{IF}}^2 \tau_{\text{eff}}^2} . \quad (7.3.26)$$

Here, R_L is the load resistance and G_{eff} is the electron-phonon thermal conductance, which is proportional to the volume V of the bolometer. We see that the conversion gain is increasing with increasing LO power and with larger dR/dT , i.e. with steeper $R(T)$ curves at the superconducting transition.⁶⁰

The mixer noise is dominated by thermal fluctuations of the electron temperature. The contribution of the Nyquist noise is generally smaller and the contribution of the shot noise is negligibly small. The

⁵⁸W.R. McGrath, J.A. Stern, H.H. Javadi, J.R. Cypher, B.D. Hunt, and H.G. LeDuc, IEEE Trans. Magn. **MAG-27**, 2650 (1995).

⁵⁹W.R. McGrath, J.A. Stern, H.H. Javadi, J.R. Cypher, B.D. Hunt, and H.G. LeDuc, IEEE Trans. Magn. **MAG-27**, 2650 (1995).

⁶⁰B.S. Karasik and A.I. Elant'ev, Proc. 6th Int. Symp. on Space Terahertz Technol., Pasadena, CA (1995), p. 229.

ultimate (SSB) mixer noise temperature, when the device is operated at temperatures $T \ll T_c$, can be expressed as⁶¹

$$T_M = (n+2) T_c . \quad (7.3.27)$$

For phonon cooled NbN mixers $n \simeq 1.6$.

Diffusion Cooling: The idea of diffusion cooling is that the hot electrons escape from the absorber into the normal metal contact pads at the ends of the microbridge in a time shorter than the electron-phonon scattering time τ_{ep} .⁶² To achieve this the length L of the bridge should be smaller than the diffusion length $\sqrt{D\tau_{\text{ep}}}$ of the hot electrons within the time scale τ_{ep} . The diffusion constants of 10 nm thick superconducting films were found to range between 0.2 (NbN) and about 10 cm²/s (Al). With $\tau_{\text{ep}} \sim 10^{-10}$ s this results in $L \lesssim 0.1 \mu\text{m}$ at $D = 1 \text{ cm}^2/\text{s}$. The related IF bandwidth is $1/2\pi\tau_{\text{ep}} = 1.6 \text{ GHz}$. Note that the IF bandwidth increases as $1/L^2$, if the length of the microbridge is reduced further.

The theory of diffusion cooled HEB mixers is still a matter of controversy. Because it is a topic of ongoing actual research it will not be discussed in more detail here.

Superconducting Inductance Thermometers

Thermometers based on a resistive read-out have certain disadvantages. For example, biasing of the superconductor in the middle of the resistive transition is required. Furthermore, self-heating due to the bias currents limits the bias current range and in turn the available output voltage. Finally, nonzero resistance always gives rise to Nyquist noise limiting the sensitivity. Therefore, it would be advantageous to use a superconductor as a thermometer in the $R = 0$ state. This can be realized by superconducting inductance thermometers.

The inductance of superconducting circuit elements is given by the sum of the geometric inductance L_{geo} and the kinetic inductance L_{kin} , which results from the inertia of the superconducting charge carriers. For a thin film element the total inductance per square can be expressed as

$$L_{\square} = L_{\text{geo}} + L_{\text{kin}} = \mu_0 \lambda_L \coth(d/\lambda_L) . \quad (7.3.28)$$

Here, d is the film thickness and λ_L the London penetration depth. The latter is strongly temperature dependent following

$$\lambda_L(t) = \frac{\lambda_L(0)}{\sqrt{1-t^4}} , \quad (7.3.29)$$

where $t = T/T_c$ is the reduced temperature. For thin films ($d/\lambda_L \lesssim 0.4$) the kinetic inductance is dominant. Approximating $\coth x \simeq 1/x$ we obtain

$$L_{\square} \simeq L_{\text{kin}} \simeq \mu_0 \frac{\lambda_L^2}{d} = \mu_0 \frac{\lambda_L^2(0)}{d(1-t^4)} . \quad (7.3.30)$$

Then

$$\frac{dL_{\square}}{L_{\square}dT} \simeq \frac{dL_{\text{kin}}}{L_{\text{kin}}dT} \simeq \frac{4t^3}{(1-t^4)T_c} . \quad (7.3.31)$$

⁶¹B.S. Karasik and W.R. McGrath, Proc. 9th Int. Symp. on Space Terahertz Technol., Pasadena, CA (1998), p. 73.

⁶²D.E. Prober, Appl. Phys. Lett. **62**, 2119 (1993).

We see that dL_{\square}/dT becomes larger when T approaches T_c , e.g. $\Delta L_{\square}/L_{\square} \simeq 18.5\Delta T/T_c$ at $t = 0.95$.

The strong temperature dependence of the kinetic inductance close to T_c results from the strong temperature dependence of the Cooper pair density in this temperature regime. It can be used for the realization of sensitive inductance thermometers. For the measurement of the inductance value sensitive SQUID sensors can be used. Although the kinetic inductance thermometers have not yet been fully optimized, a noise equivalent power of a few times $10^{-11}\text{W}/\sqrt{\text{Hz}}$ and a responsivity of a few times 10^6V/W have been achieved at $t = 0.8$ with a niobium device.⁶³

⁶³J.E. Sauvageau, D.G. McDonald, E.N. Grossman, *Superconducting kinetic inductance radiometer*, IEEE Trans. Magn. **MAG-27**, 2757-2760 (1991).

7.4 Superconducting Particle and Single Photon Detectors

With increasing quantum energy of the incoming radiation, the signal due to individual photons may become larger than the noise floor making the detection of single photon events possible. This is in contrast to the situation discussed in sections 7.2 and 7.3, where we have discussed the case that single photon events cannot be resolved and the detector only can measure the average number of photons absorbed per unit of time.

If for sufficiently large photon energy (e.g. in the visible, UV or x-ray regime) the signal generated by the absorption of a single photon exceeds the noise level, a measurable electrical signal is generated by the absorption of every single photon. Then, if the time interval between the incoming photons is larger than the characteristic time constant of the detector, one can use the detector to count the number of absorbed photons (photon counting mode). We also can average over the individual signal pulses to obtain the average rate of incoming photons (photon integrating mode). If we are able to resolve the dependence of the signal amplitude on the energy of the absorbed photon, we even can use the detector to determine the energy of each incoming photon. That is, we can use the detector as a radiation spectrometer. In this case for thermal detectors one usually refers to a ***microcalorimeter*** rather than a bolometer. Of course the various operation modes cannot only be applied to photon detection but also to the detection of particles such as electrons, protons, neutrons, α -particles, etc. which deposit their kinetic energy in the detector on absorption. Here, the particle absorption process also generates high energy excitations in the absorber material, which quickly relax down thereby heating up the electron and phonon systems in a similar way as during photon absorption.

At present two main types of high energy resolution superconducting photon/particle detectors exist. The first type, the ***superconducting tunnel junction detector (STJD)***, is a non-thermal detector. It extracts the charge carriers generated by the photon/particle absorption before they thermalize with the lattice. The other type, the ***microcalorimeter***, is a thermal detector. It measures a temperature variation generated by the photon/particle absorption. Both detector types are briefly addressed in the following subsections. Until today, superconducting particle/photon detector and spectrometers have been developed into a powerful technology. In particular, cryogenic spectrometers are beginning to enable new types of measurements. Spectrometers based on superconducting tunnel junctions (STJ) and transition edge sensors (TES) already have been used in various applications such as high sensitivity astronomical imaging in the optical to soft x-ray regime or x-ray microanalysis of biological and industrial materials.^{64,65,66,67,68,69}

7.4.1 Thermal Photon and Particle Detectors: Microcalorimeters

The operation principle of a thermal single photon/particle detector is the same as that described in section 7.3. The absorption of a single photon or particle heats up the sensor volume and the temperature rise is measured by a sensitive thermometer. If a transition-edge bolometer is used as thermometer the detectors are referred to as ***transition edge sensors (TES)***. We note that in contrast to the antenna-coupled microbolometers we do not need a collecting antenna structure, because the wavelength of the detected photons (visible to x-ray regime) and particles is smaller than the detector size. The incoming photon/particle is rather absorbed directly in the sensor volume, which may be covered by a layer of high

⁶⁴D. Twerenbold, *Cryogenic particle detectors*, Rep. Prog. Phys. **59**, 349-426 (1996).

⁶⁵K. D. Irwin, G. C. Hilton, D. A. Wollman, and J. M. Martinis, Appl. Phys. Lett. **69**, 1945 (1996).

⁶⁶F. Scott Porter, Nucl. Instrum. Methods Phys. Res. A **520**, 354 (2004).

⁶⁷D. A. Wollman, K. D. Irwin, G. C. Hilton, L. L. Dulcie, D. E. Newbury, and J. M. Martinis, J. Microsc. **188**, 196 (1997).

⁶⁸S. Friedrich et al., IEEE Trans. Appl. Supercond. **AS-7**, 3383-3386 (1997).

⁶⁹A. Peacock, P. Verhoeve, N. Rando, A. van Dordrecht, B. G. Taylor, C. Erd, M. A. C. Perryman, R. Venn, J. Howlett, D. J. Goldie, J. Lumley, and M. Wallis, *Single optical photon detection with a superconducting tunnel junction*, Nature **381**, 135-137, (1996).

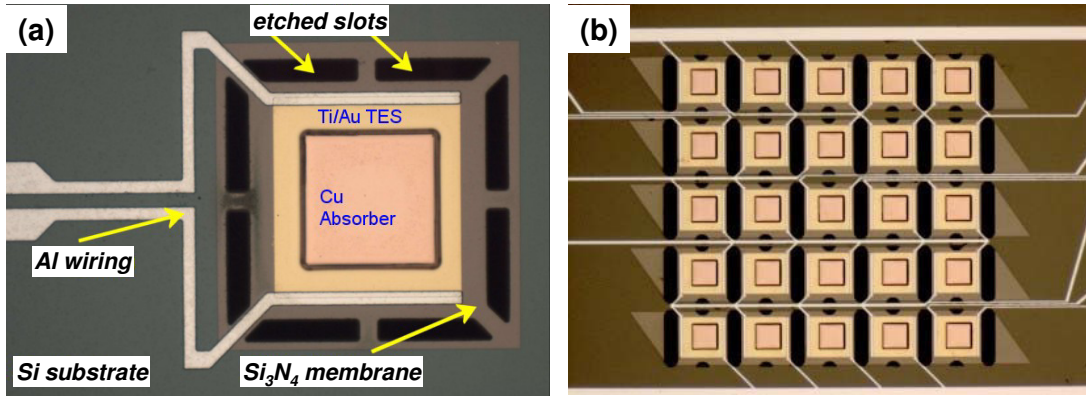


Figure 7.16: Optical micrographs of (a) a single TES and (b) a 5x5 array of TES based on Cu absorbers and Ti/Au transition-edge sensors (micrographs courtesy of SRON, The Netherlands).

absorptivity $\varepsilon \sim 1$. Note that the counting rate of the detectors is limited by the thermal time constant, which should be kept small by reducing the heat capacity of the detector.

As discussed in section 7.3.2 the energy resolution of microcalorimeters using transition edge sensors is ultimately limited by thermodynamic energy fluctuations in the detector due to the random exchange of phonons through the thermal link which connects the detector to the heat sink at temperature T_0 (phonon noise), and the Nyquist noise of the transition edge sensor. Photon noise and $1/f$ noise usually are negligible. At low temperatures in most cases the thermal noise is limiting the energy resolution. With the noise equivalent power $\text{NEP} = \sqrt{4k_B T_0^2 G}$ (for $\varepsilon = 1$, compare (7.3.12)) of the thermal fluctuation noise we obtain with the thermal time constant $\tau = C/G$ the energy resolution $\Delta E = \text{NEP} \sqrt{\tau}$ (i.e. we set the bandwidth equal to $1/\tau$) to⁷⁰

$$\Delta E_{\text{FWHM}} = 2.355 \sqrt{4k_B T_0^2 C} . \quad (7.4.1)$$

Here, the factor $2.355 = 2\sqrt{2\ln 2}$ converts from one standard deviation to FWHM. As an example, for $T_0 = 0.1$ K and $C = 10^{-12}$ J/K, corresponding to a detector volume of $100 \mu\text{m}^3$ for a specific heat capacity $c_v \sim 1 \text{ J/m}^3 \text{ K}$, we expect $\Delta E_{\text{FWHM}} \simeq 10$ eV. We see that we can improve the energy resolution by reducing T_0 and C . However, in practice this is difficult to do. Firstly, a reduction of T_0 increases the cryogenic effort in particular when going to $T < 0.1$ K. Secondly, C cannot be reduced arbitrarily by reducing the detector volume because a finite absorber volume is required to have a sufficient quantum efficiency of the detector. Thirdly, a reduction in T_0 results in a strong reduction of G (typically, due to the Kapitza boundary resistance between heat sink and sensor we have $G \propto T^3$) thereby increasing τ and hence decreasing the maximum counting rate of the detector. Therefore, one has to make a trade-off between energy resolution, cryogenic effort and counting rate. Note that the energy resolution of a detector can be derived from the NEP. For example, as already discussed in sections 7.2 and 7.3 the NEP of direct detectors and thermal detectors can be as low as 10^{-18} W/ $\sqrt{\text{Hz}}$. If such detector has a thermal time constant $\tau \simeq 1$ ms, this detector is capable of resolving an energy of a few times 10^{-19} J. This is just the energy of a soft x-ray photon with $\hbar\omega \simeq 1$ eV or a particle with the same kinetic energy.

Microcalorimeters based on transition-edge sensors (TES) positioned on Si₃N₄ membranes and using low noise SQUID preamplifier for signal amplification have been successfully fabricated and tested.

⁷⁰We also can use the following intuitive argumentation: The exchange of phonons produces random fluctuations in the energy content of the absorber and consequently fluctuations in the temperature. These fluctuations can be quantified by the fact that the effective number of phonons in the absorber is of the order C/k_B . The energy of a typical phonon is $k_B T$ and the rms fluctuation of one phonon is of the order of one, therefore the mean-squared energy fluctuation in the absorber is $(k_B T)^2 C/k_B$, i.e. $\langle \Delta E_{\text{rms}}^2 \rangle \sim k_B T^2 C$.

Usually materials with T_c well below 1 K such as Mo/Cu or Ti/Au are used. An energy resolution of a few eV at a counting rate of about 1000 counts per second at 1 keV photon energy have been reported for an effective collection area of 4 mm² and $T = 0.1$ K. These detectors are well suited for applications in X-ray microanalysis.^{71,72,73,74} Fig. 7.16 shows optical micrographs of a single TES and an array of TES based on Cu absorbers and Ti/Au transition-edge sensors. As an example, Fig. 7.17 shows the x-ray spectrum of an ⁵⁵Fe source recorded by a microcalorimeter based on a Mo/Cu transition edge sensor. From the measured spectrum an energy resolution of 4.5 ± 0.1 eV FWHM at a photon energy of 5.9 keV is determined. Successive design changes improved the measured energy resolution of the sensors from 4.5 eV FWHM to 2.4 eV.⁷⁵ Sensors with this energy resolution are well matched to applications in x-ray astrophysics and terrestrial materials analysis. The best energy resolutions (at about 6 keV) obtained so far with TESs are more than 30 times better than ubiquitous silicon-lithium sensors.^{76,77} Despite this impressive performance, the resolution of TESs has not yet reached the predicted theoretical limits and further improvements are expected.

Furthermore, superconducting transition-edge sensors for the wideband detection of individual photons from the mid infrared through the optical into the far ultraviolet have been fabricated.^{78,79} Square-shaped ($\sim 20 \mu\text{m}^2$ on a side) tungsten transition-edge sensors have been shown to be able to detect single photon events above a threshold of 0.3 eV with an energy resolution of 0.15 eV FWHM, and with a rise and fall time of 0.5 and 60 μs , respectively. The W films have a sharp superconducting transition at about 80 mK with a transition width of less than 1 mK. The Si substrate is maintained at an operating temperature of about 40 mK, half of the W transition temperature, via the Joule heating produced by the voltage bias. The intrinsic stability of the voltage bias is due to ***negative electrothermal feedback***,^{80,81} where an increase in sensor temperature and thus an increase in sensor resistance causes a decrease in Joule heating (V^2/R). Similarly, a decrease in sensor temperature causes an increase in Joule heating. This mode of operation leads to substantial improvements in resolution, linearity, dynamic range, and count rate. The improvement of the energy resolution is due to the fact that the electrothermal feedback suppresses the

⁷¹K. D. Irwin, G. C. Hilton, John M. Martinis, S. Deiker, N. Bergren, S. W. Nam, D. A. Rudman, and D. A. Wollman, *A Mo-Cu superconducting transition-edge microcalorimeter with 4.5 eV energy resolution at 6 keV*, Nucl. Instr. Meth. A **444**, 184-187 (2000).

⁷²D.A. Wollman, S.W. Nam, D.E. Newbury, G.C. Hilton, K.D. Irwin, N.F. Bergren, S. Deiker, D.A. Rudman, J.M. Martinis, *Superconducting Transition-Edge-Microcalorimeter X-ray Spectrometer with 2 eV Energy Resolution at 1.5 keV*, Nucl. Instr. Meth. A **444**, 145-150 (2000).

⁷³D.A. Wollman, S.W. Nam, G.C. Hilton, K.D. Irwin, N.F. Bergren, D.A. Rudman, J.M. Martinis, D.E. Newbury, *Microcalorimeter Energy-Dispersive Spectrometry Using a Low Voltage Scanning Electron Microscope*, J. Microscopy **199**, 37-44 (2000).

⁷⁴B. Cabrera, R. M. Clarke, P. Colling, A. J. Miller, S. Nam, and R. W. Romani, *Detection of single infrared, optical, and ultraviolet photons using superconducting transition edge sensors*, Appl. Phys. Lett. **73**, 735-737 (1998).

⁷⁵J. N. Ullom, J. A. Beall, W. B. Doriese, W. D. Duncan, L. Ferreira, G. C. Hilton, K. D. Irwin, C. D. Reintsema, and L. R. Vale, *Optimized transition-edge x-ray microcalorimeter with 2.4 eV energy resolution at 5.9 keV*, Appl. Phys. Lett. **87**, 194103 (2005).

⁷⁶W. M. Bergmann Tiest, H. F. C. Hoevers, M. P. Bruijn, W. A. Mels, M. L. Ridder, P. A. J. de Korte, and M. E. Huber, *AIP Conf. Proc.* **605**, 199 (2002).

⁷⁷C. K. Stahle, R. P. Brekosky, E. Figueroa-Feliciano, F. M. Finkbeiner, J. D. Gygax, M. J. Li, M. A. Lindeman, F. Scott Porter, and N. Tralshawala, *Proc. SPIE* **4140**, 367 (2000).

⁷⁸B. Cabrera, R. Clarke, P. Colling, A. Miller, S. Nam, R. Romani, *Detection of single infrared, optical, and ultraviolet photons using superconducting transition edge sensors*, Appl. Phys. Lett. **73**, 735 (1998).

⁷⁹J.C. Mather, *Super photon counters*, Nature **401**, 654-656 (1999).

⁸⁰K. D. Irwin, *An application of electrothermal feedback for high resolution cryogenic particle detection*, Appl. Phys. Lett. **66**, 1998 (1995).

⁸¹K. D. Irwin, G. C. Hilton, D. A. Wollman, and John M. Martinis, *X-ray detection using a superconducting transition-edge sensor microcalorimeter with electrothermal feedback*, Appl. Phys. Lett. **69**, 1945-1947 (1996).

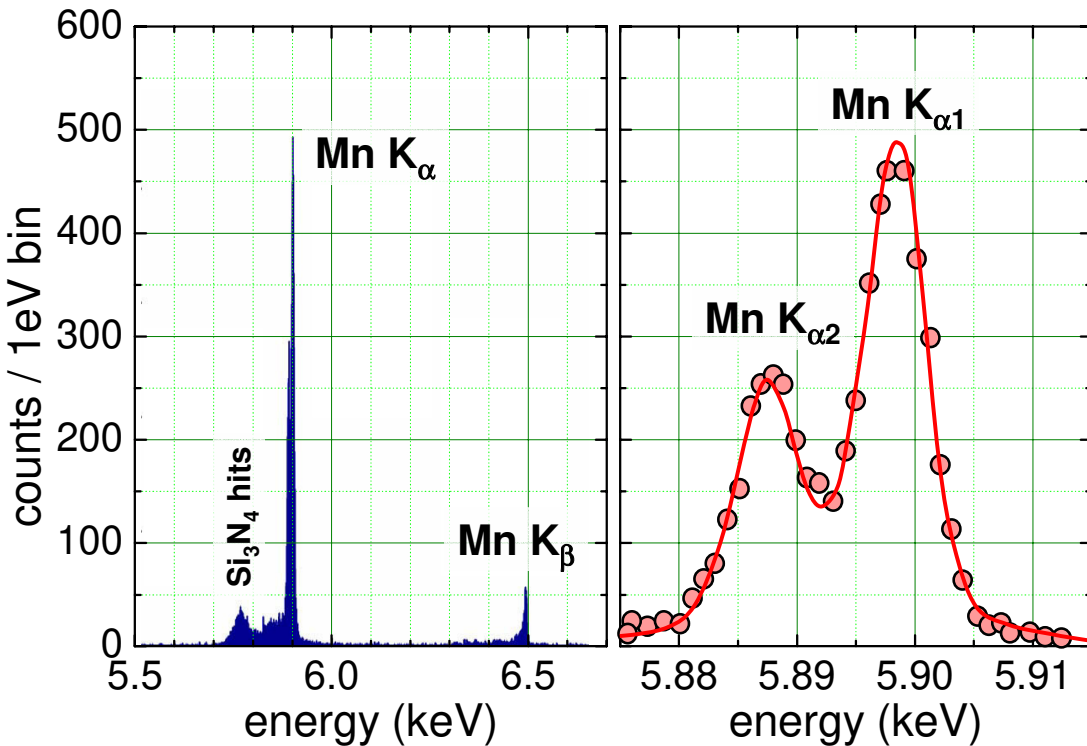


Figure 7.17: Spectrum of an ^{55}Fe source recorded by a microcalorimeter based on a Mo/Cu transition edge sensor. (a) Wide spectrum (b) a weighted least-squares fit of the Mn- K_{α} x-rays to a convolution of the theoretical line profile and a Gaussian instrument response. An instrument resolution of 4.5 ± 0.1 eV FWHM is determined (according to K.D. Irwin *et al.*, Nucl. Instr. Meth. A **444**, 184-187 (2000)).

Nyquist noise for frequencies smaller than $1/\tau_{\text{eff}}$, where τ_{eff} is the effective thermal time constant.^{82,83,84} The achieved energy resolution of ~ 0.15 eV FWHM is within a factor of 2 of the prediction based on intrinsic thermodynamic fluctuations. The quantum efficiency (the transmission coefficient times the absorption efficiency) of the W films has not been measured directly, however, from published data a value of about 50% over the wavelength range from $1\mu\text{m}$ to 350 nm dropping to below 10% for longer wavelengths is expected.

In order to achieve high energy resolution, the microcalorimeters have to be operated at low temperatures (typically below 0.1 K). Furthermore, the thermal conductance coupling the sensor volume to the heat sink has to be small resulting in large thermal time constants of the order of $100\mu\text{s}$. This limits the count rates of the microcalorimeters to a few 1000/s. These difficulties can be partly overcome by superconducting tunnel junction detectors (STJDS) discussed in the next subsection. STJDS have the potential to count at significantly higher rate because of their much faster pulse decay time. In addition, STJDS can be operated at a somewhat higher temperature of about 300-500 mK without degradation of detector performance and do not require temperature stabilization in this range. This facilitates the implementation and operation of these detectors.

⁸²By electrothermal feedback the energy resolution is improved by a factor of about $1/\sqrt{T_0\beta}$ below what is called the thermodynamic limit ($\Delta E = \sqrt{4k_B T_0^2 C}$). Here, the dimensionless quantity $T_0\beta = (T_0/R_0)(dR/dT)$ measures the sharpness of the resistive transition of the superconducting transition edge sensor.

⁸³J. N. Ullom, W. B. Doriese, G. C. Hilton, J. A. Beall, S. Decker, W. D. Duncan, L. Ferreira, K. D. Irwin, C. D. Reintsema, and L. R. Vale, *Characterization and reduction of unexplained noise in superconducting transition-edge sensors*, Appl. Phys. Lett. **84**, 4206-4208 (2004).

⁸⁴J. C. Mather, *Bolometer noise: nonequilibrium theory*, Appl. Opt. **21**, 1125 (1982).

7.4.2 Superconducting Tunnel Junction Photon and Particle Detectors

The first published experimental result of using superconducting tunnel junctions as particle detectors is from **Wood** and **White** in 1969, who detected 5.1 MeV α -particles from a ^{239}Pu source with a Sn/SnO₂/Sn tunnel junction.⁸⁵ Similar investigations were carried out by **Kurakado** and **Mazaki** about ten years later, who presented for the first time a pulse height spectrum of the α -particle energy loss in a superconducting tunnel junction.⁸⁶ Whereas in thermal photon/particle detectors the temperature increase due to an absorbed photon/particle is detected, the *superconducting tunnel junction detectors (STJDs)* are based on a non-thermal detection scheme. The incoming radiation generates an excess number N of quasiparticles, which is proportional to the energy E of the absorbed photon/particle. Detailed calculations for Nb show that^{87,88}

$$N = \frac{E}{1.74 \Delta} = \frac{E}{\varepsilon}, \quad (7.4.2)$$

where Δ is the energy gap of the superconducting material and ε the average energy required to create a single quasiparticle. This result is quite close to $N = E/\Delta$ what is expected naively, since a minimum energy of 2Δ is required to break up a Cooper pair thereby generating two quasiparticle excitations. Of course, in reality some energy is lost into other channels what is taken into account by the factor 1.74.

In order to determine the photon/particle energy, the excess quasiparticles have to be counted within their lifetime. This can be done by measuring the increase δI of the quasiparticle tunneling current due to the generated excess quasiparticles. The integral $\int \delta I dt$ is proportional to the number N of the generated excess quasiparticles, which in turn is proportional to the energy of the absorbed photon or particle. The detection scheme of a STJD is completely analogous to a semiconductor *pn*-junction. In the latter, the absorption of a photon/particle generates electron-hole pairs which are separated in the electric field of the *pn*-junction and counted by measuring the integral of the radiation induced excess current. The operation principle of the SIS tunnel junction detector is schematically shown in Fig. 7.18. The incoming photon or particle is absorbed in the junction electrodes and generates a large number of electron and hole like excess quasiparticles by breaking up Cooper pairs. The initially highly excited quasiparticles quickly relax down to the band edge by electron-electron interaction (cf. Fig. 7.12 and related discussion). As for the semiconductor *pn*-junction these excess quasiparticles are separated via the voltage drop across the tunneling barrier and counted by measuring the time integral $\int \delta I dt$ of the excess quasiparticle tunneling current.

The electronic readout of STJDs can be provided by simple FET-based charge or current sensitive preamplifiers and conventional spectroscopy shaping amplifiers. In order to measure the electrical signal from a particle interaction, the junction is usually biased at $V < 2\Delta/e$. The signal current develops a signal voltage V_s across the parallel combination of the bias resistor R_B and the amplifier input resistance R_i in parallel with the dynamic resistance R_d of the STJD at the bias point and with the junction capacitance C_J and stray plus preamplifier input capacitance C_i (see Fig. 7.19). The signal is amplified with either a voltage- or charge-sensitive preamplifier, usually with a FET input, although a SQUID amplifier can be used instead. Note that the Josephson current is reduced to zero by applying a magnetic field parallel to the tunneling barrier.

⁸⁵G.H. Wood, B.L. White, *Pulses induced in tunneling currents between superconductors by alpha-particle bombardment*, Appl. Phys. Lett. **15**, 237 (1969); Can. J. Phys. **51**, 2032 (1973).

⁸⁶M. Kurakado and H. Mazaki, *Quasiparticle excitation in a superconducting tunnel junction by α particles*, Phys. Rev. **B 22**, 168 (1980); Nucl. Instrum. Methods **185**, 141 (1981); Nucl. Instrum. Methods **185**, 149 (1981).

⁸⁷M. Kurakado, Nucl. Instrum. Methods Phys. Res. **196**, 275-277 (1982).

⁸⁸N. Rando, A. Peacock, A. v. Dordrecht, C. Foden, R. Engelhardt, B. G. Taylor, P. Gare, J. Lumley, and C. Pereira, Nucl. Instrum. Methods Phys. Res. **313**, 173 (1992).

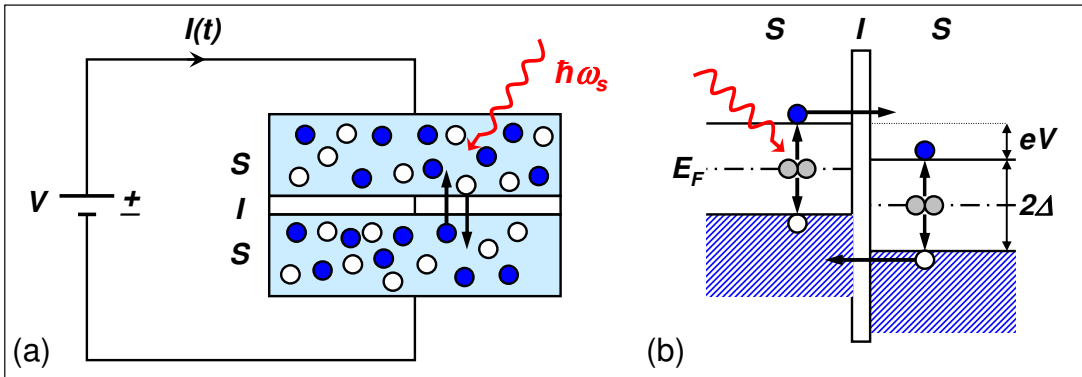


Figure 7.18: Functional principle of a superconducting tunnel junction detector. (a) A large number of electron- (full circles) and hole-like quasiparticles (open circles) are generated by breaking up Cooper pairs (shaded circles) on absorption of a photon or particle. (b) Schematic illustration of the energy diagram of a SIS junction with applied voltage V . Note that the energy of the electrons and holes is plotted up- and downwards from the Fermi level, respectively. The electron- and hole-like quasiparticles tunnel from right to left and left to right, respectively, resulting in a charge transport in the same direction.

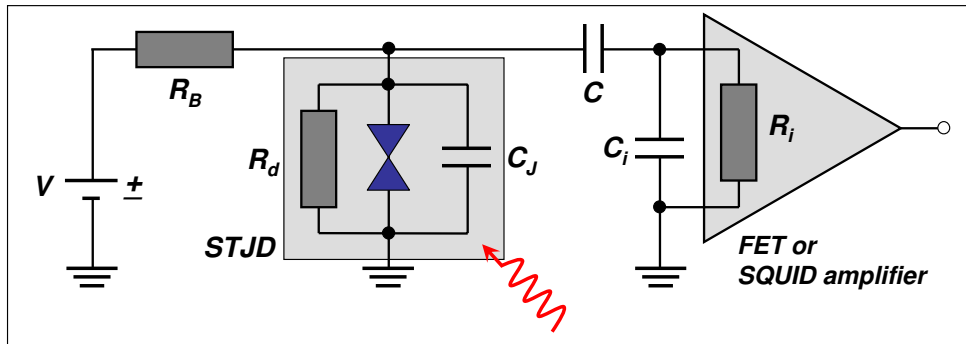


Figure 7.19: Simplified circuit diagram of a superconducting tunnel junction detector (STJD). The Josephson current through the idal Josephson element is reduced to zero by a magnetic field.

Energy Resolution

The dominating process limiting the energy resolution of STJDs is the statistical fluctuations of the number N of quasiparticles generated after the absorption of a photon or particle. The statistical fluctuation of the generated excess quasiparticle number is \sqrt{FN} , where F is the Fano factor⁸⁹ describing the statistical distribution in the number of quasiparticles. For example, for a homogeneous niobium tunnel junction, Monte Carlo simulations predict $F \simeq 0.2$. With $N = E/1.74\Delta = E/\epsilon$ the energy resolution is given by

$$\frac{\Delta E}{E} = \frac{\sqrt{FN}}{N} = \sqrt{\frac{F}{N}} = \sqrt{\frac{F\epsilon}{E}} \quad \text{or} \quad \Delta E_{\text{FWHM}} = 2.355 \sqrt{F\epsilon E}. \quad (7.4.3)$$

Here, the factor $2.355 = 2\sqrt{2\ln 2}$ converts from one standard deviation to FWHM. There may be other factors limiting the energy resolution such as (i) an insufficient counting of the generated excess quasiparticles by tunneling, (ii) spatial inhomogeneities of the detector, (iii) diffusion losses of quasiparticle into the leads or (iv) amplifier noise. Assuming that these processes result in statistically independent

⁸⁹U. Fano, *Ionization yield of rations: II. the fluctuations of the number of ions*, Phys. Rev. **72**, 26-29 (1947).

fluctuations of the number of counted excess quasiparticles, the energy resolution can be written as

$$\frac{\Delta E}{E} = \frac{1}{E} \sqrt{\Delta E_{\text{intr}}^2 + \Delta E_{\text{tun}}^2 + \Delta E_{\text{inh}}^2 + \Delta E_{\text{diff}}^2 + \Delta E_{\text{ampl}}^2 + \dots} . \quad (7.4.4)$$

Here, ΔE_{intr} is the intrinsic energy resolution given by (7.4.3).

We see that the intrinsic energy resolution increases on increasing N or, equivalently, on decreasing the average energy ε required to generate a single charge excitation. This is the basic advantage of STJDS compared to semiconductor *pn*-junction detectors. For the latter the average energy ε required for the generation of an extra electron-hole pair is given by the semiconductor energy gap E_g , which is of the order of 1 eV. In contrast, for STJDS ε is of the order of the superconducting energy gap Δ , that is typically 1 meV for most metallic superconductors. Therefore, at the same photon/particle energy, N is much larger for superconducting detectors resulting in a much better energy resolution. For comparison, the following Table summarizes the average energies required for the generation of elementary excitations in different detector systems.

<i>detector type</i>	<i>excitation</i>	ε
gas proportional counter	electron-hole pair	25-35 eV
scintillator	photon	≈ 3 eV
semiconductor detector	electron-hole pair	3.65 eV (Si), 2.85 eV (Ge)
STJD	quasiparticle	2.6 meV (Nb), 1.3 meV (Ta)
superfluid ${}^4\text{He}$	roton	0.75 meV
superfluid ${}^3\text{He}$	quasiparticle	$0.14 \mu\text{eV}$

Taking into account the statistics of the tunneling process we can rewrite (7.4.3) as

$$\Delta E_{\text{FWHM}} = 2.355 \sqrt{(F + F') \varepsilon E} . \quad (7.4.5)$$

Here we have introduced the quantity F' to account for the statistical fluctuations introduced by the tunneling process (tunneling is of course a statistical process). F' can be estimated by Monte-Carlo simulations taking into account that the quasiparticles can tunnel back and forth through the tunneling barrier several times during the lifetime. For a symmetric junction, $F' = 1 + 1/n$ is found, where n is the average number of times each quasiparticle tunnels through the barrier.^{90,91,92} As discussed

⁹⁰To estimate the effect of multiple tunneling on statistical spread we assume that each quasiparticle recombines after some time t which has a probability distribution $P(t) = \tau_R^{-1} \exp(-t/\tau_R)$, where τ_R is the recombination time. During the time interval t this quasiparticle tunnels n times. We also assume that the probability distribution for n given t is Poissonian. To get the distribution for n alone, we integrate over the lifetime distribution to obtain

$$P(n) = \int_0^\infty \frac{e^{-t/\tau_R}}{\tau_R} \frac{e^{-t/\tau_{\text{tun}}}}{n!} \left(\frac{t}{\tau_{\text{tun}}} \right)^n dt = \frac{\tau_R^n \tau_{\text{tun}}}{(\tau_{\text{tun}} + \tau_R)^{n+1}} ,$$

where τ_{tun} is the tunneling time discussed below. $P(n)$ has mean $\bar{n} = \tau_R/\tau_{\text{tun}}$ and variance $\sigma_n^2 = \bar{n}(\bar{n}+1)$. Since the tunneling and recombination events are uncorrelated, we can add the variances of the generation and the tunneling process. For the tunneling process we obtain

$$\frac{\sqrt{N_{\text{tun}}}}{N_{\text{tun}}} = \frac{\sqrt{N\bar{n}(\bar{n}+1)}}{\bar{n}N} = \frac{\sqrt{N}}{N} \sqrt{1 + \frac{1}{\bar{n}}} .$$

⁹¹C. A. Mears, S. E. Labov, and A. T. Barfknecht, *Energy-resolving superconducting x-ray detectors with charge amplification due to multiple quasiparticle tunneling*, Appl. Phys. Lett. **63**, 2961 (1993).

⁹²D. J. Goldie, P. L. Brink, C. Patel, N. E. Booth, and G. L. Salmon, *Statistical noise due to tunneling in superconducting tunnel junction detectors*, Appl. Phys. Lett. **64**, 3169 (1994).

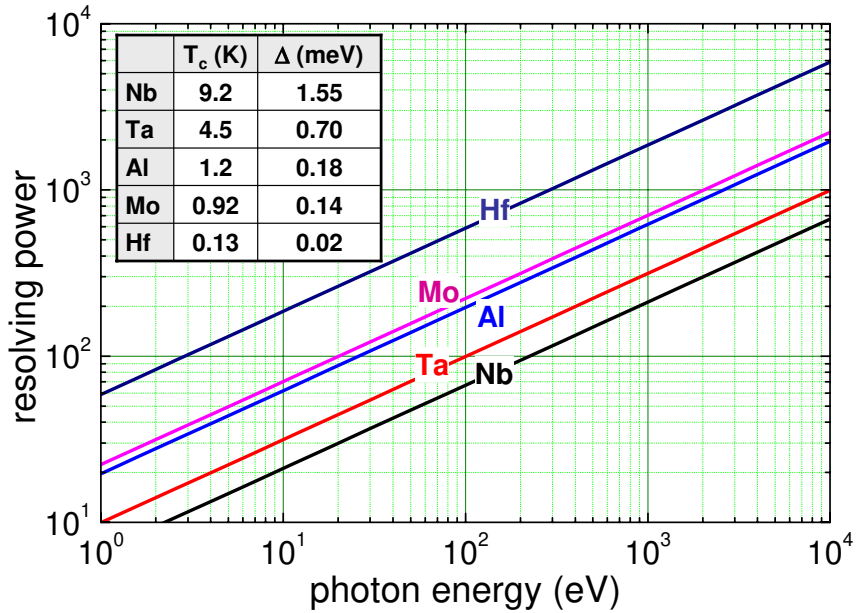


Figure 7.20: Energy resolving power of STJJs fabricated from different materials. For the calculation $F + F' = 1.5$ has been used.

below, the average number n of tunneling events per quasiparticle can be estimated by dividing the observed quasiparticle lifetime by the average tunneling time, that is, by the average time it takes each quasiparticle to tunnel. Typically, $n < 5$ is realized in STJJs. Note that for $n < 1$ only a fraction of the generated quasiparticles is counted within their lifetime. In this case the energy resolution is degraded considerably by the tunneling process.

Often the energy resolving power $R = E/\Delta E$ is used. For a symmetric tunnel junction detector the energy or wavelength resolving power R limited by the statistics of charge carrier generation (Fano noise) and tunneling (tunneling noise) is given by

$$R = \frac{1}{2.355} \sqrt{\frac{E}{(F + F') \epsilon}} . \quad (7.4.6)$$

This expression shows that the achievable relative spectral resolution of STJJs depends on the material of the electrodes (via ϵ) and other specifics of the STJD such as the tunneling time (via F'). Roughly, R is of order one part in ten to one part in a hundred in the near-UV, varying as the square root of the photon energy. Fig. 7.20 shows the resolving power of symmetric superconducting tunnel junction detectors fabricated from different materials.

By arranging a number of STJ devices into a two dimensional array, a true “three dimensional” detector can be constructed, whose output is not just the number of photons registered in each pixel of the image, but their distribution in energy throughout the UV, visible and near-IR. This unique ability to discriminate photons in wavelength without the use of filters or dispersive elements obviously comes at a price. In order to be able to distinguish the relatively feeble charges generated by the STJD above the thermal background noise, it is necessary that such devices operate at extremely low temperatures, typically below 1 K.

Quasiparticle Counting by Tunneling

Since the pioneering work by **Giaever** it is well known that the quasiparticle density can be probed by an SIS junction.^{93,94} The principle of STJDs is based on the counting of the number of excess particles generated by the incident radiation via tunneling. Since insufficient counting of the generated excess quasiparticles results in a degradation of the energy resolution, the STJDs have to be designed for optimizing the quasiparticle counting process.

The main tunneling processes in a SIS tunnel junction are sketched in Fig. 7.21. Process A describes the tunneling of a quasiparticle from superconductor 1 (S1) to superconductor 2 (S2). The probability of this process is large due to the high density of states in S1 and the large density of available empty states in S2. Process B is more complicated because it involves a Cooper pair state. In this context we emphasize that a quasiparticle excitation $|k, \sigma\rangle$, with k the momentum and σ the spin of the quasiparticle, can be electron- or hole-like with the probabilities given by the coherence factors u_k and v_k .⁹⁵ In process B a state $|k_2 \uparrow\rangle$ in S2 forms a Cooper pair with a state $| - k_2 \downarrow\rangle$, which is provided by tunneling. In S1 a state $|k_1 \uparrow\rangle$ is left. That is, in total a quasiparticle excitation is transferred from S2 to S1, however, with the total charge e transferred from S1 to S2 due to the transfer of the involved Cooper pair from S1 to S2. Process B can be viewed as the tunneling of a hole-like excitation from S2 to S1. Process B has large probability due to the high density of states in S2 and the large density of available states in S1. The processes C and D are analogous to A and B, however, with much smaller probabilities. The existence of the two processes A and B (and the analogous processes C and D) means that tunneling in itself is not a loss mechanism. Once a quasiparticle excitation had tunneled from S1 to S2 (process A) it can tunnel back again (process B) resulting in an additional charge transfer in the same direction. This occurs for either polarity of the voltage bias. That is, in contrast to a semiconductor *pn*-junction, where the charge associated with the electron-hole pair is counted only once, in a SIS tunnel junction the quasiparticle excitation can be counted several times. As will be discussed in more detail below, the counting factor depends on the ratio of the quasiparticle lifetime and the tunneling time.

Summing up the contributions of the different tunneling processes results in the total tunneling current

$$I = \frac{1}{eR_N} \int_{-\infty}^{+\infty} \rho_1(E) \rho_2(E + eV) [f_1(E) - f_2(E + eV)] dE . \quad (7.4.7)$$

Here, $f(E)$ is the Fermi function and

$$\begin{aligned} \rho(E) &= \frac{|E|}{\sqrt{E^2 - \Delta^2}} && \text{for } |E| \geq \Delta \\ \rho(E) &= 0 && \text{for } |E| < \Delta \end{aligned} \quad (7.4.8)$$

⁹³I. Giaever, *Energy Gap in Superconductors Measured by Electron Tunneling*, Phys. Rev. Lett. **5**, 147 (1960).

⁹⁴I. Giaever, *Electron tunneling and superconductivity*, Rev. Mod. Phys. **46**, 245 (1974).

⁹⁵The quasiparticle creation and annihilation operators $\beta_{k\sigma}^+$ and $\beta_{k\sigma}$ are related to the electron creation and annihilation operators $b_{k\sigma}^+$ and $b_{k\sigma}$ via the Bogoliubov-Valentin transformations

$$\begin{aligned} b_{k\uparrow} &= u_k^* \beta_{k\uparrow} + v_k \beta_{-k\downarrow}^+ \\ b_{-k\downarrow}^+ &= -v_k^* \beta_{k\uparrow} + u_k \beta_{-k\downarrow}^+ . \end{aligned}$$

Due to the fermionic nature of the electrons, the operators $b_{k\sigma}^+$ and $b_{k\sigma}$ have to satisfy canonical anti-commutation relations. It can be shown that the new operators $\beta_{k\sigma}^+$ and $\beta_{k\sigma}$ also satisfy the anti-commutation relations if $|u_k^2| + |v_k^2| = 1$. For example, the operator $\beta_{-k\downarrow}^+ = u_k^* b_{-k\downarrow}^+ + v_k^* b_{k\uparrow}$ creates an electron in the state $| - k \downarrow\rangle$ with the amplitude u_k^* and at the same time annihilates an electron in state $|k \uparrow\rangle$ with amplitude v_k^* . The calculation of the amplitudes shows that for $k \gg k_F$ we have $u_k \simeq 1, v_k \simeq 0$, i.e. here the quasiparticle excitations effectively are “electrons”, whereas for $k \ll k_F$ we have $u_k \simeq 0, v_k \simeq 1$, i.e. here the quasiparticle excitations effectively are “holes”.

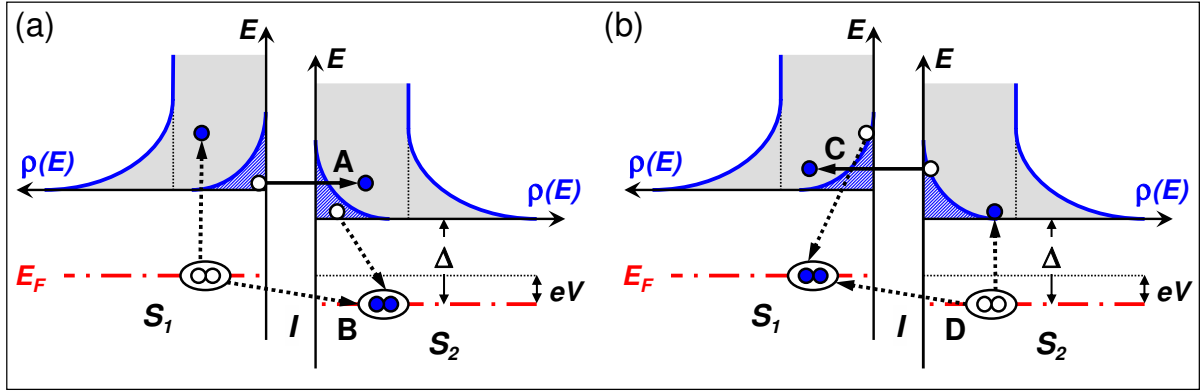


Figure 7.21: Tunneling processes in a superconducting tunnel junction. Processes A and B (a) result in charge transport from \$S_1\$ to \$S_2\$, whereas processes C and D (b) result in charge transport from \$S_2\$ to \$S_1\$. Due to the much larger probabilities of processes A and B for the chosen bias voltage a net current is obtained from \$S_1\$ to \$S_2\$. Processes B and D involve a Cooper pair state. They can be viewed as the tunneling of a hole-like quasiparticle excitation from \$S_2\$ to \$S_1\$ and vice versa, respectively. The open and full symbols mark the initial and final states, respectively.

is the normalized BCS density of states. The normal resistance \$R_N\$ is related to the normal state single spin density of states \$n_0\$ at the Fermi level as

$$R_N = \frac{4\pi e^2}{\hbar} |T^2| n_0^2 . \quad (7.4.9)$$

Here, \$|T^2|\$ is the tunneling probability, which is determined by the thickness and height of the tunneling barrier. For \$k_B T \ll |eV| < 2\Delta\$ the tunneling current as function of temperature and bias voltage can be expressed as

$$I(T, V) = \frac{n_{q,\text{th}}(T)}{2eR_N n_0} \rho(\Delta + eV) , \quad (7.4.10)$$

where

$$n_{q,\text{th}}(T) = 4n_0 \int_{\Delta_0}^{\infty} \rho(E)f(E) dE = 2n_0 \sqrt{2\pi\Delta_0 k_B T} \exp\left(-\frac{\Delta_0}{k_B T}\right) \quad (7.4.11)$$

is the thermal quasiparticle density and \$\Delta_0 = \Delta(T = 0)\$. We see that at low temperatures the thermal quasiparticle density and the associated tunneling current becomes exponentially small. For example, in a Nb tunnel junction with a volume of \$(100\mu\text{m})^2 \times 1\mu\text{m}\$ there are only about \$10^6\$ quasiparticles at \$T = 1.3\text{ K}\$. This is about the same number as generated by the absorption of a 1 keV photon. That is, at low \$T\$ the excess quasiparticle density generated due to the absorption of a photon/particle and the related extra tunneling current may become larger than the corresponding thermal quantities.

With the expression for the tunneling current we can write down the extra current due to the absorption of a photon/particle. For simplicity we assume a SIS junction consisting of two electrodes of the same material and the same thickness. The signal current \$\delta I_s\$ as a function of time may be approximated by

$$\delta I_s(t) = \delta I_s(0) e^{-t/\tau_D} = \frac{e\delta N}{\tau_{\text{tun}}} e^{-t/\tau_D} , \quad (7.4.12)$$

where $1/\tau_{\text{tun}} = \Gamma_{\text{tun}}$ is the tunneling rate, τ_D the decay time of the current pulse, and $\delta N = E/\varepsilon$ the excess quasiparticle number generated in the junction electrodes due to a radiation event. Although τ_D is the decay time of the current pulse, it is often called the rise time of the associated charge pulse

$$\delta Q_s(t) = \int_0^t \delta I_s(t') dt' = \frac{e\delta N}{\tau_{\text{tun}}} \tau_D \left[1 - e^{-t/\tau_D} \right]. \quad (7.4.13)$$

In first order approximation the total collected charge δQ is given by

$$\delta Q_s = e\delta N \frac{\tau_D}{\tau_{\text{tun}}}. \quad (7.4.14)$$

We see that the collected charge is large, if the tunneling time is large compared to the decay time of the signal pulse.

Writing expression (7.4.10) for the tunneling current as $I = en_{q,\text{th}}V/\tau_{\text{tun}}$ we obtain the tunneling time^{96,97}

$$\tau_{\text{tun}} = \frac{2e^2 n_0 A d R_N}{\rho(\Delta + eV)} = \frac{2\pi e n_0 \Delta d}{J_c \rho(\Delta + eV)}. \quad (7.4.15)$$

Here, we have used $V = Ad$ with A the junction area and d the thickness of the electrodes as well as $I_c R_N \simeq \pi \Delta/e$ and $I_c = J_c A$. We see that the tunneling time decreases with decreasing d and increasing J_c . For example, for Nb with $n_0 \simeq 4 \times 10^{22}/\text{eV cm}^3$ we obtain a tunneling time of about 60 ns for a film thickness of $d = 10 \text{ nm}$, a critical current density of $J_c = 1000 \text{ A/cm}^2$ and using $\rho \simeq 1$.

Quasiparticle Lifetime: The two tunneling processes A and B of Fig. 7.21 imply that, following an interaction in say S1, leading to an increase in the tunneling process A, there will be an increase in the quasiparticle density in S2, and in turn an increase in process B. Thus, a cyclic process can occur which leads to signal amplification.⁹⁸ This process is limited by the loss rate τ_D of the quasiparticles discussed in the following. The loss rate can be expressed as

$$\Gamma_D = \frac{1}{\tau_D} = \frac{2}{\tau_R} + \frac{1}{\tau_X}. \quad (7.4.16)$$

The rate $1/\tau_R$ is the effective quasiparticle recombination rate and the factor of two arises because two excess quasiparticles are lost in the recombination to a Cooper pair. The factor $1/\tau_X$ includes all other loss mechanisms, for example outdiffusion of quasiparticles into the connecting leads of the junction where they are unable to tunnel. In the ideal case they are negligible. The recombination rate depends on the quasiparticle density as⁹⁹

$$\frac{1}{\tau_R} = n_{q,\text{th}} \frac{1}{4n_0 \Delta_0 \tau_0} \left(\frac{2\Delta_0}{k_B T_c} \right)^3 = n_{q,\text{th}} R. \quad (7.4.17)$$

Here, R is the recombination coefficient and τ_0 is a materials constant, which is listed in Table 7.1 together with other characteristic parameters of some relevant superconductors. Note that we can use $n_q = n_{q,\text{th}}$ in (7.4.17) only if the generated excess quasiparticle density $\delta n \ll n_{q,\text{th}}$. Then we refer to the thermal

Table 7.1: Characteristic materials properties of some superconductors.

<i>property</i> ^{a,b,c}	Nb	Ta	V	Sn	Al
critical temperature T_c [K]	9.26	4.48	5.41	3.72	1.196
energy gap $2\Delta_0$ [meV]	3.05	1.5	1.6	1.15	0.34
density of states n_0 [$10^{22}/\text{cm}^3\text{eV}$]	4.06	4.08		1.45	1.56
characteristic time τ_0 [ns]	0.149	1.78		2.30	438
pair breaking time τ_B [ps]	4.2	23		110	242

^aN.W. Ashcroft and N.D. Mermin, *Solid State Physics*, Holt, Rinehard and Winston International Editions, (1987).

^bC. Kittel, *Introduction to Solid State Physics*, Oldenbourg, Munich (1983).

^cS.B. Kaplan, C.C. Chi, D.N. Langenberg, J.J. Chang, S. Jafarey, D.J. Scalapino, *Quasiparticle and phonon lifetimes in superconductors*, Phys. Rev. **B** **14**, 4854 (1976).

recombination rate. However, in STJDs this is often not the case because $n_{q,\text{th}}$ becomes exponentially small at low T . For $\delta n \gg n_{q,\text{th}}$ we have to use $n_q = \delta n$ in (7.4.17) and we obtain $d\delta n/dt = \delta n/\tau_R = R\delta n^2$.

In practice the effective quasiparticle recombination rate is reduced from its intrinsic value because the phonons emitted in the recombination process can break another Cooper pairs again, thereby replacing the quasiparticles lost by recombination. The effective recombination time can be written as

$$\tau_R^{\text{eff}} = \tau_R \left(1 - \frac{\tau_{\text{es}}}{\tau_B} \right), \quad (7.4.18)$$

where $1/\tau_{\text{es}}$ is the escape rate of the phonons to the heat sink (e.g. the substrate) and $1/\tau_B$ is the phonon pair breaking rate. The expression in brackets is denoted as the **phonon trapping factor**, which becomes large for $\tau_{\text{es}} \gg \tau_B$. The values listed in Table 7.1 show that τ_B is in ps range for Nb or Ta and therefore is usually smaller than $\tau_{\text{es}} = 4d/\gamma v_{\text{ph}}$ (compare (7.3.25)), which is in the 1 ns regime for a Nb film with a typical film thickness of a few 100 nm.

Quasiparticle Trapping: In order to achieve high detection efficiency, in particular in the x-ray regime, the thickness of the junction electrodes should be as large as possible. However, in this case the tunneling time $\tau_{\text{tun}} \propto d$ is increasing. According to (7.4.14) this in turn results in a reduction of the total collected charge. Evidently it is difficult to scale up the STJD to large volumes. A solution to the problem of scaling up the STJD is quasiparticle trapping.¹⁰⁰

The idea of quasiparticle trapping is shown in Fig. 7.22. The superconducting junction electrodes are replaced by bilayers consisting of materials with large and small energy gap, with the low gap material adjoining the barrier. Excess quasiparticles created mainly in the thick layer of large gap material diffuse into the layer of low gap material and relax down by electron-phonon scattering. This process goes as $[(\Delta - \Delta')/\Delta']^3$ and scales with $1/\tau_0$ (see Table 7.1). The quasiparticles are trapped in the thin layer of low gap material, which forms a potential well. In this way the tunneling time, which is effectively determined by the small thickness d' of the low gap material, is significantly reduced. The magnitude of the signal current is then determined to first order by tunneling from the thin trapping layer rather than

⁹⁶A.F. Cattell, A.R. Long, A.C. Hanna, and A.M. Macleod, J. Phys. F: Met. Phys. **13**, 855 (1983).

⁹⁷Note that the tunneling time includes the dominating tunneling processes A and B. If excess quasiparticles are generated for example only in S1, process B is absent and the tunneling time is increased by a factor of 2.

⁹⁸K.E. Gray, *A superconducting transistor*, Appl. Phys. Lett. **32**, 392 (1978).

⁹⁹S.B. Kaplan, C.C. Chi, D.N. Langenberg, J.J. Chang, S. Jafarey, D.J. Scalapino, *Quasiparticle and phonon lifetimes in superconductors*, Phys. Rev. **B** **14**, 4854 (1976).

¹⁰⁰N.E. Booth, *Quasiparticle trapping and the quasiparticle multiplier*, Appl. Phys. Lett. **50**, 293 (1987).

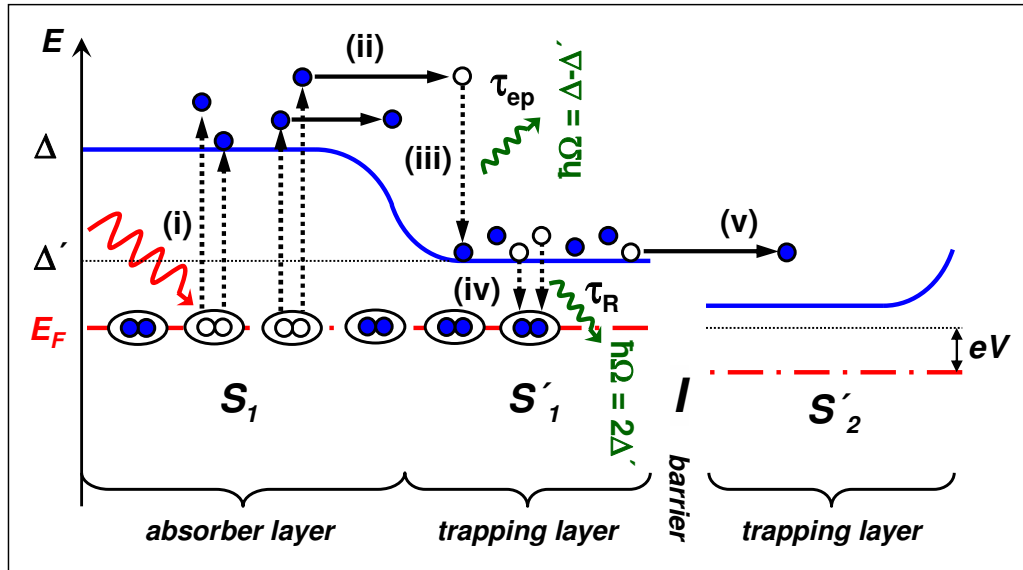


Figure 7.22: Principle of quasiparticle trapping in superconducting tunnel junction detectors. The important processes are (i) quasiparticle generation, (ii) diffusion, (iii) relaxation by electron-phonon scattering, (iv) recombination, and (v) tunneling. In the relaxation and recombination processes phonons with energy $\hbar\Omega \leq \Delta - \Delta'$ and $\hbar\Omega = 2\Delta'$ are generated. These phonons can either escape to the heat sink or break up Copper pairs again.

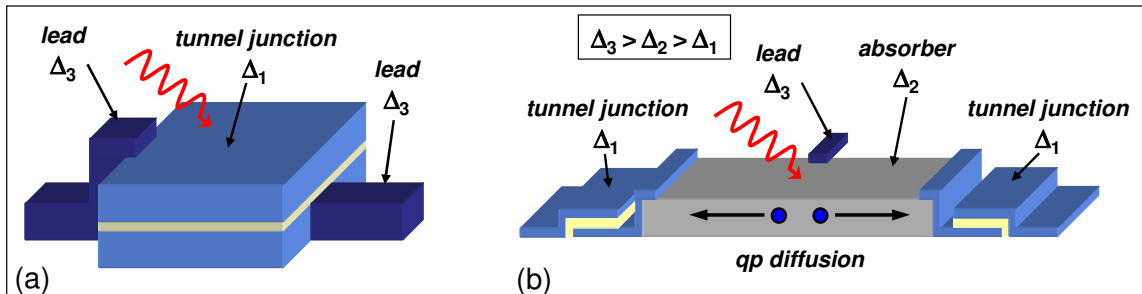


Figure 7.23: (a) STJD consisting of a low energy gap material (Δ_1 , e.g. Al) contacted by leads of large energy gap material (Δ_3 , e.g. Nb). (b) Detector configuration based on a medium energy gap absorber (Δ_2 , e.g. Ta) and low energy gap tunnel junctions (Δ_1 , e.g. Al). The absorber material is contacted by a large gap material (Δ_3 , e.g. Nb) for make electrical contact to the top electrodes of the tunnel junctions.

from the thick absorber layer. That is, by employing quasiparticle trapping the total collected charge can be increased significantly thereby improving the energy resolution.

We note that quasiparticle trapping can not only be used to trap the excess quasiparticles close to the tunneling barrier but also to avoid quasiparticle diffusion into the leads. This lateral trapping can be realized by using a material with high energy gap Δ_3 for the leads of the tunnel junction made of a superconductor with $\Delta_1 < \Delta_3$ as shown in Fig. 7.23a. Another possibility is to use an absorber of medium gap material Δ_2 and couple this absorber to a tunnel junction consisting of low gap material ($\Delta_1 < \Delta_2$) as shown in Fig. 7.23b. The excess quasiparticles generates in the absorber diffuse into the lower gap junction electrodes and are trapped there. Their number is determined by tunneling. The contact to the top electrode of the tunnel junction is made via the absorber material by a high gap material ($\Delta_3 > \Delta_2 > \Delta_1$).

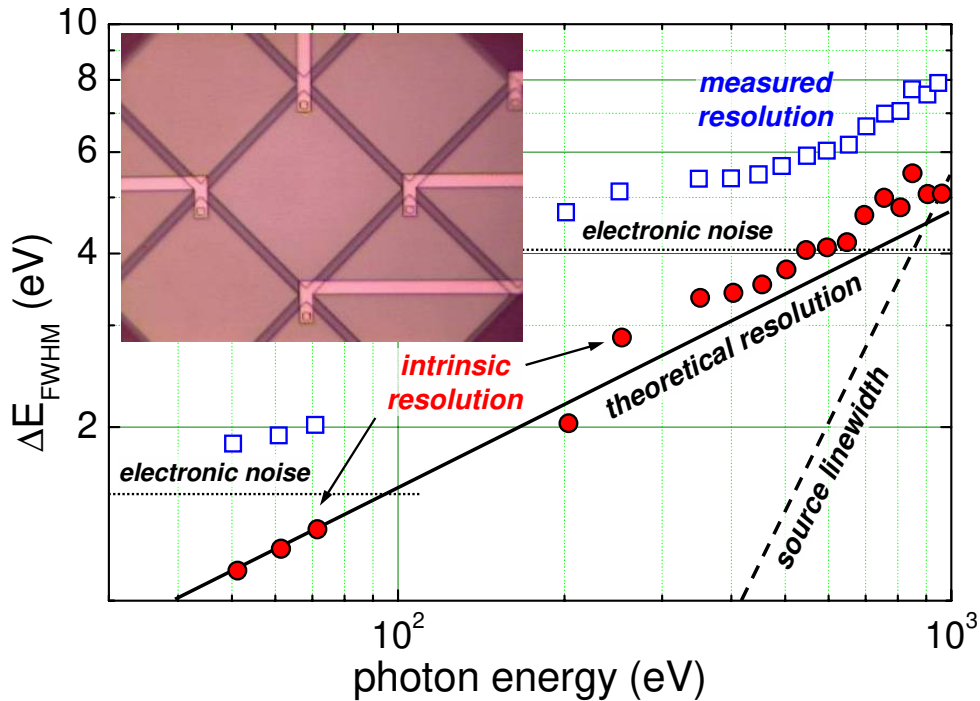


Figure 7.24: Energy resolution of a Nb/Al/AlO_x/Al/Nb STJD detector as a function of the photon energy. The intrinsic device resolution (full circles) is calculated by subtracting electronic noise (dotted lines) and monochromator line width (dashed line) in quadrature from the measured resolution (open squares). The solid line is the theoretical resolution limit calculated according to (7.4.5) using $F' = 1.3$. The inset shows an optical micrograph of a 3x3 detector array with a pixel size of $100 \times 100 \mu\text{m}^2$ (according to S. Friedrich *et al.*, IEEE Trans. Appl. Supercond. **AS-9**, 3330 (1999)).

Experimental Status

At present several groups worldwide have fabricated STJDs and detector arrays for x-ray imaging and spectroscopy based on Nb/Al/AlO_x/Al/Nb layer structures. Here, the Al layer serves for quasiparticle trapping. For these detectors an energy resolution ranging between about 2 and 10 eV FWHM has been achieved for photon energies between about 50 and 1000 eV. The detectors can be operated at count rates as high as 10 000 counts/s per pixel. Typical operation temperatures of the detectors are 0.1 K. An optical micrograph of a 3x3 detector array and the energy resolution is shown in Fig. 7.24.^{101,102}

STJDs optimized for the UV and extrem UV regime between about 20 and 200 eV based on Ta absorbers ($\Delta_2 = 700 \mu\text{eV}$) and Al/AlO_x/Al tunnel junctions ($\Delta_1 = 180 \mu\text{eV}$) have achieved a FWHM energy resolution as low as 2.15 eV, which was limited by the amplifier noise.¹⁰³ These STJDs use a lateral instead of a vertical trapping structure as sketched in Fig. 7.23b. The photons are absorber in the Ta layer and diffuse laterally into the Al tunnel junction electrode where they are trapped and counted via tunneling. Spectrometers based on STJDs already are meanwhile successfully used in many applications.¹⁰⁴

¹⁰¹S.Friedrich, J.B. le Grand, L.J. Hiller, J. Kipp, M. Frank, S.E. Labov, S.P. Cramer, and A.T. Barfknecht, *High-Resolution Tunnel Junction Extreme Ultraviolet Detectors Limited by Quasiparticle Counting Statistics*, IEEE Trans. Appl. Supercond. **AS-9**, 3330-3333 (1999).

¹⁰²S. Friedrich, K. Segall, M. C. Gaidis, C. M. Wilson, D. E. Prober, A. E. Szymkowiak and S. H. Moseley, *Experimental quasiparticle dynamics in a superconducting, imaging x-ray spectrometer*, Appl. Phys. Lett. **71**, 3901-3903 (1997).

¹⁰³Ch.M. Wilson, L. Frunzio, and D.E. Prober, *Superconducting Tunnel Junction Detectors for Extreme Ultraviolet Applications*, IEEE Trans. Appl. Supercond. **AS-13**, 1120-1123 (2003).

¹⁰⁴N. Rando *et al.*, *S-Cam: A cryogenic camera for optical astronomy based on superconducting tunnel junctions*, IEEE Trans. Appl. Supercond. **AS-10**, 1617-1625 (2000).

7.5 Other Detectors

To conclude the chapter on superconducting photon and particle detector we would like to mention a few superconducting detectors that are based on other detection schemes. The first one is based on an array of small grains consisting of a type-I superconductor. Each grain is much larger than the London penetration depth λ_L so that the grains stay in the Meißner state on applying a magnetic field. The temperature and magnetic field are chosen to keep the grains close to the phase boundary to the normal state. Therefore, when a particle is absorbed by a grain the deposited energy may be sufficient to switch the grain into the normal state. Switching the grain into the normal state lets the magnetic flux enter the grain. The change in flux distribution can be detected by a sensitive SQUID detector coupled to the grain. It has been shown that grains of the type-I superconductors Pb, Sn or In (typical diameter is $10\ \mu\text{m}$) can be operated in the so-called superheated state, where the applied magnetic field is slightly above the critical field without loosing the Meißner state. Such metastable state is possible, since the superconducting transition at finite field represents a first order phase transition. Then a very small energy deposition of the order of only 1 keV is sufficient to switch the small particle into the normal state. Such superheated superconducting granular detectors have been proposed in the search for weakly interacting massive particles (WIMPs) because large absorber masses can be realized.

The second detector to be mentioned is the magnetic monopole detector. Magnetic monopoles would carry the quantum of magnetic charge in the same way as electrons carry the quantum of electric charge. Our present experience is that magnetic monopoles do not exist in nature. All magnetic fields are magnetic dipoles generated by moving charges and magnetic field lines form closed loops. However, the existence of magnetic monopoles with magnetic charge quantized in units of h/e has been suggested by some elementary particle theories. If magnetic monopoles would exist, then the fundamental equations for magnetic and electric flux density, $\int \mathbf{B} \cdot d\mathbf{F} = Q_{\text{mag}}$ and $\int \mathbf{D} \cdot d\mathbf{F} = Q_{\text{el}}$, would be completely symmetrical. Here, Q_{mag} and Q_{el} are the magnetic and electric charge enclosed by a closed surface. The fact that magnetic monopoles have not yet been detected may just be related to their small number and weak interaction. A few researchers have attempted to search for magnetic monopoles using a superconducting detector. The functional principle of such detector is very simple. Suppose a monopole is passing a closed superconducting loop containing zero magnetic flux. As the monopole approaches the loop, the applied flux increases from zero to $\Phi_0 = h/2e$, i.e. half the total flux of the monopole. This will be compensated by a circulating current $I = \Phi_0/L$ in the loop with inductance L . As the monopole moves through the loop and away from it, the other half of the monopole flux causes the induced current to increase further to $I = \Phi_0/2L$ corresponding to the net flux $2\Phi_0$ in the loop. This is completely different to the interaction of a magnetic dipole with the loop. The passage of a dipole would first result in an increase and then on moving away from the loop in a decrease of the shielding current with no induced flux in the loop. That is, a sudden change of the magnetic flux enclosed by the superconducting loop in units of $\pm 2\Phi_0$ would be a clear signature for the passage of a magnetic monopole. This flux change can easily be detected by a SQUID sensor. Indeed, in early experiments a single event suggesting the passage of a monopole has been found.¹⁰⁵ However, this never could be reproduced later.

¹⁰⁵B. Cabrera, *First results from a superconducting detector for moving magnetic monopoles*, Phys. Rev. Lett. **48**, 1378 (1982).

Chapter 8

Microwave Applications

Superconducting devices find brought applications in passive microwave devices such as filters or resonators. These applications are based on the very small losses due to the small microwave surface resistance of superconducting materials. Therefore, the quality factor of superconducting microwave resonators and filters is larger than for equally sized normalconducting devices. In the same way, at the same quality factor superconducting microwave resonators and filters can be made much smaller. This is in particular important for satellite or space applications. In this Chapter we briefly discuss the foundations of superconducting passive microwave devices and describe a few prominent devices structures and applications.

Superconducting devices based on Josephson junctions can serve as sources for microwave radiation. Here, the underlying principle is based on the voltage-frequency relation $V = f\Phi_0$, which immediately suggests that a Josephson junction can be used as a voltage controlled oscillator with $f/V = 483\,597.9\,\text{GHz}/\text{V}$. In this Chapter we also present the foundations of superconducting microwave sources based on Josephson junction.

8.1 High Frequency Properties of Superconductors

8.1.1 The Two-Fluid Model

Already in 1934, that is long before the development of BCS theory, **Cornelius Gorter** and **H.B.G. Casimir** developed the two fluid model of superconductors.^{1,2} The model is based on the concept that there are two fluids in superconductors, namely a superfluid with carrier density n_s and a normal fluid with carrier density n_n with the total carrier density given by

$$n = n_n + \frac{n_s}{2} . \quad (8.1.1)$$

Here, the factor $\frac{1}{2}$ arises from the fact that the carriers of the superfluid are pairs with charge $-2e$. We will use the two-fluid model together with Ohm's law

$$\frac{1}{\sigma_n} \mathbf{J}_n = \mathbf{E} \quad (8.1.2)$$

and the linearized first London equation (compare (1.1.70) and (1.1.71))

$$\frac{\partial}{\partial t} (\Lambda \mathbf{J}_s) = \frac{\partial}{\partial t} (\mu_0 \lambda_L^2 \mathbf{J}_s) = \mathbf{E} \quad (8.1.3)$$

to describe the relation of the normal and superfluid current density and the electric field. In (8.1.3)

$$\Lambda \equiv \frac{m_s^*}{n_s^* q^{*2}} \quad (8.1.4)$$

is the **London coefficient** and

$$\lambda_L \equiv \sqrt{\frac{m_s^*}{\mu_0 n_s^* q^{*2}}} \quad (8.1.5)$$

the **London penetration depth** (compare (1.1.63) and (1.1.64)). Here, $q^* = -2e$ and m_s^* are the charge and the effective mass of the carrier forming the superfluid.

For a harmonic current with angular frequency ω (8.1.3) can be written as

$$\imath \omega \Lambda \mathbf{J}_s = \imath \omega \mu_0 \lambda_L^2 \mathbf{J}_s = \frac{1}{\sigma_s} \mathbf{J}_s = \mathbf{E} \quad (8.1.6)$$

with the purely imaginary conductivity of the superfluid

$$\boxed{\sigma_s = \frac{n_s^* q^{*2}}{\imath \omega m_s^*} = \frac{1}{\imath \omega \Lambda} = \frac{1}{\imath \omega \mu_0 \lambda_L^2} .} \quad (8.1.7)$$

¹D. Shoenberg, *Superconductivity*, Cambridge University Press, Cambridge (1965), pp. 194-196.

²T. van Duzer, *Principles of Superconducting Devices and Circuits*, Elsevier, New York, Amsterdam, London (1981), p. 124.

To derive the equivalent relations for the normal fluid we write the normal current as $\mathbf{J}_n = n_n e \mathbf{v}_n$, where \mathbf{v}_n is the average velocity of the normal carriers, and assume that the normal carriers have to satisfy Newton's law³

$$m_n^* \left(\frac{d\mathbf{v}_n}{dt} + \frac{\mathbf{v}_n}{\tau} \right) = e \mathbf{E} . \quad (8.1.8)$$

Here, τ is the scattering time of the normal carriers and m_n^* and e the effective mass and charge of the normal carriers. Again, for a sinusoidal current with angular frequency ω we obtain

$$\mathbf{J}_n = \left(\frac{n_n e^2}{m_n^*} \right) \frac{\tau}{1 + i\omega\tau} \mathbf{E} = \sigma_n \mathbf{E} . \quad (8.1.9)$$

The complex conductivity of the normal current can be expressed as

$$\sigma_n = \sigma_{n1} - i\sigma_{n2} = \left(\frac{n_n e^2 \tau}{m_n^*} \right) \frac{1 - i\omega\tau}{1 + (\omega\tau)^2} = \sigma_0 \frac{n_n}{n} \frac{1 - i\omega\tau}{1 + (\omega\tau)^2} . \quad (8.1.10)$$

Here, $\sigma_0 = n_n e^2 \tau / m_n^*$ is the usual normal state Drude conductivity. With (8.1.2), (8.1.3) and (8.1.6) together with the expressions for the conductivities and Maxwell's equations we can derive the high-frequency properties of superconductors.

Note that the conductivities σ_n and σ_s show a strong temperature dependence below T_c due to the temperature variation of the normal and superfluid density. At $T = T_c$ we have $n_s = 0$ and $n_n = n$. Below T_c the superfluid density increases and the normal fluid density decreases as

$$\frac{n_n}{n} = \left(\frac{T}{T_c} \right)^4 \quad (8.1.11)$$

$$\frac{n_s}{2n} = 1 - \left(\frac{T}{T_c} \right)^4 . \quad (8.1.12)$$

At $T = 0$ all the carriers are condensed into the superfluid and we have $n_s = n/2$ and $n_n = 0$.

In an electrotechnical language the two-fluid model can be visualized by the equivalent circuit shown in Fig. 8.1. The superfluid channel which does not contribute to the loss and has purely imaginary conductivity can be modeled by an inductor $L_s(T)$. The normal channel has a conductivity composed of a imaginary and a real part. The former, represented by the inductor $L_n(T)$, is due to the inertia of the charge carriers and the latter, represented by the resistor $R_n(T)$, due scattering induced loss. Note that the inductor L_n in the normal channel is often neglected which is similar to modeling the normal channel as nondispersive (frequency independent).

We can use the equivalent circuit to classify different frequency regimes. Evidently at $\omega = 0$ all the current is carried by the nondissipative superconducting channel. However, increasing the frequency the conductivity of the superfluid density becomes finite and decreases with frequency. Therefore, the contribution of \mathbf{J}_s decreases with increasing frequency and becomes equal to \mathbf{J}_n at the cross-over frequency $\omega_{ns} = R_n / L_s$. That is, the superfluid dominates in the low-frequency regime $0 \leq \omega \leq \omega_{ns}$. In the high-frequency regime the normal channel dominates. We further can discuss the question at which frequency there is a cross-over between an ohmic (nondispersive) response to an inductive (dispersive) response in

³The quantity e represents the unit of the electric charge with an electron having the charge $-e$.

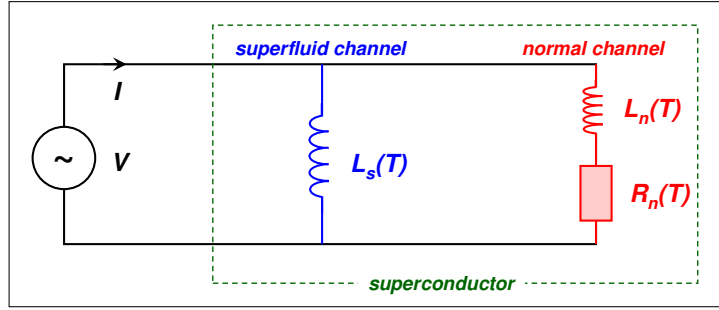


Figure 8.1: Equivalent circuit for the two-fluid model of a superconductor.

the normal channel. Evidently this occurs at the frequency $\omega_\tau = R_n/L_n = 1/\tau$. That is, in the frequency regime $\omega_{ns} \leq \omega \leq 1/\tau$ the ohmic response and for $\omega \geq 1/\tau$ the inductive response of the normal channel is dominant. In the high-frequency regime we restrict our discussion to $\omega < \omega_\Delta = \Delta/\hbar$. Above the gap frequency ω_Δ the microwave photons can break up Copper pairs and the situation becomes more complicated. For a superconductor with $\Delta = 1$ meV the gap frequency ω_Δ is about 1 THz. Note that $\tau_{ns} = L_s/R_n$ increases strongly with decreasing temperature due to the increase of L_s and the decrease of R_n associated with the temperature variation of n_n and n_s . Therefore, the cross-over frequency ω_{ns} increase with decreasing temperature and typically becomes larger than ω_τ as shown in Fig. 8.2. In this case there is no frequency regime where the ohmic normal channel dominates.

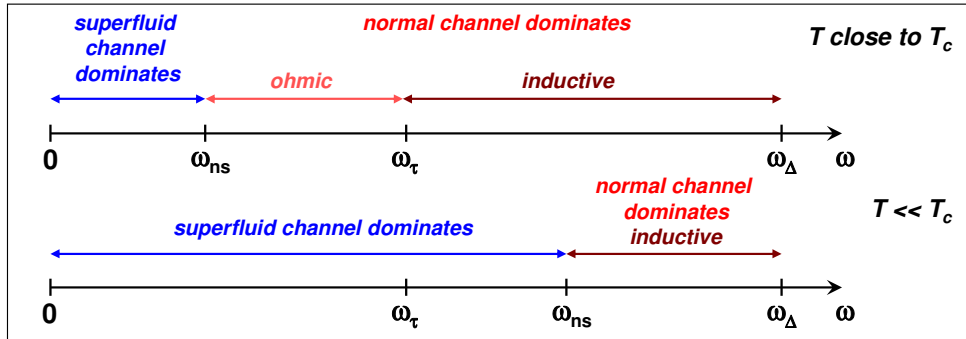


Figure 8.2: Characteristic frequency regimes for a superconductor for different temperatures.

Using equations (8.1.7) and (8.1.10) we obtain the total conductivity of a superconductor to

$$\sigma = \sigma_s + \sigma_n = \frac{n_n e^2 \tau}{m_n^*} \frac{1}{1 + (\omega \tau)^2} - i \frac{n_n e^2 \tau}{m_n^*} \frac{\omega \tau}{1 + (\omega \tau)^2} - i \frac{1}{\omega \mu_0 \lambda_L^2}. \quad (8.1.13)$$

At frequencies $\omega \tau \ll 1$ this can be simplified to

$$\sigma = \sigma_1 - i \sigma_2 = \frac{n_n e^2 \tau}{m_n^*} - i \frac{1}{\omega \mu_0 \lambda_L^2}, \quad (8.1.14)$$

where σ_1 and σ_2 are the real and imaginary components of the complex conductivity. The real part represents the loss from the normal carriers, whereas the imaginary part represents the kinetic energy of the superconductive carriers.

8.1.2 The Surface Impedance

Normal Metals

The surface impedance is defined as the characteristic impedance seen by a plane wave incident perpendicular upon a flat surface of a conductor. It is given by the ratio of the electric and the magnetic field at the surface. For thick normalconducting materials the surface impedance is equal to the bulk wave impedance Z which can be derived from Maxwell's equations to

$$Z_s = R_s + iX_s = \sqrt{\frac{i\mu_0\omega}{\sigma_0}} = (1+i)\sqrt{\frac{\mu_0\omega}{2\sigma_0}} = (1+i)\frac{\mu_0\omega\delta_0}{2}. \quad (8.1.15)$$

Here, $\sigma_0 = ne^2\tau/m^*$ is the normal state conductivity and

$$\delta_0 = \sqrt{\frac{2}{\mu_0\omega\sigma_0}} \quad (8.1.16)$$

is the normal state field penetration depth. For a normal metal at frequencies $\omega\tau \ll 1$, i.e. in the ohmic regime, the conductivity is a real number and according to (8.1.16) the surface resistance R_s and the surface reactance X_s are equal:

$$R_s = X_s = \sqrt{\frac{\mu_0\omega}{2\sigma_0}} = \frac{\mu_0\omega\delta_0}{2}. \quad (8.1.17)$$

We see that for normal metals both R_s and X_s are proportional to $\sqrt{\omega}$.

Superconductors

In order to derive the surface impedance of a superconductor we the normal state conductivity σ_0 in (8.1.16) by the total conductivity of a superconductor and obtain

$$\begin{aligned} Z_s = R_s + iX_s &= \sqrt{\frac{i\mu_0\omega}{\sigma}} = \left[\frac{\sigma_n \frac{1}{1+(\omega\tau)^2} - i\sigma_n \frac{\omega\tau}{1+(\omega\tau)^2} - i\frac{1}{\omega\mu_0\lambda_L^2}}{i\omega\mu_0} \right]^{-1/2} \\ &= i\omega\mu_0 \left[i\omega\mu_0\sigma_n \frac{1}{1+(\omega\tau)^2} + \omega\mu_0\sigma_n \frac{\omega\tau}{1+(\omega\tau)^2} + \frac{1}{\lambda_L^2} \right]^{-1/2}. \end{aligned} \quad (8.1.18)$$

At frequencies $\omega\tau \ll 1$ this can be simplified to

$$Z_s = \frac{i\omega\mu_0}{\lambda_L} \left[1 + i\omega\mu_0\lambda_L^2\sigma_n \right]^{-1/2} = i\sqrt{\frac{\omega\mu_0}{\sigma_2}} \left[1 + i\frac{\sigma_1}{\sigma_2} \right]^{-1/2}, \quad (8.1.19)$$

where we have used $\sigma = \sigma_1 + i\sigma_2$ with $\sigma_1 = \sigma_n$ and $\sigma_2 = 1/\omega\mu_0\lambda_L^2$. We can now further simplify (8.1.19) by taking into account that $\sigma_1 \ll \sigma_2$ for temperatures not to close to T_c . With $(1+x)^{-1/2} \simeq 1 - \frac{1}{2}x$ we obtain

$$Z_s = i\sqrt{\frac{\omega\mu_0}{\sigma_2}} \left(1 - i\frac{\sigma_1}{2\sigma_2} \right) = \sqrt{\frac{\omega\mu_0\sigma_1^2}{2\sigma_2^3}} + i\sqrt{\frac{\omega\mu_0}{\sigma_2}}. \quad (8.1.20)$$

Table 8.1: Conductivity σ , penetration depth δ_0 due to the normal skin effect, London penetration depth λ_L , surface resistance R_s and surface reactance X_s of normal conductors and superconductors for $\omega\tau \ll 1$ and temperatures $T \ll T_c$.

	normal conductor	superconductor
conductivity	$\sigma_0 = \frac{ne^2\tau}{m_n^*}$	$\sigma_1 + i\sigma_2 = \frac{ne^2\tau}{m_n^*} \left(\frac{n_n}{n} \right) - i \frac{1}{\omega\mu_0\lambda_L^2}$
field penetration depth	$\delta_0 = \sqrt{2/\omega\mu_0\sigma_0}$	$\delta_s = \lambda_L$
surface resistance	$R_s = \frac{1}{2}\omega\mu_0\delta_0 = \sqrt{\frac{\omega\mu_0}{2\sigma_0}}$	$R_s = \frac{1}{2}\omega^2\mu_0^2\lambda_L^3\sigma_0 \left(\frac{n_n}{n} \right)$
surface reactance	$X_s = \frac{1}{2}\omega\mu_0\delta_0 = \sqrt{\frac{\omega\mu_0}{2\sigma_0}}$	$X_s = \omega\mu_0\lambda_L$

Using expression (8.1.14) for σ_1 and σ_2 we finally obtain

$$Z_s = R_s + iX_s = \frac{\omega^2\mu_0^2\lambda_L^3 n_n e^2 \tau}{2m_n^*} + i\omega\mu_0\lambda_L = \frac{1}{2}\omega^2\mu_0^2\lambda_L^3\sigma_0 \left(\frac{n_n}{n} \right) + i\omega\mu_0\lambda_L . \quad (8.1.21)$$

We see that the surface resistance, the real part of Z_s , increases proportional to ω^2 in contrast to normal conductors, where $R_s \propto \sqrt{\omega}$. Furthermore, it increases proportional to λ_L^3 and the conductivity $\sigma_0 n_n / n$ of the normal fluid. In Table 8.1 the most main characteristics of superconductors are compared to those of normal metals.

Fig. 8.3 shows the theoretically expected surface resistance as a function of frequency for the superconductor Nb and the normal metal Cu. We see that for frequencies below about 100 GHz the surface resistance of Nb is considerably lower than for Cu at 77 K. At high frequencies there is a cross-over due to the much weaker frequency dependence of the surface resistance of normal metals. Note that the surface resistance is expected to be further reduced by going to lower temperatures due to the strong decrease of n_n . At $T/T_c \ll 1$, $\lambda_L(T) \simeq \text{const}$ and $n_n \propto \exp(-2\Delta_0/k_B T)$. Therefore, an exponential decrease of R_s with decreasing T is expected. However, this behavior is usually not observed in experiment. Rather a temperature independent residual surface resistance is measured at very low T , which is attributed to material defects. For Nb this residual resistance is as low as $10^{-9}\Omega/\square$ at 10 GHz, whereas it reaches only about $10^{-5}\Omega/\square$ for YBa₂Cu₃O_{7-δ} films.

Kinetic Inductance

The surface reactance X_s , the imaginary part of the surface impedance, is purely inductive. The equivalent inductance L_k is denoted as **kinetic inductance**

$$L_k = \mu_0\lambda_L . \quad (8.1.22)$$

The kinetic inductance reflects the kinetic energy of the carriers of the superfluid.

Finally we note that the phenomenological model used above is based on local theory, which is valid only as long as the coherence length ξ of a superconductor is much smaller than the London penetration

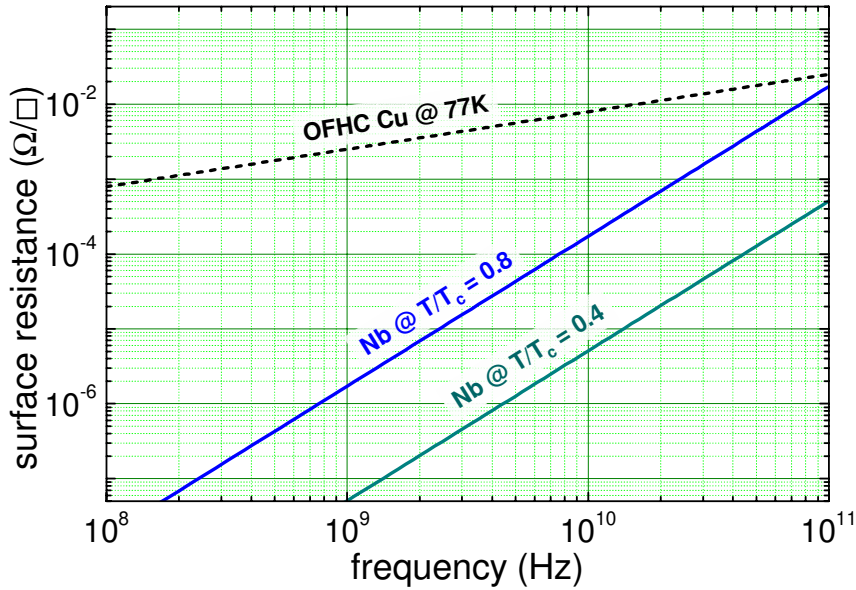


Figure 8.3: Intrinsic surface resistance versus frequency for Nb and oxygen free high conductance (OFHC) Cu. For Cu, $\sigma_0 = 10^8 \Omega^{-1} m^{-1}$, for Nb, $\lambda(0) = 85 \text{ nm}$ and $\sigma_0 = 10^8 \Omega^{-1} m^{-1}$ were used.

depth λ_L . This is for example the case for extreme type-II superconductors such as the high temperature superconductors. In contrast, for type-I superconductors we have $\xi > \lambda_L$. In this case the above treatment is non longer valid and we have to used a more complicated nonlocal theory.⁴

⁴A.B. Pippard, *An experimental and theoretical study of the relation between magnetic field and current in a superconductor*, Proc. Roy. Soc. (London), A **216**, 547-568 (1963).

8.2 Superconducting Resonators and Filters

in preparation

8.3 Superconducting Microwave Sources

in preparation

Chapter 9

Superconducting Quantum Bits

In section 3.5 we already have discussed the quantum consequences of the small capacitance of Josephson junctions leading to interesting secondary quantum macroscopic effects. The interest in macroscopic quantum effects in small capacitance Josephson junctions goes back to the 1980ies. The initial interest was to test whether or not the laws of quantum mechanics can be applied to macroscopic systems in a Hilbert space spanned by macroscopically distinct states.¹ The phase difference of the superconducting order parameter in a Josephson junction or the magnetic flux in a superconducting quantum interference devices were the degrees of freedom used in these studies. Although quantum phenomena such as macroscopic quantum tunneling and resonant tunneling of the phase difference could be demonstrated,^{2,3,4} it was impossible to observe coherent quantum oscillations between two macroscopically different (e.g. flux) states, i.e. macroscopic quantum coherence.⁵

The field of macroscopic quantum coherence in superconducting systems received new attention in the last years, when it became obvious that Josephson circuits are interesting candidates for the realization of quantum bits (qubits). The vision that superconducting devices may serve as qubits in quantum information processing and that quantum logic operations could be performed by controlling gate voltages or magnetic fields stimulated an intensive research effort.^{6,7,8,9,10,11,12} Meanwhile there has been a tremendous progress in quantum state engineering in superconducting and other solid state systems. In particular, the quantum superposition of macroscopically distinct states, coherent oscillations and entangled states of several qubits have been observed. Superconducting Josephson systems are very promising,

¹A. J. Leggett, in *Chance and Matter*, edited by J. Souletie, J. Vannimenus, and R. Stora, Elsevier, Amsterdam (1987), p. 395.

²R. F. Voss, R. A. Webb, *Macroscopic quantum tunneling in a 1 μm Nb Josephson junction*, Phys. Rev. Lett. **47**, 265 (1981).

³J. M. Martinis, M. H. Devoret, J. Clarke, *Experimental tests of the quantum behavior of a macroscopic degree of freedom: the phase difference across a Josephson junction*, Phys. Rev. B **35**, 4682 (1987).

⁴R. Rouse, S. Han, J. E. Lukens, *Observation of resonant tunneling between macroscopically distinct quantum levels*, Phys. Rev. Lett. **75**, 1614 (1995).

⁵C. D. Tesche, *Can a noninvasive measurement of magnetic flux be performed with superconducting circuits?*, Phys. Rev. Lett. **64**, 2358 (1990).

⁶V. Bouchiat, *PhD Thesis*, Université Paris VI (1997).

⁷A. Snirman, G. Schön, Z. Hermon, *Quantum manipulations of small Josephson junctions*, Phys. Rev. Lett. **79**, 2371 (1997).

⁸D. Averin, *Adiabatic quantum computation with Cooper pairs*, Solid State Com. **105**, 659 (1998).

⁹L.B. Ioffe, V.B. Geshkenbein, M.V. Feigelman, A.L. Fauchére, G. Blatter, *Quiet sds Josephson junctions for quantum computing*, Nature **398**, 679 (1999).

¹⁰Y. Makhlin, G. Schön, A. Shnirman, *Josephson junction qubits with controlled couplings*, Nature **386**, 305 (1999).

¹¹J.E. Mooij, T.P. Orlando, L. Levitov, L. Tian, C.H van der Wal, S. Lloyd, *Josephson persistent current qubit*, Science **285**, 1036 (1999).

¹²Y. Nakamura, Y.A. Pashkin, J.S. Tsai, *Coherent control of macroscopic quantum states in a single Cooper pair box*, Nature **398**, 786 (1999).

since they can be fabricated by established technologies and their control and measurement techniques are far advanced. Furthermore, superconducting qubits exploit the coherence of the superconducting state allowing the achievement of sufficiently long phase coherence times.

After giving a brief introduction to quantum information processing, in this chapter we discuss the realization of quantum bits by using superconducting Josephson junction devices.

9.1 Quantum Bits and Quantum Computers

9.1.1 Quantum Bits

Our today's classical computers represent the culmination of years of technological advancements beginning with the early ideas of **Charles Babbage** (1791-1871) and the creation of the first computer by the German engineer **Konrad Zuse** in 1941. Surprisingly however, the high speed modern computer is fundamentally not different from its gargantuan 30 ton ancestors, which were equipped with some 18 000 vacuum tubes and 500 miles of wiring. Although computers have become more compact and considerably faster in performing their task, the basic task remains the same: to manipulate and interpret an encoding of binary bits into a useful computational result. A bit is a fundamental unit of information, classically represented as a "0" or "1" in our digital computers. Each classical bit is physically realized through a macroscopic physical system, such as the magnetization on a hard disk or the charge on a capacitor. A document, for example, comprised of n -characters stored on the hard drive of a typical computer is accordingly described by a string of $8n$ zeros and ones. Herein lies a key difference between our todays classical computer and a quantum computer. Whereas a classical computer obeys the well understood laws of classical physics, a quantum computer is a device that uses physical phenomena unique to quantum mechanics (especially quantum interference) to realize a fundamentally new mode of information processing.^{13,14,15}

Whereas classical computers operate with ***classical (c-) bits*** usually represented by "0" and "1", quantum computers operate with ***quantum (qu-) bits*** usually denoted as ***qubits***. Physically, a qubit can be represented by every two level quantum system. The basic properties of such systems are discussed in detail in Appendix F. With the basis states of a two level quantum system (e.g. a spin-1/2 system, see Appendix G)

$$|\phi_1\rangle = |0\rangle = |\uparrow\rangle = \begin{pmatrix} 1 \\ 0 \end{pmatrix} \quad (9.1.1)$$

$$|\phi_2\rangle = |1\rangle = |\downarrow\rangle = \begin{pmatrix} 0 \\ 1 \end{pmatrix} \quad (9.1.2)$$

we can define a single-qubit state in the following way:

¹³T. Beth and G. Leuchs, *Quantum Information Processing*, Wiley-VCH, Berlin (2003).

¹⁴M.A. Nielsen, I.L. Chuang, *Quantum Information and Quantum Computation*, Cambridge University Press, Cambridge (2000).

¹⁵D. Bouwmeester, A. Ekert, A. Zeilinger eds., *The Physics of Quantum Information*, Springer, Berlin (2000).



Figure 9.1: Konrad Zuse 1945: Konrad Zuse was building the first binary digital computer Z1 in 1938. The first programmable electromechanical computer Z3 was completed in 1941. Zuse also developed the first algorithmic programming language called "Plankalkül".

A qubit $|\Psi\rangle$ is the superposition of two computational basis states

$$|\Psi(t)\rangle = a(t)|0\rangle + b(t)|1\rangle = \begin{pmatrix} a(t) \\ b(t) \end{pmatrix}. \quad (9.1.3)$$

Here, $a(t)$ and $b(t)$ are complex amplitudes. If we are measuring the quantum state of a qubit, we obtain the result $|0\rangle$ with probability $|a(t)|^2$ and the result $|1\rangle$ with probability $|b(t)|^2$. Since the total probability must be unity, we have to satisfy the normalization condition

$$\langle\Psi(t)|\Psi(t)\rangle = |a(t)|^2 + |b(t)|^2 = 1. \quad (9.1.4)$$

We see that the single-qubit exists in a continuum of states. It is a superposition of two basis states and therefore can be represented as a unit vector in a two-dimensional Hilbert space \mathcal{H}_2 . The key fact is that a qubit can exist not only in a state corresponding to the logical state “0” or “1” as in a classical bit, but also in states corresponding to a blend or superposition of these classical states. In other words, a qubit can exist as a zero, a one, or simultaneously as both “0” and “1”, with a numerical coefficient representing the probability for each state. This may seem counterintuitive because everyday phenomenon are governed by classical physics, not quantum mechanics – which takes over at the atomic level.

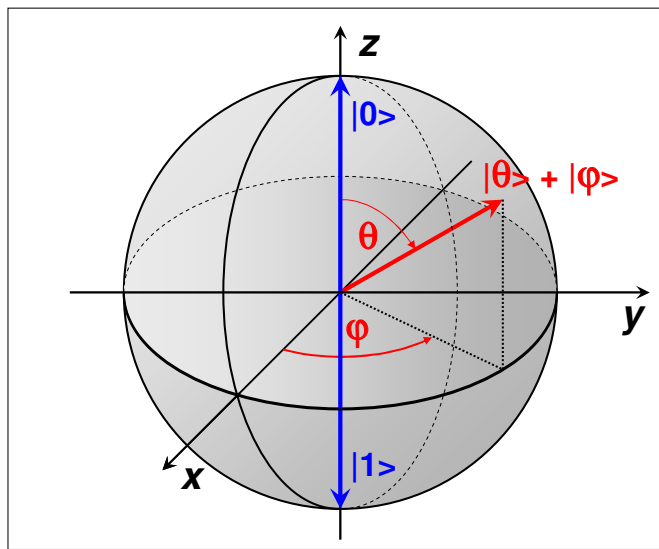


Figure 9.2: Representation of a qubit state as a vector on the Bloch sphere.

A convenient way of representing of a qubit state is as a unit vector on the Bloch sphere as shown in Fig. 9.2. With the angles θ and φ the general state can be expressed as (compare Appendix E)

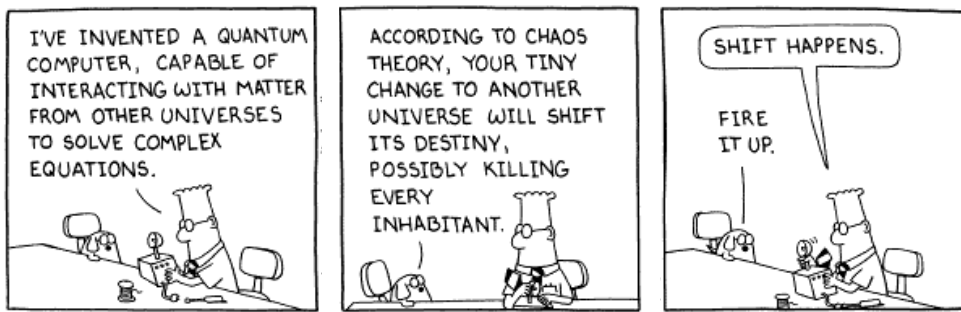
$$|\Psi\rangle = \cos \frac{\theta}{2} e^{-i\varphi/2} |0\rangle + \sin \frac{\theta}{2} e^{+i\varphi/2} |1\rangle. \quad (9.1.5)$$

Note that this state is equivalent to the general state of a spin-1/2-system (compare (G.II.20) in Appendix G). In a measurement process one has to get information on the angles θ and φ .

The foundations of single- and two-qubit states and their manipulation by unitary operators are discussed in detail in Appendix E. There, also an introduction to classical one- and two-bit gates and their quantum counterparts is given.

9.1.2 Quantum Computing

Over the last decades the performance of computers has increased tremendously. This could lead us to suppose that there is no problem that is too complicated to be solved with a classical computer. However, this is not the case. Let us consider the very simple problem of about 150 spin 1/2 particles (e.g. electrons). If we want to do a quantum mechanical description of the state of these electrons, we will exceed the capacity of every conceivable classical computer. The reason for that is that the Hilbert space of the collective spin state of these 150 electrons has the dimension $2^{150} \simeq 10^{45}$. The corresponding density matrix would have 10^{90} elements. Since to our present knowledge the number of protons in our universe is just about 10^{90} , it is just impossible to build a classical computer with the required capacity. In contrast, a quantum computer would require only a few hundred quantum bits for the simulation of the 150 electrons. This simple example shows, that for the simulation of the quantum mechanics of many particle system quantum computers would be highly desirable.



In a classical computer, information is encoded in a series of ***classical bits***, and these bits are manipulated via ***Boolean logic gates*** arranged in succession to produce an end result. In a binary systems, the bits can only have two values usually denoted as “0” and “1”. Similarly, a quantum computer manipulates ***quantum bits*** by executing a series of ***quantum gates***, each a ***unitary transformation*** acting on a single qubit or pair of qubits (for details see Appendix III and IV). The quantum bits are realized by quantum mechanical two level system with the basis state denoted as $|0\rangle$ and $|1\rangle$ or $|\uparrow\rangle$ and $|\downarrow\rangle$ (see Appendix E to G). A basic difference between classical bits and quantum bits is the fact that the superposition principle allows superpositions of qubit values as entries into a register. An example for three qubits is given in Fig. 9.3. In general, for N qubits we can form 2^N superposition states, that is, the number of superposition states grows exponentially.

The second basic ingredient of a classical computer are ***Boolean logic gates***. In a quantum computer these classical gates are replaced by ***unitary operators***. It is well known that for a classical computer there exist universal sets of gates, that are sufficient to form all other possible gates. As discuss also in Appendix IV, universal sets for classical gates are (NOT, AND) or the NAND gate alone. In complete analogy there exist sets of unitary operations allowing for the realization of all possible unitary operations. Usually, such set consists of the single bit rotation $U(\theta, \phi)$ with $U(\theta, \phi) = \cos \theta e^{-i\phi/2}|0\rangle + \sin \theta e^{+i\phi/2}|1\rangle$ (compare Appendix III), and a two-qubit-operation. Here, a common example is the ***controlled-NOT gate*** (compare (E.IV.58) in Appendix IV). With the single qubit rotation and the CNOT gate we can form every arbitrary unitary operation on N qubits allowing for the implementation of any algorithm. That is, in applying these gates in succession, a quantum computer can perform a complicated unitary transformation to a set of qubits in some initial state. The qubits can then be measured, with this measurement serving as the final computational result. A simple scheme how a quantum computer works is shown in Fig. 9.3.

Fig. 9.3 suggests that the operational principle of a classical and a quantum computer are quite similar: the successive application of gates (quantum gates) to a set of bits (qubits). This similarity in calculation between a classical and quantum computer affords that in theory, a classical computer can accurately

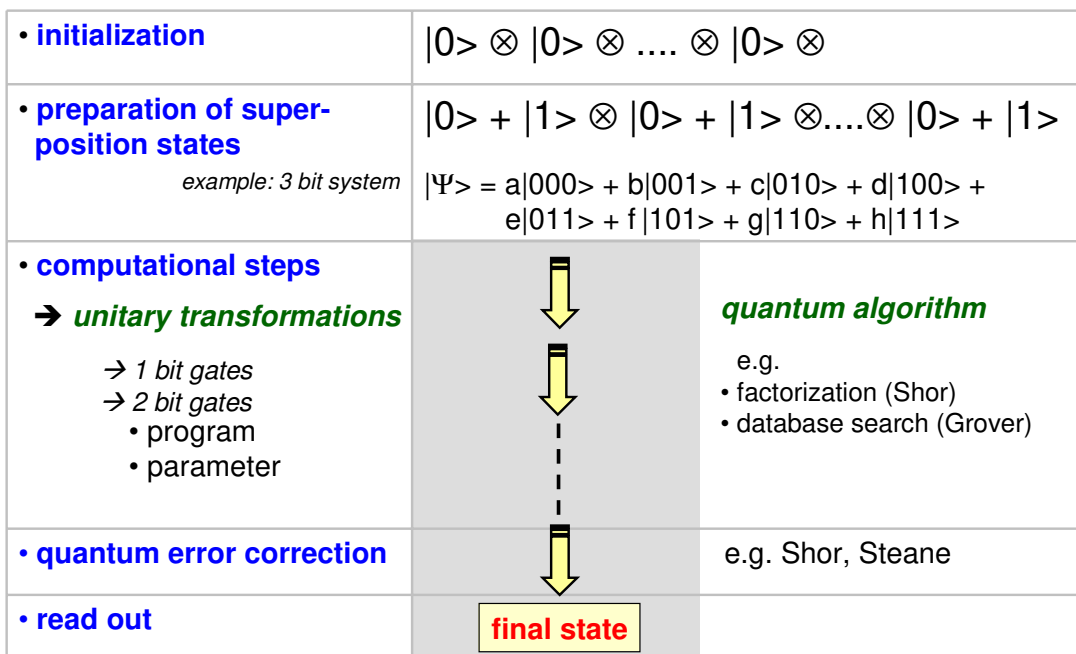


Figure 9.3: Simplified operational scheme of a quantum computer.

simulate a quantum computer. In other words, a classical computer would be able to do anything a quantum computer can. So why bother with quantum computers? Although a classical computer can theoretically simulate a quantum computer, it is incredibly inefficient, so much that a classical computer is effectively incapable of performing many tasks that a quantum computer could perform with ease. The simulation of a quantum computer on a classical one is a so-called computationally hard problem, since the correlations among quantum bits are qualitatively different from correlations among classical bits. This was first pointed out by **John Bell**. Take for example a system of only 300 qubits. This systems exists in a Hilbert space of dimension $2^{300} \simeq 10^{90}$ (quantum complexity, see Appendix VI) that in simulation would require a classical computer to work with exponentially large matrices (to perform calculations on each individual state, which is also represented as a matrix), meaning it would take an exponentially longer time than even a primitive quantum computer.

Richard Feynman was among the first to recognize the problem of handling the simulation of the quantum mechanics of many particle systems by a classical computer (already in 1981). At the same time he was pointing to the potential of quantum superposition for solving such problems much faster. As mentioned already above, a system of 300 qubits, which is impossible to simulate classically, represents a quantum superposition of as many as $2^{300} \simeq 10^{90}$ states. Each state would be classically equivalent to a single list of 300 ones and zeros. Any quantum operation on that system – a particular pulse of radio waves, for instance, whose action might be to execute a controlled-NOT operation on the 100th and 101st qubits – would simultaneously operate on all 2^{300} states. Hence, with one fell swoop, one tick of the computer clock, a quantum operation could compute not just on one machine state, as serial computers do, but on 2^{300} machine states at once! Eventually, however, observing the system would cause it to collapse into a single quantum state corresponding to a single answer, a single list of 300 ones and zeros, as dictated by the measurement axiom of quantum mechanics. The reason this is an exciting result is because this answer, derived from the massive quantum parallelism achieved through superposition, is the equivalent of performing the same operation on a classical super computer with $\sim 10^{90}$ separate processors, what is of course impossible. That is, by exploiting the massive parallelism of the coherent evolution of superpositions of states, quantum computers can perform certain tasks that

no classical computer could do in an acceptable time.^{16,17}

Already between 1982 and 1985 **David Deutsch**

provided the theoretical basis of the quantum computer by his work on quantum Turing machines. Although the early investigators in this field were naturally excited by the potential of the immense computing power, only very few people took that seriously. Only when **Peter Shor**, a research and computer scientist at AT&T's Bell Laboratories in New Jersey, provided a specific application of a quantum computer by devising the first quantum computer algorithm, the field was widely recognized and then a very active hunt was on to find something interesting for a quantum computer to do. **Shor's algorithm** uses the power of quantum superposition to rapidly factorize very large numbers (on the order $\sim 10^{200}$ digits and greater) in a matter of seconds. The premier application of a quantum computer capable of implementing this algorithm lies in the field of **encryption**, where one common encryption code,

known as RSA, relies heavily on the difficulty of factoring very large composite numbers into their primes. A computer which can do this easily is naturally of great interest to numerous government agencies that use RSA – previously considered to be “uncrackable” – and anyone interested in electronic and financial privacy.

Encryption, however, is only one application of a quantum computer. In addition, Shor has put together a toolbox of mathematical operations that can only be performed on a quantum computer, many of which he used in his factorization algorithm. Furthermore, Feynman asserted that a quantum computer could function as a kind of simulator for quantum physics, potentially opening the doors to many discoveries in the field. Currently the power and capability of a quantum computer is primarily theoretical speculation; the advent of the first fully functional quantum computer will undoubtedly bring many new and exciting applications.

A Brief History of Quantum Computing

The idea of a computational device based on quantum mechanics was first explored in the 1970's and early 1980's by physicists and computer scientists such as **Charles H. Bennett** of the IBM Thomas J. Watson Research Center, **Paul A. Benioff** of Argonne National Laboratory in Illinois, **David Deutsch** of the University of Oxford, and the late **Richard P. Feynman** of the California Institute of Technology (Caltech). The idea emerged, when scientists were pondering the fundamental limits of computation. They understood that if technology continued to abide by Moore's Law, then the continually shrinking size of circuitry packed onto silicon chips would eventually reach a point, where individual elements would be no larger than a few atoms. Here, a problem arose because at the atomic scale the physical laws that govern the behavior and properties of the circuit are inherently quantum mechanical in nature, not classical. This then raised the question of whether a new kind of computer could be devised based on the principles of quantum physics.



Figure 9.4: Quantum Computing: What's it good for?

¹⁶C. Bennett, *Quantum information and computation*, Physics Today **48**, 24 (1995).

¹⁷D. DiVincenzo, *Quantum Computation*, Science **270**, 255 (1995).

Feynman¹⁸ was among the first to attempt to provide an answer to this question by producing an abstract model in 1982 that showed how a quantum system could be used to do computations. He also explained how such a machine would be able to act as a simulator for quantum physics. In other words, a physicist would have the ability to carry out experiments in quantum physics inside a quantum mechanical computer. Later, in 1985, **Deutsch**¹⁹ realized that Feynman's assertion could eventually lead to a general purpose quantum computer and published a crucial theoretical paper showing that any physical process, in principle, could be modeled perfectly by a quantum computer. Thus, a quantum computer would have capabilities far beyond those of any traditional classical computer. After Deutsch published this paper, the search began to find interesting applications for such a machine.

Unfortunately, all that could be found were a few rather contrived mathematical problems, until **Shor**²⁰ circulated in 1994 a preprint of a paper in which he set out a method for using quantum computers to crack an important problem in number theory, namely factorization. He showed how an ensemble of mathematical operations, designed specifically for a quantum computer, could be organized to enable such a machine to factor huge numbers extremely rapidly, much faster than is possible on conventional computers. With this breakthrough, quantum computing transformed from a mere academic curiosity directly into a national and world interest.²¹

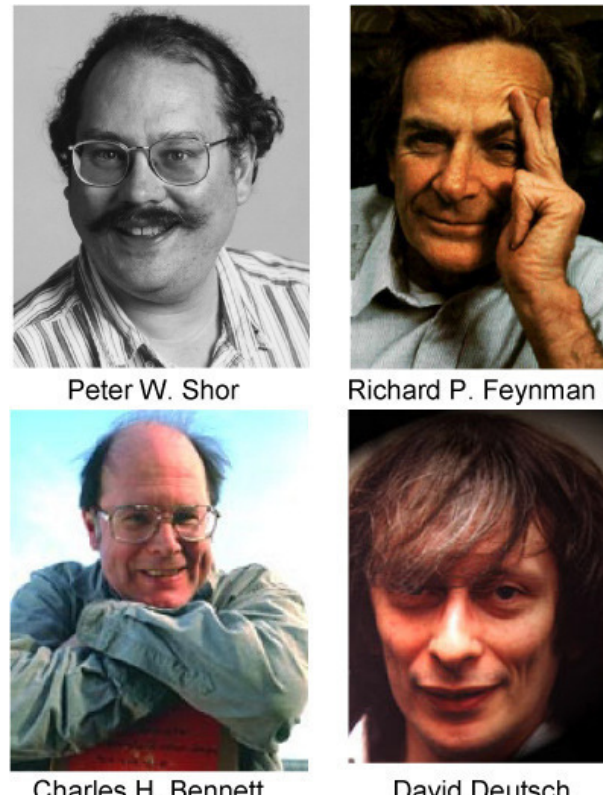


Figure 9.5: Some basic players in quantum computing.

9.1.3 Quantum Error Correction

Error correction is a well known process in classical information processing. For example, a parity bit is added to each data packet in protocols used for data transmission, where parity 0 and 1 state that the data packet has an even or odd number of "1", respectively. In this way one can check whether or not a single data bit or the parity bit has changed during transmission. If for example after transmission a single bit has changed from "1" to "0" or vice versa, the parity of the data packet does no longer correspond to the parity bit attached to the packet and one has to send the whole packet again. Obviously, such simple error correction protocol only protects against the change of an odd number of bits, whereas the change of an even number of bits remain undetected. More complicated protocols, for example the **Hamming protocol** allow for a far more extensive protection.²² In general, classical error correction operates by the judicious

¹⁸R. P. Feynman, Int. J. Theor. Phys. **21**, 467 (1982).

¹⁹D. Deutsch, Proc. Roy. Soc. London, Ser. A **400**, 97 (1985).

²⁰Shor, P. W., *Algorithms for quantum computation: Discrete logarithms and factoring*, in Proceedings of the 35th Annual Symposium on Foundations of Computer Science, IEEE Computer Society Press (1994).

²¹D. Deutsch, A. Ekert, *Quantum Computation*, Physics World, March (1998).

²²F. J. MacWilliams and N. J. A. Sloane, *The Theory of Error-Correcting Codes*, North Holland, Amsterdam (1977).

use of redundancy, that is, sending the same information many times. In this sense it is akin to making the system larger in order to make it more resistant to perturbations. However, the precise way in which the redundancy is introduced is very important. The type of redundancy, or encoding, employed must be carefully matched to the type of noise in the channel. Typically, one considers the case of random noise, which affects different bits independently, but this is not the only possible case. The encoding enables the most likely errors in the information to be identified and corrected. This corrective procedure is akin to active stabilization, and brings the associated benefits of powerful noise suppression.

Since qubits are representing superposition states $|\Psi\rangle = a|0\rangle + b|1\rangle$, it is not obvious that there are error correction protocols also for qubits. However, this is indeed the case. As has been shown by **Calderbank, Shor and Steane** that there is even a direct relationship between classical and quantum error correction protocols.^{23,24,25,26}

To understand the application of the classical ideas to the quantum regime, it is best to start with a simple example. Thus, suppose we have a collection of spin-half particles, each of which is subject independently to random “flips” or amplitude errors $|0\rangle \rightarrow |1\rangle$, but which otherwise is stable (in particular, the precession is free of phase error). Whenever such a flip occurs, the relevant two-state system may become entangled with its environment. In order to stabilize a single qubit, in the general state $a|0_L\rangle + b|1_L\rangle$, we express it by means of three two-state systems, with the “encoding” $|0_L\rangle = |000\rangle$, $|1_L\rangle = |111\rangle$. Thus, the total initial state of the three spins is $a|000\rangle + b|111\rangle$. After a period of time, during which random flips may occur, the three-spin system is measured twice. The first measurement is a projection onto the two-state basis

$$\{ |000\rangle + |111\rangle + |001\rangle + |110\rangle, \quad |010\rangle + |101\rangle + |100\rangle + |011\rangle \}$$

The second measurement is a projection onto the two-state basis

$$\{ |000\rangle + |111\rangle + |010\rangle + |101\rangle, \quad |001\rangle + |110\rangle + |100\rangle + |011\rangle \}$$

Each measurement has two possible results, which we will call 0 and 1. Depending on which results R are obtained, an appropriate action is carried out: if $R = 00$, do nothing; if $R = 01$, flip the rightmost spin; if $R = 10$, flip the middle spin; if $R = 11$, flip the leftmost spin. If, during the time interval when the system was left to evolve freely, no more than one spin flipped, then this procedure will return the three-spin state to $a|000\rangle + b|111\rangle$. It is remarkable that this can be done without gaining information about the values of a and b and thus disturbing the stored quantum information. During the correction procedure, the entanglement between the system and its environment is transferred to an entanglement between the measuring apparatus and the environment. The qubit is actively isolated from its environment by means of this carefully controlled entanglement transfer. The above error correction technique is based on the simplest classical error correcting code. More advanced techniques can be deduced from more advanced known classical codes.

Before this discovery it seemed to be impossible to carry out a longer quantum algorithm in a reliable way, since already tiny errors would spread in such way that the final result would no longer have any meaning. It now has been discussed that quantum error correction could be even more powerful than classical error correction. So called interlinked quantum error correction protocols have been shown to allow for the implementation of arbitrary quantum algorithms, since in this case the probability for a wrong result is independent of the actual length of the algorithm.

In order to achieve an error tolerant operation of a quantum computer, the error probability per gate or measurement operation has to stay below a certain level. At present this threshold level is estimated to be about 10^{-4} per memory unit, gate or read out process.

²³P. W. Shor, Phys. Rev. A **52**, R2493 (1995).

²⁴A. M. Steane, Phys. Rev. Lett. **77**, 793 (1996).

²⁵A. R. Calderbank and P. W. Shor, Phys. Rev. A **54**, 1098 (1996).

²⁶A. M. Steane, Proc. Roy. Soc. A **452**, 2551 (1996).

9.1.4 What are the Problems?

The field of quantum information processing has made numerous promising advancements since its conception. However, a few potentially large obstacles still remain that prevent us from just building a quantum computer that can rival today's modern digital computer. Among these difficulties, ***error correction, decoherence, and hardware architecture*** are probably the most formidable. Error correction is rather self explanatory, but what errors need correction? The answer is primarily those errors that arise as a direct result of decoherence, or the tendency of a quantum computer to decay from a given quantum state into an incoherent state as it interacts, or entangles, with the state of the environment. These interactions between the environment and qubits are unavoidable, and induce the breakdown of information stored in the quantum computer, and thus errors in computation. Before any quantum computer will be capable of solving hard problems, research must devise a way to maintain decoherence and other potential sources of error at an acceptable level. Thanks to the theory of quantum error correction, first proposed in 1995 and continually developed since, small scale quantum computers have been built. Probably the most important idea in this field is the application of error correction in phase coherence as a means to extract information and reduce error in a quantum system without actually measuring that system.

Today only a few of the benefits of quantum computation and quantum computers are readily obvious, but before more possibilities are uncovered theory must be put to the test. In order to do this, devices capable of quantum computation must be constructed. Unfortunately, quantum computing ***hardware*** is still in its infancy, whereas the theoretical concepts of quantum computing, the ***software***, are already rather advanced. A solid state based hardware concept seems promising, since it allows scaling and the used of well developed fabrication techniques. However, it may be that the future of quantum computer hardware architecture is very different from what we know today. Nevertheless, the current research helps to provide insight as to what obstacles the future will hold for these devices.

9.2 Implementation of Quantum Bits

Quantum bits can be implemented with every two level quantum system as shown in Fig. 9.6. The properties of such systems are summarized in Appendix F and G. In practice, quantum information processing also requires the coherent manipulation of suitable quantum systems. The coherent manipulations of the qubits can be performed, if we have sufficient control over the fields and interaction terms in the associated Hamiltonian and if the decoherence in the considered quantum systems is small enough.

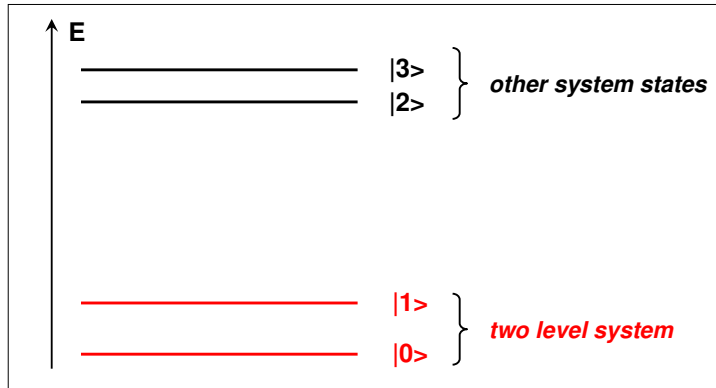


Figure 9.6: A qubit can be realized by a quantum mechanical two level system with the qubit representing the coherent superposition of the two discrete states: $|\Psi\rangle = a|0\rangle + b|1\rangle$. The only requirement is that all other states of the system are well separated from the states $|0\rangle$ and $|1\rangle$ in order to have an effective two-level system. Note that this requirement cannot be achieved for a harmonic potential, where all the states are equidistant.

As has been stressed by **DiVincenzo**,^{27,28} any physical system that is considered as a candidate for the implementation of quantum bits should satisfy the following criteria (DiVincenzo checklist):

1. **Qubits:** The system has to provide a well defined two-level quantum system. This implies that higher level states that are present in most real systems are not excited during qubit manipulations.
2. **Preparation of initial state:** It must be possible to prepare the initial state with sufficient accuracy.
3. **Decoherence:** The phase coherence time must be long enough to allow for a sufficiently large number (typically 10^4) of coherent manipulations. That is, the superposition states of the qubits are allowed to dephase only on time scales much longer than the elementary gate time.
4. **Quantum gates:** There must be sufficient control over the qubit Hamiltonian to perform the necessary unitary transformations, i.e. single- and two-qubit operations (see Appendix III). For this purpose it should be possible to control the fields at the sites of the qubits separately and to couple the qubits in a controlled way (e.g. by switching on and off the inter-qubit interactions). Then, the single- and two-qubit operations allow for the generation of arbitrary superpositions and nontrivially coupled states such as entangled states (see Appendix III and IV).
5. **Quantum measurement:** For read out of the quantum information a quantum measurement is needed. This can be either at the final stage or during the computation for the purpose of error correction.
6. **Scalability:** There should be the possibility to increase the number of qubits (scalability).

²⁷D. DiVincenzo, *The physical implementation of quantum computation*, Fortschr. Phys. **48**, 771 (2000).

²⁸D. DiVincenzo, in *Mesoscopic Electron Transport*, edited by L. Kouwenhoven, G. Schön, and L. Sohn, NATO ASI Series E: Applied Sciences No. 345, Kluwer Academic, Dordrecht (1997), p. 657.

With respect to requirement 1 we can state that there is a large number of physical systems that have been suggested as possible realizations of qubits and gates.²⁹ They are usually split up into non-solid state systems (e.g. ions in electromagnetic traps,^{30,31} nuclear magnetic resonance on ensembles of molecules in liquids,^{32,33} cavity QED systems,³⁴ and neutral atoms in optical lattices^{35,36,37}) and solid state systems. Solid state devices including the above mentioned Josephson systems have the advantage of being more easily embedded into electronic circuits and scaled up to a larger number of qubits (requirement 6). Besides the Josephson systems, electronic states and spin states in quantum dots as well as impurity spins in semiconductors are further candidates. They can be manipulated by tuning potentials and barriers.^{38,39} Finally, electrons floating on liquid helium are discussed.

Besides the advantages of solid state systems with respect to ***scalability*** and embedding into electronic circuits, ***decoherence*** is a severe problem for solid state systems (requirement 3). Unavoidable for devices that have to be controlled externally are interactions with the environment. Due to the coupling to the environment the quantum state of the qubit gets entangled (see Appendix II) with the environmental degrees of freedom. As a consequence the phase coherence is destroyed after a time scale called the ***dephasing time***. Due to the large number of environmental degrees of freedom in solid state systems, decoherence is an important issue. Maintaining coherence of a quantum device throughout the manipulation processes is therefore the major challenge for practical quantum computing. We also note that the time evolution of the quantum state may be perturbed also by other sources such as inaccuracies in the preparation of the initial state, inaccuracies in the manipulations and uncontrolled couplings between qubits.

Quantum state engineering requires the ***coherent manipulation of quantum systems***. The manipulations can be performed, if we have sufficient control over the fields and interaction terms in the Hamiltonian. In order to discuss the requirements 4 and 5 we use a model Hamiltonian of a two-state quantum system (e.g. a spin system). We will see later that under certain conditions other systems such as “charge in a box” or “flux in a SQUID loop” effectively reduce to two-state systems. Since any single two-state quantum systems can be represented as a spin-1/2 system, in the following we write down the model Hamiltonian for this system. With the effective magnetic field \mathbf{B} the Hamiltonian for the manipulation can be written as (compare Appendix III)

$$\mathcal{H}_{\text{man}}(t) = -\frac{\hbar}{2} \gamma \mathbf{B}(t) \vec{\sigma} . \quad (9.2.1)$$

Here, $\vec{\sigma} = (\mathbf{X}, \mathbf{Y}, \mathbf{Z})$ are the Pauli spin matrices in the space of states $|\uparrow\rangle$ and $|\downarrow\rangle$ (compare (E.III.25) in Appendix III) and γ the gyromagnetic ratio. These states form the basis states of a physical quantity (spin, charge, flux, ...) that has to be manipulated. Full control of the quantum dynamics of the spin is achieved,

²⁹S. Braunstein, H.-K. Lo eds., *Experimental Proposals for Quantum Computing*, Fortschr. Phys. **48**, 765 (2000).

³⁰J. I. Cirac, P. Zoller, *Quantum computation with cold trapped ions*, Phys. Rev. Lett. **74**, 4091 (1995).

³¹C. Monroe, D.M. Meekhof, B.E. King, W. M. Itano, D.J. Wineland, *Demonstration of a fundamental quantum logic gate*, Phys. Rev. Lett. **75**, 4714 (1995).

³²D. Cory, A. Fahmy, T. Havel, *Ensemble quantum computing by NMR spectroscopy*, Proc. Natl. Acad. Sci. USA **94**, 1634 (1997).

³³N. Gershenfeld, I. Chuang, *Bulk spin resonance quantum computation*, Science **275**, 350 (1997).

³⁴Q.A. Turchette, C.J. Hood, W. Lange, H. Mabuchi, H.J. Kimble, *Measurement of conditional phase shifts for quantum logic*, Phys. Rev. Lett. **75**, 4710 (1995).

³⁵T. Pellizzari, S.A. Gardiner, J.I. Cirac, P. Zoller, *Decoherence, continuous observation, and quantum computing: A cavity QED model*, Phys. Rev. Lett. **75**, 3788-3791 (1995).

³⁶P.W.H. Pineske, P. Maunz, T. Fischer, G. Rempe, *Trapping an atom with single photons*, Nature **404**, 365-368 (2000).

³⁷C.J. Hood, T.W. Lynn, A.C. Doherty, A.S. Parkin, H.J. Kimble, *The atom-cavity microscope: Single atoms bound in orbit by single photons*, Science **287**, 1477 (2000).

³⁸B.E. Kane, *A silicon based nuclear spin quantum computer*, Nature **393**, 133 (1998).

³⁹D. Loss, D.P. DiVincenzo, *Quantum computation with quantum dots*, Phys. Rev. A **57**, 120 (1998).

if the field $\mathbf{B}(t)$ can be switched arbitrarily. Actually, as shown in Appendix E, full control is already achieved, if only two field components⁴⁰ can be controlled, e.g. (compare (E.III.24) in Appendix III)

$$\mathcal{H}_{\text{man}}(t) = -\frac{\hbar}{2}\gamma B_z \mathbf{Z} - \frac{\hbar}{2}\gamma B_x \mathbf{X} . \quad (9.2.2)$$

If we want to manipulate a many-qubit system in order to perform quantum computing, we have to control the field at the sites of each spin separately. Furthermore, in addition to single-qubit operations we need two-qubit unitary operations (see Appendix III and IV). The latter require the coupling of two qubits. Including this coupling, the following model Hamiltonian seems to be suitable for a N -qubit system:

$$\mathcal{H}_{\text{man}}(t) = -\sum_{i=1}^N \frac{\hbar}{2}\gamma \mathbf{B}^i(t) \vec{\sigma}^i + \sum_{i \neq j} J_{\alpha\beta}^{ij}(t) \vec{\sigma}_\alpha^i \vec{\sigma}_\beta^j . \quad (9.2.3)$$

Here, the summation over the spin indices $\alpha, \beta = x, y, z$ is implied. Note that in this model Hamiltonian we have assumed a general form of the coupling between the qubits. In many cases simpler forms such as the pure Ising (ZZ), the XY (see Appendix III) or the Heisenberg coupling are sufficient.

In the model Hamiltonian we so far have neglected the measurement system and the coupling with the environment. This can be accounted for by the two extra terms $\mathcal{H}_{\text{meas}}$ and $\mathcal{H}_{\text{envir}}$, respectively, resulting in the total Hamiltonian

$$\mathcal{H}(t) = \mathcal{H}_{\text{man}}(t) + \mathcal{H}_{\text{meas}}(t) + \mathcal{H}_{\text{envir}} , \quad (9.2.4)$$

where we have assumed that the residual coupling to the environment is time independent. During the manipulation of the qubits the measurement device should be in the off-state, i.e. $\mathcal{H}_{\text{meas}} = 0$. Furthermore, the interaction with the environment should be as small as possible, since it results in dephasing and relaxation processes.

The ***preparation of the initial state*** (requirement 2) can be achieved by keeping the system at low temperatures so that it relaxes to the ground state. For a spin system this can be achieved for example by switching on a large field $B_z \gg k_B T$ for a sufficiently long time, while $B_x(t) = B_y(t) = 0$. Then, due to the residual interaction with the environment, each qubit relaxes into its ground state, e.g. $|\uparrow\rangle$ for a spin system. If we then switch off B_z we are left with the system in a well-defined pure ground state.

A typical experiment performed with qubits involves the preparation of the initial state, the switching of the fields $\mathbf{B}(t)$ and the coupling $J_{\alpha\beta}^{ij}(t)$ to achieve a specific unitary evolution of the qubit state, and the measurement of the final state.

⁴⁰If all three field components can be controlled, the topological or Berry phase of the systems can be manipulated as well.

9.3 Why Superconducting Qubits

On the first sight, microscopic systems seem to be ideal candidates for qubits, since they can be easily isolated from the environment thereby avoiding decoherence. However, the disadvantage of microscopic systems (e.g. ions in an electromagnetic trap) is usually scalability and the lack of simple embedding into other electronic circuits. That is, it is difficult to integrate many qubits into a more complex circuit in order to approach the vision of a practical quantum computer. Therefore, macroscopic quantum systems such as superconductors are attractive, since they offer more flexibility in scaling using standard integrated circuit technology. Until now several “macroscopic” qubits have been proposed that are based on nanostructured solid state electronic circuits, which are based either of semiconductor quantum dots or superconducting Josephson junctions.

As already mentioned above the large number of microscopic degrees of freedom in solid state devices makes it more difficult to achieve sufficiently long dephasing times. This is in particular a problem for charge based qubits, since the charge degree of freedom strongly couples to environmental degrees of freedom. Therefore, the use of isolated spins on quantum dots⁴¹ or through the deliberate doping of semiconductors⁴² seems more promising.

Quantum bits based on superconducting materials have particular advantages. First, the superconducting ground state is separated by an energy gap Δ of the order of meV from the quasiparticle excitation spectrum (see Fig. 9.7). Second, the superconducting state represents a non-degenerate macroscopic ground state and finally, superconducting metals have a large electron density resulting in a short screening length for perturbing background charges.

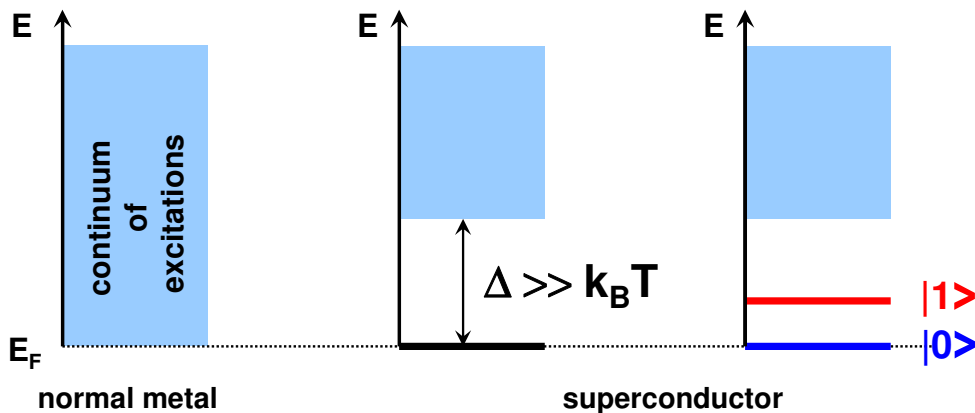


Figure 9.7: Advantage of superconductors for constructing solid state based quantum bits.

9.3.1 Superconducting Island with Leads

In order to get a feeling for the relevant energy scales for Josephson junction devices used for the realization of superconducting quantum bits we consider a superconducting island coupled to a superconducting lead via a Josephson junction that is characterized by an ideal Josephson element with Josephson inductance $L_J = \Phi_0/2\pi I_c$ (see (2.1.22)), normal resistance R_N and capacitance C as shown in Fig. 9.8. We can now consider the energy required to change the number N of Cooper pairs on the island by one and on the other hand the energy required to change the phase ϕ of the superconducting wave function by 2π .

⁴¹D. Loss, D.P. DiVincenzo, *Quantum computation with quantum dots*, Phys. Rev. A **57**, 120 (1998).

⁴²B.E. Kane, *A silicon based nuclear spin quantum computer*, Nature **393**, 133 (1998).

The first is given by the charging energy

$$E_C = \frac{q^2}{2C} \quad (9.3.1)$$

with $q = 2e$. The latter is just the energy required to change the phase difference $\varphi = \phi_{\text{island}} - \phi_{\text{reservoir}}$ across the Josephson junction by 2π or, equivalently, to move a single flux quantum Φ_0 across the Josephson junction. This energy is given by the Josephson coupling energy $E_J = E_{J0}(1 - \cos \varphi)$ with the maximum value for $\varphi = \pi$ given by

$$2E_{J0} = \frac{\Phi_0 I_c}{\pi} = \frac{(\Phi_0/\pi)^2}{2L_J} . \quad (9.3.2)$$

As already discussed in section 3.5, there is an uncertainty relation $\Delta\phi \cdot \Delta \geq 1$ for the number N of Cooper pairs and the phase ϕ . Considering the two characteristic energy scales E_C and E_{J0} we can conclude the following:

- $E_C \gg E_{J0}$:

In this case large energy is required to change N . That is, the number N of Cooper pairs or the charge state of the island is well defined, whereas according to $\Delta\phi \cdot \Delta \geq 1$ the phase ϕ is completely smeared out.

- $E_C \ll E_{J0}$:

In this case a large energy is required to change the phase ϕ , whereas the energy for changing N is small. Then, Cooper pairs easily can enter and leave the island resulting in large fluctuation of N what, in turn, causes small fluctuations of ϕ and hence in a well defined phase.

Note that in this discussion we only considered the Cooper pairs and have completely neglected the quasiparticle degrees of freedom.

We also have to consider the effect of thermal and quantum fluctuations. Thermal fluctuation do not play any role as long as

$$E_{J0}, E_C \gg k_B T . \quad (9.3.3)$$

This condition can easily satisfied with respect to E_{J0} . For example, a Josephson junction with a maximum Josephson current $I_c = 100 \mu\text{A}$ (corresponding to a junction area of $10 \times 10 \mu\text{m}^2$ at a typical current density of $J_c = 100 \text{ A/cm}^2$) has a coupling energy $E_{J0} \simeq 3 \times 10^{-18} \text{ J}$ corresponding to $T \simeq 2300 \text{ K}$. For the charging energy this is more difficult. In order to have a charging energy corresponding a temperature of only 1 K, the capacitance has to be as small as only 1 fF. With a specific capacitance of Josephson tunnel junctions of typically $100 \text{ fF}/\mu\text{m}^2$, the junction area has to be as small as $0.1 \times 0.1 \mu\text{m}^2$ requiring advanced fabrication technology.

The effect of quantum fluctuations can be estimated from energy-time uncertainty relation $\Delta E \Delta t \geq \hbar$. For the charge and the phase channel the characteristic time scales are $R_N C$ and L_J/R_N , respectively. With the condition $\Delta E \ll E_C$ and $\Delta E \ll E_{J0}$ we obtain the conditions

$$R_N \gg h/q^2 \quad \text{for } \Delta E \ll E_C \quad (9.3.4)$$

$$R_N \ll h/q^2 \quad \text{for } \Delta E \ll E_J \quad (9.3.5)$$

respectively, with $q = 2e$. We see that the resistance $R_Q/4$, where $R_Q = h/e^2$ is the quantum resistance, separates the regimes, where quantum fluctuations of the charge and the phase are dominant.

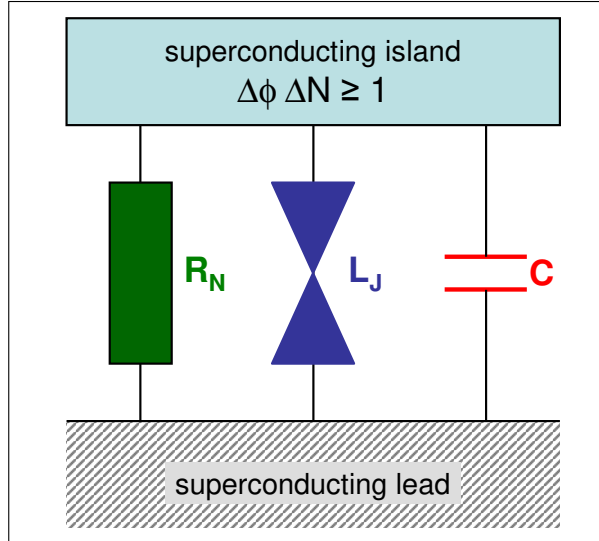


Figure 9.8: A superconducting island coupled to a superconducting lead (reservoir) via a Josephson junction characterized by an ideal Josephson element of Josephson inductance L_J , normal resistance R_N and a capacitance C .

A further characteristic energy scale of superconductors is the energy gap Δ . With the fact that the characteristic energy $eI_cR_N = eV_c \simeq \Delta$ we obtain

$$E_{J0} \simeq \frac{\hbar I_c}{2e} = \frac{\hbar}{2e^2 R_N} e I_c R_N \simeq \frac{R_Q}{4R_N} \Delta . \quad (9.3.6)$$

We see that for junctions with $R_N \gg R_Q/4$ we have $E_{J0} \ll \Delta$. Then one can always find a regime for which the two inequalities $E_{J0} \ll E_C \ll \Delta$ hold. The fact that Δ is the largest energy scale is often used in theoretical treatments. It allows to restrict to states of the island containing only an even number of electrons, which form Cooper pairs. The net charge Q on the island can then be written as $qN = 2eN$.